Lecture Notes in Nanoscale Science and Technology

Volume 13

Series Editors

Zhiming M. Wang
State Key Laboratory of Electronic, Thin Flim and Integrated Devices,
University of Electronic Science and Technology,
Chengdu, People's Republic of China

Andreas Waag
Institutfur Halbleitertechnik, TU Braunschweig, Braunschweig, Germany

Greg Salamo
Department of Physics, University of Arkansas, Fayetteville, AR, USA

Naoki Kishimoto
Quantum Beam Center, National Institue for Materials Science, Tsukuba,
Ibaraki, Japan

Stefano Bellucci
Laboratori Nazionali di Frascati, Istituto Nazionale di Fisica Nucleare,
Frascati, Italy

For further volumes:
http://www.springer.com/series/7544

Zhiming M. Wang
Editor

Quantum Dot Devices

Editor
Zhiming M. Wang
State Key Laboratory of Electronic
Thin Film and Integrated Devices
University of Electronic Science
and Technology
Chengdu
People's Republic of China

ISBN 978-1-4614-3569-3 ISBN 978-1-4614-3570-9 (eBook)
DOI 10.1007/978-1-4614-3570-9
Springer New York Heidelberg Dordrecht London

Library of Congress Control Number: 2012937780

© Springer Science+Business Media New York 2012
This work is subject to copyright. All rights are reserved by the Publisher, whether the whole or part of the material is concerned, specifically the rights of translation, reprinting, reuse of illustrations, recitation, broadcasting, reproduction on microfilms or in any other physical way, and transmission or information storage and retrieval, electronic adaptation, computer software, or by similar or dissimilar methodology now known or hereafter developed. Exempted from this legal reservation are brief excerpts in connection with reviews or scholarly analysis or material supplied specifically for the purpose of being entered and executed on a computer system, for exclusive use by the purchaser of the work. Duplication of this publication or parts thereof is permitted only under the provisions of the Copyright Law of the Publisher's location, in its current version, and permission for use must always be obtained from Springer. Permissions for use may be obtained through RightsLink at the Copyright Clearance Center. Violations are liable to prosecution under the respective Copyright Law.
The use of general descriptive names, registered names, trademarks, service marks, etc. in this publication does not imply , even in the absence of a specific statement, that such names are exempt from the relevant protective laws and regulations and therefore free for general use.
While the advice and information in this book are believed to be true and accurate at the date of publication, neither the authors nor the editors nor the publisher can accept any legal responsibility for any errors or omissions that may be made. The publisher makes no warranty, express or implied, with respect to the material contained herein.

Printed on acid-free paper

Springer is part of Springer Science+Business Media (www.springer.com)

Preface

The last 20 years have seen the rise of three-dimensional quantum-confined nanostructures, so-called quantum dots, and the birth of entirely new device architectures based on them. These structures may be fabricated by top-down methods, such as lithographic techniques, or by self-assembly, as in the formation of epitaxial quantum dots or chemical synthesis of colloidal dots. There are significant efforts to control the size, shape, and distribution of quantum dots, to characterize their optical and electronic properties, and to find their technological applications. The research on quantum dots has a strong impact in terms of both physics and devices. The future development of this field largely depends on how quantum dots can be used as nanomaterials in real-world applications. This book aims to convey the current status of quantum dot devices and how these devices take advantage of quantum features.

Quantum dot lasers have been extensively investigated and many advanced characteristics due to quantum confinement have been demonstrated. Therefore, a significant part of the chapter contributions deals with lasers. Chapter 1 covers optically injected single-mode quantum dot lasers. Chapters 2–4 focus on mode-locked lasers. Chapter 2 reviews two exotic behaviors, dark pulses mode-locking and wavelength bistability, both leading to unexpected and exciting performance characteristics. Chapter 3 analyzes the spectral splitting effects in the ground state and their influence on the performance of quantum dot mode-locked lasers. Chapter 4 reports on characteristics of passively mode-locked lasers based on quantum dots and their manipulation via external optical injection. Chapter 5 continues the focus on quantum dot lasers but emphasizes the catastrophic optical damage in high power applications.

The post-growth intermixing effect was studied in Chap. 6, not only for its impact on high power lasers but also on broadband devices such as quantum dot superluminescent diodes and amplifiers. Both Chaps. 7 and 8 cover quantum-dot applications in photonic crystals. Chapter 7 starts with the basics of photonic crystal cavities and continuous wave lasing in quantum dot nanobeam cavities, followed by a discussion on the dynamics of low-threshold quantum dot photonic crystal lasers and an introduction to electrical pumping of photonic crystal and

nanobeam devices. Chapter 8 reports on submonolayer quantum dot photonic-crystal light-emitting diodes for fiber optic applications.

Progress toward all optical signal processing is discussed in Chaps. 9–12. Chapter 9 presents a theoretical study of a quantum optical transistor with a single quantum dot in a photonic crystal nanocavity and a quantum memory for light with a quantum dot embedded in a nanomechanical resonator. Chapter 10 investigates in detail all optical quantum dot switches using a vertical cavity approach and demonstrates that quantum dots are promising candidates for next generation photonic devices needed for power efficient optical networks. Chapter 11 describes experimental studies of ultrafast carrier dynamics and all-optical switching in semiconductor quantum dots using ultrafast terahertz techniques. Chapter 12 offers an extensive overview of nonlinear optics and saturation behavior of quantum dot samples under continuous wave driving.

Quantum dot photovoltaic applications are the subject of Chaps. 13 and 14. Chapter 13 theoretically and experimentally demonstrates that quantum dots with engineered built-in charge can significantly enhance the device performances of solar cells and infrared photodetectors. Chapter 14 studies the performance of semiconductor quantum dot-sensitized solar cells employing nanostructured photoanodes with different morphologies.

Chapter 15 highlights a plethora of optoelectronic applications of colloidal quantum dots, including not only photoluminescent devices, light-emitting diodes, displays, photodetectors, and solar cells but also other novel device concepts such as biomolecule-based molecular sensors.

Last but not least, the editor wishes to thank all the authors for their excellent contributions. It took longer than planned to finalize the book because of the editor's move from the United States to China to accept a professorship in the national 1,000-talents program, and I am grateful to the chapter authors for their patience and understanding.

Chengdu, February 2012 Zhiming M. Wang

Contents

1 Optically Injected Single-Mode Quantum Dot Lasers 1
B. Kelleher, D. Goulding, S. P. Hegarty, G. Huyet, E. A. Viktorov and T. Erneux

2 Exotic Behavior in Quantum Dot Mode-Locked Lasers: Dark Pulses and Bistability 23
Kevin Silverman, Mingming Feng, Richard Mirin and Steven Cundiff

3 Spectral Splitting Effects and Their Influence to the Performance of Quantum Dot Mode Locked Lasers 49
Charis Mesaritakis and Dimitris Syvridis

4 Mode-Locked Semiconductor Lasers with Optical Injection 65
Tatiana Habruseva, Natalia Rebrova, Stephen P. Hegarty and Guillaume Huyet

5 Catastrophic Optical Damage in Quantum Dot Lasers 93
Ching Kean Chia and Mark Hopkinson

6 Post-Growth Intermixing of GaAs Based Quantum Dot Devices 109
Ziyang Zhang and R. A. Hogg

7 Photonic Crystal Cavity Lasers 131
Yiyang Gong, Bryan Ellis and Jelena Vučković

8 InGaAs Submonolayer Quantum-Dot Photonic-Crystal LEDs for Fiber-Optic Communications 159
Hung-Pin D. Yang

9 Quantum Optical Transistor and Other Devices Based on Nanostructures 173
Jin-Jin Li and Ka-Di Zhu

10 Quantum Dot Switches: Towards Nanoscale Power-Efficient All-Optical Signal Processing 197
Chao-Yuan Jin, Mark Hopkinson, Osamu Kojima, Takashi Kita, Kouichi Akahane and Osamu Wada

11 Ultrafast Terahertz Dynamics and Switching in Quantum Dots 223
Dmitry Turchinovich and Matthias C. Hoffmann

12 Nonlinear Optics and Saturation Behavior of Quantum Dot Samples Under Continuous Wave Driving 251
T. Ackemann, A. Tierno, R. Kuszelewicz, S. Barbay, M. Brambilla, C. G. Leburn and C. T. A. Brown

13 Quantum Dots with Built-in Charge for Enhancing Quantum Dot Solar Cells and Infrared Photodetectors 297
Kimberly A. Sablon, V. Mitin, J. W. Little, A. Sergeev and N. Vagidov

14 Semiconductor Quantum Dot-Sensitized Solar Cells Employing TiO_2 Nanostructured Photoanodes with Different Morphologies 317
Qing Shen and Taro Toyoda

15 Optoelectronic Applications of Colloidal Quantum Dots 351
Zhiping Wang, Nanzhu Zhang, Kimber Brenneman, Tsai Chin Wu, Hyeson Jung, Sushmita Biswas, Banani Sen, Kitt Reinhardt, Sicheng Liao, Michael A. Stroscio and Mitra Dutta

Index 369

Contributors

T. Ackemann SUPA and Department of Physics, University of Strathclyde, Glasgow, G4 0NG Scotland, UK, e-mail: thorsten.ackemann@strath.ac.uk

Kouichi Akahane National Institute of Information and Communications Technology, Tokyo 184-8795, Japan, e-mail: akahane@nict.go.jp

S. Barbay Laboratoire de Photonique et de Nanostructures, CNRS, Route de Nozay, 91460 Marcoussis, France, e-mail: sylvain.barbay@lpn.cnrs.fr

Sushmita Biswas Electrical and Computer Engineering Department, University of Illinois at Chicago (UIC), 851 S. Morgan Street, Chicago, IL 60607, USA

M. Brambilla CNISM e Dipartimento Interateneo di Fisica, via Amendola 173, 70126 Bari, Italy, e-mail: brambilla@fisica.uniba.it

Kimber Brenneman Bioengineering Department, University of Illinois at Chicago, 851 S. Morgan Street, Chicago, IL 60607, USA

C. T. A. Brown SUPA and School of Physics and Astronomy, University of St. Andrews, St. Andrews, Scotland KY16 9SS, UK, e-mail: ctab@st-andrews.ac.uk

Ching Kean Chia Institute of Materials Research and Engineering, 3 Research Link, Singapore 117602, Singapore, e-mail: ck-chia@imre.a-star.edu.sg

Steven Cundiff Quantum Physics Division, JILA National Institute of Standards and Technology and University of Colorado, Boulder, CO 80305, USA, e-mail: cundiffs@nist.gov

Mitra Dutta Electrical and Computer Engineering Department, University of Illinois at Chicago (UIC), 851 S. Morgan Street, Chicago, IL 60607, USA

Bryan Ellis Soraa Inc., 6500 Kaiser Dr, Fremont, CA 94555-3613, USADepartment of Electrical Engineering, Standford University, Stanford, CA 94305, USA

Thomas Erneux Université Libre de Bruxelles, Optique Nonlinéaire Théorique, Campus Plaine, Code Postal 231, 1050 Bruxelles, Belgium, e-mail: terneux@ulv.ac.be

Mingming Feng Optoelectronics Division, National Institute of Standards and Technology, Boulder, CO 80305, USA, e-mail: mingming@boulder.nist.gov

Tatiana Gabruseva Center of Advanced Photonics and Process Analysis, Applied Physics and Instrumentation, Cork Institute of Technology and Tyndall National Institute, Lee Maltings, Prospect Row, Cork, Ireland

Yiyang Gong Department of Electrical Engineering, Standford University, Stanford, CA 94305, USA, e-mail: yiyangg@stanford.edu

David Goulding Tyndall National Institute, University College Cork, Lee Maltings, Dyke Parade, Cork, Ireland

Stephen P. Hegarty Tyndall National Institute, University College Cork, Lee Maltings, Dyke Parade, Cork, IrelandCenter of Advanced Photonics and Process Analysis, Cork Institute of Technology and Tyndall National Institute, Cork, Ireland

Matthias C. Hoffmann Max Planck Research Department for Structural Dynamics, University of Hamburg, CFEL, 22607 Hamburg, Germany, e-mail: matthias.c.hoffman@desy.de

Richard A. Hogg ESPRC National Centre for III-V Technologies, Department of Electronic and Electrical Engineering, Centre for Nanoscience and Technology, University of Sheffield, North campus Broad lane, S3 7HQ Sheffield, UK, e-mail: r.hogg@shef.ac.uk

Mark Hopkinson Department of Electronic and Electrical Engineering, University of Sheffield, Sheffield S1 3JD, UK, e-mail: m.hopkinson@sheffield.ac.uk

Guillaume Huyet Centre for Advanced Photonics and Process Analysis, Cork Institute of Technology and Tyndall National Institute, Lee Maltings, Dyke Parade, Cork, Ireland, e-mail: guillaume.huyet@tyndall.ie

Chao-Yuan Jin COBRA Research Institute and Department of Applied Physics, Eindhoven University of Technology, 5600 MB Eindhoven, The Netherlands, e-mail: c.jin@tue.nl

Hyeson Jung Electrical and Computer Engineering Department, University of Illinois at Chicago (UIC), 851 S. Morgan Street, Chicago, IL 60607, USA

Bryan Kelleher Centre for Advanced Photonics and Process Analysis, Cork Institute of Technology and Tyndall National Institute, Lee Maltings, Dyke Parade, Cork, Ireland, e-mail: bryan.kelleher@tyndall.ie

Takashi Kita Department of Electrical and Electronic Engineering, Graduate School of Engineering, Kobe University, Kobe 657-8501, Japan, e-mail: kita@eedept.kobe-u.ac.jp

Osamu Kojima Department of Electrical and Electronic Engineering, Graduate School of Engineering, Kobe University, Kobe 657-8501, Japan, e-mail: kojima@phoenix.kobe-u.ac.jp

R. Kuszelewicz Laboratoire de Photonique et de Nanostructures, CNRS, Route de Nozay, 91460, Marcoussis, Francee-mail: robert.kuszelewicz@lpn.cnrs.fr

C. G. Leburn SUPA and School of Engineering and Physical Sciences, Heriot-Watt University, Edinburgh EH14 4AS, Scotland, UK, e-mail: C.G.Leburn@hw.ac.uk

Jin-Jin Li Department of Physics, Shanghai Jiao Tong University, 800 Dong Chuan Road, Shanghai 200240, People's Republic of China, e-mail: lijinjin.physics@gmail.com

SiCheng Liao Physics Department, University of Illinois at Chicago, 851 S. Morgan Street, Chicago, IL 60607, USA

John W. Little U.S. Army Research Laboratory, 2800 Powder Mill Road, BLDG 207 (RDRL-SEE-I), Adelphi, MD 20783, USA

Charis Mesaritakis Optical Communications Laboratory, Department of Informatics and Telecommunications, University of Athens, 15784 Athens, Greece, e-mail: cmesar.di.uoa.gr

Richard Mirin Optoelectronics Division, National Institute of Standards and Technology, Boulder, CO 80305, USA, e-mail: mirin@boulder.nist.gov

Vladimir Mitin University at Buffalo, Buffalo 14260, NY, USAU.S. Army Research Laboratory, 2800 Powder Mill Road, BLDG 207 (RDRL-SEE-I), Adelphi, MD 20783, USA

Natalia Rebrova Center of Advanced Photonics and Process Analysis, Applied Physics and Instrumentation, Cork Institute of Technology and Tyndall National Institute, Lee Maltings, Prospect Row, Cork, Ireland, e-mail: nrebrova@gmail.com

Kitt Reinhardt Physics and Electronics Directorate, Air Force Office of Scientific Research, Suite 325, 875 N. Randolph Street, Arlington, VA 22203, USA

Kimberly A. Sablon U.S. Army Research Laboratory, 2800 Powder Mill Road, BLDG 207 (RDRL-SEE-I), Adelphi, MD 20783, USA University at Buffalo, Buffalo, NY 14260, USA

Banani Sen Electrical and Computer Engineering Department, University of Illinois at Chicago (UIC), 851 S. Morgan Street, Chicago, IL 60607, USA

Andrei Sergeev University at Buffalo, Buffalo 14260, NY, USAU.S. Army Research Laboratory, 2800 Powder Mill Road, BLDG 207 (RDRL-SEE-I), Adelphi, MD 20783, USA

Qing Shen Department of Engineering Science, Informatics and Engineering, The University of Electro-Communications, 1-5-1 Chofugaoka, Chofu, Tokyo 182-8585, Japan PRESTO, Japan Science and Technology Agency, 4-1-8 Honcho, Kawaguchi, Saitama 332-0012, Japan

Kevin Silverman Optoelectronics Division, National Institute of Standards and Technology, Boulder, CO 80305, USA, e-mail: silverma@boulder.nist.gov; kevin.silverman@nist.gov

Michael A. Stroscio Electrical and Computer Engineering Department, University of Illinois at Chicago (UIC), 851 S. Morgan Street, Chicago, IL 60607, USA

Physics Department, University of Illinois at Chicago (UIC), 851 S. Morgan Street, Chicago, IL 60607, USABioengineering Department, University of Illinois at Chicago (UIC), 851 S. Morgan Street, Chicago, IL 60607, USA

Dimitris Syvridis Optical Communications Laboratory, Department of Informatics and Telecommunications, University of Athens, 15784 Athens, Greece

A. Tierno Institut Non-Linéaire de Nice, Université de Nice Sophia Antipolis, UMR 6618, Valbonne 06560, France, e-mail: alessio.tierno@inln.cnrs.fr

Taro Toyoda Department of Engineering Science, Informatics and Engineering, The University of Electro-Communications, 1-5-1 Chofugaoka, Chofu, Tokyo 182-8585, Japan, e-mail: toyoda@pc.uec.ac.jp

Dmitry Turchinovich DTU Fotonik, Department of Photonics Engineering, Technical University of Denmark, DK-2800 kongens, Lyngby, Denmark, e-mail: dmtu@fotonik.dtu.dk

Nizami Vagidov University at Buffalo, Buffalo 14260, NY, USAU.S. Army Research Laboratory, 2800 Powder Mill Road, BLDG 207 (RDRL-SEE-I), Adelphi, MD 20783, USA

Evgeny A. Viktorov Université Libre de Bruxelles, Optique Nonlinéaire Théorique, Campus Plaine, Code Postal 231, 1050 Bruxelles, Belgium

Jelena Vuckovic Ginzton Laboratory, Center for Nanoscale Science and Technology, Stanford University, 348 Via Pueblo Mall, Stanford, CA 94305, USA, e-mail: jela@stanford.edu

Osamu Wada Division of Frontier Research and Technology, CREATE, and Department of Electrical and Electronic Engineering, Graduate School of Engineering, Kobe University, Kobe 657-8501, Japan, e-mail: owada@kobe-u.ac.jp

Zhiping Wang Electrical and Computer Engineering Department, University of Illinois at Chicago (UIC), 851 S. Morgan Street, Chicago, IL 60607, USA

Department of Physics, Inner Mongolia University, 235 West University Road, Hohhot 010021, China

Tsai Chin Wu Bioengineering Department, University of Illinois at Chicago, 851 S. Morgan Street, Chicago, IL 60607, USA

Hung-Pin D. Yang Electronics and Optoelectronics Research Laboratories, Industrial Technology Re-search Institute, Chutung 310, Hsinchu, Taiwan, e-mail: hpyang@itri.org.tw

Nanzhu Zhang Electrical and Computer Engineering Department, University of Illinois at Chicago (UIC), 851 S. Morgan Street, Chicago, IL 60607, USA

Ziyang Zhang ESPRC National Centre for III-V Technologies, Department of Electronic and Electrical Engineering, Centre for Nanoscience and Technology, University of Sheffield, North campus Broad lane, S3 7HQ Sheffield, UK, e-mail: ziyang.zhang@shef.ac.ukziyang.zhang@sheffield.ac.uk

Ka-Di Zhu Department of Physics, Shanghai Jiao Tong University, 800 Dong Chuan Road, Shanghai 200240, People's Republic of China, e-mail: zhukadi@sjtu.edu.cn

Chapter 1
Optically Injected Single-Mode Quantum Dot Lasers

B. Kelleher, D. Goulding, S. P. Hegarty, G. Huyet, E. A. Viktorov and T. Erneux

Abstract The response of an optically injected quantum dot semiconductor laser is studied both experimentally and theoretically. Specifically, the locking boundaries are investigated, revealing features more commonly associated with Class A lasers rather than conventional Class B semiconductor lasers (SLs). Further, various dynamical regimes are observed including excitability and multistability. Of particular interest is the observation of a phase-locked bistability. We determine the stability diagram analytically using appropriate rate equations for quantum dot lasers. In particular, the saddle-node (SN) and Hopf bifurcations forming the locking boundaries are examined and are shown to reproduce the observed experimental stability features. The generation of the phase-locked bistability is also explained via a combination of these bifurcations.

B. Kelleher (✉) · G. Huyet
Centre for Advanced Photonics and Process Analysis,
Cork Institute of Technology and Tyndall National Institute,
Lee Maltings, Dyke Parade, Cork, Ireland
e-mail: bryan.kelleher@tyndall.ie

D. Goulding · S. P. Hegarty
Tyndall National Institute, University College Cork, Lee Maltings,
Dyke Parade, Cork, Ireland

E. A. Viktorov · T. Erneux
Université Libre de Bruxelles, Optique Nonlinéaire Théorique,
Campus Plaine, Code Postal 231, 1050 Bruxelles, Belgium
e-mail: terneux@ulb.ac.be

Z. M. Wang (ed.), *Quantum Dot Devices*, Lecture Notes in Nanoscale Science and Technology 13, DOI: 10.1007/978-1-4614-3570-9_1,
© Springer Science+Business Media New York 2012

Introduction

Semiconductor lasers (SLs) have become the optical source of choice in many applications due to their high efficiency, simplicity of modulation, and small size. However, in some applications where it is necessary for the intensity noise level to remain low, they suffer from intensity fluctuations that are enhanced by their inherent relaxation oscillations (ROs). The phenomenon of ROs is familiar in the laser physics community. When a laser is perturbed from its steady-state operation, it does not immediately return to its original position. Instead, the relaxation to the steady state typically occurs in one of two ways known as Class A and Class B behavior. In a Class A laser, the laser approaches the equilibrium exponentially like an overdamped oscillator while in a Class B laser it slowly oscillates back to its stable steady-state like an underdamped oscillator, and these are the aforementioned ROs. Class A lasers include Ar, He–Ne, and dye lasers while Class B lasers include most of the lasers used today such as CO_2, solid state and SLs. When subject to optical injection, Class A and Class B lasers exhibit quite different stability properties. Class B lasers admit a rich number of sustained pulsating intensity regimes which have been studied systematically over the last decade for semiconductor and solid-state lasers (see [24] for a recent review). Class A lasers, free of ROs, are much more stable [20]. Recent efforts to suppress the RO-induced instabilities in conventional SLs have concentrated on increasing the photon lifetime above the carrier lifetime. This can be achieved by increasing either the cavity length or the cavity finesse. The first technique has been successfully applied with a several-meter-long cavity in SLs [3]. The second alternative is technically easier and has been explored using half of a vertical cavity surface emitting laser $\left(\frac{1}{2} - \text{VCSEL}\right)$ in a short external cavity [4, 5].

The development of the QD laser was a concerted effort to combine the best features of SLs (solid state, electrically injectable, small size) with some of the best features of atomic lasers (narrow gain bandwidths, zero linewidth enhancement factor). In this work we consider both experimentally and theoretically the optical injection of a single-mode [distributed feedback (DFB)] QD laser. QD lasers experiencing optical feedback have demonstrated excellent stability properties [21] and so one might also expect enhanced stability properties for an optically injected QD laser. It is known from previous studies that QD lasers exhibit a certain number of properties that make them attractive for application [6]. A particularly attractive property is an unusually high damping of the ROs [18] in comparison to their bulk and quantum well (QW) counterparts. This high damping has been cited as the principal reason for the increased stability of such devices subject to optical feedback [21], optical injection [8, 10, 14], and mutual coupling [12, 15] configurations. We determine here an experimental stability diagram with the injection strength and the detuning as control parameters and note that it is considerably different from that of a conventional QW laser. In particular, the injected QD laser exhibits stability for arbitrary values of the injection rate provided the detuning is sufficiently low. A region of bistability between two

coexisting fixed points is also possible. While these features were noted in [8], in this work we examine the result in greater depth and the observations are substantiated analytically by studying rate equations appropriate for a QD laser.

Experimental Details

The experiment was carried out on several DFB InAs devices of similar construction to those described in detail in [19]. The devices have a 5-QD-layer structure grown by solid-source molecular beam epitaxy (MBE) and consist of 2.4 InAs monolayers topped with 5 nm GaInAs, stacked in a 200 nm thick optical cavity. A 35 nm GaAs spacer is used between the QD layers and optical confinement is provided by $Al_{0.85}Ga_{0.15}As$ cladding layers. The single-mode ridge waveguide lasers were approximately 2 μm long. The master laser was a commercial external cavity tunable device with linewidth < 100 kHz. It was tunable in steps of 0.1 pm and its output was guided in a polarization maintaining fiber and coupled into the slave waveguide using a lensed fiber via polarization controllers. To prevent undesired feedback, an optical isolator with an isolation greater than 40 dB was used at the output side of the slave. The slave laser was biased at 1.5 times threshold and its output was measured using a number of different diagnostic tools: an optical spectrum analyser; a 12 GHz photodiode, amplified and connected to an electrical spectrum analyzer; and a real-time oscilloscope of 6 GHz bandwidth and a sampling rate of 40 giga-samples per second.

There are three control parameters available experimentally, namely the master power (giving the injection rate) Γ, the slave injection current J, and the detuning Δ, defined as the angular frequency difference between the master and slave lasers. Figure 1.1 shows the evolution of the power spectrum of the slave DFB laser as the detuning is varied at a fixed relatively low injection strength. Both the power of the master and the slave injection current were fixed and the detuning was systematically varied by changing the wavelength of the master laser. At each value of the master wavelength an RF spectrum was recorded and Fig. 1.1 shows a false color plot of the spectra over a wide range of detuning. Clear from this figure are the regions of beating between the master and slave lasers far from zero detuning and a stable locked region in the center. A noteworthy feature is the large area of stable locked operation found for each injection strength tested. In particular, in stark contrast to optically injected QW lasers, stable phase-locked operation was found at zero detuning for each injection strength considered with the QD lasers.

In [10] the optical injection properties of a multimode QD laser were reported. There it was shown that for low to moderate injection strengths, fast dynamics can be observed close to the locking boundary for negative detuning. In the case of a single-mode QD laser dynamical regimes appear close to the locking boundaries for both positive and negative detunings as shown in Fig. 1.1. The nature of these regions depends on the injection strength. We define the injection strength to be the ratio of the intensity of the light injected into the lasing cavity to the intensity of the light in

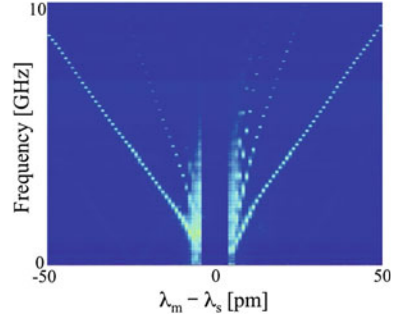

Fig. 1.1 Experimental microwave mask showing fast dynamics near both the positive and negative detuning unlocking boundaries

the cavity when free running. The lowest injection strength in this work was 0.004. For negative detuning and injection strengths up to 0.02, intensity pulses such as those in Fig. 1.2 were observed and for positive detuning and injection strengths up to 0.01, intensity pulses such as those in Fig. 1.3 were observed. These were very rare and apparently randomly spaced initially with a broad power spectrum. As the magnitude of the detuning was increased, they became more frequent, eventually becoming a periodic train of pulses much like a distorted sine curve with the fast/slow characteristic motion of the pulses with a sharply peaked power spectrum. At this point the slave had become unlocked. The shape of the pulses differs depending on the sign of the detuning since there is a nonzero α-factor. For the case of negatively detuned pulses, the intensity drops before rising above the phase-locked intensity and then returns to the steady-state value. For the positively detuned side the intensity increases, then drops below the steady-state value, and eventually again recovers to the steady-state value. These are excitable pulses resulting from 2π phase rotations of the slave electric field as shown in [14]. In [23] complicated multipulse excitability in optically injected QW lasers was predicted and has since been observed in [16]. In contrast to this, for single-mode quantum dot lasers, only single pulse excitability is observed. This has been explained as also resulting from the high RO damping in these devices in [16]. These excitable pulses arise close to the saddle-node (SN) bifurcation similar to the phase slips observed in the Adler model [1]. The logic is as follows. At very low absolute values of the detuning, the stable and unstable points are sufficiently separated to avoid any noise-induced pulsations (that is the noise is not sufficient to push the laser away from the stable point and beyond the unstable threshold point) and as a result quiet regions of locking are observed. As the magnitude of the detuning is increased, the stable and unstable fixed points become progressively closer until eventually noise is sufficient to push the system past the unstable point resulting in a 2π rotation of the electric field and a consequent intensity pulsation. As the magnitude of the detuning is increased even further the pulses occur more and more frequently until eventually the two fixed points collide and annihilate each other leaving a ghost at which point the system's time series becomes a periodic train (modulo noise) with the characteristic shape of the pulses. The dynamical behavior close to the boundaries in the microwave mask shown in Fig. 1.1 consisted of such pulses. In [15] a similar phenomenon was observed in a delayed mutually

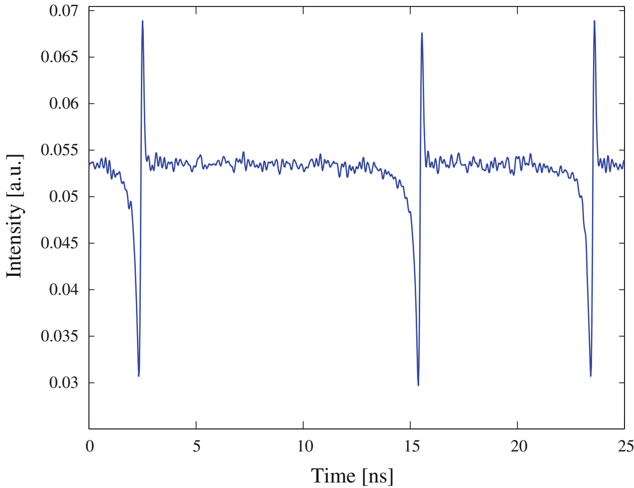

Fig. 1.2 Experimentally obtained intensity pulses for the case of negative detuning

coupled configuration of quantum dot lasers. In this case, due to the delayed mutual coupling, a pulse train is observed rather than individual pulses. As the injection strength is increased the dynamical behavior changes significantly and similar to the multimode case [10], various different dynamical regimes may be observed. The first change is the disappearance of the excitable pulses near the positive detuning unlocking boundary. These are replaced by a noise-induced switching between a stable point and a limit cycle (with a higher average power) as shown in Fig. 1.4. For the same injection power, the slave laser is still undergoing excitable pulsing close to the negatively detuned unlocking boundary, clearly showing again the asymmetry in the dynamical bifurcations in the optically injected laser system due to the nonzero α-factor. If the injection strength is increased further, this switching is replaced by chaotic behavior (Fig. 1.5) and eventually the SN bifurcation disappears and instead locking is via a Hopf bifurcation which results in the slave laser moving directly from unlocked to locked behavior as shown in Fig. 1.6. The proximity of the chaotic behavior to the disappearance of the SN and the appearance of the Hopf suggests strongly that this chaos has an organizing center in a codimension-2- fold-Hopf point at their intersection. The Hopf bifurcation first appears for injection strengths of 0.016. This is higher than that for conventional semiconductor lasers under optical injection but is consistent with measurements of the RO damping rate for quantum-dot-based devices reported in, for example, [17, 21].

At the injection strength where the positively detuned locking boundary changes to a Hopf bifurcation, excitable pulsations are still observed near the negatively detuned boundary. Increasing the injection strength still further the negatively detuned excitable pulses also disappear and are replaced with a bistability between a stable point and a limit cycle (of lower average power) as

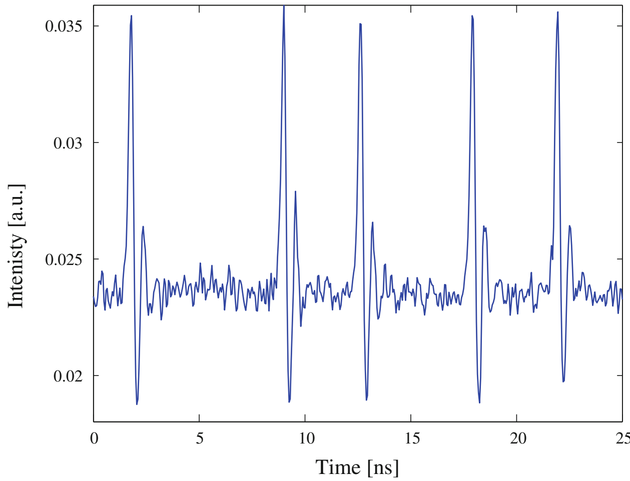

Fig. 1.3 Experimentally obtained intensity pulses for the case of positive detuning in an optically injected QD laser

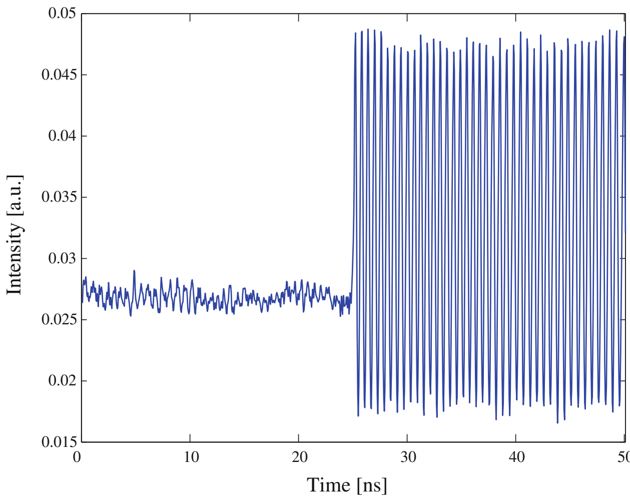

Fig. 1.4 Time trace of switch from stable state to higher average power limit cycle behavior for the case of positive detuning in an optically injected QD laser

shown in Fig. 1.7. This limit cycle undergoes a period doubling bifurcation and the switching is then between this period doubled cycle and the stable point as shown in Fig. 1.8. Finally, there is a region where two phase-locked solutions of different intensities coexist. This is the dynamical behavior of most interest for this work. Figure 1.9 shows an example of a noise-induced switching between the two locked states. The transition between the two steady states is

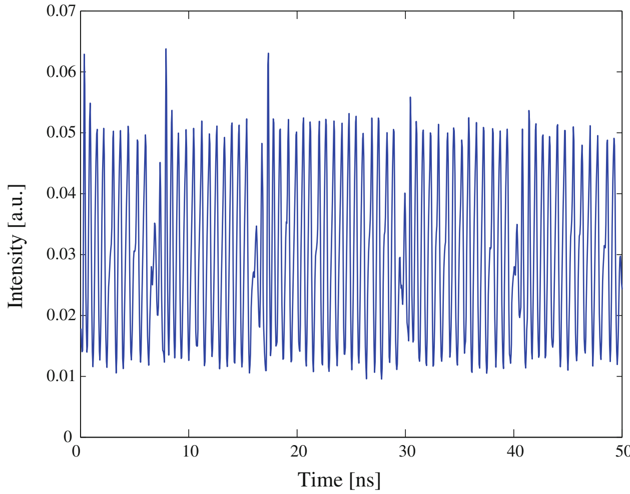

Fig. 1.5 Time trace of chaotic attractor for the case of positive detuning in an optically injected QD laser

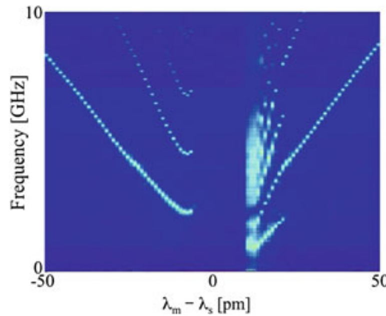

Fig. 1.6 Experimentally obtained power spectra for an optically injected QD DFB laser at a higher injection strength than that in Fig. 1.1. At this injection strength the laser moves directly from unlocked to locked on the positive detuning boundary (lower master wavelength) with no fast dynamical regime. This absence of noise-induced dynamics indicates that the locking is via a Hopf bifurcation rather than via an SN bifurcation

sharp and the relaxation includes only one spiked oscillation. It suggests that the decay of the relaxation dynamics occurs at the same time scale as that of the RO frequency in contrast to the typical Class B laser and thus we speak of the Class A limit. This behavior is not possible for a weakly damped QW laser except very close to threshold. At this injection strength the locking boundary for negative detuning is also a Hopf bifurcation. However, the SN bifurcation has not disappeared but instead lies inside the locking region where it creates the second locked solution.

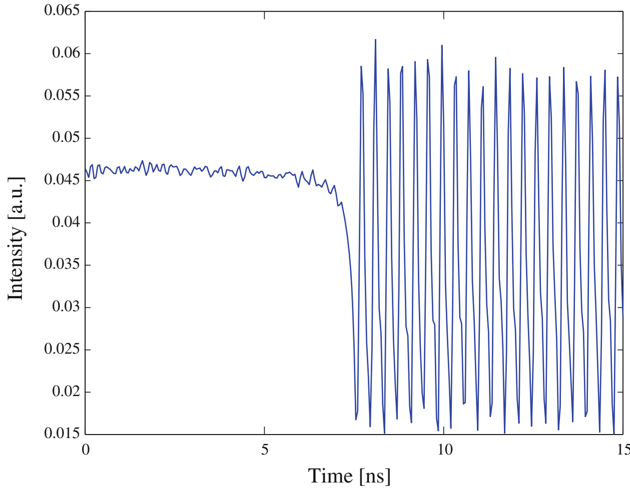

Fig. 1.7 Time trace of switch from stable state to lower average power limit cycle behavior for the case of negative detuning in an optically injected QD laser

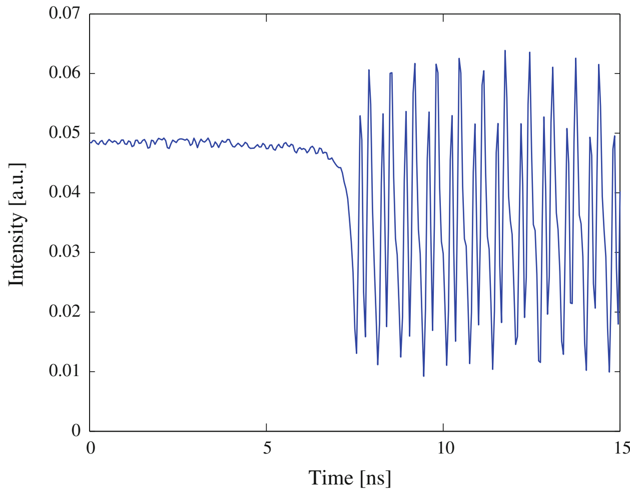

Fig. 1.8 Time trace of switch from stable state to period two limit cycle behavior for the case of negative detuning in an optically injected QD laser

The results of the experimental mapping of the observed dynamics are shown in Fig. 1.10. The black lines mark the SN bifurcations and the red lines mark the Hopf bifurcations. Between the two black lines in the upper left of the figure a phase-locked bistability was observed. A zoom of the low injection strength region is shown in Fig. 1.11 with the various dynamical regimes observed labeled.

There are a number of fundamental differences between the mappings in Figs. 1.10 and 1.11 and the injection dynamics reported in [22] for the conventional

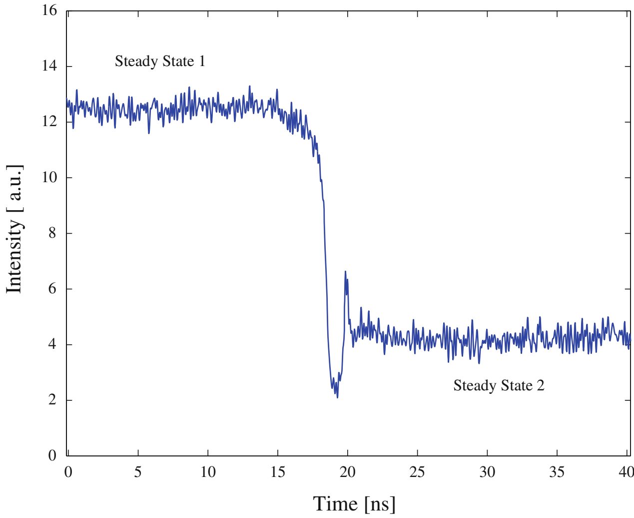

Fig. 1.9 Time trace of switch between two distinct stable phase locked states in an optically injected QD laser

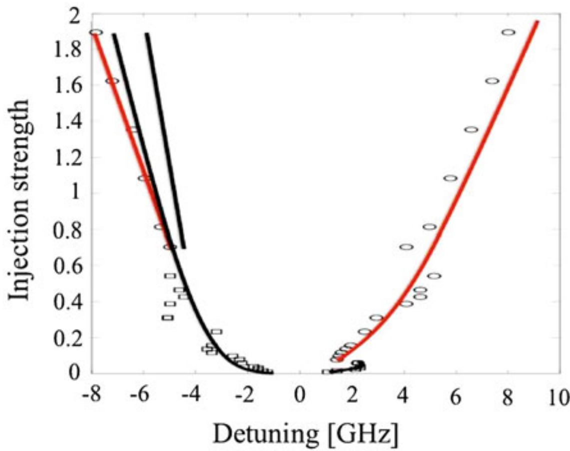

Fig. 1.10 Experimental stability diagram. The injection strength is defined as the power of the light injected into the cavity divided by the power in the cavity when free running. The *circles* and *rectangles* show the experimental points while the lines are added as a guide. The *solid black lines* (through the *rectangles*) are SN bifurcations. The *solid red lines* (through the *ellipses*) are Hopf bifurcations. Between the two *black lines* at the *top left* of the figure a phase-locked bistability is observed

QW laser and reviewed in detail in [24]. Instead, we note a similarity between the stability diagram in Fig. 1.10 and that of a Class A laser [20]. The Hopf bifurcation line differs from that which occurs for an injected QW laser and, in particular, it does not cross the zero detuning line allowing stable phase-locked behavior at zero

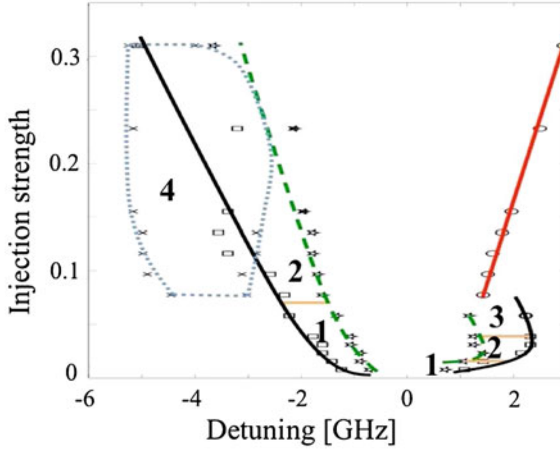

Fig. 1.11 A zoom of the low injection region of the experimental stability diagram. As before, the lines are added as guides. The *solid black lines* (through the *rectangles*) correspond to SN bifurcations and the *solid red* (through the *ellipses*) to Hopf bifurcations. The *dashed green lines* (through the *stars*) are the dynamical boundaries: between these and the *black lines* various different dynamical regimes were observed. The *blue dotted line* (through the x's) marks a period doubling line. The dynamical regions are labeled as 1 through 4. *1* Excitable pulses. *2* Switching between phase-locked behavior and a limit-cycle. *3* Switching between phase-locked behavior and a chaotic attractor. *4* Period doubling. Note that the period doubling can be both inside and outside the locking region. The same is true for the chaotic region although only that portion inside the locking region is shown

detuning for arbitrary injection strengths. Furthermore, as already stated, except very close to the laser threshold [13], the coexistence of two stable locking states is not possible for a QW laser. Also, the extent of the locking via an SN bifurcation for positive detuning is greatly increased as one would expect for a more highly damped slave laser. These observations suggest a significant impact from the nonlinear capture dynamics in QD lasers provided by the Pauli blocking factor. More precisely, QD lasers may exhibit both Class A and Class B dynamics depending on the carrier capture parameters as was shown in [7] by analyzing a three-variable rate equation model. Below, we consider these equations, adapted to include optical injection and examine the limit that leads to the highest damping of the ROs.

Modeling

We now turn our attention to a rate equation model of the optically injected quantum dot laser. We study the behavior of the system in different limits and show that the experimentally relevant case reproduces the experimental results very well. The first step is a 4-dimensional model of an optically injected quantum dot laser.

QD Laser Equations

Our rate equations for a QD laser subject to an injected signal consist of three equations for the complex electric field E, the occupation probability in a dot ρ, and the carrier density n in the wetting layers, scaled by the 2D QD density per layer. The free-running (no injection) case was studied in [7]. These are augmented with a term for the injected field and are given by

$$E' = \frac{1}{2}(1+i\alpha)[-1+g(2\rho-1)]E + \Gamma\exp(i\Delta t), \tag{1.1}$$

$$\rho' = \eta\left[Bn(1-\rho) - \rho - (2\rho-1)|E|^2\right], \tag{1.2}$$

$$n' = \eta[J - n - 2Bn(1-\rho)]. \tag{1.3}$$

Prime means differentiation with respect to $T \equiv t/\tau_{ph}$ where t is time and τ_{ph} is the photon lifetime (=2 ps for this work). Γ is the injection rate: it is proportional to the injection strength divided by the laser round-trip time (to give the correct units). The factor 2 in Eq. 1.3 accounts for the spin degeneracy in the quantum dot energy levels. J is the pump current per dot and α is the linewidth enhancement factor. The fixed parameters B and η are ratios of basic timescales and are defined as $B \equiv \tau\tau_{cap}^{-1}$ and $\eta \equiv \tau_{ph}\tau^{-1}$ where τ and τ_{cap} denote the carrier recombination and capture times, respectively. Typical values are $\tau = 1$ ns and $\tau_{cap} = 10$ ps which imply $B = 10^2$ and $\eta = 2\times10^{-3}$. The nonlinear interaction between the wetting layer and the dots is provided by the Pauli blocking factor $1-\rho$ which leads to a significant difference between QD and QW equations. As in [10], we shall consider a value of g close to one for which a good agreement between theory and experiments is observed.

Reduction to QW Laser Equations

If we consider the limit $B\to\infty$ and keep all other parameters fixed, we obtain the conventional rate equations for an injected QW laser. This can be seen by introducing the new variable

$$N = Bn \tag{1.4}$$

into Eqs. 1.1–1.3. The equations for E, ρ, and N are then given by

$$E' = \frac{1}{2}(1+i\alpha)[-1+g(2\rho-1)]E + \Gamma\exp(i\Delta t), \tag{1.5}$$

$$\rho' = \eta\left[N(1-\rho) - \rho - (2\rho-1)|E|^2\right], \tag{1.6}$$

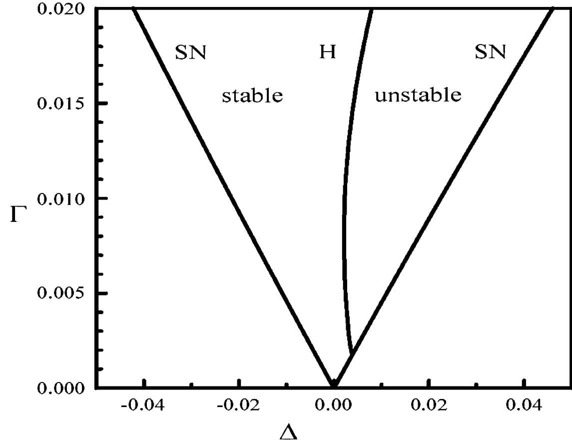

Fig. 1.12 Stability diagram in the large B limit. Steady-state locking occurs in the central region delimited by the *left* SN bifurcation line and by the Hopf (H) bifurcation line

$$N' = \eta B\left[J - B^{-1}N - 2N(1-\rho)\right]. \tag{1.7}$$

From Eqs. 1.6 and 1.7, we note that N is faster than ρ because $B \gg 1$ is multiplying the right-hand side of Eq. 1.7. This suggests the elimination of N by a quasi-steady-state approximation. Specifically, we determine N from Eq. 1.7 with $N' = 0$ and obtain

$$N = \frac{J}{2(1-\rho)} \tag{1.8}$$

as $B \to \infty$. Substituting (1.8) into Eq. 1.6, the equations for E and ρ become

$$E' = \frac{1}{2}(1 + i\alpha)[-1 + g(2\rho - 1)]E + \Gamma \exp(i\Delta t), \tag{1.9}$$

$$\rho' = \eta\left[\frac{J}{2} - \rho - (2\rho - 1)|E|^2\right]. \tag{1.10}$$

Defining

$$D = \frac{-1 + g(2\rho - 1)}{2}, \tag{1.11}$$

Eqs. 1.9 and 1.10 take the form

$$E' = (1 + i\alpha)DE + \Gamma \exp(i\Delta t), \tag{1.12}$$

$$D' = \eta\left[P - D - (1 + 2D)|E|^2\right], \tag{1.13}$$

where

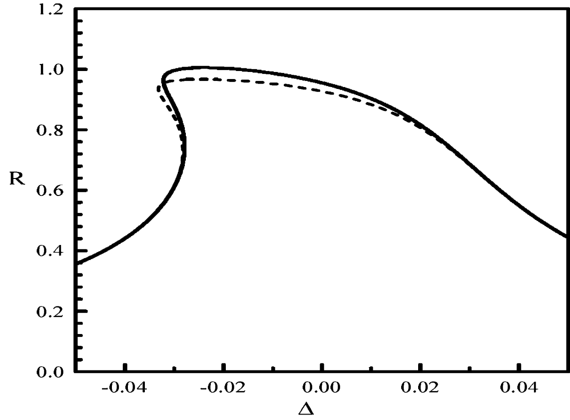

Fig. 1.13 Bifurcation diagram of the steady-state solutions. The values of the fixed parameters are those in (1.15) plus $B = 10^2$ and $\Gamma = 0.02$. The broken line is the approximation given by (1.34) and (1.35) found in the limit $\varepsilon = g - 1 \to 0$ and $B\varepsilon = O(1)$.

$$P \equiv \frac{g}{2}(J - 1 - g^{-1}) \tag{1.14}$$

is defined as the pump parameter above threshold ($J_{\rm th} = 1 + g^{-1}$). Equations 1.12 and 1.13 are the rate equations for an optically injected QW laser [9]. A typical stability diagram is shown in Fig. 1.12.

The values of the fixed parameters α, η and g are the same for all our bifurcation studies. They are given by

$$\alpha = 1.2, \quad \eta = 2 \times 10^{-3}, \quad \text{and} \quad g = 1.02. \tag{1.15}$$

We consider $J = 1.5\,J_{\rm th} = 2.97$ which implies from (1.14) that $P = 0.51$. In Fig. 1.12, the Hopf bifurcation line emerges from a fold-Hopf bifurcation point located on the right SN bifurcation line. As the injection rate progressively increases, the Hopf line moves slightly to the left before folding back to the right. If α is larger, the Hopf line crosses the zero detuning axis before folding back. A detailed investigation of the stability diagram in Fig. 1.12 can be found in [24].

Steady States and Stability Analysis

We next determine the basic steady-state solutions. We make the substitution $E = R\exp(i(\Delta T + \phi))$ in Eqs. 1.1–1.3 and look for solutions satisfying $R' = \phi' = \rho' = n' = 0$. Using Δ as the bifurcation parameter, the solution in parametric form (where n is the parameter) is given by

$$\rho = 1 - \frac{J - n}{2Bn}, \tag{1.16}$$

$$R^2 = \frac{1}{2[(B+1)n - J]}[Bn(J - n - 2) + J - n] \geq 0, \tag{1.17}$$

$$\Delta = F\alpha \pm \sqrt{\Gamma^2 R^{-2} - F^2} \text{ with } (\Gamma^2 R^{-2} - F^2 \geq 0) \tag{1.18}$$

where

$$F \equiv \frac{1}{2}\left[-1 + g\left(1 - \frac{J-n}{Bn}\right)\right]. \tag{1.19}$$

Note that the condition $0 \leq \rho \leq 1$ restricts the values of n to the interval

$$\frac{J}{2B+1} \leq n \leq J. \tag{1.20}$$

The steady-state solution for R is shown in Fig. 1.13. It exhibits an S-shape for negative detuning.

In the case of the solitary laser ($\Gamma = 0$), the linear stability properties of the steady states depend on an effective capture rate $B_e \equiv B(g-1)$ [7]. Because B is large and $\varepsilon \equiv g - 1$ is small, we need to specify how these quantities are related. The most interesting case that does not lead to the conventional QW laser rate equations is based on the limit

$$B = O(\varepsilon^{-1}) \text{ as } \varepsilon \to 0. \tag{1.21}$$

After introducing $g = 1 + \varepsilon$ into Eq. 1.1, the expression in brackets becomes $[-2 + 2\rho + \varepsilon(2\rho - 1)]$ and motivates the introduction of u where

$$\rho = 1 + \varepsilon u \tag{1.22}$$

to balance all terms. The expression in brackets is then proportional to ε and motivates the new time

$$s \equiv \varepsilon T \tag{1.23}$$

to balance the left- and right-hand sides of Eq. 1.1. In terms of u and s, Eqs. 1.1–1.3 become

$$E' = \frac{1}{2}(1 + i\alpha)[1 + 2u(1+\varepsilon)]E + \gamma \exp(i\delta s), \tag{1.24}$$

$$u' = \varepsilon^{-2}\eta\left[-B\varepsilon nu - 1 - \varepsilon u - (1 + 2u\varepsilon)|E|^2\right], \tag{1.25}$$

$$n' = \varepsilon^{-1}\eta[J - n + 2B\varepsilon nu] \tag{1.26}$$

where prime now means differentiation with respect to s. The new control parameters are the scaled injection strength γ and the scaled detuning δ. They are defined by

$$\gamma \equiv \varepsilon^{-1}\Gamma \text{ and } \delta \equiv \varepsilon^{-1}\Delta. \tag{1.27}$$

Adiabatic Elimination

Since $\varepsilon^{-2} \gg \varepsilon^{-1}$ as $\varepsilon \to 0$, Eqs. 1.25 and 1.26 suggest that u is faster than n. Consequently, we eliminate u by a quasi-steady-state approximation. From Eq. 1.25 with $u' = 0$, we obtain

$$u = -\frac{1+E^2}{B\varepsilon n} \tag{1.28}$$

as $\varepsilon \to 0$. Substituting (1.28) into Eqs. 1.24 and 1.26, the equations for E and n become

$$E' = \frac{1}{2}\left(1 - \frac{2(1+|E|^2)}{B\varepsilon n}\right)(1+i\alpha)E + \gamma\exp(i\delta s), \tag{1.29}$$

$$n' = \varepsilon^{-1}\eta\left[J - n - 2(1+|E|^2)\right]. \tag{1.30}$$

Introducing the decomposition $E = R\exp(i(\delta s + \phi))$ into Eqs. 1.29 and 1.30 leads to the following three equations for R, ϕ, and n

$$R' = \frac{1}{2}\left(1 - \frac{2(1+R^2)}{B\varepsilon n}\right)R + \gamma\cos(\phi), \tag{1.31}$$

$$\phi' = -\delta + \frac{1}{2}\left(1 - \frac{2(1+R^2)}{B\varepsilon n}\right)\alpha - \frac{\gamma}{R}\sin(\phi), \tag{1.32}$$

$$n' = \varepsilon^{-1}\eta\left[J - n - 2(1+R^2)\right]. \tag{1.33}$$

Steady States

The steady-state solutions can be determined analytically in the parametric form $n = n(R^2)$ and $\gamma = \gamma(R^2)$. We find

$$n = J - 2(1+R^2), \tag{1.34}$$

$$\gamma^2 = \left[F^2 + (-\delta + F\alpha)^2\right]R^2 \tag{1.35}$$

where

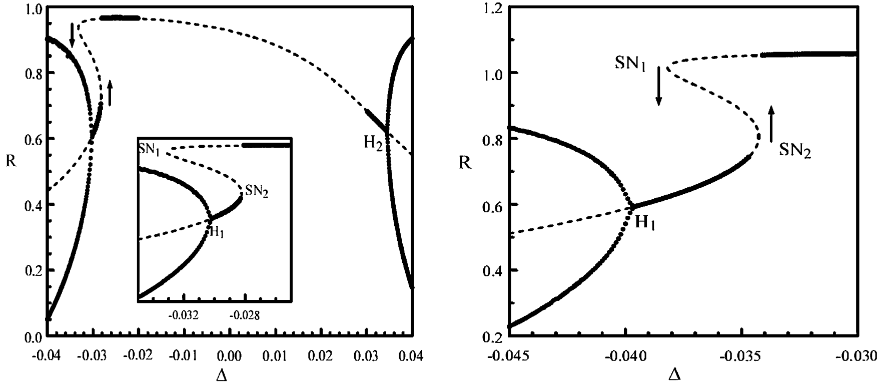

Fig. 1.14 Two bifurcation diagrams. The figure on the *left* is a bifurcation diagram of the bistability between stable steady and periodic solutions. The branch of steady-state solutions is given by Eqs. 1.34–1.36 (*broken line*). The extrema of the stable periodic solutions have been obtained by integrating Eqs. 1.31–1.33. The bistability between steady states is possible due to the Hopf bifurcation H_1 that stabilizes the lower branch of steady states. The values of the parameters are those in (1.15) plus $B = 10^2$, $J = 1.5\,J_{\text{th}} = 4.5$ and $\Gamma = 0.02$. The location of the Hopf and SN bifurcation points is in agreement with the predictions of the linearized theory (Fig. 1.15a). The figure on the *right* shows the full phase-locked bistability. The extrema of R are shown as functions of the detuning Δ. The complete S-shaped branch of steady states is shown by a *broken line*. The values of the parameters are those in (1.15) plus $B = 0.7 \times 10^2$, $J = 1.5\,J_{\text{th}} = 5.14$ and $\Gamma = 0.025$

$$F \equiv \frac{1}{2}\left(1 - \frac{2(1+R^2)}{B\varepsilon(J - 2(1+R^2))}\right). \tag{1.36}$$

The branch of steady states is shown in Fig. 1.14 by a broken line. The condition $n > 0$ implies, using (1.34), that $R^2 < (J-2)/2$. Under this condition, we note from (1.28) that $\rho < 1$ as must be the case.

Linear Stability

We next examine the stability of the steady states. From the linearized equations, we determine the following characteristic equation for the growth rate λ

$$\lambda^3 + a_1\lambda^2 + a_2\lambda + a_3 = 0 \tag{1.37}$$

where the coefficients are all expressed as functions of the steady-state intensity R^2. They are given by

$$a_1 = -G - F + \varepsilon^{-1}\eta, \tag{1.38}$$

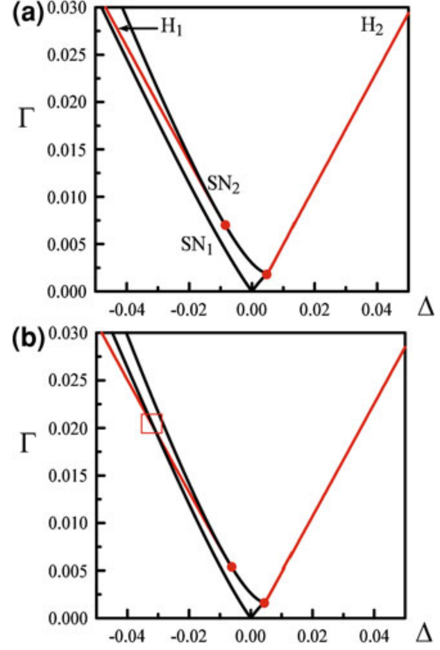

Fig. 1.15 Stability diagrams for the case $\varepsilon = g - 1 \to 0$ and $B\varepsilon = O(1)$. **a** $B = 10^2$ and $J = 1.5\,J_{th} = 4.5$; **b** $B = 0.7 \times 10^2$ and $J = 1.5\,J_{th} = 5.14$. All remaining parameters are given in (1.15). The *square* in Fig. (**b**) indicates the point where H_1 and SN_1 admit the same value of Δ. Above this point, full bistability between steady states is possible. The laser threshold of the solitary laser is determined from $J_{th} = 1 + g^{-1} + (g+1)/(B\varepsilon)$ [7]

$$\begin{aligned} a_2 =& GF + H\alpha(\delta - F\alpha) + (\delta - F\alpha)^2 \\ & - \varepsilon^{-1}\eta(G+F) + \varepsilon^{-1}\eta 4R^2K, \end{aligned} \tag{1.39}$$

$$\begin{aligned} a_3 =& \varepsilon^{-1}\eta\left[GF + H\alpha(\delta - F\alpha) + (\delta - F\alpha)^2\right] \\ & \varepsilon^{-1}\eta 4R^2K[\alpha(\delta - F\alpha) - F]. \end{aligned} \tag{1.40}$$

The functions $G = G(R^2)$, $H = H(R^2)$, and $K = K(R^2)$ are defined by

$$G \equiv \frac{1}{2}\left[1 - \frac{2(1+3R^2)}{B\varepsilon(J - 2(1+R^2))}\right], \tag{1.41}$$

$$H \equiv \frac{2R^2}{B\varepsilon(J - 2(1+R^2))}, \tag{1.42}$$

$$K \equiv \frac{1+R^2}{B\varepsilon(J - 2(1+R^2))^2}. \tag{1.43}$$

The Routh–Hurtwitz stability conditions for a stable steady-state require that [11]

$$a_1a_2 - a_3 > 0, a_1 > 0 \text{ and } a_3 > 0. \tag{1.44}$$

A change of stability occurs through either an SN bifurcation or a Hopf bifurcation. The SN bifurcation point is characterized by a zero eigenvalue and satisfies the condition

$$a_3 = 0. \tag{1.45}$$

A Hopf bifurcation point is characterized by a pair of purely imaginary eigenvalues and satisfies the conditions

$$a_1 a_2 - a_3 = 0 \tag{1.46}$$

and

$$a_2 > 0. \tag{1.47}$$

Both Eqs. 1.45 and 1.46 can be solved analytically because they are quadratic expressions in the detuning δ. Specifically, we first determine δ as a function of R^2 from either Eqs. 1.45 or 1.46. We then obtain γ as a function of δ by using the steady-state Eq. 1.35. Two stability diagrams exhibiting the SN and Hopf bifurcation lines are shown in Fig. 1.15 for two different values of B. For clarity, only the Hopf bifurcation points from a stable steady state are shown $(a_1 a_2 - a_3 = 0,\ a_1 > 0, \text{ and } a_3 > 0)$.

Comparing Fig. 1.15 with the stability diagram of the conventional QW laser (Fig. 1.12), we note two distinct differences. First, a Hopf bifurcation line emerges from the SN bifurcation line at a positive detuning and moves immediately to the right. Second, an additional Hopf bifurcation emerges from the SN bifurcation line at a negative detuning. This second Hopf bifurcation allows the coexistence of either two stable steady states (bistability) or the coexistence of one stable steady state and one pulsating time-periodic regime. These predictions from the linearized theory are verified by direct simulations of Eqs. 1.31–1.33 (see Fig. 1.14).

The stability diagram in Fig. 1.15 is qualitatively similar to the experimental map. Both the experimental and analytical stability diagrams predict stable locking for a larger domain of detuning compared to a QW laser. Moreover, there are no Hopf bifurcations at low injection strengths as previously demonstrated experimentally in [14]. At higher injection strengths and for a sufficiently large positive detuning, steady-state locking occurs through a Hopf bifurcation (H_2 in Fig. 1.14) and not through an SN bifurcation. For negative detunings, there is a domain of bistability between two locked states. As previously stated, this bistability phenomenon is possible because of a Hopf bifurcation that stabilizes the lower intensity branch (H_1 in Fig. 1.14).

Because the Hopf bifurcation lines do not cross the $\Delta = 0$ axis as is the case for QW lasers [9], the injected QD laser exhibits greater stability properties. We should, however, emphasize that this results from the fact that $g - 1 \ll 1$ and $(g - 1)B = O(1)$. Other ranges of values of the parameters $g - 1$ and B are possible because of the large diversity of QD structures that are currently designed.

The stability diagram shown in Fig. 1.15 bears striking similarities with that of an optically injected Class A laser with a nonzero linewidth enhancement factor. We consider this system in the next section.

Class A Laser

Mayol et al investigated the equations for an optically injected Class A laser with a nonzero linewidth enhancement factor α in [20]. These equations are given by

$$E' = \left(\frac{A}{1+|E|^2} - 1\right)(1+i\alpha)E + \Gamma\exp(i\Delta t) \tag{1.48}$$

where A is the normalized pump parameter (laser threshold is $A = 1$) and α is the linewidth enhancement factor. The control parameters are the injection rate Γ and the detuning Δ. Introducing $E = R\exp(i(\Delta t + \phi))$ into (1.48), we obtain

$$R' = \left(\frac{A}{1+R^2} - 1\right)R + \Gamma\cos(\phi), \tag{1.49}$$

$$\phi' = -\Delta + \left(\frac{A}{1+R^2} - 1\right)\alpha - \frac{\Gamma}{R}\sin(\phi). \tag{1.50}$$

The steady-state intensity $R^2 = R^2(\Gamma)$ satisfies

$$\Gamma^2 = R^2\left\{\left(\frac{A}{1+R^2} - 1\right)^2 + \left[-\Delta + \left(\frac{A}{1+R^2} - 1\right)\alpha\right]^2\right\}. \tag{1.51}$$

From the linearized equations, we then obtain the characteristic equation for the growth rate λ

$$\lambda^2 + b_1\lambda + b_2 = 0 \tag{1.52}$$

where

$$b_1 = 2\left(1 - \frac{A}{(1+R^2)^2}\right), \tag{1.53}$$

$$\begin{aligned} b_2 = {} & \left(\frac{A}{1+R^2} - 1\right)\left[\frac{A(1-R^2)}{(1+R^2)^2} - 1\right] + \left[\Delta - \left(\frac{A}{1+R^2} - 1\right)\alpha\right]^2 \\ & + \frac{2AR^2\alpha}{(1+R^2)^2}\left[\Delta - \left(\frac{A}{1+R^2} - 1\right)\alpha\right]. \end{aligned} \tag{1.54}$$

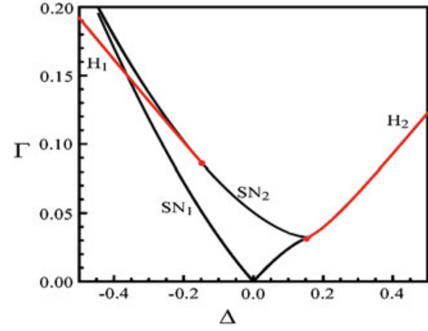

Fig. 1.16 Stability diagram for an optically injected class A laser with $\alpha = A = 1.2$.

The condition for an SN stability boundary is $b_2 = 0$ which is a quadratic equation for $\Delta - \left(\frac{A}{1+R^2} - 1\right)\alpha$. By gradually changing R^2 from zero, we first determine Δ from this quadratic equation and then evaluate Γ using Eq. 1.51 (see Fig. 1.16). The conditions for a Hopf bifurcation are $b_1 = 0$ and $b_2 > 0$. From 1.53, we find that $b_1 = 0$ if

$$R^2 = R_H^2 = \sqrt{A} - 1 \tag{1.55}$$

with $\sqrt{A} \geq 1$ and from (1.54) we find

$$b_2(R_H^2) = \left(\Delta - R_H^2\sqrt{\alpha^2+1}\right)\left(\Delta + R_H^2\sqrt{\alpha^2+1}\right). \tag{1.56}$$

We conclude that $b_2(R_H^2) > 0$ if either $\Delta < -R_H^2\sqrt{\alpha^2+1}$ or $\Delta > R_H^2\sqrt{\alpha^2+1}$. The Hopf bifurcation lines are obtained by substituting (1.55) into Eq. 1.51 and satisfy

$$\Gamma^2 = (\sqrt{A} - 1)\left\{(1+\alpha^2)(\sqrt{A}-1)^2 - 2\Delta(\sqrt{A}-1)\alpha^2 + \Delta^2\right\}. \tag{1.57}$$

The critical points $\Delta = \pm R_H^2\sqrt{\alpha^2+1}$ correspond to double zero eigenvalues and are indicated by dots in Fig. 1.16.

This stability diagram bears a striking resemblance to those in Fig. 1.15 and to the experimentally obtained diagram in Fig. 1.10. This highlights again the large RO damping associated with quantum dot lasers. However, this similarity is restricted to the stability diagram and does not extend to some features such as the presence of chaos. Since the optically injected Class A laser is a 2-dimensional system it does not admit deterministic chaos while we saw that chaotic attractors do feature in the optically injected QD laser in Fig. 1.5. Thus, the optically injected QD laser occupies a sort of middle ground between weakly damped QW lasers and Class A lasers.

Conclusions

In conclusion, we have performed an experimental and theoretical study of an optically injected single-mode QD laser. Various dynamical regimes were observed experimentally. Among these were excitability for both positive and negative detuning and a number of bistabilities including most strikingly, a phase-locked bistability over a relatively large area. An experimental stability diagram was obtained and was shown to differ significantly from that of an optically injected QW laser. In particular, the Hopf bifurcation typically induced by ROs is absent from a large region of the stability diagram. Furthermore, the phase-locked bistability is not possible with weakly damped QW devices except close to threshold. A rate equation model of the system was considered and reproduced both the bistability and the qualitative features of the stability diagram. Finally, the stability diagram was shown to strongly resemble that of an optically injected Class A laser with a nonzero α-factor, further underlining the importance of the strong RO damping in QD lasers.

Acknowledgments This work was conducted under the framework of the INSPIRE programme, funded by the Irish Governments Programme for Research in Third Level Institutions, Cycle 4, National Development Plan 2007–2013 and the authors also gratefully acknowledge the support of Science Foundation Ireland (SFI) under the contract number 07/IN.1/I929 and also through the Centre for Telecommunications Value-Chain Research (CTVR), the Irish Research Council for Science, Engineering and Technology (IRCSET), the EU FP7 Marie Curie Action FP7-PEOPLE-2010-ITN through the PROPHET project, Grand No. 264687 and the Tyndall National Access Programme. The authors in Bruxelles acknowledge support of the Fonds National de la Recherche Scientifique (Belgium). The research by T. Erneux was also supported by the Air Force Office of Scientific Research (AFOSR) grant FA8655-09-1-3068.

References

1. Adler, R.: Study of locking phenomena in oscillators. Proc. IRE **34**, 351–357 (1946)
2. Arecchi, F.T., Lippi, G.L., Puccioni, G.P., Tredicce, J.R.: Deterministic chaos in laser with injected signal. Opt. Commun. **51**, 308–314 (1984)
3. Baili, G., Alouini, M., Moronvalle, C., Dolfi, D., Bretenaker, F.: Broad-bandwidth shot-noise-limited class-A operation of a monomode semiconductor fiber-based ring laser. Opt. Lett. **31**, 62–64 (2006)
4. Baili, G., Alouini, M., Dolfi, D., Bretenaker, F., Sagnes, I., Garnache, A.: Shot-noise-limited operation of a monomode high-cavity-finesse semiconductor laser for microwave photonics applications. Opt. Lett. **32**, 650–652 (2007)
5. Baili, G., Alouini, M., Malherbe, T., Dolfi, D., Sagnes, I., Bretenaker, F.: Direct observation of the class-B to class-A transition in the dynamical behavior of a semiconductor laser. Eur. Phys. Lett. **87**, 44005 (2009)
6. Bimberg, D., Grundmann, M., Ledentsov, N.N.: Quantum Dot Heterostructures. Wiley, NY (1999)
7. Erneux, T., Viktorov, E.A., Mandel, P.: Time scales and relaxation dynamics in quantum-dot lasers. Phys. Rev. A **76**, 023819 (2007)
8. Erneux, T., Viktorov, E.A., Kelleher, B., Goulding, D., Hegarty, S.P., Huyet, G.: Optically injected quantum dot lasers. Opt. Lett. **35**, 937–939 (2010)

9. Erneux, T., Glorieux, P.: Laser Dynamics. Cambridge University Press, Cambridge (2010)
10. Goulding, D., Hegarty, S.P., Rasskazov, O., Melnik, S., Hartnett, M., Greene, G., McInerney, J.G., Rachinskii, D., Huyet, G.: Excitability in a quantum dot semiconductor laser with optical injection. Phys. Rev. Lett. **98**, 153903 (2007)
11. Gradshteyn, I.S., Ryzhik, I.M.: Routh-Hurwitz Theorem. In: Tables of Integrals, Series, and Products. 6th edn. Academic Press, San Diego (2000)
12. Hegarty, S.P., Goulding, D., Kelleher, B., Huyet, G., Todaro, M.T., Salhi, A., Passaseo, A., De Vittorio, M.: Phase-locked mutually coupled 1.3 μm quantum-dot lasers. Opt. Lett. **32**, 3245–3247 (2007)
13. Hohl, A., van der Linden, H.J.C., Roy, R., Goldsztein, G., Broner, F., Strogatz, S.H.: Scaling laws for dynamical hysteresis in a multidimensional laser system. Phys. Rev. Lett. **74**, 2220–2223 (1995)
14. Kelleher, B., Goulding, D., Hegarty, S.P., Huyet, G., Ding-Yi, C., Martinez, A., Lemaître, A., Ramdane, A., Fischer, M., Gerschütz, F., Koeth, J.: Excitable phase slips in an injection-locked single-mode quantum-dot laser. Opt. Lett. **34**, 40–42 (2009)
15. Kelleher, B., Bonatto, C., Skoda, P., Hegarty, S.P., Huyet, G.: Excitation regeneration in delay-coupled oscillators. Phys. Rev. E **81**, 036204 (2010)
16. Kelleher, B., Bonatto, C., Huyet, G., Hegarty, S.P.: Excitability in optically injected semiconductor lasers: contrasting quantum-well- and quantum-dot-based devices. Phys. Rev. E **83**, 026207 (2011)
17. Kuntz, M., Ledentsov, N.N., Bimberg, D., Kovsh, A.R., Ustinov, V.M., Zhukov, A.E., Shernyakov, Y.M.: Spectrotemporal response of 1.3 μm quantum-dot lasers. Appl. Phys. Lett. **81**, 3846–3848 (2002)
18. Lüdge, K., Bormann, M.J.P., Malic, E., Hövel, P., Kuntz, M., Bimberg, D., Knorr, A., Schöll, E.: Turn-on dynamics and modulation response in semiconductor quantum dot lasers. Phys. Rev. B **78**, 035316 (2008)
19. Martinez, A., Lemaître, A., Merghem, K., Ferlazzo, L., Dupuis, C., Ramdane, A., Provost, J.G., Dagens, B., Le Gouezigou, O., Gauthier-Lafaye, O.: Static and dynamic measurements of the α-factor of five-quantum-dot-layer single-mode lasers emitting at 1.3 μm on GaAs. Appl. Phys. Lett. **86**, 211115 (2005)
20. Mayol, C., Toral, R., Mirasso, C.R., Natiello, M.A.: Class-A lasers with injected signal: bifurcation set and Lyapunov-potential function. Phys. Rev. A **66**, 013808 (2002)
21. O'Brien, D., Hegarty, S.P., Huyet, G., Uskov, A.V.: Sensitivity of quantum-dot semiconductor lasers to optical feedback. Opt. Lett. **29**, 1072–1074 (2004)
22. Simpson, T.B.: Mapping the nonlinear dynamics of a distributed feedback semiconductor laser subject to external optical injection. Opt. Commun. **215**, 135–151 (2003)
23. Wieczorek, S., Krauskopf, B., Lenstra, D.: Multipulse excitability in a semiconductor laser with optical injection. Phys. Rev. Lett. **88**, 063901 (2002)
24. Wieczorek, S., Krauskopf, B., Simpson, T.B., Lenstra, D.: The dynamical complexity of optically injected semiconductor lasers. Phys. Rep. **416**, 1–128 (2005)

Chapter 2
Exotic Behavior in Quantum Dot Mode-Locked Lasers: Dark Pulses and Bistability

Kevin Silverman, Mingming Feng, Richard Mirin and Steven Cundiff

Abstract Passively mode-locked semiconductor lasers with self-assembled quantum dot active regions can be operated in exotic output modes, stabilized by the complex gain and absorption dynamics inherent in these structures. One such device emits dark pulses—sharp dips on an otherwise stable continuous wave background—in an extended cavity design. We show that a dark pulse train is a solution to the master equation for mode-locked lasers and perform numerical modeling to test the stability of such a solution. A separate, monolithic design displays wavelength bistability and can be electrically switched between these two modes within just a few cavity round trips. This device can be made to switch between two stable wavelengths separated by just 7 nm up to over 40 nm with a contrast ratio of over 40 dB.

K. Silverman (✉) · M. Feng · R. Mirin
Optoelectronics Division, National Institute of Standards and Technology, Boulder, CO 80305, USA
e-mail: silverma@boulder.nist.gov; kevin.silverman@nist.gov

M. Feng
e-mail: mingming@boulder.nist.gov

R. Mirin
e-mail: mirin@boulder.nist.gov

S. Cundiff
Quantum Physics Division, JILA, National Institute of Standards and Technology and University of Colorado, Boulder, CO 80305, USA
e-mail: cundiffs@nist.gov

Z. M. Wang (ed.), *Quantum Dot Devices*, Lecture Notes in Nanoscale Science and Technology 13, DOI: 10.1007/978-1-4614-3570-9_2,
© Springer Science+Business Media New York 2012

Introduction

Background

Mode-locked lasers have become an essential tool in both industrial applications and scientific investigations. They are capable of generating ultrashort pulses (down to below 10 fs) enabling ultra-high peak powers and unbeatable time resolution of optically generated excitations in a wide variety of materials. There are many applications of ultrashort/broadband optical pulses that are hindered by the cost, complexity, and inefficiency of the mode-locked lasers used to produce such pulses. This reasoning led to significant effort in mode-locked diode lasers 10–15 years ago. However, these efforts ran up against a fundamental barrier that limited the brevity of the pulses, falling well short of the performance required for the most promising applications. Initially, diode lasers based on self-assembled quantum dots (QDs) were proposed to break this barrier. This optimism was fuelled by two unique properties of QDs. First, the large gain bandwidth (up to over 100 nm) of these materials, attributable to the inherent size and composition distribution of the individual QDs could easily support ultrashort pulses. Second, it was theorized that QDs would have a very small linewidth enhancement factor (LEF) because of the symmetric gain coefficient attributable to 3D confinement [1, 2]. The LEF determines the amount of nonlinear chirp imparted on the mode-locked pulse during amplification and seriously limits the duration and quality of the pulses generated [1]. After long attempts by many groups, using monolithic [3] and extended cavity schemes, QD mode-locked diode lasers have failed to reach the ultrashort pulse regime, although small improvements over quantum well material have been realized. Subsequent measurements have revealed that the gain dynamics in the QD active region under normal operating conditions are not as simple as initially thought. For instance, it has been shown that the LEF is not only significant, but that it has a strong dependence on carrier injection levels [4]. As is often the case, it turns out that these unwanted, unanticipated, properties lead to unexpected, exciting performance as well. Two such novel operating regimes discovered in QD-based mode-locked lasers are the subjects of this chapter.

QD Gain Chip

The design of the QD gain chip for both monolithic and extended cavity structures is that of a standard double heterostructure laser. The active region consists of a 10-fold stack of InGaAs QD layers embedded in a GaAs waveguide, which is sandwiched between AlGaAs cladding layers. A cross section detailing the layer growth and etch profile is displayed in Fig. 2.1. The upper and lower AlGaAs cladding is doped to facilitate current injection.

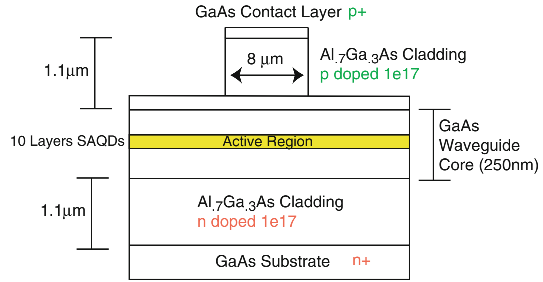

Fig. 2.1 Layer structure for the epitaxial material used in this work

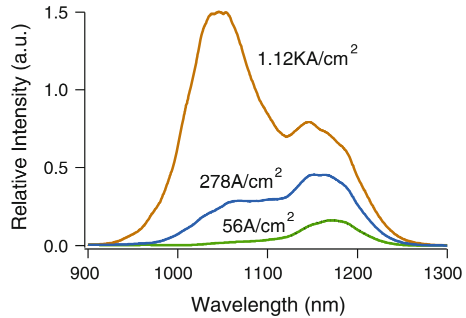

Fig. 2.2 Electroluminescence at various injection levels collected from the AR-coated QD gain chip

Standard photolithography and wet etching were used to etch a ridge into the top cladding layer. Electroluminescence from a typical device is displayed in Fig. 2.2. Clearly evident is the exceptionally large gain bandwidth mentioned in the Introduction. Also present is a strong rise in the excited state (ES) emission at higher injection levels due to state-filling effects. With inclusion of ES emission, the luminescence bandwidth of this device is greater than 150 nm. The ground-state transition alone has sufficient broadening to generate sub-100 fs pulses if used to its full potential.

Gain and Absorption Dynamics

Key to understanding the novel effects in a QD mode-locked laser is a detailed knowledge of the gain and absorption dynamics. It is the details of these processes that are responsible for stabilizing dark pulses and providing an appropriate operating region for bistable operation. It is therefore necessary to measure these properties of the laser material under operating conditions as close to the actual operating conditions as possible. The standard method for resolving these dynamics is ultrafast differential transmission spectroscopy, and many excellent reviews of the technique are available [5]. The experiment involves inducing a non-equilibrium carrier population in the gain medium with a resonant ultrafast laser pulse and then probing the decay of this excitation with a second time-delayed version of the pulse. All time-

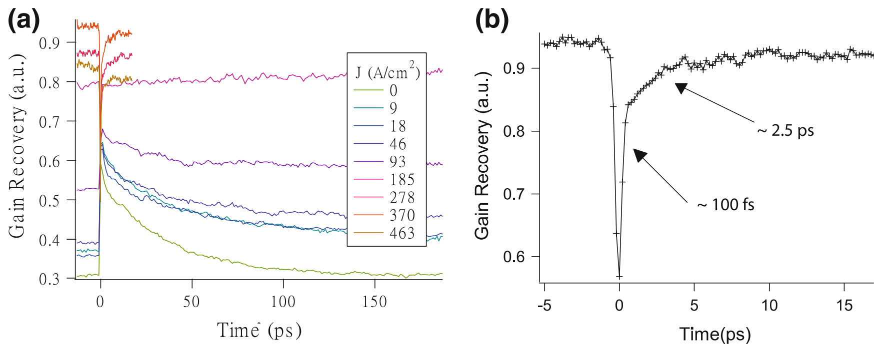

Fig. 2.3 **a** Recovery dynamics of the QD waveguide under various injection conditions. Current increases from *bottom* of figure to *top*. **b** Close-up view of the gain recovery at 278 A/cm^2

resolved data shown in this section was collected with differential transmission spectroscopy. Samples were antireflection coated or angle-cleaved in order to inhibit lasing at injection levels typical for laser operation.

Unfortunately, the desire to perform measurements on actual laser chips necessitates a substantial increase in the complexity of the DT measurement as compared to standard approaches. The difficulty arises when attempting to separate the pump from probe pulses for background-free detection of the probe transmission. The pump and probe propagate co-polarized through the QD waveguide in the same spatial mode. Therefore, the standard techniques of selecting the probe beam by its polarization or k-vector is not applicable. We choose to circumvent this problem by using a heterodyne pump-probe scheme as detailed by Hall et al. [6]. We give the probe beam a small frequency shift with an acousto-optic modulator and then beat the output of the waveguide with a local oscillator (LO) beam that does not interact with the sample. The probe beam can then be detected, without contamination from the pump beam, as a 60 MHz beat note between probe and LO.

Gain Recovery Dynamics

To investigate the recovery dynamics of the QD gain medium a positive bias must be applied to the p-i-n diode structure. Figure 2.3 shows differential transmission traces with the QD chip biased to different current densities. For reference, the transparency current density of this device is about 180 A/cm^2. Below this injection level the QDs are absorbing. When the current is higher than the transparency density, the QDs provide gain.

In Fig. 2.3a, the gain recovery dynamics at various injection levels is displayed. At time t = 0 the first pulse arrives and modifies the QD states. This depletes some of the gain (or saturates absorption), resulting in decreased (increased) transmission through the waveguide. There is a stark contrast between the dynamics

observed above and below transparency. Below transparency the absorption recovers by a combination of radiative recombination of photo-generated carriers and redistribution of those carriers over all dots in the ensemble. These are relatively slow processes proceeding on the 50 ps–1 ns timescale. The gain, on the other hand, recovers via the refilling of the active states from either ESs of the same dot or extended states that couple to all dots simultaneously. Recovery is clearly seen to proceed on two different, extremely fast, timescales. This is evident from Fig. 2.3a, in which the early time evolution of the QD population is shown in detail for a current bias of 278 A/cm^2. These two components of the decay can be extracted from the traces by fitting to a biexponential function. In general, the ultrafast response remains fairly constant over a broad range of currents above transparency with a value around 100 fs, possibly resolution limited. The second time constant indicated in Fig. 2.3b is in the single picosecond range and has a weak, but observable, dependence on injection current. In addition to the ultrafast processes, a longer recovery time, usually greater than 100 ps, is also observed.

QD gain recovery is usually described as proceeding in three steps: (1) intra-dot relaxation (sub-picoseconds), (2) carrier capture from the wetting layer to the dots (picoseconds), and (3) overall recovery of the carrier density of the electron injection on a timescale of hundreds of picoseconds. Dynamics on multiple timescales in QD gain materials are a unique property compared to other semiconductor gain materials.

Absorption Recovery Dynamics

When the QD ridge waveguide is reverse biased, it becomes a saturable absorber. The recovery dynamics of a QD saturable absorber differs dramatically from the case of a QD amplifier as the dots are initially empty, and photo-generated carriers fill the ground-state hole and electron levels. There is very little interaction with the wetting layer and ES carriers that dominates the response under carrier injection. We systematically investigated the recovery behavior of a QD saturable absorber with a pump-probe technique.

Pump-probe traces in transmission at different reverse bias voltages are shown in Fig. 2.4a. The traces are fitted with a biexponential function, where T_{a1} and T_{a2} are the two fast-recovery time constants, and A_{a1} and A_{a2} are the amplitudes. The results of the fitting time constants and amplitudes are shown in Fig. 2.4b. The plots show a picosecond-range, bias-independent recovery (T_{a1}) followed by a slower recovery (T_{a2}) decreasing from 38 to 2 ps as the reverse bias is increased from 0 to −9 V. When the reverse bias is higher than −4 V, the fast recovery time dominates the process. The shortest recovery time is 680 fs when the reverse bias is −9 V.

This behavior is consistent with a model [7] in which a QD's absorption recovery is considered to be the result of a combination of (1) fast thermal excitation of the injected ground-state carriers to higher states and (2) tunneling of the

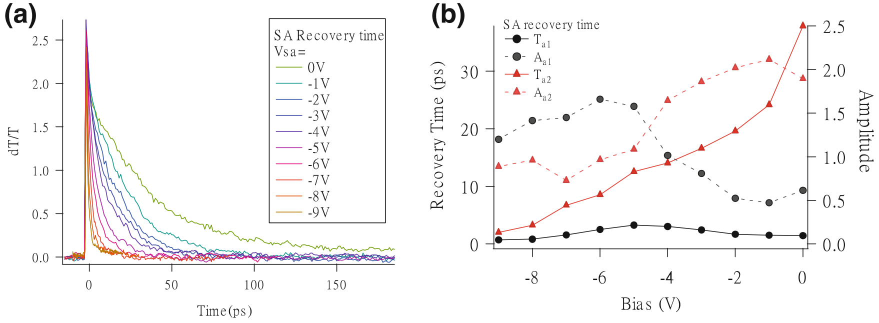

Fig. 2.4 **a** Absorption recovery dynamics for various reverse biases. Recovery duration decreases monotonically with increasing reverse bias. **b** Results of bi-exponential fit to the data displayed in **a**

excited carriers out of the dot. The timescale of the former process is bias independent, while the latter process becomes faster with increasing reverse bias. When bias is lower than −5 V, the tunneling of the carriers dominates the recovery of absorption. When the bias is higher than −5 V, thermal excitation is the primary process.

Our measured recovery times are comparable to those reported for a QD saturable absorber [8, 9]. In shallower dots, a shorter recovery time has been seen [10], which was interpreted as thermal escape.

Quantum dots under strong electric fields are powerful tools when used as saturable absorbers in mode-locked lasers. Under appropriate bias they display fast, sub-picosecond recovery dynamics capable of supporting 100 fs pulses. The fast recovery dynamics are promising for the optimization of saturable absorbers used for passive mode-locking of semiconductor lasers with ultrashort pulses and high repetition-rate pulses.

Dark Pulse Laser

Here, we discuss the first novel effect attributable to the unique gain dynamics in self-assembled QDs: the dark pulsed laser. Furthermore, we show that a dark pulse is a straightforward solution to the linearized version of the equation that describes the operation of a passively mode-locked laser [11]. To determine whether the solution is stable, and over what range of parameters, we perform simulations for the full (not linearized) equation. We show that the parameters of our laser fall in the range predicted to have stable dark pulses.

Dark pulses received considerable interest some years ago for their potential in the field of optical communications. When properly prepared as dark solitons, they propagate without distortion in material of normal dispersion [12], potentially opening up new transmission frequency choices for certain protocols [12].

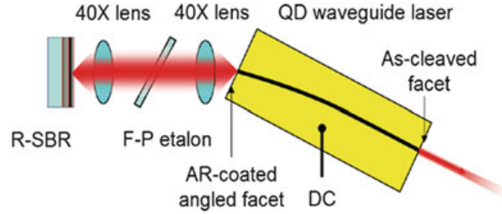

Fig. 2.5 Schematic of the extended-cavity semiconductor laser used for *dark* pulse generation. *R-SBR* resonant saturable absorber, *F–P* Fabry–Perot

Early attempts at generating dark pulses were made with bright pulse sources and external pulse shaping [13, 14]. Only recently, by our group and one other [15], have true mode-locked dark pulses been emitted directly from a laser. These recent successes have also led to some theoretical work into determining the conditions necessary for dark pulse generation [16].

We use an external cavity semiconductor diode laser to demonstrate the generation of dark pulses (Fig. 2.5). The gain section is a 5 mm long single-mode semiconductor ridge waveguide with InAs self-assembled QDs buried in the core. Light amplified by the QD active region is collimated, filtered by a Fabry–Perot etalon and focused on a saturable absorber to initiate mode-locking. The saturable absorbing medium, a few intentionally damaged semiconductor quantum wells, is grown in an integrated resonant structure to increase the electric field intensity and lower the saturation fluence. The saturable absorber structure also acts as an end mirror for the laser cavity. Spectral filtering to tune and restrict the lasing bandwidth was provided by a Fabry–Perot etalon with a transmission bandwidth of 10 nm. The flat facet of the semiconductor diode is used as the output coupler and has a reflectivity of approximately 30%. When the laser cavity is well aligned, lasing action occurs with 60 mA of current injected into the gain medium.

We monitored the output of the laser using a fast photodetector and recorded the output on a high-speed oscilloscope (shown in Fig. 2.6). A dark pulse train is clearly observed. The width of the pulses is measured to be 92 ps (a fit is shown in red in Fig. 2.6) and the modulation depth is approximately 70% [the ratio of the depth of the dark pulse to continuous wave (CW) level]. The clear comb confirmed the stability of the pulse train with narrow lines in the radio frequency spectrum of the photodiode output (shown in Fig. 2.6). We carefully calibrated the measurement system with a source of ultrafast bright pulses and determined the time resolution of our system to be about 60 ps, mostly limited by the sampling oscilloscope. This calibration also confirms that the signal is due to dark pulses and not artifacts of the detection system. A simple deconvolution of the instrument response function yields a true pulse width of 70 ps. Some ringing is evident in the signal for both dark and bright pulses, as is typically the case. Based on the calibration, we conclude that the pulses are dark pulses, although they are not "black" pulses, i.e., going to zero power, but rather "gray" pulses. The contrast ratio and modulation depth depend on the lasing wavelength (see supplementary material). Optical feedback into diode lasers can also result in trains of intensity dips that are attributed to coherence collapse [17, 18]. While there may be a

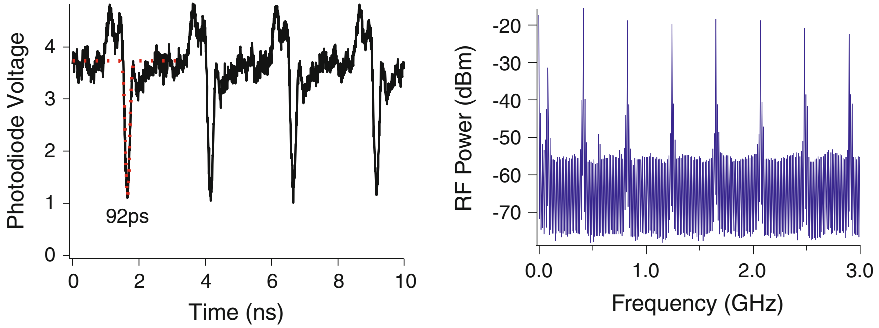

Fig. 2.6 Pulse train emitted from the *dark* pulse laser shown in the time and frequency domain

connection to our observations, the situation is quite different. Coherence collapse occurs when weak feedback is introduced to a chip-scale diode laser already above threshold. Our chip will not lase without the strong feedback from the extended cavity under any of the injection levels explored here, and pulsed operation does not occur without a saturable absorber in the cavity.

The question now becomes, what makes it possible for this dark pulse to exist? We can begin to understand the process by analogy with bright laser pulses. When a bright pulse interacts with a saturable absorbing medium, the pulse is shortened due to the increased transmission of the high intensity portion on the pulse with respect to the lower energy "wings". Now, let us assume that the saturable medium is already highly saturated by continuous radiation. If a small dark pulse interacts with this absorber it will be shortened as well, as the lower intensity portion on the pulse receives increased attenuation as the absorber is pulled out of saturation. We have shown this schematically in Fig. 2.7. This is the basic idea behind dark pulse generation. We will show later that our absorber is already in a highly saturated regime under CW excitation. In the following we will take a more formal approach to dark pulse generation, which confirms our basic understanding of the process and reveals the conditions necessary for observing this effect.

The theoretical understanding of mode-locked lasers typically starts from the "master equation" model developed by Haus [11]. In steady state, the pulse must reproduce itself every round trip. Considering only fast saturable gain, fast saturable absorption and spectral filtering due to the finite gain bandwidth yields the steady-state condition where u is the pulse amplitude, q (g) is the small-signal absorption (gain) coefficient normalized to the non-saturable loss in the cavity, E_a (E_g) is the saturation intensity for the absorber (gain), and ${\omega_g}^2$ is the gain bandwidth. This equation cannot be solved analytically, so we start by linearizing the gain and absorption saturation terms, giving

$$\left[1+\frac{q}{1+|u|^2/E_a}-\frac{g}{1+|u|^2/E_g}-\frac{g}{\omega_g^2}\frac{d^2}{dt^2}\right]u=0 \qquad (2.1)$$

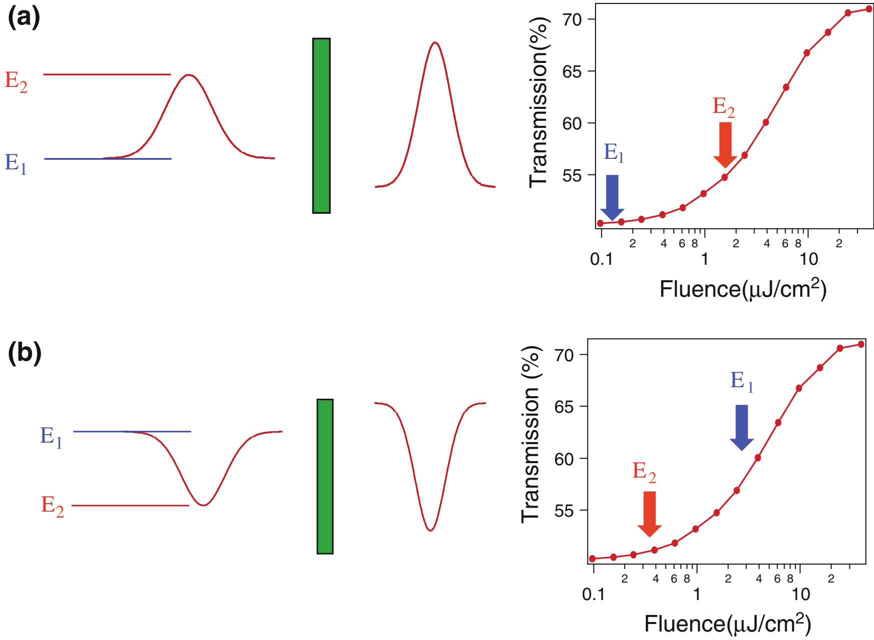

Fig. 2.7 Cartoons describing pulse shaping via interaction with a saturable absorber. **a** Conventional *bright* pulse shaping mechanism. **b** *Dark* pulse being accentuated by interacting with an absorber in a high degree of saturation

where u is the pulse amplitude, q (g) is the small-signal absorber (gain) coefficient normalized to the non-saturable loss in the cavity, E_a (E_g) is the saturation intensity for the absorber (gain), and $\omega_g{}^2$ is the gain bandwidth. This equation cannot be solved analytically, so we start by linearizing the gain and absorption saturation terms, giving

$$\left[1 + q\left(1 - \frac{|u|^2}{E_a}\right) - g\left(1 - \frac{|u|^2}{E_a}\right) - \frac{g}{\omega_g^2}\frac{d^2}{dt^2}\right]u = 0 \qquad (2.2)$$

A solution to this equation has the form of $u = u_0 \tanh(\tau/\tau_p)$. This solution corresponds to a CW wave of amplitude u_0 with a dip at $t = 0$ that has a width τ_p. The CW wave before the dip has a π phase shift compared to that after the dip. While this analysis shows that a dark pulse is a solution, it does not show that it is stable against perturbations, which is also a requirement for it to exist in a physical system such as a laser. Stability arises from the interplay of saturation and the spectral filtering. The linearized equation does not adequately capture the interplay, indeed bright pulses are not stable solutions. To study stability, we resort to numerical simulations of Eq. 2.1.

In a numerical simulation, additional terms can be added to more accurately model the real laser. This includes the biexponential gain recovery of QDs. We attribute these times to intra-dot relaxation and to refilling of the dots from the wetting layer,

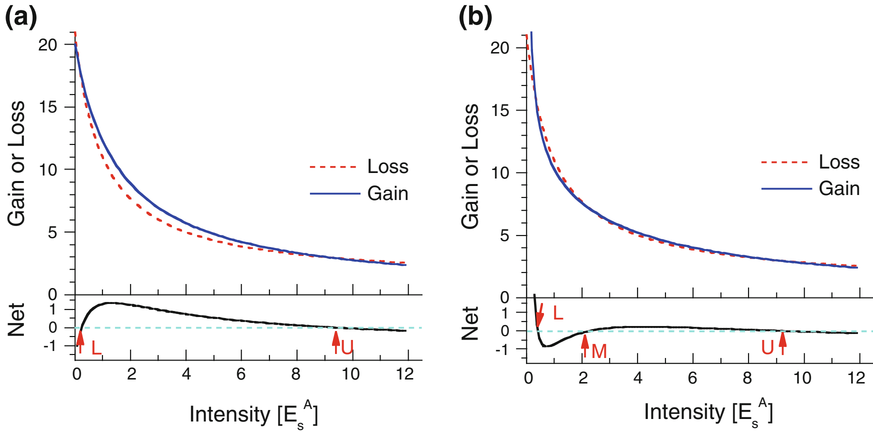

Fig. 2.8 Saturation of the absorption and **a** single-component gain and **b** two-component gain. The intensity is in units of the absorber's saturation intensity and the gain and loss are in units of the nonsaturable loss. The *lower* panels in **a** and **b** show the net gain (gain minus loss). The points where the net gain is zero are stable and labeled

respectively, as described in "Gain and Absorption Dynamics". Both time constants are fast compared to the measured width of the dark pulse, thus the approximation of fast dynamics is still valid; however, the model can better account for this behavior if the gain saturation includes two components with differing saturation powers. Furthermore, the gain will show very slow saturation determined by the carrier injection rate, which means a slow gain saturation part should be included in the gain simulation model. We model this effect by including a term that saturates based on the total energy in the cavity, rather than the instantaneous power. A split-step algorithm simulates each round trip through the laser cavity, calculating the saturation terms in the time domain and the spectral filtering in the frequency domain. Given an arbitrary input condition, usually a pulse, we track the evolution through many round trips until the change between successive round-trips is negligible. To test that the simulation is working properly, we verified that it did produce stable bright pulses with pulse parameters in agreement with previously published results [19].

We find that the simulation produces stable dark pulses when we include the two-component fast gain saturation and the slow saturation. Examining how the gain and absorption saturate, as is often done when discussing the stability of bright pulses in a mode-locked laser, gives insight into why the two-component saturation results in stable dark pulses. In Fig. 2.8, we plot the gain and absorption as a function of intensity for (a) single-component gain saturation and (b) two-component gain saturation. The net gain is plotted in the lower panel for each case. In both cases, the absorption is given by the first two terms in Eq. 2.1 and the intensity is normalized to E_a. Figure 2.2a shows the saturation curves for the situation where the absorber has lower saturation intensity than the gain, but the unsaturated absorption is higher than the unsaturated gain. For this situation, there are two intensities at which the gain and loss cross. Below the lower point,

denoted by "*L*" in Fig. 2.2a, the net gain is negative, so intensities in this range will decay to zero. Above intensity *L*, but below the upper crossing point, denoted by "*U*", there is net gain, so intensities in this range will grow until they reach intensity *U*. Above *U*, the net gain is again negative, so intensities will decay back to point *U*. It is easy to see that an initial bright pulse, or fluctuation, that exceeds intensity *L* will grow until its peak intensity reaches intensity *U*. This simple picture yields a threshold behavior, which produces a rectangular bright pulse. The spectral filter limits the rise and fall times of the pulse, resulting in a smooth pulse with a minimum duration determined by the bandwidth of the spectral filter.

By similar reasoning it initially appears that these conditions would also support a dark pulse. Consider CW operation at intensity *U*, which is stable, with a fluctuation that drops below point *L*. Again the threshold will drive the fluctuation to zero intensity, resulting in a rectangular dark pulse when the spectral filter is omitted. However, in contrast to the bright pulse, simulations show that the inclusion of the spectral filter actually destabilizes the dark pulse, causing it to evolve into a bright pulse.

Stable dark pulses appear in the simulation when we include two-component fast saturation and slow saturation in the model. Figure 2.2b shows the saturation curves for conditions that give a stable dark pulse. A third crossing point, denoted by "*M*" in Fig. 2.8b, occurs with net loss below it and net gain above. CW lasing at intensity above *M* will evolve to intensity *U*. If an intensity fluctuation occurs that crosses below *M*, it will evolve toward *L*. Again, if the spectral filter is omitted, a rectangular dark (gray) pulse will result. However, the inclusion of the spectral filter results in a stable, smooth dark pulse. The evolution of an initial bright pulse into a stable dark (actually gray) pulse is shown in Fig. 2.9a.

We have systematically explored parameter space to determine whether the formation of dark pulses is a robust phenomenon. For each parameter set, we run the simulation until a steady state evolves. We then categorize the steady state as being (1) CW, defined as having an intensity modulation less than 10%, (2) a dark pulse, defined as a dip in the intensity of greater than 10% with dark duration that is less than 40% of the round trip time, (3) a bright pulse, defined as a positive going excursion in the intensity of greater than 10% with bright duration that is less than 40% of the round-trip time, or (4) a pulsation, which is a modulation of greater than 10% that does not fulfill the criteria for a bright or dark pulse. Note that our definition of a dark pulse allows for a gray pulse and the definition of a bright pulse allows it to ride on a CW background. In Fig. 2.9b and c, we plot a "phase space" diagram for the laser showing what output it gives as we vary the two fast gain saturation parameters (larger fast gain saturation intensity I_{gh} and smaller fast gain saturation intensity I_{gl}, both are normalized to the absorption saturation parameter I_q). As I_{gh} increases, the laser goes from CW, to dark pulses, to pulsations and finally to bright pulses. This sequence remains the same as I_{gl} is varied, although the transition between the regimes occurs at a higher I_{gh} as the I_{gl} is increased. We have also varied other parameters and find that the basic structure of this map does not change. The contours in the dark pulse region are lines of constant modulation depth. The darker shaded regions have a modulation closer to one (black pulse). The dark pulse modulation depth is increased (the dark pulses change from gray pulses to black pulses) when I_{gh} and I_{gl} are increased.

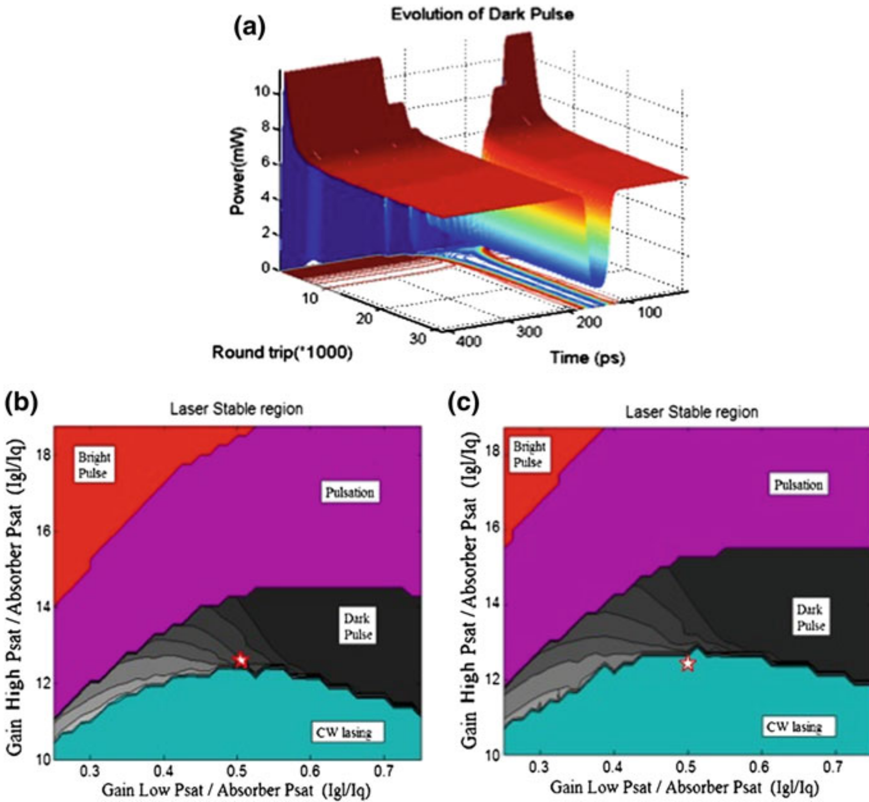

Fig. 2.9 Simulation results. **a** Evolution of initial bright pulse seed into a steady-state solution showing a gray pulse. **b** Phase space map showing stable solution for various parameters. Star indicates the best estimate of the operating point for the experimental conditions when the laser produces dark pulses. **c** Phase space map and estimated operating point for increased injection current, where laser produces a CW output

We have made our best estimate of the operating parameters corresponding to the experimental observation of dark pulses (see supplementary material) and mark it with a star in Fig. 2.3b. It falls well within the region predicted to produce dark pulses. Experimentally, it is difficult to systematically vary the operating parameters. We did increase the injection current and find that a transition from dark pulses to CW operation occurs. A higher injection current means a higher slow gain. In Fig. 2.3c we show the phase space diagram for a higher slow gain where CW operation occurs and find that our best estimate of the operating point falls within the region predicted for CW operation.

Our results experimentally demonstrate a new operating regime for lasers, namely the generation of a train of dark pulses. The theoretical analysis shows that dark pulses are solutions to the master equation describing mode-locked lasers and simulations show that dark pulses are stable. It is the complex dynamics of the QD active region that stabilizes the dark pulse train.

Bistable Quantum Dot Lasers

Introduction

Wavelength bistable lasers are attractive devices for incorporation in next generation optical networks where the time-consuming and component-intensive tasks of optical-to-electrical and electrical-to-optical conversion need to be minimized [20]. They may be employed as compact and fast wavelength switching devices or as memory elements in photonic circuits, due to their robust latching properties [21, 22]. For such devices to be cost competitive they should also be compatible with chip-level optical architecture. Therefore, monolithic devices such as semiconductor diode lasers are more desirable than other types of optical bistable lasers, such as fiber lasers and external cavity lasers [23]. Conventional diode lasers do not normally exhibit wavelength bistability, so we must look to a design with added flexibility while still being monolithic. Two-section diode lasers that are currently being used to generate ultrafast mode-locked pulses are a potential candidate. Working with mode-locked lasers also offers the additional advantage of being able to support extremely high-speed applications.

In two-section diode lasers, the ability to separately control the gain and absorbing regions can lead to various forms of optical bistability. In particular, these lasers can exhibit power bistability when the current applied to the gain section is swept [24, 25]. Wavelength bistability has been more difficult to achieve, but was observed in continuous-wave, two-section distributed feedback (DFB) diode lasers almost two decades ago [26]. There have been relatively few results on bistable wavelength diode lasers since then. In the last few years, the success of mode-locked, two-section QD diode lasers has led to new and exciting results in the area of wavelength bistability [27]. For example, bistability was recently demonstrated between the ground and ES transitions of the QD gain medium [28]. In this case the subordinate mode was not completely quenched throughout the bistable region, possibly due to the fact that cross-gain saturation between ground and ESs was not strong enough. In our earlier work, we reported wavelength bistability from a two-section QD diode laser with a very high contrast between two lasing wavelengths both supported by the ground state (GS) gain [29].

In this section, we present a full investigation of wavelength bistability in two-section QD diode lasers. We first analyze simplified coupled mode equations as a model for the observed bistability. With this simple understanding we can explain why the unique gain dynamics of QD ensembles lead to some of the new results. We then present our experimental results on wavelength bistability from three different two-section passively, mode-locked diode lasers. The devices are not always mode-locked, but when we study the bistability, we only investigate devices working in the stable mode-locked region. All three lasers show wavelength bistability when the reverse bias voltage on the saturable absorber is swept, but they have different wavelength spacings between two bistable branches. Because our lasers operate in the mode-locked region, there are a group of longitudinal modes in one lasing wavelength. Here, the word “mode” refers to one lasing wavelength.

Mode Competition

To gain a general understanding of the important features of our bistable laser, we analyze a simplified set of coupled differential equations [30]. The two-section laser contains regions of both saturable gain and absorption in which lasing modes experience gain or loss and interact with each other. If we include both gain and absorption regions in the same term, assume fast dynamics in the gain and saturable absorber, and make a "weak" saturation approximation, then the intensities of two lasing modes, I_1 and I_2, evolve according to rate equations

$$\frac{dI_1}{dt} = (\alpha_1 - \beta_1 I_1 - \theta_{12} I_2) \times I_1, \tag{2.3a}$$

$$\frac{dI_2}{dt} = (\alpha_2 - \beta_2 I_2 - \theta_{21} I_1) \times I_2, \tag{2.3b}$$

where α_i is the small-signal gain minus loss for each mode, and β_i and θ_{ij} represent the self- and cross-saturation coefficients. These are the Lotka-Volterra equations, which are often used to describe competition between biological species [31]. For certain values of the constants in Eq. 2.3a, there are exactly two steady-state solutions that are characterized by nonzero intensity in only one of the two potential modes. These solutions correspond to one mode (species) always winning out over the other regardless of initial conditions. We are interested in the case in which both modes are simultaneously stable. If this solution is stable to small perturbations, then both modes will coexist in the steady state. If this point is not stable, the system will progress toward one or the other solutions with its ultimate destination being determined by initial conditions. Bistability occurs in this regime.

To reveal the conditions required for bistable operation we can perform a perturbation analysis around the dual mode solution. This point is unstable, and therefore bistable behavior is predicted if

$$\frac{\theta_{12}\theta_{21}}{\beta_1\beta_2} > 1. \tag{2.4}$$

This condition requires the cross-saturation between the two modes to be stronger than the self-saturation. Obviously achieving this condition is quite difficult in a single-section laser. On the other hand, if we include a separate saturable absorption region, the cross-saturation term now consists of two terms

$$\theta_{12} \approx \theta_{21} = \theta_{12}^{g} - \theta_{12}^{a}, \tag{2.5}$$

as does the self-saturation term

$$\beta_1 \approx \beta_2 = \beta_1^{g} - \beta_1^{a}. \tag{2.6}$$

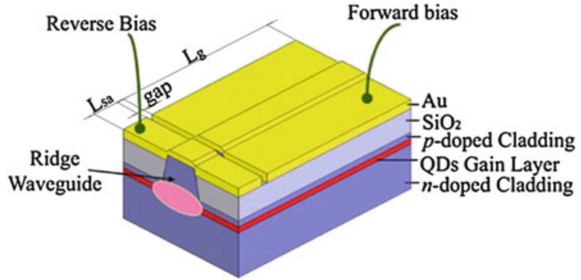

Fig. 2.10 Schematic of the two-section quantum dot diode laser

These add flexibility such that Eq. 2.6 can be satisfied in a system with strong cross-saturation in the gain region and weak cross-saturation in the absorption region. One final consideration is that the overall gain in the two potential modes must be similar. Without this balance, the dual-mode solution will no longer satisfy Eq. 2.4, and stable single-mode operation will prevail.

It is possible to extend the analysis presented here by including full saturation of the absorption and gain [32]. This model predicts more exotic forms of bistability such as that observed in Ref. [28] where single-mode and dual-mode operation are bistable with respect to each other.

Device Structure and Characterization

We fabricated and tested three different two-section QD lasers. A schematic of a generic laser design is shown in Fig. 2.1, as in [29]. It consists of a two-section ridge waveguide where one section is electrically pumped while the other section is reverse biased as a saturable absorber. The active region of all devices consists of a 10-fold stack of InGaAs QD layers embedded in a GaAs waveguide, which is sandwiched between $Al_{0.7}Ga_{0.3}As$ cladding layers. The epitaxial structure is identical to the one used in the extended cavity configuration in order to generate dark pulses. The waveguide was fabricated by standard photolithography and wet etching. A strip waveguide was etched in the top cladding layer followed by the removal of a small section of the heavily doped cap layer to provide isolation between the two sections. The lengths of the gain section and the saturable absorber section are L_g and L_{sa}, respectively. *P*-and *n*-type ohmic contacts were established with Ti/Au and Ni/AuGe/Ni/Au, respectively. No coating was applied to the cleaved facets. The device was mounted *p*-side up on a copper heat sink that was thermoelectrically temperature controlled (Fig. 2.10).

The same QD material was used in all three devices. The QDs have a GS transition at ~ 1,170 nm, with a full-width at half maximum of 60 nm, as determined by a fit to the low excitation electroluminescence data in Fig. 2.2. At higher injection levels, an ES centered at approximately 1,050 nm becomes apparent. This broad, inhomogeneous, gain spectrum is indicative of the size/shape distribution of the QD ensemble.

Table 2.1 Relevant parameters for the three devices tested in this section

	L_g(mm)	L_{sa}(mm)	Guide width (micrometers)	J_{th}(A/cm^2)
Device 1	5.5	0.3	6	136
Device 2	5.5	0.3	6	142
Device 3	2.8	0.3	8	290

It is interesting that the gain spectrum becomes fairly flat over an approximately 200 nm range at injection levels around 300 A/cm^2. This situation leads to interesting mode competition effects in the laser cavity as discussed above. Wavelength bistability is studied in three different laser geometries. The relevant parameters for the three different lasers are summarized in Table 2.1. All three lasers exhibit similar characteristics, thus we will discuss the general features of the first device in-depth as a representative example and then compare and contrast all three devices.

Device 1

The first device we tested has a waveguide width of 6 μm. The length of the gain section (L_g) is 5.5 mm, and the length of the saturable absorber section (L_{sa}) is 0.3 mm. The operating temperature is 12°C. With the saturable absorber region electrically floating, the threshold current is 45 mA (threshold current density is 136 A/cm^2), and the lasing wavelength is 1,173 nm.

The optical spectrum and output power of the QD laser were measured with current injection into the gain section and a reverse-bias voltage applied to the saturable absorber section. With a fixed reverse bias on the saturable absorber.

The optical spectrum and output power of the QD laser were measured with current injection into the gain section and a reverse-bias voltage applied to the saturable absorber section. With a fixed reverse bias on the saturable absorber, the laser exhibits a hysteresis loop in the power-current characteristics [33, 34]. This typical behavior for mode-locked diode lasers can be attributed to the strong hole-burning in the absorber region that allows the laser to stay above threshold even when the injection level is brought below the unsaturated zero-gain point.

When the laser is operated with fixed injection current to the gain region and a varying bias on the saturable absorber region, hysteresis and bistability are observed in the lasing wavelength, as shown in Fig. 2.3a. Throughout the saturable absorber bias range of −6 to −1 V, the laser has two stable wavelengths, 1,163 and 1,173 nm.

By comparing with the electroluminescence data in Fig. 2.2, it is clear that ground-state emission is responsible for both lasing states. As is evident from Fig. 2.11b, the two lasing modes are well separated, and the power contrast between them is more than 30 dB. The switchable wavelength range remains relatively constant throughout the region and is around 7.7 nm when $V_{sa} = -3$ V.

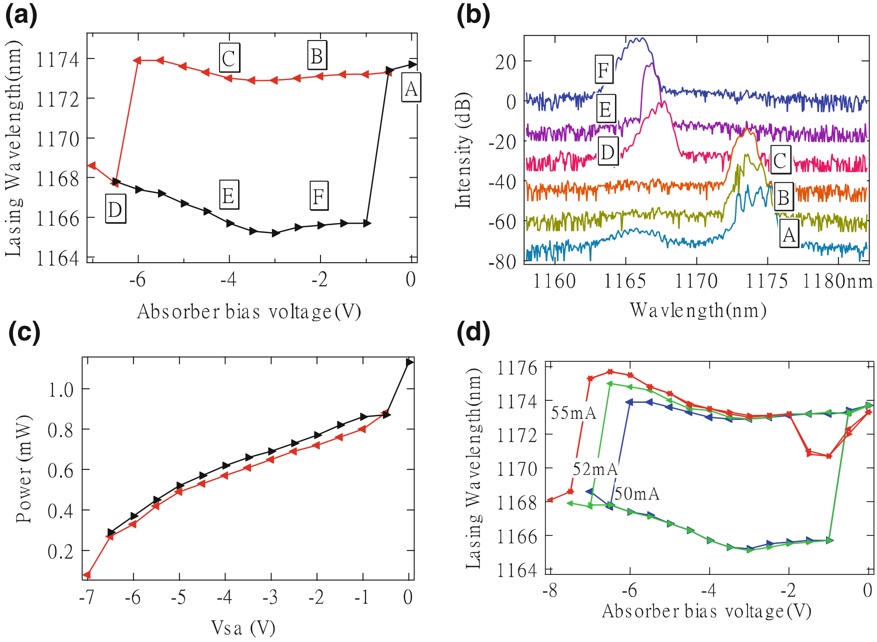

Fig. 2.11 **a** Wavelength of laser emission as a function of saturable absorber bias (V_{sa}) at a fixed gain section current of 50 mA. **b** Optical spectra at various positions in the *left* hysteresis curve (the curves are offset for clarity). **c** Optical power as a function of V_{sa}. **d** Lasing wavelength vs V_{sa} at different gain currents. The *left-pointing triangle* means the trace is taken with the bias ramped up, from 0 to −7 V; The *right-pointing triangle* means the trace is taken with the bias ramped down, from −7 to 0 V

Moreover, the power in each of the two lasing modes is almost identical, as shown in Fig. 2.11c. For example, at $V_{sa} = -4$ V, the power ratio between 1,173 nm (0.57 mW) and 1,166 nm (0.62 mW) is 0.92.

We also found that wavelength bistability can be observed only in the narrow range of gain currents between 50 and 52 mA, as shown in Fig. 2.11d. When the current is too low, the laser is either unstable or only one lasing wavelength is observed at a single saturable absorber bias voltage. When the current is too high, e.g., at the 55 mA shown in Fig. 2.11d, the lasing wavelength varies almost continuously as the saturable absorber bias voltage is varied, and there is no bistability. Note that the bistable area at 52 mA is slightly bigger than the area at 50 mA, with the higher energy mode surviving at larger reverse biases. This is easily explained by the additional gain provided to the shorter wavelength mode at higher injection levels due to the strong state-filling effects in QDs. Therefore, the points where the gain of the two modes becomes dissimilar to support bistable operation moves to lower reverse bias voltage.

We also measured the pulse characteristics of the laser output in the two branches of the hysteresis loop shown in Fig. 2.11. We observed that stable

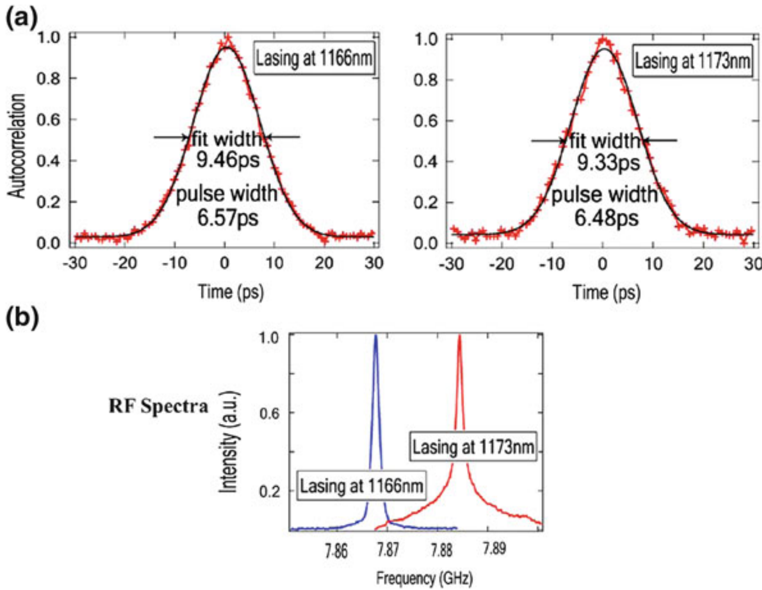

Fig. 2.12 **a** Intensity autocorrelation for the mode-locked pulses on different branches of the hysteresis curve, both at −4 V *reverse* bias. **b** Corresponding radio-frequency spectra

mode-locking occurs in both branches of the hysteresis loop. An autocorrelation trace measured with the laser operating in each branch at $V_{sa} = -4$ V is displayed in Fig. 2.12a. The corresponding pulse width is about 6.5 ps, assuming a Gaussian pulse shape, and is essentially identical in both branches. The pulse could be shortened by increasing the reverse bias, and the shortest value obtained is 3 ps at −6 V. Figure 2.12b shows the radio-frequency (RF) spectra of the device. It indicates a pulse train with a repetition rate of around 7.9 GHz corresponding to a round-trip time of 120 ps. The difference in frequency between the two branches is approximately 15 MHz, with the longer wavelength branch at higher frequency, as expected from the normal dispersion in the GaAs waveguide.

Devices 2 and 3

We tested two other lasers exhibiting bistability (see Table 2.1), a laser that was nominally identical to the first one but with a higher threshold current (device 2) and one with a different ratio of gain length to absorber length (device 3). As expected, device 2 showed qualitatively similar performance to device 1. Bistability is observed at current injection levels between 55 and 64 mA, which is a slightly higher injection level than for device 1. Figure 2.13a compares the two hysteresis curves. Device 2 exhibits a much larger wavelength spacing between the modes, with the shorter wavelength mode at approximately the same location. This

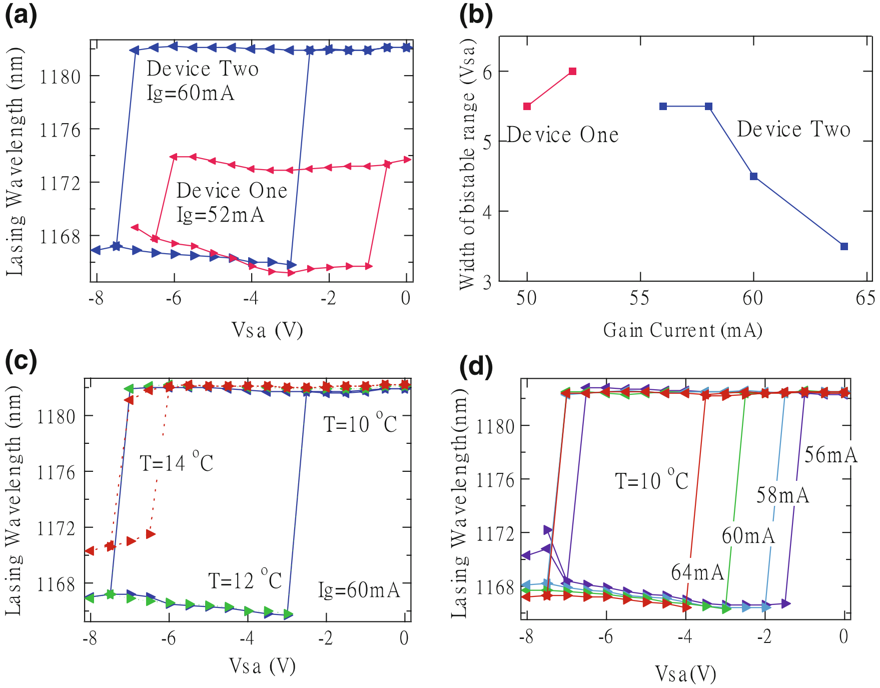

Fig. 2.13 Wavelength bistability comparison between device 1 (in *red* line) and device 2 (in *blue* line). **a** Laser emission as a function of saturable absorber bias (V_{sa}). **b** Width of bistability at different gain current injection. Device 2's lasing wavelengths as a function of saturable absorber bias (V_{sa}). Wavelength bistability data for device 2: **c** At different temperatures (gain current 60 mA). **d** At different gain currents. The *left-pointing triangle* means the trace is taken with the bias ramped up from 0 to −8 V. The *right-pointing triangle* means the trace is taken with the bias ramped down from −8 to 0 V

result is consistent with the higher injection level producing a wider gain bandwidth due to stronger state-filling effects at higher current. These results clearly demonstrate the ability to tune the switchable range in this laser by simple adjustments to the amount of gain and/or loss present in the device.

In Fig. 2.13b, we compare the width of the bistability region for the first two devices as a function of current injected to the gain section. The bistable region decreases with injection current for device 2, which is the complete opposite behavior of the first device. The reason for this difference is that the hysteresis loop for device 2 collapses on the low energy side while device 1 shuts down on the higher energy side. Again, this is consistent with the higher energy mode beginning to dominate at higher injection levels. The detailed bistable data for device 2 are present in Fig. 2.13c for different device temperatures and Fig. 2.13d for different gain currents.

The third laser we tested had a different geometry, with $L_{sa} = 0.3$ mm, $L_g = 2.8$ mm, and a waveguide width = 8 μm. With the saturable absorber region floating and a temperature of 10°C, the threshold current is 65 mA (threshold

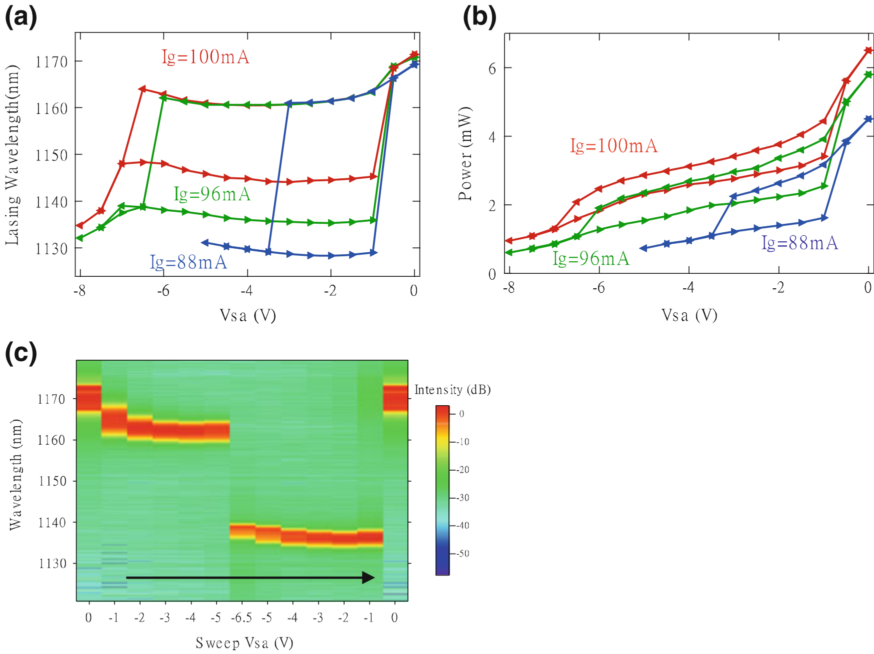

Fig. 2.14 Device 3 lasing wavelengths as a function of saturable absorber bias (V_{sa}). **a** Different gain currents when the temperature is 10°C. **b** Power bistability at different currents. **c** 3D optical spectrum when V_{sa} is swept from 0 to −6.5 V and back to 0 V at I_g = 96 mA. The direction is shown by the arrow (the intensity is on a log scale). In **a** and **b**, the *left-pointing triangle* means the trace is taken with the bias ramped up from 0 to −8 V; The *right-pointing triangle* means the trace is taken with the bias ramped down from −8 to 0 V

current density is 290 A/cm^2). This threshold current density is about twice that of the first device because more injection current is needed to overcome the mirror loss due to a shorter gain segment. The initial lasing mode is at 1,170 nm, which is slightly shorter than those of the first two devices. The reason is that the gain region current density is much higher for the third device, and the overall gain peak blue shifts because of state filling. With the significantly higher current density injection, the overall gain profile is much larger and flatter compared to the first two devices (see the EL spectra in Fig. 2.2), resulting in a very large wavelength range in which modes experience similar amounts of gain. This fact leads to more complicated and interesting properties for device 3.

The wavelength-bias voltage hysteresis curve for the third device taken at various injection currents is shown in Fig. 2.14a. The switchable range is 32 nm when the gain current is 88 mA (current density is 393 A/cm^2). When the current is increased to 96 mA (current density is 428 A/cm^2) and 100 mA (current density is 446 A/cm^2), the ranges change to 25 and 16 nm, respectively. The gain region current range for wavelength bistability is from approximately 84–104 mA. Throughout this region, the spacing between laser modes takes on three discrete values, as shown in Fig. 2.14a.

We also show the power-bias voltage hysteresis curve in Fig. 2.14b for different pump currents. The power difference between the two branches is the largest at low current. The difference decreases monotonically as the current is increased while the wavelength difference in the two branches decreases. To demonstrate the high isolation between the two lasing branches, a 3D optical spectrum is plotted for $I_g = 96$ mA in Fig. 2.14c. The black arrow shows the direction of the sweep for the saturable absorber bias. The modes in the two branches are well distinguished and isolated.

The most interesting property of this device is that the switchable range changes with gain current, which did not happen with the first two devices. As the injection to the gain region is increased, the separation between the lasing modes becomes smaller. The longer wavelength mode stays relatively constant, while the shorter wavelength mode moves progressively longer. This behavior is different than the trend observed in the first two devices. It is also counterintuitive, since one would expect higher energy modes to have relatively more gain at higher current densities, due to state filling.

There are two factors that, in combination, may be responsible for these results. At these higher current densities the gain curve is fairly flat, and therefore subtle changes can dictate which mode becomes the eventual winner. Because the gain curve is flat, the relative amounts of gain and loss determine where the gain peak occurs. Since the loss in the absorber region is monotonically increasing in this region (unlike the gain), the net gain peak shifts to lower energies as the relative strength of the absorption grows. This scenario fits well with the observation of higher energy modes lasing as the gain is increased (absorption relatively decreased).

Switching Mechanism

An additional requirement for a practical bistable laser is an effective switching mechanism. The lasers in this work can be switched electrically by modulating the bias voltage on the absorber. There is a strong red shift of the QD transition energy with the application of an electric field. This shift is known as the quantum-confined Stark effect (QCSE) and has been measured to be up to 2 nm/V in similar structures [35]. The effect on the overall laser cavity (i.e., saturable absorber plus gain region) is to shift the peak gain to shorter wavelengths. Once one laser mode becomes too highly favored over the other, bistability breaks down and single mode operation occurs, causing the laser to abruptly change modes.

To measure this shift, we monitored the electroluminescence spectrum as a function of saturable absorber bias from the first laser. In this experiment, one of the facets was antireflection coated to inhibit lasing, and light was extracted from the facet adjacent to the saturable absorber region. The result is shown in Fig. 2.15. Although not a quantitative measure of the gain spectrum in our laser cavity, it is clear that the effect of the increased bias is not only to reduce the overall gain, but also to shift the peak. This peak shift explains why the low-bias lasing mode is always red-shifted compared to the high-bias lasing mode.

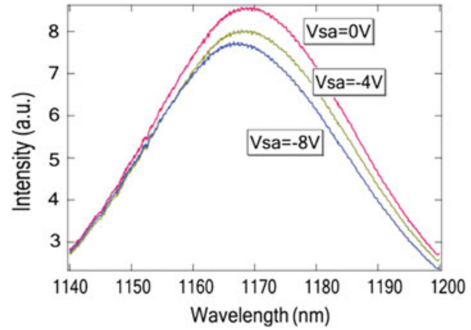

Fig. 2.15 Electroluminescence spectra taken from a sample similar to the first laser, but with an antireflection coating to inhibit lasing. The light was extracted from the facet adjacent to the saturable absorber region. V_{sa} is the bias voltage of the saturable absorber region

Switchable Spacing

The three devices were made from the same wafer, but because of their different structures, the characteristics, including threshold current density and lasing wavelength, of the three lasers were different. Nevertheless, at different pump-current densities, all three devices showed lasing-wavelength bistability. There is also a remarkable characteristic that stands out when the switchable spacings of all three devices (Fig. 2.16) are plotted together. First, the spacing between modes for devices 2 and 3 at the lowest current overlap almost exactly throughout the entire bistable range. Second, the switching occurs in discrete steps. Observed values are 7, 16, 25, and 33 nm; all are roughly multiples of 8–9 nm. This behavior is especially interesting, because there are only two modes lasing at one time. The spacing is maintained for widely spaced modes even without the intermediate modes being active.

Time-resolved and spectral hole-burning measurements have shown that the homogeneous linewidth of InGaAs self-assembled QDs is roughly 10 nm at room temperature [36]. The reverse biased section is depleted of carriers; therefore, this width is a reasonable value to assume for the QDs in this section of the laser. To avoid excessive cross-saturation in the absorber region, modes must be spaced by more than the homogeneous linewidth, a criterion for bistable operation, as explained above. With this reasoning we could expect to never observe bistability of two modes that are separated by less than about 10 nm. This fact would also explain the similar spacing seen for different devices, as it is the optical properties of the QDs that set the scaling.

More difficult to explain is the consistent spacing of widely separated modes in integer multiples of 8–9 nm. This strongly suggests that although only two modes are seen to lase at one time, the other dormant modes still play a role in the laser dynamics.

Switching Time

The wavelength hysteresis loop for a QD diode laser could be used for applications that require switching between wavelengths on a short timescale. When the saturable absorber is biased in the middle of the hysteresis loop, the output

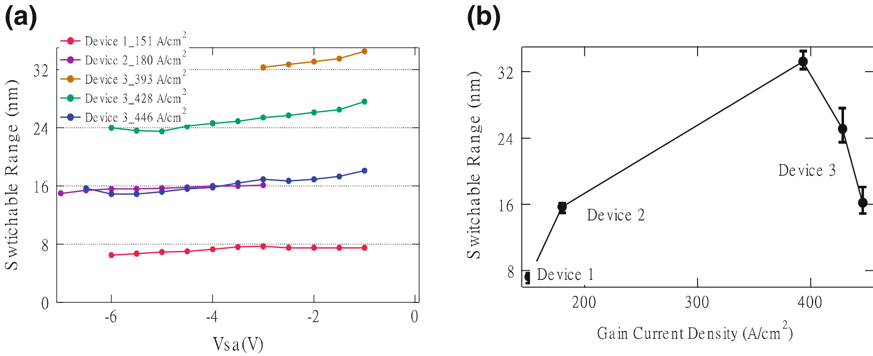

Fig. 2.16 Comparison of the switchable range of the three devices. **a** Different saturable absorber bias voltage. **b** Different gain-current densities. The error bars are the maximum and minimum ranges

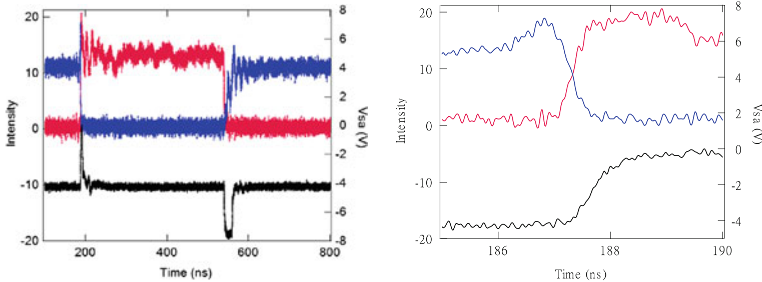

Fig. 2.17 Switching wavelengths between two bistable wavelengths in device 3. The *red* line is the intensity of *long* wavelength branch (1,170 nm), the *blue* line is the intensity of *short* wavelength branch (1,140 nm), and the *black* line is the V_{sa} voltage

wavelength can be switched by an ultrafast electrical pulse of the required polarity. Since no current is injected into the saturable absorber region, the modification of the saturable absorber that selects the lasing mode should be as fast as the pulse injected. Therefore, the lower limit of switching time between the two stable states for a two-section diode laser is determined by the saturation recovery time of the saturable absorber section, as in Ref. [25]. In QDs, carrier recovery time can be sub-picosecond, as measured in "Gain and Absorption Dynamics". In our case, the output of the diode laser is a pulse train, and a minimum of one round-trip is needed for the next lasing state to be established. This timescale is longer than the saturation recovery in our absorber, therefore the wavelength-switching time should be on the order of the round-trip time of the diode laser.

To measure the switching time we dispersed the output of device 3 with a grating and measured each wavelength mode independently. A high-speed electrical pulse was applied to the saturable absorber, and output power data was collected with two high-speed photodiodes and an oscilloscope. The measured switching dynamics are presented in Fig. 2.17. If we define the switching time to

be measured as the time from 90% of the intensity of the wavelength one mode to 90% intensity of the wavelength mode two, then the time to switch from the short wavelength branch to the long wavelength branch is about 150 ps. In this case the switch occurs faster than the voltage pulse, indicating that the jump in wavelength takes place on a narrow voltage range. This measured switching time is only about two round-trips time of the laser.

Conclusion

In conclusion, we have reviewed two novel effects displayed in QD lasers, wavelength bistability, and dark pulse mode-locking. Both these effects are attributable to the complicated recovery dynamics of the QD gain and absorber material. The dark pulse laser was one of the first of its kind and may find application where broadening-free propagation of optical pulses is required in materials with normal dispersion. The bistable laser is electrically switchable within just a few round trips of the cavity and may find use as an optical memory element in next generation optical networks due to its robust latching properties.

References

1. Coldren, L.A., Corzine, S.W.: Diode Lasers and Photonic Integrated Circuits. Wiley, New York (1995)
2. Borri, P., Langbein, W., Hvam, J.M., Heinrichsdorff, E., Mao, M.H., Bimberg, D.: Ultrafast gain dynamics in InAs-InGaAs quantum-dot amplifiers. IEEE Photonics Technol. Lett. **12**(6), 594 (2000)
3. Rafailov, E.U., Cataluna, M.A., Sibbett, W., Il'inskaya, N.D., Zadiranov, Y.M., Zhukov, A.E., Ustinov, V.M., Livshits, D.A., Kovsh, A.R., Ledentsov, N.N.: High-power picosecond and femtosecond pulse generation from a two-section mode-locked quantum-dot laser. Appl. Phys. Lett. **87**(8), 081107 (2005)
4. Schneider, S., Borri, P., Langbein, W., Woggon, U., Sellin, R.L., Ouyang, D., Bimberg, D.: Linewidth enhancement factor in InGaAs quantum-dot amplifiers. IEEE J. Quantum Electron. **40**(10), 1423 (2004)
5. Diels, J.-C., Rudolph, W.: Ultrashort Laser Pulse Phenomena, 2nd edn. Academic, New York (2006)
6. Hall, K.L., Lenz, G., Ippen, E.P., Raybon, G.: Heterodyne pump-probe technique for time-domain studies of optical nonlinearities in waveguides. Opt. Lett. **17**(12), 874 (1999)
7. Kapteyn, C.M.A., Lion, M., Heitz, R., Bimberg, D., Brunkov, P.N., Volovik, B.V., Konnikov, S.G., Kovsh, A.R., Ustinov, V.M.: Hole and electron emission from InAs quantum dots. Appl. Phys. Lett. **76**(12), 1573 (2000)
8. Rafailov, E.U., McRobbie, A.D., Cataluna, M.A., O'Faolain, L., Sibbett, W., Livshits, D.A.: Investigation of transition dynamics in a quantum-dot laser optically pumped by femtosecond pulses. Appl. Phys. Lett. **88**(4), 041101 (2006)
9. Malins, D.B., Gomez-Iglesias, A., White, S.J., Sibbett, W., Miller, A., Rafailov, E.U.: Ultrafast electroabsorption dynamics in an InAs quantum dot saturable absorber at 1.3 mm. Appl. Phys. Lett. **89**(17), 171111 (2006)

10. Borri, P., Langbein, W., Hvam, J.M., Heinrichsdorff, F., Mao, M.H., Bimberg, D.: Spectral hole-burning and carrier-heating dynamics in InGaAs quantum-dot amplifiers. IEEE J. Sel. Top. Quantum Electron. **6**(3), 544 (2000)
11. Haus, H.A.: Mode-locking with a fast saturable absorber. J. Appl. Phys. **46**, 3049 (1975)
12. Kivshar, Y.S., Luther-Davies, B.: Dark optical solitons: physics and applications. Phys. Rep.-Rev. Sect. Phys. Lett. **298**(2–3), 81 (1998)
13. Haelterman, M., Emplit, P.: Optical dark soliton trains generated by passive spectral filtering technique. Electron. Lett. **29**(4), 356 (1993)
14. Weiner, A.M., Heritage, J.P., Hawkins, R.J., Thurston, R.N., Kirschner, E.M., Leaird, D.E., Tomlinson, W.J.: Experimental observation of the fundamental dark soliton in optical fibers. Phys. Rev. Lett. **61**(21), 2445 (1988)
15. Zhang, H., Tang, D.Y., Zhao, L.M., Wu, X.: Dark pulse emission of a fiber laser. Phys. Rev. A **80**(4), 045803 (2009)
16. Ablowitz, M.J., Horikis, T., Nixon, S., Frantzeskakis, D.: Dark solitons in mode-locked lasers. Opt. Lett. **36**(6), 793 (2001)
17. Lenstra, D., et al.: Coherence collapse in single-mode semiconductor lasers due to optical feedback. IEEE J. Quantum Electron. **QE-21**(6), 674–679 (1985)
18. Carroll, O., et al.: Feedback induced instabilities in a quantum dot semiconductor laser. Opt. Express **14**(22), 10831 (2006). 30 Oct
19. Kärtner, F.X., Kopf, D., Keller, U.: J. Opt. Soc. Am. B **12**, 486–496 (1995)
20. Kawaguchi, H.: Bistable laser diodes and their applications: state of the art. IEEE J. Sel. Top. Quantum Electron. **3**(5), 1254 (1997)
21. Kawaguchi, H., Mori, T., Sato, Y., Yamayoshi, Y.: Optical buffer memory using polarization-bistable vertical-cavity surface-emitting lasers. Japan. J. Appl. Phys. Part 2-Lett. Express Lett. **45**(33–36), L894 (2006)
22. White, I., Penty, R., Webster, M., Chai, Y.J., Wonfor, A., Shahkooh, S.: Wavelength switching components for future photonic networks. IEEE Commun. Mag. **40**(9), 74 (2002)
23. Tangdiongga, E., Yang, X.L., Li, Z.G., Liu, Y., Lenstra, D., Khoe, G.D., Dorren, H.J.S.: Optical flip-flop: based on two-coupled mode-locked ring lasers. IEEE Photonics Technol. Lett. **17**(1), 208 (2005)
24. Qasaimeh, O., Zhou, W.D., Phillips, J., Krishna, S., Bhattacharya, P., Dutta, M.: Bistability and self-pulsation in quantum-dot lasers with intracavity quantum-dot saturable absorbers. Appl. Phys. Lett. **74**(12), 1654 (1999)
25. Uenohara, H., Takahashi, R., Kawamura, Y., Iwamura, H.: Static and dynamic response of multiple-quantum-well voltage-controlled bistable laser diodes. IEEE J. Quantum Electron. **32**(5), 873 (1996)
26. Shoji, H., Arakawa, Y., Fujii, Y.: Fast bistable wavelength switching characteristics in 2-electrode distributed feedback laser. IEEE Photonics Technol. Lett. **2**(2), 109 (1990)
27. Huang, X.D., Stintz, A., Li, H., Rice, A., Liu, G.T., Lester, L.F., Cheng, J., Malloy, K.J.: Bistable operation of a two-section 1.3 mm InAs quantum dot laser—absorption saturation and the quantum confined stark effect. IEEE J. Quantum Electron. **37**(3), 414 (2001)
28. Cataluna, M.A., Sibbett, W., Livshits, D.A., Weimert, J., Kovsh, A.R., Rafailov, E.U.: Stable mode locking via ground- or excited-state transitions in a two-section quantum-dot laser. Appl. Phys. Lett. **89**(8), 081124 (2006)
29. Feng, M., Brilliant, N.A., Cundiff, S.T., Mirin, R.P., Silverman, K.L.: Wavelength bistability in two-section mode-locked quantum-dot diode lasers. IEEE Photonics Technol. Lett. **19**(9–12), 804 (2007)
30. Siegman, A.E.: Lasers. University Science Books, Sausalito (1986)
31. Murray, J.D.: Mathematical Biology I: An Introduction. Springer, Berlin (2003)
32. Lin, C.F., Ku, P.C.: Analysis of stability in two-mode laser systems. IEEE J. Quantum Electron. **32**(8), 1377 (1996)
33. Thompson, M.G., Rae, A., Sellin, R.L., Marinelli, C., Penty, R.V., White, I.H., Kovsh, A.R., Mikhrin, S.S., Livshits, D.A., Krestnikov, I.L.: Subpicosecond high-power mode locking using flared waveguide monolithic quantum-dot lasers. Appl. Phys. Lett. **88**(13), 133119 (2006)

34. Thompson, M.G., Rae, A.R., Xia, M., Penty, R., White, I.H.: InGaAs quantum-dot mode-locked laser diodes. IEEE J. Sel. Top. Quantum Electron. **15**(3), 661 (2009)
35. Alen, B., Bickel, F., Karrai, K., Warburton, R.J., Petroff, P.M.: Stark-shift modulation absorption spectroscopy of single quantum dots. Appl. Phys. Lett. **83**(11), 2235 (2003)
36. Borri, P., Langbein, W., Schneider, S., Woggon, U., Sellin, R.L., Ouyang, D., Bimberg, D.: Exciton relaxation and dephasing in quantum-dot amplifiers from room to cryogenic temperature. IEEE J. Sel. Top. Quantum Electron. **8**(5), 984 (2002)

Chapter 3
Spectral Splitting Effects and Their Influence to the Performance of Quantum Dot Mode Locked Lasers

Charis Mesaritakis and Dimitris Syvridis

Abstract In this chapter the multi-wavelength emission capabilities of quantum dot (QD) lasers, due to splitting effects in the ground-state (GS), are analyzed. These emission sub-bands are not related to carrier transitions from different excitation levels like GS/excited-state (ES) emission, but are strongly depended on gain saturation effects. The existence of these sub-bands alongside their wavelength tuning capabilities, have enabled the identification of novel regimes of operation like pulse width narrowing in the presence of dual GS emission, and tunable dual state mode locking. The exploitation of these regimes can allow the deployment of QD mode locked lasers into newly emerging applications both in the telecomm and medical field.

Introduction

Quantum dot (QD) mode locked lasers have attracted the spotlight of attention due to many inherent advantages they posses in comparison with conventional quantum well (QW) lasers. These advantages originate from the 3D spatial confinement of carriers and the corresponding discrete-atom-like density of states observed at these materials. Low linewidth enhancement factor [1], low thermal sensitivity [2], and ultra fast carrier dynamics [3] are some characteristics of QD based lasers that make them excellent candidates for ultra short pulse generation. Especially, through the mechanism of passive mode locking sub-picosecond pulses have been

C. Mesaritakis (✉) · D. Syvridis
Optical Communications Laboratory, Department of Informatics and Telecommunications, University of Athens, GR-15784 Athens, Greece
e-mail: cmesar@di.uoa.gr

Z. M. Wang (ed.), *Quantum Dot Devices*, Lecture Notes in Nanoscale Science and Technology 13, DOI: 10.1007/978-1-4614-3570-9_3,
© Springer Science+Business Media New York 2012

achieved, repetition rate that extends to hundreds of GHz and peak power in the order of few Watts [4–7].

These achievements of QD based lasers are still inferior to the performance of standard solid state laser (Ti.Saphire e.g.). Nonetheless constant improvement of the temporal and power characteristics of the pulses generated by QD lasers, alongside the high integration capabilities, the low manufacturing and maintenance cost, can enable the widespread use of QD mode locked lasers into newly emerging applications like, low coherence tomography [8], optical clock recovery in high speed communication networks [9, 10], and all optical signal processing [11, 12].

One aspect of QD lasers that has attracted considerable attention is the multi-wavelength emission capabilities. These discrete emission wavebands occur due to radiative recombination of carriers from different excitation energies [ground-state (GS), excited-state (ES)] [13]. Although these effects are also present in QW based lasers, extreme pumping conditions are required in order to be triggered. On the other hand the unique electronic structure of QD gain media allow easy excitation of these energy states and enable multi-wavelength emission at moderate pumping levels. The existence of these multiple wavebands in QD materials have been recently exploited using passive mode locking techniques, in order to achieve several novel regimes of operation like, pulse generation from the GS or ES [14], dual state mode locking from the GS and ES [15], and pulse width reduction due to the presence of CW emission form the ES [16, 17].

Further experimental investigation of QD lasers allowed the identification of a new multi-wavelength regime that is related to the splitting of the GS band into two independent sub-bands [18–21]. This effect manifests under strong pumping conditions, whereas the spectral separation between the two sub-bands is tunable with current and can extend to several nanometers [19–21]. The physical mechanism of this effect is not associated to carrier recombination from higher energy bands, whereas two different interpretations have been already proposed. The first is related to enhanced quantum effects in QD materials [19], while the second approach gives credit to gain saturation effects [20, 21]. Although the origin of ground-state splitting (GSS) is still a matter of debate, new applications, which are associated to GSS have already emerged, like tunable dual mode locking from the two GS sub-bands [19] and pulse width narrowing due to GS splitting effects [21]. The exploitation of these two effects can unlock the deployment of QD monolithic lasers into new areas of applications. The dual state tunable mode locking can be utilized in order to produce a tunable pulsed Terahertz source, while the pulse width narrowing effect can be utilized in nano-surgery application, where the simultaneous high peak and average power is a highly desired feature.

In the context of this chapter the potential origin of this effect will be discussed in detail. The two independent approaches will be analyzed and further experimental results will be presented that help establish a valid interpretations of this effect. Furthermore the potential applications like tunable dual state mode locking and especially pulse width narrowing with increasing gain current, that emerge from this regime of operation will be presented. Finally further experimental

results will be presented allowing the identification of some basic device's structural parameters like cavity length and number of QD layers that enhance spectrum splitting effects.

Ground-State Splitting

The GSS consists of a strong suppression of lasing action in the center of spectrum that creates two independent emission bands. This effect manifests at strong pumping conditions, whereas further current increase broadens in the spectral separation of the two sub-bands. This behavior has been firstly observed both numerically and experimentally in the pioneer work of Sugawara et al. [18]. In this work an InAs/InGaAs QD laser was studied with length of 700 μm, ridge width of 5 μm and only one layer of QDs. In the case where injection current increased and just before the onset of ES lasing, the spectrum of the GS appeared to have two discrete emission peaks with a spectral separation in the order of 4.5 meV. In order to confirm these findings Sugawara et al. developed a detailed numerical model based on multi-population rate equations that include three different energy levels (GS, ES, upper-continuum state). Free carriers were pumped from the wetting layer (WL) and were able to either recombine through the mechanism of stimulated-spontaneous emission or to excite/relax to different energy states. The characteristic time for each transition is governed by the carrier population at each state.

This numerical approach provided accurate results in full agreement with the experimental behavior. In detail, at low bias conditions both the experiment and simulation show stimulated emission only from the GS, whereas if current is further increased the GS band is splitted to two independent emission wavebands. In the case that current increase enabled stimulated emission from the ES, the GS splitting effect diminished. The explanation provided for this effect was that, central lasing modes are depleted from carriers due to stimulated emission from side modes. This carrier transition occurs to QD based devices through the inhomogeneous broadening of the gain. The fact that ES lasing drove the GS emission to single emission was attributed to the fact that "all the dot groups with the modal gain above the total cavity loss come to contribute to the central lasing modes due to the increase in the ground-state homogeneous broadening" [18].

Liu et al. [19] also observed the same effect in a Kerr-lens self-mode locked InP-based QD laser. The GSS effect manifested again for high injection current and the spectral separation between the two sub-bands was also tunable with current. The absence of ES emission from this device hindered the ability to confirm the Sugawara claims regarding the effect of ES lasing on the GSS. In this case the authors attributed the splitting to quantum effects that are greatly enhanced in QD based materials due to the excitonic nature of the carriers-holes. In detail the enhanced electrostatic force between the electrons and holes interact with photons inside the cavity and causes splitting according to Stark effect and

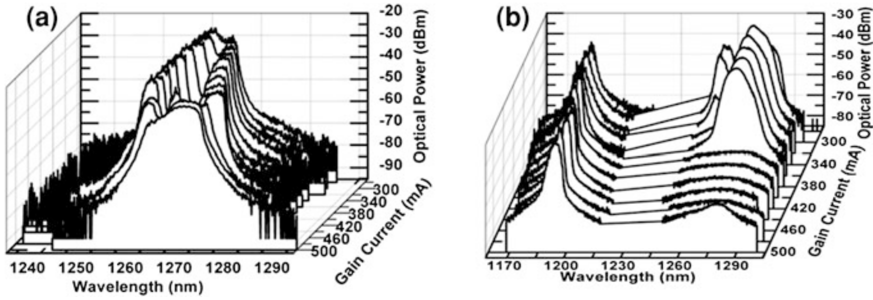

Fig. 3.1 Optical spectra for different gain currents. **a** $V_{abs} = 0$ V. **b** $V_{abs} = -7$ V

Rabi oscillations. Taking into account that the magnitude of such effects are proportional to the intra-cavity photon density, this theoretical explanation, although possible, cannot explain the fact that GSS stops on the onset of ES lasing, or the fact that maximum splitting does not coincide with maximum optical power in many cases.

Recently the same effect has been observed in a passively mode locked InAs/InGaAs QD based device [21]. In detail the device was a multi-sectional QD laser, where the absorber was split into two sections 0.3 mm each of them and reverse biased, while the rest were forward biased. The laser structure includes five self-assembled InAs/InGaAs QD layers surrounded with $Al_{35\%}Ga_{65\%}As$ claddings. The laser chip had a total length of 4 mm and the ridge width of 6 μm. The intra-cavity saturable absorber was utilized in order to achieve pulsed operation through the mechanism of passive mode locking. Its existence did not seem to affect GSS, apart from the fact that due to increased cavity losses the required electrical pumping was much stronger.

In Fig. 3.1a, b the emitted spectra are presented for different bias conditions. The first case corresponds to weak reverse voltage (Fig. 3.1a), where only GS emission is present at the recorded optical spectrum. In this regime of operation, if current is increased beyond a voltage depended limit GSS is evident, whereas current increase induces a widening of the spectral separation that can extend to 14 nm. The second regime is achieved when a higher reverse voltage is applied at the absorbing section (Fig. 3.1b). In this case the bias conditions enable ES lasing, while GSS is hardly noticeable and it diminishes rapidly on the onset of ES. These results although they involve a passively mode locked device, with an intra-cavity saturable absorber, appear to be in full accordance with numerical and experimental results of Sugawara et al.

In order to distinguish the exact origin of this effect and exclude one of the two interpretations', further measurements were performed. In the case that this phenomenon was Rabi-oscillations related, then the spectral separation of the two sub-bands should be linearly related to the square root of the emitted power. On the contrary as it can be seen in Fig. 3.2 this is not the case for the device under test

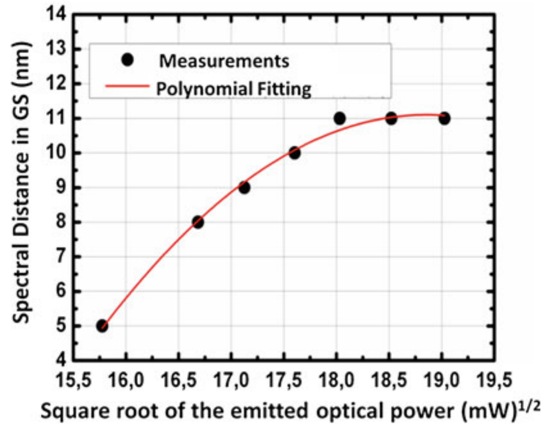

Fig. 3.2 Spectral distance of the two GS sub-bands versus the square root of the emitted power

where the spectral separation appears to have an almost parabolic relationship with optical power. Moreover, the maximum spectral separation between the two sub-bands did not coincide in many cases with the maximum intra-cavity optical power.

Taking into consideration the bias conditions at which the effect is manifested alongside the parabolic relation of the intra-cavity optical power and the spectral separation, an explanation can be derived. In detail as gain current increases then the central lasing modes are subjected to stronger non linear gain suppression effects like spectral hole burning (SHB). This gain suppression mechanism depletes the central lasing modes from free carriers and lasing action is suppressed. The free carriers are redistributed through the large inhomogeneous broadening to outer modes and enable lasing action. According to this approach the widening of the spectral separation can be attributed to the fact that as gain current is further increased more central modes are subject to SHB and are clamped, while more outer modes from both sides of the spectral deep surpass the threshold condition.

On the other hand the relationship between the GSS and ES can be attributed to the fact that ES lasing enable a decrease in the available gain in the GS [19]. In detail according to both numerical simulations and experimental data, ES lasing significantly alters the characteristic time of carrier relaxation and recombination at the GS. This variation results to the fact that free carriers tend to recombine radiative from the ES rather than accumulate to the lower energy state (GS), thus GS gain is reduced. According to this approach, GS gain decrease suppresses the effects that trigger GSS and consequently the spectral emission of GS shifts back to the conventional case. Finally, by comparing all available experimental results it can be concluded that GSS is an intrinsic property of the QD material and it is not affected by the existence of an intra-cavity saturable absorber. The only difference between the three cases (CW-passive mode locking and Kerr-lens mode locking) is the stronger pumping conditions that are required to achieve GSS due to the absorber induced unsaturated losses.

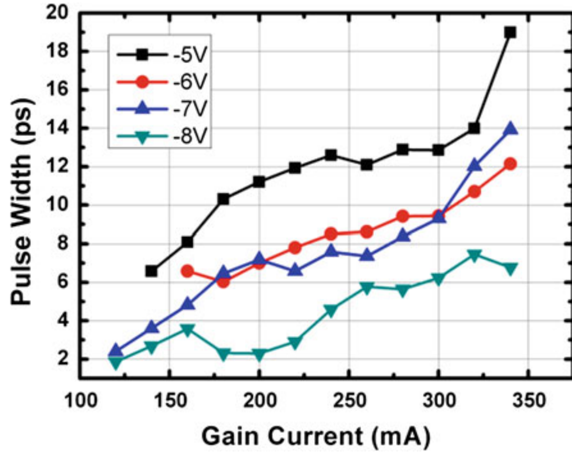

Fig. 3.3 Pulse width versus gain current for different reverse voltage

Pulse Width Narrowing Due to GSS

The existence of an intra-cavity absorber in the aforementioned device enabled pulsed operation through the mechanism of passive mode locking in the presence of GSS. In particular the temporal properties of the generated pulses were recorded through an optical auto correlator based on second harmonic generation (SHG). The bias conditions at the gain and absorbing section were varied and the pulse width was measured, by assuming the pulses were of Gaussian shape.

In the case that the reverse voltage was high ES lasing was favored and GSS effect was literally absent. In this regime of operation pulse width evolution with bias conditions is typical and a characteristic case is presented in Fig. 3.3. As it can be concluded from the figure, reverse voltage increase induces a severe pulse width decrease, which originates from the exponential relationship of reverse voltage and carrier recovery time [22, 23]. On the other hand, higher reverse voltage is also associated with increased non-saturated losses in the cavity, which in turn drastically reduces the average emitted power. Taking into consideration the fact that the peak power is proportional to the average power and reverse proportional to pulse width, it can be concluded that peak power does not exhibit monotonical behavior with reverse voltage. Instead, local maxima are recorded which are associated to either broad pulses with high average power or short pulses with low average power. In Fig. 3.4 the aforementioned dependence is demonstrated for the same bias condition used in Fig. 3.3.

Regarding the evolution of pulse width with gain current, a similar trade off has been observed. Gain current increase enhances effects like self-phase modulation, which in combination with the positive dispersion effects present at the gain section cause severe pulse width broadening [24]. In terms of peak power gain current also establishes a strict trade off. Pumping enhancement induces average power increase, whereas in the case of mode locked lasers it also induces pulse

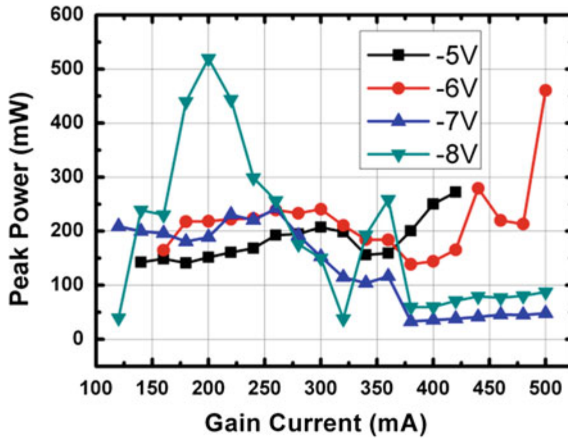

Fig. 3.4 Peak power versus gain current for different reverse voltage

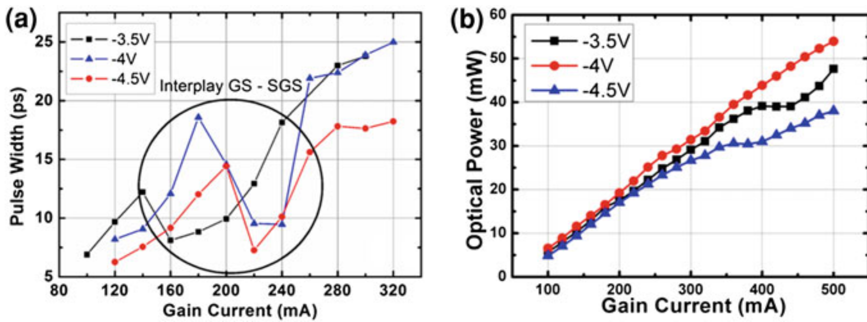

Fig. 3.5 **a** Pulse width versus gain current for different reverse voltage the area in *circle* corresponds to the existence of GSS. **b** Average power versus gain current for different reverse voltages

width broadening, thus local maxima in terms of peak power are recorded in this case also. The aforementioned bias induced trade off can significantly hinter the deployment of QD devices in many cutting-edge applications where simultaneous peak power and average power is a highly required feature.

In the second regime of operation where the reverse voltage is reduced GSS effect is achieved as mentioned in the previous paragraphs, whereas pulse width evolution with current exhibits a significant different behavior with increasing current. In Fig. 3.5a the pulse width is presented for different reverse voltages versus the gain current. It can be observed that for a specific voltage depended injection current and higher, the pulse width is drastically reduced. Characteristic is the case when the reverse voltage is set to −4 V the gain current is increased by 180–240 mA. In this case the recorded pulses exhibit a reduction in pulse width in the order of 10 ps, whereas the examination of the evolution of average optical power with gain current revealed a monotonically increment without any

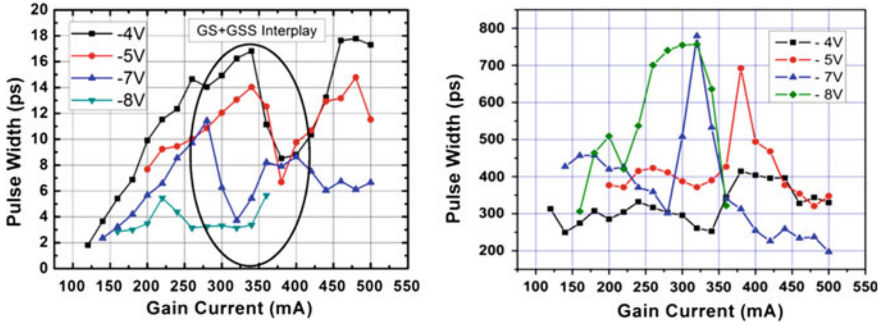

Fig. 3.6 Pulse width evolution with bias conditions for a similar device as the one used for Fig. 3.5 (*left*). Peak power evolution with bias conditions (*right*)

noticeable kinks (Fig. 3.5b). The accumulative effect of these two observed behaviors is an abrupt increase in the pulse's peak power.

The confirmation of this new regime of operation was established by further experimental investigation of similar devices. In these cases similar results were obtained, whereas in the presence of GSS the recorded optical pulses exhibited reduced width and increased average power. In particular some devices that their structural characteristics did not enable ES lasing, exhibited enhanced GSS for a broader range of bias conditions and the observed pulse width narrowing was more profound. In Fig. 3.6, pulse width and peak power measurements versus gain current for different reverse voltage at the absorbing section is presented for the aforementioned device. The pulse width decrease in this case induces a strong increase in the pulse's peak power that for $V_{\text{abs}} = -7$ V and current variation from 260 to 340 mA it was in the order of 300%.

The fact that the pulse width narrowing effect is observed only when the bias conditions enable GSS, implies that these two phenomena are closely related. As shown in Fig. 3.7 the device's behavior can be classified into three discrete regimes.

The first regime is characterized as "typical" device behavior, and consists of pulse width broadening due to increased non linear effects like self-phase modulation and chromatic dispersion. In this regime of operation no GSS is evident, whereas injection current increase induces a strong enhancement in the optical bandwidth. This bandwidth increase results to an increased number of longitudinal modes that surpass the lasing threshold. Theoretically, through this mechanism a larger amount of modes could attain the same phase and consequently enable the production of optical pulses with reduced temporal bandwidth. Nonetheless, the non ideal time-bandwidth product of the recorded pulses imply that the optical power of these modes fluctuate with random phase, thus they do not contribute to pulse formation but on the contrary are responsible for the laser's increased phase noise and pulse destabilization due to severe competition effects.

In the second regime, current increase marks the onset of GSS and GS emission is divided into two independent sub-bands. In this regime the lasing suppression in

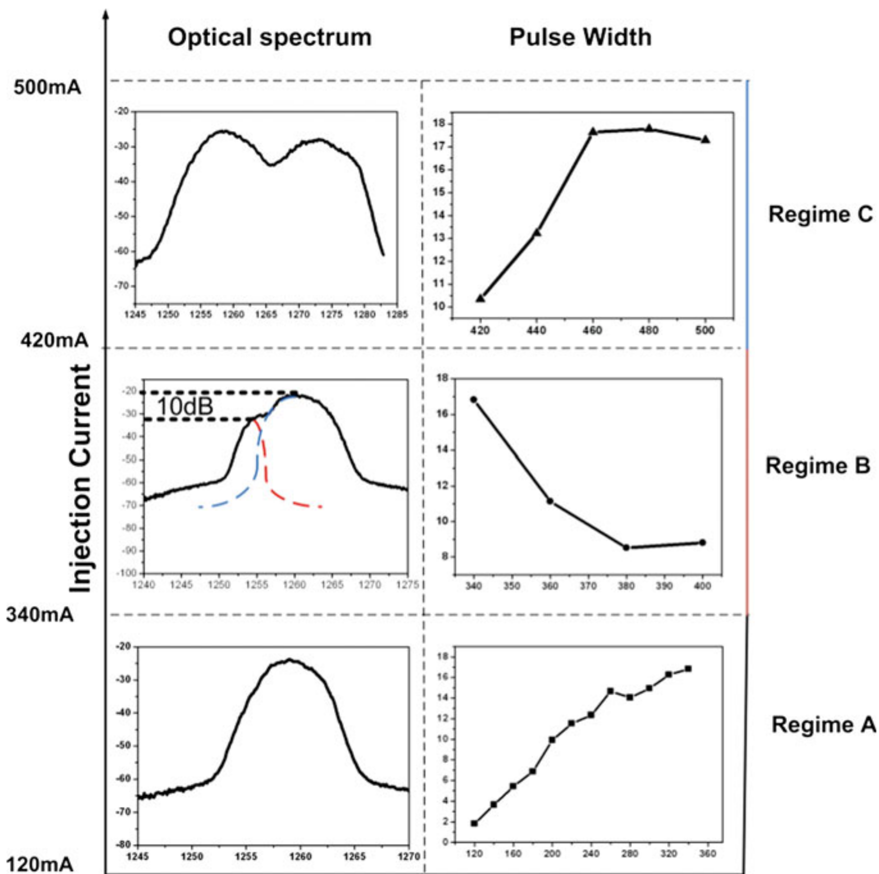

Fig. 3.7 Pulse width evolution (*left column*) and characteristic optical spectrum (*right column*)

the middle of the gain forces a severe reduction in the optical bandwidth of the spectral peak that is responsible for pulse formation. Through this effect the number of modes that participate in phase locking is reduced, thus phase noise is also reduced. Furthermore the second sub-band (not mode locked) exhibits reduced power thus its lasing modes cannot destabilize mode locking through competition effects.

The third regime of operation manifests when the injection current is further increased. In this case, the enhanced electrical pumping allows two effects. The first corresponds to optical bandwidth increase in both sub-bands, whereas the second is related to the fact that both sub-bands acquire similar optical power. These two effects enhance the competition effects between the two groups of longitudinal modes, whereas bandwidth increase also induces an increase in the number of randomly fluctuating modes at each band. The accumulative result of these effects is pulse width deterioration, which can be monitored either as a strong pulse width broadening or even as mode locking collapse in some cases.

Dual State Mode Locking Due to GSS

The existence of two independent wavebands in the spectral region of GS, can provide the possibility to achieve simultaneous mode locking from both the sub-bands in a similar way that GS–ES mode locking has been demonstrated [15]. Taking also into consideration that the spectral separation of the GS sub-bands is tunable with bias, such a device could be used in order to fabricate a monolithic pulsed source. In [19] this effect has been demonstrated for the first time in an InP-based QD device. In this case two independent trains of pulses, originating from the spectral band of the GS, have been generated, whereas the recorded pulse width was in the femtosecond range. The generated pulses exhibited very low pulse width without the utilization of any additional dispersion-minimization component, whereas the device tested did not have an intra-cavity saturable absorber nor the gain current was externally modulated, consequently Liu et al. [19] assumed that the mechanism that enables pulse generation was related to Kerr-lens effect. The origin of this effect is the abrupt change in the material's refractive index due to increased intra-cavity optical power. The amplitude of the optical power is assumed to have a Gaussian profile, thus the refractive index variation in the tails of the beam is less severe than in the center. This fact results to a spatial inhomogeneous variation of the refractive index that forces the gain medium to operate like a focusing lens. The ultra short optical pulses together with the absence of a saturable absorber that reduces optical power, makes this mode locking technique very interesting for new applications. Nonetheless, assuming that the mechanism behind pulse generation is kerr-lens mode locking, many issues arise such as the long term stability of the process, the hard electric pumping required in order to excite Kerr-lens effect and finally design issues related to the structural parameters of the laser-resonator.

More recently the same effect has been demonstrated in a conventional InAs/InGaAs QD based device and mode locking was achieved through the well documented mechanism of passive mode locking. The device employed had a length of 4 mm, five QD layers and ridge width of 6 μm (the same device mentioned in the previous section), whereas the reverse voltage used was significantly reduced in order to allow dual state mode locking. The identification of this operating regime has been performed through simultaneous measurements of the electrical and optical spectrum of the laser. In detail, dual state mode locking can be identified through the existence of two discrete RF peaks that correspond to phase-locked lasing modes from different emission bands. The different central wavelength of the two sub-bands impose a slightly different refractive index that allow pulses from each band to be guided with a different effective cavity length. In the case that simultaneous GS/ES mode locking is achieved, the spectral difference is ≈ 80 nm which results to a repetition rate variation in the order of 500 MHz. On the other hand, in the case of dual GS mode locking the optical spectral separation was significantly smaller (2–14 nm) and consequently the refractive index variation was less strong, resulting in a repetition rate variation in

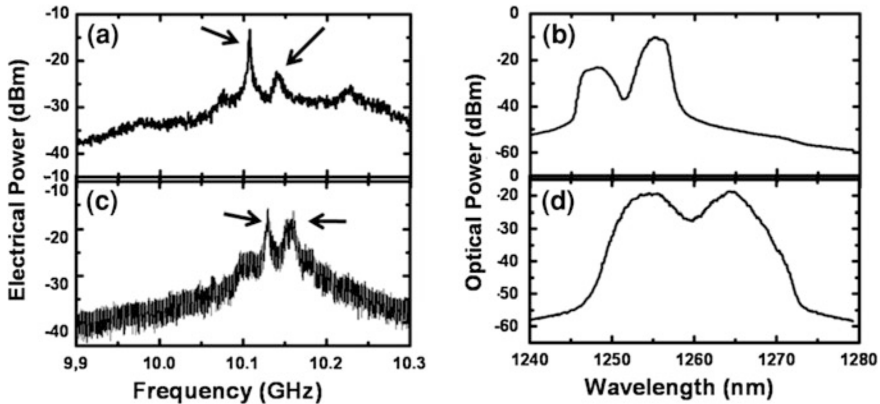

Fig. 3.8 RF spectra (*left column*) and corresponding optical spectra (*right column*)

the order of 30 MHz. In Fig. 3.8 both the optical and RF spectrum are presented for a typical case. Two peaks can be clearly distinguished having a frequency spacing of 30 MHz. The two peaks have an amplitude difference which can be attributed to the different optical power of the two sub-bands (Fig. 3.8).

Although RF and optical measurements can provide strong evidence on the existence of two independent pulses, in order to further confirm this regime autocorrelation traces have been also acquired. In the case that two pulse-trains with different repetition rates are injected to the auto correlator, the output signal is the result of the overlap of both pulses. This complex autocorrelation results to a single trace with increased pulse width compared to the case where each train was fed to the auto correlator independently. Based on this fact two autocorrelation traces have been acquired: the first corresponds to the original output of the laser (Fig. 3.1a), while in the second case an optical band-pass filter was employed in order to filter one sub-band. If only one train of pulses was generated, the optical filtering would not affect the pulse width. On the contrary in our case a pulse width decrease was observed that imply the existence of two independent pulse-trains (Fig. 3.9).

Device's Structural Parameters that Enable GSS

Taking into consideration the possible applications that originate from GSS a critical issue arises. Which structural parameters allow the existence of GSS? In the previous paragraphs it was pointed out that GSS is closely related to gain saturation effects, while it vanishes in the presence of ES lasing, due to the GS gain suppression imposed by the stimulated emission of free carriers from the ES energy band. In order to confirm the relationship between GSS and saturation

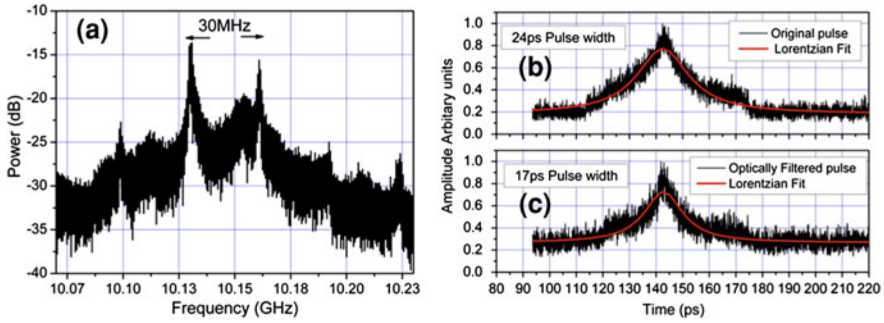

Fig. 3.9 **a** RF spectrum and corresponding autocorrelation traces **b** without and **c** with optical filtering

effects, a characterization of QD based laser cavities having different structural parameters has been performed. In detail the devices tested varied in terms of cavity length (2-4-8 mm), number of QD layers (5-10-15) and width of the waveguide ridge (4–6 μm).

Experimental investigation of the optical spectrum revealed that GSS was evident only for devices having five QD layers, length greater than 4 mm, while the cavity width did not affect significantly the spectral splitting effect. The length dependence of GSS can be attributed to the fact that small cavities enable the fast feeling of the GS with free carriers and consequently early ES lasing [24]. In this context, device with length smaller than 2 mm exhibited ES lasing under relative weak pumping conditions resulting to suppressed GS gain and consequently absence of GSS. On the other hand, 4 and 8 mm devices did not allow early ES lasing, thus stronger electrical pumping was employed that allowed strong gain saturation effects.

In terms of QD layers, the relationship between gain saturation and number of layers is not straightforward. In general, more QD layers were proposed in order to increase differential gain, reduce the inhomogeneous broadening of the optical spectrum and improve the optical efficiency of the laser [25, 26]. Nonetheless variation of the number of QD layers can alter the geometry of the device and consequently change the wave guiding properties of the laser. In order to identify the impact of QD layers to the gain dynamics, two types of simulations have been performed. The first consists of wave guiding simulation and in particular 2D beam propagation using commercial available software (R-Soft) in order to extract the confinement factor (Γ) for each structure. The second utilized the steady-state solutions of multi-population rate equations [27] in order to fit experimental obtained ASE spectra. Through this technique basic parameters like waveguide-mirror losses and material gain could be extracted. In Fig. 3.10 the confinement factor and material gain are presented versus the number of QD layers.

By differentiating material gain near threshold the differential gain could be extracted. As pointed out in Fig. 3.10 neither the confinement factor nor the

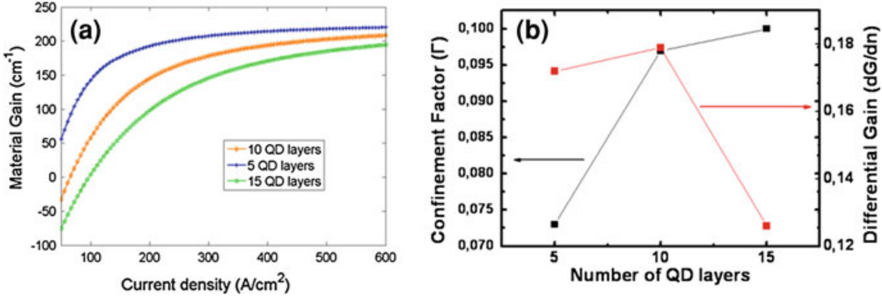

Fig. 3.10 **a** Material gain for different number of QD layers. **b** Confinement factor and differential gain versus the number of QD layers

differential gain exhibit monotonical relationship with the number of QD layers. This fact can be attributed to the geometry of the devices and in particular QD increment beyond 10 layers does not enhance confinement factor, due to the strong interaction of the optical field with the waveguide-air interface. In the case of 15 QD layers the optical field is guided close to the air-waveguide interface and consequently the confinement factor is mostly affected by this index variation (GaAs-air) than by the actual number of QD layers. The saturation energy for each structure, which is defined as Eq. 3.1

$$E_{\mathrm{sat}} = \frac{h v A_{\mathrm{eff}}}{\mathrm{d}G/\mathrm{d}N} \tag{3.1}$$

$$E_{\mathrm{sat}} = \frac{h v \times w \times d}{\Gamma \times (\mathrm{d}G/\mathrm{d}N)} \tag{3.2}$$

or by substituting A_{eff} we can derive Eq. 3.2 where h is plank's constant, v is the optical frequency, w is the waveguide width, d is the device's height (which increases with QD layers), Γ is the confinement factor, and $\mathrm{d}G/\mathrm{d}N$ is the differential gain. By comparing the saturation energy between the different structures it can be concluded that the increase of device's height greatly enhances saturation energy, while the impact of differential gain and confinement factor is not so significant. Consequently smaller devices can be saturated more easily and thus GSS effects are also greatly enhanced.

Conclusion

In the context of this chapter the splitting effects in the GS and the potential application that can emerge from this effect are presented. In detail, in the first part the origin of the effect is discussed in detail and further experimental evidence are demonstrated in order to confirm the effect. In the second part the splitting effect is

exploited for two applications. Pulse width narrowing in the presence of GSS in a passively mode locked InAs/InGaAs QD laser is presented, whereas dual GS state mode locking is also demonstrated and experimentally verified. Finally in the last part through characterization of several devices having different structural parameters like number of QD layers and length, some basic design rules have been extracted that enable/enhance GSS effects.

References

1. Shernyakov, Y.M., Bedarev, D.A., Kondrateva, E.Y., Kopev, P.S., Kovsh, A.R., Maleev, N.A., Maximov, M.V., Mikhrin, S.S., Tsatsulnikov, A.F., Ustinov, V.M., Volovic, B.V., Zhukov, A.E., Alferov, Z.I., Ledenstov, N.N., Bimberg, D.: 1.3 μm GaAs-based laser using quantum dots obtained by spinodal decomposition. IEEE Electron. Lett. **35**, 898 (1999)
2. Prasankumar, R.P., Attaluri, R.S., Averitt, R.D., Urayama, J., Bernstein, N.W., Rotella, P., Stintz, A.D., Krishna, S., Taylor, A.J.: Ultrafast carrier dynamics in an InAs/InGaAs quantum dots in a well heterostructure. Opt. Express **16**, 1165 (2008)
3. Oksanen, J., Tulkki, J.: Linewidth enhancement factor and chirp in quantum dot lasers. J. Appl. Phys. **94**, 1983 (2003)
4. Rae, A.R., Thompson, M.G., Penty, R.V., White, I.H., Kovsh, A.R., Mikhrin, S.S., Livshits, D.A., Krestnikov, I.: In: Proceedings of the LEOS Annual Meeting Conference, vol. 1, p. 874 (2006)
5. Rafailov, E.U., Cataluna, M.A., Sibbet, W., Il'inskaya, N.D., Zadiranov, Y.M., Zhukov, A.E., Ustinov, V.M., Livshits, D.A., Kovsh, A.R., Ledentsov, N.N.: High power picosecond and femtosecond pulse generation from a two section mode-locked quantum dot laser. Appl. Phys. Lett. **87**, 081107 (2005)
6. Gubenko, A., Livshits, D., Krestnikov, I., Mikhrin, S., Kozhukhov, A., Kovsh, A., Ledentsov, N., Zhukov, A., Portnoi, E., Ioffe, A.F.: High power monolithic passively mode-locked quantum-dot laser. IEEE Electron. Lett. **41**, 1124 (2005)
7. Rae, A.R., Thompson, M.G., Kovsh, A.R., Penty, R.V., White, I.H.: InGaAs-GaAs quantum dot mode-locked laser diodes: optimization of geometry for subpicosecond pulse generation. IEEE Photonics Technol. Lett. **21**, 307 (2009)
8. Djie, H.S., Ooi, B.S., Fang, X.-M., Wu, Y., Fastenau, J.M., Liu, W.K., Hopkinson, M.: Room temperature broadband emission of an InGaAs/GaAs quantum dot lasers. Opt. Lett. **32**(1), 44–46 (2007)
9. Tang, X., Cartledge, J.C., Shen, A., Akrout, A., Duan, G.H.: Low-timing-jitter all-optical clock recovery for 40 Gbits/s RZ-DPSK and NRZ-DPSK signals using a passively mode-locked quantum-dot Fabry–Perot semiconductor laser. Opt. Lett. **34**(7), 899–901 (2009)
10. Silva, M.C., Lagrost, A., Bramerie, L., Gay, M., Besnard, P., Joindot, M., Simon, J.C., Shen, A., Duan, G.H.: Up to 427 GHz all optical frequency down-conversion clock recovery based on quantum-dash Fabry–Perot mode-locked laser. IEEE J. Lightwave Technol. **29**(4), 609–615 (2011)
11. Bimberg, D., Meuer C., Laemmlin, M., Liebich, S., Kim, J., Eisenstein, G., Kovsh, A.R.: Quantum dot semiconductor optical amplifiers for wavelength conversion using cross-gain modulation. In: 10th Anniversary International Conference on Transparent Optical Networks, ICTON 2008, no. 22–25, pp. 141–144 (2008)
12. Nielsen, D., Chuang, S.L.: Four wave mixing and wavelength conversion in quantum dots. Phys. Rev. B **81**(3), 035305 (2010)
13. Leburn, C.G., Metzger, N.K., Lagatsky, A.A., Brown, C.T., Sibbett, W., Lumb, M., Clarke, E., Murray, R.: Advanced Solid-State Photonics, OSA Technical Digest Series (CD). Optical Society of America, Washington (2009)

14. Cataluna, M.A., Sibbet, W., Livshits, D.A., Weimert, J., Kovsh, A.R., Rafailov, E.U.: Stable mode locking via ground—or excited state transitions in a two section quantum dot laser. Appl. Phys. Lett. **89**, 081124 (2006)
15. Cataluna, M.A., Nikitichev, D.I., Mikroulis, S., Simos, H., Simos, C., Mesaritakis, C., Syvridis, D., Krestnikov, I., Livshits, D., Rafailov, E.U.: Dual-wavelength mode-locked quantum-dot laser, via ground and excited state transitions: experimental and theoretical investigation. Opt. Express **18**(12), 12832–12838 (2010)
16. Kim, J., Choi, M.T., Delfyett, P.J.: Pulse generation and compression via ground and excited state from a grating coupled passively mode-locked quantum dot two section diode laser. Appl. Phys. Lett. **89**, 261106 (2006)
17. Cataluna, M.A., McRobbie, A.D., Sibbett, W., Livshits, D.A., Kovsh, A.R., Rafailov, E.U.: New mode-locking regime in a quantum-dot laser: enhancement by simultaneous CW excited-state emission. In: CLEO 2006, Paper CThH3, Long Beach, USA (2006)
18. Sugawara, M., Hatori, N., Ebe, H., Ishida, M., Arakawa, Y., Akiyama, T., Otsubo, K., Nakata, Y.: Modelling of room temperature lasing spectra of 1.3 μm self-assembled InAs/GaAs quantum dot lasers: homogenous broadening of optical gain under current injection. J. Appl. Phys. **97**, 043523 (2005)
19. Liu, J., Lu, Z., Raymond, S., Poole, P.J., Barrios, P.J., Poitras, D.: Dual-wavelength 92.5 GHz self-mode-locked InP-based quantum dot laser. Opt. Lett. **33**, 1702 (2008)
20. Li, S.G., Gong, Q., Lao, Y.F., Yang, H.D., Gao, S., Chen, P., Zhang, Y.G., Feng, S.L., Wang, H.L.: Two color quantum dot laser with tunable gap. Appl. Phys. Lett. **95**, 251111 (2009)
21. Mesaritakis, C., Simos, C., Simos, H., Mikroulis, S., Krestnikov, I., Syvridis, D.: Pulse width narrowing due to dual ground state emission in quantum dot passively mode locked lasers. Appl. Phys. Lett. **96**, 211110 (2010)
22. Malins, D.B., Gomez-Iglesias, A., White, S.J., Sibbett, W., Miller, A., Rafailov, E.U.: Ultrafast electroabsorption dynamics in an InAs quantum dot saturable absorber. Appl. Phys. Lett. **89**(17), 171111 (2006)
23. Thompson, M.G., Marinelli, C., Chu, Y., Sellin, R.L., Penty, R.V., White, L.H., Poel, V., Birkedal, M., Hvam, D., Ustinov, J., Lammlin, V.M., Bimberg, M.: Properties of InGaAs quantum dot saturable absorbers in monolithic mode-locked lasers. In: Semiconductor Laser Conference, 2004, Conference Digest. 2004 IEEE 19th International, pp. 53–54, (2004)
24. Markus, A., Chen, J.X., Paranthoën, C., Fiore, A., Platz, C., Gauthier-Lafaye, O.: Simultaneous two-state lasing in quantum-dot lasers. Appl. Phys. Lett. **82**, 1818 (2003)
25. Solomon, J.S., Trezza, J.A., Marshall, A.F., Harris, J.S.: Vertically aligned and electronically coupled growth induced InAs Islands in GaAs. Phys. Rev. Lett. **76**(6), 952 (1995)
26. Mukai, K., Nakata, Y., Otsubo, K., Sugawara, M., Yokoyama, N., Ishigawa, H.: 1.3 μm CW lasing characteristics of self-assembled InGaAs/GaAs quantum dots. IEEE J. Quantum. Electron. **36**(4), 472 (2000)
27. Rossetti, M., Bardella, P., Montrosset, I.: Time-domain travelling-wave model for quantum dot passively mode-locked lasers. IEEE J. Quantum Electron. **47**(2), 139–150 (2011)

Chapter 4
Mode-Locked Semiconductor Lasers with Optical Injection

Tatiana Habruseva, Natalia Rebrova, Stephen P. Hegarty and Guillaume Huyet

Abstract We perform characterization of the pulse shape and noise properties of quantum dot passively mode-locked lasers (PMLLs). We propose a novel method to determine the RF linewidth and timing jitter, applicable to high repetition rate PMLLs, through the dependence of modal linewidth on the mode number. Complex electric field measurements show asymmetric pulses with parabolic phase close to threshold, with the appearance of waveform instabilities at higher currents. We demonstrate that the waveform instabilities can be overcome through optical injection-locking to the continues wave (CW) master laser, leading to time-bandwidth product (TBP) improvement, spectral narrowing, and spectral tunability. We discuss the benefits of single- and dual-tone master sources and demonstrate that dual-tone optical injection can additionally improve the noise properties of the slave laser with RF linewidth reduction below instrument limits (1 kHz) and integrated timing jitter values below 300 fs. Dual-tone injection allowed slave laser repetition rate control over a 25 MHz range with reduction of all modal optical linewidths to the master source linewidth, demonstrating phase-locking of all slave modes and coherence improvement.

T. Habruseva (✉) · N. Rebrova · S. P. Hegarty · G. Huyet
Center of Advanced Photonics and Process Analysis,
Cork Institute of Technology and Tyndall National Institute,
Cork, Ireland
e-mail: tatiana.gabruseva@gmail.com

N. Rebrova
e-mail: nrebrova@gmail.com

S. P. Hegarty
e-mail: stephen.hegarty@tyndall.ie

G. Huyet
e-mail: guillaume.huyet@tyndall.ie

Z. M. Wang (ed.), *Quantum Dot Devices*, Lecture Notes in Nanoscale Science and Technology 13, DOI: 10.1007/978-1-4614-3570-9_4,
© Springer Science+Business Media New York 2012

Introduction

Synchronization of the relative phases of the longitudinal modes of a laser is called "mode-locking", and typically results in the formation of short high intensity pulses. The general principle of mode-locked operation is to induce all longitudinal modes of the laser cavity to oscillate with a fixed phase relation between them. There are a number of techniques commonly employed to fix mode phase relationships, including, but not limited to, active [1], passive [2, 3], hybrid [4, 5], colliding pulse [6–9], and harmonic mode-locking [10]. In this chapter we focus on the characteristics of passively mode-locked lasers (PMLLs) based on quantum dots (QDs) and their manipulation via external optical injection.

Monolithic PMLLs were divided into two or more electrically isolated sections, with saturable absorption providing the mode-locking mechanism. The forward-biased sections provided sufficient gain to overcome cavity, scattering, and absorption losses, while the absorber sections were usually reverse biased to provide faster photocarrier sweepout and thus absorption recovery. A photograph of a two-section PMLL used in these experiments is shown in Fig. 4.1.

The dynamics of the saturable gain and loss functions, and pulse intensity (see "Numerical simulations"), calculated for a two-section QD device is shown in Fig. 4.2. Between two consequent pulses losses are greater than gain (see Fig. 4.2a) so the absorber remains opaque and hence no signal is produced. This is the so-called "slow stage". When the pulse arrives the low intensity light (leading edge of the pulse) is absorbed and thus it saturates the absorber which then transmits high intensity light. This part of the laser output is called the "fast stage".

Since the absorber recovers much faster than the gain [11, 12] the emitted pulse have a faster leading edge and a slower trailing edge (see Fig. 4.2b). The result may be further improved by reducing absorber recovery time with the reverse bias [13], which results in a generally shorter pulsewidth at higher voltages applied to the absorber section.

Devices Description and Fabrication

The PMLLs used in this work were two-section monolithic InAs/GaAs devices. The active region consisted of 15 layers of InAs QDs grown by molecular beam epitaxy (Stranski–Krastanov growth) on GaAs substrate at Innolume GmbH. Dot layers were separated by 33 nm of GaAs and optical confinement in the growth direction was provided by $Al_{0.35}Ga_{0.65}As$ cladding layers. The detailed layer structure of the wafer is shown in Table 4.1.

Four-step photolithography together with etching were used to create the ridge etches of 1.7 μm depth and 3 μm width. Individual sections were separated by etching a 20−50 μm wide trench into the doped region, providing $> 1\,k\Omega$ electrical isolation between sections. At the last step the metal contacts were evaporated on the top layer of the matrix. A scanning electron microscope image of the

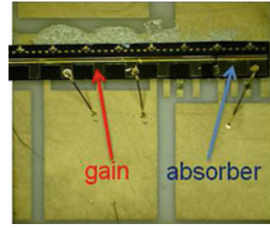

Fig. 4.1 Mounted PMLL with wire bonded gain and absorber sections. A common ground connection is provided through the substrate

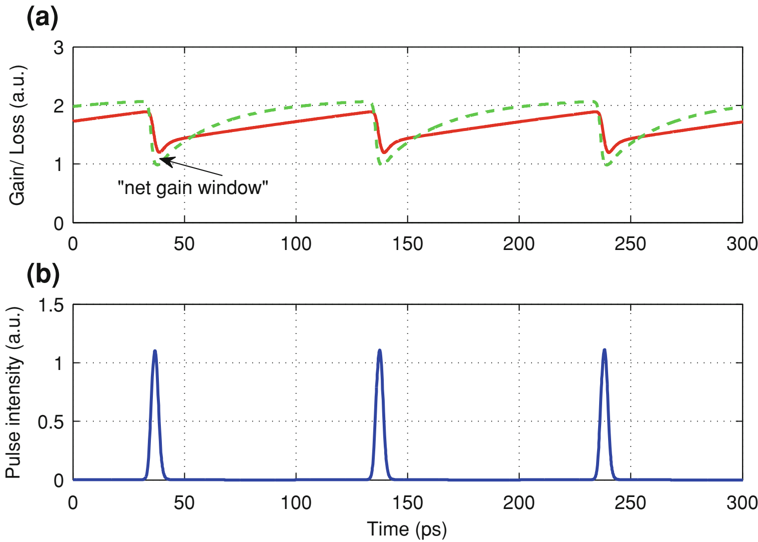

Fig. 4.2 **a** Saturable gain (*red solid line*) and loss (*green dashed line*). **b** Calculated pulses

ridge profile with dimensions is shown in Fig. 4.3. Further details of the fabrication process and equipment used can be found in [14].

After fabrication, the devices were cleaved with no coatings applied to the facets and mounted on a temperature controlled stage at 19.5°C. We used devices with a variety of absorber sections as shown in Table 4.2. The absorber section percentage length is shown relative to the total device length (in mm). Typically, the lasers emitted pulses of a few picoseconds duration at 1.3 μm with a repetition rate around 10 GHz.

Noise Properties of PMLLs

In this section we present experimental study of QD-PMLL noise properties. Low timing jitter of the pulse source is essential requirements for optical time-division multiplexing and optical sampling, while narrow optical linewidth and highly coherent frequency comb are required for coherent communications [15, 16] and frequency metrology [17].

Table 4.1 Material layer structure

Layer	Material	Repeat	Thickness	Type	Dopant
12	GaAs		200	P	C
11	$Al_{0.35}Ga_{0.65}As$		15	P	C
10	$Al_{0.35}Ga_{0.65}As$		1,000	P	C
9	$Al_{0.35}Ga_{0.65}As$		500	P	C
8	GaAs	45	33	U/D	U/D
7	$In_{0.15}Ga_{0.85}As$	15	5	U/D	None
6	InAs	15	0.8	U/D	None
5	GaAs		33	U/D	None
4	$Al_{0.35}Ga_{0.65}As$		500	N	Si
3	$Al_{0.35}Ga_{0.65}As$		1,000	N	Si
2	$Al_{0.35}Ga_{0.65}As$		15	N	Si
1	GaAs		300	N	C
0	GaAs substrate				

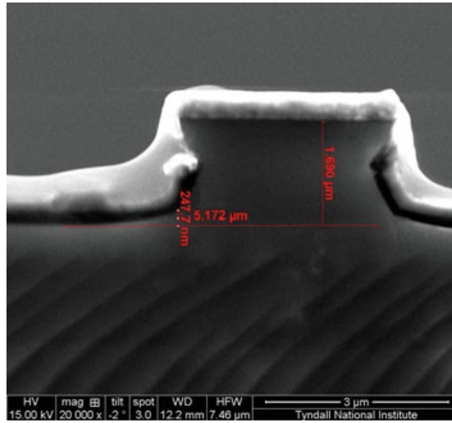

Fig. 4.3 Electron microscope image of the laser waveguide viewed from facet. The indicated waveguide width is 5.172 μm, depth is 1.690 μm.

Table 4.2 Characteristics of QD-PMLLs used in the experiments

Device	Length (mm)	Absorber (%)	F_{rep}(GHz)	Doping
P_1	4.3	10	9.4	p-doped
P_2	4.3	12	9.4	p-doped
P_3	4.3	17	9.4	p-doped
P_4	4.3	23	9.4	p-doped

RF Linewidth of PMLLs

The stochastic dynamics of noisy MLLs can be described by a set of Langevin equations [18] capturing the evolution of the power, frequency, timing jitter and optical phase of the laser. The RF linewidth is mainly determined by amplitude

noise and pulse-to-pulse timing fluctuations [19]. Taking into account only these factors the optical field of a PMLL can be written as:

$$A(t,T) = \sum_{m=-\infty}^{\infty} \Big(a(T, t - mT_{\mathrm{r}} - \Delta t(m)) + \Delta a(T)\Big) \times e^{-i\omega_0(t-mT_{\mathrm{r}})-i\phi}, \quad (4.1)$$

where t and T are the fast and slow time variables, respectively, a is the optical pulse envelope, $\omega_0(t - mT_{\mathrm{r}}) + \phi$ is the optical phase of the m th pulse, T_r is the device repetition rate, and ω_0 is the center frequency. The functions $\Delta a(T)$ and $\Delta t(m)$ are random variables that describe amplitude noise and pulse-to-pulse timing fluctuations of the pulse train.

If the amplitude noise is negligible when compared with the timing jitter, the optical field of a PMLL is [20]:

$$A(t) = \sum_{m=-\infty}^{\infty} a(t - mT_{\mathrm{r}} - \Delta t(m)) \times e^{-i\omega_0(t-mT_{\mathrm{r}})-i\phi}, \quad (4.2)$$

and the power spectrum of photocurrent signal is:

$$S_{\mathrm{RF}}(\omega) \sim \sum_{m=-\infty}^{\infty} \frac{2\Delta\omega_{\mathrm{RF},m}}{(\omega - m\omega_{\mathrm{r}})^2 + \Delta\omega_{\mathrm{RF},m}^2}. \quad (4.3)$$

Equation 4.3 shows the power spectrum of a PMLL with the above assumptions consists of a set of Lorentzian lines centered at $m\omega_{\mathrm{r}} = 2m\pi/T_{\mathrm{r}}$ with the RF linewidth of the mth harmonic proportional to the square of the harmonic number $(\Delta\omega_{\mathrm{RF},m} \sim m^2)$.

For RF spectral measurements light from the laser was coupled to an amplified high frequency photodetector, XPDV 2320R u^2t photonics. The first five harmonics of the 10 GHz PMLL were measured using a 50 GHz Agilent 8565 EC electronic spectrum analyzer (ESA).

The lineshapes approximated well with a Lorentzian fit for the first four harmonics. Figure. 4.4a shows an example of the first harmonic measurement (red) together with the Lorentzian fit (black) for laser P_3. For a Lorentzian lineshape, the integrated and pulse-to-pulse timing jitter can be determined from the RF linewidth of the first harmonic $\Delta\nu_{\mathrm{RF},1}$ (in Hz) and pulse train period T_{r} via [21]:

$$\sigma^i(f_1, f_2) = \frac{T_{\mathrm{r}}\sqrt{\Delta\nu_{\mathrm{RF},1}}}{2\pi^{3/2}} \sqrt{\frac{1}{f_1} - \frac{1}{f_2}} \quad (4.4)$$

and

$$\sigma^{pp}(N) = \frac{T_{\mathrm{r}}}{\pi} \sqrt{\frac{\Delta\nu_{\mathrm{RF},1} N T_{\mathrm{r}}}{2\pi}}. \quad (4.5)$$

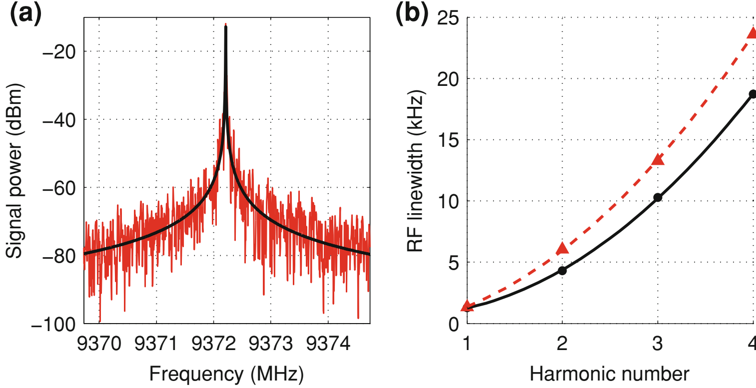

Fig. 4.4 **a** Measured RF signal of the first harmonic (*red*, *narrow line*) and Lorentzian fit (*black*, *bold lined*). **b** RF linewidth of the first four harmonics measured via Lorentzian fitting versus harmonic number and parabolic fit for 120 mA (*black circles*, *solid line*) and 160 mA (*red triangles*, *dotted line*). Laser P_3, bias: $-1.0\,\mathrm{V}$.

For the first four harmonics, the measured $-3\,\mathrm{dB}$ linewidth increased quadratically with harmonic number, as shown in Fig. 4.4b. As the quadratic increase of the RF linewidth with the harmonic number is valid only for the case of low amplitude noise, the results obtained demonstrate that the RF spectrum is dominated by the timing jitter contribution and amplitude noise can be neglected [19].

Modal Optical Linewidth of PMLL

From [20], a set of Lorentzian lines with frequencies ω_n and linewidths $\Delta\omega_n$ compose the optical spectrum of a PMLL:

$$S(\omega) = \frac{|\hat{a}(\omega - \omega_0)|^2}{{T_\mathrm{r}}^2} \sum_{n=-\infty}^{\infty} \frac{2\Delta\omega_n}{(\omega_0 - \omega_n)^2 + \Delta\omega_n^2}, \tag{4.6}$$

where $\hat{a}$ is the Fourier transform of the steady-state pulse

$$\hat{a}(\omega) = \int_{-\infty}^{+\infty} a(t) e^{i\omega t} dt. \tag{4.7}$$

The power spectrum of the intensity, S_RF, is also a set of Lorentzians with the linewidths $\Delta\omega_{\mathrm{RF},m}$. From (4.3) and (4.6) the optical and RF linewidths of the first harmonic ($\Delta\omega_n$ and $\Delta\omega_{\mathrm{RF},1}$, respectively) are related as:

$$\Delta\omega_n = \Delta\omega_0 + \Delta\omega_{\mathrm{RF},1}(n - n_0)^2, \tag{4.8}$$

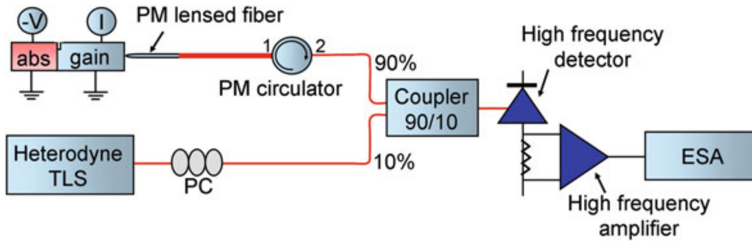

Fig. 4.5 Experimental setup for modal optical linewidth measurements

where n is the mode number and n_0 is the mode number corresponding to the minimum linewidth $\Delta\omega_0$. Thus, knowing the modal optical linewidths, a parabolic fit would give values for the RF first harmonic linewidth, $\Delta\omega_{RF,1}$.

We measured the modal optical linewidths using a heterodyne technique. The beating of each longitudinal mode with a narrow linewidth tunable laser source (TLS) was recorded with a high speed photodetector connected to an amplifier and an ESA, as shown in Fig. 4.5. The -3 dB linewidths were extracted from the Lorentzian fits. The TLS linewidth of $\sim$200 kHz was negligible compared with that of the PMLL.

Sets of individual modal linewidths were collected over a range of gain currents and bias voltages. The modal optical linewidth of the devices varied from 10 to 100s of MHz, exhibited Lorentzian lineshapes, and demonstrated a strong parabolic dependence on the mode number [22, 23]. Figure 4.6 shows measured beating signal (red) and corresponding Lorenzian fit (black, bold line).

Figure 4.7 shows measured optical linewidths (filled circles) versus mode number at a variety of bias currents. For convenience we have set $n_0 = 0$ in these plots. The red lines show root-mean-square parabolic fit, while the black dashed lines show the theoretical fit with fixed value of $\Delta\omega_{RF,1}$, measured directly from ESA (from Lorentzian fit).

The comparison between the directly measured RF linewidth and the fitted $\Delta\omega_{RF,1}$ is made in Fig. 4.8. Within the accuracy of the experiment, measured and calculated RF linewidth values largely agree, confirming that modal optical linewidth measurement can give a measure of the $\Delta\omega_{RF,1}$ via Eq. 4.8. This technique can be very advantageous when measuring the RF linewidth and timing jitter of short PMLLs with high repetition rates, where the RF peak of the first harmonic can not be measured directly. It has none of the limitations of von der Linde's method imposed by the requirement of large bandwidth equipment nor the experimental awkwardness and large power of the cross-correlation method.

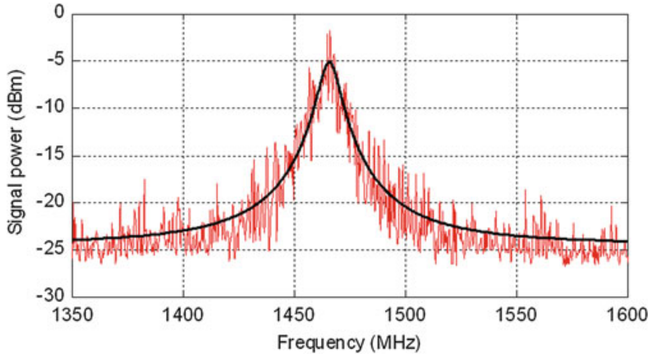

Fig. 4.6 Heterodyne beating signal measured by ESA (*red*) and the corresponding Lorenzian fit (*black*, *bold line*). Laser P_3; gain: 150 mA; absorber bias: $-1.0\,\text{V}$.

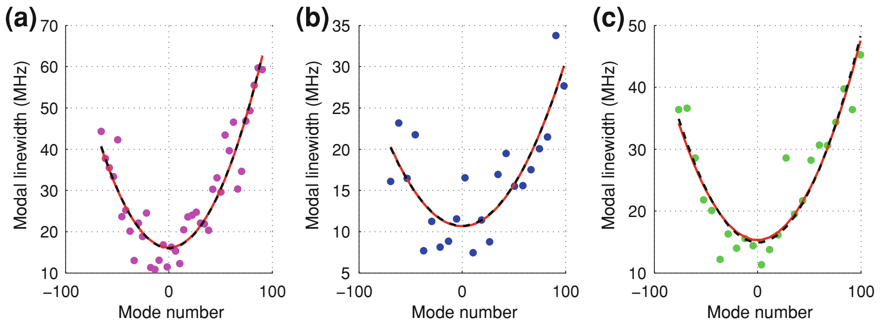

Fig. 4.7 Optical linewidth as a function of mode number (*filled circles*), a root-mean-square parabolic fit (*solid red lines*) and the theoretical fit from Eq. 4.8 (*dashed black lines*) at 120 mA (**a**), 140 mA (**b**) and 160 mA (**c**). Laser P_3; absorber bias: $-2.0\,\text{V}$.

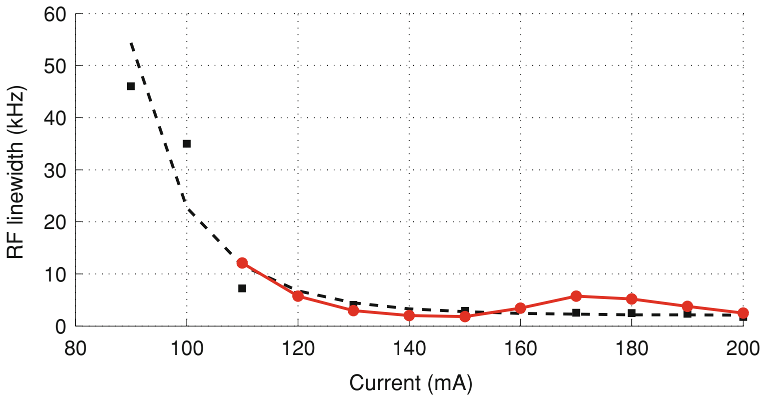

Fig. 4.8 RF linewidth as a function of bias current. *Black squares*: extracted from parabolic fit to modal linewidths. *Red circles*: directly measured by ESA. Laser P_3; absorber bias: $-2.0\,\text{V}$.

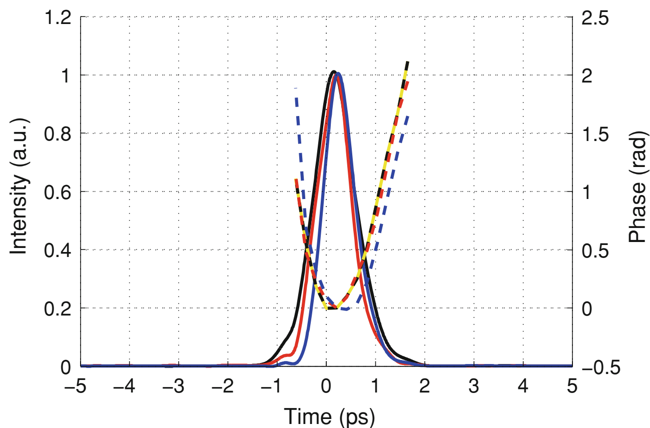

Fig. 4.9 Pulse shapes (*solid lines*) and phases (*dotted lines*) recovered from three different FRMZG measurements, identical conditions

Direct Electric Field Measurements

To completely characterize a periodic pulse train, one may give a set of modal intensities and phases. One nonlinear method to measure this is frequency-resolved optical gating (FROG) [24]. In this work a frequency resolved Mach-Zehnder gating (FRMZG) was used for complete pulse characterization. FRMZG is a linear spectrographic technique which allows recovery of low power pulses [25]. This technique, developed by Southern Photonics, is similar to frequency-resolved electro-absorbance gating, which has been shown to be an accurate method of pulse recovery [26], but in FRMZG the electro-absorbtion modulator is replaced with a Mach-Zehnder modulator.

For FRMZG measurements the light from one of the laser facets was passed through a Mach-Zehnder modulator, which was used as a gate, and then sent to a spectrometer (scanning Fabry-Pérot interferometer). As the lasers were passively mode-locked the trigger for the gate was derived from the laser output. The gate position was shifted along the pulse via a phase shifter and different parts of pulses were spectrally resolved as a function of the sampling time shift giving the spectrogram.

Direct electric field measurements for PMLL P_2 shown in Fig. 4.9 demonstrated asymmetrical pulse shape with faster leading edge and slower trailing edge (solid lines). The time dependence of the pulse phases (dotted lines) was close to a parabola, which indicated almost linear chirp of the pulses. From threshold ($I_{th} = 85\,\mathrm{mA}$) up to $1.4I_{th}$ (120 mA) the FRMZG reconstruction algorithm converged and the recovered pulse shape and phase were confirmed by comparison with the optical spectrum analyzer and autocorrelation measurements. However, for the currents above $1.4I_{th}$ the FRMZG algorithm failed to recover physical pulse shapes. This is in accordance with previous work using a high-sensitivity FROG

[27] and was interpreted as an outcome of waveform instabilities. A detailed discussion of this will be given in "Numerical simulations".

Thus, we can see that over large operation ranges at higher currents the performance of QD-PMLL is not optimal suffering waveform instabilities, highly chirped pulses, significant phase noise and large timing jitter. Therefore, other methods should be used to improve PMLL performance characteristics.

One common method is the electrical modulation of the laser absorber, 'hybrid' mode-locking. For InAs/GaAs QD mode-locked lasers, hybrid modulation [5] allows repetition rate control within a 30 MHz range [28] with integrated timing jitter values of hundreds of femtoseconds to a picosecond [29]. Another technique to improve laser noise performance can be optical feedback, when the light from the laser is reflected by a mirror and coupled back to the laser's cavity [30, 31]. At appropriate optical feedback level RF linewidth reduction below 1 kHz and timing jitter reduction to 1 ps (integration range from 10 kHz to 1 GHz) were achieved for PMLLs based on InAs/GaAs QDs [32, 33]. However, optical feedback does not allow control of the laser optical properties and can lead to instabilities [34], linewidth broadening [35], coherence collapse, and chaos. We use external continuous-wave (CW) optical injection to improve PMLL characteristics. An overview of the advantages and achievements of this technique is given in the next section.

Improvement of QD-MLLs Characteristics Applying Optical Injection

In optical injection, light from a master laser is coupled unidirectionally into the cavity of a slave laser. When the frequency of injected light is close to the frequency of one of the slave's longitudinal modes, the slave laser can lock to the master frequency. We call the slave 'phase-locked' to the master when the phase of injected slave mode is fixed in relation to the master source phase.

CW optical injection has been shown to be an effective method for noise reduction in semiconductor MLLs. Modal optical linewidth reduction below 20 kHz [36] due to phase locking of all slave modes to the master laser has been demonstrated in actively mode-locked MQW devices [37, 38]. Timing jitter reduction to 0.85 ps (integrated from 10 kHz to 50 MHz) and 20 dB phase noise suppression has been achieved in gain-switched DFB laser [39] and harmonically MLL [40], respectively. Optical spectrum narrowing with enhancement of injected mode and suppressed side modes under CW optical injection has been demonstrated in bulk semiconductor MLL [41].

QD CW lasers have shown very stable optical injection locking characteristics, with no instabilities observed at zero detuning frequency over a wide range of master powers [42]. Exited state pulse injection into QD-PMLL oscillating on the ground-state transition demonstrated phase and amplitude noise reduction of the slave laser [43]. These observations suggest that QD-PMLLs characteristics could

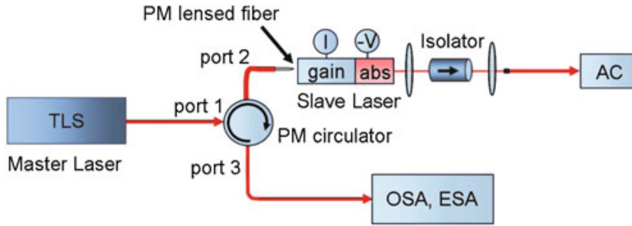

Fig. 4.10 Experimental setup for CW optical injection

be further improved and controlled through optical injection locking, for example, for applications such as remote coherent receivers [44].

Injection-Locking to a Single-Tone CW Master Source

In this section we consider QD-PMLLs under CW optical injection. The effect of optical injection on the slave laser optical spectrum, pulsewidth, noise performance, and modal optical linewidth is described. We demonstrate optical spectrum narrowing and tuning over a 10 nm range, time-bandwidth product (TBP) reduction down to the Fourier limit, and pulse train stabilization under optical injection. The numerical simulations reproduced observed phenomena, showing waveform instability suppression under CW optical injection.

Experimental Setup

For single-tone injection, light from a CW master laser (Agilent 81672 B) was coupled to the slave QD-MLL through a polarization maintaining (PM) fiber circulator, as shown in Fig. 4.10. Port 2 of the circulator was coupled to the gain section of the slave QD-MLL via a PM lensed fiber and port 3 used for diagnostics. Temperature control to 10 mK was achieved by the exclusion of air currents in addition to the actively controlled submount temperature.

Optical Spectrum of Injection-Locked QD-MLL

When the slave was injected within the locking range of one of its resonator modes, its repetition rate, optical spectrum, power, timing jitter, and phase noise were affected. Generally, the optical power was reduced with injection-locking and the repetition rate was shifted by 10–100s of MHz to higher frequencies.

Figure 4.11a shows the optical spectra of free-running (black) and injection-locked laser P_3 (colors) for a number of master wavelengths (shown with arrows). Injection-locking resulted in significant optical spectrum narrowing, with a 3 dB

bandwidth 10–20 times smaller compared to the free-running case, and tunability of the slave's optical spectrum via the master wavelength over a 10 nm range. The slave's output shape was remarkably consistent at different injection wavelengths, with very little laser power at wavelengths below the injection wavelength and the peak output shifted by 0.5–1.5 nm to longer wavelengths. Numerical simulations performed in "Numerical simulations" have shown that this red shift may be attributed to the difference in α-factors of the gain and absorber sections.

The strength of the injected power had a critical influence on the slave laser behavior. At excessive injection power ($> 80\,\mu W$) only one mode at the injection wavelength was amplified and the laser operated in a single mode CW regime [45], with too little master power ($< 1\,\mu W$) injection had no significant effect on the device. The locking range increased with the injection power achieving several GHz range; similarly to that observed for multimode [42] and DFB [46] QD lasers. However, an increase of injection strength resulted in a larger power drop, optical spectrum narrowing and hence pulse broadening. Figure. 4.12 shows optical spectra (a), autocorrelation traces (b) and recovered pulse profiles (c) for a number of injection powers.

At low injection powers, the autocorrelation pulsewidths of injection-locked lasers (see Fig. 4.11b, red dash–dotted line) were approximately the same as for free- running (black solid line), while the optical spectrum width was considerably reduced (see Fig. 4.11a, red). This resulted in TBP reduction; from values between 6 to 10 when free-running (black circles) down to 0.4 with injection (red triangles), as shown in Fig. 4.13. TBP was calculated as a product of the 3 dB optical bandwidth and the pulsewidth measured from autocorrelation trace, assuming a Gaussian pulse shape. FRMZG measurements (see Fig. 4.15, red) showed TBP reduction so that the pulses were nearly Fourier-transform limited even for small injection powers. The appropriate master power injected into the device was about from 2 to 5% of the slave power of $\sim 1\,mW$.

Remarkably, with injection-locking, the FRMZG recovery always converged for the range of biases examined (up to 200 mA). The retrieved pulses shown in Fig. 4.14 demonstrated an asymmetrical pulse shape with faster leading edge and slower trailing edge at smaller gain currents and pulse doubling at higher currents.

The recovered pulse shapes were verified by comparison with direct optical spectrum and autocorrelation measurements. Figure 4.15 shows a comparison between the directly measured optical spectrum (a, black solid line) and auto-correlation (b, black solid line), and recovered from FRMZG spectrogram (a, b, red circles).

Numerical Simulations

To describe the injection-locking phenomena we used the model proposed in [28, 47] for a PML ring cavity laser with Lorentzian spectral filtering profile and unidirectional operation. The model equations extend the classical model of Haus [48] to MLLs with large gain and losses per cavity round trip, i.e., the situation

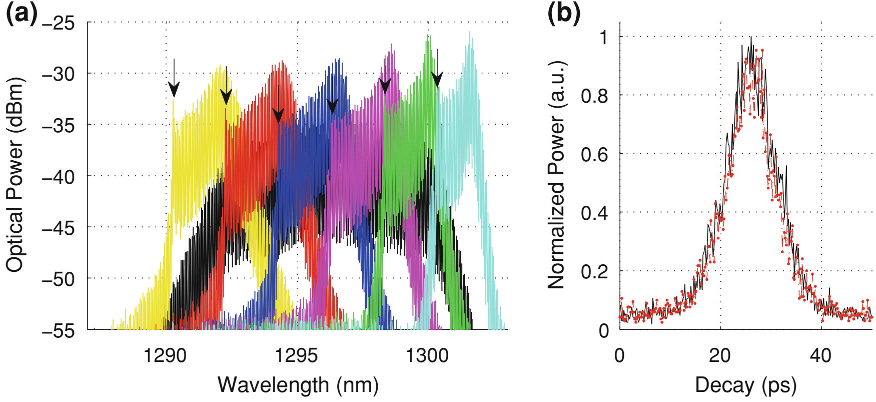

Fig. 4.11 **a** Optical spectra of the free-running laser P_3 (*black*) and injection-locked (*colors*) for different master wavelengths (shown with *arrows*). **b** Autocorrelation traces of the slave laser when free-running (*black*, *solid line*) and injection-locked (*red*, *dash–dotted line*) for one of the master wavelengths. Gain: 180 mA, absorber bias: −2.0 V.

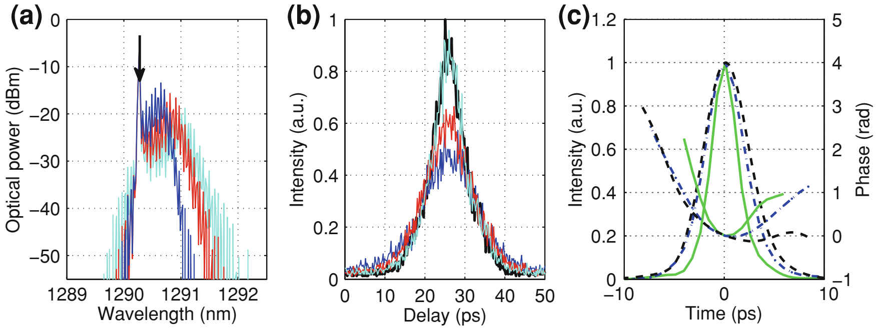

Fig. 4.12 **a** Optical spectra of injection-locked laser P_4 for injection powers of 23 µW (*cyan*), 54 µW (*red*), and 80 µW (*blue*). **b** Corresponding autocorrelation traces of the slave laser when free-running (*black*, *bold line*) and injection-locked (*colors*). Gain: 132 mA, absorber bias: −2.0 V. **c** Recovered pulses and phases for 6.4 µW (*green solid line*), 30 µW (*blue dash–dotted line*), and 43 µW (*black dashed line*) injection powers. Laser P_2; gain current: 104 mA; absorber bias: −6 V.

typical for semiconductor lasers. The model expressed in dimensionless terms reads

$$\gamma^{-1}\dot{A} + A = \sqrt{\kappa}e^{(1-i\alpha_g)G(t-T)/2-(1-i\alpha_q)Q(t-T)/2}A(t-T), \tag{4.9}$$

$$\dot{\rho}_g = -\gamma_g\rho_g + F_g(\rho_g, N_g) - e^{-Q}(e^G - 1)|A|^2, \tag{4.10}$$

$$\dot{N}_g = N_{g0} - \Gamma_g N_g - 2F_g(\rho_g, N_g), \tag{4.11}$$

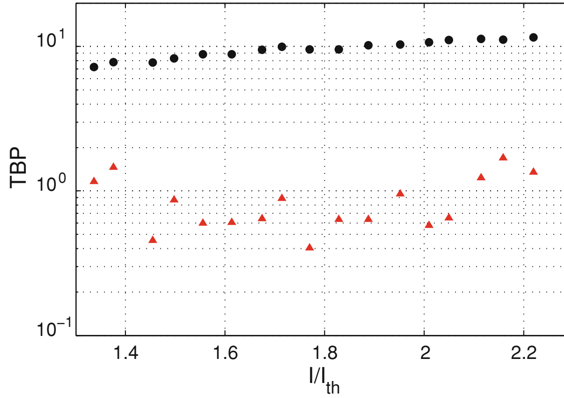

Fig. 4.13 TBP of laser P_3 when free-running (*black*) and with single-tone (*red*) injection. Absorber bias: -2 V.

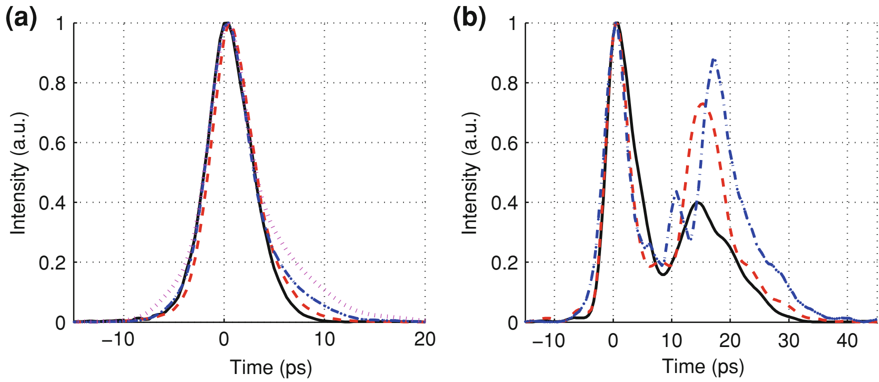

Fig. 4.14 **a** Recovered pulse intensity profiles for the injection-locked laser P_2 at 100 mA (*black*, *solid line*), 110 mA (*red*, *dashed line*), 120 mA (*blue*, *dot–dashed line*), 130 mA (*magenta*, *dotted line*). **b** Recovered pulse profiles at 150 mA (*black*, *solid line*), 160 mA (*red*, *dashed line*), 170 mA (*blue*, *dot–dashed line*). Absorber bias: -2.0 V.

$$\dot{\rho}_q = -\gamma_q \rho_q + F_q(\rho_q, N_q) - s(1 - e^{-Q})|A|^2, \tag{4.12}$$

$$\dot{N}_q = N_{q0} - \Gamma_q N_q - 2F_q(\rho_q, N_q), \tag{4.13}$$

$$\text{with} \qquad G(t) = 2L_g g_g(2\rho_g - 1), \qquad Q(t) = 2L_q g_q(2\rho_g^g - 1) \tag{4.14}$$

where A is an electric field envelope, $\rho_{g,q}$ and $N_{g,q}$ occupation probability in a dot and carrier density in the wetting layer in gain (absorber) section; T is the cold cavity round trip time; parameter γ represents the gain/losses bandwidth, κ is the attenuation factor describing linear non-resonant intensity losses per cavity

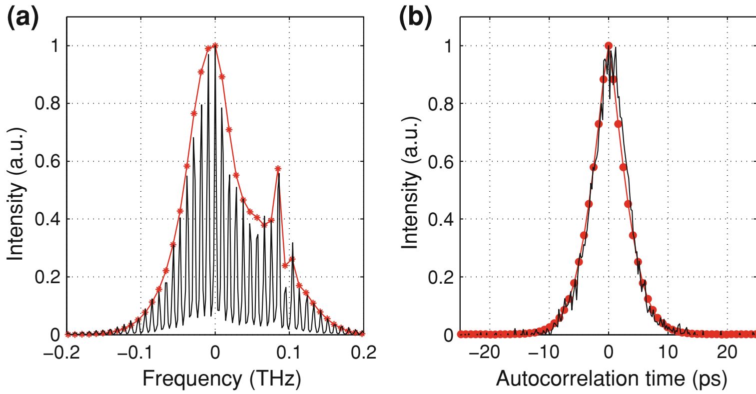

Fig. 4.15 **a** Directly measured optical spectrum of injection-locked laser (*black*, *solid line*) and recovered from FRMZG spectrogram (*red*, *circles*). **b** Autocorrelation trace for injection-locked laser output (*black*, *solid line*) and calculated autocorrelation from recovered pulse (*red*, *circles*). Laser P_2; current: 118 mA; bias: −6.0 V.

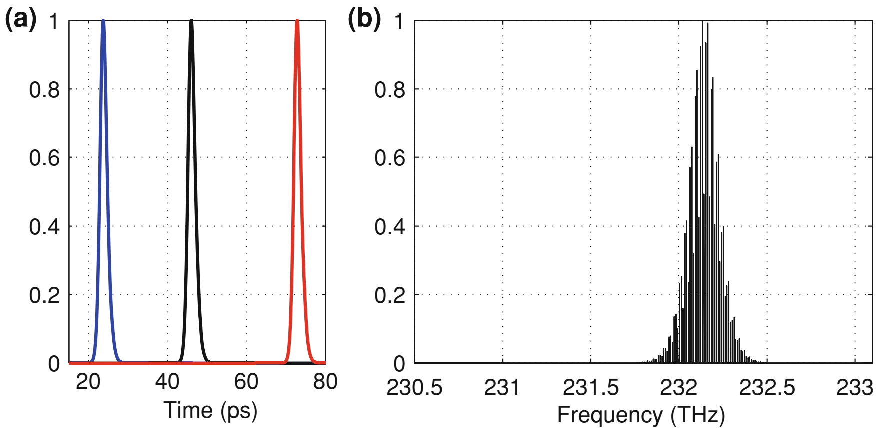

Fig. 4.16 **a** Three pulses from the stable pulse train. **b** Optical spectrum of the stable pulse train. $N_{g_0} = 0.06$

round trip. The parameters $g_{g,q}$, $\Gamma_{g,q}$ and $\gamma_{g,q}$ are the differential gains, the carrier relaxation rates in the wetting layers, and the carrier relaxation rates in the dots, respectively. The dimensionless parameters N_{g0} and N_{q0} describe the pumping processes in the amplifier and the absorber sections; s is the ratio of the saturation intensities in gain and absorber media. Finally, α_g and α_q are linewidth enhancement factors in gain and absorber sections and L_g and L_q correspond to the lengths of gain and absorber section.

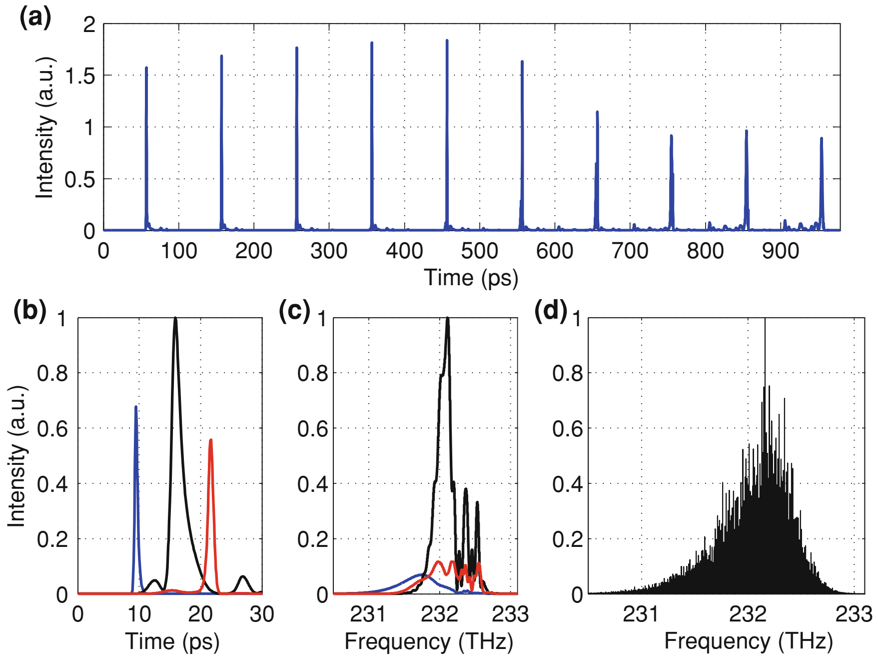

Fig. 4.17 **a** Example of unstable pulse train. **b** Three non-consecutive pulses forms from unstable pulse train. **c** Fourier transforms of three pulses shown in (b). **d** Optical spectrum of the unstable pulse train. $N_{g_0} = 0.1$

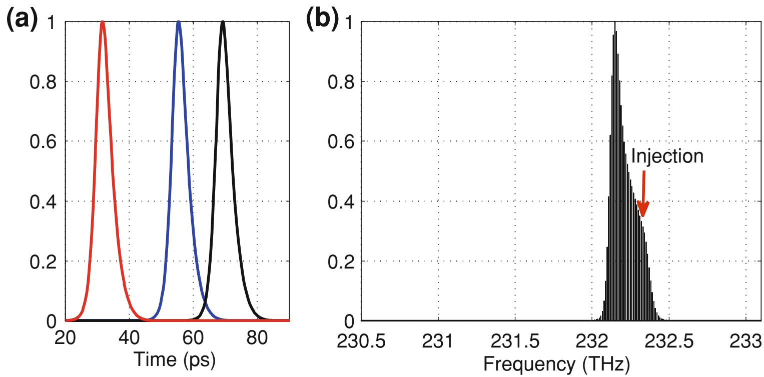

Fig. 4.18 **a** Pulses are stabilized with injection. **b** Optical spectrum of the injected laser. $N_{g_0} = 0.1$, $\omega = -0.203$, $\eta = 0.005$.

The functions $F_{g,q}(\rho_{g,q}, N_{g,q})$ describe the carrier exchange rate between the wetting layers and the dots. In the most general form, the carrier exchange can be written as

$$F_{g,q}(\rho_{g,q}, N_{g,q}) = R^{\text{cap}}_{g,q}(1 - \rho_{g,q}) - R^{\text{esc}}_{g,q}\rho_{g,q}, \tag{4.15}$$

where $(1 - \rho_{g,q})$ is the Pauli blocking factor, $R^{\text{cap}}_{g,q} = B_{g,q}N_{g,q}$ describes the carrier capture from the wetting layer to the dots with the rate $B_{g,q} \times R^{\text{esc}}_{g,q}$ is a temperature-dependent coefficient defining carrier escape from the dots to the wetting layer.

We numerically integrated equations for a laser with $L_g = 0.88$, $L_q = 0.12$, $\alpha_g = 2$, $\alpha_q = 1$, $\gamma = 20$, $\kappa = 0.5$, $B_g = 5$, $B_q = 5$, $R^{\text{esg}}_g = 0.4$, $R^{\text{esq}}_q = 1$, $g_g = 6$, $g_q = 10$, $N_{q_0} = 2$, $s = 25$, $\gamma_g = 0.01$, $\gamma_q = 0.01$, $\Gamma_g = 0.01$, $\Gamma_q = 1$, $T = 10$. This corresponds to a mode-locked laser with a 10 GHz repetition rate with 17 nm gain bandwidth, an absorber recovery time of 13 ps and a gain recovery time of 100 ps as extracted from pump-probe spectroscopy measurements [49, 50]. For these parameters the mode-locking threshold occurs at $N_{g0,\text{th}} = 0.022$ and a periodic pulse train is emitted, as shown in Fig. 4.16a which repeat Lorentzian optical spectrum calculated over the long pulse train (see Fig. 4.16b).

These pulses remain stable for $N_{g_0} < 0.1$ and become unstable for higher values of N_{g_0}. In such a case a waveform instability appears hence causing the optical spectrum broadening. Figure 4.17a demonstrates an example of an unstable pulse train. Figure 4.17b and c shows three non-consecutive pulses (black, red, blue) and their corresponding Fourier transforms, demonstrating the changing pulse shapes. Figure 4.17d shows the optical spectrum of the long pulse train.

To model optical injection we added a term $\eta e^{i\omega t}$ into Eq. 4.9, where η is the injection amplitude and ω is the detuning from the central frequency. With appropriate choice of η and ω we observed that injection suppressed the waveform instabilities which resulted in pulse stabilization (see Fig. 4.18a) and spectral narrowing (see Fig. 4.18b).

The injected slave spectrum is shifted to the red side of the master wavelength as seen in Figs. 4.11a (from experiment) and 4.18b (numerical simulations). We found that this effect can be observed when using parameters $\alpha_g > \alpha_q$. Indeed, this condition and inequality $G - Q > \ln(\kappa)$ (which holds during the pulse) result in $\alpha_g G - \alpha_q Q > 0$, which causes the red frequency shift $-\Delta\omega = \alpha_g G - \alpha_q Q$, from the imaginary part of exponent in (4.9).

Modal Optical Linewidth

In previous sections we have shown the positive effect of CW optical injection, however, single-tone injection does not allow control of the device repetition rate, and can lead to frequency pulling, timing jitter increase and amplitude modulation. Figure 4.19 shows first harmonic signals of free-running (black solid line) and injection-locked (red dash-dotted line) QD-PMLLs, demonstrating RF linewidth reduction (a), RF linewidth increase (b), and modulation (c), depending on the bias conditions and device characteristics.

Figure 4.20 shows the optical spectra (a) and individual modal linewidths (b) for a PMLL when free-running (black) and with single-tone optical injection (cyan).

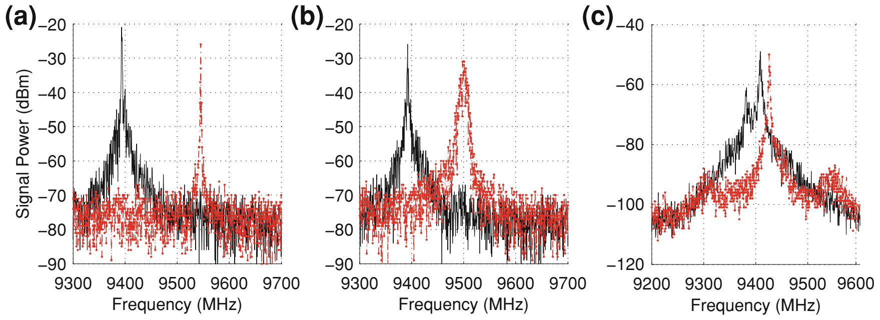

Fig. 4.19 Measured first harmonic spectra for free-running (*black solid line*) and injection-locked (*red dash–dotted line*) lasers. **a** Laser P_4; gain: 170 mA; absorber bias: −3.0 V. **b** Laser P_4; gain: 183 mA; absorber bias: −3.0 V. **c** Laser P_2; gain: 140 mA; absorber bias: −6.0 V.

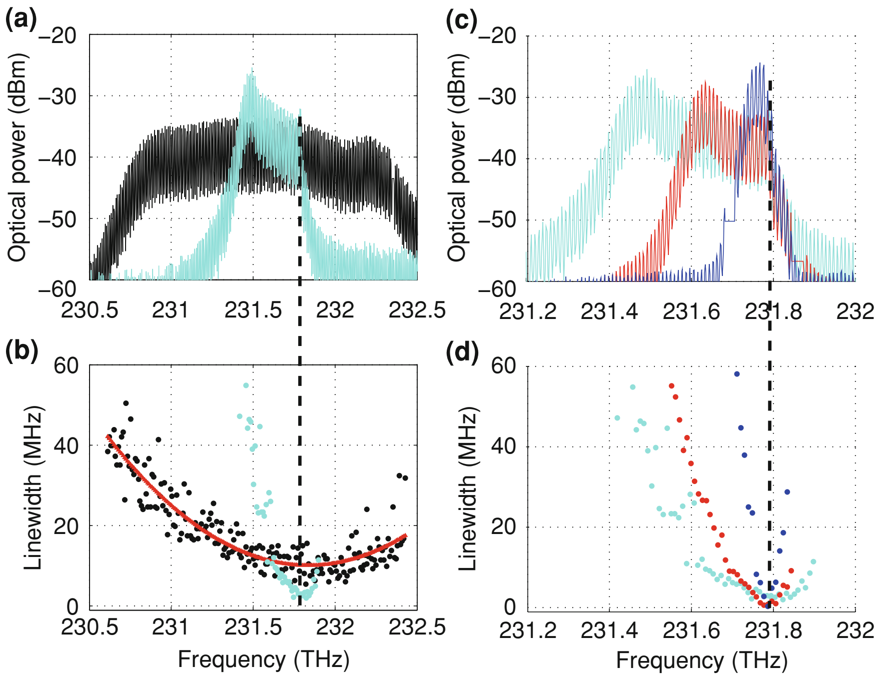

Fig. 4.20 **a** Optical spectra of slave laser when free-running (*black*) and injection-locked (*cyan*). **b** Modal optical linewidth of injected laser (*black*) and when free running (*cyan*). Reprinted from [51]. **c** Optical spectra for injection-locked slave at 25, 78, and135 μW injection power. **d** Corresponding modal optical linewidth. Laser P_3; gain: 160 mA; absorber bias: −4.0 V.

Single-tone injection reduced greatly the phase noise of the device in the vicinity of the injection wavelength. Several modes close to the injection frequency (dotted line) were phase-locked to the master (that is, they attained the narrow linewidth of

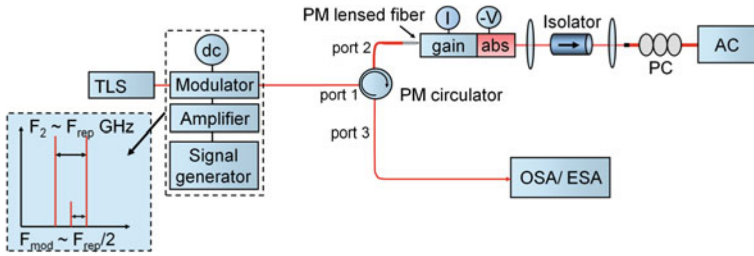

Fig. 4.21 Experimental setup for dual-tone coherent injection. *Inset* shows schematic diagram of the modulator optical specrum with the suppressed carrier frequency

the master TLS). However, moving further away from the injection frequency the modal linewidth increased and could achieve larger values than those of the free-running case, subject to the bias conditions and device characteristics. Increase of the master power exacerbated the effect, as shown in Fig. 4.20c, d.

Thus, further efforts should be made to reduce the noise, control the repetition rate of the device, and achieve a highly coherent frequency comb, for example, injection-locking to a two-tone coherent master source [52], or combination of single-tone CW injection and active/hybrid mode-locking [36, 38].

Injection of two-tone coherent lines generated by phase/amplitude modulation of the CW master source was first demonstrated experimentally by Goldberg et al. [53] using the frequency-modulated sidebands of a GaAlAs diode lasers. Sidebands injection-locking has been shown a successful technique to improve the noise properties in InGaAsP DFB lasers [54], led to RF linewidth reduction and repetition rate control over 170 MHz range in DBR PMLL [52], and allowed synchronization of frequency combs of multiple sources [44].

Injection-Locking to a Dual-Tone Coherent Master Source

In this Section we present studies of injection-locking of a slave laser by a dual-tone coherent master source. The light from the TLS was amplitude modulated by a Mach-Zehnder modulator driven via an amplified Rohde and Schwarz SMR 60 signal generator to generate coherent tones. The diagram of the experimental setup is presented in Fig. 4.21. The modulator was biased at the transmission minimum, which resulted in the generation of two coherent sidebands, with a suppressed carrier frequency. The frequency of the driver was chosen close to half the repetition rate of the slave laser, so that the separation between the sidebands was close to the fundamental frequency of mode-locking.

Similar to injection-locking to a single-tone source, locking to the dual-tone source resulted in PMLL optical spectrum narrowing (see Fig. 4.22a), tuning with the master wavelength [55], and TBP improvement (see Fig. 4.23).

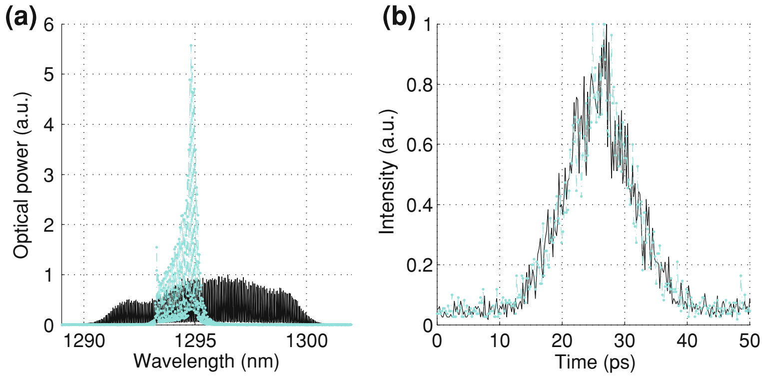

Fig. 4.22 Optical spectra (**a**) and SHG autocorrelation traces (**b**) of laser P_3 when free-running (*black*, *solid line*) and with dual-tone coherent injection (*cyan*, *dot–dashed line*)

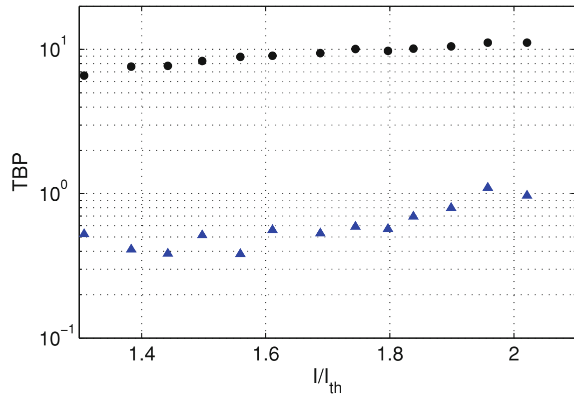

Fig. 4.23 TBP of laser P_3 when free-running (*black circles*) and with single-tone (*blue triangles*) injection. Absorber bias: -2 V.

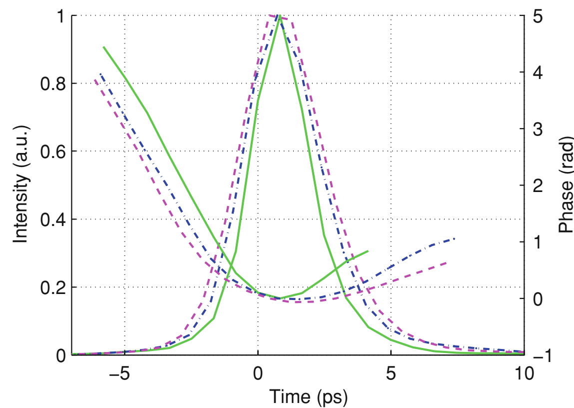

Fig. 4.24 Recovered pulses and phases for 7 µW (*green solid line*), 40 µW (*blue dash–dotted line*) and 50 µW (*magenta dashed line*) injection powers. Laser P_2; gain current: 104 mA; absorber bias: -6 V.

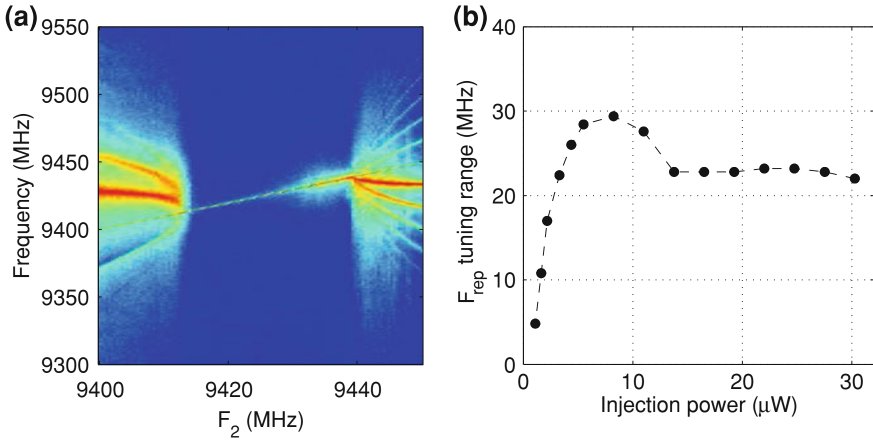

Fig. 4.25 **a** Evolution of the slave PMLL electronic spectrum with modulator frequency detuning. **b** The slave frequency detuning range as a function of the injected optical power. Reprinted from [45]. Laser P_2; gain current: 100 mA; absorber bias: −6.0 V.

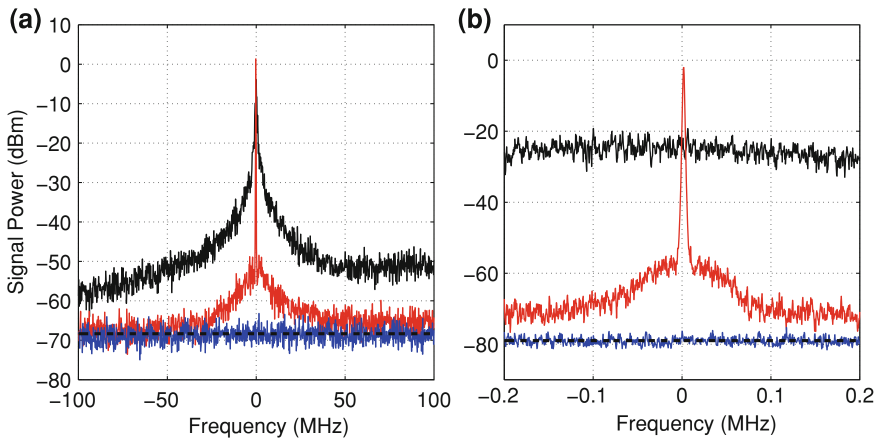

Fig. 4.26 RF signals of the slave laser P_2 when free-running (*black*) and with dual-tone injection (*red*). Gain: 90 mA, absorber bias: −6 V. *Blue line* and *black dotted line* show the noise signal and noise level, respectively. **a** 200 MHz span, RBW = 100 kHz, VBW = 10 kHz; **b** 400 kHz span, RBW = 1 kHz, VBW = 100 Hz

FRMZG measurement have shown the stabilizing effect of the dual-tone injection upon the slave laser pulse train as the slave pulses could be recovered for a wide range of currents and injection powers (see Fig. 4.24). Similar to the previously discussed results for single-tone injection, an increase of the dual-tone injection strength resulted in pulse broadening and optical spectrum narrowing; however, no single-mode CW regime could be observed for dual-tone injection. The optimal range of

injection strength was around 5% of the slave laser power, when the pulsewidth broadening with respect to the free-running laser was not observed (see Fig. 4.22b) and the pulses were close to transform-limited, as shown in Fig. 4.23.

Dual-tone injection-locking requires not only that both injected optical frequencies are close to the respective slave laser longitudinal modes, but also that the beating frequency, F_2, between the master modes lies within a narrow range around the injected laser repetition rate. Stable operation was achieved over a range of $\pm 10\,\mathrm{MHz}$ around the injected laser repetition rate, which was shifted from the free-running F_{rep} by $\sim 10-100\,\mathrm{s}$ of MHz, depending on the laser used and bias conditions. The evolution of the slave RF spectrum with modulator frequency detuning, F_2, is shown in Fig. 4.25a. Dual-tone locking allowed tuning of the slave repetition rate over a 25 MHz range with a significant jitter reduction. F_{rep} tuning range increased with optical injection power at low injection levels, and saturated at injection powers of $\sim 8\,\mu\mathrm{W}$ (see Fig. 4.25b), which is consistent with results reported for distributed Bragg grating PMLL [52]. Thus, low injection levels allowed optical spectrum narrowing and TBP improvement without visible pulse broadening, along with a large range of F_{rep} frequency tuning.

When the slave was locked to a dual-tone coherent source, the RF linewidth of its first harmonic was reduced greatly, from hundreds of kHz for free-running case to below 1 kHz resolution bandwidth (RBW) of the ESA when injection-locked. The ESA filter width was 4 kHz at −20 dB level measured RF signals for the free-running laser (black) and with dual-tone injection (red) are shown in Fig. 4.26. This instrument limited spike sat above a phase noise pedestal, as shown for the small span in Fig. 4.26b, which led to the measurable jitter of the slave (see Fig. 4.27a). The signal noise floor was reduced below the instrument noise level (blue) at 50 MHz from the signal peak.

The timing jitter was calculated via integration of the phase noise of the slave's first harmonic signal in the range from 20 kHz to 80 MHz. Dual-tone injection-locking resulted in reduction of the integrated timing jitter from 11 to 21 ps for free-running regime, to 300 fs–1 ps, as shown in Fig. 4.27a. Timing jitter decreased with injection strength increase until achieving minimal value at injection powers of $> 10\,\mu\mathrm{W}$, as shown in Fig. 4.27b. Timing jitter values of 210 fs were achieved for some bias conditions and injection powers (see Fig. 4.27b, black circles), which is consistent with the best published results for similar devices with hybrid mode-locking [56].

With dual-tone injection-locking all measurable modal optical linewidths of the slave's modes (see Fig. 4.28a, blue) were reduced to the master source linewidth, within the resolution of the experiment (chosen RBW of ESA was 300 kHz). Figure 4.27a shows optical spectra of the laser P_3 without injection (black) and when phase-locked to the dual-tone master source (cyan); Fig. 4.27b shows corresponding modal linewidths. Similar results have been observed in MQW devices for the combination of active mode-locking and CW optical injection [37]. Here, instead of using an electroabsorption modulator (active mode-locking) or applying

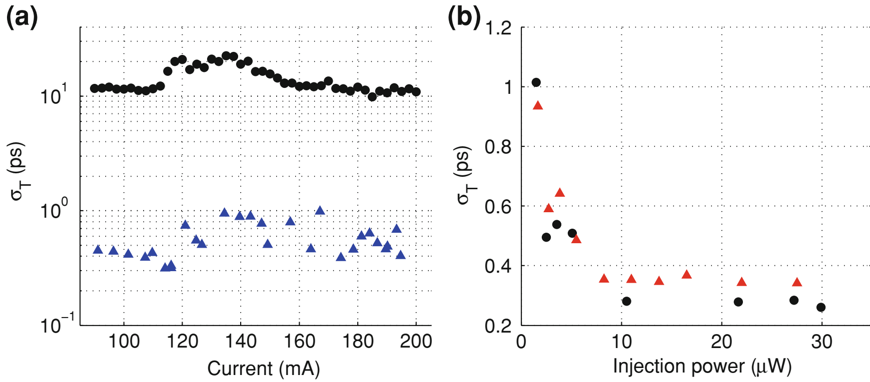

Fig. 4.27 **a** Integrated timing jitter of a free-running PMLL (*black*), and with dual-tone injection (*blue*). Reprinted from [55]. **b** Integrated timing jitter as a function of the injected optical power at 118 mA (*black*, *circles*) and 100 mA (*red*, *triangles*) gain currents. Laser P_2; absorber bias: −6 V.

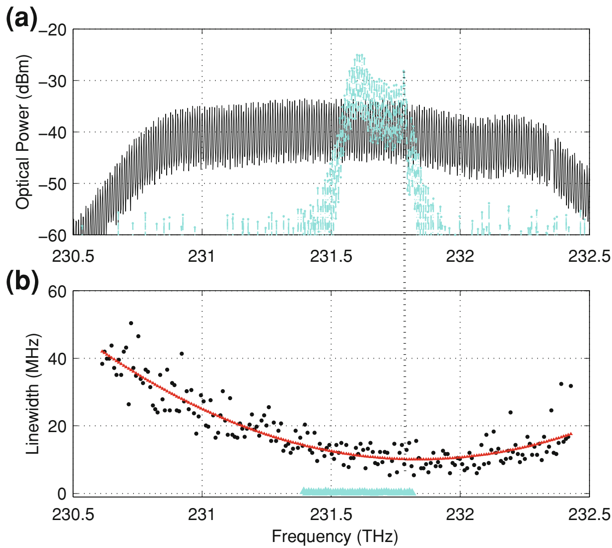

Fig. 4.28 **a** Optical spectra for slave laser P_3 when free-running (*black*) and dual-tone injection-locked (*cyan*). **b** individual optical linewidth of injected laser (*cyan*, *triangles*) compared to free-running (*black*, *circles*). *Red line* shows parabolic fit to the measured linewidths of free-running laser Gain: 160 mA, absorber bias: −4.0 V. Reprinted from [57]

modulated signal to the absorber section (hybrid mode-locking), we modulate the field in the laser cavity with dual-tone injection, thus clocking the passive absorber section.

Thus, dual-tone coherent injection has shown to be a promising technique to control and enhance the performance of QD-PMLLs. Large reductions of pulse TBP and stable pulses have been obtained by dual-mode injection-locking, as well as optical spectrum tuning and all-modal linewidth narrowing. Integrated timing jitter values below 300 fs (20 kHz–80 MHz) were achieved at small injection levels along with slave F_{rep} tuning over a 25 MHz range, consistent with tuning ranges reported for hybridly mode-locked samples [28]. The technique presented here can also be considered as a form of hybrid mode-locking, but it has added advantages such as the spectral narrowing and wavelength tuning. Similar benefits can be achieved by a combination of hybrid mode-locking with optical injection. The ability to tune the wavelength without detrimental effect on the pulseshape is essential for optical communications and clock recovery [58, 59]. The considerable reduction of timing jitter and optical linewidth after injection also makes this arrangement attractive for time-division-multiplexing [60], wavelength-division-multiplexing [61], and optical sampling.

Conclusions

QD-PMLL noise characterization has shown the dominance of the timing jitter fluctuations over the amplitude noise. The modal optical linewidth measurements have confirmed the theoretically predicted parabolic dependence of the optical linewidth versus the modal number, with the slope of the parabola equal to the RF linewidth of the first harmonic. This observation provides a novel technique for RF linewidth and timing jitter measurement in ultrafast MLLs, whose repetition rate exceeds ESA limits.

Direct electric field measurements performed using a linear pulse reconstruction technique have shown asymmetric pulse shapes and linear chirp of the passively mode-locked pulses at small gain currents and the appearance of waveform instabilities at higher currents, which has been recreated via numerical simulations.

CW optical injection is a relevant instrument to improve QD-PMLL performance leading to waveform instability suppression, optical spectrum narrowing, and center wavelength tuning over a 10 nm range. Optimal values of injected power, where optical spectrum narrowing was not accompanied by pulse broadening, have been found to be around $\sim 5-10\%$ of the slave power. TBP values of 0.4, close to the Fourier limit, have been demonstrated for a wide range of currents. However, single-tone injection has induced phase noise increase and small amplitude intensity modulation, which may necessitate further efforts for the complete control of PMLL properties.

Injection-locking to a dual-tone coherent optical source have shown to be a promising technique to enhance and control laser performance. The benefits obtained by means of single-tone injection have been retained with dual-tone master source, with additional improvement of the slave's noise properties. RF linewidth reduction below instrument limits of 1 kHz, repetition rate control over a

25 MHz range, integrated timing jitter (20 kHz–80 MHz) values below 300 fs, with a record values of 210 fs has been demonstrated under dual-tone injection-locking, along with all-modal optical linewidth narrowing. This ease of control further recommends QD-MLL as a flexible, high performance solution for pulsed laser diode applications.

References

1. Hargrove, L.E., Fork, R.L., Pollack, M.A.: Appl. Phys. Lett. **5**(1) (1964)
2. DeMaria, A.J., Stetser, D.A., Heynau, H.: Appl. Phys. Lett. **8**(7) (1966)
3. Keller, U., Miller, D.A.B., Boyd, G.D., Chiu, T.H., Ferguson, J.F., Asom, M.T.: Opt. Lett. **17**(7) (1992)
4. Weber, A.G., Schell, M., Fischbeck, G., Bimberg, D.: IEEE J. Quantum Electron. **28**(10) (1992)
5. Thompson, M.G., Marinelli, C., Tan, K.T., Williams, K.A., Penty, R.V., White, I.H., Kaiander, I.N., Sellin, R.L., Bimberg, D., Kang, D.J., Blamire, M.G., Visinka, F., Jochum, S., Hansmann, S.: Electron. Lett. **39**(15) (2003)
6. Fork, R.L., Greene, B.I., Shank, C.V.: Appl. Phys. Lett. **38**(9), 25 (1981)
7. Wu, M.C., Chen, Y.K., Tanbun-Ek, T., Logan, R.A., Chin M.A., Raybon, G.: Appl. Phys. Lett. **57**(8) (1990)
8. Chen, Y.K., Wu, M.C., Tanbun-Ek, T., Logan, R.A., Chin, M.A.: Appl. Phys. Lett. **58**(12) (1991)
9. Thompson, M.G., Marinelli, C., Zhao, X., Sellin, R.L., Penty, R.V., White, I.H., Kaiander, I.H., Bimberg, D., Kang, D.J., Blamire, M.G.: Electron. Lett. **42**(5) (2007)
10. Arahira, S., Oshiba, S., Matsui, Y., Kunii, T., Ogawa, Y.: Opt. Lett. **19**(11) (1994)
11. Viktorov, E.A., Erneux, T., Mandel, P., Piwonski, T., Madden, G., Pulka, J., Huyet, G., Houlihan, J.: Appl. Phys. Lett. **94**, 263502 (2009)
12. Piwonski, T., Pulka, J., Madden, G., Huyet, G., Houlihan, J., Pozo, J., Vogiatzis, N., Ivanov, P., Rorison, J.M., Barrios, P.J., Gupta, J.A.: Appl. Phys. Lett. **106**, 083104 (2009)
13. Piwonski, T., Pulka, J., Madden, G., Huyet, G., Houlihan, J., Viktorov, E.A., Erneux, T., Mandel, P.: Appl. Phys. Lett. 94(12) (2009)
14. O'Donoghue, S.: Investigation and optimisation of mode-locked semiconductor quantum dot lasers. Ph.D. thesis, University College Cork (2011)
15. Delfyett, P.J., Gee, S., Choi, M.T., Izadpanah, H., Lee, W., Ozharar, S., Quinlan, F., Yilmaz, T.: J. Lightwave Technol. **24**(7), 2701 (2006)
16. Lee, W., Izadpanah, H., Menendez, R., Etemad, S., Delfyett, P.J.: J. Lightwave Technol. **26**(8), 908 (2008)
17. Udem, T., Holzwarth, R., Hansch, T.W.: Nature **46**, 233 (2002)
18. Haus, H.A., Mecozzi A.: IEEE J. Quantum Electron. **29**(3) (1993)
19. von der Linde, D.: Appl. Phys. B **39** (1988)
20. Kärtner, F.X., Morgner, U., Schibli, T., Ell, R., Haus, H.A., Fujimoto, J.G., Ippen, E.P.: Top. Appl. Phys. **95** (2004)
21. Kèfèlian, F., O'Donoghue, S., Todaro, M.T., McInerney, J.G., Huyet, G.: IEEE Photonics Technol. Lett. **20**(16) (2008)
22. Takushima, Y., Sotobayashi, H., Grein, M.E., Ippen, E.P., Haus, H.A.: Proc. SPIE **5595** (2004)
23. Habruseva, T., O'Donoghue, S., Rebrova, N., Kèfèlian, F., Hegarty, S.P., Huyet, G.: Opt. Lett. **34**(21) (2009)
24. Kane, D.J., Trebino, R., J. Quantum Electron. **29**(2) (1993)

25. Thomsen, B.C., Roelens, M.A.F., Watts, R.T., Richardson, D.J.: IEEE Photonics Technol. Lett. **17**(9) (2005)
26. Dorrer, C., Kang, I., Opt. Lett. **27**(15) (2002)
27. Xin, Y.C., Kane, D.J., Lester, L.F.: Electron. Lett. **44**(21) (2008)
28. Fiol, G., Arsenijevic, D., Bimberg, D., Vladimirov, A.G., Wolfrum, M., Viktorov, E.A., Mandel, P.: Appl. Phys. Lett. **96**, 011104 (2010)
29. Thompson, M.G., Larsson, D., Rae, A., Yvind, K., Penty, R.V., White, I.H., Hvam, J. Kovsh, A.R., Mikhrin, D.L. S., Krestnikov I.: In: Proceedings of ECOC (2006)
30. Lang, R., Kobayashi, K.: IEEE J. Quantum Electron. **16**(3) (1980)
31. O'Brien, D., Hegarty, S.P., Huyet, G., McInerney, J.G., Kettler, T., Laemmlin, M., Bimberg, D., Ustinov, V.M., Zhukov, A.E., Mikhrin, S.S., Kovsh, A.R.: Electron. Lett. **39**(25) (2003)
32. Lin, C.Y., Grillot, F., Naderi, N.A., Lester, Y.L.L.F.: Appl. Phys. Lett. **96**(5), 051118 (2010)
33. Fiol, G., Kleinert, M., Arsenijevic, D., Bimberg, D.: Semicond. Sci. Technol. **26**, 014006 (2011)
34. Grillot, F., Lin, C.Y., Naderi, N.A., Pochet, M., Lester, L.F.: Appl. Phys. Lett. **94**, 153503 (2009)
35. Tkach, R., Chraplyvy, A.R.: J. Lightwave Technol. **4**(11), 1655 (1986)
36. Takada, A., Imajuku W.: IEEE Photonics Technol. Lett. **9**(10) (1997)
37. Teshima, M., Sato, K., Koga, M.: J. Quantum Electron. **34**(9), 1588 (1998)
38. Jung, T. Shen, J.L., Tong, D.T.K., Murthy, S., Wu, M.C., Tanbun-Ek, T., Wang, W., Lodenkamper, R., Davis, R., Lembo, L.J., Brock, J.C.: IEEE Trans. Microw. Theory Tech. **47**(7) (1999)
39. Seo, D.S., Kim, D.Y., Liu, H.F.: Electron. Lett. **32**(1), 44 (1996)
40. Quinlan, F., Gee, S., Ozharar, S., Delfyett, P.J.: IEEE Photonics Technol. Lett. **19**(16) (2007)
41. Joneckis, L.G., Ho, P.T., Burdge, G.L.: J. Quantum Electron. **27**(1), 1854 (1991)
42. Goulding, D., Hegarty, S.P., Rasskazov, O., Melnik, S., Hartnett, M., Greene, G., McInerney, J.G., Rachinskii, D., Huyet, G.: Phys. Rev. Lett. **98**(15) (2007)
43. Kim, J., Delfyett, P.: Opt. Express **16**, 11153 (2008)
44. Lee, W., Delfyett, P.J.: Electron. Lett. **40**(19) (2004)
45. Habruseva, T., Huyet, G., Hegarty, S.: J. Sel. Top. Quantum Electron. **4** (2011)
46. Kelleher, B., Goulding, D., Hegarty, S.P., Huyet, G., Cong, D.Y., Martinez, A., Lemaitre, A., Ramdane, A., Fischer, M., Gerschuetz, F., Koeth, J.: Opt. Lett. **34**(4), 440 (2009)
47. Vladimirov, A., Turaev, D.: Phys. Rev. A **72**, 033808 (2005)
48. Haus, H.A.: J. Appl. Phys. **46** (1975)
49. O'Driscoll, I., Piwonski, T., Houlihan, J., Huyet, G., Manning, R.J., Corbett, B.: Appl. Phys. Lett. **91**, 263506 (2007)
50. O'Driscoll, I., Piwonski, T., Schleussner, C.F., Houlihan, J., Huyet, G., Manning, R.: Appl. Phys. **L91**, 071111 (2007)
51. Habruseva, T., O'Donoghue, S., Rebrova, N., Hegarty, S.P., Huyet, G.: SPIE Proc. **7608**, 760803 (2010)
52. Ahmed, Z., Liu, H.F., Novak, D., Ogawa, Y., Pelusi, M.D., Kim, D.Y.: IEEE Photonics Technol. Lett. **8**(1), 37 (1996)
53. Goldberg, L., Taylor, H.F., Weller, J.F.: Electron. Lett. **18**((11), 1019 (1982)
54. Kikuchi, K., Zan, C.E., Lee, T.P.: J. Lightwave Technol. **6**((12), 1821 (1988)
55. Habruseva, T., O'Donoghue, S., Rebrova, N., Reid, D.A., Barry, L., Rachinskii, D., Huyet, G., Hegarty, S.P.: IEEE Photonics Technol. Lett. **22**(6) (2010)
56. Carpintero, M., Thompson, M.G., Penty, R.V., White, I.H.: IEEE Photonics Technol. Lett. **21**(6) (2009)
57. Habruseva, T., Rebrova, N., Hegarty, S.P., Huyet, G.: SPIE Proc. **7720**, 77200Z (2010)
58. Renaudier, J., Lavigne, B., Jourdan, M., Gallion, P., Lelarge, F., Dagens, B., Accard, A., Legouezigou, O., Duan, G.H.: In: Proceedings of European Conference Exhibition on Optical Communications (ECOC), pp. 31–32 (2005)

59. e Silva, M.C., Lagrost, A., Bramerie, L., Gay, M., Besnard, P., Joindot, M., Simon, J.C., Shen, A., Duan, G.: In: National Fiber Optic Engineers Conference (NFOEC) (2010)
60. e Silva, M.C., Lagrost, A., Bramerie, L., Gay, M., Besnard, P., Joindot, M., Simon, J.C., Shen, A., Duan, G.H.: J. Lightwave Technol. **29**(4)(2011)
61. Nguyen, Q.T., Besnard, P., Bramerie, L., Shen, A., Kazmierski, C., Chanlou, P., Duan, G.H., Member, S., Simon, J.C.: IEEE Photonics Technol. Lett. **22**(11), 733 (2010)

Chapter 5
Catastrophic Optical Damage in Quantum Dot Lasers

Ching Kean Chia and Mark Hopkinson

Abstract A review of the high power performance of quantum dot (QD) lasers and one of its failure modes by catastrophic optical damage (COD) is presented. Since the first lasing action reported in 1994, a rapid advancement in the output power of QD lasers has been achieved. QD lasers with excellent optical power from a few mW to more than 11 W have been reported. As the QD laser output power continues to reach higher levels, problems such as COD which causes sudden failure of the laser inevitably become a problem that requires an immediate solution. Over the years, COD failure has been widely reported in QD lasers with emission wavelengths varying from 0.9 to 1.3 μm. In this chapter, factors contributing to the COD failure in high power QD lasers are discussed and existing methods to suppress the COD are assessed. Finally, a novel laser annealing technique with in situ monitoring and control capabilities for the formation of non-absorbing mirrors in QD laser is described.

Introduction

The first semiconductor laser, which used a bulk active layer, was demonstrated by Hall et al. [1], followed by Marshall and co-workers [2] in 1962. This achievement followed very soon after the first lasing action in ruby was achieved by Maiman [3]

C. K. Chia (✉)
Institute of Materials Research and Engineering, 3 Research Link,
Singapore 117602, Singapore
e-mail: ck-chia@imre.a-star.edu.sg

M. Hopkinson
Department of Electronic and Electrical Engineering, University of Sheffield,
Sheffield, S1 3JD, UK
e-mail: m.hopkinson@sheffield.ac.uk

Z. M. Wang (ed.), *Quantum Dot Devices*, Lecture Notes in Nanoscale Science and Technology 13, DOI: 10.1007/978-1-4614-3570-9_5,
© Springer Science+Business Media New York 2012

in 1960 and is a very significant landmark in the development of semiconductor devices. Over the years quantum well (QW) [4], quantum wire [5], and quantum dot (QD) lasers [6] have been developed with each step demonstrating continued advancement in laser performance. The evolution of diode laser active layer from bulk layers to a zero dimension QD structure has happened in less than three decades and since their first demonstration in 1994 [6, 7], QD lasers have advanced rapidly. Of relevance here is that the power performance has improved significantly such that a high output power of more than 11 W under quasi-cw operation can be readily achieved [8]. Evidence of the QD laser's superior characteristics, such as enhanced differential efficiency, reduced threshold current density, high temperature stability, and low wavelength chirping, has been regularly reported [9–11]. These days, commercial-grade QD lasers are available and may shortly replace QW lasers in applications such as metropolitan fiber-optic networks [10]. In 2010, collaboration between the University of Tokyo, Fujitsu Laboratories, and QD Laser Inc. has resulted in a 1.3 μm QD laser capable of high-speed data transmission up to 25 Gbps [11] under direct modulation.

However, despite the excellent properties mentioned above, QD lasers face some of the same fundamental problems found in QW lasers. They share the very same failure modes, for instance, the phenomenon of COD which causes the sudden failure of the diode laser. As evidenced by Sellin and co-workers [8], the output power of their QD laser was limited by COD, which failed when the power density reaches 19.5 MW/cm^2. Over the years, COD failure in QD lasers emitting at 0.94 [12], 0.98 [13], 1.068 [14], 1.135 [8], and 1.3 μm [15] has been reported.

It was initially thought that reduced non-radiative surface recombination as a consequence of the strong spatial localization of charge-carrier would decrease facet overheating in QD lasers and therefore a larger COD threshold would be expected [16]. However, Chia et al. [15] found that COD is prominent in QD lasers due to exposed relaxed QDs at the cleaved facet, as illustrated in Fig. 5.1. These relaxed QDs can contribute to extra non-radiative surface recombination, aggravating the facet heating problem.

In this chapter, we will discuss the high power performance of the QD laser and one of the factors limiting its output power; COD. The COD failure mode causes the sudden failure of ridge waveguide QD lasers due to thermal runaway. Methods to suppress the COD will be reviewed.

High Power Performance in QD Lasers

To date, InGaAs/GaAs QD lasers with optical power from a few mW to greater than 11 W have been demonstrated [8, 12–14]. The laser emission wavelength can be widely tuned from 0.87 to 1.3 μm [8, 12–15, 17–20] by altering the indium composition and growth conditions of the QDs. The possibility remains to extend this operation toward the 1.5–1.6 μm range [21].

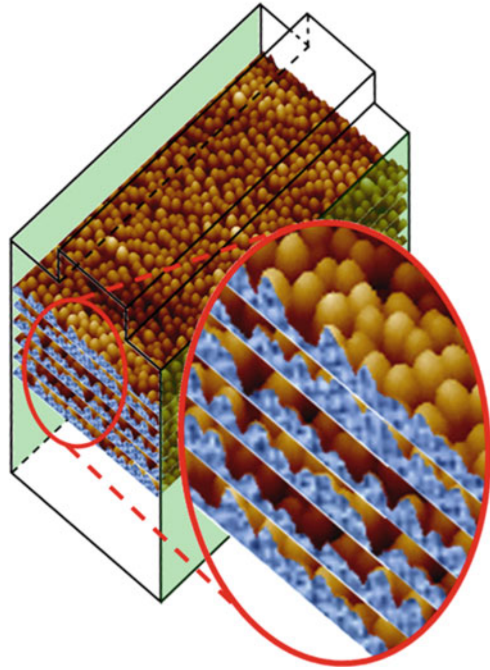

Fig. 5.1 The relaxed QDs exposed at the cleaved facet of the laser can contribute to extra non-radiative surface recombination, causing additional facet overheating effect during operation. Reprinted with permission from [15]. Copyright 2009, American Institute of Physics

Typical failure scenarios for high power semiconductor lasers are illustrated in Fig. 5.2. Line A shows a gradual degradation in power over time, which would be typical of the response of many semiconductor lasers to stress mechanisms. Line B represents the output power of a semiconductor laser that is dropping rapidly in a linear fashion over time and for which the device has short lifetime. The effect would be indicative of materials issues or processing imperfections and from a manufacturing point of view can be dealt by performing "burn-in" of the devices in initial testing. A response such as that in line C is more problematic for the application of high power semiconductor lasers. Here the drop in laser output power is gradual at the initial stage and may not show up in initial testing. However, at a later stage, a drastic drop in power to zero occurs all of a sudden. This response is typical of COD. Ziegler et al. [22] studied the gradual degradation of the output power in a 650 nm QW laser with facet optical power density of 4 mW/μm. They found the presence of packaging-induced strain acted as the driving force for gradual degradation, although the edges of the metallized emitter stripes were identified as the starting points for this failure. Alternatively, Martin–Martin et al. [23] have suggested a thermo-mechanical model for the mechanism of rapid degradation in semiconductor laser diodes. They modeled the rapid degradation observed in an 808 nm AlGaAs-based high power QW laser bar in terms of the thermal stress gradient induced by the overheating produced at a facet defect by self-absorption and the resulting non-radiative recombination. Localized heating at the defect is shown to induce local stress above the yield strength

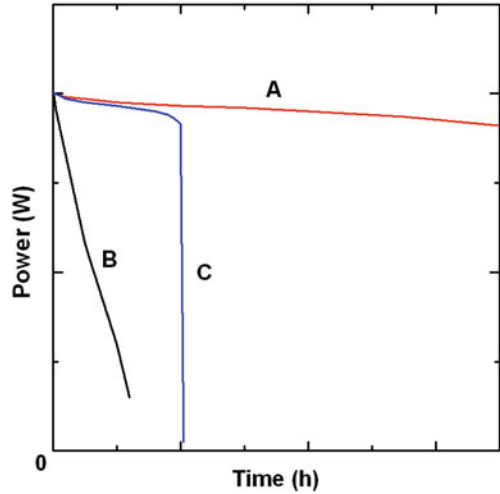

Fig. 5.2 Illustration of failure modes in semiconductor laser: gradual (*A*), rapid (*B*), and sudden (*C*) drop in output power

necessary for plastic deformation. They conclude that packaging stress and defect-related local temperature enhancement significantly lowered the degradation threshold for laser bars, accelerating the degradation of the laser output power. Evidently, both gradual and rapid degradation of the laser output power are related to packaging-induced strain. The sudden failure of high power lasers represents a somewhat different mechanism and is the result of thermal runaway at optical facets. Both QW and QD lasers are found to share the same failure modes.

High power QW lasers emitting between 0.6 and 1.0 μm wavelengths have been shown to fail mainly because of COD. QW lasers for telecommunications which emit at longer wavelength, however, appear to be less affected by this failure mode. Like QW lasers, most high power QD lasers are subject to COD failure as a result of the thermal runaway problem. However, the wavelength dependence of COD is somewhat different in QD lasers. Chia et al. [15] found that COD is prominent in QD lasers emitting at long wavelengths. They conclude that in addition to the dangling bonds at the cleaved facet that give rise to defect states and the effect of strain relaxation which can couple confined states with surface states [24, 25], the exposed relaxed QDs at the cleaved surface also must contribute to extra non-radiative surface recombination. As the QD laser output power continues to reach new highs, problems such as COD inevitably require urgent attention.

Thermal Runaway and COD

COD is one of the failure modes in high power semiconductor diode laser that has haunted laser scientists for decades. Its origins have been investigated extensively over the years [26–28] and it is now well accepted that the origin of this failure

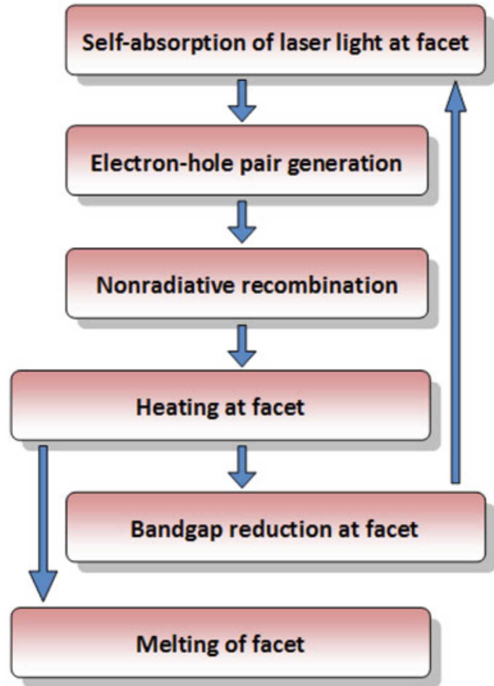

Fig. 5.3 Thermal runaway process at laser facet which causes COD

mode is the thermal runaway effect at the laser facet as illustrated in Fig. 5.3. Compared to the bulk properties within the crystal, the atomic states at the cleavage plane of the laser facet are altered by the termination of the periodic lattice at that plane. At the cleaved plane the translation symmetry is lost and surface reconstruction takes place resulting in formation of dangling bonds. These surface states at the cleaved plane have energy levels within the band gap of the semiconductor. Hence, at the cleaved facets, the defect states of the dangling bonds are highly absorbing to the laser light, resulting in generation of the electron–hole pairs at this region. The non-radiative recombination of these carriers leads to a highly localized thermal loading of the facet.

The efficiency of the carrier recombination at the facet is quantified by the surface recombination velocity, v_s, given by

$$v_s = -D\partial/\partial x[\delta n]/\delta n(x)|_{x=0,l} \tag{5.1}$$

where $\delta n(x = 0, l)$ is the carrier concentration at facet, $\partial/\partial x[\delta n]$ is the gradient of carrier concentration, D is the diffusion coefficient, and l is the device cavity length. As the facet heats up, the local bandgap decreases and optical absorption increases. This causes carriers to drift toward the facets because of the carrier concentration gradient $\partial/\partial x[\delta n]$ and as a result, v_s is increased and this leads to a

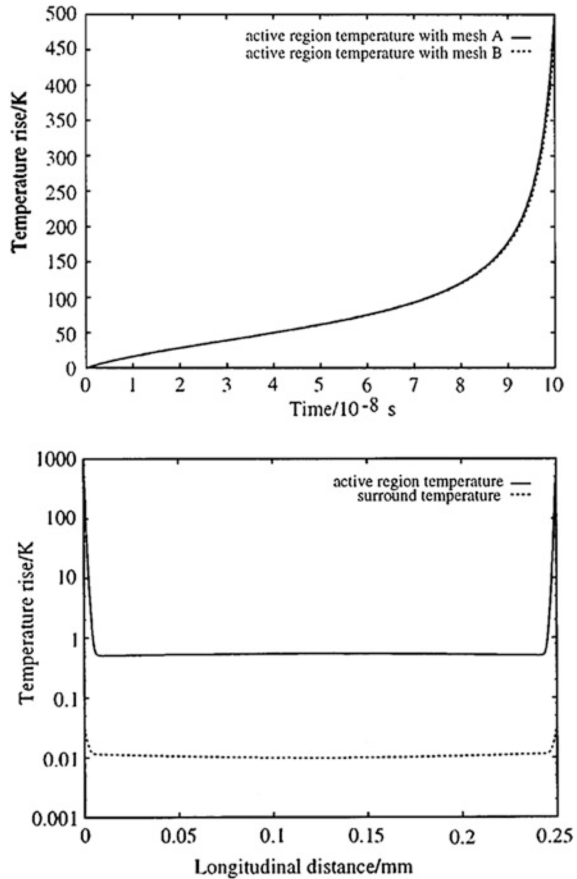

Fig. 5.4 Numerical solution for the temperature rise of the active region on the mirror facet using two spatial meshes. Mesh *A* has 280 points and mesh *B* has 220 points (*Top*). The temperature rise of the active region and the surround at $t = 1 \times 10^{-7}$ s (*Bottom*). Reprinted with permission from [29]. Copyright 2000, American Institute of Physics

further rise in the local temperature. Eventually, the facets, acting as an additional localized recombination channel, are subject to irreversible COD as a result of this thermal runaway effect.

Using a mathematical model describing the coupling of electrical, optical and thermal effects in a semiconductor laser, Smith [29] has shown the temperature rise at the facet is significantly higher than that inside the cavity of the laser due to the thermal runaway effect. The calculated temperature rise at the laser facet as a function of time; and the temperature rise in the active region and the surround (cladding layers) as a function of longitudinal length are shown in Fig. 5.4. The temperature at the facet can exceed the melting point of the laser crystal, leading to the type of COD damage observed in many experiments. Examples of COD failure as a result of the melting of the facet in QW [30] and QD [15] lasers are shown in Fig. 5.5.

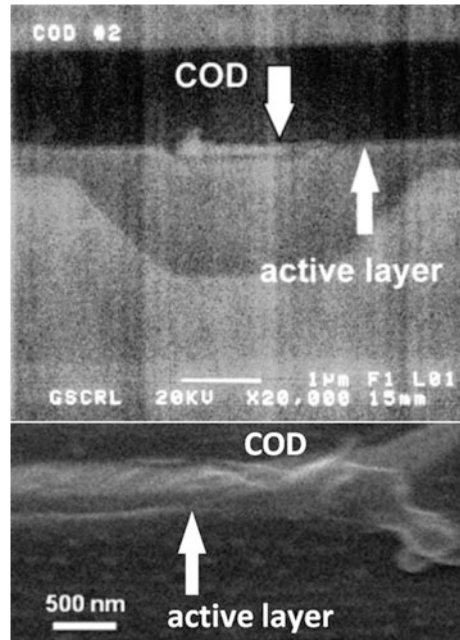

Fig. 5.5 SEM images show example of COD failure in QW laser (*top* reprinted from [30] with kind permission from Springer Science+Business Media B.V., © 1999 Springer) and QD laser (*bottom* reprinted with permission from [15]. Copyright 2009, American Institute of Physics)

Suppression of COD

Attempts to tackle the COD problem can be traced back to as early as the 1970s. Facet passivation by depositing a thin film such as aluminum oxide over the surface, was one of the very first methods used. A reduction in the recombination velocity of surface states can be achieved by cleaving the crystals in high vacuum environment and immediately depositing a suitable passivation layer. Over the years, numerous alternative approaches have been proposed and demonstrated to suppress COD in high power semiconductor QW lasers, such as introduction of a current blocking layer [31], formation of non-injecting mirrors (NIMs) [32], and non-absorbing mirrors (NAMs) [30, 33]. These methods are also applicable to QD–based lasers.

The method of using a current blocking layer is described by Rinner et al. [31]. The facet heating of a single-QW InGaAs/AlGaAs laser was reduced by the introduction of a 30 μm long current blocking region formed by inserting a SiN layer below the front facet of the laser, as illustrated in Fig. 5.6. The blocking of the pump current close to the facet reduces the carrier density and then the surface recombination current. The temperature rise of a broad area high power laser emitting at 940 nm was reduced by a factor of ~4. A schematic diagram of a semiconductor laser with the NIM or NAM approaches used at both ends is presented in Fig. 5.7. Marsh et al. [32] fabricated three types of QW laser using a combination of these approaches and compared the COD limit in each case. It was

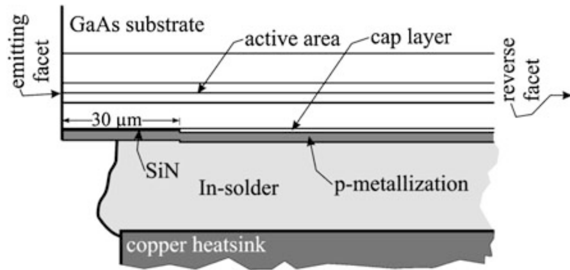

Fig. 5.6 A SiN current blocking layer is inserted at the bottom contact near the facet. Reprinted with permission from [31]. Copyright 2003, American Institute of Physics

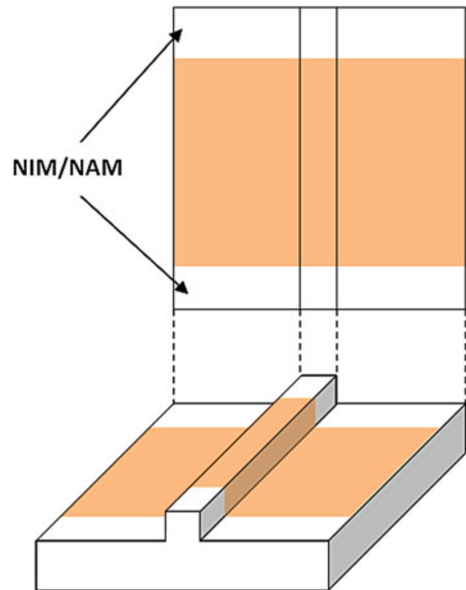

Fig. 5.7 Schematic of a ridge waveguide laser with NIM or NAM at both ends

found that the device with both NIM and NAM outperformed the devices with only NIM and with a conventional mirror. This is because the device using both NIM and NAM approaches has the combined benefit of excluding carriers from the facet region (NIM) and increasing the local bandgap at the facet (NAM).

One of the most effective ways to suppress COD in semiconductor lasers is to widen the energy bandgap at the facets to form NAMs [30, 33]. NAMs can suppress COD by restricting the number of carriers that drift from the center of the laser to the facet region, and by reducing the band-to-band absorption at facet region. NAMs can be created using a selective intermixing process [33, 34]. Conventionally, in such a process the whole device structure is subject to high temperature rapid thermal annealing (RTA which leads to possible degradation in the device active region and unwanted wavelength blueshift [35, 36]. Degradation often results in a modest increase in lasing threshold current density after RTA [33].

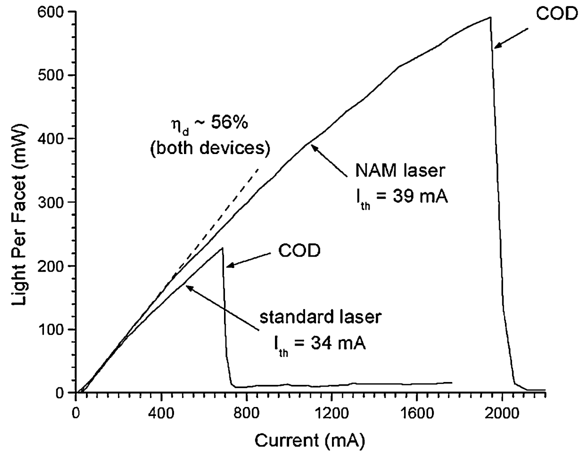

Fig. 5.8 Pulsed light–current characteristics of standard and NAM ridge lasers. Reprinted with permission from [32], © 2002 IEEE

Walker et al. [33] showed that a 3-fold increase in COD optical power level can be obtained in lasers with NAMs compared to conventional lasers, as depicted in Fig. 5.8. The COD threshold was shown to increase from 200 to 600 mW in their double-QW GaAs/AlGaAs laser structure. The differential quantum efficiencies they obtained were around 56%, which is approximately the same for both devices with and without NAMs. However, a 15% increase in the threshold current for the NAM laser is observed.

An alternative approach to the formation of NAMs is to use selective laser annealing (LA) at the facets. The advantage of LA is that the beam can be scanned in a small region close to the facets, avoiding unwanted modification to the device center active region and possible structural degradation that might occur from this. By forming non-absorbing mirrors on the facets in an InAs/GaAs QD laser operating at 1.3 μm, Chia et al. [15] have shown a notable enhancement in optical output power P and external differential quantum efficiency n_d, with improvement factors of up to 2.4 and 1.7 times, respectively. A unique selective LA technique for the formation of non-absorbing mirrors is detailed in the following section.

Formation of Non-absorbing Mirror by Laser Annealing

LA of semiconductor devices has decades of history [37]. For photonic devices in particular, selective area LA can avoid unintentional modification to the device active region and therefore the quality of the photonic structures may not be compromised after annealing. This ability to selectively anneal the facet should be contrasted with other annealing techniques such as the dielectric capped intermixing processes [35, 38–42], in which the whole device structure is subject to a high temperature rapid thermal annealing step

As initially reported by Lee and co-workers, the LA technique has been utilized to form non-absorbing mirrors in ridge waveguide semiconductor laser structure [43]. High power density laser pulses were directed to the semiconductor laser facet to intermix the atoms near the facet. The authors show an enhancement in the COD threshold after performing pulsed LA on a 980 nm QW laser facet. An improvement of up to 38% in COD threshold was demonstrated. An excimer laser with wavelength of 248 nm and pulse width of 25 ns was used in the processing and the power density of the laser was controlled between 0.25 and 9 MW/cm^2. However, using such a short and intense pulsed source, it is difficult to control the degree of atomic intermixing and there is a risk of possible damage to the facet. Lee and co-workers showed that excessive damage can occur when a high energy single excimer laser pulse was used. The damage mechanism is thought to be the formation of point defects due to bond breaking. Such lattice disruption created by laser pulses needs a subsequent thermal annealing step to induce interdiffusion and to recover the quality of the material [44]. It has been shown that using cw laser irradiation has the advantage of eliminating the necessity of the subsequent thermal annealing process [35].

Chia et al. [45] have proposed an apparatus which allows real-time monitoring of the intermixing in a targeted area during LA. Before that, LA methods have never being able to provide in situ monitor and control of the annealing process, in particular over the effectiveness and degree of atomic intermixing in semiconductors. Without an in situ monitor, extensive experiments are often required to estimate the degree of intermixing after multiple attempts at the process [46]. Other issues affecting the consistency of the LA results, including repeatability due to experimental variations in the optical alignment and setup parameters, can be effectively addressed. The apparatus for LA with in situ control and monitor capacities proposed by Chia et al. is shown in Fig. 5.9. The formation of the non-absorbing mirror at a 3 mm long QD laser facets using the setup was demonstrated. In this approach, the QD laser, an optical spectrum analyzer (OSA) and a 972 nm high power laser source were linked up using a 50:50 1$\times$2 fiber splitter. The QD laser was electrically probed on a sample stage and under cw operation and injected using a constant current (c.c.) source.

Because the QD laser was under c.c. injection, its electroluminescence (EL) can be collected by the optical fiber. Using the OSA as a power meter, a precise alignment of the fiber tip with the QD laser in the same optical axis can be readily achieved by adjusting the xyz stage to optimize the maximum EL output collected from the QD laser. High energy photons from the 972 nm high power annealing light source are then delivered to the QD laser facet for targeted area annealing. The power density of the 972 nm annealing light source chosen for cw LA was 5.0 kW/cm^2, much lower than that in pulsed laser technique (250 kW/cm^2–9 MW/cm^2). Hence this minimizes possible damage to the facet. McKee et al. [47] have shown that heating up the substrate to reduce the temperature gradient between the QD layer and its surrounding matrix can substantially reduce the power density required for efficient LA. In this experiment, the QD device which is under c.c. injection generates heat within the structure itself, providing the background heat

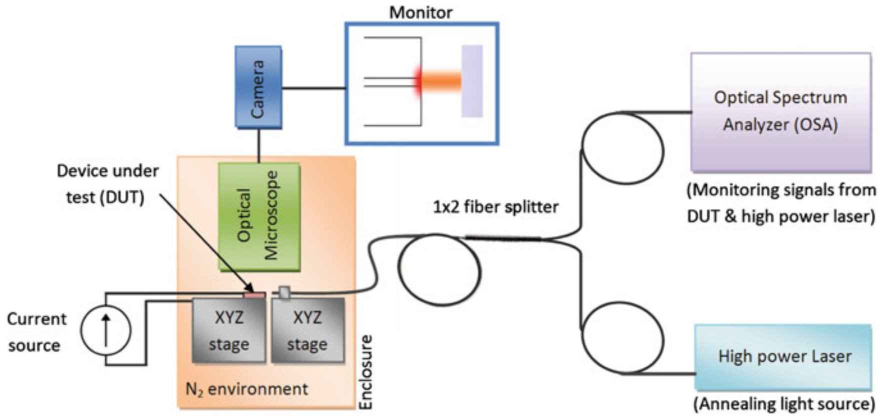

Fig. 5.9 LA experimental setup with in situ control and monitoring capacities. The device under test (DUT) is a 3 mm long ridge waveguide QD laser. Reprinted with permission from [45], © 2011 OSA

required. The laser diode facet could be damaged if a 972 nm laser with much higher power density were to be used for annealing, so operation below the critical laser power density for facet damage is essential in this approach.

Using this technique, Chia et al. showed that during LA, a progressive blueshift in emission wavelength of the EL from the QD laser can be monitored in real time on the OSA, which was continuously scanned over the wavelength range of interest. Figure 5.10 shows the spectra recorded during LA. The wavelength blueshift, $\Delta\lambda$, of the QD ridge waveguide diode during LA, is attributed to the reduced "effective" device length, due to two competing effects, namely wavelength lengthening due to Joule heating, $\Delta\lambda_{\mathrm{Joule}}$, where heating of the lattice can result in a redshift in the emission wavelength; and wavelength shortening due to a reduction in the cavity length, L, which is now minus the portion which has undergone intermixing, ΔL. The shift follows the $\Delta\lambda_{\mathrm{length}} = 2 \times \Delta L/n$ relationship, where n is an integer and ΔL is the reduction of the effective cavity length which is therefore a negative value. This shift originates because the section under annealing has undergone a rearrangement of atoms and hence the "effective" mirror of the device during LA is at a shorter position.

The progressive blueshift in EL is a result of the extension of intermixing depth deeper into the laser facet which causes the effective L to become shorter over time. From these arguments, the spectral blueshift observed in Fig. 5.10 is a net result of $\Delta\lambda_{\mathrm{length}} + \Delta\lambda_{\mathrm{Joule}}$. Wavelength shortening as a result of a change in the refractive index resulting from a change in carrier density during direct modulation is not considered here, because the change in carrier density can be neglected in a QD laser that is operating in cw mode.

The blueshift in EL spectrum during LA shown in Fig. 5.10 is temporary and can be recovered back to the original position after the LA process has ended, because atoms in the intermixed section eventually stabilize and return back to

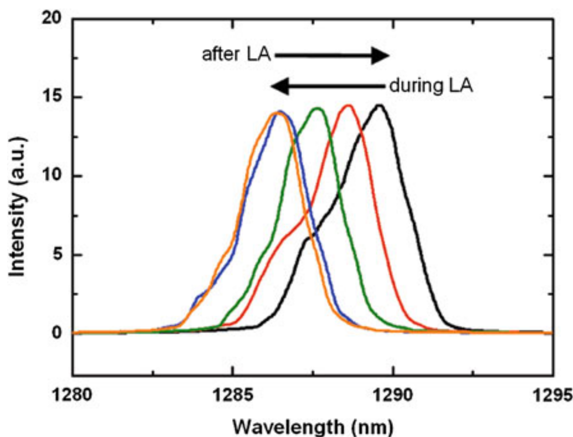

Fig. 5.10 Progressive *blueshift* of the EL spectrum of the InAs/GaAs QD laser during annealing. From *right to left*: 0, 1, 3, 7, and 10 min after the 972 nm annealing light source was turned on. The spectrum reverts back to the original position after the LA process has ended. Reprinted with permission from [45], © 2011 OSA

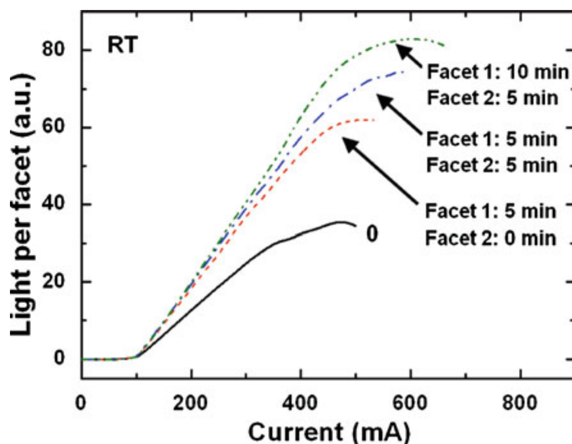

Fig. 5.11 Light–current characteristics measured from the same QD laser before (*solid line*) and after facet 1 annealed for 5 min (*broken line*); facets 1 and 2 annealed for 5 min each (*dot-dashed line*); and facet 1 annealed for 10 min, facet 2 annealed for 5 min (*dot–dot-dashed line*). Reprinted with permission from [44], © 2011 OSA

crystalline lattice, then L will return back to its original length with the removal of the cw source. The QD laser lasing peak wavelength was therefore found to remain unchanged before and after LA process [15], because L remains the same, even though the actual gain region has been reduced after the formation of non-absorbing mirrors.

The in situ monitor technique provides real-time control of the LA process, being both capable of delivering high energy photons to anneal the QD laser and simultaneously measuring the EL spectrum.

The effectiveness of this apparatus in forming non-absorbing mirror on QD ridge waveguide laser is summarized in Fig. 5.11 in terms of the effect on the light current characteristics of the QD laser. The success in the formation of non-absorbing mirrors is demonstrated by the enhancement in the optical output and slot efficiency of the QD laser. This is because LA has widened the energy

bandgap at the facets and hence reduced the carrier recombination velocity and optical absorption from the facets. The overall result is to greatly suppress thermal runaway and raise the COD threshold.

Conclusions

Issues related to thermal runaway and COD in high power QD lasers with emission wavelength varying from 0.9 to 1.3 μm have been discussed. Contrary to previous expectations, QD lasers are just as susceptible to COD as QW structures and in fact may be even more degraded by an additional non-radiative recombination mechanism resulting from the relaxation of exposed QDs at the facet surface. For the effective use of QD lasers it is therefore important to find an approach to suppress this mechanism.

Existing methods to suppress the COD in semiconductor lasers have been assessed. These include facet passivation to reduce the recombination velocity of surface states; the introduction of a current blocking layer to reduce the carrier density and therefore the surface recombination current; the formation of NIMs to exclude the carriers from the facet region; and NAMs to increase in the local bandgap at the facet. While such methods have been proven to be effective, they can also show some degradation in properties such as lasing threshold which are a consequence of the need to thermal process the whole device. To address this issue, we describe a novel LA technique which has in situ control and monitor capabilities for the targeted formation of a non-absorbing laser facet. The setup utilizes an optical fiber splitter which delivers photons to selectively anneal the photonic device at a targeted area and simultaneously measures the emission spectra from the device to monitor the intermixing process in real time. The in situ monitoring of the LA process for the modification of a QD laser diode facet is demonstrated. A progressive blueshift in the emission wavelength of the QD laser can clearly be observed in real time while high energy photons are delivered to anneal the device facet, hence enabling the control on the degree of intermixing required. The approach is one which could easily lend itself to automation if combined with a high quality wafer translation stage.

References

1. Hall, R.N., Fenner, G.E., Kingsley, J.D., Soltys, T.J., Carlson, R.O.: Coherent light emission from GaAs junctions. Phys. Rev. Lett. **9**, 366–368 (1962)
2. Nathan, M.I., Dumke, W.P., Burns, G., Dill, F.H., Lasher, G.: Stimulated emission of radiation from GaAs p-n junctions. Appl. Phys. Lett. **1**, 62 (1962)
3. Maiman, T.H.: Stimulated optical radiation in ruby. Nature **187**, 493–494 (1960)
4. Dingle, R., Henry, C.H.: Quantum effects in heterostructure lasers, U.S. Patent #3,982,207, filed 7 March 1975, issued 21 Sept 1976

5. Kapon, E., Hwang, D.M., Bhat, R.: Stimulated-emission in semiconductor quantum wire heterostructures. Phys. Rev. Lett. **63**, 430–433 (1989)
6. Ledentsov, N.N., Ustinov, V.M., Egorov, A.Y., Zhukov, A.E., Maksimov, M.V., Tabatadze, I.G., Kopev, P.S.: Optical-properties of heterostructures with InGaAs-GaAs quantum clusters. Semiconductors **28**, 832–834 (1994)
7. Kirstaedter, N., Ledentsov, N.N., Grundmann, M., Bimberg, D., Ustinov, V.M., Ruvimov, S.S., Maximov, M.V., Kop'ev, P.S., Alferov, Zh.I., Richter, U., Werner, P., Gosele, U., Heydenreich, J.: Low threshold, large T_o injection laser emission from (InGa)As quantum dots. Electron. Lett. **30**, 1416–1417 (1994)
8. Sellin, R.L., Ribbat, C., Bimberg, D., Rinner, F., Konstanzer, H., Kelemen, M.T., Mikulla, M.: High-reliability MOCVD-grown quantum dot laser. Electron. Lett. **38**, 883–884 (2002)
9. Kovsh, A.R., Maleev, N.A., Zhukov, A.E., Mikhrin, S.S., Vasil'ev, A.P., Shemyakov, Yu.M., Maximov, M.V., Livshits, D.A., Ustinov, V.M.: Alferov, Zh.1., Ledentsov, N.N., Bimberg, D.: InAs/lnGaAs/GaAs quantum dot lasers of 1.3 μm range with high (88%) differential efficiency. Electron. Lett. **38**, 1104–1106 (2002)
10. Sugawara, M., Usami, M.: Quantum dot devices: handling the heat. Nat. Photon. **3**, 30–31 (2009)
11. Tanaka, Y., Ishida, M., Takada, K., Yamamoto, T., Song H.-Z., Nakata, Y., Yamaguchi, M., Nishi, K., Sugawara, M., Arakawa, Y.: 25 Gbps direct modulation in 1.3 μm InAs/GaAs high-density quantum dot lasers, conference on lasers and electro-optics (CLEO) and quantum electronics and laser science conference (QELS), 16–21 May, pp. 1–2 (2010)
12. Maximov, M.V., Shernyakov, Yu.M., Tsatsul'nikov, A.F., Lunev, A.V., Sakharov, A.V., Ustinov, V.M., Egorov, A.Yu., Zhukov, A.E., Kovsh, A.R., Kop'ev, P.S., Asryan, L.V., Alferov, Zh.I., Ledentsov, N.N., Bimberg, D., Kosogov, A.O., Werner, P.: High-power continuous-wave operation of a InGaAs/AlGaAs quantum dot laser. J. Appl. Phys. **83**, 5561–5563 (1998)
13. Sumpf, B., Deubert, S., Erbert, G., Fricke, J., Reithmaier, J.P., Forchel, A., Staske, R., Trankle, G.: High-power 980 nm quantum dot broad area lasers. Electron. Lett. **39**, 1655–1657 (2003)
14. Heinrichsdorff, F., Ribbat, Ch., Grundmann, M., Bimberg, D.: High-power quantum-dot lasers at 1,100 nm. Appl. Phys. Lett. **76**, 556–558 (2000)
15. Chia, C.K., Suryana, M., Hopkinson, M.: Thermal runaway and optical efficiency in InAs/GaAs quantum dot laser. Appl. Phys. Lett. **95**, 141106 (2009)
16. Grundmann, M., Heinrichsdorff, F., Ribbat, C., Mao, M.-H., Bimberg, D.: Quantum dot lasers: recent progress in theoretical understanding and demonstration of high-output-power operation. Appl. Phys. B **69**, 413–416 (1999)
17. Kovsh, A.R., Livshits, D.A., Zhukov, A.E., Egorov, A.Yu., Maximov, M.V., Ustinov, V.M., Tarasov, I.S., Ledentsov, N.N., Kop'ev, P.S., Alferov, Zh.I., Bimberg, D.: Quantum-dot injection heterolaser with 3.3 W output power. Tech. Phys. Lett. **25**, 438–439 (1999)
18. Huffaker, D.L., Park, G., Zou, Z., Shchekin, O.B., Deppe, D.G.: 1.3 μm room-temperature GaAs-based quantum-dot laser. Appl. Phys. Lett. **73**, 2564–2566 (1998)
19. Liu, H.Y., Liew, S.L., Badcock, T., Mowbray, D.J., Skolnick, M.S., Ray, S.K., Choi, T.L., Groom, K.M., Stevens, B., Hasbullah, F., Jin, C.Y., Hopkinson, M., Hogg, R.A.: p-doped 1.3 μm InAs/GaAs quantum-dot laser with a low threshold current density and high differential efficiency. Appl. Phys. Lett. **89**, 073113 (2006)
20. Grundmann, M., Heinrichsdorff, F., Ledentsov, N.N., Ribbat, C., Bimberg, D., Zhukov, A.E., Kovsh, A.R., Maximov, M.V., Shernyakov, Y.M., Lifshits, D.A., Ustinov, V.M., Alferov, Zh.I.: Progress in quantum dot lasers: 1,100 nm, 1,300 nm, and high power applications. Jpn. J. Appl. Phys. Part **1**(39), 2341–2343 (2000)
21. Polyakov, N.K., Samsonenko, Yu.B., Ustinov, V.M., Zakharov, N.D., Werner, P.: Room-temperature 1.5–1.6 μm photoluminescence from InGaAs/GaAs heterostructures grown at low substrate temperature. Semiconductors **37**, 1406–1410 (2003)

22. Ziegler, M., Tien, T.Q., Schwirzke-Schaaf, S., Tomm, J.W., Sumpf, B., Erbert, G., Oudart, M., Nagle, J.: Gradual degradation of red-emitting high-power diode laser bars. Appl. Phys. Lett. **90**, 171113 (2007)
23. Martín-Martín, A., Avella, M., Iñiguez, M.P., Jiménez, J., Oudart, M., Nagle, J.: A physical model for the rapid degradation of semiconductor laser diodes. Appl. Phys. Lett. **93**, 171106 (2008)
24. Moison, J.M., Elcess, K., Houzay, F., Marzin, J.Y., Gerard, J.M., Barthe, F., Bensoussan, M.: Near-surface GaAs/$Ga_{0.7}Al_{0.3}As$ quantum wells: interaction with the surface states. Phys. Rev. B **41**, 12945–12948 (1990)
25. Saito, H., Nishi, K., Sugou, S.: Influence of GaAs capping on the optical properties of InGaAs/GaAs surface quantum dots with 1.5 μm emission. Appl. Phys. Lett. **73**, 2742–2744 (1998)
26. Nakwaski, W.: Thermal analysis of the catastrophic mirror damage in laser diodes. J. Appl. Phys. **57**, 2424 (1985)
27. Ziegler, M., Tomm, J.W., Reeber, D., Elsaesser, T., Zeimer, U., Larsen, H.E., Petersen, P.M., Andersen, P.E.: Catastrophic optical mirror damage in diode lasers monitored during single-pulse operation. Appl. Phys. Lett. **94**, 191101 (2009)
28. Hempel, M., Tomm, J.W., Ziegler, M., Elsaesser, T., Michel, N., Krakowski, M.: Catastrophic optical damage at front and rear facets of diode lasers. Appl. Phys. Lett. **97**, 231101 (2010)
29. Smith, W.R.: Mathematical modeling of thermal runaway in semiconductor laser operation. J. Appl. Phys. **87**, 8276–8285 (2000)
30. Ko, H.-C., Cho, M.-W., Chang, J.-H., Yang, M.: A new structure of 780 nm AlGaAs/GaAs high power laser diode with non-absorbing mirrors. Appl. Phys. A **68**, 467–470 (1999)
31. Rinner, F., Rogg, J., Kelemen, M.T., Mikulla, M., Weimann, G., Tomm, J.W., Thamm, E., Poprawe, R.: Facet temperature reduction by a current blocking layer at the front facets of high-power InGaAs/AlGaAs lasers. J. Appl. Phys. **93**, 1848–1850 (2003)
32. Marsh, J.H.: The role of monolithic integration in advanced laser products. J. Cryst. Growth **288**, 2–6 (2006)
33. Walker, C.L., Bryce, A.C., Marsh, J.H.: Improved catastrophic optical damage level from laser with nonabsorbing mirrors. IEEE Photon. Technol. Lett. **14**, 1394–1396 (2002)
34. Kawazu, Z., Tashiro, Y., Shima, A., Suzuki, D., Nishiguchi, H., Yagi, T., Omura, E.: Over 200 mW operation of single-lateral mode 780 nm laser diodes with window–mirror structure. IEEE Photon. Technol. Lett. **7**, 184–187 (2001)
35. Chia, C.K., Chua, S.J., Tripathy, S., Dong, J.R.: Group-V intermixing in InAs/InP quantum dots. Appl. Phys. Lett. **86**, 051905 (2005)
36. Cusumano, P., Ooi, B.S., Helmy, A.S., Ayling, S.G., Bryce, A.C., Marsh, J.H., Voegele, B., Rose, M.J.: Suppression of quantum well intermixing in GaAs/AlGaAs laser structures using phosphorus-doped SiO_2 encapsulant layer. J. Appl. Phys. **81**, 2445–2447 (1997)
37. Boyd, I.W., Wilson, J.I.B.: Laser annealing for semiconductor devices. Nature **287**, 278 (1980)
38. Deppe, D.G., Holonyak, N.Jr.: Atom diffusion and impurity-induced layer disordering in quantum well III-V semiconductor heterostructures. J. Appl. Phys. **64**, R93–R113 (1988)
39. Laidig, W.D., Holonyak, N.Jr., Camras, M.D., Hess, K., Coleman, J.J., Kapkus, P.K., Bardeen, J.: Disorder of an AlAs-GaAs superlattice by impurity diffusion. Appl. Phys. Lett. **38**, 776–778 (1981)
40. Djie, H.S., Mei, T., Arokiaraj, J., Sookdhis, C., Yu, S.F., Ang, L.K., Tang, X.H.: Experimental and theoretical analysis of argon plasma-enhanced quantum-well intermixing. IEEE J. Quantum Electron. **40**, 166–174 (2004)
41. Barik, S., Tan, H.H., Jagadish, C.: High temperature rapid thermal annealing of phosphorous ion implanted InAs/InP quantum dots. Appl. Phys. Lett. **90**, 093106 (2007)
42. Barik, S., Fu, L., Tan, H.H., Jagadish, C.: Impurity-free disordering of InAs/InP quantum dots. Appl. Phys. Lett. **90**, 243114 (2007)

43. Lee, J.H., Choo, A.G., Lee, W.T., Yu, J.S., Park, G.G., Kim, T.I.: Enhanced COD of pump laser diode by laser annealing of the facet, the 4th IEEE international conference on VLSI and CAD, ICVC'95, 15–18 Oct 1995, Seoul, Korea (IEEE, New York), pp. 337–339 (1995)
44. Qiu, B.C., Bryce, A.C., De La Rue, R.M., Marsh, J.H.: Monolithic integration in InGaAs–InGaAsP multiquantum-well structure using laser processing. IEEE Photonics Technol. Lett. **10**, 769–771 (1998)
45. Chia, C.K., Suryana, M., Hopkinson, M.: In situ control and monitoring of photonic device intermixing during laser irradiation. Opt. Express **19**, 9535–9540 (2011)
46. Djie, H.S., Ooi, B.S., Gunawan, O.: Quantum dot intermixing using excimer laser irradiation. Appl. Phys. Lett. **89**, 081901 (2006)
47. McKee, A., McLean, C.J., Lullo, G., Bryce, A.C., De La Rue, R.M., Marsh, J.H., Button, C.C.: Monolithic integration in InGaAs–InGaAsP multiple quantum well structures using laser intermixing. IEEE J. Quantum Electron. **33**, 45–55 (1997)

Chapter 6
Post-Growth Intermixing of GaAs Based Quantum Dot Devices

Ziyang Zhang and R. A. Hogg

Abstract Post-growth intermixing is a powerful technique currently applied in areas such as high power laser arrays and photonics integrated circuits. The application of this technique to quantum dot (QD) based laser materials is of significant interest offering new types of device and allows large-scale integrated devices, but brings about new challenges. In this paper, we will initially review quantum well (QW) intermixing processes and applications and move on to describe specific differences between QW and QD based materials and review the literature on various forms of QD intermixing. Structural and spectroscopic studies of intermixed QD materials will be discussed, and the importance of modulation p-doping of structures will be highlighted. We will then go on to describe active intermixed QD devices including both lasers and broadband devices such as super luminescent diodes and amplifiers, and conclude with our latest results on selective area intermixed devices.

Z. Zhang (✉) · R. A. Hogg
EPSRC National Centre for III-V Technologies,
Department of Electronic and Electrical Engineering,
Centre for Nanoscience and Technology,
University of Sheffield, North Campus Broad Lane,
Sheffield, S3 7HQ, UK
e-mail: ziyang.zhang@shef.ac.ukziyang.zhang@sheffield.ac.uk

R. A. Hogg
e-mail: r.hogg@shef.ac.uk

Z. M. Wang (ed.), *Quantum Dot Devices*, Lecture Notes in Nanoscale Science and Technology 13, DOI: 10.1007/978-1-4614-3570-9_6,
© Springer Science+Business Media New York 2012

Introduction

Quantum Well Intermixing

Quantum well (QW) intermixing is a process in which atoms from QW and their surrounding matrix interdiffuse, to modify the shape and depth of the QW, and hence change the quantized energy state [1]. Generally, after the intermixing process, a blue-shift of the quantized energy state is observed, due to the interdiffusion between the QW materials and the barrier materials. The interdiffusion can be enhanced by using; high annealing temperatures, long annealing duration times, or using enhanced intermixing techniques. Impurity-induced disordering (IID) utilizes impurities/dopants to change the equilibrium defect concentration in the crystal and hence to enhance the group III or V self-diffusion length to promote the degree of intermixing [2]. Impurity-free vacancy disordering (IFVD) utilizes capping materials which introduce vacancies at the interface which are subsequently diffused into the crystal by a subsequent thermal annealing process. The propagation of these vacancies induces adjacent atoms to exchange places, therefore enhancing the intermixing process. For the GaAs material system, this method usually uses a SiO_2 dielectric layer to induce the out-diffusion of Ga atoms into the SiO_2 network to increase the Ga vacancies in the epitaxial structure hence promoting the degree of interdiffusion [3]. As it is essentially impurity free, the optical loss and degradation of electrical properties induced by free-carrier absorption can be avoided to a great extent, which makes IFVD exhibit advantages of maintaining a high degree of crystal quality and higher device performance. The ability to control the absorption band edge after epitaxial growth for QW materials provides great flexibility in many applications in photonic materials and devices [4]. The development of QWI technique becomes more attractive and promising along with the prospect of selective area QWI (SAQWI). Due to the ability to spatially modify the band-edge, SAQWI can be used for fabricating monolithic photonic integrated circuits (PIC), in which the ability to control the bandgap across one single semiconductor wafer is a key requirement to achieve passive waveguide element. To date, QWI has been recognized as a well-established technique, which has been widely investigated by many researchers/laboratories. There are many developed materials characterization techniques such as Auger electron spectra [5] and secondary ion mass spectroscopy [6] for analyzing the interdiffusion process in QW materials. And so far SAQWI has been successfully applied commercially to inhibit catastrophic optical damage of laser facets by making them non-absorbing to improve the device performance and reliability of laser diodes [7].

Quantum Dot Intermixing

The optical and electrical properties of self-assembled quantum dots (SAQD) directly grown by the Stranski–Krastanow growth mode have attracted great interest in both fundamental physics and device applications in the past $\sim$30 years.

For device applications, by utilizing the atom like density of states from SAQD's due to the three-dimensional quantum confinement of charge carriers, high performance lasers have been realized exhibiting low threshold current densities, low chirp under direct modulation, and reduced temperature sensitivity [8–10]. Exploiting the large dot size and composition inhomogeneous distribution and state filling effects, high power and broadband quantum dot (QD) light sources have been achieved [11–13]. The combination of band-gap tuning with the attractive characteristics which SAQDs offer, quantum dot intermixing (QDI) becomes a very attractive subject that is currently being pursued in a number of commercial and academic laboratories worldwide.

Similar to QWI, QDI takes place when the elements from surrounding barrier layers and the QD interdiffuse. But QDI is more complicated than QWI because the intermixing process is not only decided by the difference in thermal expansion coefficients between the QDs and the surrounding matrix, but is also strongly affected by the shape, size and strain distribution in and around QDs [14]. In addition, although cross-sectional tunneling and transmission electron microscopy can provide atomic resolution images before/after the intermixing process of similar QD, compared to QWI, the lack of precise materials characterization methods makes the QDI process difficult to be accurately understand and control. These are the main reasons why QDI has so far been limited to photoluminescence studies (PL) of materials and the creation of passive devices [15].

Generally, a narrowing of the PL linewidth, large blueshift of the emission spectrum and significant reduction in the energy separation of electronic states of the QDs has been observed, which are attributed to inter-diffusion between the QD and the surrounding barrier layers [16–18]. These properties are very promising for application in semiconductor QD lasers [19] and QD photo-detectors [20]. Furthermore, post-growth rapid thermal annealing (RTA) and laser-induced annealing (LIA) processes have been widely used to modify the optical properties of SAQD based devices. In addition to the PL linewidth narrowing by intermixing, it should also be noted that the In-Ga intermixing during the RTA or LIA process can also broaden the emission spectrum under appropriate "low" annealing temperatures due to the increased fluctuation of the interface between the QD and the surrounding matrix [21], which could be used for the fabrication of broadband light sources and amplifiers [22, 23]. Based on the above mentioned intermixing techniques to vary the peak emission wavelength and linewidth for QD based devices application, similar to the SAQWI, the development of selective area QDI (SAQDI) to implement a spatial variation in bandgap of QDs have also been attracting considerable interest and have been suggested as a feasible route leading to photonic integration. However, the study so far is limited to materials and passive devices, with only a few reports on active devices. One main reason is that QD structures are highly sensitive to the annealing parameters, with high annealing temperature or long annealing times sharply degrading the devices' performances.

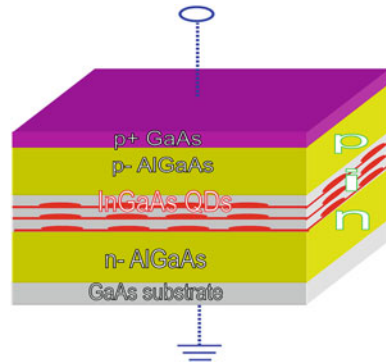

Fig. 6.1 A schematic of GaAs based InGaAs quantum dot laser diode epitaxial structure

Effects of Intermixing on In(Ga)As/GaAs Quantum Dot and Potential Device Applications

Post-Growth Intermixing and High Temperature Epitaxial Growth

The initial studies of thermal treatment of QD structures by Leon et al., [24] and Kosogov et al. [25] investigated the luminescence characteristics from strained InGaAs/InAs QDs ensemble by post-growth annealing (PGA) and by raising the upper cladding layer growth temperature. They suggested that the observed emission wavelength shift is because of the interdiffusion/intermixing of the interfaces rather than strain effects due to the variation in capping layer thickness [24]. Temperature dependant PL indicated a change of the shape and depth of QD confining potential with this becoming less abrupt and well defined due to PGA or by high growth temperature capping. As PGA has similar thermal effects as high temperature epitaxial growth of waveguide and upper cladding layers, it is possible to directly compare with results from epitaxial growth studies of QD where the growth parameters and procedures are adjusted/modified. A schematic of a typical QD based laser diodes (QD-LD) structure, is shown in Fig. 6.1. This InGaAs/GaAs QD-LD epitaxial structure is based on a typical p-i-n configuration, which usually contains a thick p-AlGaAs top cladding layer above the In(Ga)As QD active layers. The high quality epitaxial p-AlGaAs/n-AlGaAs layers require high temperature growth, which is equivalent to a relatively strong annealing process for the QD active region. This will lead to a significant change of the optical properties and quality of the QDs. Too high a growth temperature or too long a duration time will induce dots/islands "dissolving" or with the appearance of dislocations by large strain relaxation. So carefully optimizing and controlling the growth parameter, and especially the growth temperature for the cladding layers is a key factor to realize high quality QD-LD epitaxial structures [26].

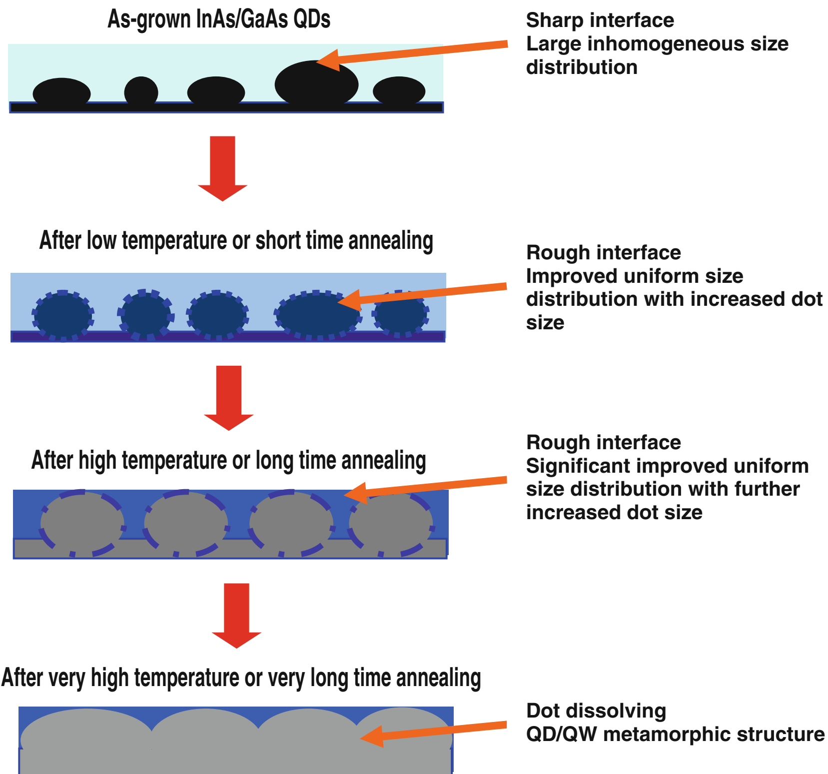

Fig. 6.2 A schematic of the evolution of InAs/GaAs QDs during intermixing process

Post-growth Intermixing Induced Optical Properties and Quality Changing of InGa(Al)As/GaAs QDs and Potential Device Applications

Recent studies of thermal interdiffusion of QD have shown that in addition to a blue-shift of the emission spectrum, there are reductions in the PL emission linewidth and the energy separation of confined states in the InGaAs/GaAs QDs. These changing optical properties and the related evolution of the QD structure with intermixing have been widely investigated by many research groups [14, 17, 27–30].

A schematic diagram of the evolution of the QD structures under different annealing parameters is shown in Fig. 6.2. Structural and spectroscopic studies of the QD material have been discussed in detail. As seen in Fig. 6.2, during the intermixing process, the interfaces between QDs and the surrounding matrix become rough due to interdiffusion, along with improved size uniformity by increasing the dot size. By very high temperature or very long duration time annealing process, the QDs will vanish, as the system becomes a random bulk

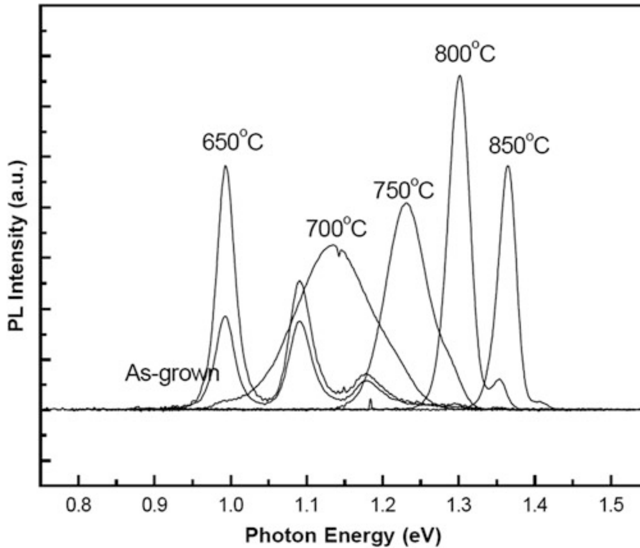

Fig. 6.3 77 K PL spectra of a InGa(Al)As/GaAs QD as grown sample and annealed samples under different annealing temperature. Adapted with permission from Ref. [26] (@ 2003 ELSEVIER)

alloy of InGaAs. For less extreme cases a thick 2D InGaAs layer or a QD/QW metamorphic structure may be formed, due to strong lateral In/Ga Interdiffusion.

Figure 6.3 shows the PL spectra of a InGa(Al)As/GaAs QD sample. PL from the as grown sample and for a range of different annealing temperature treatments. This example depicts a range of changes to the optical properties during the intermixing process.

(1) **PL emission peak.** There are two key factors which dictate the emission wavelength shift. One is, during intermixing process, the QD size increases compared to that of the as grown QDs as seen in Fig. 6.2, which will lead to the quantized energy states red-shifting due to reduced confinement energy. The other effect is the increased Ga composition in QDs by In-Ga interdiffusion between the QDs and the surrounding matrix, which leads to a reduction in the depth of the confining potential and an emission blue-shift. Usually the second effect is dominant, so the emission wavelength is observed to blue-shift due to intermixing. This is observed in the PL spectra in Fig. 6.3, where the emission energy of the QDs continues shifting to higher energy with increasing annealing temperature. Moreover, a large tuning range of over 200 nm by intermixing is demonstrated, considerably larger than emission energy shifts reported by QWI [31], indicating possible greater functionality for QDI devices.

(2) **PL emission linewidth.** The PL emission linewidth initially broadens and subsequently narrows for high temperature annealing. As seen in Fig. 6.2, there are two main structural changes during intermixing; one is the dot size/composition uniformity is improved leading to a PL linewidth narrowing; the other is

attributed to increased interface fluctuations between the QD and the surrounding matrix. In the as grown case the inhomogeneous line-width is governed by QD size and composition variations. The inhomogeneity may increase when different intermixing effects due to differing composition gradients drive the diffusion process [15, 19]. Under low temperature annealing process, the effect of broadening is dominant so the PL linewidth initially increases. This broadening of the emission spectrum makes QDI an attractive method to fabricate broadband QD light sources and amplifiers [16, 22]. Under relatively high annealing temperature, the effect of dot size uniformity improving becomes dominant, so the PL linewidth continues to narrow until the dot disappears. Dubowski et al. [32] reported a very small full width at half maximum (FWHM) of 8 meV in a 77 K spectrum from a laser annealed InAs/GaAs QD sample. This significant reduction in FWHM for QD samples by intermixing may find use in enhancing device performance where peak gain is critical, such as for high characteristic temperature, high modulation rate, and low current density QD-LDs [7, 9].

(3) **PL intensity.** From Fig. 6.3, it can be seen that there is an increase in integrated PL intensity by annealing. This is attributed to a reduction in the density of grown-in defects and is a function of both the annealing process conditions and the epitaxial growth processes [18]. Sometimes, at higher annealing conditions, a reduction in integrated PL intensity compared to the case for PL intensity in as grown sample or low temperature annealed samples can be observed. This reduction in PL intensity is associated with the formation of dislocations by strain relaxation during the intermixing process or carrier escape from the more shallowly confined potential barrier due to the interdiffusion. The change of PL intensity is strongly affected by the annealing temperature, so careful optimization of the annealing temperature and duration is a key factor in determining the performance of intermixed devices.

(4) **Energy Separation of QD transitions in PL spectra.** InGaAs/GaAs QDs have an asymmetric shape, with the height being much smaller than the width. As a consequence the emission energy is mainly decided by the height of QDs, and the energy separation is governed by the width of QDs [22]. During the intermixing process, interdiffusion takes place in both vertical and horizontal directions. This is driven by the density of defects such as vacancies, interstitials, and dislocations. The small ratio of height to width for QDs will lead to an anisotropic strain distribution at the interface between the QDs and the surrounding matrix, so that the intermixing will mainly increase the lateral size of QDs rather than their height. This increased lateral size of QDs will lead to a reduced energy separation. A widely tuned energy spacing of QD optical transitions from 90.9 to 14.6 meV has been observed by Wang et al. [13]. In addition, Babinski et al. [26], has demonstrated that strong lateral interdiffusion is responsible for the fast disappearance of the QDs by the RTA process. The ability to widely tune the energy separation of QDs by intermixing offers many potential applications such as in infrared photo-detectors [33] and lasers based on intrasubband transitions of the QDs [34].

Effects of Caps on the Post-Growth Intermixing of InGaAs/GaAs QDs

The QD intermixing process is strongly affected by the density of defects such as vacancies, interstitials and dislocations, so utilizing caps over QD samples during the annealing process will play a crucial role in determining the degree of intermixing. Many dielectric films, metal films and proximity caps have been used to enhance or inhibit QDI.

The thermal expansion coefficient of SiO_2 is around ten times smaller than that of GaAs, so during the intermixing process, the GaAs surface is under compressive stress, which has the tend to relieve by out diffusion Ga. Due to the porous structure of SiO_2 deposited by plasma-enhanced chemical-vapor deposition (PECVD) [3], the Ga has a high solubility in SiO_2, and will form a number of Ga vacancies, and hence enhance QDI. Kowalski et al. [35] believed that the intermixing degree will be further enhanced if the SiO_2 is deposited by a sputtering process due to the increased point defects induced by the bombardment of the Ar ion plasma. Si_3N_4 and SrF_2 have been used to partially suppress the degree of intermixing due to the low solubility of Ga in them, and hence the low density of Ga vacancies generated in the crystal [36, 37]. However, the density of vacancies is dependent on the Si_3N_4 film growth condition, and Si_3N_4 has also been found to enhance the degree of intermixing [38, 39]. Si_3N_4 and SrF_2 are usually combined with SiO_2 to spatially control of the degree of bandgap energy shift across a single semiconductor wafer to realize a selective area intermixing process [3, 32]. Fu et al. [40] have proposed a SiO_2/TiO_2 bilayer cap technique, in which a significant increase in the overall thermal expansion coefficient of SiO_2/TiO_2 compared to a single layer of SiO_2 results in a significant reduction in Ga diffusion, and hence a concomitant decrease in the density of Ga vacancies and an inhibition to the degree of intermixing. Similar to the above SiO_2/TiO_2 bilayer cap, a phosphorus-doped SiO_2 (SiO_2: P) cap has also been demonstrated to suppress intermixing attributed to the fact that SiO_2: P is more dense and void free during the annealing process [41]. Contrary to the Ga vacancies, the Ga interstitials will suppress intermixing. The Ga interstitials can be formed by using an Al layer deposited upon the GaAs layer. During the intermixing process, the Al and Ga_2O_3 will interchange to form Al_2O_3 and Ga. The excess Ga interstitial concentration reduces the Ga vacancies to suppress the intermixing [42]. In addition, another simple method is using a GaAs proximity cap. During the annealing process As will be desorbed from the GaAs surface resulting in a Ga rich surface and subsequent diffusion of Ga into the sample increasing the concentration of group III interstitials to inhibit intermixing [43].

QDI for Opto-Electronic Devices Application

The application of QDI technique, offering new types of devices and allowing large-scale integrated devices, but brings about new challenges. So far, most reports have focused on the investigation of materials or passive devices, with only

a few reports on active intermixed device fabrication [27, 41, 43, 44]. In this section, we describe active intermixed QD devices for both lasers and broadband devices such as QD super luminescent diodes (QD-SLED) and amplifiers, and conclude with our latest results on selective area intermixed devices.

Tunable Interband and Intersubband Transitions in Modulation C-doped InGaAs/GaAs Quantum Dot Lasers by a Post-Growth Intermixing Process

As QDs are highly sensitive to the annealing process, in order to make a high performance intermixed active devices, it is necessary to find methods to weaken the degree of intermixing. As mentioned in "Effects of Caps on the Post-Growth Intermixing of InGaAs/GaAs QDs", Ga vacancies are a key driver in determining the interdiffusion, and some caps act as good candidates for this purpose. In addition to the capping techniques, engineering of the epitaxial structure of the QD active layers also provides an effective way to decrease the degree of intermixing. In this section, PGA is applied to modulation carbon-doped (C-doped) InAs/InGaAs/GaAs QD structures [38]. As the propagation of Ga vacancies is suppressed in the p-type materials, the intermixing is significantly inhibited.

As seen in the insets of Fig. 6.4, the C-doped and un-doped QD samples were identical except for modulation p-doping with carbon to a concentration of 3e17 in a 10 nm wide layer located in the GaAs spacer layer 14 nm above each InAs/InGaAs layer [38]. Figure 6.4a, b show the room temperature (RT) PL spectra of un-doped and C-doped samples respectively, as a function of annealing temperatures from 700 to 775°C. Data for as grown material is also plotted. For the un-doped sample it is clear that for all annealing treatments, the PL intensity is significantly reduced as well as the emission wavelength is significantly blue-shifted. The strong reduction in integrated PL intensity indicates that the optical quality is significantly degraded due to the formation of dislocations by strain relaxation during the intermixing process or carrier escape from the more shallowly confined potential barrier by interdiffusion procedure. This suggests that the intermixed un-doped QD sample is not a good candidate for subsequent device fabrication. However, for the C-doped samples, the 700°C annealed sample shows an almost identical integrated PL emission compared to the as grown material. For higher annealing temperatures a reduction in integrated emission intensity compared to the as grown sample is also observed. However, the rate of reduction of intensity is less severe as the case for the un-doped sample. There are two factors to determine the strong difference in optical quality of the annealed samples for un-doped and modulation p-doped samples. Firstly, modulation doping may assist in saturating non-radiative recombination centres. Secondly the modulation doping inhibit the diffusion of Ga vacancies [38], reducing the penetration of non-radiative centres into the active region of the device.

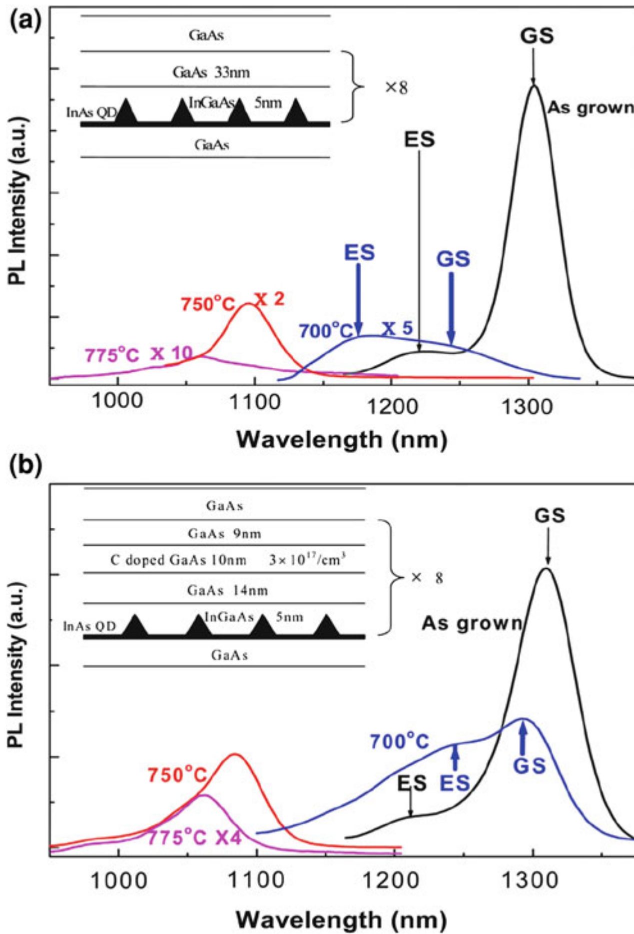

Fig. 6.4 (**a**) Room temperature PL spectra of un-doped as grown QD sample and annealed samples at different temperatures. Inset to Fig. 6.4a: schematic structure of the active region of the un-doped QD laser. (**b**) Room temperature PL spectra of C-doped as grown QD sample and annealed samples at different temperatures. Inset to Fig. 6.4b: schematic structure of the active region of the C-doped QD laser. Figure adapted with permission from Ref. [43] (@ 2008 AIP)

The as grown and 700°C annealed C-doped QD samples were selected for broad area (50 μm wide) LD fabrication, and the laser characteristics of these devices are shown in Fig. 6.5a, b. Simultaneous GS and ES lasing were observed in 1 mm long un-annealed lasers and 3 mm long annealed lasers. The intermixed laser exhibits comparable light–current characteristics after the GS bandgap is blueshift by 13 nm and the inter-sublevel energy spacing is reduced by 30 nm compare to the as grown device. In summary, modulation C-doped InAs/InGaAs/GaAs QD structures with PGA treatments are demonstrated as an effective method to tailor the bandgap energy and energy separation between quantized sates in QD lasers [43].

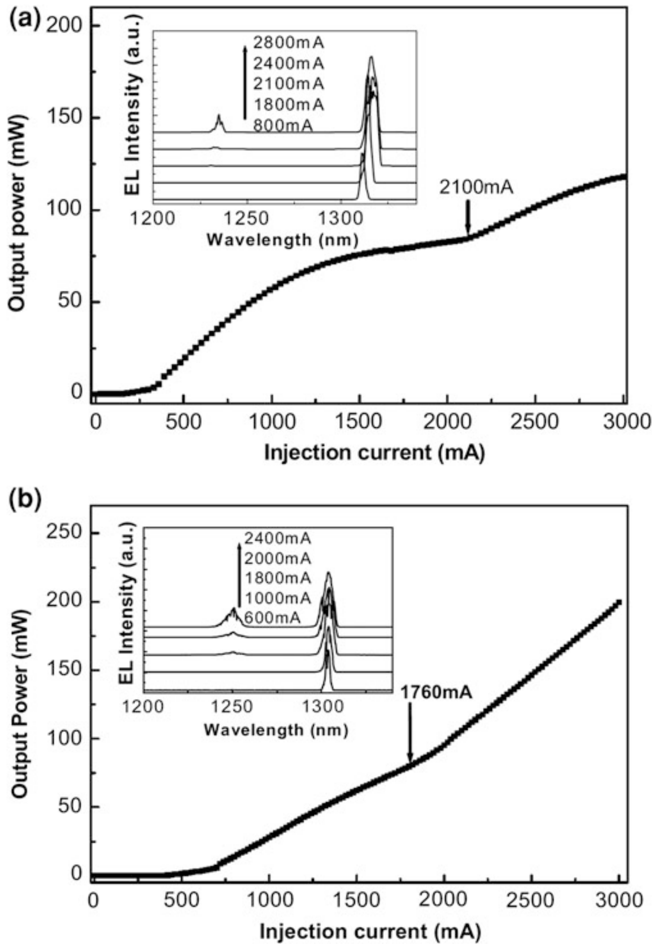

Fig. 6.5 (**a**) Light-injection current curve of the 1 mm as grown C-doped QD laser. Inset to (**a**): corresponding lasing spectra of the device under various injection currents. (**b**) Light-injection current curve of the 3 mm annealed C-doped QD laser. Inset to (**b**): corresponding lasing spectra of the device under various injection currents. Figure adapted with permission from Ref. [43] (@ 2008 AIP)

The Fabrication of High Power and Broadband QD-SLEDs by Post-Growth Intermixing Process

(1) **980 nm QD-SLEDs by intermixing based on a un-doped QD structure**

As mentioned in "Post-growth Intermixing Induced Optical Properties and Quality Changing of InGa(Al)As/GaAs QDs and Potential Device Applications", the broadening of the emission spectrum by low temperature intermixing makes QDI a very useful method to fabricate broadband QD light sources and amplifiers [16, 21].

The first demonstration of the creation of a broadband QD-SLED by RTA was reported in 2008 [21]. By carefully controlling the annealing process parameters, a CW QD SLED with a 146 nm broad emission spectra and output power as high as 15mW was achieved at RT, utilizing an intermixing process. This result is in a calculated coherence length of 6.6 μm. The bandwidth of the intermixed device was found to increase by >2 times with the central emission peak blueshifted by ~50 nm compare to the as grown device. This band-width increase is at the expense of output power which is decreased by a factor of ~6 compared to the as grown QD-SLED, in line with the commensurate reduction in peak gain. This observation strongly suggests that the intermixing process has not significantly degraded the optical property of the QD active material. In addition, a QD-SLED under higher annealing temperature treatment also has been demonstrated exhibiting a 102 nm bandwidth with central emission wavelength further blueshift to 917 nm, but with no obvious state filling effects observed in the EL emission spectra [21]. This lack of state-filling suggests that a non-uniform QW or a QW/QD metamorphic structure is created by the high temperature annealing process, which is consistent with the evolution of QD materials during intermixing as described in "Post-growth Intermixing Induced Optical Properties and Quality Changing of InGa(Al)As/GaAs QDs and Potential Device Applications".

Although high performance QD-SLEDs have been realized by a post-growth intermixing process, from our experiments, we found that the intermixing procedure is extremely difficult to control. It is well known that the QD materials are highly sensitive to the annealing parameters. For the fabrication of broadband intermixed QD-SLED, we require a broadening to the emission, corresponding to a low degree of intermixing. This is much more difficult to achieve than if only an emission wavelength shift is required, and results in significant effort to determine suitable annealing temperatures and times to achieve the desired effect.

(2) **1.3 μm QD-SLEDs by intermixing based on a C-doped QD structure**

The C-doped QD structure has been successfully utilized for fabricating a tunable interband and intersubband QD-LD [38], in which the p-doping has played a crucial role for inhibiting the degree of intermixing. This motivated us to make an intermixed QD-SLED based on a p-doped QD active region.

The RT-PL spectra under identical excitation power densities of the C-doped as grown sample, 700°C annealed SiO_2 capped sample and 700°C annealed GaAs capped sample are shown in Fig. 6.6. It is clear that the energy separation between the GS and ES is significantly reduced from 95 nm (1,310–1,215 nm) of as grown sample to 60 nm (1,286–1,226 nm) of the SiO_2 capped and annealed sample and 48 nm (1,292–1,244 nm) of the GaAs capped and annealed sample. The linewidth of the GS is measured to be 45, 53 and 62 nm for the as grown, SiO_2 capped and GaAs capped samples, respectively. As the energy separation is reduced and linewidth is increased, a much smaller dip in the PL spectrum will be obtained, which is critical for getting a flat emission spectrum of a QD-SLED. The energy peaks and energy splitting between the two annealed p-doped QD samples are found to be different, which is attributed to the different caps used during annealing.

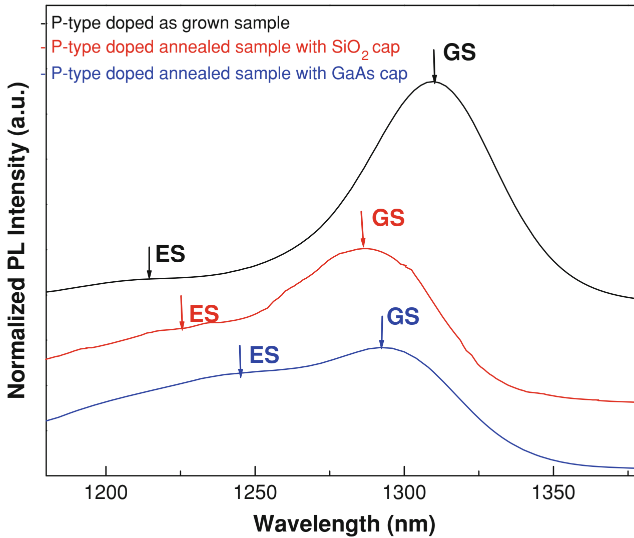

Fig. 6.6 RT-PL spectra of the p-doped as grown sample, p-doped 700°C annealed sample with SiO_2 cap and p-doped 700°C annealed sample with GaAs cap. Figure adapted with permission from Ref. [23] (@ 2009 IOP)

A large number of Ga vacancies are known to form at the SiO_2/GaAs interface during the annealing process with a SiO_2 cap, and enhance the In/Ga interdiffusion through the dot/cap interface, compared to that for the annealed sample with a GaAs proximity cap. This intermixing process mainly modifies the height of the QD, which results in a blueshift of the emission wavelength. Referenced to the as grown sample, the blueshift of the GS emission wavelength is 24 nm (1,310–1,286 nm) for the SiO_2 capped sample compare to 18 nm for the GaAs capped sample. The density of Ga vacancies introduced during annealing with a SiO_2 cap is likely to be greater than the concentration of strain induced vacancies around the QD. So the lateral intermixing, which mainly influences the energy separation of the QD, may be weaker in the SiO_2 capped QD sample compared to that for the GaAs capped QD sample [23]. This is consistent with the smaller reduction of energy splitting of 35 nm for the SiO_2 capped sample compared to 47 nm for the GaAs capped sample.

Based on the PL results in Fig. 6.6, the 700°C annealed GaAs capped sample, with the smallest energy separation among those QD samples, was selected for subsequent QD-SLED fabrication. The QD-SLED was fabricated as a 15° angled facet device structure by focus ion beam etching technique of a 2.7 mm long laser diode structure. A 3 dB bandwidth of 132 nm and very flat emission spectrum (spectral dip of $\sim$1.2 dB) covering 1,325–1,193 nm with an output power of $\sim$2 mW was acquired which is attributed to the simultaneous contribution of the GS and ES1 of QDs. These states have significantly reduced energy separation and increased linewidth due to PGA [23].

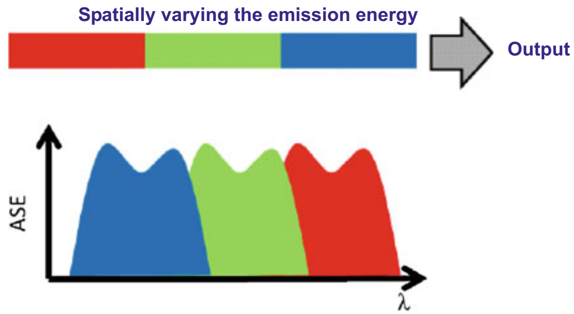

Fig. 6.7 A broadband light source combining spatially varied emissions within one single wafer

(3) **1.3 μm QD-SLEDs by intermixing based on a Be-doped QD structure**

In order to achieve an ultra-broad-band source, one important approach for future research is to vary the emission wavelength spatially and selectively within a device as shown schematically in Fig. 6.7. This may be achieved by selective area epitaxy growth [45] or by selective area post-growth intermixing [22, 46]. As most high quality QD-SLED structures are grown by MBE, the later is preferred as selective area epitaxy is very challenging via MBE. Additionally, as mentioned above SAQDI has great potential for fabricating monolithic PIC, so SAQDI has been attracted considerable interests and has been widely investigated [29].

Modulation C-doped QD structures have been successfully employed as the active region for the fabrication of intermixed QD lasers and intermixed QD-SLEDs. These devices exhibited small emission wavelength shift of ~10 nm blueshift of the GS emission, a decrease in splitting between GS and ES, and a broadening of the inhomogeneous broadening of these states. However, the very low diffusion rate of carbon dopants and the corresponding relatively high thermally stable nature of C-doped QD samples makes them unsuitable for SAQDI, which requires a combination of un-shifted and blue-shifted regions to contribute to the emission spectrum.

In this section, we discuss modulation-doped structures where beryllium (Be) replaces carbon as the p dopant in the QD active region for the fabrication of intermixed QD-SLEDs. Beryllium has a large diffusion rate compared to carbon, providing an additional degree of freedom in the design of an intermixed device [47].

Figure 6.8 shows RT-PL spectra of the samples under identical excitation power of 9.5 mW (HeNe laser emitting at 633 nm), as a function of annealing temperature and time using a GaAs proximity cap and a SiO_2 cap. Data for the as grown sample is also plotted. For the as grown sample the GS emission peak is at 1,296 nm, and ES peak at 1,214 nm. The FWHM of the GS and ES are ~70 and 90 nm, respectively. The PL linewidth of the 700°C annealed sample with GaAs proximity cap are significantly broadened with a GS emission peak blue-shifted to 1,234 nm (FWHM ~145 nm) and an ES peak to 1,194 nm (FWHM ~140 nm). This increase in linewidth is attributed to increased interface fluctuations between the QD and the surrounding matrix. For the sample annealed for 5 min at 700°C the peak intensity is observed to reduce to around half that of the as grown sample.

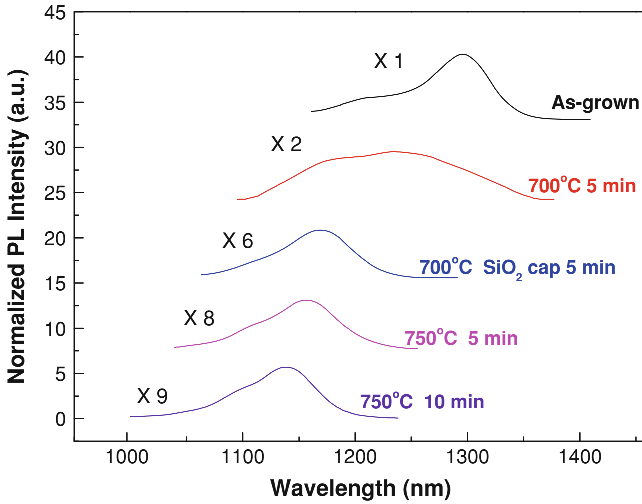

Fig. 6.8 RT- PL spectra of the as grown QD sample and annealed QD samples by using different annealing temperature, different time, and different caps during annealing process. Figure adapted with permission from Ref. [47] (@ 2010 OSA)

However, the integrated intensity is very similar between these two samples due to the significant increase in line-width of the states. This suggests the optical quality of the QDs has been preserved at this annealing condition. The sample annealed at 700°C for 5 min with a SiO_2 cap exhibits a larger GS emission peak blue-shift of ~126 nm (from 1,296 to 1,170 nm) with around a factor of six reduction in PL intensity compared to the as grown sample.

Samples annealed at 750°C for 5 min and 10 min with GaAs proximity caps also exhibit large GS emission peak blue-shifts to ~1,155 and 1,140 nm, respectively with large PL intensity reductions compared to the as grown sample. These observations are in agreement with a stronger interdiffusion under these annealing conditions at higher temperatures and longer times than those discussed previously. Based on the observations from PL test samples, the as grown sample, and samples annealed at 700°C with GaAs proximity cap and SiO_2 cap were fabricated into QD-SLEDs. These selected samples were processed into 5 μm wide ridge waveguide structures, which oriented at ~7° from the facet normal to suppress lasing. 6 mm long bars were mounted on gold plated copper tiles without antireflection coating on the facets. Device characterisation was performed at RT under pulsed operations (5 μs pulse width, 1% duty cycle) to eliminate the effects of self-heating.

Figure 6.9a shows the EL spectra as a function of drive current for the as grown QD-SLED. Under low drive currents, the emission is mainly from the GS of the QDs with central emission peak at ~1,316 nm. With increasing injection current, the ES gradually dominates the emission spectra, with peak emission at around 1,242 nm. This is due to the saturation of the GS and increased population of the ES due to Pauli-blocking. The large energy splitting of the ES and GS results in a large

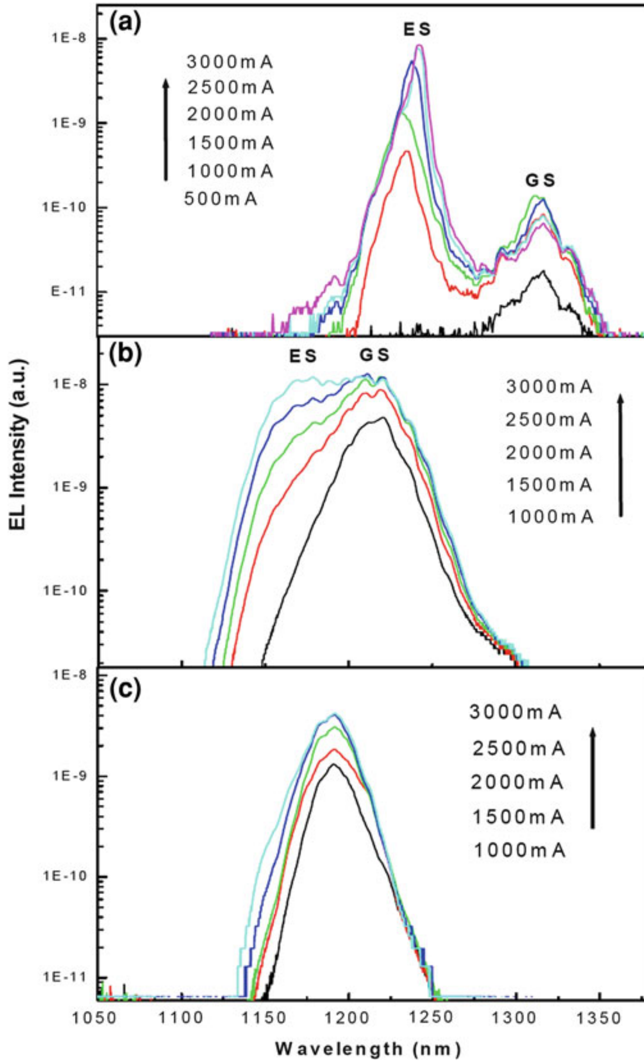

Fig. 6.9 EL spectra as a function of drive currents of as grown QD-SLED,700°C intermixed QD-SLED with GaAs proximity cap and 700°C intermixed QD-SLED with SiO2 cap during annealing process. Figure adapted with permission from Ref. [47] (@ 2010 OSA)

spectral dip occurring in the EL spectrum. For single contact QD-SLEDs the length of the device dictates the power at maximum bandwidth, corresponding to the balance of GS and ES power. The presence of large spectral dips at this condition of maximum bandwidth is undesirable for interferometric applications [48].

The EL spectra as a function of injection current for the device fabricated from 700°C annealed material with GaAs proximity cap is shown in Fig. 6.9b. At low currents the emission is dominated by the QD GS emission which has been shifted

to ~1,212 nm. As current is increased, the ES emission (peak emission ~1,176 nm) increases in power to provide an equal contribution to total output power at ~3 A. Due to the significantly reduced energy separation of QD states in this intermixed device (40 nm compared to 82 nm in the as grown material from PL) and an increase in inhomogeneous linewidth compared to that in the as grown material from PL as shown in Fig. 6.8, a flat topped (spectral dip <0.8 dB) emission spectrum was achieved. A small spectral modulation is highly desirable for high resolution optical coherence tomography image application [48]. A bandwidth of 78 nm from 1,155 to 1,233 nm with output power of 190 mW is achieved at 3 A drive current in this device.

The EL spectra as a function of injection current for the device fabricated from 700°C SiO_2 cap annealed material is shown in Fig. 6.9c. A single peak is observed at all powers centered at ~1,190 nm with ~30 nm bandwidth. The emission spectra show neither appreciable change in bandwidth nor strong shift in the emission peak with increasing injection current, which indicates a QD/QW metamorphic structure formed by this annealing condition.

(4) **QD-SLED fabrication by selective area intermixing on a Be-doped QD structure**

Based on the above results, as the effects of inter-diffusion are quite different between the intermixed device with GaAs proximity cap and the intermixed device with SiO_2 cap, a QD-SLED has been fabricated comprising regions with different cap along it's length. This was realized by combining the GaAs proximity cap with a sample selectively patterned with SiO_2. The schematic for this device is shown in Fig. 6.10a. The device is identical to those discussed previously in 1.3 μm QD-SLEDs by intermixing based on a Be-doped QD structure terms of length (6 mm), ridge width (5 μm) and 7° angle of the waveguide to the normal to the cleaved facet. This selective area intermixed QD-SLED device consists of a 4 mm long QD-SLED A (capped by a SiO_2 layer during annealing) and a 2 mm long QD-SLED B (GaAs proximity cap during annealing).

The L-I characteristics from the two different ends of this device are shown in Fig. 6.10b. The associated emission spectrum from each end of the device, obtained at the maximum current of 3 A is shown as an inset. As expected for such an asymmetric device, the power-current characteristics and emission spectrum are different for the two ends of the device. From facet A, a maximum power of ~120 mW is obtained and at this maximum in drive current a ~45 nm 3 dB band-width is measured centred at ~1,185 nm. From facet B a maximum power of ~79 mW is obtained and at this maximum in drive current a ~60 nm 3 dB band-width is measured centered at 1,170 nm. The modeling of such a device is complex, requiring a time dependant travelling wave solution, incorporating a number of currently unknown material parameters for the two intermixed sections [49]. However, we are able to derive an expectation of the resultant device characteristics if we consider two SLEDs with different gain and ASE bandwidths acting as signal and amplifier. Due to the mismatch in bandwidths we can expect a lower power when compared to a single device of equivalent length. This is in

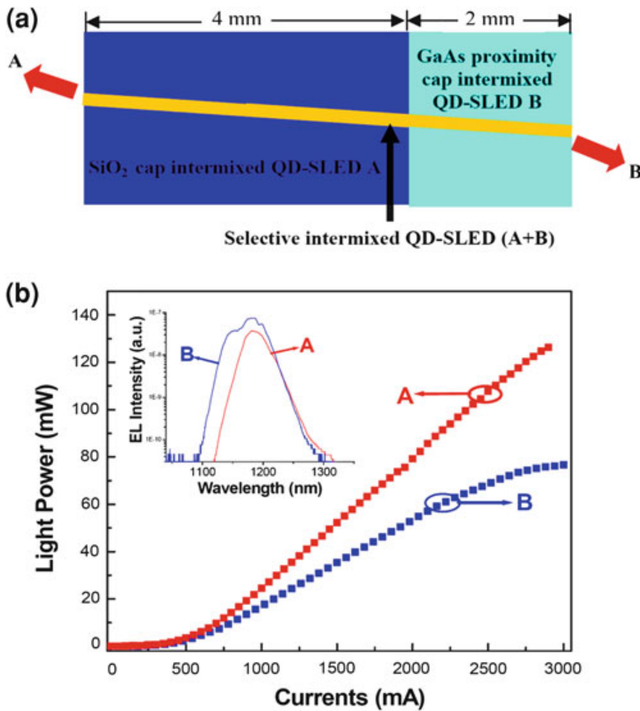

Fig. 6.10 (**a**) Schematic device structure of the selective area intermixed QD-SLED; (**b**). L-I curves of the selective area intermixed QD-SLED measured from front and back facet, respectively. Inset: the corresponding spectra of the device at 3A. Figure adapted with permission from Ref. [47] (@ 2010 OSA)

agreement with what we observe from both facets of the device. Similarly, the narrower bandwidth source can have its emission broadened due to the additional ASE of the other device in the case of a strong spectral overlap [47]. This is also observed from facet A. The spectral overlap of the current device is not optimal for obtaining ultra-broadband emission. However, we believe that if the spectral overlapping occurs at the edge of the two emission spectra, not overlapped centrally as in the present case as shown in Fig. 6.9, an ultra broad emission spectrum would be achieved. This may be possible via the use of different cap materials (e.g. sputtered SiO_2 [35] and TiO_2 [40]) or by laser annealing [46].

Conclusion for QDI and Outlook for Further Developments

Following a review of QW intermixing processes, we have described specific differences between QW and QD materials and intermixing processes. The evolution of the optical properties and physical structure of QDs during intermixing

processes have been discussed in detail. Modulation p-doping with carbon and beryllium is demonstrated as a key factor in realizing high performance QD intermixed devices. A monolithically integrated QD-SLED is demonstrated utilizing a selective area intermixing process. Here, patterning of different cap layers plays a crucial role.

Within the last few years, many reports have appeared on the realization of high quality QD materials and high performance QD devices utilizing PGA processes. Post-growth intermixing has been employed as a very powerful technique for many applications, such as for the fabrication of high power QD-LD, wavelength tunable QD lasers, broadband QD LEDs and QD-SLEDs. The development of the QD intermixing technique is a very attractive research subject which is currently being pursued in a number of commercial and academic laboratories world-wide.

Future challenges and development of QD post-growth intermixing techniques will be mainly application driven, where the spatial variation of emission wavelength allows new device functionality. These include PIC incorporating active elements of different wavelengths and passive elements to act as waveguide elements. GaAs based QDs allow the access of 900–1,300 nm allowing frequency doubling to wavelengths of importance for display applications. These wavelengths are also of interest for biomedical imaging. GaAs based QDs are currently pushing towards 1,550 nm, a crucially important wavelength for optical communications where non-linear absorbers play key roles in both edge emitting [50–52] and surface emitting devices [53, 54]. The modification of single QDs is also of importance for quantum information processing applications [55, 56]. The development of this process in InP [36] and GaN [57] based systems is also expected. In all areas, the development of epitaxial structure hand-in-hand with intermixing process will be critical and the development of in situ control techniques for QDI will greatly accelerate the development of such intermixing process.

References

1. Sengupta, D., Jandhyala, V., Kim, S., Fang, W., Malin, J., Apostolakis, P., Hseih, K.C., Chang, Y.C., Chuang, S.L., Bandara, S., Gunapala, S., Feng, M., Michielssen, E., Stillman, G.: Redshifting and broadening of quantum-well infrared photodetector's response via impurity-free vacancy disordering. IEEE J. Sel. Top. Quantum Electron. **4**(4), 746–757 (1998)
2. Deppe, D.G., Holonyak, N.: Atom diffusion and impurity-induced layer disordering in quantum well III-V semiconductor heterostructures. J. Appl. Phys. **64**(12), R93–R113 (1988)
3. Ooi, B.S., McIlvaney, K., Street, M.W., Helmy, A.S., Ayling, S.G., Bryce, A.C., Marsh, J.H., Roberts, J.S.: Selective quantum-well intermixing in GaAs-AlGaAs structures using impurity-free vacancy diffusion. IEEE J. Quantum Electron. **33**(10), 1784–1793 (1997)
4. Marsh, J.H.: Quantum-well intermixing. Semicond. Sci. Technol. **8**(6), 1136–1155 (1993)
5. Chang, L.L., Koma, A.: Interdiffusion between GaAs and AlAs. Appl. Phys. Lett. **29**(3), 138–141 (1976)
6. Mei, P., Yoon, H.W., Venkatesan, T., Schwarz, S.A., Harbison, J.P.: Kinetics of silicon-induced mixing of AlAs-GaAs super lattices. Appl. Phys. Lett. **50**(25), 1823–1825 (1987)
7. http://www.intenseco.com/

8. Shchekin, O.B., Deppe, D.G.: 1.3 μ m InAs quantum dot laser with T-o = 161 K from 0 to 80°C. Appl. Phys. Lett. **80**(18), 3277–3279 (2002)
9. Huang, X.D., Stintz, A., Hains, C.P., Liu, G.T., Cheng, J., Malloy, K.J.: Very low threshold current density room temperature continuous-wave lasing from a single-layer InAs quantum-dot laser. IEEE Photonics Technol. Lett. **12**(3), 227–229 (2000)
10. Otsubo, K., Hatori, N., Ishida, M., Okumura, S., Akiyama, T., Nakata, Y., Ebe, H., Sugawara, M., Arakawa, Y.: Temperature-insensitive eye-opening under 10 Gb/s modulation of 1.3 μm p-doped quantum-dot lasers without current adjustments. Jpn. J. Appl. Phys., Part 2-Lett. Express Lett. **43**(8B), L1124–L1126 (2004)
11. Djie, H.S., Dimas, C.E., Wang, D.N., Ooi, B.S., Hwang, J.C.M., Dang, G.T., Chang, W.H.: InGaAs/GaAs quantum-dot super luminescent diode for optical sensor and imaging. IEEE Sens. J. **7**(1–2), 251–257 (2007)
12. Xin, Y.C., Martinez, A., Saiz, T., Moscho, A.J., Li, Y., Nilsen, T.A., Gray, A.L., Lester, L.F.: 1.3 μm quantum-dot multisection super luminescent diodes with extremely broad bandwidth. IEEE Photonics Technol. Lett. **19**(5–8), 501–503 (2007)
13. Zhang, Z.Y., Wang, Z.G., Xu, B., Jin, P., Sun, Z.Z., Liu, F.Q.: High-performance quantum-dot super luminescent diodes. IEEE Photonics Technol. Lett. **16**(1), 27–29 (2004)
14. Wang, X.C., Xu, S.J., Chua, S.J., Zhang, Z.H., Fan, W.J., Wang, C.H., Jiang, J., Xie, X.G.: Widely tunable intersubband energy spacing of self-assembled InAs/GaAs quantum dots due to interface intermixing. J. Appl. Phys. **86**(5), 2687–2690 (1999)
15. Zhang, Z.Y., Hogg, R.A., Lv, X.Q., Wang, Z.G.: Self-assembled quantum-dot super luminescent light-emitting diodes. Adv. Opt. Photon **2**, 201–228 (2010)
16. Djie, H.S., Wang, Y., Ding, Y.H., Wang, D.N., Hwang, J.C.M., Fang, X.M., Wu, Y., Fastenau, J.M., Liu, A.W.K., Dang, G.T., Chang, W.H., Ooi, B.S.: Quantum dash intermixing. IEEE J. Sel. Top. Quantum Electron. **14**(4), 1239–1249 (2008)
17. Fafard, S., Allen, C.N.: Intermixing in quantum-dot ensembles with sharp adjustable shells. Appl. Phys. Lett. **75**(16), 2374–2376 (1999)
18. Heinrichsdorff, F., Grundmann, M., Stier, O., Krost, A., Bimberg, D.: Influence of In/Ga intermixing on the optical properties of InGaAsInGaAs/GaAs quantum dots. J. Cryst. Growth **195**(1–4), 540–545 (1998)
19. Djie, H.S., Wang, Y., Ooi, B.S., Wang, D.N., Hwang, J.C.M., Fang, X.M., Wu, Y., Fastenau, J.M., Liu, W.K., Dang, G.T., Chang, W.H.: Wavelength tuning of InAs/InAlGaAs quantum-dash-in-well laser using post growth intermixing. Electron. Lett. **43**(1), 33–35 (2007)
20. Fu, L., McKerracher, I., Tan, H.H., Jagadish, C.: Thermal annealing study on InGaAs/GaAs quantum dot infrared photo detectors. In: International Conference on Nanoscience and Nanotechnology, vols. 1 and 2, pp. 550–553 (2006)
21. Zhang, Z.Y., Hogg, R.A., Xu, B., Jin, P., Wang, Z.G.: Realization of extremely broadband quantum-dot super luminescent light-emitting diodes by rapid thermal-annealing process. Opt. Lett. **33**(11), 1210–1212 (2008)
22. Chia, C.K., Chua, S.J., Dong, J.R., Teo, S.L.: Ultrawide band quantum dot light emitting device by post fabrication laser annealing. Appl. Phys. Lett. **90**(6), 061101 (2007)
23. Zhang, Z.Y., Jiang, Q., Luxmoore, I.J., Hogg, R.A.: A p-type-doped quantum dot super luminescent LED with broadband and flat-topped emission spectra obtained by post-growth intermixing under a GaAs proximity cap. Nanotechnology **20**(5), 055204 (2009)
24. Leon, R., Kim, Y., Jagadish, C., Gal, M., Zou, J., Cockayne, D.J.H.: Effects of interdiffusion on the luminescence of InGaAs/GaAs quantum dots. Appl. Phys. Lett. **69**(13), 1888–1890 (1996)
25. Kosogov, A.O., Werner, P., Gosele, U., Ledentsov, N.N., Bimberg, D., Ustinov, V.M., Egorov, A.Y., Zhukov, A.E., Kopev, P.S., Bert, N.A., Alferov, Z.I.: Structural and optical properties of InAs-GaAs quantum dots subjected to high temperature annealing. Appl. Phys. Lett. **69**(20), 3072–3074 (1996)
26. Zhang, Z.Y., Jin, P., Li, C.M., Ye, X.L., Meng, X.Q., Xu, B., Liu, F.Q., Wang, Z.G.: The evolution of InAs/InAlAs/InGaAlAs quantum dots after rapid thermal annealing. J. Cryst. Growth **253**(1–4), 59–63 (2003)

27. Djie, H.S., Gunawan, O., Wang, D.N., Ooi, B.S., Hwang, J.C.M.: Group-III vacancy induced InxGa1-xAs quantum dot interdiffusion. Phys. Rev. B **73**(15), 1–6 (2006)
28. Babinski, A., Jasinski, J., Bozek, R., Szepielow, A., Baranowski, J.M.: Rapid thermal annealing of InAs/GaAs quantum dots under a GaAs proximity cap. Appl. Phys. Lett. **79**(16), 2576–2578 (2001)
29. Bhattacharyya, D., Helmy, A.S., Bryce, A.C., Avrutin, E.A., Marsh, J.H.: Selective control of self-organized In0.5Ga0.5As/GaAs quantum dot properties: quantum dot intermixing. J. Appl. Phys. **88**(8), 4619–4622 (2000)
30. Lobo, C., Leon, R., Fafard, S., Piva, P.G.: Intermixing induced changes in the radiative emission from III-V quantum dots. Appl. Phys. Lett. **72**(22), 2850–2852 (1998)
31. Chia, C.K., Dong, J.R., Chua, S.J., Tripathy, S.: Band gap engineering in semiconductor quantum dots. J. Cryst. Growth **288**(1), 57–60 (2006)
32. Dubowski, J.J., Allen, C.N., Fafard, S.: Laser-induced InAs/GaAs quantum dot intermixing. Appl. Phys. Lett. **77**(22), 3583–3585 (2000)
33. Pan, D., Towe, E., Kennerly, S.: Normal-incidence intersubband (In, Ga)As/GaAs quantum dot infrared photo detectors. Appl. Phys. Lett. **73**(14), 1937–1939 (1998)
34. Krishna, S., Bhattacharya, P., McCann, P.J., Namjou, K.: Room-temperature long-wavelength ($\lambda = 13.3$ μm) unipolar quantum dot intersubband laser. Electron. Lett. **36**(18), 1550–1551 (2000)
35. Kowalski, O.P., Hamilton, C.J., McDougall, S.D., Marsh, J.H., Bryce, A.C., De la Rue, R.M., Vogele, B., Stanley, C.R., Button, C.C., Roberts, J.S.: A universal damage induced technique for quantum well intermixing. Appl. Phys. Lett. **72**(5), 581–583 (1998)
36. Beauvais, J., Marsh, J.H., Kean, A.H., Bryce, A.C., Button, C.: Suppression of bandgap shifts in GaAs/AlGaAs quantum-wells using strontium fluoride caps. Electron. Lett. **28**(17), 1670–1672 (1992)
37. Deppe, D.G., Guido, L.J., Holonyak, N., Hsieh, K.C., Burnham, R.D., Thornton, R.L., Paoli, T.L.: Stripe-geometry quantum-well hetero structure AlxGa1-xAs-GaAs lasers defined by defect diffusion. Appl. Phys. Lett. **49**(9), 510–512 (1986)
38. Choi, W.J., Lee, J.I., Han, I.K., Kang, K.N., Kim, Y., Park, H.L., Cho, K.: Enhanced disordering of GAAS/ALGAAS multiple-quantum-well by rapid thermal annealing using plasma-enhanced chemical-vapor-deposited sin capping layer grown at high RF power condition. J. Mater. Sci. Lett. **13**(5), 326–328 (1994)
39. Ribot, H., Lee, K.W., Simes, R.J., Yan, R.H., Coldren, L.A.: Disordering of GaAs AlGaAs multiple quantum well structures by thermal annealing for monolithic integration of laser and phase modulator. Appl. Phys. Lett. **55**(7), 672–674 (1989)
40. Fu, L., Lever, P., Tan, H.H., Jagadish, C., Reece, P., Gal, M.: Suppression of interdiffusion in InGaAs/GaAs quantum dots using dielectric layer of titanium dioxide. Appl. Phys. Lett. **82**(16), 2613–2615 (2003)
41. Cusumano, P., Ooi, B.S., Helmy, A.S., Ayling, S.G., Bryce, A.C., Marsh, J.H., Voegele, B., Rose, M.J.: Suppression of quantum well intermixing in GaAs/AlGaAs laser structures using phosphorus-doped SiO_2 encapsulant layer. J. Appl. Phys. **81**(5), 2445–2447 (1997)
42. Cohen, R.M., Li, G., Jagadish, C., Burke, P.T., Gal, M.: Native defect engineering of interdiffusion using thermally grown oxides of GaAs. Appl. Phys. Lett. **73**(6), 803–805 (1998)
43. Zhang, Z.Y., Jiang, Q., Hogg, R.A.: Tunable interband and intersubband transitions in modulation C-doped InGaAs/GaAs quantum dot lasers by postgrowth annealing process. Appl. Phys. Lett. **93**(7), 071111–0711113 (2008)
44. Mokkapati, S., Du, S., Buda, M., Fu, L., Tan, H.H., Jagadish, C.: Multiple wavelength InGaAs quantum dot lasers using ion implantation induced intermixing. Nanoscale Res. Lett. **2**(11), 550–553 (2007)
45. Song, J.H., Kim, K., Leem, Y.A., Kim, G.: High-power broadband super luminescent diode using selective area growth at 1.5 μm wavelength. IEEE Photonics Technol. Lett. **19**, 1415–1417 (2007)

46. Ong, T.K., Yin, M., Yu, Z., Chan, Y.C., Lam, Y.L.: High performance quantum well intermixed super luminescent diodes. Meas. Sci. Technol. **15**(8), 1591–1595 (2004)
47. Zhang, Z.Y., Jiang, Q., Hopkinson, M., Hogg, R.A.: Effects of intermixing on modulation p-doped quantum dot super luminescent light emitting diodes. Opt. Express **18**(7), 7055–7063 (2010)
48. Drexler, W.: Ultrahigh-resolution optical coherence tomography. J. Biomed. Opt. **9**(1), 47–74 (2004)
49. Bardella, P., Rossetti, M., Montrosset, I.: Modeling of broadband chirped quantum-dot superluminescent diodes. IEEE J. Sel. Top. Quantum Electron. **15**(3), 785–791 (2009)
50. Sugimoto, Y., Tanaka, Y., Ikeda, N., Nakamura, Y., Asakawa, K., Inoue, K.: Low propagation loss of 0.76 dB/mm in GaAs-based single-line-defect two-dimensional photonic crystal slab waveguides up to 1 cm in length. Opt. Express **12**(6), 1090–1096 (2004)
51. Rafailov, E.U., Cataluna, M.A., Sibbett, W.: Mode-locked quantum-dot lasers. Nat. Photonics **1**(7), 395–401 (2007)
52. Thompson, M.G., Rae, A.R., Xia, M., Penty, R.V., White, I.H.: InGaAs quantum-dot mode-locked laser diodes. IEEE J. Sel. Top. Quantum Electron. **15**(3), 661–672 (2009)
53. Rafailov, E.U., White, S.J., Lagatsky, A.A., Miller, A., Sibbett, W., Livshits, D.A., Zhukov, A.E., Ustinov, V.M.: Fast quantum-dot saturable absorber for passive mode-locking of solid-state lasers. IEEE Photonics Technol. Lett. **16**(11), 2439–2441 (2004)
54. Scurtescu, C., Zhang, Z.Y., Alcock, J., Fedosejevs, R., Blumin, M., Saveliev, I., Yang, S., Ruda, H., Tsui, Y.Y.: Quantum dot saturable absorber for passive mode locking of Nd : YVO4 lasers at 1,064 nm. Appl. Phys. B-Lasers Opt. **87**(4), 671–675 (2007)
55. Stevenson, R.M., Young, R.J., Atkinson, P., Cooper, K., Ritchie, D.A., Shields, A.J.: A semiconductor source of triggered entangled photon pairs. Nature **439**(7073), 179–182 (2006)
56. Shields, A.J.: Semiconductor quantum light sources. Nat. Photonics **1**(4), 215–223 (2007)
57. Wang, Q., Wang, T., Bai, J., Cullis, A.G., Parbrook, P.J., Ranalli, F.: Influence of annealing temperature on optical properties of InGaN quantum dot based light emitting diodes. Appl. Phys. Lett. **93**(8), 081915 (2008)

Chapter 7
Photonic Crystal Cavity Lasers

Yiyang Gong, Bryan Ellis and Jelena Vučković

Abstract Photonic laser sources have great potential in communication and lighting applications. Optical resonators reduce the lasing threshold by enhancing the light-matter interaction, increasing the efficiency and modulation rate. We explore the design, fabrication, and characterization of lasers based on photonic crystal (PC) cavities. We first describe the fundamentals of the PC cavity in one dimensional (1D) and two dimensional (2D) settings, and how cavity designs enable high quality factor, low mode volume resonators that facilitate high Purcell enhancements. Next, we show how such designs are implemented to fabricate low threshold lasers using quantum dot(QD) materials. Experimentally under optical injection, we are able to obtain lasing thresholds of microwatts at room temperature and cryogenic temperature, fitting the behavior of different lasers to rate equations. We also theoretically and experimentally characterize the time dynamics of the lasers at cryogenic temperature under modulated pumping, observing that the lasers can be modulated at 30 GHz. Finally, we explore novel approaches to electrically inject PC cavity devices using a lithographically defined lateral p-i-n junction, and demonstrate a lateral junction PC cavity light-emitting device.

Yiyang Gong and Bryan Ellis contributed equally.

Y. Gong (✉) · B. Ellis
Department of Electrical Engineering, Stanford University, Stanford, CA 94305, USA
e-mail: yiyangg@stanford.edu

B. Ellis
e-mail: bellis@soraa.com

B. Ellis
Soraa Inc., 6500 Kaiser Dr, Fremont, CA 94555-3613, USA

J. Vučković
Ginzton Laboratory, Center for Nanoscale Science and Technology, Stanford University,
348 Via Pueblo Mall, Stanford, CA 94305, USA
e-mail: jela@stanford.edu

Z. M. Wang (ed.), *Quantum Dot Devices*, Lecture Notes in Nanoscale Science and Technology 13, DOI: 10.1007/978-1-4614-3570-9_7,
© Springer Science+Business Media New York 2012

Introduction

In the information age, the need for bandwidth to pass data between computation centers has greatly increased. In addition to the growth of the fiber-optic communication bandwidth for long distance data transfer, the growth of the local data centers, computer clusters, and multi-core processors has motivated the development of optical communications for short distances. Here, and especially for chip-to-chip communications, optical interconnects have distinct advantages over conventional electrical interconnects as device sizes are decreased to increase the information density [1]. In particular, the resistance and time constant of wires transporting electrical data increase as device dimensions are scaled down, leading to high energy costs for transporting information. On the other hand, the energy cost for optical interconnects scale down with the size of the transmitter and receiver, and could be decreased with the device design.

The emission and control of light on such nanoscales could be done by a variety of optical cavities [2]. The two key figures of merit for an optical cavity at frequency ω (and wavelength $\lambda = 2\pi c/\omega$, where c is the speed of light) are the quality (Q) factor and the mode volume (V_m). The Q-factor can be defined in the optical spectrum of the cavity as $Q = \omega/\Delta\omega = \lambda/\Delta\lambda$, where $\Delta\omega$ and $\Delta\lambda$ are the full-width at half-maximum (FWHM) of the cavity spectrum in the frequency and wavelength domains, and is a measure of the temporal confinement of the photons. On the other hand, the mode volume of the cavity is a measure of the volume that the photonic field occupies when confined to the cavity. It is defined as:

$$V_{\mathrm{m}} = \frac{\int \varepsilon(\vec{r})|E(\vec{r})|^2 \mathrm{d}V}{\max\left[\varepsilon(\vec{r})|E(\vec{r})|^2\right]} \tag{7.1}$$

where $E(\vec{r})$ is the spatial distribution of the electrical field of the cavity mode, and $\varepsilon(\vec{r})$ is the dielectric structure of the cavity. In short, it measures the spatial confinement of photons in the cavity. In particular, increasing Q and decreasing V_m increases the light-matter interaction inside of a photonic cavity. In the weak-coupling, or Purcell, regime of cavity quantum electrodynamics (cQED), the spontaneous emission (SE) rate of an emitter coupled to a cavity is enhanced by the Purcell factor, defined as [3]:

$$F = \frac{3}{4\pi^2}\left(\frac{\lambda}{n}\right)^3\left(\frac{Q}{V_{\mathrm{m}}}\right)\overline{\psi(\theta, \vec{r}, v)} \tag{7.2}$$

where $\psi\ (\theta,\ \vec{r}, v)$ includes the decrease of enhancement for spatially and spectrally detuned emitters from the cavity mode. Defined for a dipole emitter with frequency v (spectrally detuned from the cavity frequency, ω) at a position $\vec{r}$ that forms an angle θ with the cavity E-field at the same position, $\psi(\theta,\ \vec{r}, v)$ takes the form:

$$\psi(\theta, \vec{r}, v) = \left|\frac{E(\vec{r})}{E_{\max}}\right|^2 \frac{\left(\frac{v}{2Q}\right)^2}{(v-\omega)^2 + \left(\frac{v}{2Q}\right)^2}\cos^2(\theta) \tag{7.3}$$

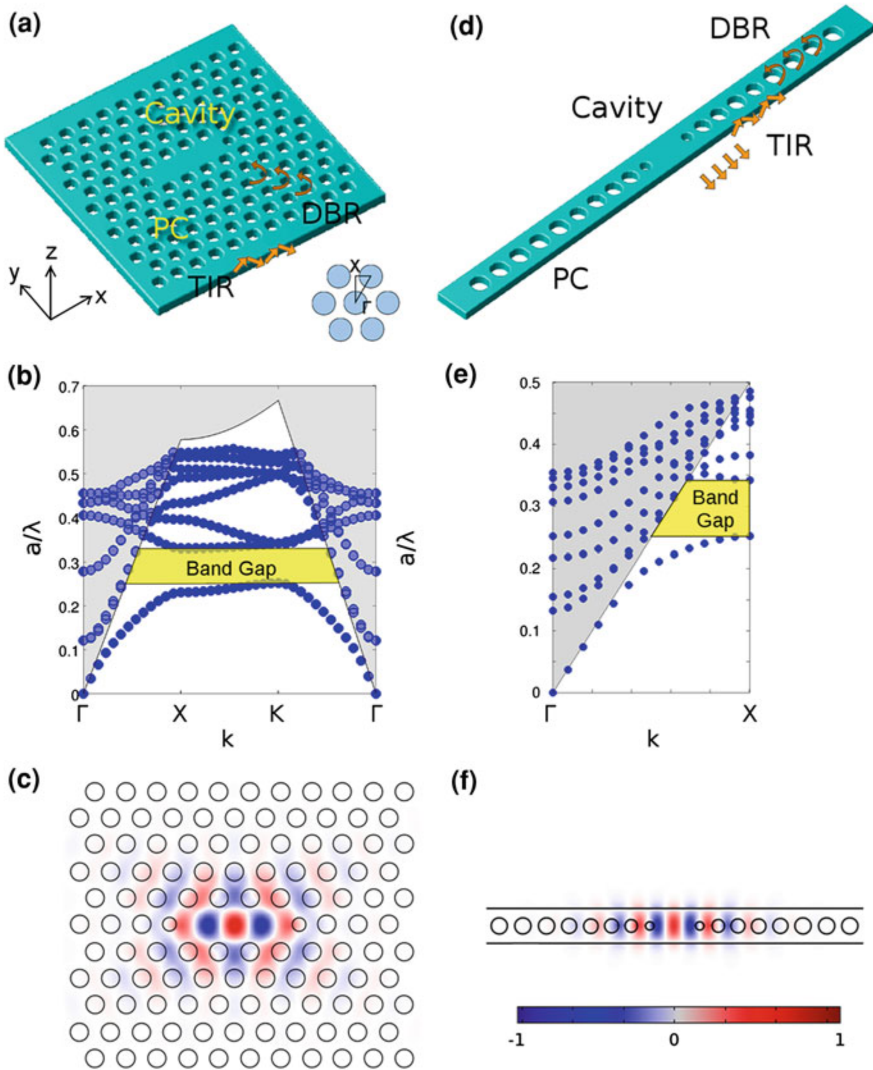

Fig. 7.1 **a** The 2D PC cavity system in a suspended membrane, with the cavity defect and the periodic air holes that form the triangular lattice PC. TIR confines the light in the out-of-plane directions of the membrane, while DBR confines the light in the directions in the plane of the membrane. The *inset* shows the irreducible Brillouin zone in the reciprocal space for the triangular lattice, along with the labeled high-symmetry points. **b** A representative band diagram for the TE-like polarization along the high-symmetry directions, for a slab with index of refraction $n = 3.5$. The *solid line* is the light line, which separates the states confined by the TIR (*below* the line) from those that leak in the direction perpendicular to the membrane. The optical bandgap is seen *below* the light line and between normalized frequencies $a/\lambda = 0.25$ and 0.33. **c** The E_y field of the fundamental mode for the 2D PC cavity. **d** The 1D PC nanobeam cavity system. Here, DBR confines the light in the direction along the beam, and TIR confines the light in the other two directions. **e** Band diagram for the 1D system also for $n = 3.5$. A bandgap forms around the same frequencies as the 2D PC system. **f** The E_y field of the fundamental mode for the 1D PC cavity

where E_{max} is the *E*-field amplitude at the location of the maximum *E*-field energy density, $\varepsilon|E|^2$. Intuitively, enhancing *Q* increases the photon storage time, while decreasing V_m increases the local photon energy density, both increasing the interaction (emission and absorption) between the emitter and photons in the optical cavity mode and increasing the SE of emitters into the cavity mode [4].

Photonic crystal (PC) cavities have had a large impact in the field of low threshold lasers [5, 6], as these high *Q* factor and small V_m resonators reduce the lasing threshold by enhancing the SE rate of the emitters into the cavity and lasing mode. In addition, the increased *Q* and reduced V_m reduce the lasing threshold for active materials, as the increased photon storage time enhances stimulated emission processes, while the reduced mode volume allows inversion with reduced pump power by reducing the amount of active material in the cavity. Due to the low threshold and small volumes, PC cavities enable lasers with very fast direct modulation speeds exceeding 100 GHz [7, 8], which have the potential to be used in opto-electronic communications. Finally, the use of quantum dot (QD) active material inside PC cavity lasers to further lower the lasing threshold (by minimizing non-radiative surface recombination effects) has been studied [9–13]. Other potential applications of these devices include compact chemical or mass sensors [14].

The outline of this chapter will be as follows: In "PC Cavities", we discuss the basics of PC cavities. In "1D PC Laser", we discuss a one dimensional (1D) PC cavity laser. In "High Speed Modulation of PC Lasers", we discuss the dynamics of PC lasers and ultrafast operation. Finally, in "Electrical Pumping of PC Lasers", we introduce novel approaches to PC laser design and electrical injection of PC cavities.

PC Cavities

The PC cavity system, with high *Q*-factor and low V_m, can be employed to enhance the SE rate via Purcell enhancement and reduce the threshold to lasing. First proposed by Yablonovitch [15] and John [16], the PC is a structure with a periodic variation in dielectric constant. Much like how the periodic arrangement of atoms in solids leads to a bandgap in allowed energies for electrons, the periodic arrangement of the dielectric constant leads to a photonic bandgap in the allowed energies for photons. This photonic bandgap can be used to direct light, as photons with energies inside of the bandgap will be reflected by the PC structure.

The periodicity of the material system creates coupling between forward and backward propagating waves with certain wave vectors *k* and frequencies ω, and for certain ranges of the ω-*k* relationship can enable complete reflection in a process known as distributed Bragg reflection (DBR). Although 3D PCs can confine light in all directions and their fabrication has been recently improved (including high *Q* cavities) [17–21], the fabrication process for these multilayered structures is extremely difficult. Similarly, 1D PCs made up of stacks of alternating materials have been used in vertical cavity surface-emitting lasers (VCSELs) [22],

but require very well-controlled growth of multilayer structures. In this chapter, we focus on 1D or 2D cavities that are fabricated in an one-step lithography and etching process to form suspended membranes. Because 1D and 2D PCs only confine light in the direction with periodic dielectric constant, total internal reflection (TIR) arising from the index contrast between the slab material and the surrounding medium is used to confine light in the remaining directions.

The basic 2D PC cavity system is shown in Fig. 7.1a, where a three-hole defect is formed in a periodic triangular lattice of air holes in a dielectric slab. As shown, the planar 2D PC confines light to the cavity defect by DBR in the plane of the structure, and by TIR out of the plane. By solving the electromagnetic eigenvalue equation in the infinitely periodic system (i.e., without the cavity defect):

$$\frac{1}{\varepsilon}\nabla \times \nabla \times \vec{E} = \left(\frac{\omega}{c}\right)^2 \vec{E} \tag{7.4}$$

for the possible directions of propagation $(\vec{k})$ in the plane of the membrane in the PC region, we obtain the energy band diagram of the photonic system shown in Fig. 7.1b. For infinitely periodic structures, the solutions to Eq. 7.4 must satisfy periodic Bloch boundary conditions: $E(\vec{r}+\vec{a}) = e^{i\vec{k}\cdot\vec{a}}E(\vec{r})$, where $\vec{a}$ is a lattice vector of the periodic system. In this case, the allowable modes of the ω-k relationship is shown for the transverse-electric (TE)-like polarization, which has non-zero components for only (E_x, E_y, H_z) on the midplane of the z-direction, where E_x and E_y are in the plane of the membrane, and H_z is perpendicular to the plane of the membrane. The high symmetry directions of the triangular lattice, which forms the boundary of the irreducible Brillouin zone in the reciprocal lattice space, are plotted in Fig. 7.1a, inset. The solid lines in Fig. 7.1b correspond to the light line, which follow the relation $c|k|/n$, where n is the refractive index of the PC material and $|k| = 2\pi/\lambda$ is the norm of the wave vector. The gray region of the band diagram (known as "above the light-line") denotes the region where TIR does not confine photons in the direction normal to the plane of the membrane. Below the light line, we see a range of energies where no photonic modes exist, and thus a range of energies where the PC would confine light through the combination of DBR and TIR. Because the photonic bandgap exists for all directions below the light line, photons confined to the cavity region would not be able to escape through the PC in directions parallel to the plane of the membrane. Thus, the confinement of a PC cavity is limited by the radiation lost in the directions not confined by the DBR, i.e., the cavity field components located above the light line. Designs to manipulate the spatial profile of the cavity mode and minimize radiation in the above light line directions have been implemented to improve Q-factors [23, 24].

From Fig. 7.1b, we also observe that the lattice constant that creates a bandgap is generally on the order of $a = \lambda/n$, where n is the refractive index of the PC slab material. With proper design, the V_m of PC cavities is expected to be below $(\lambda/n)^3$. By simulating the three-hole defect cavity shown in Fig. 7.1a with finite different time-domain (FDTD) simulations, we find that the cavity supports a fundamental cavity mode (which satisfies Eq. 7.4 without periodic boundary conditions) with a

dominant E_y profile shown in Fig. 7.1c, $Q > 4 \times 10^4$, and $V_m < (\lambda/n)^3$. Compared to other cavities, such as the micropillar ($Q = 2{,}000$, $V_m > 5\ (\lambda/n)^3$), microdisk ($Q > 10^4$, $V_m > 6\ (\lambda/n)^3$), microtoroid ($Q > 10^8$, $V_m \sim 10^2\ (\lambda/n)^3$), and microsphere ($Q > 10^9$, $V_m > 10^3\ (\lambda/n)^3$), the 2D PC cavity offers a different regime of moderate Q and low V_m, which is useful for reaching the Purcell regime and enhancing light emission into a particular mode [2].

The 2D PC cavity has been well established, with $Q > 10^6$ having been theoretically and experimentally achieved in a high index material (silicon, $n = 3.5$) [23, 25, 26]. In addition, moderate Q cavities have been proposed in low index materials such as diamond ($n = 2.4$) [27, 28] and silicon nitride (Si_3N_4, $n = 2.0$) [29, 30], with experimental $Q > 3{,}000$. While high Q cavities in 2D PCs are difficult to achieve in low index materials, 1D nanobeam cavities support cavity modes in many materials. These beams confine modes by DBR with a periodic lattice along the length of the beam and by TIR in the two directions perpendicular to the length of the beam (Fig. 7.1d). In the 1D setting, photonic bandgaps formed in high index materials with $n = 3.5$ are comparable to the bandgaps in 2D PCs (Fig. 7.1e), and bandgaps exist even for low index contrast systems [31]. As one of the first PC cavities designed and fabricated [32], the nanobeam cavity can achieve strong reflection along the length of the beam due to the photonic bandgap of reduced dimensionality, while TIR efficiently confines cavity modes derived from lossless waveguide modes of the beam. For example, the beam structure in Fig. 7.1d forms a cavity by removing holes from the beam and modifying the holes sizes around the defect. This structure supports the fundamental mode with a dominant E_y field shown in Fig. 7.1f, with $Q > 10^5$ and $V_m < (\lambda/n)^3$. Recent developments in 1D nanobeam cavities with "potential well" designs have achieved the same Q-factors in silicon as in 2D PC cavities with comparable mode volumes [33], while also opening the door for high-Q cavities in Si_3N_4 for applications of optomechanics [34] and coupling to active materials [35]. In particular, the experimentally demonstrated Qs exceed 10^5 for Si [33], 10^4 for Si_3N_4 ($n = 2.0$) [34], and 10^3 for SiO_2 ($n = 1.46$) [31]. Because of their versatility, the nanobeam design can be applied to a variety of materials to engineer high-Q, low V_m cavity modes that enhance radiation from emitters embedded in the cavity.

The planar PC offers simple fabrication with one lithography step, such as the procedure shown in Fig. 7.2. First, the wafer is grown with the eventual PC membrane (including the active layer) on top of a sacrificial layer that offers selective etching properties compared to the PC membrane (Fig. 7.2a). Then a layer of resist (either polymer or deposited material) is coated on the wafer (Fig. 7.2b). Electron beam lithography is used to define the PC pattern into the resist, and the pattern is transferred into the PC membrane using a directional dry etch (Fig. 7.2c–d). Finally, the resist is removed, and a selective wet etch is used to remove the sacrificial layer under the PC membrane to form a free-standing planar PC (Fig. 7.2e–f).

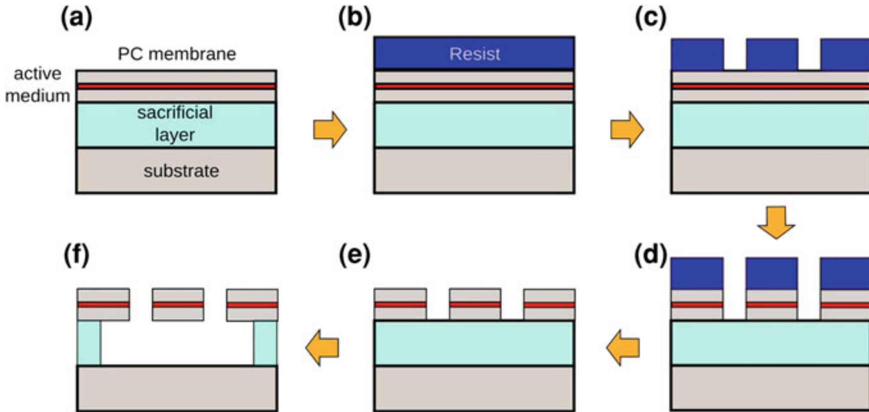

Fig. 7.2 The PC fabrication process: **a** The grown wafer with layered structure. **b** Deposition of resist. **c** exposure and patterning of the resist. **d** Transfer of the resist pattern to the PC membrane. **e** Removal of resist. **f** Selective undercut of the sacrificial layer to suspend the membrane

1D PC Laser

In this section, we study the lasing properties of GaAs nanobeam cavities with InAs QDs at room temperature. 1D nanobeam cavities have been previously designed and fabricated in a variety of passive materials, such as Si [32, 33], Si_3N_4 [34], and SiO_2 [31]. Very recently, lasing in such cavities incorporating quantum well material has been demonstrated [36, 37, 38]. Because of their small footprint, such 1D PC cavities also have potential as compact light sources for on-chip optical communications, and proposals for employing nanomechanical properties of such structures to build tunable lasers have been made [39]. Much like 2D PC cavities, nanobeam cavities have high Q and low V_m, thereby potentially decreasing the lasing threshold via the Purcell enhancement of SE rate.

The cavity design is based on a beam having thickness d and width w, and circular holes are patterned along the beam with period a and radii $r = 0.3a$ in the PC mirror region (Fig. 7.3a). The cavity comprised of holes spaced at $a' = 0.84a$ at the center of the cavity, and holes size of $r' = 0.84r$. The hole spacing and size increased parabolically from the center of the cavity outwards, extending six holes on either side of the cavity. The cavity is designed with $d = 0.7a$ and $w = 1.3a$, and is simulated by the 3D-FDTD method with 20 units per lattice constant (a) and perfectly matched layer (PML) absorbing boundary conditions. We computed the Q of the cavity using $Q = \omega U/P$, where ω is the frequency of the cavity, U is the total energy of the mode, and P is the time-averaged energy radiated transverse to the beam length (i.e., not through the ends of the beams, where the leakage is suppressed by the DBR). Using the FDTD simulation, we found the $|E|^2$ field profile of the fundamental TE-like cavity mode shown in Fig. 7.3b, which is dominated by the E_y component. We also found that further increase in the number of PC mirror layers beyond 15 did not increase the overall Q of the cavity. Finally, from the simulations,

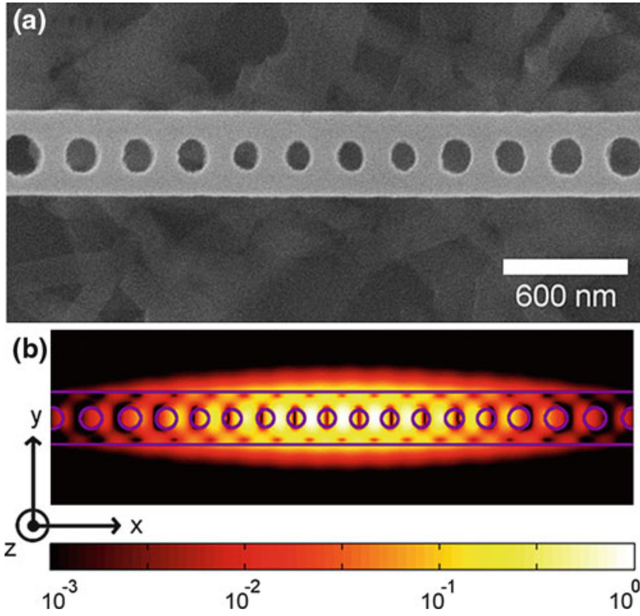

Fig. 7.3 **a** The fabricated 1D nanobeam cavity. **b** The electric field intensity ($|E|^2$) of the fundamental mode supported by the cavity. Reproduced with permission from [38]. Copyright 2010 OSA

we obtained $Q = 1.2 \times 10^5$, $V_m = 0.8\ (\lambda/n)^3$, and normalized frequency of $a/\lambda = 0.25$. While the beam also supports higher order modes that sit farther from the central defect and have lower frequency [33, 34], we worked with the fundamental TE mode as it has the highest Q and lowest V_m among all TE modes. In experiment, we observed a significant reduction in Q relative to theoretical prediction (by a factor of 5–10), resulting from fabrication imperfections (such as edge roughness from the dry etch and lithographic tolerances to the hole position), or from absorption losses in the QDs and the wetting layer.

The employed membrane structure was grown by molecular beam epitaxy (MBE) and consists of a 1 μm $Al_{0.8}Ga_{0.2}As$ sacrificial layer and a 240 nm GaAs membrane that contains three layers of InAs QDs separated by 50 nm GaAs spacers. To achieve emission at 1.3 μm, the dots were capped with a 6 nm $In_{0.15}Ga_{0.85}As$ strain-reducing layer. The QDs were formed by depositing 2.8 monolayers (ML) of InAs at 510°C using a growth rate of 0.05 ML/s. These growth conditions result in a dot density of 3×10^{10} cm^{-2}, as estimated from atomic force microscopy (AFM) measurements of uncapped QD samples. Fabrication of the PC cavities is done by procedures similar to the one shown in Fig. 7.2. First, a 300 nm layer of the electron beam resist ZEP-520A is spun on top of the wafer, e-beam lithography is performed to define the cavity design. The written pattern is then transferred to the GaAs membrane using a Cl_2:BCl_3 dry etch. Finally, the nanobeam is undercut with a 7% HF solution in water. An example fabricated structure is shown in Fig. 7.3a. In fact, by simulating this structure directly [40] without absorption losses, we observe a reduction in Q to $Q = 20{,}000$.

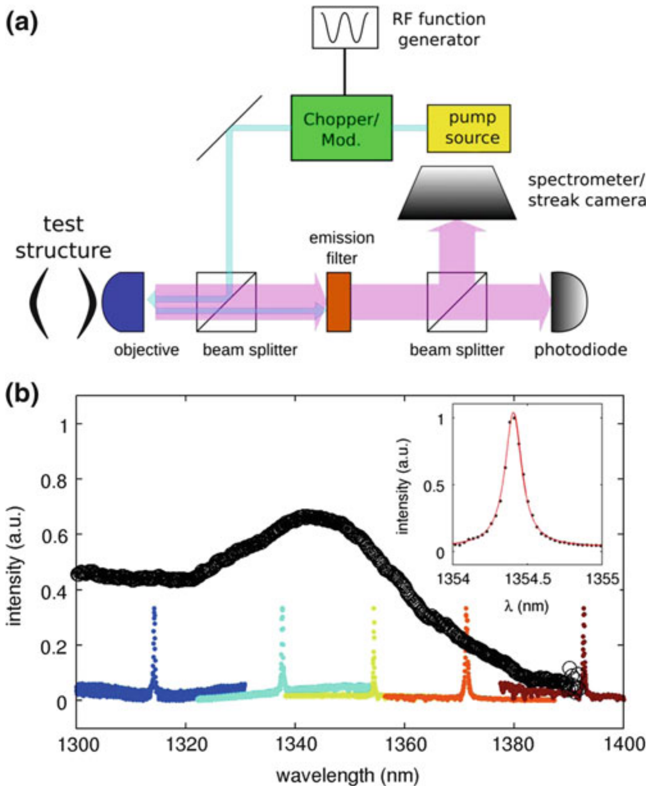

Fig. 7.4 **a** Experimental configuration. **b** Normalized PL spectra from representative cavities above lasing threshold (*colored points*). The PL spectrum from QDs in bulk (unpatterned film) is also shown (*gray circles*). The *inset* shows a zoomed-in cavity spectrum (pumped at 14 μW, below the lasing threshold) and its fit to a Lorentzian lineshape, corresponding to $Q = 9{,}700$. Reproduced with permission from [38]. Copyright 2010 OSA

We pump the cavities at both 780 nm (above the GaAs band gap positioned at $\lambda_g = 870$ nm) and at 980 nm (below λ_g, but above the emission wavelength of the QDs, and slightly above the emission wavelength of the quantum well wetting layer at 1,000 nm), both at room temperature using the micro-photoluminescence (μ-PL) setup shown in Fig. 7.4a. The continuous wave (CW) pump laser is focused onto the beam from normal incidence with a 100 × objective lens with numerical aperture NA = 0.5. The photoluminescence (PL) from the sample is also collected from the direction perpendicular to the plane of the chip and sent to a spectrometer with an InGaAs CCD array. Suspended bridge nanobeam cavities have been shown to have very small heat conduction [41]. However, the 980 nm pumping avoids heating of the cavity at high pump powers, and allows high power CW pumping. The PL from QDs in an unpatterned region of the sample is shown in Fig. 7.4b. The PL spectra of various cavities with slightly different lattice constants and radii are also shown in Fig. 7.4b, with pump powers above threshold

with the 980 nm pump. The Lorentzian fit to a cavity spectrum (pumped at 14 μW, below threshold) with $Q = 9{,}700$ is shown in the inset of Fig. 7.4b.

We studied the pump power dependence of cavities by varying the pump power of an unchopped CW 980 nm pump laser from as little as 0.1 μW to as much as 10 mW. The output power of the nanobeam laser as a function of the pump power is shown in Fig. 7.5a. The experiment is repeated with the same cavity, but with the 780 nm pump (Fig. 7.5b). We fit the data to the standard rate equations [42]:

$$\frac{\mathrm{d}N}{\mathrm{d}t} = \eta \frac{L_{\mathrm{in}}}{\hbar\omega V_{\mathrm{a}}} - N\left(\frac{F}{\tau_{\mathrm{r}}} + \frac{1}{\tau_{\mathrm{nr}}}\right) - v_{\mathrm{g}}gP \tag{7.5}$$

$$\frac{\mathrm{d}P}{\mathrm{d}t} = \Gamma v_{\mathrm{g}}gP + \Gamma\beta\left(\frac{N}{\tau_{\mathrm{r}}} + \frac{P}{\tau_{\mathrm{p}}}\right) \tag{7.6}$$

where $N(P)$ represents the carrier (photon) density, F is the Purcell factor, η represents the fraction of incident pump power (L_{in}) absorbed in the active region, V_{a} is the active volume of the laser, τ_{r} (τ_{nr}) is the radiative (non-radiative) recombination lifetime, $v_{\mathrm{g}} = 1 \times 10^{10}$ cm/s is the group velocity of light in the active medium, τ_{p} is the photon lifetime of the cavity, β is the fraction of SE coupled to the cavity mode, and Γ is the mode overlap with the QDs. Because the homogeneous linewidth of such QDs at room temperature is approximately 10 meV [10], which far exceeds the cavity linewidth, the Purcell enhancement was negligible (F $\sim$ 1) [43]. A logarithmic gain model $g = g_0 \ln(N/N_{\mathrm{tr}})$ is used where g_0 is the gain coefficient in units of cm^{-1} and N_{tr} is the transparency carrier density in units of cm^{-3} [10]. The photon lifetime $\tau_{\mathrm{p}} = Q/\omega$ was estimated from the linewidth of the cavity resonance around threshold to be 7.1 ps. The QD radiative lifetime in bulk, τ_{r}, was estimated from the literature to be about 3 ns [10], and the non-radiative lifetime, τ_{nr}, was too long to significantly affect the fits. We also expect that the non-radiative recombination occurring at the surfaces in our structures is significantly lower than in quantum well lasers, as a result of the spatial confinement of the QD excitons. This small non-radiative recombination rate, in addition to low threshold, caused a soft turn-on of the laser structures shown in Fig. 7.5a.

Since it is difficult to estimate the gain parameters and the fraction of absorbed pump power in our structures, we fit the rate equations with β, g_0, N_{tr}, and η as variable parameters. We simultaneously fit the data from the 780 nm pump and the 980 nm pump to the model with the same β, g_0, and N_{tr}, but different η. The best fit to the data was obtained with $g_0 = 6.2 \times 10^4$ cm^{-1} and $N_{\mathrm{tr}} = 7.9 \times 10^{15}$ cm^{-3}, comparable to previous studies with similar QDs [10]. For our lasers we find $\beta = 0.88$, $\eta = 1.3 \times 10^{-5}$ for the 980 nm pump, and $\eta = 6.3 \times 10^{-4}$ for the 780 nm pump. The difference in η for the two pump powers is expected, since the 980 nm pump laser has lower energy than the GaAs band gap and therefore is weakly absorbed (only by QDs and the wetting layer). Despite low Purcell enhancement, a high β factor was achieved, resulting from redirection of SE into a single mode, similar to vertical nanowire antennas [44, 45]. To find the threshold

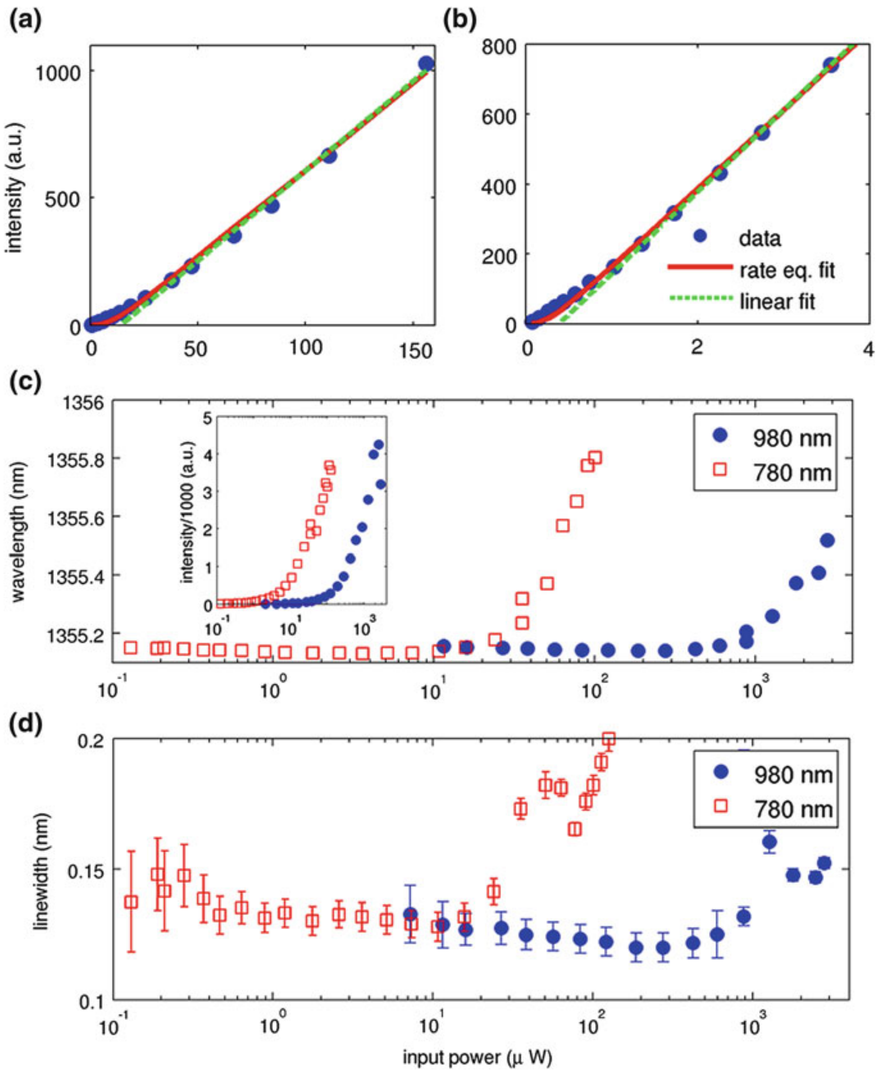

Fig. 7.5 The L–L curves of a representative cavity, using **a** the 980 nm pump, and **b** the 780 nm pump laser. Fits from the rate equations, and linear fits to the above threshold behavior are also shown. **c** The power dependence of the cavity wavelength with 780 and 980 nm pump. The redshift at high pump powers indicates structure heating, and it occurs at lower input powers if the above-GaAs bandgap laser (780 nm) is employed, as expected. The *inset* shows the cavity intensity for larger pump powers, where the beginning of saturation is observed toward the end of both traces. **d** The power dependence of the cavity linewidth with 780 and 980 nm pump. The pump power (horizontal axis) is measured before the objective in all cases. Reproduced with permission from [38]. Copyright 2010 OSA

of the laser we used a linear fit to the light-in light-out (L–L) curve above threshold, and found the thresholds to be 19 and 0.3 μW, for the 980 and 780 nm pump, respectively. Again, the reduction in threshold highlights the improved

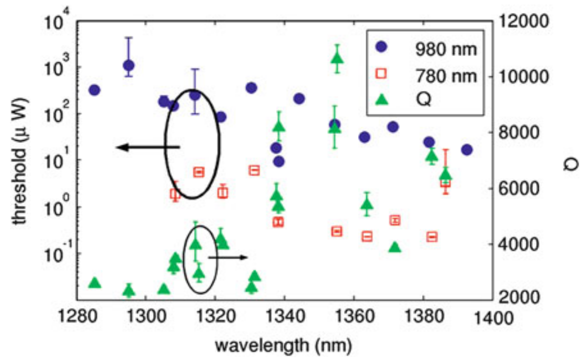

Fig. 7.6 The thresholds of various nanobeam lasers obtained by linear fit to the above threshold behavior, using both the 780 nm and the 980 nm pump. Threshold pump powers are measured before the objective lens in all cases. The *Q*s of various cavities (all below threshold) are also shown. Reproduced with permission from [38]. Copyright 2010 OSA

pump efficiency with the 780 nm pump. The threshold with the 780 nm pump is an order of magnitude lower than that (25 μW) reported in Ref. [10], where a chopped CW pump (100 μs on in a period of 1 ms) was used to reduce heating effects, and that (2.5 μW, in front of the objective) in Ref. [11], with CW pumping. We observed a reduction in threshold despite not using any chopping, which could come from the reduced number of QD layers in our structure, or from the high β-factor of this cavity design.

In addition, we noticed that two pump wavelengths create different behavior in the cavity heating. For both pump wavelengths, the cavity wavelength was unchanged at low pump powers, but red shifted at high pump powers (Fig. 7.5c). Moreover, the wavelength shift for the 780 nm pump began at lower powers than the one for the 980 nm pump, which is expected, as the 780 nm pump is more efficiently absorbed in the material. We also studied the cavity linewidth as a function of pump power, but observed only a small narrowing (Fig. 7.5d), as the cavity linewidth is near the resolution of our spectrometer and small linewidth narrowing at threshold is a signature of high β factor lasers [46]. There was a noticeable increase in linewidth above 10 μW pump power associated with heating losses, and again occurring sooner with the 780 nm pump. Finally, in the inset of Fig. 7.5c, we show the high pump power dependence of the cavity output intensity, and the end of each trace represents the pump power where the cavity output started to decrease. While the two pump wavelengths show approximately the same power output, the cavity linewidth was irreversibly broadened with the 780 nm before the saturation behavior (as in Fig. 7.5d), suggesting heating damage to the cavity. On the other hand, damage to the cavity was not observed with the 980 nm pump.

We also investigated multiple cavities throughout the PL spectrum of the QDs, finding each threshold by a linear fit to the above threshold behavior and plotting the results in Fig. 7.6. First, we noticed that the thresholds increased by nearly an order of magnitude as we move toward the blue side of the PL spectrum, for both the 780 nm and the 980 nm pump. This results from the degradation of the cavity Q-factor with decreasing wavelength (Fig. 7.6). As more QDs are able to absorb the emission from the cavity, the Q falls well below the radiation limited Q found

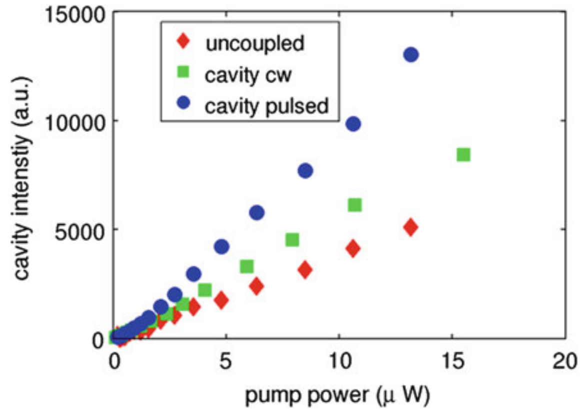

Fig. 7.7 The L–L curve for the same cavity as in Fig. 7.5a–b, pumped with a pulsed 830 nm laser, and by a CW 830 nm laser. The emission from a portion of the PL spectrum not coupled to the cavity is also shown. Pump powers are measured in front of the objective. Reproduced with permission from [38]. Copyright 2010 OSA

by simulation. In addition, we also observed that the use of the 780 nm pump always results in lower thresholds than the 980 nm, by approximately two orders of magnitude. Again, this corroborates the fact that the pumping above the GaAs bandgap efficiently delivers carriers to the QDs.

In order to check the lossy mechanisms due to heating, we also pumped the cavity with a pulsed 830 nm laser (35 ns pulse, 150 ns repetition period). It should be noted that this corresponds to a quasi-CW regime, as the pulse duration is much longer than any recombination time scales of the system, but the modulation helps reduce heating losses. The cavity emission as a function of the peak CW power is plotted in Fig. 7.7 for the various cases of CW and pulsed pumping. Lasing was observed in both cases, but the pulsed pump generated a higher slope of the L–L curve. Moreover, the saturation at higher pump powers was delayed in the case of the pulsed pumping. This is attributed to the reduction of the heating effect, which leads to higher laser efficiency.

High Speed Modulation of PC Lasers

Many potential applications of 2D PC and nanobeam lasers such as short distance optical communications and optical interconnects require high speed modulation. Because edge-emitting and VCSELs cannot be modulated at very high speeds, an external modulator is used to modulate the laser source in conventional optical communication systems. Removing the optical modulator and directly modulating the laser would simplify the architecture and reduce the power consumption of the optical source. However, ultrafast optical sources would need to be developed to satisfy the bandwidth requirements of these applications. Although a practical demonstration of an electrically pumped PC laser modulated at frequencies exceeding those demonstrated in edge-emitting or VCSEL devices has not been achieved, researchers have theoretically and experimentally demonstrated that

high-β lasers such as those discussed in this chapter can be modulated at ultrafast frequencies far exceeding those of conventional lasers [7, 47]. Modulation rates exceeding 100 GHz are feasible in quantum well PC lasers [7] and QD PC lasers have been demonstrated to have large-signal modulation rates of 30 GHz [9]. An optically pumped PC laser transmitter operating with only 13 fJ/bit energy consumption has been demonstrated at 5.5 Gb/s, demonstrating that these devices can be practical in low-power optical communication links [48]. This section will discuss the theory and experimental demonstration of high speed modulation in PC lasers.

In theory it is not necessary to use a laser to achieve high modulation rates. Purcell enhancement can be used to speed up the maximum modulation frequency of a cavity-enhanced light-emitting diode (LED) [49]. In any LED, the modulation rate will be limited by the radiative recombination lifetime of the emitting medium, and thus high speed modulation can be achieved by coupling the active medium to a cavity. Since the unenhanced radiative recombination lifetime in practical emitters is slow compared to stimulated emission rates achieved in lasers, a very high Purcell factor is necessary to achieve high modulation speeds [50]. For example, the radiative recombination lifetime of InAs QDs is on the order of 1 ns. Therefore, to achieve modulation rates of 100 GHz, a Purcell factor of 100 averaged over the entire pumped active region is necessary. At present it is not clear that any micro- or nanocavity can be designed to achieve an average Purcell factor this high.

Another way to achieve this high speed modulation is to use non-radiative recombination. For example, surface recombination at the sidewalls of the etched holes in quantum well PCs causes the non-radiative recombination time constant to be only a few tens of picoseconds at room temperature [50]. If this quantum well PC is used to make an LED, modulation rates exceeding 10 GHz can be achieved. The main disadvantage of this technique is that LEDs with high non-radiative recombination rates will be very inefficient, as the non-radiative pathways channel excitation from radiative recombination. For example, in a quantum well PC laser below threshold, the non-radiative recombination lifetime was measured to be 36 ps while the radiative recombination lifetime was 654 ps [50]. This means that the maximum achievable efficiency of an LED made from this material is only:

$$\eta = \frac{1/\tau_{\mathrm{r}}}{1/\tau_{\mathrm{r}} + 1/\tau_{\mathrm{nr}}} = 5\% \tag{7.7}$$

and is even lower if parasitic loss mechanisms such as light emitted into modes other than that of the PC or inefficient pumping are included.

Clearly, the best approach to achieve high modulation rates is to use a laser instead of an LED, as stimulated emission will direct a large fraction of the pumping energy into a single optical mode when a laser is pumped well above threshold, allowing the device efficiency to approach 100%. At the same time, the stimulated emission rate can be very fast, meaning that high modulation rates can be achieved. The large-signal modulation properties of optically pumped quantum well PC lasers have been studied [7]. The lasers were made using quadrupole

modes in a square lattice PC, and InGaAs quantum wells were used as the gain material. The lasers were optically pumped with ultrashort pulses from a mode-locked laser, and the response of the PC laser was measured. When pumped far above threshold, it was found that the rise time of the lasers could be as short as 1.5 ps, and the fall time was only 2 ps, comparable to the photon lifetime in the cavity. Pumping the cavity with a series of optical pulses demonstrated that it is feasible to modulate the lasers at speeds greater than 100 GHz. However, since the PC holes are etched through the active region exposing the quantum wells to the sidewall surfaces, the non-radiative recombination lifetime in these lasers is also very fast (31 ps) [7]. This harmful effect increases the device's lasing thresholds (10–100 μW) and limits its practicality for low-power applications.

To develop optical sources with very low-power consumption and high modulation rates, researchers have developed QD-based PC lasers [9, 38]. Streak camera measurements of the rise time of PL from InAs QDs in bulk GaAs indicate that the carrier capture time is around 10 ps in InAs QDs for a wide range of pump powers. In practice, this short relaxation time means that non-radiative recombination at the etched sidewalls is negligible. Because of this, QD PC lasers have been demonstrated with thresholds of only a few nanowatts and high efficiencies [12]. In this section, we cover our experimental and theoretical results studying the modulation of QD PC lasers, showing that high modulation rates can be combined with ultralow thresholds.

To accurately model the PC laser modulation characteristics, the rate equations (Eqs. 7.5, 7.6) must be adapted to include the finite relaxation time into the QDs. We employed a three-level rate equation model adapted from references [42, 51]:

$$\frac{\mathrm{d}N_\mathrm{w}}{\mathrm{d}t} = \eta \frac{L_\mathrm{in}}{\hbar\omega V_\mathrm{a}} - \frac{N_\mathrm{w}}{\tau_\mathrm{w}} + \frac{N_\mathrm{w}}{\tau_\mathrm{c}} \tag{7.8}$$

$$\frac{\mathrm{d}N_\mathrm{g}}{\mathrm{d}t} = \frac{N_\mathrm{w}}{\tau_\mathrm{c}} - N_\mathrm{g}\left(\frac{F}{\tau_\mathrm{r}} + \frac{1}{\tau_\mathrm{nr}}\right) - v_\mathrm{g} g P \tag{7.9}$$

$$\frac{\mathrm{d}P}{\mathrm{d}t} = \Gamma v_\mathrm{g} g P + \Gamma\beta\left(\frac{N_\mathrm{g}}{\tau_\mathrm{r}} + \frac{P}{\tau_\mathrm{p}}\right) \tag{7.10}$$

To Eqs. 7.5 and 7.6, we have added a rate equation for N_W representing the carrier density in the wetting layer. N_g represents the carrier density in the ground state of the QDs, τ_w represents the wetting layer lifetime, and τ_c represents the carrier capture time into the QDs. For large-signal modulation, these rate equations must be solved numerically. To simulate the properties of these PC lasers, a linear gain model is assumed:

$$g = g_\mathrm{o}(N - N_\mathrm{tr}) \tag{7.11}$$

Here g_o is the linear gain coefficient and N_tr is the transparency current density.

The laser cavities employed in our experiment are high-Q linear three-hole defect PC cavities in a GaAs membrane. Finite-difference time domain simulations

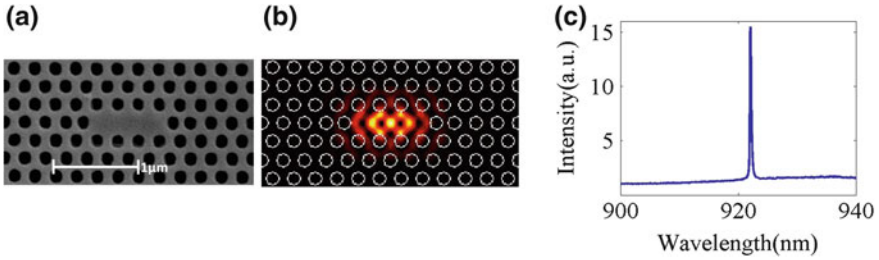

Fig. 7.8 **a** Scanning electron microscope image of linear three-hole defect PC cavity. **b** Finite-difference time domain simulation of the electric field amplitude of the fundamental mode of the PC cavity. **c** Spectrum of the PC laser just above threshold showing single mode operation. Reproduced with permission from [9]. Copyright 2007 American Institute of Physics

were used to design the cavities to have a high-Q resonance near the center of the QD gain spectrum (Fig. 7.8c). The membrane is approximately 135 nm thick and contains one layer of high density (600 μm^{-2}) InAs QDs. The cavities were fabricated using the procedure illustrated in Fig. 7.2. After fabrication the structures were placed inside a He-flow cryostat and cooled to 5 K. This cooling was necessary because the InAs/GaAs QDs used in this work have shallow quantum confinement and do not emit at temperatures above about 50 K. InAs QDs with deeper quantum confinement have been used to demonstrate room temperature operation of QD PC lasers [10, 38] and our results are applicable to more practical lasers working at higher temperatures.

The lasers were optically pumped using a mode-locked Ti–Sapphire laser, and the emission was detected using a spectrometer with a liquid nitrogen cooled InGaAs CCD camera for spectral measurements or a streak camera for time resolved measurements (similar to the setup in Fig. 7.3a). To determine the cavity photon lifetime τ_p, the quality factors of the cavities were measured well below threshold using CW pumping. Fits to a Lorentzian lineshape indicated that the cold-cavity quality factors were around 3,000, corresponding to a cavity photon lifetime of about 1.5 ps. To investigate the dynamics of the structures, we pumped the cavities with 3 ps pulses at an 80 MHz repetition rate using the Ti–Sapphire laser, which corresponds to a duty cycle of 0.2%. Streak camera measurements of the wetting layer response indicated that for our samples $\tau_w \approx 100\,\text{ps}$. From the overlap of the mode volume with the gain medium found using FDTD, we estimate that $\Gamma = 0.028$ in our lasers. The non-radiative lifetime of our QDs was assumed to be too long to affect the behavior of the lasers, as has been found previously using similar QDs [12]. To confirm that the SE rate in our cavities is significantly enhanced, we used a streak camera to compare the decay time of PL from QDs in bulk GaAs and cavity-coupled dots in non-lasing devices. The measurements show that the dot lifetime was significantly reduced from the bulk value of 2.5 ns to 300 ps when the QDs were on resonance and spatially coupled to the PC cavity. The parameters for this laser are summarized in Table 7.1.

Table 7.1 Parameters of the PC laser used in the dynamic simulation

Name	Symbol	Value
Active volume	V_a	4.2×10^{12} cm^3
Mode volume	V_{mode}	1.5×10^{14} cm^3
Confinement factor	Γ	0.028
Wetting layer lifetime	τ_w	100 ps
Carrier capture time	τ_c	10 ps
Radiative recombination lifetime	τ_r	2.5 ns
Nonradiative recombination lifetime	τ_{nr}	10 ns
Photon lifetime	τ_p	1.5 ps

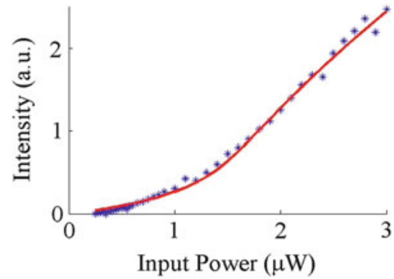

Fig. 7.9 Pulsed L–L curve for the PC laser. The *blue data points* represent experimental data and the *red line* represents a fit to the rate equations (Eqs. 7.8–7.11). Reproduced with permission from [9]. Copyright 2007 AIP

Figure 7.9 shows an L–L curve taken under pulsed optical pumping conditions (blue data points). The red line shows a fit to the rate equations (Eqs. 7.8–7.11) using the parameters shown in Table 7.1. The gain coefficient g_c, the transparency carrier density N_{tr}, β, and the carrier injection efficiency η were variable parameters in the fit. From the fit we estimated that in our system $v_g g_o = 8.13 \times 10^{-6}$ cm^3/s, $N_{tr} = 3.22 \times 10^{17}$ cm^{-3}, and $\beta = 0.2$. The L–L curve exhibited a threshold kink around the pump power of 1 μW, confirming that the structures were lasing. In the best structures (where the cavity mode is near the center of the gain spectrum) threshold values were around 250 nW average power, while in other structures with more absorption and less gain, threshold values were measured at several microwatts average power.

To investigate the large-signal modulation response, emission from the lasers above threshold was collected by the streak camera when the lasers are pumped by 3 ps pulses from the mode-locked laser. Figure 7.10a shows the response of the laser pumped at five times threshold, where the fall time (8.5 ps) was found by fitting an exponential decay to the trailing edge of the pulse. One of the main advantages of cavity-QED enhanced lasers is the decreased rise time because SE rapidly builds up the photon number in the laser mode. Experimentally, we found that as the pump power is increased, the rise time is reduced to 7.5 ps when the laser is pumped at about five times threshold (Fig. 7.10b). Experiments performed at 10 and 15 times threshold indicated that the rise time is pinned at about 12 ps even at very high pump powers. This is close to the measured carrier capture time of the QDs, and by comparing with simulations we conclude that the rise time of QD lasers is limited by the carrier capture time. In high-β lasers this limit is practically achievable because

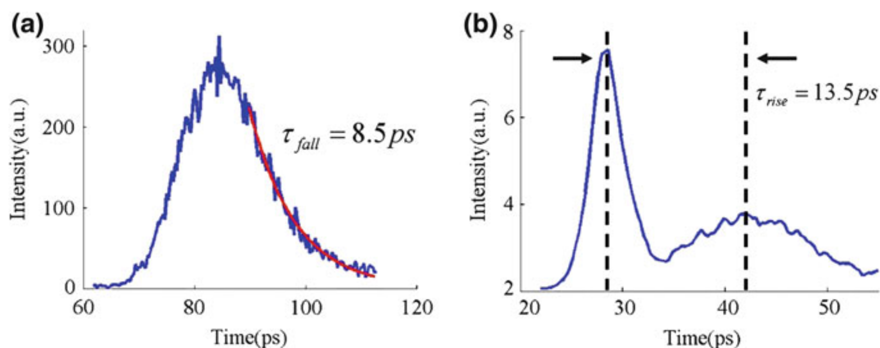

Fig. 7.10 **a** Response of the PC laser to a pump pulse of 3 ps well above threshold. The fall time is found to be approximately 8.5 ps by fitting the exponential decay at the end of the pulse. **b** Measurement of the rise time of the PC laser well above threshold. The pump pulse is redirected onto the streak camera so that the pump pulse and laser response can be seen simultaneously. The left peak is the pump pulse, and the right peak is the laser response. Reproduced with permission from [9]. Copyright 2007 AIP

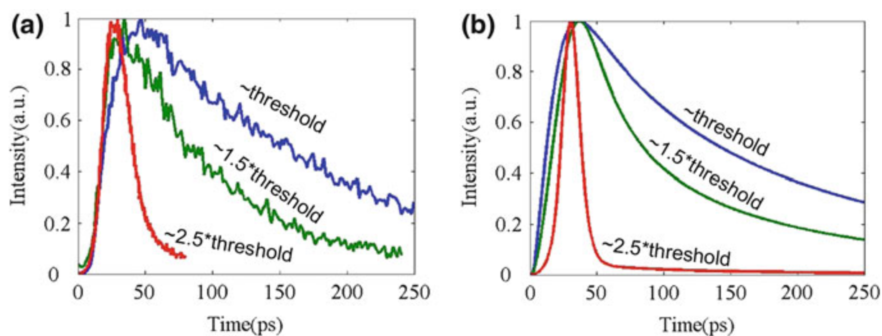

Fig. 7.11 **a** Experimental laser response taken at pump powers of around threshold, 1.5 times threshold and 2.5 times threshold (as labeled). **b** Simulated laser response based on the rate equations (Eqs. 7.8–7.11) and the parameters given in Table 7.1 showing good agreement with experiment. Reproduced with permission from [9]. Copyright 2007 AIP

it is approached at lower pump powers relative to threshold (as opposed to QD lasers not employing strong cavity effects where higher power pumping is needed).

Above threshold, higher pump powers lead to faster decay times due to increased stimulated emission rates. Figure 7.11a shows the laser response at various pump powers, demonstrating the reduction in decay time with increasing pump power. We observed a minimum decay time of 8.5 ps at pump powers around five times threshold (Fig. 7.10a). For higher pump powers the laser response appeared largely unchanged. We attribute this to large carrier densities causing the gain to saturate, preventing further decrease of the decay time, but more work is necessary to characterize saturation effects in our QDs. Figure 7.11b shows the simulated laser response at various pump powers based on the rate

equations (Eqs. 7.8–7.11) and the parameters given in Table 7.1, showing good agreement between theory and experiment. By numerically solving this model for realistic operating conditions, we predict that our lasers can be modulated at speeds up to 30 GHz. We believe that these results are also applicable to nanobeam lasers discussed earlier in this chapter.

This result shows that PC and nanobeam lasers with enhanced SE have an enhanced modulation bandwidth relative to conventional lasers. This is because in large-signal modulation, the enhanced SE into the cavity mode builds up the laser mode and the rise time of the lasers is limited only by the rate of carrier capture into the QDs, which can be as fast as a few picoseconds [52]. This can be compared to the turn-on delay times of conventional lasers which have been measured at around 1 ns [53].

Electrical Pumping of PC Lasers

As emphasized above, PC nanocavities are an ideal platform for low-power laser sources because of the flexibility provided by the photonic bandgap. PC lasers have been proven to have the performance required in many emerging applications such as optical interconnects. However, in order for them to be practical for applications outside the laboratory, an electrical driving scheme must be developed. The main challenge of electrically pumping PC membrane nanocavities is efficiently injecting current into the cavity region. Due to the membrane geometry, this is very difficult to do using a vertical p-i-n junction. The reason is that the membrane typically has to be less than 200 nm thick so that the membrane is single mode and supports a photonic bandgap. This restricts the doped layers to be less than 100 nm thick (typically much less to avoid free carrier absorption). In practice, the layers are not thick enough to spread current effectively throughout the PC. In addition, since the vertical junction has uniform doping in the plane of the PC, there is no way to efficiently inject current to only the cavity region without incurring inefficient pumping to the rest of the device [54].

However, lasing has been demonstrated in an electrically pumped PC nanocavity by directing the current to the cavity region using a vertical p-i-n junction and a current post [55, 56]. The disadvantage of using a current post is that the fabrication process is further complicated. The post must be small enough that it does not affect the optical properties of the cavity, but big enough to carry enough current to the active region. Therefore, the undercut step must be precisely timed [56] and the quality factor of the cavity is substantially degraded by the post. Because the size of the post depends on the size and location of the PC holes, an arbitrary PC design also cannot be used, limiting practical implementation options such as the addition of a waveguide to efficiently extract the laser emission. In addition, a high threshold current of 260 μA (corresponding to 260 μW power dissipation) was observed, significantly higher than in optically pumped PC devices and exceeding even that of VCSELs [57].

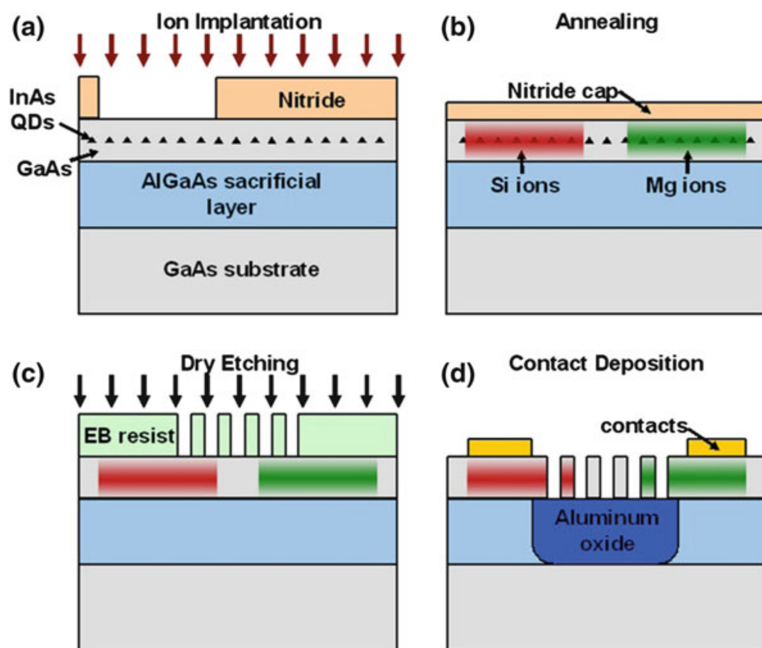

Fig. 7.12 Schematic of the fabrication process. **a** Si and Mg ions are implanted through a silicon nitride mask patterned by electron beam lithography. **b** The implanted dopants are activated by annealing at 900°C for 30 s with a nitride cap which is subsequently removed by dry etching. **c** The PC pattern is defined in a resist by electron beam lithography and transferred to the GaAs membrane by dry etching. **d** The sacrificial layer is oxidized and the p and n contacts are deposited by photolithography and liftoff. Reproduced with permission from [58]. Copyright 2010 AIP

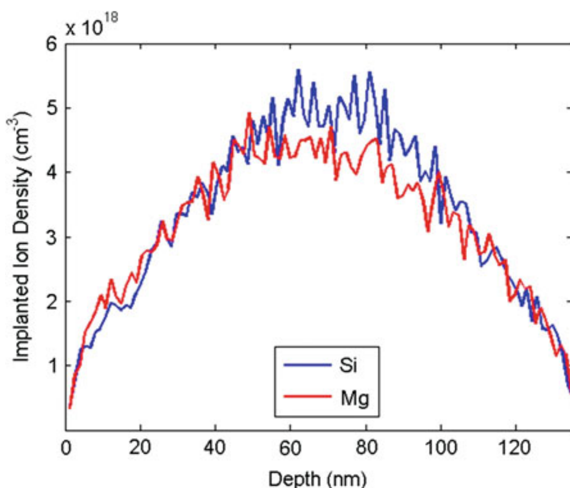

Fig. 7.13 Density of implanted ions as a function of depth simulated by Monte Carlo simulations for the ion energies and doses given in the text. Reproduced with permission from [58]. Copyright 2010 AIP

A lateral p-i-n junction presents a solution to this problem since the current flow can be defined lithographically to be very efficient, and therefore is compatible with arbitrary PC designs [59]. Ideally this doping can be performed during growth using two regrowth steps. Because this is a time consuming and difficult process, ion implantation is typically used. Ion implantation is a standard method of doping in the electronics industry, and can also be used to dope III–V materials with a lateral junction on a submicron scale. Previous studies of edge-emitting lateral current injection lasers found that the performance was worse than in comparable vertical injection lasers due to a non-uniform carrier distribution in the active region [60, 61]. This is because the lasers were fabricated with intrinsic regions wider than the ambipolar diffusion length, which in most III–V materials is approximately 1 μm. Improvements in fabrication technology have allowed the intrinsic region to be reduced significantly, leading to better performance. Here, we describe a practical technique to electrically pump PC devices using an ion implanted lateral p-i-n junction.

A schematic of the fabrication procedure is shown in Fig. 7.12. The wafer used in this experiment is the same as that described in the previous section. First, a dry-etcher was used to define alignment marks. Next, Si ions at an energy of 71 keV and a dose of 4×10^{13} cm^{-2} and Mg ions at an energy of 55 keV and a dose of 5×10^{13} cm^{-2} were implanted using a 330 nm thick nitride mask that is patterned by electron beam lithography. Si and Mg ions were chosen because they offer the best combination of low damage, high activation efficiency, and a low diffusion coefficient. The depth distribution of the ions can be calculated with freely available Monte Carlo software and is shown in Fig. 7.13 [62]. To maximize the electrical pumping efficiency of the device, the energies of the ions were chosen so that the maximum of the dopant distribution is in the middle of the membrane and the doses were chosen to be well below the amorphization dose. Next, the samples were annealed at 900°C for 30 s to remove most of the ion implantation-induced damage and to activate the dopants. It was found that a 30 nm nitride cap was necessary to prevent arsenic outdiffusion during the anneal step. After the annealing, PC patterns were defined by electron beam lithography and dry-etched into the membrane. The sacrificial layer underneath the GaAs membrane was oxidized in an oxidation furnace. Next an Au-Ge-Ni-Au n-type contact and an Au-Zn-Au p-type contact were deposited, and the contacts were annealed at 450°C for 1 min. Based on the results of Hall effect and electrochemical capacitance voltage measurements, we estimate the maximum n-type doping concentration in the middle of the membrane to be about 8×10^{17} cm^{-3} and the maximum p-type doping concentration to be about 3×10^{18} cm^{-3}.

To study the effect of the doping process on the QD PL, the samples were cooled to 30 K. A continuous He-flow cryostat with a custom coldfinger was used, and the sample was attached to an alumina chip carrier with vacuum grease. Contact was made to the devices by wirebonding the gold pads to the pads of the chip carrier using aluminum wirebonds. Figure 7.14 shows the normalized QD PL from a region with no implanted ions before and after the activation anneal. The QD density in our wafer was too high to see the emission lines of individual QDs,

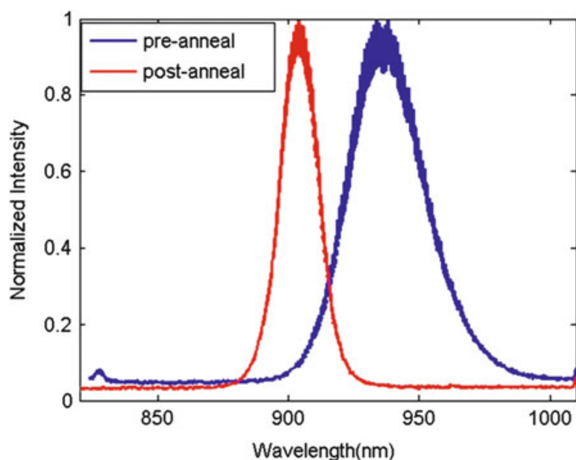

Fig. 7.14 Normalized QD PL before and after the activation anneal. The activation anneal blueshifts the PL and narrows the FWHM. Reproduced with permission from [58]. Copyright 2010 AIP

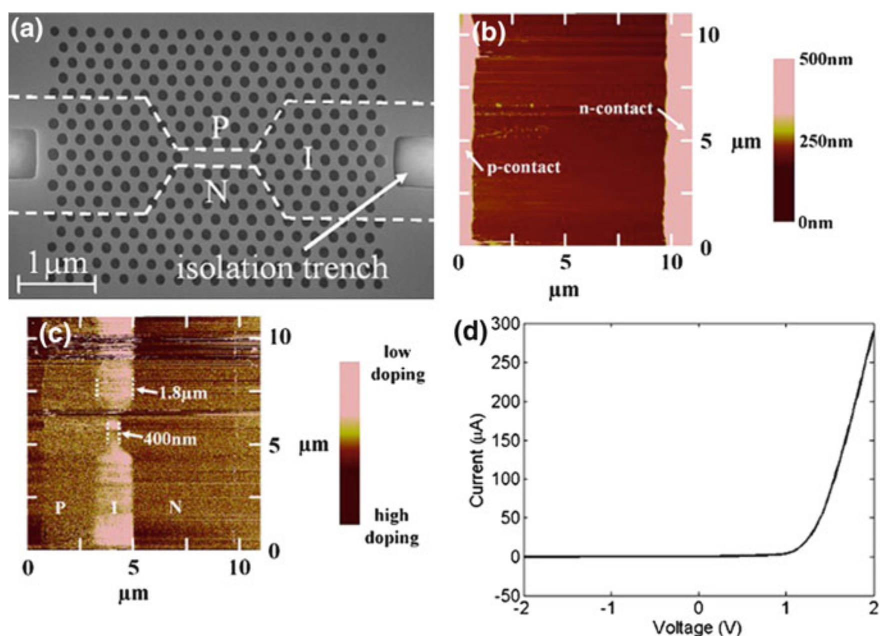

Fig. 7.15 **a** Schematic diagram of the doping layout of the PC LED. **b** AFM image of the doped region of a device without PCs. **c** Scanning capacitance microscopy image of the same doped region as in **b** showing the presence of the desired doping without topographical effects. **d** Current–voltage characteristics of 10 PC cavities connected in parallel showing low leakage current. Reproduced with permission from [58]. Copyright 2010 AIP

and we instead saw a Gaussian distribution of emission where the full-width half-maximum (FWHM) was determined by the inhomogeneous broadening of the QD ensemble. The QD emission is grown to be centered at 940 nm; however, the activation anneal step caused the dots to blueshift by about 30 nm. Interestingly, the FWHM of the QD emission was reduced by a factor of 2, indicating a reduction of the inhomogeneous broadening. Previous studies of this effect have found that rapid thermal annealing of QDs can actually be beneficial for laser applications because the FWHM of the dot distribution narrows, increasing the available gain [63]. However, the blueshift of the emission wavelength must be compensated for during the growth. Ion implantation-induced damage introduces non-radiative recombination centers, and the PL intensity was observed to decrease significantly in the implanted regions, similar to what has been observed in other experiments [60, 61]. The unimplanted regions are left undamaged, so the emission intensity there was unaffected.

A schematic diagram of the doping layout is shown in Fig. 7.15a, on top of a linear three-hole defect cavity design. The intrinsic region is wider than the ambipolar diffusion length outside of the cavity region. The combination of the wide intrinsic region of the diode and the PC holes form a high resistance region reducing the leakage current. In the cavity region the intrinsic region of the diode is designed to be between 200 and 400 nm wide. To confirm that dopant diffusion during the activation anneal does not drastically change the dopant layout, a scanning capacitance atomic force microscope (SCM) was used to image the dopant distribution on devices without PCs. SCM data are a combination of the phase and amplitude of capacitance data taken spatially across the sample, where the gold AFM tip and sample act as the capacitor plates and the native oxide as an insulator between them. The strength of the signal is directly proportional to the intensity of doping in the local region underneath the tip. Figure 7.15b shows the AFM topography image of the device, and Fig. 7.15c shows the change in capacitance with applied voltage (dC/dV) amplitude image. Together these indicate the presence of the desired doping without topographical effects. The current–voltage (IV) curve of 10 cavities in parallel is shown in Fig. 7.15d. From this we infer that the current density in the cavity region is high, around 10^3 A/cm^2 at an applied voltage of 1.5 V. Previous studies of the electrical properties of doped PCs found that the surface depletion region around the holes affects the series resistance [64]. This is because the depletion regions at the top and bottom of the membrane, as well as at the hole edges, decrease the available volume for conduction. Carrier transport in the PC is determined by the electrical effective air fill factor [64]:

$$f_{\mathrm{elec}} = \frac{\pi}{2\sqrt{3}}\left[\frac{(d+2\delta)^2}{a^2}\right] \tag{7.12}$$

Here δ is the depletion width, d is the membrane thickness, and a is the spacing between PC holes. We estimate that the depletion width δ is approximately 45 and 30 nm in the n- and p-type regions, respectively, indicating that the membrane is not fully depleted.

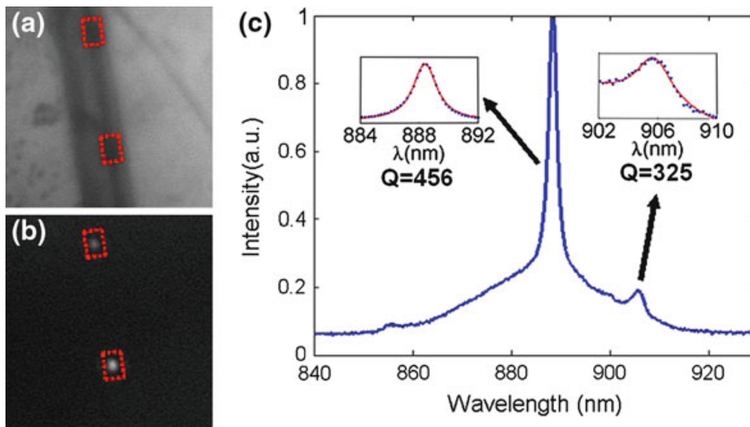

Fig. 7.16 **a** Microscope image of PC cavities. **b** Corresponding image of the electroluminescence at 1.6 V. **c** Electroluminescence spectrum of the cavity on the top in part **b**. The *insets* show Lorentzian fits (*solid lines*) to the experimental cavity spectrum (*data points*) to determine the quality factor. Reproduced with permission from [58]. Copyright 2010 AIP

To test the electroluminescence of the cavities, 1.6 V of forward bias was applied. The EL was imaged by a confocal microscope setup. Figure 7.16a shows the microscope image of the cavities under white light illumination, and Fig. 7.16b shows the corresponding image of the EL. The EL was confined to the cavity region, confirming the devices have low leakage current. A pinhole was used to collect the emission from only one cavity, and the spectrum of a single cavity is shown in Fig. 7.16c. Two cavity modes were observed with quality factors of approximately 400. Finite-difference time domain simulations indicate that the highest wavelength mode is the fundamental mode of the cavity, with a simulated Q of approximately 2,000. The low Q of the design is limited by the high refractive index ($n \approx 1.72$) aluminum oxide layer under the cavity.

As is demonstrated in Fig. 7.16, this technique is a very efficient way to electrically pump PC nanocavities. Recently this technique was used to demonstrate ultralow threshold electrically pumped PC lasers with thresholds of only 181 nA at 50 K [65].

Future Directions and Outlook

In this chapter we have introduced the concept of PC and nanobeam lasers, and explained how high Purcell factor cavities can be used to make highly efficient and high modulation rate lasers. The basics of PC physics were introduced, and we covered our results on CW lasing in QD nanobeam cavities. Next, we examined the dynamics of low threshold QD PC lasers and introduced an efficient and practical technique to electrically pump PC and nanobeam devices.

A critical challenge for researchers in the field of PC nanocavity lasers is to demonstrate a practical electrically pumped room temperature laser with a high modulation rate. This would open up many new applications in low-power optical communication systems. In addition, many applications require high outcoupling efficiency, so techniques to efficiently extract the light from PC and nanobeam devices must be developed. Finally, PC devices have proven promising in many interesting applications such as sensing and optomechanics, and electrically pumped lasing devices provide a means to transition these laboratory demonstrations to practical implementation.

Acknowledgments The authors would like to acknowledge the Interconnect Focus Center (IFC), the NSF graduate research fellowship (YG), and the Stanford Graduate Fellowship (YG, BE) for funding. Fabrication was done at Stanford Nanofabrication Facilities.

References

1. Miller, D.A.B.: Device requirements for optical interconnects to silicon chips. Proc. IEEE **97**((7, Sp. Iss. SI)), 1166–1185 (2009)
2. Vahala, K.J.: Optical microcavities. Nature **424**(6950), 839–846 (2003)
3. Purcell, E.M.: Spontaneous emission probabilities at radio frequencies. Phys. Rev. **69**(11–1), 681 (1946)
4. Scully, M., Zubairy, M.S.: Quantum Optics. Cambridge University Press, Cambridge (1997)
5. Painter, O., Lee, R.K., Scherer, A., Yariv, A., O'Brien, J.D., Dapkus, P.D., Kim, I.: Two-dimensional photonic band-gap defect mode laser. Science **284**(5421), 1819–1821 (1999)
6. Loncar, M., Yoshie, T., Okamoto, K., Qiu, Y.M., Vuckovic, J., Scherer, A.: Planar photonic crystal nanolasers (I): porous cavity lasers. IEICE Trans. Electron. **E87C**(3), 291–299 (2004)
7. Altug, H., Englund, D., Vuckovic, J.: Ultrafast photonic crystal nanocavity laser. Nat. Phys. **2**(7), 484–488 (2006)
8. Englund, D., Altug, H., Fushman, I., Vuckovic, J.: Efficient terahertz room-temperature photonic crystal nanocavity laser. Appl. Phys. Lett. **91**(7), 071126 (2007)
9. Ellis, B., Fushman, I., Englund, D., Zhang, B., Yamamoto, Y., Vuckovic, J.: Dynamics of quantum dot photonic crystal lasers. Appl. Phys. Lett. **90**(15), 151102–1–151102–3 (2007)
10. Nomura, M., Iwamoto, S., Watanabe, K., Kumagai, N., Nakata, Y., Ishida, S., Arakawa, Y.: Room temperature continuous-wave lasing in photonic crystal nanocavity. Opt. Express **14**(13), 6308–6315 (2006)
11. Nomura, M., Iwamoto, S., Kumagai, N., Arakawa, Y.: Temporal coherence of a photonic crystal nanocavity laser with high spontaneous emission coupling factor. Phys. Rev. B **75**(19), 195313 (2007)
12. Strauf, S., Hennessy, K., Rakher, M.T., Choi, Y.-S., Badolato, A., Andreani, L.C., Hu, E.L., Petroff, P.M., Bouwmeester, D.: Self-tuned quantum dot gain in photonic crystal lasers. Phys. Rev. Lett. **96**(12), 127404/1–4 (2006)
13. Nomura, M., Kumagai, N., Iwamoto, S., Ota, Y., Arakawa, Y.: Photonic crystal nanocavity laser with a single quantum dot gain. Opt. Express **17**(18), 15975–15982 (2009)
14. Loncar, M., Scherer, A., Qiu, Y.M.: Photonic crystal laser sources for chemical detection. Appl. Phys. Lett. **82**(26), 4648–4650 (2003)
15. Yablonovitch, E.: Inhibited spontaneous emission in solid-state physics and electronics. Phys. Rev. Lett. **58**(20), 2059–2062 (1987)

16. John, S.: Strong localization of photonics in certain disordered dielectric superlattices. Phys. Rev. Lett. **58**(23), 2486–2489 (1987)
17. Lin, S.Y., Fleming, J.G., Hetherington, D.L., Smith, B.K., Biswas, R., Ho, K.M., Sigalas, M.M., Zubrzycki, W., Kurtz, S.R., Bur, J.: A three-dimensional photonic crystal operating at infrared wavelengths. Nature **394**(6690), 251–253 (1998)
18. Lodahl, P., van Driel, A.F., Nikolaev, I.S., Irman, A., Overgaag, K., Vanmaekelbergh, D.L., Vos, W.L.: Controlling the dynamics of spontaneous emission from quantum dots by photonic crystals. Nature **430**(7000), 654–657 (2004)
19. Qi, M., Lidorikis, E., Rakich, P.T., Johnson, S.G., Joannopoulos, J., Ippen, E.P., Smith, H.I.: A three-dimensional optical photonic crystal with designed point defects. Nature **429**(6991), 538–542 (2004)
20. Aoki, K., Guimard, D., Nishioka, M., Nomura, M., Iwamoto, S., Arakawa, Y.: Coupling of quantum-dot light emission with a three-dimensional photonic-crystal nanocavity. Nat. Photonics **2**(11), 688–692 (2008)
21. Takahashi, S., Suzuki, K., Okano, M., Imada, M., Nakamori, T., Ota, Y., Susumu, K.I., Noda, S.: Direct creation of three-dimensional photonic crystals by a top–down approach. Nat. Mater. **8**(9), 721–725 (2009)
22. Jewell, J.L., Harbison, J.P., Scherer, A., Lee, Y.H., Florez, L.T.: Vertical-cavity surface-emitting lasers: design, growth, fabrication, characterization. IEEE J. Quantum Electron. **27**(6), 1332–1346 (1991)
23. Song, B.-S., Noda, S., Asano, T., Akahane., Y.: Ultra-high-Q photonic double-heterostructure nanocavity. Nat. Mater. **4**(3), 207–210 (2005)
24. Englund, D., Fushman, I., Vuckovic, J.: General recipe for designing photonic crystal cavities. Opt. Express **13**(16), 5961–5975 (2005)
25. Notomi, M., Tanabe, T., Shinya, A., Kuramochi, E., Taniyama, H., Mitsugi, S., Morita, M.: Nonlinear and adiabatic control of high-q photonic crystal nanocavities. Opt. Express **15**(26), 17458–17481 (2007)
26. Takahashi, Y., Hagino, H., Tanaka, Y., Song, B.-S., Asano, T., Noda, S.: High-Q nanocavity with a 2 ns photon lifetime. Opt. Express **15**(25), 17206–17213 (2007)
27. Wang, C.F., Hanson, R., Awschalom, D.D., Hu, E.L., Feygelson, T., Yang, J., Butler, J.E.: Fabrication and characterization of two-dimensional photonic crystal microcavities in nanocrys talline diamond. Appl. Phys. Lett. **91**(20), 201112–1–201112–3 (2007)
28. Kreuzer, C., Riedrich-Moeller, J., Neu, E., Becher, C.: Design of photonic crystal microcavities in diamond films. Opt. Express **16**(3), 1632–1644 (2008)
29. Barth, M., Nuesse, N., Stingl, J., Loechel, B., Benson, O.: Emission properties of high-Q silicon nitride photonic crystal heterostructure cavities. Appl. Phys. Lett. **93**(2), 021112 (2008)
30. Makarova, M., Vuckovic, J., Sanda, H., Nishi, Y.: Silicon-based photonic crystal nanocavity light emitters. Appl. Phys. Lett. **89**(22), 221101 (2006)
31. Gong, Y., Vuckovic, J.: Photonic crystal cavities in silicon dioxide. Appl. Phys. Lett. **96**(3), 031107 (2010)
32. Foresi, J.S., Villeneuve, P.R., Ferrera, J., Thoen, E.R., Steinmeyer, G., Fan, S., Joannopoulos, J.D., Kimerling, L.C., Smith, H.I., Ippen, E.P.: Photonic-bandgap microcavities in optical waveguides. Nature **390**(6656), 143–145 (1997)
33. Deotare, P.B., McCutcheon, M.W., Frank, I.W., Khan, M., Loncar, M.: High quality factor photonic crystal nanobeam cavities. Appl. Phys. Lett. **94**(12), 121106 (2009)
34. Eichenfield, M., Camacho, R., Chan, J., Vahala, K.J., Painter, O.: A picogram- and nanometre-scale photonic-crystal optomechanical cavity. Nature **459**(7246), 550–U79 (2009)
35. McCutcheon, M.W., Loncar, M.: Design of a silicon nitride photonic crystal nanocavity with a quality factor of one million for coupling to a diamond nanocrystal. Opt. Express **16**(23), 19136–19145 (2008)
36. Zhang, Y., Khan, M., Huang, Y., Ryou, J., Deotare, P., Dupuis, R., Loncar, M.: Photonic crystal nanobeam lasers. Appl. Phys. Lett. **97**(5), 051104–051107 (2010)

37. Ahn, B.-H., Kang, J.-H., Kim, M.-K., Song, J.-H., Min, B., Kim, K.-S., Lee, Y.-H.: One-dimensional parabolic-beam photonic crystal laser. Opt. Express **18**(6), 5654–5660 (2010)
38. Gong, Y., Ellis, B., Shambat, G., Sarmiento, T., Harris, J., Vuckovic, J.: Nanobeam photoniccrystal cavity quantum dot laser. Opt. Express **18**(9), 8781–8789 (2010)
39. Alegre, T.P.M., Perahia, R., Painter, O.: Optomechanical zipper cavity lasers: theoretical analysis of tuning range and stability. Opt. Express **18**(8), 7872–7885 (2010)
40. Englund, D., Vuckovic, J.: A direct analysis of photonic nanostructures. Opt. Express **14**(8), 3472–3483 (2006)
41. Haret, L.-D., Tanabe, T., Kuramochi, E., Notomi, M.: Extremely low power optical bistability in silicon demonstrated using 1D photonic crystal nanocavity. Opt. Express **17**(23), 21108–21117 (2009)
42. Coldren, L., Corzine, S.: Diode Lasers and Photonic Integrated Circuits. Wiley, New York (1995)
43. van Exter, M.P., Nienhuis, G., Woerdman, J.P.: Two simple expressions for the spontaneous emission factor beta. Phys. Rev. A **54**(4), 3553–3558 (1996)
44. Friedler, I., Sauvan, C., Hugonin, J.P., Lalanne, P., Claudon, J., Gerard, J.M.: Solid-state single photon sources: the nanowire antenna. Opt. Express **17**(4), 2095–2110 (2009)
45. Babinec, T.M., Hausmann, B.J.M., Khan, M., Zhang, Y., Maze, J.R., Hemmer, P.R., Loncar, M.: A diamond nanowire single-photon source. Nat. Nanotechnol. **5**(3), 195–199 (2010)
46. Mohideen, U., Slusher, R.E., Jahnke, F., Koch, S.W.: Semiconductor microlaser linewidths. Phys. Rev. Lett. **73**(13), 1785–1788 (1994)
47. Bjork, G., Yamamoto, Y.: Analysis of semiconductor microcavity lasers using rate equations. IEEE J. Quantum Electron. **27**(11), 2386–2396 (1991)
48. Matsuo, S., Shinya, A., Kakitsuka, T., Nozaki, K., Segawa, T., Sato, T., Kawaguchi, Y., Notomi, M.: High-speed ultracompact buried heterostructure photonic crystal laser with 13 fJ of energy consumed per bit transmitted. Nat. Photonics **4**, 648–654 (2010)
49. Lau, E., Lakhani, A., Tucker, R., Wu, M.: Enhanced modulation bandwidth of nanocavity light emitting devices. Opt. Express **17**(10), 7790–7799 (2009)
50. Englund, D., Altug, H., Vuckovic, J.: Low threshold surface-passivated photonic crystal nanocavity laser. Appl. Phys. Lett. **91**, 071124 (2007)
51. O'Brien, D., Hegarty, S., Huyet, G., Uskov, A.: Sensitivity of quantum-dot semiconductor lasers to optical feedback. Opt. Lett. **29**(10), 1072–1074 (2004)
52. Bhattacharya, P., Ghosh, S., Pradhan, S., Singh, J., Wu, Z., Urayama, J., Kim, K., Norris, T.: Carrier dynamics and high-speed modulation properties of tunnel injection InGaAs-GaAs quantum-dot lasers. IEEE J. Quantum Electron. **39**(8), 952–962 (2003)
53. Grundmann, M.: How a quantum dot laser turns on. Appl. Phys. Lett. **77**, 1428 (2000)
54. Francardi, M., Balet, L., Gerardino, A., Chauvin, N., Bitauld, D., Li, L., Alloing, B., Fiore, A.: Enhanced spontaneous emission in a photonic crystal light emitting diode. Appl. Phys. Lett. **93**, 143102 (2008)
55. Park, H., Kim, S., Kwon, S., Ju, Y., Yang, J., Baek, J., Kim, S., Lee, Y.: Electrically driven single-cell photonic crystal laser. Science **305**, 1444–1447 (2004)
56. Park, H., Kim, S., Seo, M., Ju, Y., Kim, S., Lee, Y.: Characteristics of electrically driven two-dimensional photonic crystal lasers. IEEE J. Quantum Electron. **41**(9), 1131–1141 (2005)
57. Macdougal, M., Dapkus, P., Pudlikov, V., Zhao, H., Yang, G.: Ultralow threshold current vertical-cavity surface emitting lasers with AlAs oxide-GaAs distributed Bragg reflectors. IEEE Photonics Technol. Lett. **7**, 229–231 (1995)
58. Ellis, B., Sarmiento, T., Mayer, M., Zhang, B., Harris, J., Haller, E., Vuckovic, J: Electrically pumped photonic crystal nanocavity light sources using a laterally doped p-i-n junction. Appl. Phys. Lett. **96**, 181103 (2010)
59. Long, C., Giannopoulos, A., Choquette, K.: Modified spontaneous emission from laterally injected photonic crystal emitter. Electron. Lett. **45**(4), 227–228 (2009)
60. Sargent, E., Tan, G., Xu, J.: Physical model of OEIC-compatible lateral current injection lasers. IEEE J. Sel. Top. Quantum Electron. **3**(2), 507–512 (1997)

61. Tager, A., Gaska, R., Avrutsky, I., Fay, M., Chik, H., SpringThorpe, A., Eicher, S., Xu, J., Shur, M.: Ion-implanted GaAs-InGaAs lateral current injection laser. IEEE J. Sel. Top. Quantum Electron. **5**(3), 664–672 (1999)
62. Ziegler, J., Ziegler, M., Biersach, J.: SRIM—the stopping and range of ions in matter, version 2008.03. www.srim.org (2008)
63. Malik, S., Roberts, C., Murray, R., Pate, M.: Tuning self-assembled InAs quantum dots by rapid thermal annealing. Appl. Phys. Lett. **71**, 1987 (1997)
64. Berrier, A., Mulot, M., Malm, G., Ostling, M., Anand, S.: Carrier transport through a dry-etched InP-based two-dimensional photonic crystal. J. Appl. Phys. **101**, 123101 (2007)
65. Ellis, B., Mayer, M., Shambat, G., Sarmiento, T., Harris, J., Haller, E., Vuckovic, J.: Ultralow threshold electrically pumped quantum dot photonic crystal laser. Nat. Photonics **5**, 297–300 (2011)

Chapter 8
InGaAs Submonolayer Quantum-Dot Photonic-Crystal LEDs for Fiber-Optic Communications

Hung-Pin D. Yang

Abstract An InGaAs submonolayer (SML) quantum-dot photonic-crystal light-emitting diode (QD PhC-LED) with for fiber-optic applications is reported. The active region of the device contains three InGaAs SML QD layers. Each of the InGaAs SML QD layers is formed by alternate depositions of InAs (<1 ML) and GaAs. A maximum CW output power of 0.34 mW at 20 mA has been obtained in the 980 nm range. The internally reflected spontaneous emission can be extracted and collimated out of the photonic-crystal etched holes. High-resolution imaging studies indicate that the device emits narrower light beams mainly through the photonic-crystal etched holes making it suitable for fiber-optic applications.

Introduction

High brightness (HB) light-emitting diodes (LEDs) have drawn a lot of attentions because of their applications in mobile electronics, flat panel displays, automobiles, traffic signals, large outdoor displays, and general lighting [1]. More recently, photonic-crystal light-emitting diodes (PhC-LEDs) have achieved higher external quantum efficiency [2–17], as compared to conventional LEDs. The increase in series resistance of the PhC-LEDs is mainly

H.-P. D. Yang (✉)
Electronics and Optoelectronics Research Laboratories, Industrial Technology Research Institute, Chutung 310, Hsinchu, Taiwan
e-mail: hpyang@itri.org.tw

Z. M. Wang (ed.), *Quantum Dot Devices*, Lecture Notes in Nanoscale Science and Technology 13, DOI: 10.1007/978-1-4614-3570-9_8,
© Springer Science+Business Media New York 2012

because of photonic-crystal (PhC) hole etching which partly blocks current conduction. For fiber-optic applications, LEDs made with smaller light-emitting apertures are needed because of their smaller optical beams and better optical-fiber coupling efficiency. For LEDs made with small oxide-confined structure, the device may have reliability problem, similar to that of vertical-cavity surface-emitting lasers (VCSELs) [18]. For LEDs made with integrated lenses, the deep wet chemical etch to form lenses is difficult to control uniformity in lens curvature and diameter. Small-aperture LEDs are designed for small light beam emission at lower currents for better optical-fiber coupling. The current spreading can be improved for devices with smaller aperture, as compared to the large-aperture LEDs ($\geq$300 μm in diameter). Higher coupling efficiency can be achieved with the emitted light beam size smaller than core diameter of the optical fiber. Moreover, epitaxially grown distributed Bragg reflectors (DBRs) can be used to form microcavity for enhanced light emission of the microcavity (or resonant cavity) LEDs [19–36]. The absorption of the spontaneous emission by the substrate can be minimized. Also, microhole array LEDs have demonstrated enhanced light output recently [37]. The light emission can be extracted out of the microhole array. Moreover, holey LEDs made with different holey structures were reported [38, 39]. For longer wavelength applications, InAs and InGaAs quantum-dot (QD) edge-emitting lasers [40–47], VCSELs [48–53], and InAs photonic-crystal VCSELs (PhC-VCSELs) [54] achieved laser emission up to 1,300 nm and above. For shorter wavelength emission, InGaAs/GaAs submonolayer (SML) QD embedded in a GaAs matrix shows luminescence peaks and high-power lasing performance in the 0.92–1 μm range [55–64]. The thickness of the InAs QD layer is less than one monolayer (<1 ML), so that the emission wavelength of the device is shorter. The advantages of InGaAs SML QDs include better growth uniformity, narrower gain spectrum, higher differential gain, and lower threshold current density [55–64], as compared with the 980 nm $In_{0.2}Ga_{0.8}As$/GaAs QW VCSELs, lasers, and LEDs. Broad-area InGaAs SML QDs VCSELs very high output power was also reported [62]. In this chapter, we report our results on the InGaAs SML QD PhC-LEDs within the 980 nm range. The PhC structure in this work is the arrangement of etched holes as a triangular PhC structure with larger lattice constant (5 μm) and etched hole diameters (2–2.5 μm) [2–17]. The PhC structure of this work was made with larger lattice constant and etched hole diameters, which can also provide a similar intensity enhancement effect for the device. The unetched areas of the PhC structure can be used for current spreading so that the overall light emission can be improved. Two-dimensional (2-D) PhC etched holes were formed within the p-type ohmic contact ring for light extraction and collimation. The collimation of the output light beam can be further improved by using the sidewalls within the etched holes for light deflection. A maximum continuous-wave (CW) output power of over 0.34 mW has been obtained. High-resolution imaging studies show that the device emits light beams mainly through the etched holes.

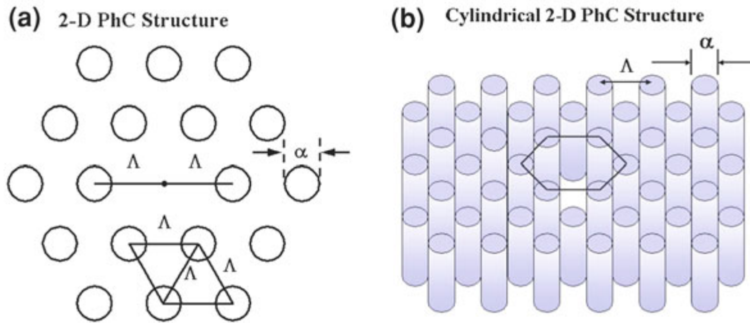

Fig. 8.1 **a** Plane-view, and **b** cylindrical etched holes of the 2-D photonic-crystal (PhC) structure

Epitaxial Growth of the InGaAs SML QD LEDs and Device Fabrication of the PhC-LEDs

The schematic diagrams of the 2-D PhC structure (consists of an array of cylindrical air holes) are shown in Fig. 8.1. The lattice constant of the PhC structure is Λ, and the hole diameter is α. The epitaxial layers of the InGaAs SML QD LED wafers (structure shown in Fig. 8.2a) were grown on 3-in. n^+-GaAs (001) substrates by molecular beam epitaxy (MBE) in a Riber 49 chamber. The bottom DBR consists of a 33-pair n-type (Si-doped) quarter-wave stack ($\lambda/4$) of $Al_{0.9}Ga_{0.1}As$/GaAs. The top DBR consists of a 20-pair p-type (carbon-doped) $Al_{0.9}Ga_{0.1}As$/GaAs quarter-wave stack. Above the top DBR, is a heavily doped p-type GaAs contact layer. The undoped 1λ cavity contains three 8 nm InGaAs SML QD layers, separated by 10 nm GaAs barrier layers. Each of the InGaAs SML QD layers is formed by alternate depositions of InAs (<1 ML) and GaAs. The current confinement of the device was carried out using a selectively oxidized AlO_x tapered aperture. Firstly, mesas with diameters varying from 68 to 78 μm were defined by reactive ion etching (RIE). The mesa dimension of the device is designed to be close to the core diameter (typically 50–100 μm) of the multimode optical fiber for better coupling efficiency. The p-ohmic contact ring with an inner diameter of 46–56 μm larger than the oxide aperture was formed on top of the p-contact layer. The AlAs layer within the $Al_{0.9}Ga_{0.1}As$ confinement layers was selectively oxidized to AlO_x. The oxidation depth was about 15–16 μm toward the center from the mesa edge so that the resulting oxide aperture varied from 36 to 48 μm in diameter. The oxide aperture was introduced in a minimum of optical field to reduce the lateral optical loss and the leakage current. The n-ohmic contact was formed at the bottom of the n^+-GaAs substrate.

After that, triangular lattice patterns of PhC structure (Fig. 8.1a) with a single-point defect in the center were defined within the p-contact ring using deep ultraviolet (UV) photolithography and etched through the p-type DBR using RIE. The hole diameter (α) is 2–2.5 μm and the lattice constant (Λ) is 5 μm in the PhC

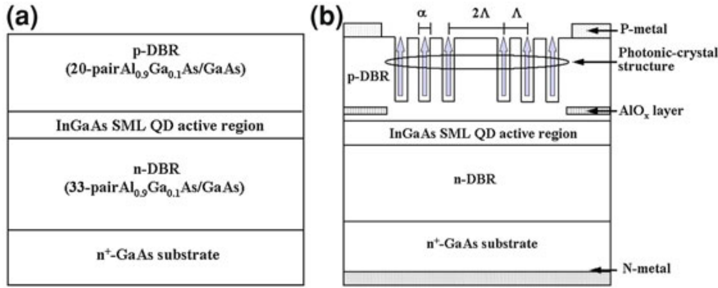

Fig. 8.2 Schematics of the **a** epitaxial structure, and **b** device structure of the PhC-LED

structure (Fig. 8.1). The PhC structure in this work was made with larger hole diameters and lattice constant, as compared with the previously reported PhC-LEDs [2, 3]. The etching depth of the holes is about 16-pair thick into the 20-pair top DBR layer. The distance between etched holes is approximately 2.5–3 μm for conduction current to flow through and therefore better current spreading. The device structure is shown in Fig. 8.2b. We use the oxide aperture for current confinement and the PhC structure within the p-ohmic contact ring for light extraction.

Measurement Results and Analysis of the InGaAs SML QD PhC-LEDs

Figure 8.3 shows the CW light–current–voltage (L–I–V) output of the InGaAs SML QD PhC-LEDs. The lattice constant (Λ) is 5 μm and the hole diameter (α) is 2.5 μm for both the 68 and 78 μm-mesa devices. Thermal rollover of the output power occurs near 13 mA for the 68 μm-mesa devices. The average differential series resistances are 300 and 267 Ω for the 68 and 78 μm-mesa devices, respectively. The differential series resistance increases with decreasing device mesa diameter. The differential series resistances of the PhC-LEDs are larger, as compared with the LEDs without PhC structure, mainly because of the reduced device areas by etching of the PhC structure. Figure 8.4 shows the CW light–current (L–I) output of the two typical InGaAs SML QD PhC-LEDs with different mesa sizes. The PhC-LEDs show maximum output powers of 0.19 and 0.34 mW for the 68 and 78 μm-mesa devices, respectively. The device emits a higher output power with larger oxide aperture and more etched holes. The lower output power of the devices is due to smaller oxide apertures for light emission (approximately 36 and 48 μm in diameter), as compared to other larger area LEDs.

Figure 8.5 shows the micrographs of the InGaAs SML QD PhC-LED at 0, 5, 10, and 15 mA. The lattice constant Λ is 5 μm and the hole diameter α is 2.5 μm for the PhC structure. The mesa of the device is 78 μm in diameter.

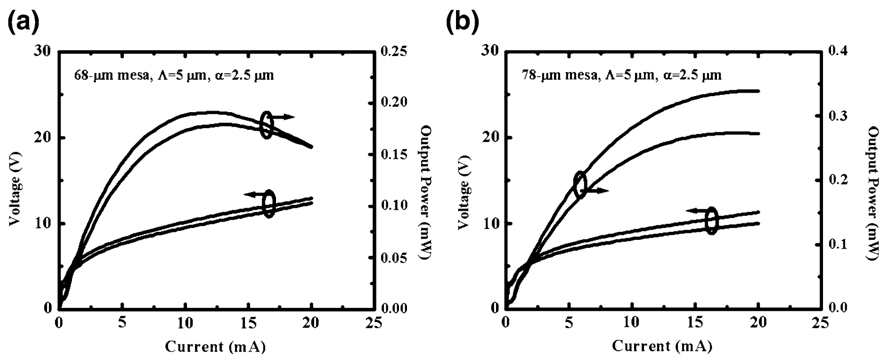

Fig. 8.3 L–I–V characteristics of the **a** 68 μm-mesa, and **b** 78 μm-mesa InGaAs SML QD PhC-LEDs

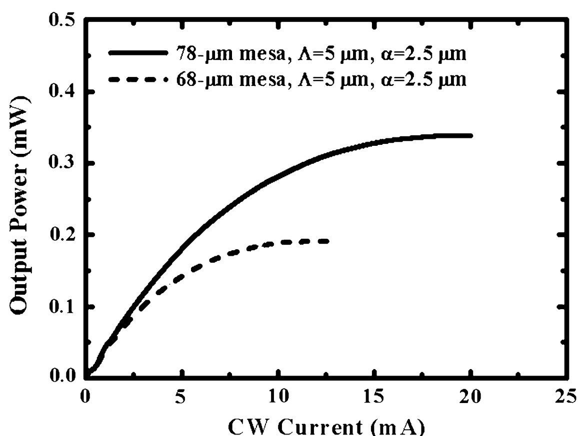

Fig. 8.4 L–I–V characteristics of the 68 and 78 μm-mesa InGaAs SML QD PhC-LEDs

The micrographs were taken by a high-resolution charge-coupled device (CCD) imaging system. Figure 8.5a was taken with additional light illumination on the device to clearly show the PhC structure of the device. As shown in Figs. 8.5b–f, the spontaneous emission mainly emits out of the PhC etched holes of the device. The intensity of the light emission increases with increasing current. The reflectance within the PhC etched holes is reduced by RIE (16 pairs of the top DBR being etched off), so that most of the internally reflected spontaneous emission (by the top- and bottom-DBRs) can be transmitted out of the PhC holes. Weaker light emission was also observed near the central un-etched device area. The light emission in this area is blocked by top DBR. The overall light emission in other area of the device is limited by AlO_x layer

The 2-D intensity profile of the same device is shown in Fig. 8.6. The three-dimensional (3-D) intensity profiles of the device are shown in Fig. 8.7. Neutral density (ND) filters were added to attenuate the output beam, to avoid saturation

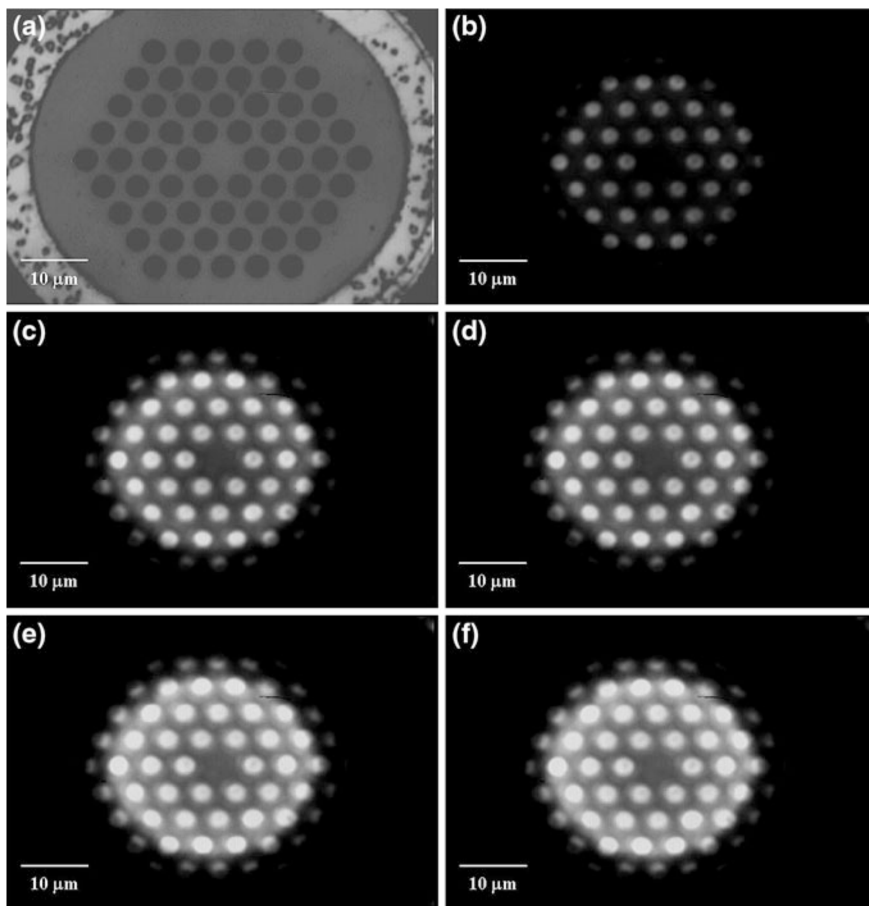

Fig. 8.5 **a** Micrographs of the InGaAs SML QD PhC-LED at **a** 0, **b** 5 mA, **c** 8 mA, **d** 10 mA, **e** 15 mA, and **f** 18 mA. The lattice constant (Λ) of the photonic-crystal structure is 5 μm and the hole diameter (α) is 2.5 μm. The mesa of the device is 78 μm in diameter

of the high-resolution CCD system at higher currents, so that the light intensity variation out of the PhC etched holes could be observed. The output of the CCD system was connected to another image board of a computer, with a beam analyzing software (Beam View) to analyze the light output of the device.

The results in Figs. 8.5, 8.6 and 8.7 clearly show the spontaneous emission mainly emits out of the PhC etched holes of the device. The height of the 3-D intensity profile represents the intensity of the light output. As shown in Fig. 8.7, the light emits out of the PhC etched holes and the light intensity increases with increasing current. The reflectance within the etched holes are reduced by RIE (16 pairs of the top DBR being etched off), so that the internally reflected spontaneous emission (by the DBRs) and light emission under the etched hole region can be transmitted out of the PhC etched holes (Fig. 8.2b).

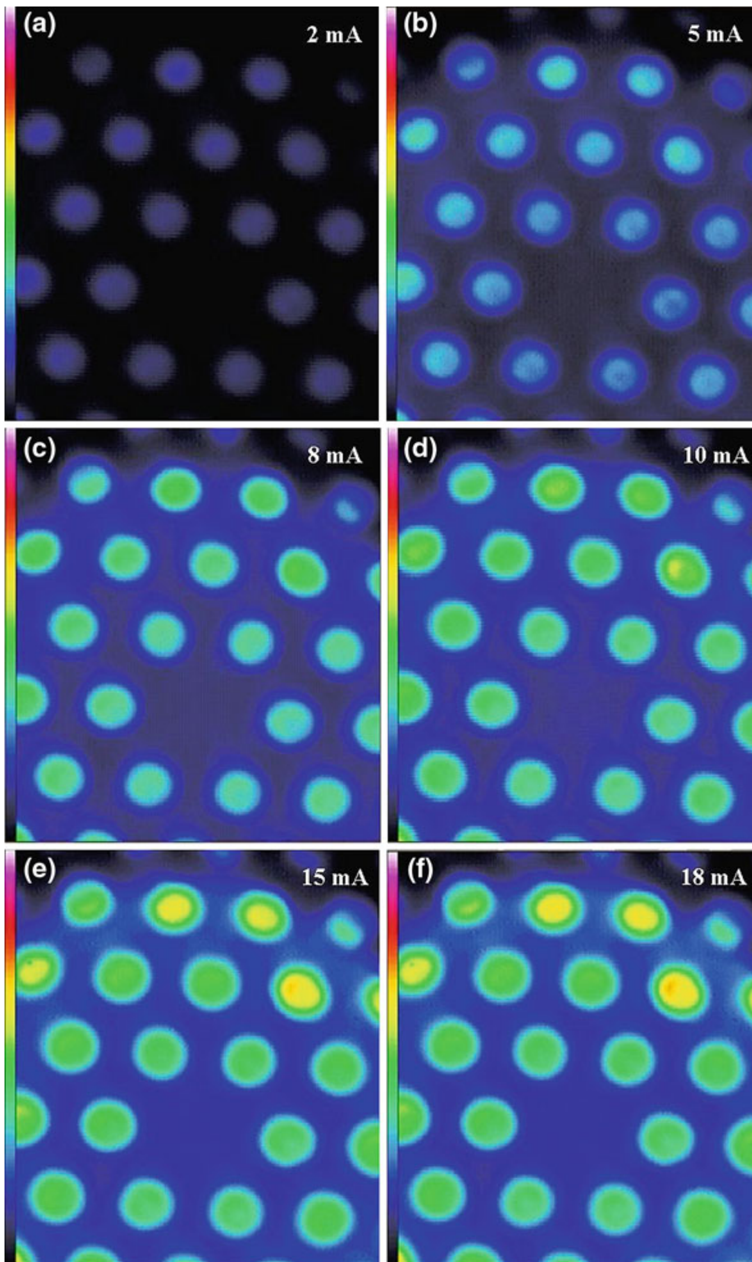

Fig. 8.6 2-D intensity profile at **a** 2 mA, **b** 5 mA, **c** 8 mA, **d** 10 mA, **e** 15 mA, and **f** 15 mA of the InGaAs SML QD PhC-LED. Neutral density (ND) filters were added to attenuate the beam, to avoid saturation of the charge-coupled device (CCD) imaging system. The lattice constant (Λ) of the PhC structure is 5 μm and the hole diameter (α) is 2.5 μm

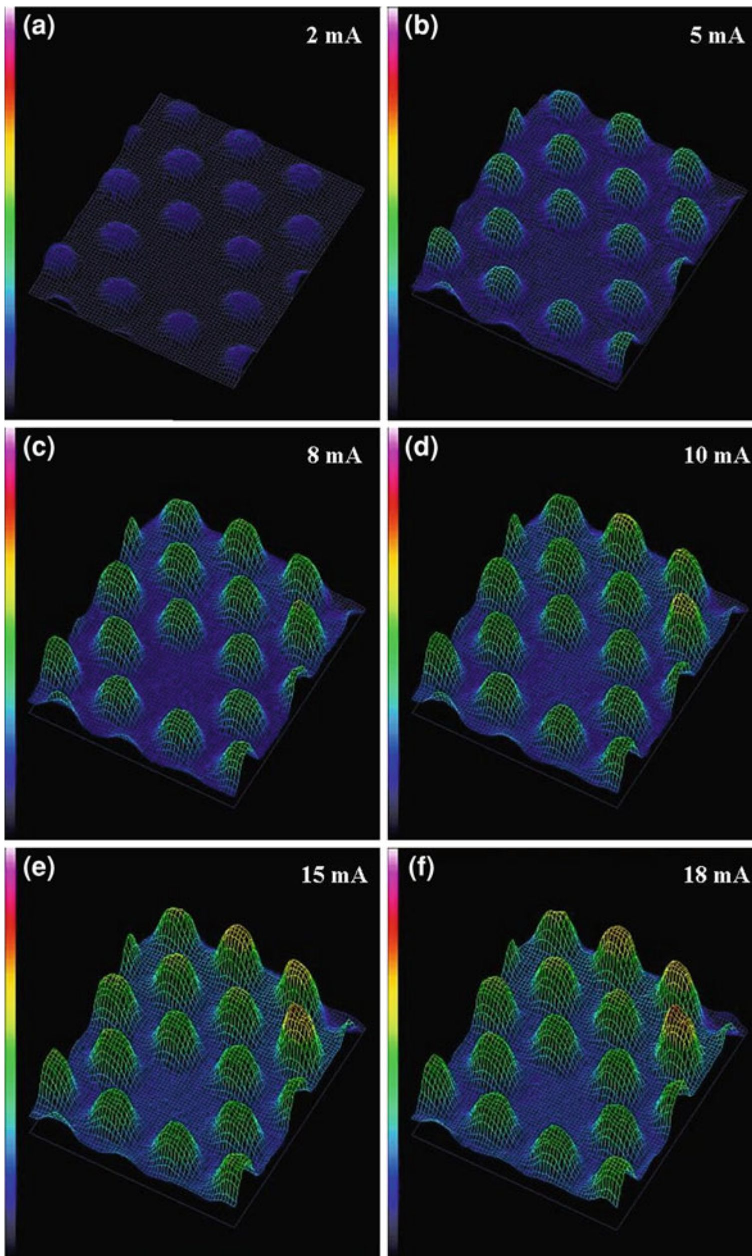

Fig. 8.7 3-D intensity profile at **a** 2 mA, **b** 5 mA, **c** 10 mA, and **d** 15 mA of the InGaAs SML QD PhC-LED. Neutral density (ND) filters were added to attenuate the beam, to avoid saturation of the charge-coupled device (CCD) imaging system. The lattice constant (Λ) of the PhC structure is 5 μm and the hole diameter (α) is 2.5 μm

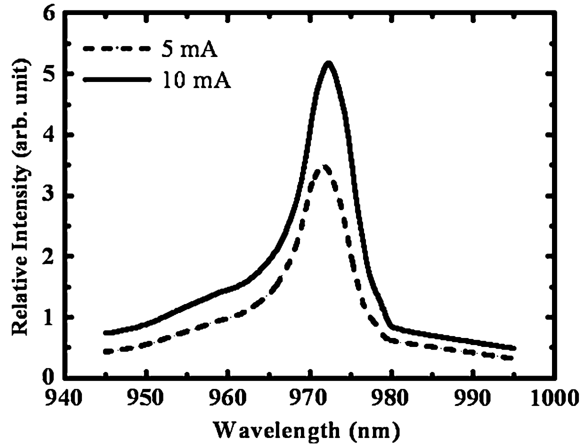

Fig. 8.8 Spectra of the InGaAs SML QD PhC-LED at 5 and 10 mA. The lattice constant (Λ) of the photonic-crystal structure is 5 μm and the hole diameter (α) is 2.5 μm

The spectra of the InGaAs SML QD PhC-LED at 5 and 10 mA are shown in Fig. 8.8. The peak emission wavelengths are 971.6 and 972.2 nm at 5 and 10 mA, respectively. The linewidth ($\Delta\lambda$) of the light emission, which is the full width at half-maximum (FWHM) of the peak intensity value, are 8.4 and 8.5 nm at 5 and 10 mA, respectively. These linewidth values are slightly larger than the linewidths (3–6 nm) of typical Fabry–Perot (FP) lasers. The narrower linewidth of the emission spectra is mainly due to the highly uniform grown QDs size and narrower gain spectrum of the QDs. The narrower linewidth also related to the resonant cavity properties of the PhC-LED. The internally reflected light within the resonant cavity can transmit out of the PhC etched holes because of the lowered reflectance within the etched holes. The emission wavelength of the SML QD PhC-LED is similar to those of the $In_{0.2}Ga_{0.8}As$/GaAs quantum-well (QW) LEDs. The InGaAs SML QD PhC-LEDs in this work emit with much narrower linewidths. Figure 8.9 shows the current-dependent peak wavelength of the InGaAs SML QD PhC-LED. The emission wavelength varies between 971 and 975 nm as current increases from 2 to 19 mA.

The light emission of SML QD PhC-LED is the combination of the confined emission from the InAs SML QD and the surrounding GaAs layers. The resonant light emission within the 1λ cavity narrows the emission linewidth down to $\sim$8 nm. For fiber-optic communications, narrower linewidth light sources can be used for longer distance transmission because of reduced dispersion in the optical fibers [65].

Compared to the previous studies of PhC-LEDs [2–17], our PhC-LEDs (oxide aperture = 48 μm in diameter) emit with higher output power of 0.34 mW. This output power value is lower than other PhC-LEDs [10] made with much larger device sizes (500 × 500 μm with output power larger than 44 mW). The average out power per unit area of our PhC-LED is 18.8 W/cm^2, which is comparable to other PhC-LEDs at similar current levels (17.6 W/cm^2 at 60 mA).

The sidewall of cylindrical PhC air holes in this work also deflect the output light so as to make the light beam more collimated. The collimated light beam can

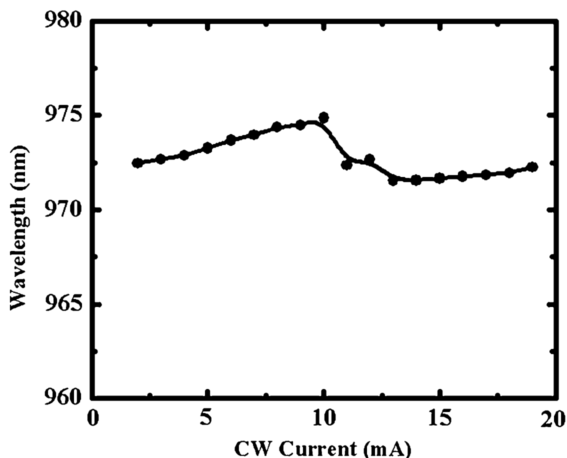

Fig. 8.9 Current-dependent peak wavelength of the InGaAs SML QD PhC-LED. The lattice constant (Λ) of the photonic-crystal structure is 5 μm and the hole diameter (α) is 2.5 μm

therefore be more easily coupled into the core of the optical fiber so that the coupling efficiency is higher. The two 1/4-λ DBRs that form the reflectors of the resonant cavity of the LED can also make the output light emit with narrower linewidth. The reflectance of the top- and bottom-DBRs need to be greater than 98%. The growth uniformity and high precision thickness control of the epitaxial layers are important issues to obtain exactly 1λ optical cavity of the devices, so as to achieve cavity resonance of the light emission. The remaining DBR layers ($\sim$4-pair $Al_{0.9}Ga_{0.1}As$/GaAs) of the PhC etched holes still can be used as the lower reflectance top-reflector of the resonant cavity.

Conclusions

In conclusion, we report InGaAs SML QD PhC-LEDs for fiber-optic communications. A maximum CW output power of 0.34 mW has been obtained. The present results indicate that a PhC-LED using an oxide layer for current confinement and a PhC structure for light extraction is an alternative approach to achieve small light beam output for optical-fiber coupling.

References

1. Steigerwald, D.A., Bhat, J.C., Collins, D., Flectcher, R.M., Holcomb, M.O., Ludowise, M.J., Martin, P.S., Rudaz, S.L.: Illumination with solid state lighting technology. IEEE J. Sel. Top. Quantum Electron. **8**, 310–312 (2002)
2. Kim, T., Danner, A.J., Choquette, K.D.: Enhancement in external quantum efficiency of blue light-emitting diode by photonic crystal surface grating. Electron. Lett. **41**, 1138–1140 (2005)
3. Ishikawa, H., Baba, T.: Efficiency enhancement in a light-emitting diode with a two-dimensional surface grating photonic crystal. Appl. Phys. Lett. **84**, 457–459 (2004)

4. Rangel, E., Matioli, E., Choi, Y.S., Weisbuch, C., Speck, J.S., Hu, E.L.: Directionality control through selective excitation of low-order guided modes in thin-film InGaN photonic crystal light-emitting diodes. Appl. Phys. Lett. **98**, 081104 (2011)
5. Kim, J.Y., Kwon, M.K., Park, S.J., Kim, S.H., Lee, K.D.: Enhancement of light extraction from GaN-based green light-emitting diodes using selective area photonic crystal. Appl. Phys. Lett. **96**, 251103 (2010)
6. Yang, H.P.D., Liu, J.N., Lai, F.I., Hao-Chung Kuo, H.C., Chi, J.Y.: Photonic-crystal light-emitting diodes on p-type GaAs substrates for optical communications. J. Modern Opt. **55**, 1509–1517 (2008)
7. Lai, C.F., Chao, C.H., Kuo, H.C., Yu, P., Yen, H.H., Yung Yeh, W.Y.: GaN thickness effect on directional light enhancement from GaN-based film-transferred photonic crystal light-emitting diodes. Jpn. J. Appl. Phys. **49**, 04DG09 (2010)
8. Shin, Y.C., Dong Ho Kim, D.H., Chae, D.J., Ji Won Yang, J. W., Shim, J.I., Park, J.M., Ho, K.M., Constant, K., Ryu, H.Y., Tae Geun Kim, T.G.: Effects of nanometer-scale photonic crystal structures on the light extraction from gan light-emitting diodes. IEEE J. Quantum Electron. **49**, 1375–1380 (2010)
9. Long, D.H., Hwang, I.K., Ryu, S.W.: Analysis of disordered photonic crystal implemented in light-emitting diode for high light extraction efficiency. Jpn. J. Appl. Phys. **47**, 4527–4530 (2008)
10. Lee, J., Ahn, S., Kim, S., Kim, D.U., Jeon, H., Lee, S.J., Baek, J.H.: GaN light-emitting diode with monolithically integrated photonic crystals and angled sidewall deflectors for efficient surface emission. Appl. Phys. Lett. **94**, 101105 (2009)
11. Francardi, M., Balet, L., Gerardino, A., Chauvin, N., Bitauld, D., Li, L.H., Alloing, B., Fiore, A.: Enhanced spontaneous emission in a photonic-crystal light-emitting diode. Appl. Phys. Lett. **93**, 143102 (2008)
12. Byeon, K.J., Hwang, S.Y., Lee, H.: Fabrication of two-dimensional photonic crystal patterns on GaN-based light-emitting diodes using thermally curable monomer-based nanoimprint lithography. Appl. Phys. Lett. **91**, 091106 (2007)
13. Mastro, M.A., Kim, C.S., Kim, M., Caldwell, J., Holm, R.T., Vurgaftman, I., Kim, J., Eddy Jr, C.R., Meyer, J.R.: Zinc Sulphide overlayer two-dimensional photonic crystal for enhanced extraction of light from a micro cavity light-emitting diode. Jpn. J. Appl. Phys. **47**, 7827–7830 (2008)
14. Su, Y.K., Chen, J.J., Lin, C.L., Shi-Ming Chen, S.M., Li, W.L., Kao, C.C.: GaN-based light-emitting diodes grown on photonic crystal-patterned sapphire substrates by nanosphere lithography. Jpn. J. Appl. Phys. **47**, 6706–6708 (2008)
15. Iwamoto, S., Tatebayashi, J., Fukuda, T., Nakaoka, T., Ishida, S., Arakawa, Y.: Observation of 1.55 μm light emission from InAs quantum dots in photonic crystal microcavity. Jpn. J. Appl. Phys. **44**, 2579–2583 (2005)
16. Wierer, J.J., Krames, M.R., Epler, J.E., Gardner, N.F., Craford, M.G., Wendt, J.R., Simmons, J.A., Sigalas, M.M.: InGaN/GaN quantum-well hetero-structure light-emitting diodes employing photonic crystal structures. Appl. Phys. Lett. **84**, 3885–3887 (2004)
17. Cho, H.K., Kim, S.K., Bae, D.K., Kang, B.C., Lee, J.S., Lee, Y.H.: Laser liftoff GaN thin-film photonic crystal GaN-based light-emitting diodes. IEEE Photonics Technol. Lett. **20**, 2096–2098 (2008)
18. Hawkins, B.M., Hawthorne III, R.A., Guenter, J.K., Tatum, J.A., Biard, J.R.: Reliability of various size oxide aperture VCSELs. 52nd electronic components and technology conference proceedings, p. 540 (2002)
19. Chang, S.J., Chang, C.S., Su, Y.K., Chang, P.T., Wu, Y.R., Huang, K.H., Chen, T.P.: Chirped GaAs-AlAs distributed Bragg reflectors for high brightness yellow-green light-emitting diodes. IEEE Photonics Technol. Lett. **9**, 182–184 (1997)
20. Modak, P., D'Hondt, M., Delbeke, D., Moerman, I., Van Daele, P., Baets, R., Demeester, P., Mijlemans, P.: AlGaInP microcavity light-emitting diodes at 650 nm on Ge substrates. IEEE Photonics Technol. Lett. **12**, 957–959 (2000)

21. Sharma, R., Choi, Y., Wang, C.F., David, A., Weisbuch, C., Nakamura, S., Hu, E.L.: Gallium-nitride-based microcavity light-emitting diodes with air-gap distributed Bragg reflectors. Appl. Phys. Lett. **91**, 211108 (2007)
22. Huang, G.S., Lu, T.C., Kuo, H.C., Wang, S.C., Chen, H.G.: Fabrication of microcavity light-emitting diodes using highly reflective AlN–GaN and Ta_2O_5–SiO_2 distributed Bragg mirrors. IEEE Photon. Technol. Lett. **19**, 999–1001 (2007)
23. Huang, H., Deppe, D.G.: Obtaining high efficiency at low power using a quantum-dot microcavity light-emitting diode. IEEE J. Quantum Electron. **36**, 674–679 (2000)
24. Zhou, W., Bhattacharya, P., Qasaimeh, O.: InP-based cylindrical microcavity light-emitting diodes. IEEE J. Quantum Electron. **37**, 48–54 (2001)
25. Chen, H., Zou, Z., Cao, C., Deppe, D.G.: High differential efficiency (16%) quantum dot microcavity light emitting diode. Appl. Phys. Lett. **80**, 350–352 (2002)
26. Dorsaz, J., Carlin, J.-F., Gradecak, S., Ilegems, M.: Progress in AlInN–GaN Bragg reflectors: application to a microcavity light emitting diode. J. Appl. Phys. **97**, 084505 (2005)
27. Tasco, V., Todaro, M.T., De Vittorio, M., De Giorgi, M., Cingolani, R., Passaseo, A., Ratajczak, J., Katcki, J.W.: Electrically injected InGaAs/GaAs quantum-dot microcavity diode operating at 1.3 μm and grown by metalorganic chemical vapor deposition. Appl. Phys. Lett. **84**, 4155–4157 (2004)
28. Qasaimeh, O., Zhou, W.-D., Bhattacharya, P., Huffaker, D., Deppe, D.G.: Monolithically integrated low-power phototransceiver incorporating InGaAs/GaAs quantum-dot microcavity LED and modulated barrier photodiode. Electron. Lett. **36**, 1955–1957 (2000)
29. Pratt, A.R., Takamori, T., Kamijoh, T.: Cavity detuning effects in semiconductor microcavity light emitting diodes. J. Appl. Phys. **87**, 8243–8250 (2000)
30. Song, Y.-K., Diagne, M., Zhou, H., Nurmikko, A.V., Schneider, R.P., Takeuchi, T.: Resonant-cavity InGaN quantum-well blue light-emitting diodes. Appl. Phys. Lett. **77**, 1744–1746 (2000)
31. Todaro, M.T., Tasco, V., De Giorgi, M., Martiradonna, L., Raino, G., De Vittorio, M., Passaseo, A., Cingolani, R.: High-efficiency 1.3 μm InGaAs/GaAs quantum-dot microcavity light-emitting diodes grown by metalorganic chemical vapor deposition. Appl. Phys. Lett. **86**, 15118 (2005)
32. Royo, P., Stanley, R.P., Ilegems, M., Streubel, K., Gulden, K.H.: Experimental determination of the internal quantum efficiency of AlGaInP microcavity light-emitting diodes. J. Appl. Phys. **91**, 2563–2568 (2002)
33. Takamori, T., Pratt, A.R., Kamijoh, T.: Temperature dependence of InGaAs/GaAs quantum well microcavity light-emitting diodes. Appl. Phys. Lett. **74**, 3598–3600 (1999)
34. Depreter, B., Moerman, I., Baets, R., Van Daele, P., Demeester, P.: InP-based 1300 nm microcavity LEDs with 9% quantum efficiency. Electron. Lett. **36**, 1303–1304 (2000)
35. Unlu, M.S., Strite, S.: Resonant cavity enhanced photonic devices. J. Appl. Phys. **78**, 607–639 (1995)
36. Krestnikov, I.L., Maleev, N.A., Sakharov, A.V., Kovsh, A.R., Zhukov, A.E., Tsatsul'nikov, A.F., Ustinov, V.M., Alferov, Zh.I., Ledentsov, N.N., Bimberg, D., Lott, J.A.: 1.3 μm resonant-cavity InGaAs/GaAs quantum dot light-emitting devices. Semicond. Sci. Technol. **16**, 844–848 (2001)
37. Hsueh, T.H., Sheu, J.K., Huang, H.W., Chu, J.Y., Kao, C.C., Kuo, H.C., Wang, S.C.: Enhancement in light output of InGaN-based microhole array light-emitting diodes. IEEE Photonics Technol. Lett. **17**, 1163–1165 (2005)
38. Yang, H.P.D., Yeh, Z.E., Lai, F.I., Kuo, H.C., Chi, J.Y.: Characteristics of multileaf holey light-emitting diodes for fiber-optic communications. Jpn. J. Appl. Phys. Part. **1**(47), 974–976 (2008)
39. Yang, H.P.D., Liu, J.N., Lai, F.I., Kuo, H.C., Chi, J.Y.: Characteristics of p-substrate small-aperture light-emitting diodes for fiber-optic applications. Jpn. J. Appl. Phys. Part. **1**(46), 2941–2943 (2007)
40. Amano, T., Sugaya, T., Komori, K.: 1.3 μm InAs quantum-dot laser with high dot density and high uniformity. IEEE Photon. Technol. Lett. **18**, 619–621 (2006)

41. Thompson, M.G., Rae, A.R., Mo, X., Penty, R.V., White, I.H.: InGaAs quantum-dot mode-locked laser diodes. IEEE J. Sel. Top. Quantum Electron. **15**, 661–672 (2009)
42. Moore, S.A., O'Faolain, L., Cataluna, M.A., Flynn, M.B., Kotlyar, M.V., Krauss, T.F.: Reduced surface sidewall recombination and diffusion in quantum-dot lasers. IEEE Photon. Technol. Lett. **18**, 1861–1863 (2006)
43. Park, G., Shchekin, O.B., Huffaker, D.L., Deppe, D.G.: Low-threshold oxide-confined 1.3 μm quantum-dot laser. IEEE Photon. Technol. Lett. **12**, 230–232 (2000)
44. Kim, J., Su, H., Minin, S., Chuang, C.L.: Comparison of linewidth enhancement factor between p-doped and undoped quantum-dot lasers. IEEE Photon. Technol. Lett. **18**, 1022–1024 (2006)
45. Mi, Z., Yang, J., Bhattacharya, P., Qin, G., Ma, Z.: High-performance quantum dot lasers and integrated optoelectronics on Si. Proc. IEEE **97**, 1239–1249 (2009)
46. Asryan, L.V., Luryi, S.: Tunneling-injection quantum-dot laser: ultrahigh temperature stability. IEEE J. Quantum Electron. **37**, 905–910 (2001)
47. Fischer, M., Bisping, D., Marquardt, B., Forchel, A.: High-temperature continuous-wave operation of GaInAsN–GaAs quantum-dot laser diodes beyond 1.3 μm. IEEE Photon. Technol. Lett. **19**, 1030–1032 (2007)
48. Lester, L.F., Stintz, A., Li, H., Newell, T.C., Pease, E.A., Fuchs, B.A., Malloy, K.J.: Optical characteristics of 1.24 μm InAs quantum-dot laser diodes. IEEE Photon. Technol. Lett. **11**, 931–933 (1999)
49. Yu, H.C., Wang, J.S., Su, Y.K., Chang, S.J., Lai, F.Y., Chang, Y.H., Kuo, H.C., Sung, C.P., Yang, H.P.D., Lin, K.F., Wang, J.M., Chi, J.Y., Hsiao, R.S., Mikhrin, S.: 1.3 μm InAs–InGaAs quantum-dot vertical-cavity surface-emitting laser with fully doped DBRs grown by MBE. IEEE Photon. Technol. Lett. **18**, 418–420 (2006)
50. Chang, Y.H., Peng, P.C., Tsai, W.K., Lin, G., Lai, F.I., Hsiao, R.S., Yang, H.P., Yu, H.C., Lin, K.F., Chi, J.Y., Wang, S.C., Kuo, H.C.: Single-mode monolithic quantum-dot VCSEL in 1.3 μm with sidemode suppression ratio over 30 dB. IEEE Photon. Technol. Lett. **18**, 847–849 (2006)
51. Lott, J.A., Ledentsov, N.N., Ustinov, V.M., Mallev, N.A., Zhukov, A.E., Kovsh, A.R., Maximov, M.V., Volvovik, B.V., Alferov, Z.H.I., Bimberg, D.: InAs-InGaAs quantum dot VCSELs on GaAs substrates emitting at 1.3 μm. Electron. Lett. **36**, 1384–1385 (2000)
52. Peng, P.C., Lin, C.T., Kuo, H.C., Tsai, W.K., Liu, J.N., Chi, S., Wang, S.C., Lin, G., Yang, H.P., Lin, K.F., Chi, J.Y.: Tunable slow light device using quantum dot semiconductor laser. Opt. Express **14**, 12880–12886 (2006)
53. Peng, P.C., Lin, C.T., Kuo, H.C., Lin, G., Tsai, W.K., Yang, H.P., Lin, K.F., Chi, J.Y., Chi, S., Wang, S.C.: Tunable optical group delay in quantum dot vertical-cavity surface-emitting laser at 10 GHz. Electron. Lett. **42**, 1036–1037 (2006)
54. Peng, P.C., Chang, Y.H., Kuo, H.C., Tsai, W.K., Lin, G., Lin, C.T., Yu, H.C., Yang, H.P., Hsiao, R.S., Lin, K.F., Chi, J.Y., Chi, S., Wang, S.C.: 1.3 μm quantum dot vertical-cavity surface-emitting laser with external light injection. Electron. Lett. **41**, 1222–1223 (2005)
55. Yang, H.P.D., Chang, Y.H., Lai, F.I., Yu, H.C., Hsu, Y.J., Lin, G., Hsiao, R.S., Kuo, H.C., Wang, S.C., Chi, J.Y.: Singlemode InAs quantum dot photonic crystal VCSELs. Electron. Lett. **41**, 1130–1132 (2005)
56. Mikhrin, S.S., Zhukov, A.E., Kovsh, A.R., Maleev, N.A., Ustinov, V.M., Shernyakov, Yu.M., Soshnikov, I.P., Livshits, D.A., Tarasov, I.S., Bedarev, D.A., Volovik, B.V., Maximov, M.V., Tsatsul'nikov, A.F., Ledentsov, N.N., Kop'ev, P.S., Bimberg, D., Alferov, Z.H.I.: 0.94 μm diode lasers based on Stranski-Krastanow and sub-monolayer quantum dots. Semicond. Sci. Technol. **15**, 1061–1064 (2000)
57. Zhukov, A.E., Kovsh, A.R., Mikhrin, S.S., Maleev, N.A., Ustinov, V.M., Livshits, D.A., Tarasov, I.S., Bedarev, D.A., Maximov, M.V., Tsatsul'nikov, A.F., Soshnikov, I.P., Kop'ev, P.S., Alferov, Zh.I., Ledentsov, N.N., Bimberg, D.: 3.9 W CW power from sub-monolayer quantum dot diode laser. Electron. Lett. **35**, 1845–1847 (1999)
58. Blokhin, S.A., Sakharov, A.V., Maleev, N.A., Kulagina, M.M., Shernyakov, Yu.M., Novikov, I.I., Gordeev, N.Yu., Maximov, M.V., Kuzmenkov, A.G., Ustinov, V.M.,

Ledentsov, N.N., Kovsh, A.R., Mikhrin, S.S., Lin, G., Chi, J.Y.: The impact of thermal effects on the performance of vertical-cavity surface-emitting lasers based on sub-monolayer InGaAs quantum dots. Semicond. Sci. Technol. **22**, 203–208 (2007)

59. Blokhin, S.A., Maleev, N.A., Kuzmenkov, A.G., Sakharov, A.V., Kulagina, M.M., Shernyakov, Y.M., Novikov, I.I., Maximov, M.V., Ustinov, V.M., Kovsh, A.R., Mikhrin, S.S., Ledentsov, N.N., Lin, G., Chi, J.Y.: Vertical-cavity surface-emitting lasers based on submonolayer InGaAs quantum dots. IEEE J. Quantum Electron. **42**, 851–858 (2006)
60. Hopfer, F., Mutig, A., Kuntz, M., Fiol, G., Bimberg, D., Ledentsov, N.N., Shchukin, V.A., Mikhrin, S.S., Livshits, D.L., Krestnikov, I.L., Kovsh, A.R., Zakharov, N.D., Werner, P.: Single-mode submonolayer quantum-dot vertical-cavity surface-emitting lasers with high modulation bandwidth. Appl. Phys. Lett. **89**, 141106 (2006)
61. Blokhin, S.A., Maleev, N.A., Kuzmenkov, A.G., Shernyakov, Yu.M., Novikov, I.I., Gordeev, N.Yu., Sokolovskii, G.S., Dudelev, V.V., Kuchinskii, V.I., Kulagina, M.M., Maximov, M.V., Ustinov, V.M., Kovsh, A.R., Mikhrin, S.S., Ledentsov, N.N.: VCSELs based on arrays of sub-monolayer InGaAs quantum dots. Semiconductors **40**, 615–619 (2006)
62. Kuzmenkov, A.G., Ustinov, V.M., Sokolovskii, G.S., Maleev, N.A., Blokhin, S.A., Deryagin, A.G., Chumak, S.V., Shulenkov, A.S., Mikhrin, S.S., Kovsh, A.R., McRobbie, A.D., Sibbett, W., Cataluna, M.A., Rafailov, B.U.: Self-sustained pulsation in the oxide-confined vertical-cavity surface-emitting lasers based on submonolayer InGaAs quantum dots. Appl. Phys. Lett. **91**, 121106 (2007)
63. Germann, T.D., Strittmatter, A., Pohl, J., Pohl, U.W., Bimberg, D., Rautiainen, J., Guina, M., Okhotnikov, O.G.: High-power semiconductor disk laser based on InAs/GaAs submonolayer quantum dots. Appl. Phys. Lett. **92**, 101123 (2008)
64. Yang, H.P.D., Hsu, I.C., Lai, F.Y., Lin, G., Hsiao, R.S., Maleev, N.A., Blokhin, S.A., Kuo, H.C., Chi, J.Y.: Characteristics of broad-area InGaAs submonolayer quantum-dot vertical-cavity surface-emitting lasers. Jpn. J. Appl. Phys. **46**, 6670–6672 (2007)
65. Powers, J.P.: An Introduction to Fiber Optic Systems. Aksen Associates, Homewood (1993)

Chapter 9
Quantum Optical Transistor and Other Devices Based on Nanostructures

Jin-Jin Li and Ka-Di Zhu

Abstract Laser and strong coupling can coexist in a single quantum dot (QD) coupled to nanostructures. This provides an important clue toward the realization of quantum optical devices, such as quantum optical transistor, slow light device, fast light device, or light storage device. In contrast to conventional electronic transistor, a quantum optical transistor uses photons as signal carriers rather than electrons, which has a faster and more powerful transfer efficiency. Under the radiation of a strong pump laser, a signal laser can be amplified or attenuated via passing through a single quantum dot coupled to a photonic crystal (PC) nanocavity system. Such a switching and amplifying behavior can really implement the quantum optical transistor. By simply turning on or off the input pump laser, the amplified or attenuated signal laser can be obtained immediately. Based on this transistor, we further propose a method to measure the vacuum Rabi splitting of exciton in all-optical domain. Besides, we study the light propagation in a coupled QD and nanomechanical resonator (NR) system. We demonstrate that it is possible to achieve the slow light, fast light, and quantum memory for light on demand, which is based on the mechanically induced coherent population oscillation (MICPO) and exciton polaritons. These QD devices offer a route toward the use of all-optical technique to investigate the coupled QD systems and will make contributions to quantum internets and quantum computers.

J.-J. Li (✉) · K.-D. Zhu
Department of Physics, Shanghai Jiao Tong University, 800 Dong Chuan Road, 200240 Shanghai, People's Republic of China
e-mail: lijinjin.physics@gmail.com

K.-D. Zhu
e-mail: zhukadi@sjtu.edu.cn

Z. M. Wang (ed.), *Quantum Dot Devices*, Lecture Notes in Nanoscale Science and Technology 13, DOI: 10.1007/978-1-4614-3570-9_9,
© Springer Science+Business Media New York 2012

Introduction

Transistor is a semiconductor device used for amplification and switching electronic signals [1, 2]. It consists of three terminals for connecting to an external circuit, two in-port terminals and one out-port terminal (Fig. 9.1a). A voltage or current applied to one in-port of the transistor leads to the current change of another in-port terminal, and eventually results in the out-port signal switched or amplified. The transistor based on electrons was released in the early 1950s, which revolutionized the field of electronics, and paved the way for smaller and cheaper radios, computers, and networks.

Nowadays, more widespread and faster information transmission technology becomes the hot pursuit for scientific researchers, especially for the internet connections and computers, which need to be ever faster and more powerful. However, the information transmission that uses electron as signal carrier limits the performance of computers and networks due to the power dissipations, consequent hardware heating, and others. The continued increase in global network bandwidth demand highlights the need for new devices that reduce the effects of this electron bottleneck by operating entirely in the optical domain. Therefore, it has been a trend for scientists to try to find other objects to substitute electrons as signal carriers. Photon is a better choice than electron in powering processors because it causes much less heat than regular processors and enables much higher transfer rates within the device. Consequently, optical transistors are an attractive sought goal because they could form the basis of optical computers that use photons instead of electrons as signal carriers.

A photonic transistor is a device where a strong pump laser is used to control the propagation of another weak signal laser via a nonlinear optical interaction. In analogy with the electronic transistor, photons in optical transistor do not perturb each other that enhance the signal's transfer efficiency and increase the transfer speed. The transistor using photons other than electrons brings new hope for the development of internet connections and computers. Furthermore, a quantum optical transistor requires a nonlinear transmission medium (Fig. 9.1b). In general, the nonlinear response of most materials is too small to create an all-optical device that operates at the few-photon level, which requires strong nonlinear light-matter interactions. Some systems have a weak light-matter coupling and do not miniaturize conveniently due to the complex structures and the material properties, such as atomic gas [3], optical fibers [4], and so on. To this end, there has also been a notable effort to create all-optical devices using semiconductor materials where manufacturing and miniaturization processes are well understood.

Quantum dots (QDs), the most familiar and simple semiconductor structure, have been theoretically and experimentally studied very thoroughly over a long period of time [5]. The unique size-dependent, narrow, symmetric, bright, and stable fluorescence of QDs have made them the best choice in solar cells, LEDs, infrared photodetector, and medical imaging [6–8]. QDs, also known as quantum boxes, are nanometer scale structures in which electrons and holes are confined in 3D potential boxes. Because of strong confinement imposed on all three spatial

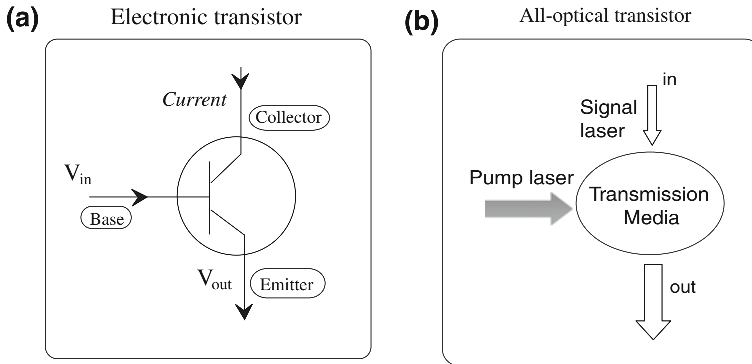

Fig. 9.1 Comparison of conventional electronic transistor and all-optical transistor. (**a**)Transistor based on electrons, which consists of three parts a *base*, a *collector*, and an *emitter*. The small change of V_{in} produces large changes of V_{out} via the collector of the transistor and makes the output signal switched or amplified. (**b**) Optical transistor, which is in analogy with electronic transistor. The output signal laser can be switched or amplified by regulating the input pump laser properly, via the pump laser passing through the specific media previously

dimensions, QDs are similar to atoms. They are often referred as artificial atoms. These attractive features of quantum dots have realized some QD devices [9]. In 1999, Imamoḡlu et al. [10] have proposed quantum information processing in terms of QD spins and cavity QED. And then, quantum information, quantum storage, and quantum measurement based on QDs began to grow and became a separate subject itself. Recently, Heiss et al. [11] have reported the investigation of charge storage device based on a single quantum dot. The device allows selective optical charging of a single dot with electrons. The storage of these charges over timescales is much longer than microseconds. Another QD-based storage sensor has been proposed by Kłopotowskia et al. [12], who have demonstrated the storage of photoexcited electrons in a layer of the self-assembled CdTe QDs embedded in a field-effect structure. Using the QD, the persisting time of the electrons is as long as 9 ms, which may achieve the quantum information and storage. Additionally, there are a large number of QD devices, such as the infrared photodetector and Kerr devices based on surface plasmon coupled to QDs [13–15]. The QD infrared sensors with a photonic crystal (PC) cavity [16], Kerr modulator [17], and fast light/slow light switch [18] based on QDs coupled to a nanomechanical resonator (NR). These QDs-based quantum devices open a new chapter during these years in the field of nanotechnology [19–23].

In this chapter, attractive QD devices are introduced to extend the subject of QDs to high level photonic device, using the two-laser technique [24–27]. "A Quantum Optical Transistor with a Single QD in a Photonic Crystal Nanocavity" gives a physical illustration of a quantum optical transistor with a single quantum dot in a PC nanocavity [19]. Using experimental realistic parameters, theoretical analysis shows that such a quantum optical transistor can be switched on or off by turning on or off the pump laser, which corresponds to attenuation or amplification

of the signal laser, respectively. Furthermore, based on this quantum optical transistor, an all-optical measurement of the vacuum Rabi splitting is also presented. In "Light Manipulation Devices in a QD Coupled to a NR System", we investigate the coupled QD and NR system and demonstrate that it is possible to achieve the slow light and fast light effects, and even to store and read out the quantum signal pulse by switching off and on the pump pulse, respectively [18, 21]. It is shown that the vibration of NR leads to the dressed metastable energy level of QD, which provides a temporary accommodation for electrons. This dressed exciton dark-state polaritons can be reaccelerated and converted back into a photon pulse via a tunable pump laser.

A Quantum Optical Transistor with a Single QD in a Photonic Crystal Nanocavity

Optical transistor is an attractive sought goal because it could form the basis of optical computers and quantum computers that use photons instead of electrons as signal carriers. Recently, a breakthrough of a single molecule optical transistor was achieved by Hwang et al. [28]. They experimentally described how the transmission of a light can be modulated by another light using just one molecule. However, because of the weak light-matter coupling and the unstable photonic signals, the practical optical transistors still possess a significant challenge, which will, to a large extent, limit the development of quantum transmission [29, 30]. A promising avenue is to trap a register of atoms inside an optical cavity [31, 32], where the high reflectivity of cavity can increase the optical path length and the strength of matter-light interaction. A inside atom/nanoparticle/QD can provide an extra energy and assist the light transmission. Furthermore, PCs have some advantages in optics, which make them the best optical cavity candidate to modulate the flow of light [33–35]. For example, optical devices enabled by PC designs can be smaller than the wavelength of light, operated at very low powers, and with bandwidths that are very difficult to achieve electronically.

In this section, by combining the advantages of photons as information carriers and QD as single quantum emitter, we report a quantum optical transistor where a two-level QD is embedded in a PC nanocavity. In the presence of a strong pump laser and a weak signal laser, the output signal laser can be switched on or off while turning on or off the input pump laser, respectively. Furthermore, we give an all-optical technique to detect the normal mode splitting of QD-cavity system (vacuum Rabi splitting), which is better than traditional circuit-assistant method [36]. The proposal of a quantum optical transistor will pave the way toward many important applications such as efficient photon detection and quantum information science.

Figure 9.2 shows the setup of how to realize a quantum optical transistor, where a single QD is embedded in a photonic crystal nanocavity, in the presence of two optical fields. In the PC nanocavity. the artificial defects, formed by small regions of disorder can serve as an effective resonant cavity, since they would be able

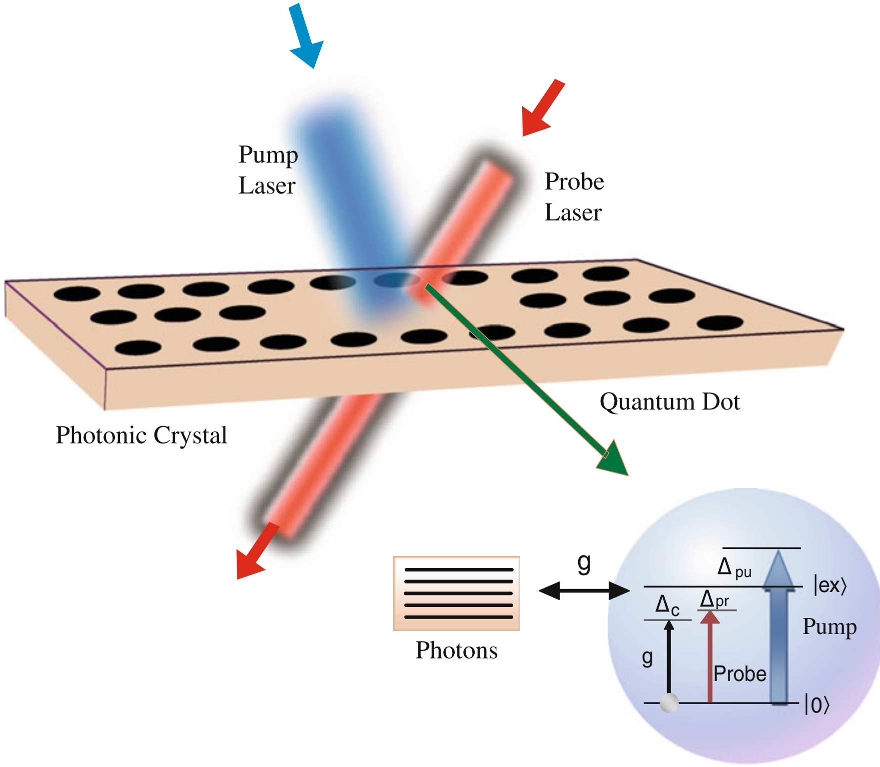

Fig. 9.2 Setup of a quantum optical transistor, where an InAs/GaAs QD is embedded in the center of a photonic crystal nanocavity. Two optical fields are aimed for the coupled system. The inset shows the energy levels of a QD, which is coupled to a single cavity mode and two optical fields

to control the behavior of photons and would hardly suffer any losses. Such a PC nanocavity has both high Q and small modal volume V as required for strong light-matter interactions. Inside the PC nanocavity, a single quantum is placed in the center during growth. At low temperatures, the two-level QD consists of the ground-state $|0\rangle$ and the first excited state (single exciton) $|ex\rangle$, which can be characterized by the pseudospin $-1/2$ operators $\sigma^{\pm}$ and σ^{z}.

The master equation describing the dynamics of a coherently driven single QD coupled to a single cavity mode with the creation operator a^{+} and the annihilation operator a is given by [19, 37]

$$\frac{\mathrm{d}\rho}{\mathrm{d}t} = -\frac{i}{\hbar}[H,\rho] + \kappa\ell[a] + \Gamma_1\ell[\sigma^-] + \frac{\Gamma_2}{2}(\sigma_z\rho\sigma_z - \rho), \tag{9.1}$$

where ρ is the density matrix of the coupled cavity/QD system, $2\Gamma_1$ and 2κ are the QD spontaneous emission rate and the cavity field decay rate, respectively, Γ_2 is the pure dephasing rate of the QD, $\ell[D]$ is the Lindbald operator corresponding to a

collapse operator D. This is used to model the incoherent decays and is given by: $\ell[D] = 2D\rho D^{+} - D^{+}D\rho - \rho D^{+}D$.

In the rotating frame at the pump field frequency ω_p, the total Hamiltonian is described by

$$\begin{aligned} H = & \hbar\Delta_p\sigma^z + \hbar\Delta\omega a^+ a + \hbar g(\sigma^+ a + \sigma^- a^+) \\ & - \hbar\Omega_p(\sigma^+ + \sigma^-) - \mu E_s(\sigma^+ e^{-i\delta t} + \sigma^- e^{i\delta t}), \end{aligned} \tag{9.2}$$

where $\Delta_p = \omega_{ex} - \omega_p$, $\Delta\omega = \omega_c - \omega_p$, and $\delta = \omega_s - \omega_p$ are the exciton-pump laser detuning, the PC-pump laser detuning, and the signal-pump laser detuning, respectively. ω_{ex} and ω_c are the frequency of exciton and nanocavity, respectively. g is the coupling strength between QD and cavity. We apply two classical optical fields in this system, where one is strong pump beam with amplitude E_p and frequency ω_p, the other is relatively weak signal beam with amplitude E_s and frequency ω_s. Ω_p is the Rabi frequency of the pump laser and is given by $\Omega_p = \mu E_p/\hbar$.

The Markovian interaction with reservoirs determining the decay rates Γ_1 and κ for the QD exciton and the nanocavity mode, respectively, is described by the following Liouvillian terms: [37, 38] $\ell[a] = 2a\rho a^+ - a^+ a\rho - \rho a^+ a$, $\ell[\sigma^-] = 2\sigma^-\rho\sigma^+ - \sigma^+\sigma^-\rho - \rho\sigma^+\sigma^-$.

Starting from Eq. 9.1, the equations of motion for the cavity field expectation values $\langle a\rangle \equiv \mathrm{Tr}[a\rho]$, $\langle\sigma^-\rangle \equiv \mathrm{Tr}[\sigma^-\rho]$ and $\langle\sigma^z\rangle \equiv [\mathrm{Tr}\sigma^z\rho]$ can be obtained by

$$\frac{\mathrm{d}\langle a\rangle}{\mathrm{d}t} = -(i\Delta\omega + \frac{\kappa}{2})\langle a\rangle - ig\langle\sigma^-\rangle, \tag{9.3}$$

$$\frac{\mathrm{d}\langle\sigma^-\rangle}{\mathrm{d}t} = -(i\Delta_p + \Gamma_2)\langle\sigma^-\rangle + 2ig\langle\sigma^z\rangle\langle a\rangle - 2i\Omega_p\langle\sigma^z\rangle - \frac{2i\mu E_s}{\hbar}e^{-i\delta t}, \tag{9.4}$$

$$\begin{aligned} \frac{\mathrm{d}\langle\sigma^z\rangle}{\mathrm{d}t} = & -\Gamma_1(\langle\sigma^z\rangle + 1) - ig(\langle\sigma^+\rangle\langle a\rangle - \langle\sigma^-\rangle\langle a^+\rangle) \\ & + i\Omega_p(\langle\sigma^+\rangle - \langle\sigma^-\rangle) + \frac{i\mu E_s}{\hbar}(\langle\sigma^+\rangle e^{-i\delta t} + \langle\sigma^-\rangle e^{i\delta t}). \end{aligned} \tag{9.5}$$

In order to solve the Eqs. 9.3–9.5, use the following ansatz [39]: $\langle a(t)\rangle = a_0 + a_+ e^{-i\delta t} + a_- e^{i\delta t}$, $\langle\sigma^-(t)\rangle = \sigma_0 + \sigma_+ e^{-i\delta t} + \sigma_- e^{i\delta t}$, $\langle\sigma^z(t)\rangle = \sigma_0^z + \sigma_+^z e^{-i\delta t} + \sigma_-^z e^{i\delta t}$. Upon substituting these approximation to Eqs. 9.3–9.5, and upon working to the lowest order in E_s but to all orders in E_p, we can obtain σ_+, which corresponds to the linear optical susceptibility through a single QD as follows: $\chi^{(1)}(\omega_s) = \mu\sigma_+/E_s = (\mu^2/\hbar)\chi(\omega_s)$, where $\chi(\omega_s)$ is given by

$$\chi(\omega_s) = \frac{iF_6 fp - w_0}{ifp[\Omega_p + gF_6(F_3 - F_2)] - q}, \tag{9.6}$$

where $\Delta_c = \omega_c - \omega_{ex}, F_1 = -ig/[i(\Delta_c + \Delta_p) + \kappa/2], F_2 = ig/[-i(\Delta_c + \Delta_p) + \kappa/2], F_3 = ig/[i(\delta - \Delta_c - \Delta_p) - \kappa/2]$, $F_4 = -ig/[i(\delta + \Delta_c + \Delta_p) - \kappa/2]$, $F_5 =$

$\Omega_p w_0/(g w_0 F_1 - \Delta_p + i\Gamma_2)$, $F_6 = \Omega_p w_0/(g w_0 F_2 - \Delta_p - i\Gamma_2)$, $p = g w_0 F_4 - \Delta_p - i\Gamma_2 - \delta$, $q = g w_0 F_3 - \Delta_p + i\Gamma_2 + \delta$, and

$$f = \frac{2(\Omega_p - gF_1F_5)}{(i\delta - \Gamma_1)p + 2i(\Omega_p - gF_2F_6)[\Omega_p + gF_5(F_4 - F_1)]}. \tag{9.7}$$

The population inversion ($w_0 = \sigma_0^z$) of the exciton is determined by the following equation:

$$\begin{aligned} &\{\Gamma_1(w_0 + 1)[(g^2 w_0 + \Delta_p\Delta\omega - \kappa/2)^2 + (\Delta\omega + \Delta_p\kappa/2)^2]\} \\ &+ 4\Gamma_2\Omega_p^2 w_0(\Delta\omega^2 + \kappa^2/4) = 0, \end{aligned} \tag{9.8}$$

where $\Delta\omega = \Delta_c + \Delta_p$.

Figure 9.2 shows an InAs/GaAs QD embedded in a photonic crystal nanocavity system, in the simultaneous presence of a strong pump beam and a weak signal beam. In the weak coupling regime ($g < \Gamma_1, \kappa$), the Purcell effect [40] can either enhance or inhibit the decay rate of irreversible spontaneous emission. On the other hand, when $g > \Gamma_1, \kappa$, this is in the regime of the strong coupling. Here we consider the strong coupling case for $(g, \kappa, \Gamma_1) = (25, 8, 5.2)$ MHz [41]. This two-level QD trapped inside the PC cavity is dressed by cavity photons as shown in the inset of Fig. 9.2. In the following, we will demonstrate that, under the radiation of two optical fields, such coupled QD-PC system can be used to measure the vacuum Rabi splitting and serve as a quantum optical transistor.

Measurement of Vacuum Rabi Splitting

In the first step of protocol, we tune the cavity frequency and pump laser frequency simultaneously to the frequency of exciton $\Delta_c = \Delta_p = 0$, and detect the signal transmission spectrum. Figure 9.3a plots the signal absorption spectrum versus the signal detuning ($\Delta_s = \omega_s - \omega_{\text{ex}}$). This spectrum contains two sharp peaks representing the vacuum Rabi splitting. This manifests itself as two distinct Lorentzian peaks and an anticrossing behavior. We note that the distance of these two peaks become larger as the QD-cavity coupling strength increases. Figure 9.3b illustrates the energy levels and transitions, where the excited state $|ex\rangle$ splits into two dressed state $|ex, n+1\rangle$ and $|ex, n\rangle$ after aiming for a strong pump laser on the QD. The energy gap of $|ex, n+1\rangle$ and $|ex, n\rangle$ is $2g$. The linear relationship between the peak splitting distance and the QD-cavity coupling strength is shown in Fig. 9.3c, which provides an effective method to measure the vacuum Rabi splitting of a single QD in a PC nanocavity. Therefore, if we first fix the cavity frequency and the pump laser frequency on the resonance of exciton simultaneously, according to the distance of two sharp peaks, the vacuum Rabi splitting strength can be obtained in the signal absorption spectrum.

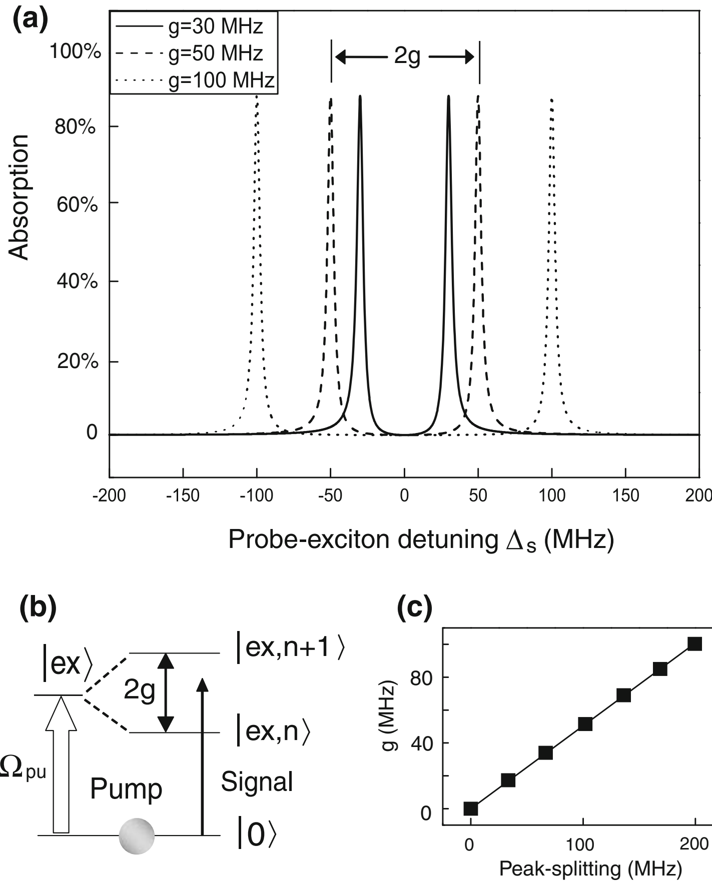

Fig. 9.3 (**a**) The absorption spectrum of the signal beam as a function of the detuning Δ_s for three different QD-cavity coupling strengths. The other parameters used are $\Omega_p^2 = (50\,\text{MHz})^2$, $\kappa = 8\,\text{MHz}$, $\Gamma_1 = 5.2\,\text{MHz}$, $\Delta_p = 0$ and $\Delta_c = 0$. (**b**) The energy levels of the dressed states ($|n\rangle$ denotes the number states of photons). (**c**)The linear relationship between the peak splitting distance and the QD-cavity coupling strength

A Quantum Optical Transistor

If we tune the cavity frequency and the pump frequency away from the exciton frequency, the output signal field turns to different behavior. Figure 9.4a displays the situation when shelving the pump beam but only applying a signal beam, which shows that in the absence of the pump beam the system attenuates the weak signal beam totally. This dip arises from the usual excitonic absorption resonance. The inset of Fig. 9.4a gives a pictorial temporal view of the energy levels of the QD. However, when turning on the pump beam, the dip becomes a peak immediately. As the pump power increases even further, we can observe more

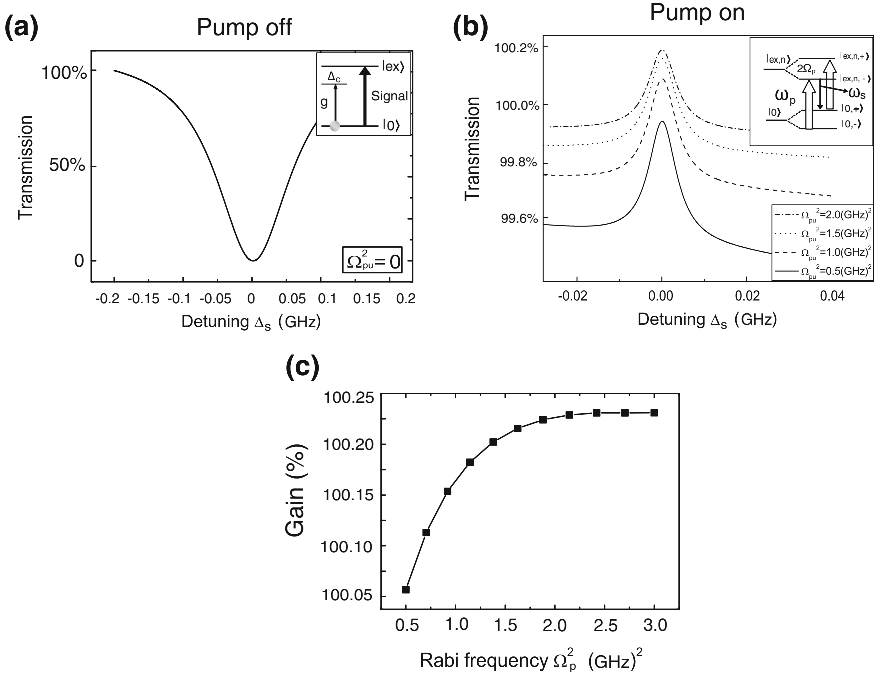

Fig. 9.4 The signal transmission spectrum with the parameters $g = 25\,\text{MHz}$, $\kappa = 8\,\text{MHz}$, $\Delta_p = 0.2\,\text{GHz}$ and $\Delta_c = -0.4\,\text{GHz}$. (**a**) The attenuation spectrum of the signal beam as a function of its frequency detuning from the exciton in the absence of the pump beam. (**b**) When turning on the pump beam, the amplification of signal laser enlarges as the power of pump beam increases. (**c**) The relationship of the magnitude of amplification and the Rabi frequency of pump beam illustrates the characteristic of quantum optical transistor

amplification of the signal beam as shown in Fig. 9.4b. In this case, the pump beam, much like a switch, dramatically controls the transmission of the signal beam. The plots in Fig. 9.4b demonstrate that a single QD can indeed act as an optical transistor when coupled to a single mode nanocavity. The characteristic behavior of these transmission curves are in excellent agreement with the experimental results of a single-molecule optical transistor by Hwang et al. [28]. This amplification behavior is caused by quantum interference between the dressed states while applying two optical fields. The inset of Fig. 9.4b shows the origin of this three-photon resonance physical process. Here the electron makes a transition from the lowest energy level $\mid 0, -\rangle$ to the dressed level $\mid ex, n, +\rangle$ by the simultaneous absorption of two pump photons and emission of a photon at $\Delta_s = 0$, as indicated by the region of amplification of the signal beam in Fig. 9.4b. For more specific description, Fig. 9.4c gives a transistor characteristic curve by plotting the amplification of signal beam as a function of the pump beam power. The gain shown in Fig. 9.4c increases with the increase of pump laser power.

The amplification of the signal laser is a strong evidence for quantum optical transistor with a QD embedded in photonic crystal nanocavity. In the presence of

two optical fields, proper control of the input pump laser leads to the desirable output signal laser on-demand. The output signal laser can be turned off or amplified quickly by turning off or increasing the input pump laser directly. The scheme proposed here will provide an important clue toward the realization of all-optical logic elements and quantum computers.

Light Manipulation Devices in a QD Coupled to a NR System

Bestriding the realms of classical and quantum mechanics, NR has limited environment, small size, high Q factor, and long vibration lifetime, which offers great promise for a huge variety of applications and fundamental research [42–44]. There has been a flurry of activity aiming at the development of NR and its coupled system, such as the detection of qubit-oscillator entanglement in nanomechanical systems by coupling a superconducting qubits [45], the investigation of dynamical properties of a vibrating molecular QD in a Josephson junction [46], and cooling the vibrations of a nanotubes with constant electron current [47]. Recently, Bennett et al. [48] have experimentally studied the strong coupling effects in an electromechanical system consisting of a QD and a mechanical resonator.

The interaction of light with matter can lead to extreme changes of light velocity, i.e., fast light, slow light, and even stored light, which have been investigated in several systems, mainly using electromagnetically induced transparency (EIT), coherent population oscillation (CPO), and stimulated Brillouin scattering (SBS). These phenomena have been investigated in different kinds of media ranging from atomic vapors [49], solid materials [50] to cavity optomechanical system [26]. The first published results of slow light is to minimize the signal absorption based on EIT, while retaining the large contribution to the group index associated with working close to an atomic absorption frequency. Like EIT, CPO is a process that can lead to decreased absorption and rapid spectral variation of the refractive index, and producing a strong slow-light effect. However, CPO is highly insensitive to the presence of dephasing collisions and thus can occur in room-temperature solids. For the light storage device, the major importance in precision measurements and quantum computing tasks is achieving long lifetime of coherence [51]. This requires to seek some special materials, which have relatively long coherence lifetime or elimination of decoherence arising from inhomogeneous external fields and trapping potentials. In atomic system, long coherence times have been observed using clock transitions, which are first-order insensitive to magnetic fields.

In the this section, we theoretically investigate the coupled QD and NR system, and propose three all-optical devices: slow light device, fast light device, and quantum memory device, according to mechanically induced coherent population oscillation (MICPO) [22]. Detailed analysis shows that the signal laser displays the superluminal and ultraslow light characteristics via passing through a coupled QD

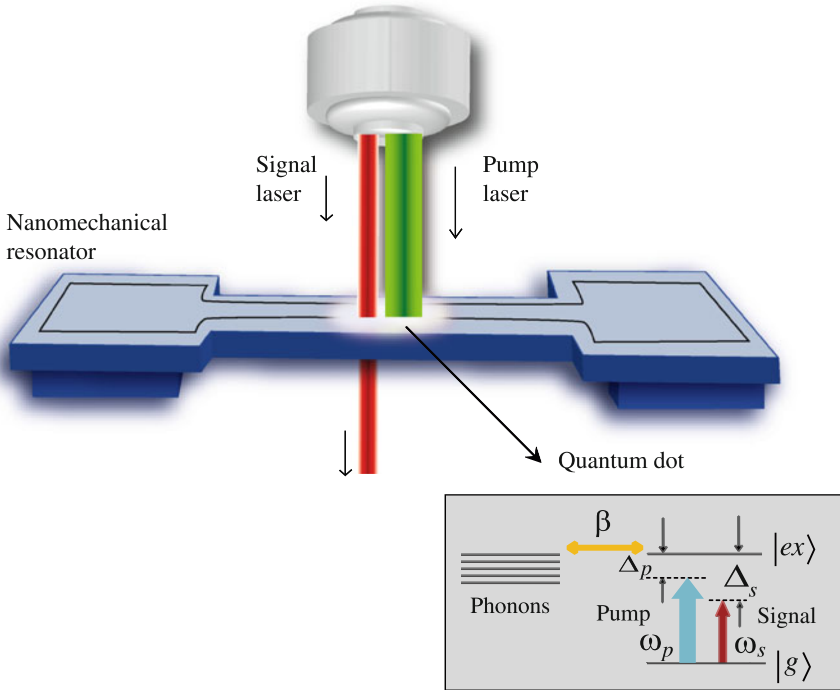

Fig. 9.5 Schematic of a GaAs NR with an embedded InAs QD driven by a strong control laser and probed by a weak signal laser. The inset is energy level description of a QD, while dressing with the vibrational modes of NR. Here the vibrational modes of NR can be treated as phonon modes

and NR system, while the incident pump laser is off-detuned and detuned with the exciton frequency, respectively. And then we demonstrate that it is possible to store and read out the quantum signal pulse in this promising system, by switching off and on the pump pulse, respectively. The vibration of NR leads to the dressed metastable energy level of QD, which provides a temporary accommodation for electrons. This dressed exciton dark-state polaritons can be reaccelerated and converted back into a photon pulse via a tunable pump laser. Thanks to the long lifetime of NR, the signal pulse can stay for a long time compared with other semiconductor systems.

We consider a system composed of a two-level semiconductor quantum dot and a NR in the simultaneous presence of a strong pump field and a weak signal field, as shown in Fig. 9.5. Recently, the two-laser technique has been experimentally demonstrated by Kippenberg et al. [24, 27] in radiation-pressure coupling of an optical and a mechanical mode system. They predicted that this technique can be used for slowing and on-chip storage of light pulses in the future. At low temperatures, the two-level semiconductor QD consists of the ground state $|g\rangle$ and the first excited state (single exciton) $|e\rangle$. The QD via exciton interacts with a strong

pump field (ω_p) and a weak quantum signal field (ω_s). Such NR-QD system has been experimentally demonstrated by Bennett et al. [48] using atomic force microscope (AFM) to probe quantum electronic systems. As usual, the two-level QD system can be characterized by the pseudospin $-1/2$ operators $S^{\pm}$ and S^z. Then the Hamiltonian of this two-level exciton can be described as $H_{\text{ex}} = \hbar\omega_{\text{ex}}S^z$, where ω_{ex} is the frequency of exciton. Besides, we assume the doubly clamped suspended NR vibrates in its fundamental mode [52]. The lowest energy resonance of NR corresponds to the fundamental flexural mode with the frequency ω_n and the resonator is assumed to be characterized by sufficiently high quality factors [52]. The eigenmode of NR can be described by a quantum harmonic oscillator, with a and a^+ the bosonic annihilation and creation operators of energy $\hbar\omega_n$. The Hamiltonian of NR is given by $H_n = \hbar\omega_n a^+ a$.

The Hamiltonian of this coupled QD-nanomechanical resonator and two optical fields in a rotating frame at the pump field frequency ω_p reads as follows [18]

$$H = \hbar\Delta_p S^z + \hbar\omega_n a^+ a + \hbar S^z \omega_n \beta(a^+ + a) - \hbar(\Omega S^+ + \Omega^* S^-) - \frac{\mu}{\hbar}(S^+ E_s e^{-i\delta t} + S^- E_s^* e^{i\delta t}), \tag{9.9}$$

where $\Delta_p = \omega_{\text{ex}} - \omega_p$, β is coupling strength of NR and QD; $\Omega = \mu E_p/\hbar$ is the Rabi frequency of the pump field; E_p and E_s are the slowly varying envelope of the pump field and signal field; μ is the electric dipole moment of the exciton, assumed to be real; $\delta = \omega_s - \omega_p$ is the detuning of the signal and the pump field, respectively.

According to the Heisenberg equation of motion $i\hbar\, \mathrm{d}O/\mathrm{d}t = [O, H]$ and the commutation relation $[S^z, S^{\pm}] = \pm S^{\pm}, [S^+, S^-] = 2S^z$, $[a, a^+] = 1$. The temporal evolutions of the exciton and NR system are given by setting $N = a^+ + a$. For calculations of the absorption spectrum , we can use the semiclassical approach where the optical fields are taken to be classical. The results of calculations in the limits appropriated to this work are read as follows:

$$\frac{\mathrm{d}S^-}{\mathrm{d}t} = [-\Gamma_2 - i(\Delta_p + \omega_n \beta N)]S^- - 2i\Omega S^z - 2i\frac{\mu}{\hbar}E_s e^{-i\delta t} S^z, \tag{9.10}$$

$$\frac{\mathrm{d}S^z}{\mathrm{d}t} = -(S^z + \frac{1}{2})\Gamma_1 + i\Omega(S^+ - S^-) + i\frac{\mu}{\hbar}(S^+ E_s e^{-i\delta t} - S^- E_s^* e^{i\delta t}), \tag{9.11}$$

$$\frac{\mathrm{d}^2 N}{\mathrm{d}t^2} + \gamma_n \frac{\mathrm{d}N}{\mathrm{d}t} + \omega_n^2 N = -2\omega_n^2 \beta S^z, \tag{9.12}$$

where Γ_1 is the exciton relaxation rate, Γ_2 is the exciton dephasing rate, γ_n is the decay rate of the NR due to the coupling to a reservoir of "background" modes and the other intrinsic processes [52]. In order to solve Eqs. 9.10–9.12, we make the ansatz [39] $S^-(t) = S_0 + S_+ e^{-i\delta t} + S_- e^{i\delta t}$, $S^z(t) = S_0^z + S_+^z e^{-i\delta t} + S_-^z e^{i\delta t}$, $N(t) = N_0 + N_+ e^{-i\delta t} + N_- e^{i\delta t}$. Upon working to the lowest order in E_s, but

to all orders in E_p, we can obtain S_+, which corresponds to the linear optical susceptibility as follows: $\chi_{\text{eff}}^{(1)}(\omega_s) = \rho\mu S_+/E_s = \rho\mu^2\chi^{(1)}(\omega_s)/\hbar\Gamma_2$, and the dimensionless susceptibility is given by

$$\chi^{(1)}(\omega_s) = \frac{2Bw_0(\Omega_R^2 + C) - Ew_0}{AE - 2B(\Omega_R^2 + C)(B - \delta_0)}, \tag{9.13}$$

where we have assumed that many QDs couple to a single mechanical resonator, so here ρ is the number density of QDs. $\Gamma_1 = 2\Gamma_2, \omega_{n_0} = \omega_n/\Gamma_2, \gamma_{n0} = \gamma_n/\Gamma_2, \Omega_R = \Omega/\Gamma_2, \delta_0 = \delta/\Gamma_2, \Delta_{p0} = \Delta_p/\Gamma_2$, $A = \Delta_{p0} - \omega_{n0}\beta^2 w_0 - i - \delta_0$, $B = \Delta_{p0} - \omega_{n0}\beta^2 w_0 + i + \delta_0$, $C = \Omega_R^2\omega_{n0}\beta^2\eta w_0/(\Delta_{p0} - \omega_{n0}\beta^2 w_0 - i)$, $D = \Omega_R^2\omega_{n0}\beta^2\eta w_0/(\Delta_{p0} - \omega_{n0}\beta^2 w_0 + i)$, $E = (2\Omega_R^2 + 2D - 2iB - B\delta_0)(B - \delta_0)$, and $\eta = \omega_{n0}^2/(\omega_{n0}^2 - i\delta_0\gamma_{n0} - \delta_0^2)$ is the auxiliary function.

The population inversion of the exciton w_0 is determined by the following equation

$$(w_0 + 1)[(\Delta_{p0} - \beta^2\omega_{n0}w_0)^2 + 1] + 2\Omega_R^2 w_0 = 0. \tag{9.14}$$

In terms of this model, we can determine the light group velocity as $v_g = c/[n + \omega_s(\mathrm{d}n/\mathrm{d}\omega_s)]$, where $n \approx 1 + 2\pi\chi_{\text{eff}}^{(1)}$, and then

$$\frac{c}{v_g} = 1 + 2\pi Re\chi_{\text{eff}}^{(1)}(\omega_s)_{\omega_s=\omega_{\text{ex}}} + 2\pi\omega_s Re\left(\frac{d\chi_{\text{eff}}^{(1)}}{d\omega_s}\right)_{\omega_s=\omega_{\text{ex}}}. \tag{9.15}$$

It is clear from this expression for v_g that when $Re\chi(\omega_s)_{\omega_s=\omega_{\text{ex}}}$ is zero and the dispersion is steeply positive or negative, the group velocity is significantly reduced or increased, and then

$$\frac{c}{v_g} - 1 = \frac{2\pi\omega_{\text{ex}}\rho\mu^2}{\hbar\Gamma_2}Re\left(\frac{\mathrm{d}\chi^{(1)}(\omega_s)}{\mathrm{d}\omega_s}\right)_{\omega_s=\omega_{\text{ex}}} = \Gamma_2\Sigma Re\left(\frac{\mathrm{d}\chi^{(1)}(\omega_s)}{\mathrm{d}\omega_s}\right)_{\omega_s=\omega_{\text{ex}}}, \tag{9.16}$$

where $\Sigma = 2\pi\omega_{\text{ex}}\rho\mu^2/\hbar\Gamma_2^2$.

Figure 9.6 shows the signal absorption spectrum as a function of signal-pump detuning. We notice that there are three prominent features in Fig. 9.6a: the left amplified peak (2), the middle peak (3), and the right absorption peak (4). These new peaks attribute to the longitudinal vibration of NR. In analogy with atomic two-level systems in quantum optics, we call this effect as MICPO. Figure 9.6b gives the origin of these new features. Part (1) of Fig. 9.6b shows the dressed states of exciton ($|n\rangle$ denotes the number states of the NR). Part (2) shows the origin of mechanically induced three-photon resonance. Here the electron makes a transition from the lowest dressed level $|g, n\rangle$ to the highest dressed level $|ex, n+1\rangle$ by the simultaneous absorption of two pump beam photons and emission of a photon at $\omega_p - \omega_n$. This process can amplify a wave at $\delta = -\omega_n$, as indicated by the region of negative absorption in Fig. 9.6a. Part (3) shows the origin of mechanically induced stimulated Rayleigh resonance. The Rayleigh resonance corresponds

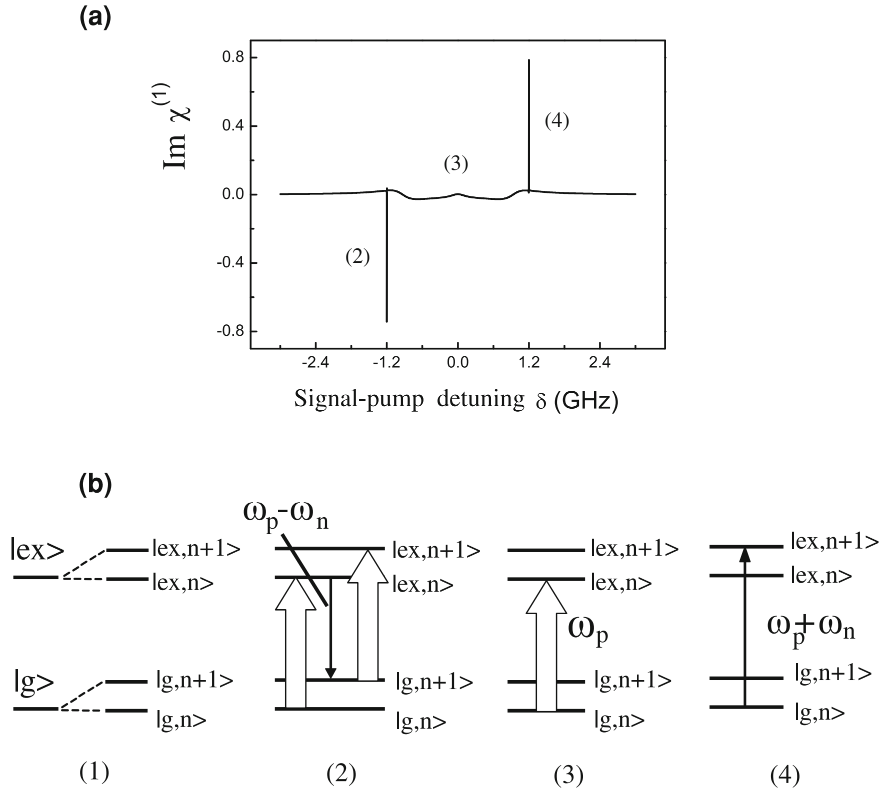

Fig. 9.6 (**a**)The signal absorption spectrum as a function of signal-pump detuning δ. The other parameters used are $\Omega^2 = 0.15\,(\mathrm{GHz})^2$, $\omega_n = 1.2\,\mathrm{GHz}$, $\Delta_p = 1.2\,\mathrm{GHz}$, $\gamma_n = 4 \times 10^{-5}\,\mathrm{GHz}$, and $\beta = 0.06$. (**b**) New features in the spectrum shown in (**a**) are identified by the corresponding transition between the dressed states of the exciton

to a transition from the lowest dressed level $|g,n\rangle$ to the dressed level $|ex,n\rangle$. Each of these transitions is centered on the frequency of the pump field. The rightmost part (4) corresponds to the mechanically induced absorption resonance as modified by the ac Stark effect.

Slow Light and Fast Light

Figure 9.7 displays the fast light and slow light curves in the coupled QD and NR system. The left part shows the slow light spectrum with $\Delta_p = \omega_n$, while the right part exhibits the fast light situation with $\Delta_p = 0$. Figure 9.7a shows the imaginary part and real part of linear optical susceptibility while fixing $\Delta_p = \omega_n$, which correspond to the absorption and dispersion of the signal light, respectively.

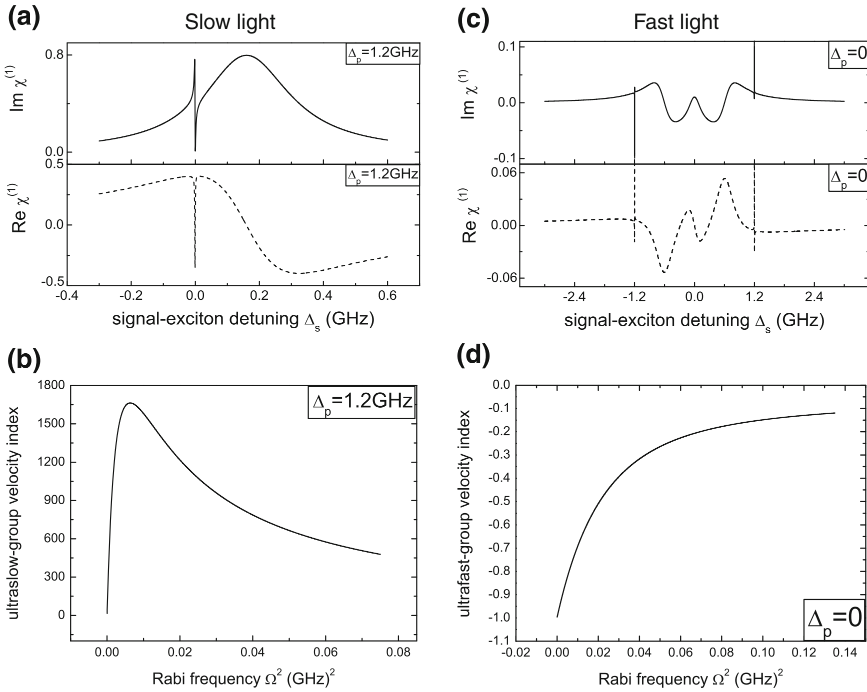

Fig. 9.7 (**a**)The imaginary part and real part of the linear optical susceptibility as a function of the signal detuning form exciton resonance Δ_s with parameters $\Omega^2 = 0.15(\text{GHz})^2$, $\omega_n = 1.2\,\text{GHz}$, $\Delta_p = 1.2\,\text{GHz}$, $\gamma_n = 4 \times 10^{-5}\,\text{GHz}$, and $\beta = 0.06$. (**b**)The group velocity index $n_g(= c/v_g)$ of slow light (in units of Σ) as a function of Rabi frequency of pump laser. (**c**)The absorption and dispersion curves of fast light, while fixing $\Delta_p = 0$. The other parameters are the same with (**a**). (**d**)The group velocity index $n_g(=c/v_g)$ of superluminal light (in units of Σ) as a function of the Rabi frequency of pump laser

From this figure, we find that the the imaginary part has a zero absorption and the real part has a positive steep slope at $\Delta_s = 0$, which signifies the potential of slow light achievement. We next plot the group velocity index of signal laser n_g (in the unit of Σ) as a function of the Rabi frequency Ω^2, as shown in Fig. 9.7b. Figure 9.7b indicates that the output signal pulse can be about 1,800 times slower than input signal pulse in vacuum simply via tuning the $\Delta_p = \omega_n$. Furthermore, in the case of $\Delta_p = 0$, the imaginary part and real part of linear optical susceptibility exhibit zero absorption and negative steep slope at $\Delta_s = 0$ in Fig. 9.7c, which denotes the possibility of superluminal light realization. Figure 9.7d exhibits the fast light curve, where the most fast-light index can be produced in the coupled QD-NR device as 10 times. That is, the output signal pulse can be 10 times faster than the input light with the help of a single NR. The total magnitude of slow light and fast light is determined by the number density of NR. The physical origin of this result is the coupling between exciton and mechanical vibration, which makes

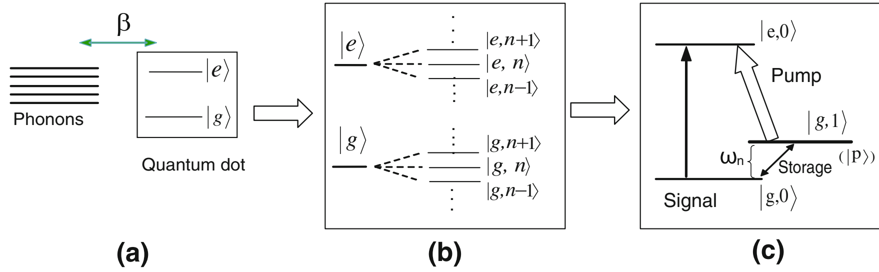

Fig. 9.8 (**a**) The initial model of a two-level QD and a nanomechanical resonator(*NR*). $|g\rangle$ and $|e\rangle$ are the ground state and the excited state of QD, respectively, β is the coupling between the QD and the NR. The vibration modes of NR are treated as phonons modes. (**b**) The split energy levels of QD when dressing with NR. $|g,n\rangle = |g\rangle|n\rangle$ and $|e,n\rangle = |e\rangle|n\rangle$, where $|n\rangle$ denotes the number states of the NR. (**c**) The process of quantum memory for light, where the $|g,1\rangle \rightarrow |e,0\rangle$ and $|g,0\rangle \rightarrow |e,0\rangle$ transitions can be induced by the pump beam and signal beam, respectively. $|g,1\rangle$ denoted by $|p\rangle$ is the metastable state caused by mechanical vibration. The signal pulse is temporarily stored between $|g,1\rangle$ and $|g,0\rangle$

quantum interference between the NR and the two optical fields via the exciton. Such nonlinear process is due to MICPO, which has been discussed in Fig. 9.6.

Here coupling to a mechanical resonator seems to provide the exciton with additional energy level to realize MICPO effect. Therefore in our structure one can obtain the slow and superluminal signal light without absorption only by simply fixing the pump-exciton detuning equal to the frequency of NR and zero, respectively. Actually, this additional energy level produced by the mechanical vibration provides a temporary accommodation for electrons, which makes the long lifetime storage for light to become a reality.

Quantum Memory for Light

Since achieving the slow light and fast light in a coupled NR-QD system, according to MICPO, we next demonstrate that it is possible to store and read out the quantum signal pulse in this promising system, by switching off and on the pump pulse. Detailed analysis shows that the vibration of NR leads to the dressed metastable energy level of QD, which provides a temporary accommodation for electrons. This dressed exciton dark-state polaritons can be reaccelerated and converted back into a photon pulse via a tunable pump laser. Thanks to the long lifetime of NR, the signal pulse can stay for a long time compared with other semiconductor systems.

As shown in Fig. 9.8b, the two-level exciton in QD can be dressed by an infinite number of possible phonon states. Compared with the transition from $|g,n\rangle$ to $|e,n\rangle$, the transition from $|g,n+1\rangle$ to $|e,n+1\rangle$ can be neglected when the system is radiated by a weak signal beam. In Fig. 9.8c, we select $|g,0\rangle$, $|e,0\rangle$ and $|g,1\rangle$ as

a three-level system, while the transition from $|g,0\rangle$ to $|e,0\rangle$ corresponding to the zero-phonon line [53]. The mechanism of quantum memory by adiabatic passage is well-known when the medium is made of lambda three-state atoms. The storage is achieved through the coherence of the atomic ground states. The idea of present work is to replace the lambda atoms by a two-level QD dressed by the NR as done in [52] and to take advantage of the long coherence induced by the resonator.

We follow the treatment in [54, 55], which consists of one propagating beam $\hat{\varepsilon}(z,t)$ passing through a medium of length L. $\hat{\varepsilon}(z,t)$ is a weak signal field that couples the ground state $|g,0\rangle$ and the first excited state $|e,0\rangle$, and is related to the positive frequency part of the electric field by

$$\hat{E}_s^+(z,t) = \sqrt{\frac{\hbar\omega_{\text{ex}}}{2\varepsilon_0 V}}\hat{\varepsilon}(z,t)e^{i(\omega_{\text{ex}}/c)(z-ct)}, \tag{9.17}$$

where ω_{ex} is the frequency of the $|e,0\rangle \to |g,0\rangle$ transition, V is the quantization volume of the electromagnetic field, ε_0 is the free space permittivity, z is the direction along the medium of length L.

In what follows, we introduce the locally averaged, slowly varying operators as $\hat{\sigma}_{\mu\nu}(z_j,t) = \frac{1}{N_{z_j}}\sum_{z_j \in N_z} \hat{\sigma}^j_{\mu\nu}(t)e^{i(\omega_{\mu\nu}/c)(z_j-ct)}$, where $\hat{\sigma}^j_{\mu\nu}(t) = |\mu^j(t)\rangle\langle\nu^j(t)|$ is the jth QD $(\mu,\ \nu = g,e,p)$. In the continuum limit, the effective interaction Hamiltonian for the reduced three-level system can be written as [56]

$$\hat{H} = -\int \frac{N\hbar}{L}[g\hat{\sigma}_{\text{eg}}(z,t)\hat{\varepsilon}(z,t) + \Omega_p\hat{\sigma}_{\text{ep}}(z,t) + \text{H.c.}]\mathrm{d}z, \tag{9.18}$$

where N is the number density of the QD. $g = \mu\sqrt{\omega_{\text{ex}}/2\varepsilon_0 V\hbar}$ is the exciton-quantum signal field coupling constant. $\Omega_p = \langle 1,g|\,\mu_{\text{ep}}\,\mathbf{E(t)}|e,0\rangle/2\hbar$ describes the coupling between the pump field and the transition, where $\mathbf{E(t)}$ is the amplitude of the pump field, μ_{ep} is the electric dipole moment that corresponds to the transition between $|e,0\rangle$ and state $|g,1\rangle$.

We make the approximation that the quantum signal field intensity is much less than the pump field and assume all the excitons are initially in the state $|g,0\rangle$. Then the exciton evolution is governed by a set of Heisenberg-Langevin equations

$$\frac{\partial}{\partial t}\hat{\sigma}_{\text{ge}} = -\gamma_{\text{ge}}\hat{\sigma}_{\text{ge}} + ig\hat{\varepsilon} + i\Omega_p\hat{\sigma}_{\text{gp}} + \hat{F}_{\text{ge}}, \tag{9.19}$$

$$\frac{\partial}{\partial t}\hat{\sigma}_{\text{gp}} = -\gamma_{\text{gp}}\hat{\sigma}_{\text{gp}} + +i\Omega_p\hat{\sigma}_{\text{ge}} + \hat{F}_{\text{gp}}, \tag{9.20}$$

where γ_{ge} and γ_{gp} are the decay rates of $|e,0\rangle \to |g,0\rangle$ and $|g,1\rangle \to |g,0\rangle$, respectively. If we assume the pump laser power changed slowly and neglect the decay rate γ_{gp} of the exciton [54], then $\hat{\sigma}_{\text{ge}}(z,t) \approx -\frac{i}{\Omega_p}\frac{\partial}{\partial t}\hat{\sigma}_{\text{gp}}(z,t)$, $\hat{\sigma}_{\text{gp}}(z,t) \approx -g\frac{\hat{\varepsilon}(z,t)}{\Omega_p}$, and the propagation equation of quantum light pulse in the NR-QD system is written by

$$(\frac{\partial}{\partial t} + c\frac{\partial}{\partial z})\hat{\varepsilon}(z,t) = -\frac{g^2N}{\Omega_p}\frac{\partial}{\partial t}\frac{\hat{\varepsilon}(z,t)}{\Omega_p}. \quad (9.21)$$

We introduce a new quantum field operator $\hat{\Psi}(z,t)$,

$$\hat{\Psi}(z,t) = \cos\theta(t)\hat{\varepsilon}(z,t) - \sin\theta(t)\sqrt{N}\hat{\sigma}_{\mathrm{gp}}(z,t) \quad (9.22)$$

where $\tan^2\theta(t) = g^2N/\Omega_p^2(t)$. The operator $\hat{\Psi}(z,t)$ satisfies the following equation of motion

$$\left[\frac{\partial}{\partial t} + c\cos^2\theta(t)\frac{\partial}{\partial z}\right]\hat{\Psi}(z,t) = 0, \quad (9.23)$$

which describes a shape-preserving propagation with velocity $v = v_g(t) = c\cos^2\theta(t)$. It should be noted here that $\hat{\sigma}_{\mathrm{gp}}(z,t)$ corresponds to the creation operator of the $|g,0\rangle \to |g,1\rangle$, which is different from atomic spin operator as in three-level atomic systems [56]. In the linear limit, this operator obeys the Bosonic commutation relation and we can refer this new Bosonic particle to mechanically induced exciton polariton.

We can decelerate and stop the signal pulse by rotating θ from 0 to $\pi/2$ via a tunable pump laser: (1) when $\theta \to 0$, $\Omega^2 \gg g^2N$ (the strong drive field), the polariton has purely photonic character and the signal propagation velocity equals to the vacuum speed of light, where we have $\hat{\Psi}(z,t) = \hat{\varepsilon}(z,t)$; (2) when $\theta \to \pi/2$, the polariton becomes exciton like, and the signal propagation velocity approaches zero. During this process, the quantum signal field are mapped onto mechanically induced excitons which are different from the atomic spins in three-level atomic systems. The mechanically induced exciton polariton can be reaccelerated to the vacuum speed of light in which the stored quantum states are transferred back to the photonic state. Here, we show an example of the signal storage and recall on demand. When the pump laser is switched off, the signal laser information is stored in the coherence between the $|g,0\rangle$ and $|g,1\rangle$ subbands. Turning on the pump laser results in a retrieved signal pulse. There is no additional distortion during the storage because the width of the signal pulse spectrum is much less than the width of the MICPO window [22].

Furthermore, the features of the field are described as a spin wave in the atomic ensemble, when storing light in atomic systems based on EIT effect. The storage time is determined by the coherence times of the hyperfine transitions. Here, the term "storage " in the NR-QD system denotes the conversion of signal pulse into the electronic coherence σ_{gp}, whose lifetime is determined by the vibrational lifetime of NR. Recently, Verbridge et al. [57] experimentally showed that for a doubly clamped silicon nitride NR, the radiative lifetime of resonator can be reached from 0.8 μs to 0.1 s via different tensile stress. Such data provide us a tunable storage time in the coupled QD and NR system, which means the light storage time can reach a ideal situation if we select a long vibration lifetime of NR.

Conclusions

In summary, based on pump-signal technique, in this chapter we propose some QD devices, such as the quantum optical transistor, the switch from slow light and fast light, and the quantum memory device. On the one hand, we demonstrate that a coupled QD-PC nanocavity system can act as quantum optical transistor media. The signal spectra indicates that this coupled system has the transistor properties such as the switching or amplification of the signal laser, under the radiation of another strong pump laser. This switched or amplified signal laser can be achieved by turning the strong pump laser appropriately via passing through the optical transistor media. Turning on and off the incident pump laser results in the amplification and attenuation of the signal laser, respectively. The pump laser, input signal, and output signal are analogous with the switch, signal carrier, and transmission channel, respectively. On the other hand, we theoretically present a highly efficient optical method to achieve the light manipulation in a coupled system consisting of a NR and a QD, i.e., slow light, fast light, and stopped light, in terms of MICPO. Turning on or turning off the specific detuning of pump field from exciton resonance, this coupling system can provide us a direct optical way to obtain the slow or fast group velocity without absorption. We further find that the vibration of NR leads to the dressed metastable energy level of QD, which provides a temporary accommodation for electrons. This dressed exciton dark-state polaritons can be reaccelerated and converted back into a photon pulse via a tunable pump laser, which realize the long lifetime storage for light. The two-laser technique would give rise to some new all-optical devices and solve some detection disadvantages existing in conventional electric measurement or single-laser technique.

Outlook

One of the most important applications of quantum optical transistor is the all-optical repeater in signal transmission, which may be a good substitute for electronic repeater. A conventional electronic repeater is a signal transmission device, which receives signal and retransmits it with higher power or transfers to another part of the obstacle, in order to make the signal amplified and cover longer distance. However, there are several conditions which limit the development of conventional repeater based on electrons. For example, the charges that electrons carry may interfere with each other and directly affect the signal's quality in turn. Several parts of carried signals may be lost via passing through the electronic repeater due to the perturbation of electrons. Besides, the transmission speed and the working temperature of electrons also limits the performance of electronic repeaters. With this backdrop, an optical-electrical-optical (OEO) repeater is invented in a fiber-optic communication system to regenerate an optical signal by

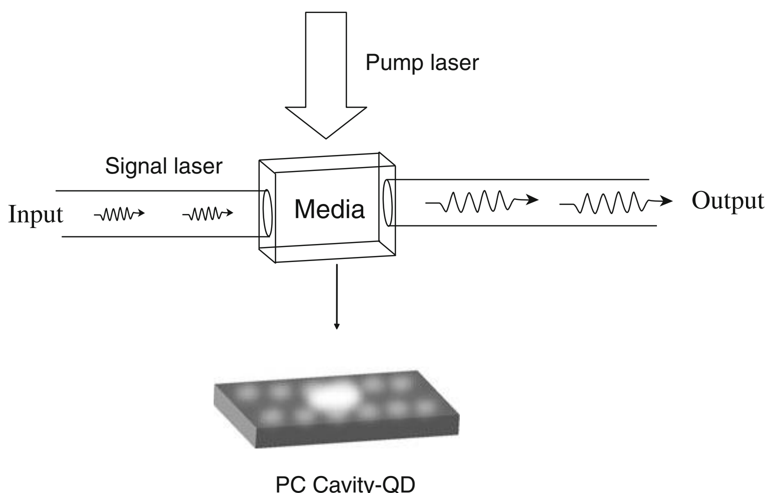

Fig. 9.9 Quantum optical transistor, in which the pump laser, input signal, and transmission media are in analogy with switch, signal carrier, and transmission channel, respectively. The transmission media can be a single QD embedded in a PC nanocavity, which has been discussed in "A Quantum Optical Transistor with a Single QD in a Photonic Crystal Nanocavity"

converting it to an electrical signal, processing electrical signal, and retransmitting it to optical signal. Unfortunately, there are several problems limiting the performance of OEO repeater, i.e., one wavelength of the signal requires one OEO repeater to support, thus many different wavelengths of light signal transmission require a lot of repeaters, which require a lot of equipments for each fiber. In this case, the practical OEO repeaters based on optical fibers are expensive and difficult to construct.

Figure 9.9 shows a simple model of all-optically controlled transistor, which consists of a weak signal laser to carry signals, a strong pump laser, and a specific transmission media. During the all-optical process, the pump laser like a switch supervises the magnitude of signal laser, where turning on and off the pump laser corresponds to the output signal on and off, respectively. Regulating the pump laser appropriately can make the output signal amplified efficiently. The optical transistor media will act as a light transmission channel while the strong pump laser serves as a switch controlling the signal light transmission through the transmission media. But most importantly, the key element of quantum optical transistor is the transmission media which generates the switch behavior and amplified behavior simultaneously. Obviously, the transmission media can be the coupled QD-photonic crystal system, which has some well-known advantages such as lower cost and mature production process. We believe that quantum optical transistors will make quantum internet and quantum information technology easier and faster, and bring people's life into a new chapter.

Acknowledgements This work was supported by the Natural Science Foundation of China (No. 10774101 and No. 10974133), the National Ministry of Education Program for Ph.D., the Foundation for Excellent Doctoral Dissertation of Shanghai Jiao Tong University, the Award for Excellent New Doctoral Student (Ministry of Education), and the Key Laboratory of Artificial Structures and Quantum Control (Ministry of Education).

References

1. Amos, S.W., James, M.R.: Principles of transistor circuits. 9th edn. Elsevier (1969)
2. Bunis, M., Bunis, S.: Collector's guide to transistor radios identification and values, collector books publisher, Paducah (1996)
3. Ooi, C.H.R.: Controlling irreversibility and directionality of light via atomic motion: optical transistor and quantum velocimeter. New J. Phys. **10**, 123024 (2008)
4. Kalithasan, B., Porsezian, K., Dinda, P.T.: Modulational instability in resonant optical fiber with higher-order dispersion effect. J. Opt. **12**, 035210 (2010)
5. Zhang, J.J., Wang, Z.L., Liu, J., Chen, S., Liu, G.: Self-assembled nanostructures. Kluwer Academic/Plenum Publishers, NY (2003)
6. Fu, A., Gu, W.W., Larabell, C., Alivisatos, A.P.: Semiconductor nanocrystals for biological imaging. Curr. Opin. Neurobiol. **15**, 568 (2005)
7. Jabbour, G.E., Doderer, D.: Quantum dot solar cells: the best of both worlds. Nat. Photonics **4**, 604 (2010)
8. Liu, H.C.: Quantum dot infrered photodetector. Opto-electron. Rev. **11**, 1–5 (2003)
9. Bimberg, D., Grundmann, M., Ledentsov, N.N.: Quantum dot heterostructures. Wiley, Chichester (1999)
10. Imamoḡlu, A., Awschalom, D.D., Burkard, G., DiVincenzo, D.P., Loss, D., Sherwin, M., Small, A.: Quantum information processing using quantum dot spins and cavity QED. Phys. Rev. Lett. **83**, 4204–4207 (1999)
11. Heiss, D., Jovanov, V., Caesar, M., Bichler, M., Abstreiter, G., Finley, J.J.: Selective optical charge generation, storage, and readout in a single self-assembled quantum dot. Appl. Phys. Lett. **94**, 072108 (2009)
12. Kłopotowskia, L., Gorycab, M., Kossackib, P., Kudelski, A., Krebs, O., Wojnara, P., Wojtowicza, T., Karczewskia, G.: Charge storage in self-assembled CdTe quantum dots. J. Phys.: Conf. Ser. **210**, 012007 (2010)
13. Chang, C.-C., Sharma, Y.D., Kim, Y.-S., Bur, J.A., Shenoi, R.V., Krishna, S., Huang, D., Lin, S.-Y.: A surface plasmon enhanced infrared photodetector based on InAs quantum dots. Nano Lett. **10**, 1704–1709 (2010)
14. Wang, H., Zhu, K.D.: Coherent optical spectroscopy of a hybrid nanocrystal complex embedded in a nanomechanical resonator. Opt. Express **18**, 16175 (2010)
15. Wang, H., Zhu, K.D.: Large optical Kerr effect in a nanocrystal complex coupled to a nanomechanical resonator. Europhys. Lett. **92**, 47008 (2010)
16. Posani, K.T., Tripathi, V., Annamalai, S., Weisse-Bernstein, N.R., Krishna, S., Perahia, R., Crisafulli, O., Painter, O.J.: Nanoscale quantum dot infrared sensors with photonic crystal cavity. Appl. Phys. Lett. **88**, 151104 (2006)
17. Li, J.J., Zhu, K.D.: A tunable optical Kerr switch based on a nanomechanical resonator coupled to a quantum dot. Nanotechnol. **21**, 205501 (2010)
18. Li, J.J., Zhu, K.D.: An efficient optical knob from slow light to fast light in a coupled nanomechanical resonator-quantum dot system. Opt. Express **17**, 19874–19881 (2009)
19. Li, J.J., Zhu, K.D.: A quantum optical transistor with a single quantum dot in a photonic crystal nanocavity. Nanotechnology **22**, 055202 (2011)
20. Li, J.J., Zhu, K.D.: A scheme for measuring vibrational frequency and coupling strength in a coupled annomechancial resonator-quantum dto system, Appl. Phys. Lett. **94**, 063116–063118, 249903 (2009)

21. Li, J.J., Zhu, K.D.: Quantum memory for light with a quantum dot system coupled to a nanomechanical resonator. Quantum Inf. Comput. **11**, 0456–0465 (2011)
22. Li, J.J., Zhu, K.D.: Mechanical vibration-induced coherent optical spectroscopy in a single quantum dot coupled to a nanomechanical resonator. J. Phys. B **43**, 155504 (2010)
23. Li, J.J., Zhu, K.D.: Coherent optical spectroscopy due to lattice vibrations in a single quantum dot. Eur. Phys. J. D **59**, 305–308 (2010)
24. Weis, S., Rivière, R., Deléglise, S., Gavartin, E., Arcizet, O., Schliesser, A., Kippenberg, T.J.: Optomechanically induced transparency. Science **330**, 1520 (2010)
25. Teufel, J.D., Li, D., Allman, M.S., Cicak, K., Sirois, A.J., Whittaker, J.D., Simmonds, R.W.: Circuit cavity electromechanics in the strong-coupling regime. Nature **471**, 204–208 (2011)
26. Safavi-Naeini, A.H., Mayer Alegre, T.P., Chan, J., Eichenfield, M., Winger, M., Lin, Q., Hill, J.T., Chang, D.E., Painter, O.: Electromagnetically induced transparency and slow light with optomechanics. Nature **472**, 69–73 (2011)
27. Verhagen, E., Deléglise, S., Weis, S., Schliesser, A., Kippenberg, T.J.: Quantum-coherent coupling of a mechanical oscillator to an optical cavity mode. Nature **482**, 63–67 (2012)
28. Hwang, J., Pototschnig, M., Lettow, R., Zumofen, G., Renn, A., Götzinger, S., Sandoghdar, V.A.: Single-molecule optical transistor. Nature **460**, 76–80 (2009)
29. Nomura, M., Kumagai, N., Iwamoto, S., Ota, Y., Arakawa, Y.: Laser oscillation in a strongly coupled single-quantum-dot-nanocavity system. Nat. Phys. **6**, 279–283 (2010)
30. Mücke, M., Figueroa, E., Bochmann, J., Hahn, C., Murr, K., Ritter, S., Villas-Boas, C.J., Rempe, G.: Electromagnetically induced transparency with single atoms in a cavity. Nature **465**, 755–758 (2010)
31. Faraon, A., Majumdar, A., Kim, H., Petroff, P., Vučković, J.: Fast electrical control of a quantum dot strongly coupled to a nano-resonator. Phy. Rev. Lett. **104**, 047402–047405 (2010)
32. Chauvin, N., Zinoni, C., Francardi, M., Gerardino, A., Balet, L., Alloing, B., Li, L.H., Fiore, A.: Controlling the charge environment of single quantum dots in a photonic-crystal cavity. Phys. Rev. B **80**, 241306–241309(R) (2009)
33. Arlandis, J., Centeno, E., Pollès, R., Moreau, A., Campos, J., Gauthier-Lafaye, O., Monmayrant, A.: Mesoscopic self-collimation and slow light in all-positive index layered photonic crystals. Phys. Rev. Lett. **108**, 037401 (2012)
34. Figotin, A., Vitebskiy, I.: Slow wave phenomena in photonic crystals. Laser Photonics Rev. **5**, 201–213 (2011)
35. Kim, M.-K., Kim, J.-Y., Kang, J.-H., Ahn, B.-H., Lee, Y.-H.: On-demand photonic crystal resonators. Laser Photonics Rev. **5**, 479–495 (2011)
36. Yoshie, T., Scherer, A., Hendrickson, J., Khitrova, G., Gibbs, H.M., Rupper, G., Ell, C., Shchekin, O.B., Deppe, D.G.: Vacuum Rabi splitting with a single quantum dot in a photonic crystal nanocavity. Nature **432**, 200–203 (2004)
37. Gardiner, C.W., Zoller, P.: Quantum noise. Springer Verlag, Berlin (2005)
38. Scully, M.O., Zubairy, M.S.: Quantum optics. Cambridge University Press, Cambridge (1997)
39. Boyd, R.W.: Nonlinear optics, pp. 313. Academic, Amsterdam (2008)
40. Purcell, E.M.: Spontaneous emission probabilities at radio frequencies. Phys. Rev. Lett. **69**, 681 (1946)
41. Duan, L.-M., Kimble, H.J.: Scalable photonic quantum computation through cavity-assisted interactions. Phys. Rev. Lett. **92**, 127902 (2004)
42. Safavi-Naeini, A.H., Chan, J., Hill, J.T., Alegre, T.P.M., Krause, A., Painter, O.: Observation of quantum motion of a nanomechanical resonator. Phys. Rev. Lett. **108**, 033602 (2012)
43. Massel, F., Heikkilä, T.T., Pirkkalainen, J.-M., Cho, S.U., Saloniemi, H., Hakonen, P.J., Sillanpää M., A.: Microwave amplification with nanomechanical resonators. Nature **480**, 351–354 (2011)
44. Bagheri, M., Poot, M., Li, M., Pernice, W.P.H., Tang H., X.: Dynamic manipulation of nanomechanical resonators in the high-amplitude regime and non-volatile mechanical memory operation. Nat. Nanotechnol. **6**, 726–732 (2011)

45. Schmidt, T.L., Børkje, K., Bruder, C., Trauzettel, B.: Detection of qubit-oscillator entanglement in nanoelectromechanical systems. Phys. Rev. Lett. **104**, 177205 (2010)
46. Fransson, J., Balatsky, A.V., Zhu, J.X.: Dynamical properties of a vibrating molecular quantum dot in a Josephson junction. Phys. Rev. B **81**, 155440 (2010)
47. Zippilli, S., Bachtold, A., Morigi, G.: Ground-state-cooling vibrations of suspended carbon nanotubes with constant electron current. Phys. Rev. B **81**, 205408 (2010)
48. Bennett, S.D., Cockins, L., Miyahara, Y., Grütter, P., Clerk, A.A.: Strong electromechanical coupling of an atomic force microscope cantilever to a quantum dot. Phys. Rev. Lett. **104**, 017203 (2010)
49. Wu, B., Hulbert, J.F., Lunt, E.J., Hurd, K., Hawkins, A.R., Schmidt, H.: Slow light on a chip via atomic quantum state control. Nat. Photonics **4**, 776 (2010)
50. Stepanov, S., Sánchez, M.P.: Slow and fast light via two-wave mixing in erbium-doped fibers with saturable absorption. Phys. Rev. A **80**, 053830 (2009)
51. Dudin, Y.O., Zhao, R., Kennedy, T.A.B., Kuzmich, A.: Light storage in a magnetically dressed optical lattice. Phys. Rev. A **81**, 041805 (2010)
52. Wilson-Rae, I., Zoller, P., Imamoḡlu, A.: Laser cooling of a nanomechanical resonator mode to its quantum ground state. Phys. Rev. Lett. **92**, 075507 (2004)
53. Mahan, G.D.: Many-particle physics, 2nd edn. pp. 304. Plenum Press, NY (1990)
54. Fleischhauer, M., Lukin, M.D.: Quantum memory for photons: dark-state polaritons. Phys. Rev. A **65**, 022314 (2002)
55. Peng, A., Johnsson, M., Bowen, W.P., Lam, P.K., Bachor, H.A., Hope, J.J.: Squeezing and entanglement delay using slow light. Phys. Rev. A **71**, 033809 (2005)
56. Fleischhauer, M., Lukin, M.D.: Dark-state polaritons in electromagnetically induced transparency. Phys. Rev. Lett. **84**, 5094 (2000)
57. Verbridge, S.S., Shapiro, D.F., Craighead, H.G., Parpia J., M.: Macroscopic tuning of nanomechanics: substrate bending for reversible control of frequency and quality factor of nanostring resonators. Nano Lett. **7**, 1728 (2007)

Chapter 10
Quantum Dot Switches: Towards Nanoscale Power-Efficient All-Optical Signal Processing

Chao-Yuan Jin, Mark Hopkinson, Osamu Kojima, Takashi Kita, Kouichi Akahane and Osamu Wada

Abstract Photonic devices employing semiconductor quantum dots (QDs) are anticipated to play an important role within power-efficient optical networks. In this chapter, we consider the prospects for signal processing using all-optical QD switches. Vertical cavity structures have been developed to enhance the light-QD interaction and accordingly the optical nonlinearity of QDs which leads to low

C.-Y. Jin (✉)
COBRA Research Institute and Department of Applied Physics,
Eindhoven University of Technology, 5600 MB, Eindhoven, The Netherlands
e-mail: c.jin@tue.nl

M. Hopkinson
Department of Electronic and Electrical Engineering, University of Sheffield,
Sheffield, S1 3JD, UK
e-mail: m.hopkinson@sheffield.ac.uk

O. Kojima · T. Kita
Department of Electrical and Electronic Engineering,
Graduate School of Engineering, Kobe University, Kobe, 657-8501, Japan
e-mail: kojima@phoenix.kobe-u.ac.jp

T. Kita
e-mail: kita@eedept.kobe-u.ac.jp

K. Akahane
National Institute of Information and Communications Technology,
Tokyo, 184-8795, Japan
e-mail: akahane@nict.go.jp

O. Wada
Division of Frontier Research and Technology,
CREATE and Department of Electrical and Electronic Engineering,
Graduate School of Engineering, Kobe University, Kobe, 657-8501, Japan
e-mail: owada@kobe-u.ac.jp

Z. M. Wang (ed.), *Quantum Dot Devices*, Lecture Notes in Nanoscale Science and Technology 13, DOI: 10.1007/978-1-4614-3570-9_10,
© Springer Science+Business Media New York 2012

energy consumption. Such structures show great potential for the realization of power-efficient, polarization-insensitive and micrometer-size switching devices for future photonic signal processing systems.

Introduction

Semiconductor quantum dots (QDs) are known to demonstrate electronic structure resembling that of an artificial atom. Specifically they exhibit three dimensional confined quantum states localized within nm-sized clusters [1]. During the past 2 decades, the unique nature of their δ-function-like density of states has lead to the demonstration of a number of revolutionary photonic device concepts [2], with the prospect of temperature-insensitive lasing characteristics initially predicted to be one of the major merits of QD-based photonic devices [3].

In the 1980s, Goldstein et al. demonstrated the possibility to self-assemble three dimensional InAs clusters in a GaAs matrix by molecular beam epitaxy (MBE) [4]. The clusters are formed by a surface instability which occurs when the thickness of the highly mismatched InAs exceeds a certain value ($\sim$0.5 nm). Over the next 2 decades this method, commonly ascribed as the Stransky–Krastanov growth mode [5], has made it possible to construct defect-free laser diodes based on semiconductor nanostructures. Following the first demonstration in 1994 [6], the performance of QD lasers has improved considerably with a significantly lower threshold and higher temperature stability achieved by many research groups [7–10].

In the meantime, QDs have found their various applications in ultrafast photonics. The ultrabroad optical spectrum of self-assembled QDs has been utilized as an absorption saturator in mode-locked QD lasers and QD semiconductor saturable absorber mirrors (QD-SESAMs) [11]. QD semiconductor optical amplifiers (QD-SOAs) have also been extensively investigated. Under high current injection such devices can demonstrate sub-picosecond ($<10^{12}$ s) gain recovery times [12, 13]. With this impressive early-stage performance, it is anticipated that QD photonic devices could constitute indispensable components in the future signal processing network and have a significant potential to be operated up to 1 Tb/s.

Current Status of QD-Based Ultrafast Photonic Devices

Although semiconductor QDs have already shown their promise in various device applications, the practical advantages of QDs for ultrafast photonic devices are somewhat debated when compared to their counterparts such as quantum well (QW) devices. In Table 10.1, we attempt to list the current status of several typical QD devices which might find their way in the application of future optical signal processing systems. We can conclude from the table that QD-based ultrafast

Table 10.1 Current status of QD-based ultrafast devices and their major advantages compared to their QW counterparts

QD Devices	Ultrafast parameters	Advantages compared to QW devices
Lasers	Direct modulation bandwidth = 11 GHz [14] for ridge-waveguide lasers, 13.7 GHz for QD-VCSELs [15][a]	Low threshold current [7], temperature-insensitive threshold [9, 10] and emission wavelength [16]
Mode-locked lasers	Repetition rate = 80 GHz [17], pulse width = 393 fs [18]	Ultra low noise [19], high temperature stability [20], ultralow jitter [21]
SOAs	Recovery time = 170 fs [22], repetition rate = 40 GHz [23]	Low noise figure [24], broad bandwidth [25], pattern effect free [23]
SESAMs	Recovery time = 820 fs [11]	Broad bandwidth [26]
All-optical switches	Switching time = 16 ps [27], repetition rate = 40 GHz [28]	Broad bandwidth [29], low operation power [30]

[a] For QD vertical cavity surface emitting lasers (QD-VCSELs), the current reported results show 13.7 GHz modulation bandwidth (- 3 dB) based on submonolayer QDs emitting at 980 nm [15]. The modulation bandwidth of QD-VCSELs at communication wavelength (* 1.31/1.55 μm) is still below 10 GHz. This would be an important reason to investigate external modulation using optical switches/modulators.

devices could offer operation speeds from 10 to 100 GHz or even higher. This performance is potentially competitive to QW-based photonic devices that have been employed in present optical networks.

The major advantages of QD-based devices include: (1) Power efficiency, as shown in low-threshold QD lasers and low-operation-power QD all-optical switches. (2) High thermal stability, as shown in temperature-insensitive lasers and ultralow-noise pattern-effect-free QD-SOAs. (3) Broad bandwidth, as shown in SOA, SESAMs and also being applied as broadband incoherent sources (super-luminescent diodes). These three advantages construct a solid ground for QD devices to be naturally attractive for the application in future power-efficient optical networks or sometimes referred as "Green internet" in a macro scale [31], which requires low-power, low-noise and broadband operation.

Power-Efficient All-Optical QD Switches

One of the key devices to establish a high-bit-rate optical network is an optical switch which functions within an ultra-short delay time [32]. The idea of using all-optical switches to replace present day optoelectronic switches is driven by the power hungry nature of the electronic to optical conversion. There is also a speed

limitation for any electronic interface; despite impressive advancements in materials and device technology, the current record f_{max} of any transistor technology lies at around 700 GHz [33], and the speed record of the off-chip interconnection is at around 10 Gb/s [34]. The all-optical switch controls optical signals directly by another light beam without the need for an electronic interface. With potential recovery times in the picosecond range (or lower) has the capability for terahertz switching speeds. Its availability would provide therefore a promising step towards a high speed, cost-effective and power-efficient networks.

Despite the inherent advantages of the all-optical approach there is a major problem to source an optimum non-linear material to act as the switching medium. For most optical materials the excitation power required to access to the nonlinear operation regime is fairly high and device performance is therefore limited (the well-known problem of the "power/speed trade-off" [35, 36]). For the development of optical networks between chips and at chip level, the required energy per pulse is expected to be less than 1 pJ/bit [37, 38]. Most of the existing candidates for all-optical switching would fail this target [32, 39]. However, as we discussed above, semiconductor nanostructures such as QDs may be able to meet such a system goal as a consequence of their small volume and atom-like density of states which leads to very high differential gain/absorption parameters. For this reason, QD based structures are anticipated to generate high optical nonlinearity with ultralow energy consumption.

Figure 10.1 shows a schematic diagram of the all-optical switch using self-assembled InAs/GaAs QDs. The QD image is typical of that obtained by atomic force microscopy and shows an ensemble of QDs with an average surface density $N_{QD} = 3 \times 10^{10}\ \mathrm{cm}^{-2}$. Due to the state filling effect in QDs, one dot only absorbs one phonon and as it does this it moves from absorption to transparency [40]. Assuming that the control light is fully absorbed by the QDs and turns the QD from absorption to transparency, the total energy consumption can be shown to be:

$$E = h\nu N_{QD}\Gamma\sigma \cong 0.05\, fJ/\mu\mathrm{m}^2 \times \alpha V \tag{10.1}$$

where $\Gamma \approx \alpha L$ is absorption in QDs, α is the absorption coefficient, σ is the effective absorption cross section, L is the effective length of the QD region, and V is the effective volume. Although the above equation depends on the particular device geometry employed, it is clear that ultra low energy consumption of less than femto-joule per pulse is possible in principle for these QD nanostructures. In comparison QW materials have density of states values above two orders of magnitude larger than QDs and therefore the transition to transparency in these materials requires correspondingly higher pulse energies.

Optical Nonlinearity and Carrier Dynamics

In addition to the power efficiency, two other parameters, the differential reflectivity (or transmission) and the switching time, are particularly important for the characterization of all-optical switches [32]. In the case of QD switches, these

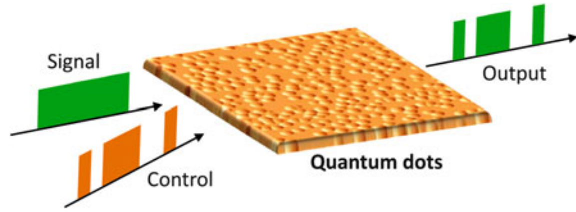

Fig. 10.1 Schematic diagram of all-optical switching using self-assembled QDs. The QD image is obtained from atomic force microscopy

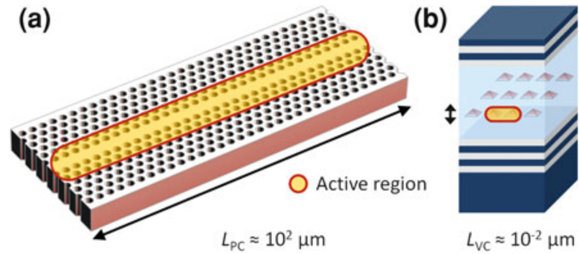

Fig. 10.2 Schematic comparison between two QD switches using (**a**) photonic crystal waveguides, and (**b**) vertical cavities

parameters correspond to two major limitations of QDs, i.e. (1) the magnitude of the optical nonlinearity and (2) the speed of the carrier dynamics.

Firstly, the effective cross section and interaction length are extremely small in self-assembled QDs due to their dispersive distribution in both real and frequency space. An enhancement of the light-QD interaction is therefore required in practical devices to achieve high optical nonlinearity and through this a high differential reflectivity (or transmission). The problem of the weak interaction of light with QDs can be partially solved by combining QDs with either two dimensional photonic crystal waveguides or vertical cavities [29, 41]. Figure 10.2 shows schematically a photonic crystal waveguide switch and a vertical cavity switch. For the photonic crystal waveguide case, the waveguide size is of a few hundred microns aside with hundreds of photonic air holes, which makes the device relatively large area and potentially high cost. From Eq. 10.1, a large effective QD volume in the photonic crystal waveguide will also consume more energy. From a power efficiency point of view, vertical cavity QD switches would be a better choice. The vertical cavity, also known as a one-dimensional photonic crystal, enhances the light-QD interaction whilst preserving the advantage of low energy consumption. Such a vertical geometry structure could potentially provide power-efficient, polarization-insensitive and micrometer-size switching devices based on QD materials.

The second issue we must address is the carrier dynamics of the QDs. There is nothing intrinsically fast about QD interband transitions compared to say QW devices. The presence of such relatively slow recombination rates can limit the switching performance of the device. As with QW materials it is possible to introduce non-radiative channels using such methods as impurity doping or low-temperature growth [42]. However, these methods reduce the absorption strength and hence degrade the optical nonlinearity. Such methods could be employed with

QDs, however, due to the low absorption values the application of defect-related methods needs to be handled extremely carefully. Fortunately, the presence of discrete energy states in the QDs offers another routing mechanism to manipulate the switching dynamics. The fast inter-subband carrier relaxation between QD high energy states and the ground state can be utilized to enhance the device performance.

This Chapter is organized as follows: We first describe the theory for the design of vertical cavities in Section "Design of Vertical Cavities". In Section "Growth of the Vertical Cavity and QDs", we present the growth of QD nanostructures. In Section "Switching Based on Absorption Nonlinearity", the device characterization and faster switching using interband transitions are discussed. We also show the initial results to utilize vertical cavity QD switches as a phase modulator in Section "Exploring the Phase Properties". Finally, we summarize our work in Section "Summary".

Design of Vertical Cavities

Zero Reflection Condition

Figure 10.3 schematically illustrates the operation principle of a QD switch using a vertical Febry-Perot (FP) cavity. The cavity consists of two distributed Bragg reflector (DBR) mirrors which consist of multiple pairs of alternating high and low refractive index layers. The two DBR mirrors are named the front and back mirrors according to the output direction. Each individual layer of the DBR mirror has a thickness of $\lambda/4n$, where λ is the operation wavelength and n is the refractive index of the corresponding layers. The cavity region between two DBR mirrors has a thickness L equal to an integer multiple of $\lambda/2n$, which is the so-called λ cavity. When a λ-cavity is considered, the reflectivity at the cavity mode is expressed as [30],

$$R_{\mathrm{CM}} = R_{\mathrm{F}} \left[\frac{1 - (R_{\mathrm{B}}/R_{\mathrm{F}})^{1/2} e^{-\Gamma}}{1 - (R_{\mathrm{B}} R_{\mathrm{F}})^{1/2} e^{-\Gamma}} \right]^2, \tag{10.2}$$

where R_{F} and R_{B} are the reflectivity of the front and back mirrors, respectively, and $\Gamma = 2\int_L \alpha(l)dl$ is the integrated absorption in QDs

When signal light is injected into the cavity, the light reflected by the front mirror can be fully cancelled by the effective reflection from the back mirror at the cavity resonant mode with these two reflected beams out of phase with one another. This mechanism has been employed in vertical-geometry optical switches using both QW and bulk materials [42–44]. This so-called 'zero reflectivity condition' can be described by the relation between the front and back reflectivity [30]

$$R_{\mathrm{F}} = R_{\mathrm{B}} e^{-2\Gamma}, \tag{10.3}$$

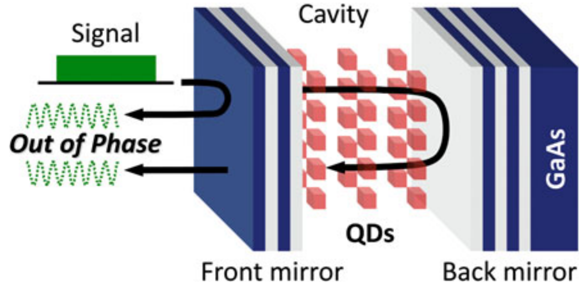

Fig. 10.3 Schematic diagram for the operation principle of an all-optical switch using QDs in a vertical cavity. Zero reflectivity at cavity resonant mode holds when two reflected light beams from the front and back mirrors are out of phase

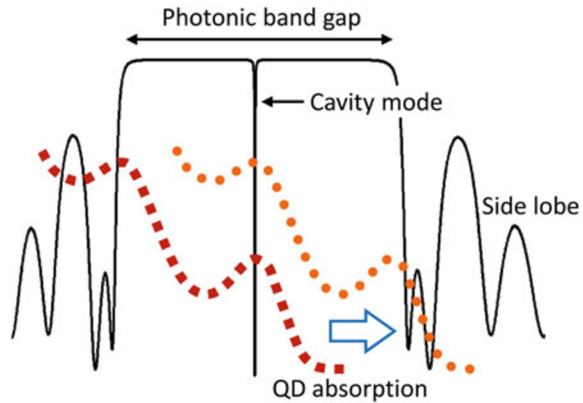

Fig. 10.4 Cavity reflectivity spectrum shown under the zero reflectivity condition (*solid curve*). The QD absorption spectra are plotted with GS (*solid squares*) and ES (*solid circles*) transitions matching at the cavity mode

where R_F and R_B are the optical reflectivity of the front and back mirrors at the cavity resonant mode, respectively.

Figure 10.4 presents a typical reflectivity spectrum from a λ cavity at the zero reflectivity condition. A photonic bandgap region can be observed with high reflectivity close 100%. At the cavity resonant mode, the light beam can fully penetrate into the cavity without reflection when the zero reflectivity condition holds. When strong optical pumping occurs at the cavity resonant mode, the absorption of the QDs saturates. This disturbs the zero reflectivity condition and the device switches mode. Efficient switching requires high differential reflectivity between the operation states of with and without optical pumping. To achieve a high differential reflectivity, the cavity should be operated under the following design criterion

$$R_F = \left(\frac{\sqrt{3} R_B^{1/2} e^{-\Gamma} - 1}{\sqrt{3} - R_B^{1/2} e^{-\Gamma}} \right)^2 < R_B e^{-2\Gamma}. \tag{10.4}$$

It should be noted that the above equations are derived at the cavity resonant wavelength. Both equations require an asymmetric geometry of the cavity. In the case of QW or bulk materials, a large Γ value exists, which suggests a small

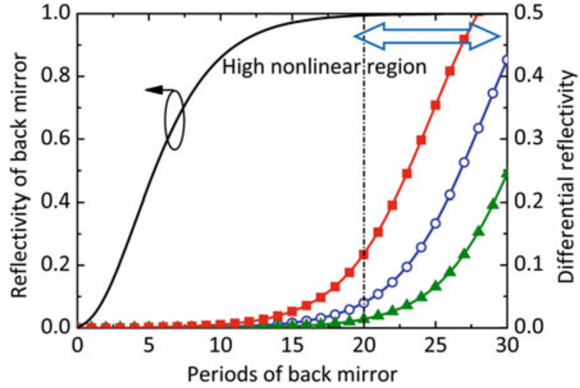

Fig. 10.5 The QD/cavity nonlinearity represented by the differential reflectivity at the cavity mode with $\Gamma = 1 \times 10^{-4}$ (*open triangles*), 3×10^{-4} (*open circles*) and 1×10^{-3} (*solid squares*), respectively

reflectivity of the front mirror. A low-finesses cavity therefore works well for QW and bulk materials [42, 43]. However, the Γ value is extremely small for QD structures, normally at a magnitude order of 10^{-4}. Hence, a high-finesse design needs to be employed for the QD switch.

Absorption Nonlinearity

To study the absorption nonlinearity of the QD-cavity combination, the relation between the front and back mirror periods is fixed at the maximum differential reflectivity condition. In Fig. 10.5, the cavity reflectivity with different periods of the back mirror is simulated by using Eq. 10.4. When the period of the back mirror increases, the reflectivity of the back mirror is significantly enhanced. After exceeding 20 periods, the reflectivity of the back mirror almost reaches one, whilst the differential reflectivity of vertical cavities increases rapidly. Three test values of Γ are used in the figure, with $\Gamma = 1 \times 10^{-4}$ (open triangles), 3×10^{-4} (open circles) and 1×10^{-3} (solid squares), respectively. The region of 20–30 periods of the back mirror is so-called the high nonlinear region where we focused for the design of QD switches.

Nonlinear Refractive Index

The refractive index change due to the Kramers–Krönig relation is usually considered as another optical nonlinear mechanism induced by the absorption nonlinearity, which can be described as [45],

$$\Delta n(\omega) = \frac{c}{\pi} P \int_0^{\infty} \frac{\Delta\alpha(\omega\prime)}{\omega\prime^2 - \omega^2} d\omega\prime \qquad (10.5)$$

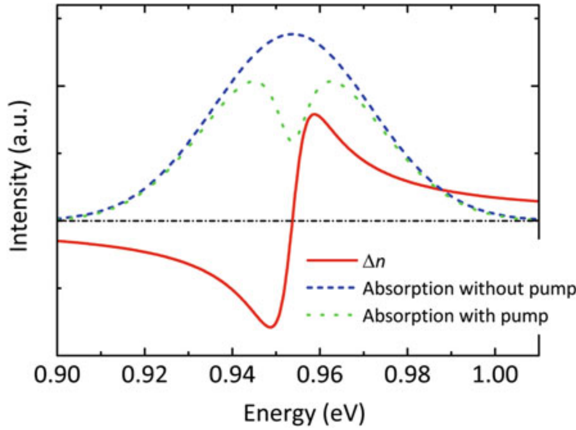

Fig. 10.6 The refractive index change within the QD ensemble calculated by using the Kramers-Krönig relation

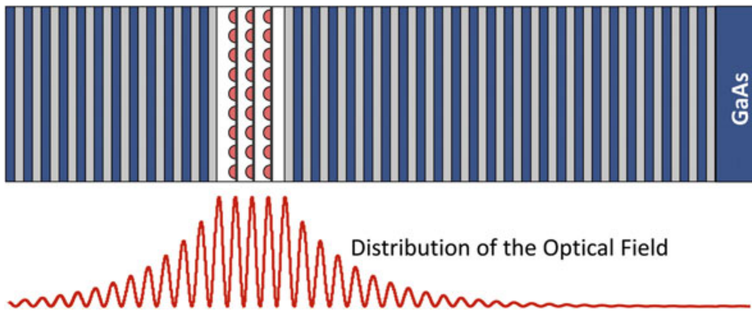

Fig. 10.7 Detailed structure of the QD switch designed in this article. The distribution of the optical filed inside the cavity is plotted by an oscillation curve

where ω is the optical frequency, and n is the refractive index. With considering a light beam injected into a large-finesses vertical cavity, the absorption linewidth is mainly determined by the homogenous broadening of QD materials. The refractive index change of QDs inside cavity is calculated using Eq. 10.5, as shown in Fig. 10.6.

Designed Structure

Based on the principles discussed above, we have designed a cavity structure for the QD switch as shown in Fig. 10.7. Three layers of self-assembled InAs QDs have been inserted into a vertical cavity which consists of 12 (25) period GaAs/ $Al_{0.8}Ga_{0.2}As$ for the front (back) mirror. Twenty percent Ga is added into the AlGaAs layer to prevent lateral oxidization of Al atoms. The thickness of the

GaAs and AlGaAs layers is chose to be 89 and 102 nm, respectively. The spatial distribution of the electric field inside the cavity is calculated by a transfer matrix method. An enhancement of 22 times is theoretically estimated for the optical field inside the cavity.

Growth of the Vertical Cavity and QDs

The fabrication of vertical cavity structures places great emphasis on the accurate control and stability of growth rates during epitaxial growth processes [46]. It is necessary to have both an accurate placement of the cavity wavelength (set by the cavity thickness) and the DBR centre wavelength (set by the mirror thickness) with the optical spectrum of the QDs which of course should be at the designed operation wavelength of the optical switch. The relatively broad spectrum of an ensemble of QDs allows a little more freedom than for QW samples but nevertheless the required wavelength tolerance range is still in the range of ± 10 nm leading to a requirement for thickness accuracies in the range of $\pm 1\%$.

The QD switch samples we have produced were grown by MBE using a VG V90 machine. Epitaxy took place on 3 in. n^+ doped GaAs (001) substrates. As previously discussed the samples are composed of three components, a back mirror, a cavity and a front mirror, with the mirrors being formed from GaAs/$Al_{0.8}Ga_{0.2}As$ $\lambda/4n$ pairs and the cavity of $3\lambda/2n$ thickness and comprised of GaAs with a plane of InAs QDs at the three cavity antinodes.

Thickness control of $\pm 1\%$ or better is highly demanding of any growth technique and two problems in particular affect MBE growth in this respect; source stability and source flux transients. The stability of MBE sources is generally good if allowed to thermally stabilize for a sufficient time and if temperature cycling is minimized. However, the sources also naturally deplete of material over time reducing the evaporant surface area and moving the melt further back in the crucible. The vertical cavity structures are ~ 8 μm thick and have an 8–10 h growth duration, during which there is a small but significant source depletion. We have addressed this by introducing a small compensating temperature ramp $\sim +1$–2°C to the cell temperature during the growth of these structures. The second relates to MBE source flux transients which occur as a consequence of opening and closing the shutters associated with each cell. This can lead to a difference between the steady state growth rate and the instantaneous growth rate after opening the shutter due to the differences in thermal environment. The typical flux transients we observe for the indium, gallium and aluminium sources are of the order of 2, 3 and 8% respectively and last between 2 and 6 min. These values are not untypical of other MBE equipment. As a result, one must be careful to account for these effects. For aluminium in particular it is important to take into account that the growth rate of AlGaAs during the Bragg reflector sequence will be higher than its steady state value, since during that sequence the Al source is subjected to an open–close shutter cycle with a period ~ 10 min.

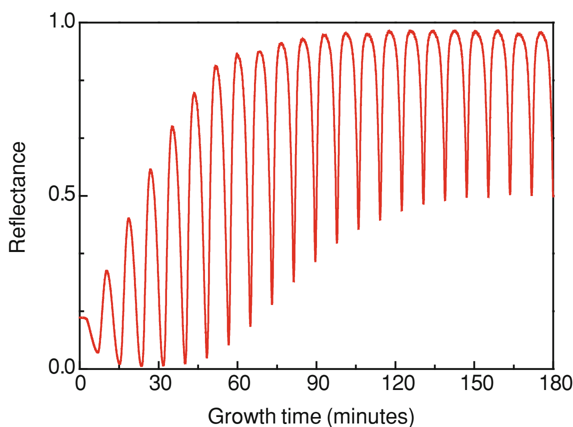

Fig. 10.8 Reflectivity profile during the initial growth of a DBR structure, measured at the temperature-shifted cavity wavelength

Due to the required thickness accuracy, it is often necessary to produce a number of calibration samples prior to attempting the full growth, for example of partical DBR structures with or without cavities and then assess them by optical reflectivity and x-ray diffraction. The data from these methods can be simulated and the growth thicknesses can be obtained to a reasonable accuracy, providing input for revised growth recipe timing. However, we also have access to in situ optical reflectivity (*Laytec EpIR*) via a window on the MBE which allows near surface normal light to access the wafer [47]. The use of in situ optical reflectivity provides a very useful short-cut to the calibration process. Its application is now commonplace in epitaxial growth systems, but it is useful to discuss the particular methods we have employed here.

For effective real time monitoring we observe the time dependence of the wafer reflectivity at a wavelength corresponding to the growth temperature shifted cavity wavelength. The structure is simulated and then the refractive index values adjusted to those calculated for the DBR growth temperature, which is $\sim$600°C. At this wavelength the wafer reflectivity undergoes an oscillation which reaches a maximum or minimum every time a $\lambda/4n$ layer is completed, as shown in a typical trace in Fig. 10.8. If these layers remain in phase, the reflectivity maxima will rise towards 100% and the minima falls initially towards 0% and then rises to an intermediate value. To a good approximation, the switching between $\lambda/4n$ pairs must occur at these maxima and minima. Real time data can be observed and the MBE timing sequence can be adjusted if any drift in the coincidence is detected. The method can also be used to monitor the cavity thickness by observing oscillations due to $\lambda/4n$ GaAs pairs. However, it cannot be extended to effectively monitor the top pair since as the cavity is formed the time dependence of the reflectivity profile becomes very dependent on the precise positioning of the monitor wavelength with respect to the cavity.

Within the cavity of the switch samples are placed three layers of QDs. To access the wavelength range $\sim$1,300 nm we have used the dot-in-well (DWELL)

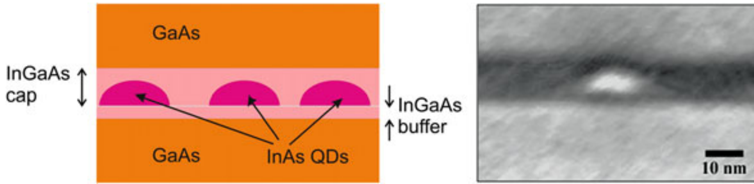

Fig. 10.9 DWELL QD schematic together with a typical cross sectional TEM image of one of the dots in the structure

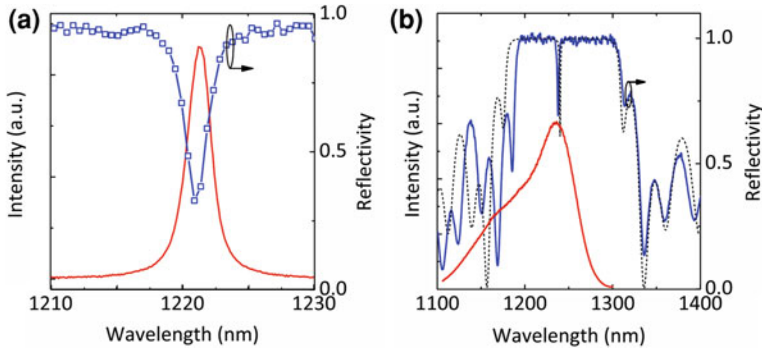

Fig. 10.10 **a** Surface emission PL (*solid curve*) and cavity reflectivity spectra (*open squares*) near the cavity resonant mode. **b** Edge emission PL (*solid curve*). The cavity reflectivity spectra are obtained from the measurement (*dashed curve*) and calculation (*dot–dashed curve*), respectively

configuration in which InAs QDs are surrounded by an $In_{.15}Ga_{.85}As$ cap layer and thin $In_{.15}Ga_{.85}As$ buffer layer. A schematic of this approach, which follows that published by of Lester [48] is shown in Fig. 10.9, together with a cross sectional transmission electron microscope image of a typical QD in the structure.

A layer of DWELL QDs is placed at each antinode of the GaAs cavity, a process which can be monitored using in situ reflectivity. At this point the substrate was cooled from the GaAs growth temperature of ~580°C to a value ~510°C and the deposition of 1–2 nm of $In_{0.15}Ga_{0.85}As$ took place to form the lower buffer. InAs was then deposited to a thickness of 2.5 monolayers at a growth rate of 0.1 ml s^{-1} which are typical conditions to produce a mature array of QDs with a density in the range of $2–3 \times 10^{10}$ cm^{-2}. The QDs were subsequently capped with 6 nm of $In_{0.15}Ga_{0.85}As$. It is the presence of this layer and principally its effect on the strain of the QD which shifts the wavelength from around 1.1 μm in the case of InAs QDs on GaAs to around 1.3 μm in the case of the DWELL. On completion of the $In_{0.15}Ga_{0.85}As$ cap, 2 nm of GaAs was grown at low temperature before an interrupt and high temperature anneal step (~610°C, 2–3 min) was performed. We have found this step to be important in reducing the density of large dots formed by coalescence and its effect on properties of laser samples using a similar method have been well reported [49].

Switching Based on Absorption Nonlinearity

Characterization of All-Optical QD Switches

The solid curve in Fig. 10.10a presents the photoluminescence (PL) spectra collected from the upper surface of the vertical cavity, which exhibits a significant narrowing of the QD emission. The reflectivity spectra near the cavity resonant mode is also plotted to give a comparison (open squares). Both the surface PL and reflectivity spectra have a linewidth around 2 nm, corresponding to a cavity quality factor of $\sim$600. These results indicate the surface PL is strongly modified by the cavity resonance. The PL signal from the sample edge was also measured, as shown in Fig. 10.10b by the solid curve. The edge emission PL gives QD GS emission peak at 1,235 nm and the first excited state (ES) peak at 1,170 nm. Cavity reflectivity spectra are also shown in the figure by the dashed curve. The cavity mode wavelength is 1,238 nm which is close to the GS emission wavelength of QDs. The dot–dashed curve in the figure indicates a theoretical design from transfer matrix simulation. It is well matched by the experimental result.

Switching Dynamics

Conventional pump-probe measurements (Fig. 10.11) were carried out at room temperature to study the switching dynamics using orthogonally polarized pump and probe beams. 130 fs optical pulses with a typical bandwidth of 20 nm and a repetition rate of 80 MHz were generated by an optical parametric oscillator (OPO). When the pump beam excited the front cavity mirror at the cavity resonant wavelength, the differential reflectivity was traced by the probe beam. A switching process with a time constant of 80 ps has been demonstrated for the GS-switching sample as shown in Fig. 10.12, which exhibits comparable results with previously reported values for a QD-based optical switch using two-dimensional photonic crystal waveguides [41]. An ultra-fast component within a few picoseconds was observed at the first part of the dynamic curve, in agreement with a previous report on QDs [50].

Since the QDs occupy a small volume within the cavity an ultra-low saturation power is expected for the operation of QD switches. In our measurement, the probe beam power is set at one hundredth of that of the pump beam. The optical pulse has a bandwidth of 20 nm which is about ten times of the cavity mode linewidth. Therefore to estimate the power consumption and differential reflectivity, we have simply assumed that one tenth of the power has been used in the switching process. Figure 10.12b shows the differential reflectivity as a function of the excitation power density. An ultra-low power density less than 1 fJ/μm^2 has been obtained.

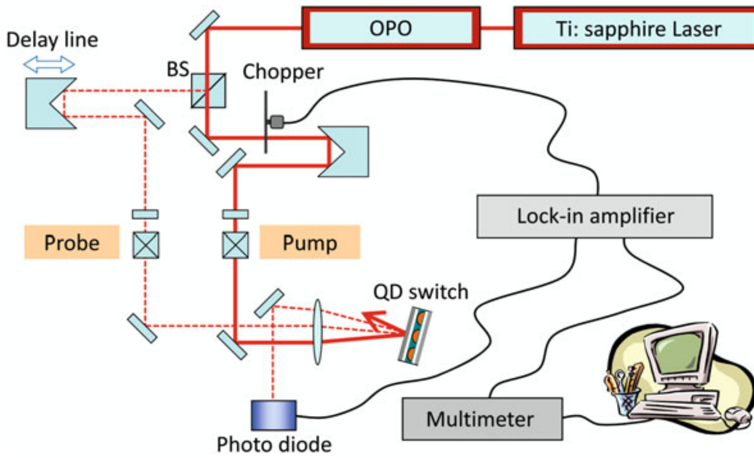

Fig. 10.11 Schematic diagram of the pump-probe setup used for the measurement of the switching dynamics

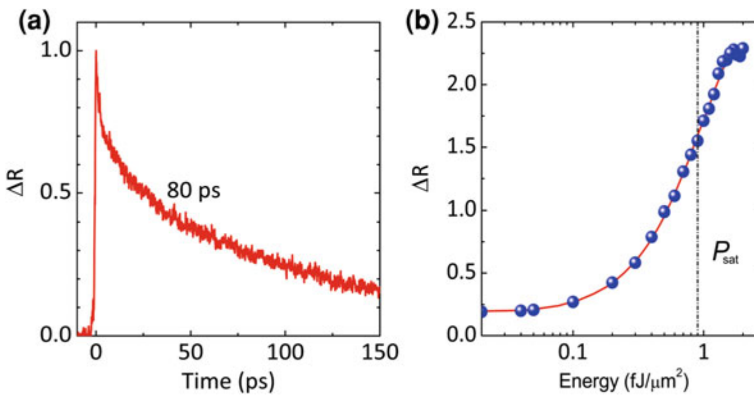

Fig. 10.12 **a** Differential reflectivity as a function of delay time for a switching processes via GS transition of QDs. **b** Differential reflectivity (time = 0) as a function of power density

The saturation behavior can be simulated assuming the QD absorption follows the saturation function,

$$\Gamma = \frac{\Gamma_0}{1 + (P/P_s)} \tag{10.6}$$

where P is the excitation power density and P_s is the saturation power density. $P_s = 0.9$ fJ/μm^2 is used for the simulation which makes good agreement with the experimental data.

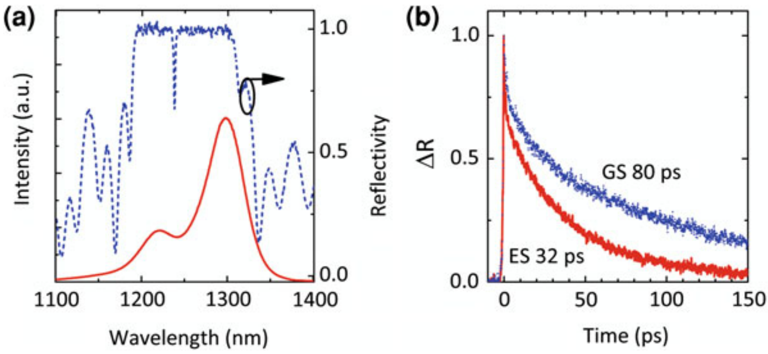

Fig. 10.13 **a** Edge emission PL (*solid curve*) and the cavity reflectivity spectra (*dashed curve*). **b** Differential reflectivity as a function of delay time for switching processes via either ES transition (*solid curve*) or GS transition of QDs (*dotted curve*)

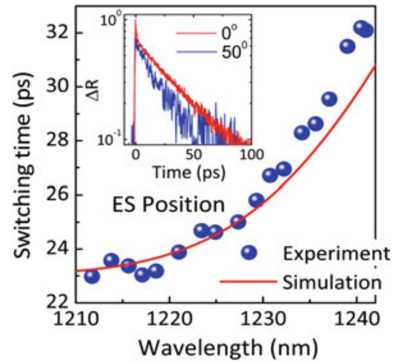

Fig. 10.14 Switching time as a function of cavity resonant wavelength from the measurement (*open circles*) and simulation (*dashed curve*). The inset gives two switching curves with operation wavelength at 1,240 and 1,219 nm, which correspond to incident angles of 0 and 50°, respectively

Excited State Switching

As discussed in the introduction, high energy states in QDs can be employed to enhance the switching dynamics. The edge emission PL from the ES switching sample gives peaks with the GS emission at 1,298 nm and the ES emission at 1,220 nm (solid curve). The ES transition is close to the cavity mode. This ES-switching sample shows a switching time of 32 ps as shown in Fig. 10.13b. The significantly faster response for the ES sample can be explained by the rapid intersubband relaxation of carriers [12]. The absorption of the ES becomes saturated when an ultra-fast optical pulse pumps at the ES wavelength. After the pump pulse is removed, a fast relaxation of carriers into the GS takes place, which recovers the absorption at the ES. As a consequence, a faster switching time is suggested and is now demonstrated in experiments.

Broadband Operation with Angular-Dependent Switching

Since the cavity resonant mode determines the operation wavelength of the device, this QD switch can only work in a very narrow wavelength region. To overcome this drawback, we have investigated the incident angle dependence of the switching performance using the ES switching sample. By changing the incident angle of the optical pulses from 0 to 50°, the operation wavelength is varied near the ES emission peak from 1,240 to 1,210 nm. This degree of tuning is certainly possible because the inhomogeneous broadening of QD absorption spectra is usually over a range of 40–50 nm. The angle-dependent switching time (open circles in Fig. 10.14) decreases when the operation wavelength is going to shorter. A minimum switching time of 23 ps is reached using this configuration near the QD ES emission. For wavelengths shorter than 1,220 nm, the switching time almost keeps constant. The inset in Fig. 10.14 presents two switching dynamics curves with operation wavelength at 1,240 and 1,219 nm. The present QD switch using the ES has been shown to operate over a wavelength range of 30 nm with a 23–32 ps switching time.

The wavelength dependence of the switching time can be further explained by a photon coupling process, which occurs due to the overlap between the absorption spectra of the QD ES and GS [10, 51]. For 1.3 μm QDs with a DWELL structure, a bi-modal distribution of QDs has been always observed in our samples and appears to present in many other published reports [52]. The second subset of QDs in the bi-mode, most likely due to a distribution of smaller dots, presents an optical transition which partially overlaps the ES transition peak. The optical absorption near the ES emission peak therefore is from a combination of different-size QDs which may have either ES or GS transitions. If we assume the absorption intensities of the GS and ES are A_1 and A_2, respectively, the absorption change as function of time can be described by a summation of two exponential decays:

$$\Delta\alpha(t) = A_1 \exp\left(-\frac{t}{\tau_{gs}}\right) + A_2 \exp\left(-\frac{t}{\tau_{es}}\right) \quad (10.7)$$

In the case of $A_2 \gg A_1$, by using the second term expansion of the Taylor series,

$$\Delta\alpha(t) \approx (A_1 + A_2) \exp\left(-\frac{t}{\tau_1}\right) \quad (10.8)$$

where

$$\tau_1 = \left(\frac{A_2}{A_1 + A_2}\tau_0^{-1} + \tau_{gs}^{-1}\right)^{-1} \quad (10.9)$$

is the observed angular-dependent switching time. In the simulation, we have assumed that the second distribution in the bi-mode has a GS peak at 1,260 nm. The carrier decay times of the GS and ES are 80 and 23 ps as measured. This simulation reproduces very similar behavior to the wavelength-dependent

switching time in Fig. 10.14. The deviation in the longer wavelength region is caused by the increasing violation of the inequality, $A_2 \gg A_1$, when the operating wavelength approaches that of the bi-modal GS peak.

Enhance the Absorption Nonlinearity

In the characteristics of the switching device, the differential reflectivity indicates 2–3% variation of the cavity reflectivity, e.g. $\Delta R/R = 2\text{–}3\%$, as shown in Fig. 10.12. Through simulations, a contrast ratio of 2–3% corresponds to an absorption strength of $\Gamma \approx 2.5 \times 10^{-4}\ \text{cm}^{-1}$, which is close to one of the test values used in Fig. 10.5 (hollow circles). This small contrast ratio of the QD switch is caused by the small volume occupied by the QDs. The total number of carrier states in the QD layer is about one hundredth of its counterparts, such as the QW or bulk materials. The small number of carrier states requires fewer carriers to saturate the absorption. This is advantageous for ultra-low power consumption but the low contrast ratio is problematic for practical application. The contrast ratio can be optimized by increasing the optical enhancement inside the cavity, which would cause a trade-off between the contrast ratio and the cavity response time, or by simply increasing the number of carrier states in the active region using high density dots or multiple layers of QDs, which would cause a trade-off between the contrast ratio and the power consumption [30].

An increase of the QD density and number of QD layers in the cavity is an effective means to increase the optical nonlinearity. We have revised our design to include three closely spaced DWELLs at each antinode of the $3\lambda/2$ cavity. The structure therefore has 3×3 dot layers inside the cavity. The increased absorption dictates a small change in the design such that it now has $p = 16$ and $q = 30$ periods of GaAs/AlGaAs DBR mirrors. As for the previous samples, the QD ES emission peak is assigned to match the cavity resonant mode at 1,240 nm. A switching process with a time constant of 20 ps has been demonstrated as shown in Fig. 10.15a. The power-dependent differential reflectivity measurement indicates a saturation power density of 2.5 fJ/μm^2 and a maximum differential reflectivity close to 10% of the original intensity of the probe beam. The differential reflectivity is significantly enhanced from previous results, which indicates that the device is now working within a higher nonlinear region.

Exploring the Phase Properties

It has been shown above that using inter-sublevel transitions is an efficient mean to accelerate the switching dynamics. However, this improved performance is still limited by the intrinsic carrier dynamics inside QDs, which has been realized not always fast. It is therefore worthwhile to examine other possibilities such as a

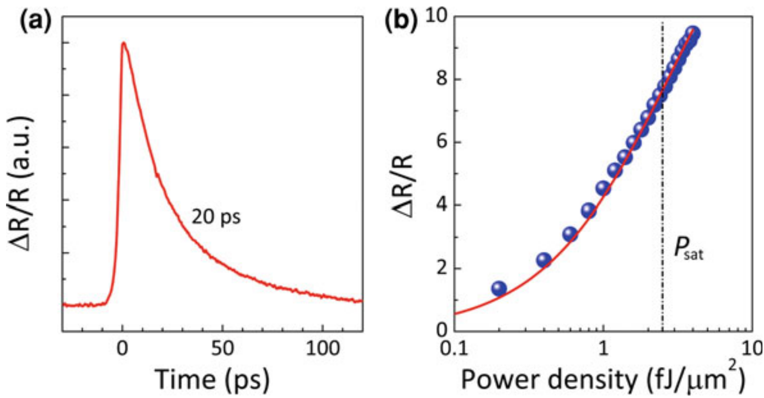

Fig. 10.15 **a** Switching dynamics from all-optical QD switches with 16/25 periods GaAs/AlGaAs for the front/back DBR mirror. **b** Differential refractivity as a function of pumping power density. The *solid curve* shows simulation results considering saturable absorption in the dot layers, using a theoretical model described in Ref. [29]

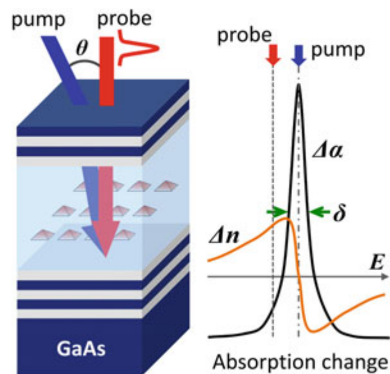

Fig. 10.16 A schematic diagram of working principles for a vertical cavity QD switch. The *right hand side* diagram shows both the differential absorption and refractive index change in the dot layer

Mach–Zehnder (MZ) configuration which employs the phase nonlinearity rather than the absorption dynamics. The optical phase nonlinearity of QDs has been observed in two dimensional photonic waveguides for the development of an all-optical MZ switch [41]. However, to employ this vertical structure as a practical optical nonlinear phase shifter, some further optimization of the device is required.

Figure 10.16 presents a schematic diagram of the vertical-cavity QD switch. In this structure, the centre wavelength of the absorption saturation is defined by the wavelength of the cavity mode. Pump light injected into the cavity saturates the QD absorption and hence results in a differential reflectivity of the probe light. The QD absorption saturates with a spectral linewidth of δ, which is limited by the homogenous broadening of the absorption spectra of the QD ensemble. The change of the refractive index in the dot layer follows the Kramers–Kronig relation, as shown in the right hand side in Fig. 10.16. Assuming no carrier heating

effects occur in the passive QD structure, the refractive index change becomes close to zero at the centre wavelength. Away from the centre wavelength, if the probe light is tuned to a different value within the spectral linewidth of the ensemble, the probe light will now experience a small refractive index change in the dot layer. This small change of the refractive index induces a phase shift when the light passes though the whole structure. Assuming a transfer matrix for an approximately quarter-wave layer with a small thickness deviation of $\varepsilon\lambda/2\pi$ which has the form of

$$M_{\lambda/4} = \begin{bmatrix} -\varepsilon & i/n_{\mathrm{H}} \\ in_{\mathrm{H}} & -\varepsilon \end{bmatrix} \tag{10.10}$$

where n_{H} is the refractive index of the GaAs. For the $m\lambda/2$ cavity, the transfer matrix of the active region becomes

$$M_{\mathrm{active}} = \begin{bmatrix} -1 & -2mi\varepsilon/n_{\mathrm{H}} \\ -2mi\varepsilon n_{\mathrm{H}} & -1 \end{bmatrix} \tag{10.11}$$

By writing down the transfer matrix for the whole structure including all DBR layers, the phase shift is derived as

$$\Delta\phi \cong \tan\Delta\phi = \frac{-2m\varepsilon n_{\mathrm{H}}\left(\frac{n_{\mathrm{H}}}{n_{\mathrm{L}}}\right)^{2p}}{1 + n_{\mathrm{H}}\left(-\frac{n_{\mathrm{L}}}{n_{\mathrm{H}}}\right)^{-2p+2q}} \tag{10.12}$$

where n_{L} is the refractive index of AlGaAs, and p and q are the period number of the GaAs/AlGaAs layers in the front and back DBR mirrors. In the case of an asymmetric cavity with $q \gg p$, the phase shift can be simplified to be

$$\Delta\phi \cong -2m\varepsilon n_{\mathrm{H}}\left(\frac{n_{\mathrm{H}}}{n_{\mathrm{L}}}\right)^{2p} \tag{10.13}$$

The factor $(n_{\mathrm{H}}/n_{\mathrm{L}})^{2p}$ represents the enhancement due to the vertical cavity. Hence, by increasing the number of periods of the front mirror, p, the optical phase shift for the whole structure can be amplified dramatically. It is therefore possible to achieve a large nonlinear phase shift in the vertical direction for QDs.

Following the above discussion, a switch device with $p = 16$ and $q = 30$ periods of GaAs/AlGaAs DBR mirrors has been employed, with switching performance as shown in Fig. 10.15. Figure 10.17 describes a MZ interferometer setup for the evaluation of phase shifts in vertical cavity QD switches. To achieve the small wavelength shift between the pump and probe beams, as suggested in Fig. 10.16, the pump beam was slightly tilted with a angle $\theta = 20°\mathrm{C}$. Since the femtosecond pulses in the system have a spectral broadening of around 20 nm, the use of angled injection automatically selects a pump wavelength 5 nm shorter than the probe. Thus, a 5 nm detuning is achieved with the degenerated pump-probe setup. The spectral linewidth of the absorption saturation in the dot ensemble is limited by the homogeneous broadening linewidth at room temperature, which has

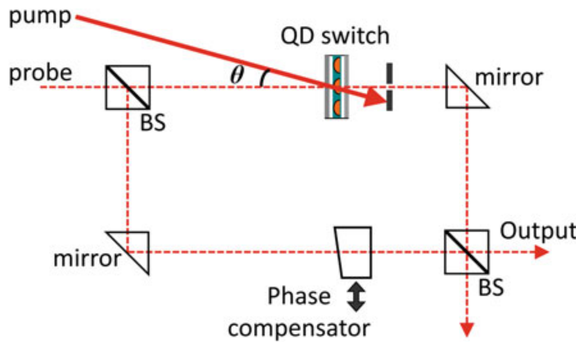

Fig. 10.17 A schematic diagram of a Mach–Zehnder interferometer setup for the evaluation of optical phase shifts inside QDs. Beam splitter (*BS*)

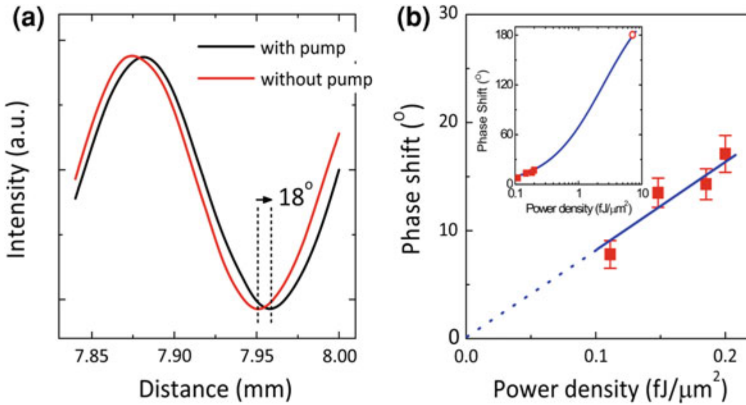

Fig. 10.18 **a** Interference patterns from the MZ interferometer with and without optical pumping of the QD switch sample. The *inset* shows the phase dynamics (*solid curve*) compared to the absorption dynamics (*dashed curve*). **b** Phase shifts as a function of pumping power density. The *inset* shows simulation results assuming that the refractive index change inside QDs follows a saturation function. The *solid squares* are from the experimental data shown in the main figure. The *open circle* indicates a π phase shift could be achieved with a pump power intensity of 7 fJ/μm2 with the present device

a typical value around 6 meV [53]. Therefore the 5 nm detuning is approaching the maximum refractivity change defined by the Kromers–Kronig relation. In the MZ scheme, the probe beam is divided into two beams with an optical beam splitter (BS). One of the beams passes through the optically pumped QD switching sample and the other beam is modified by an optical phase compensator. Those two beams join together after a BS and give the output signal. All the optical components in this setup are integrated into a compact box with fiber based input and output connections to achieve high signal to noise ratio. Very small optical phase shifts ($\sim 0.5^{o}$) can be evaluated by this arrangement by comparing the interference patterns with and without the pump beam.

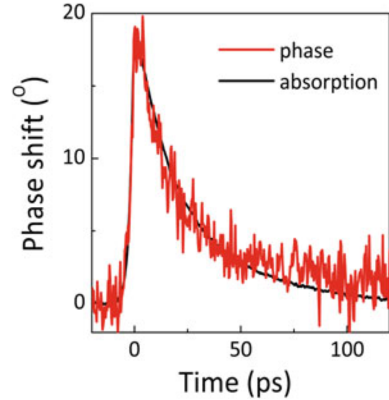

Fig. 10.19 Comparison between the absorption and phase dynamics using the MZ interferometer setup

Figure 10.18a shows the results of the phase shift measurement. By adjusting the phase compensator, the output intensity follows a sinusoid function with observable bright and dark regions in the interference pattern. By pumping the QD switch with a 20 pJ optical pulse, the pattern is shifted by 9.0 μm, which corresponds to an 18° phase shift inside the switching device. The phase dynamics has been measured by tracing the intensity change of the interference pattern in the time scale, which was further converted into the phase space as shown in the inset of Fig. 10.19. The switching curve in terms of the absorption dynamics (dashed curve) has been rescaled to compare with the phase dynamics (solid curve). The phase dynamics follows almost the same tendency as the absorption dynamics, although the last part of it is slightly slower, similar as the previous reports on the QD-photonic crystal switches [54] and the passive region of QD-SOAs [55].

Using Eq. 10.13, the refractive index change in the dot layer can be calculated

$$\Delta n_{\mathrm{QD}} = \frac{D_{\mathrm{a}}}{d_{\mathrm{QD}}} \times \frac{\varepsilon}{\pi/2} = -\frac{D_{\mathrm{a}}}{d_{\mathrm{QD}}} \times \frac{\Delta\varphi}{\pi m n_{\mathrm{H}} \left(\frac{n_{\mathrm{H}}}{n_{\mathrm{L}}}\right)^{2p}} \tag{10.14}$$

where $D_{\mathrm{a}} = 3\lambda/2$ is the thickness of the active region, $d_{\mathrm{QD}} = 10$ nm is the thickness of each individual dot layer. With $n_{\mathrm{H}} = 3.461$, $n_{\mathrm{L}} = 3.045$, and $m = 3$, the refractive index change is evaluated to be $\sim 0.3\%$ of the original value of QDs. This value of refractivity nonlinearity is smaller than previous reported values. The reason for this decrease is that the pump beam from the fiber has a spot size of ~ 300 μm, which provides a pump power density of 0.22 fJ/μm^2. This is at least a decade below the saturation fluence, which will be around 2.5 fJ/μm^2. A linear dependence of the optical phase shift on the pump beam power is observed, as shown in Fig. 10.18b. The inset in Fig. 10.17b presents the power-dependent phase shift in a large scale from the simulation result in which we assumes the refractive index change follows a saturation function. Accordingly, up to a π phase shift from the device could be achieved if an additional focusing component were to be integrated into the compact system. Another possible approach to enhance

the phase shift is to increase the number of periods of the DBR mirror as indicated in Eq. 10.13, although this requires the growth of thicker vertical cavities.

Several approaches have been already proposed to accelerate the switching dynamics for vertical cavity QD switches down to the picosecond timescale using mechanisms such as the optical Kerr nonlinearity [56, 57], carrier tunneling mechanisms from an additional QW [58], or impurity doping [59]. Comparing these previous approaches to the optical phase nonlinearity in a MZ scheme, this new approach could potentially achieve ultrafast switching with fewer limitations placed on it by the carrier dynamics inside the QDs, whilst also retaining ultralow power operation [60, 61] at the femto-joule level.

Summary

We have investigated in details all-optical QD switches using a vertical cavity approach which enhances the absorption and phase nonlinearity of QD materials. The device shows switching dynamics down to 20 ps, a differential reflectivity of ~10%, a broad modulation bandwidth of ~30 nm, and an ultralow energy consumption of 1–2.5 fJ/μm^2. An 18° phase shift has been initially observed in the vertical geometry using a tilted pumping scheme. These results demonstrate that QD nanostructures are promising candidates for next generation photonic devices needed for power-efficient optical networks.

Acknowledgments We are grateful to Dr. H. Ishikawa and Dr. R. Akimoto at AIST, Tsukuba, Japan, Dr. N. Ozaki at Wakayama University, Japan, and Dr. T. Inoue at Kobe University, Japan for helpful discussions and supports. This work is partially supported by the Ministry of Education, Culture, Sports, Science and Technology of Japan and by the Royal Society, U.K. One of the authors, C.Y. Jin, acknowledges financial support from Japan Society for the Promotion of Science.

References

1. Ashoori, R.C.: Electrons in artificial atoms. Nature **379**, 413–419 (1996)
2. Bimberg, D., Grundmann, M., Ledentsov, N.N.: Quantum Dot Heterostructures. Wiley, UK (1998)
3. Arakawa, Y., Sakaki, H.: Multidimensional quantum well laser and temperature dependence of its threshold current. Appl. Phys. Lett. **40**, 939–941 (1982)
4. Goldstein, L., Glas, F., Marzin, J.Y., Charasse, M.N., LeRoux, G.: Growth by molecular beam epitaxy and characterization of InAs/GaAs strained-layer superlattices. Appl. Phys. Lett. **47**, 1099–1101 (1985)
5. Walther, T., Cullis, A.G., Norris, D.J., Hopkinson, M.: Nature of the Stranski–Krastanow transition during epitaxy of InGaAs on GaAs. Phys. Rev. Lett. **86**, 2381–2384 (2001)
6. Kirstaedter, N., Ledentsov, N.N., Grundmann, M., Bimberg, D., Ustinov, V.M., Ruvinov, S.S., Maximov, M.V., Kop'ev, P.S., Alferov, Z.I., Richter, U., Werner, P., Gosele, U., Heydenreich, J.: Low threshold large T_0 injection laser emission from (InGa)As quantum dots. Electron. Lett. **30**, 1416–1417 (1994)

7. Liu, H.Y., Childs, D.T., Badcock, T.J., Groom, K.M., Sellers, I.R., Hopkinson, M., Hogg, R.A., Robbins, D.J., Mowbray, D.J., Skolnick, M.S.: High-performance three-layer 1.3 μm InAs–GaAs quantum-dot lasers with very low continuous-wave room-temperature threshold currents. IEEE Photonics Technol. Lett. **17**, 1139–1141 (2005)
8. Shchekin, O.B., Deppe, D.G.: 1.3 μm InAs quantum dot laser with $T_0 = 161$ K from 0 to 80°C. Appl. Phys. Lett. **80**, 3277–3279 (2002)
9. Fathpour, S., Mi, Z., Bhattacharya, P., Kovsh, A.R., Mikhrin, S.S., Krestnikov, I.L., Kozhukhov, A.V., Ledentsov, N.N.: The role of auger recombination in the temperature-dependent output characteristics ($T_0 = \infty$) of *p*-doped 1.3 μm quantum dot lasers. Appl. Phys. Lett. **85**, 5164–5166 (2004)
10. Jin, C.Y., Badcock, T.J., Liu, H.Y., Groom, K.M., Royce, R.J., Mowbray, D.J., Hopkinson, M.: Observation and modeling of a room-temperature negative characteristic temperature 1.3 μm *p*-type modulation-doped quantum-dot laser. IEEE J. Quantum Electron. **42**, 1259–1266 (2006)
11. Rafailov, E.U., White, S.J., Lagatsky, A.A., Miller, A., Sibbett, W., Livshits, D.A., Zhukov, A.E., Ustinov, V.M.: Fast quantum-dot saturable absorber for passive mode-locking of solid-state lasers. IEEE Photonics Technol. Lett. **16**, 2439–2441 (2004)
12. Akiyama, T., Wada, O., Kuwatsuka, H., Simoyama, T., Nakata, Y., Mukai, K., Sugawara, M., Ishikawa, H.: Nonlinear processes responsible for nondegenerate four-wave mixing in quantum-dot optical amplifiers. Appl. Phys. Lett. **77**, 1753–1755 (2000)
13. Borri, P., Langbein, W., Hvam, J.M., Heinrichsdorff, F., Mao, M.-H., Bimberg, D.: Time-resolved four-wave mixing in InAs/InGaAs quantum-dot amplifiers under electrical injection. Appl. Phys. Lett. **76**, 1380–1382 (2000)
14. Mi, Z., Bhattacharya, P., Fathpour, S.: High-speed 1.3 μm tunnel injection quantum-dot lasers. Appl. Phys. Lett. **86**, 153109 (2005)
15. Mutig, A., Fiol, G., Moser, P., Arsenijevic, D., Shchukin, V.A., Ledentsov, N.N., Mikhrin, S.S., Krestnikov, I.L., Livshits, D.A., Kovsh, A.R., Hopfer, F., Bimberg, D.: 120°C 20 Gbit/s operation of 980 nm VCSEL. Electron. Lett. **44**, 1305–1306 (2008)
16. Liu, H.Y., Badcock, T.J., Jin, C.Y., Nabavi, E., Groom, K.M., Hopkinson, M., Mowbray, D.J.: Reduced temperature sensitivity of lasing wavelength in near-1.3 μm InAs/GaAs quantum-dot laser with stepped composition strain-reducing layer. Electron. Lett. **43**, 670–672 (2007)
17. Laemmlin, M., Fiol, G., Meuer, C., Kuntz, M., Hopfer, F., Kovsh, A.R., Ledentsov, N.N., Bimberg, D.: Distortion-free optical amplification of 20–80 GHz modelocked laser pulses at 1.3 μm using quantum dots. Electron. Lett. **42**, 697–699 (2006)
18. Rafailov, E.U., Cataluna, M.A., Sibbett, W., Il'inskaya, N.D., Zadiranov, Yu.M., Zhukov, A.E., Ustinov, V.M., Livshits, D.A., Kovsh, A.R., Ledentsov, N.N.: High-power picosecond and femtosecond pulse generation from a two-section mode-locked quantum-dot laser. Appl. Phys. Lett. **87**, 081107 (2005)
19. Choi, M.-T., Kim, J.-M., Lee, W., Delfyett, P.J.: Ultralow noise optical pulse generation in an actively mode-locked quantum-dot semiconductor laser. Appl. Phys. Lett. **88**, 131106 (2006)
20. Viktorov, E.A., Mandel, P., Kuntz, M., Fiol, G., Bimberg, D., Vladimirov, A.G., Wolfrum, M.: Stability of the mode-locked regime in quantum dot lasers. Appl. Phys. Lett. **91**, 231116 (2007)
21. Thompson, M.G., Rae, A.R., Xia, M., Penty, R.V., White, I.H.: InGaAs quantum-dot mode-locked laser diodes. IEEE J. Sel. Top. Quantum Electron. **15**, 661 (2009)
22. Schneider, S., Borri, P., Langbein, W., Woggon, U., Sellin, R.L., Ouyang, D., Bimberg, D.: Excited-state gain dynamics in InGaAs quantum-dot amplifiers. IEEE Photonics Technol. Lett. **17**, 2014–2016 (2005)
23. Akiyama, T., Hatori, N., Nakata, Y., Ebe, H., Sugawara, M.: Pattern-effect-free amplification and cross-gain modulation achieved by using ultrafast gain nonlinearity in quantum-dot semiconductor optical amplifiers. Phys. Status Solidi B **238**, 301–304 (2003)
24. Borghesani, A., Fensom, N., Scott, A., Crow, G., Johnston, L.M., King, J.A., Rivers, L.J., Cole, S., Perrin, S.D., Scrase, D., Bonfrate, G., Ellis, A.D., Crouzel, G., Chun, L.S.H.K., Lupu, A., Mahe, E., Maigne, P., Lealman, I.F.: High Saturation Power (>16.5 dBm) and Low Noise Figure (<6 dB) Semiconductor Optical Amplifier for C-Band Operation. OFC Atlanta, USA (2003)

25. Akiyama, T., Ekawa, M., Sugawara, M., Sudo, H., Kawaguchi, K., Kuramata, A., Ebe, H., Morito, K., Imai, H., Arakawa, Y.: An Ultrawide-Band (120 nm) Semiconductor Optical Amplifier Having an Extremely-High Penalty-Free Output Power of 23 dBm Realized with Quantum-Dot Active Layers. OFC Los Angeles, USA (2004)
26. Lumb, M.P., Clarke, E., Harbord, E., Spencer, P., Murray, R., Masia, F., Borri, P., Langbein, W., Leburn, C.G., Jappy, C., Metzger, N.K., Brown, C.T.A., Sibbett, W.: Ultrafast absorption recovery dynamics of 1,300 nm quantum dot saturable absorber mirrors. Appl. Phys. Lett. **95**, 041101 (2009)
27. Takahashi, T., Mukai, T., Morita, K., Kitada, T., Isu, T.: GaAs/AlAs multilayer cavity with InAs quantum dots embedded in strain-relaxed barriers for planar-type optical Kerr gate switches. Jpn. J. Appl. Phys. **49**, 04DG02 (2010)
28. Kitagawa, Y., Ozaki, N., Takata, Y., Ikeda, N., Watanabe, Y., Sugimoto, Y., Asakawa, K.: Sequential operations of quantum dot/photonic crystal all-optical switch with high repetitive frequency pumping. J. Lightwave Technol. **27**, 1241–1247 (2009)
29. Jin, C.Y., Kojima, O., Kita, T., Wada, O., Hopkinson, M., Akahane, K.: Vertical-geometry all-optical switches based on InAs/GaAs quantum dots in a cavity. Appl. Phys. Lett. **95**, 021109 (2009)
30. Jin, C.Y., Kojima, O., Inoue, T., Kita, T., Wada, O., Hopkinson, M., Akahane, K.: Detailed design and characterization of all-optical switches based on InAs/GaAs quantum dots in a vertical cavity. IEEE J. Quantum Electron. **46**, 1582 (2010)
31. Tucker, R.S.: A green internet. In: The 21st Annual Meeting of the LEOS (2008)
32. Wada, O.: Femtosecond all-optical devices for ultrafast communication and signal processing. New J. Phys. **6**, 183 (2004)
33. Kim, D.-H., del Alamo, J.A.: 30 nm InAs pseudomorphic HEMTs on an InP substrate with a current-gain cutoff frequency of 628 GHz. IEEE Electron Device Letts. **29**, 830–833 (2008)
34. Emami-Neyestanak, A., Varzaghani, A., Bulzacchelli, J. F., Rylyakov, A., Yang, C.-K. K., and Friedman, D. J.: A 6.0-mW 10.0-Gb/s receiver with switched-capacitor summation DFE. IEEE J. Solid-state Circuits 42, 889–896 (2007)
35. Smith, P.W.: Application of all-optical switching and logic. Philos. Trans. R. Soc. Lond. Ser. A **313**, 349–355 (1984)
36. Wada, O.: Femtosecond semiconductor-based optoelectronic devices for optical-communication systems. Opt. Quantum Electron. **32**, 453–471 (2000)
37. Miller, D.A.B.: Device requirements for optical interconnects to silicon chips. Proc. IEEE **97**, 1166–1185 (2009)
38. Miller, D.A.B.: Are optical transistors the logical next step. Nat. Photonics **4**, 3–5 (2010)
39. Wada, O.: Recent progress in semiconductor-based photonic signal-processing devices. IEEE J. Sel. Top. Quantum Electron. **17**, 309–319 (2011)
40. Prasanth, R., Haverkort, J.E.M., Deepthy, A., Bogaart, E.W., van der Tol, J.J.G.M., Patent, E.A., Zhao, G., Gong, Q., van Veldhoven, P.J., Nötzel, R., Wolter, J.H.: All-optical switching due to state filling in quantum dots. Appl. Phys. Lett. **84**, 4059–4061 (2004)
41. Nakamura, H., Sugimoto, Y., Kanamoto, K., Ikeda, N., Tanaka, Y., Nakamura, Y., Ohkouchi, S., Watanabe, Y., Inoue, K., Ishikawa, H., Asakawa, K.: Ultra-fast photonic crystal/quantum dot all optical switch for future photonic networks. Opt. Express **12**, 6606–6614 (2004)
42. Takahashi, R., Kawamura, Y., Iwamura, H.: Ultrafast 1.55 μm all-optical switching using low-temperature-grown multiple quantum wells. Appl. Phys. Lett. **68**, 153–155 (1996)
43. Loka, H.S., Smith, P.W.E.: Ultrafast all-optical switching with an asymmetric Fabry-Pérot devices using low-temperature-grown GaAs: material and device issues. IEEE J. Quantum Electron. **36**, 100–111 (2000)
44. Gupta, S., Frankel, M.Y., Valdmanis, J.A., Whitaker, J.F., Mourou, G.A., Smith, F.W., Calawa, A.R.: Subpicosecond carrier lifetime in GaAs grown by molecular beam epitaxy at low substrate temperatures. Appl. Phys. Lett. **59**, 3276–3278 (1991)
45. Hutchings, D.C., Sheik-Bahae, M., Hagan, D.J., van Stryland, E.W.: Kramers-Krönig relations in nonlinear optics. Opt. Quantum Electron. **24**, 1–30 (1992)

46. Houng, Y.M., Tang, M.R.T.: MBE growth of highly reproducible VCSELs. J. Crys. Growth **175/176**, 352–358 (1995)
47. Killeen, K.P., Breiland, W.P.: In situ spectral reflectance monitoring of III-V epitaxy. J. Electron. Mater. **23**, 179–183 (1994)
48. Stintz, A., Liu, G.T., Li, H., Lester, L.F., Malloy, K.J.: Low-threshold current density 1.3 μm InAs quantum-dot lasers with the dots-in-a-well (DWELL) structure. IEEE Photonics Technol. Lett. **12**, 591–593 (2000)
49. Liu, H.Y., Sellers, I.R., Badcock, T.J., Mowbray, D.J., Skolnick, M.S., Groom, K.M., Gutierrez, M., Hopkinson, M., Ng, J.S., David, J.P.R., Beanland, R.: Improved performance of 1.3 μm multilayer InAs quantum-dot lasers using a high-growth-temperature GaAs spacer layer. Appl. Phys. Lett. **85**, 704–706 (2004)
50. Malins, D.B., Gomez-Iglesias, A., White, S.J., Sibbett, W., Miller, A., Rafailov, E.U.: Ultrafast electroabsorption dynamics in an InAs quantum dot saturable absorber at 1.3 μm. Appl. Phys. Lett. **89**, 171111 (2006)
51. Jin, C.Y., Liu, H.Y., Groom, K.M., Jiang, Q., Hopkinson, M., Badcock, T.J., Royce, R.J., Mowbray, D.J.: Effects of photon and thermal coupling mechanisms on the characteristics of self-assembled InAs/GaAs quantum dot lasers. Phys. Rev. B **76**, 085315–085326 (2007)
52. Liu, H.Y., Sellers, I.R., Gutierrez, M., Groom, K.M., Soong, W.M., Hopkinson, M., David, J.P.R., Beanland, R., Badcock, T.J., Mowbray, D.J., Skolnick, M.S.: Influences of the spacer layer growth temperature on multilayer InAs/GaAs quantum dot structures. J. Appl. Phys. **96**, 1988–1992 (2004)
53. Borri, P., Langbein, W., Schneider, S., Woggon, U., Sellin, R.L., Ouyang, D., Bimberg, D.: Ultralong dephasing time in InGaAs quantum dots. Phys. Rev. Lett. **87**, 157401 (2001)
54. Asakawa, K., Sugimoto, Y., Watanabe, Y., Ozaki, N., Mizutani, A., Takata, Y., Kitagawa, Y., Ishikawa, H., Ikeda, N., Awazu, K., Wang, X., Watanabe, A., Nakamura, S., Ohkouchi, S., Inoue, K., Kristensen, M., Sigmund, O., Borel, P.I., Baets, R.: New J. Phys. **8**, 208 (2006)
55. Cesari, V., Borri, P., Rossetti, M., Fiore, A., Langbein, W.: Refractive index dynamics and linewidth enhancement factor in *p*-doped InAs/GaAs quantum-dot amplifiers. IEEE J. Quantum Electron. **45**, 579–585 (2009)
56. Kitada, T., Kanbara, T., Morita, K., Isu, T.: GaAs/AlAs multilayer cavity with InAs quantum dots embedded in strain-relaxed barriers for planar-type optical Kerr gate switches. Appl. Phys. Exp. **1**, 092302 (2008)
57. Morita, K., Takahashi, T., Kitada, T., Isu, T.: Enhanced optical Kerr signal of GaAs/AlAs multilayer cavity with InAs quantum dots embedded in strain-relaxed barriers. Appl. Phys. Exp. **2**, 082001 (2009)
58. Jin, C.Y., Ohta, S., Hopkinson, M., Kojima, O., Kita, T., Wada, O.: Temperature-dependent carrier tunneling for self-assembled InAs/GaAs quantum dots with a GaAsN quantum well injector. Appl. Phys. Lett. **96**, 151104 (2010)
59. Sridharan, D., Waks, E.: All-optical switch using quantum-dot saturable absorbers in a DBR microcavity. IEEE J. Quantum Electron. **47**, 31–39 (2011)
60. Nakamura, S., Tajima, K., Sugimoto, Y.: Experimental investigation on high-speed switching characteristics of a novel symmetric Mach–Zehnder all-optical switch. Appl. Phys. Lett. **65**, 283–285 (1994)
61. Jin, C.Y., Kojima, O., Kita, T., Wada, O., Hopkinson, M.: Observation of phase shifts in a vertical cavity quantum dot switch. Appl. Phys. Lett. **98**, 231101 (2011)

Chapter 11
Ultrafast Terahertz Dynamics and Switching in Quantum Dots

Dmitry Turchinovich and Matthias C. Hoffmann

Abstract In this Chapter we describe the experimental studies of ultrafast carrier dynamics and all-optical switching in semiconductor quantum dots (QDs) using ultrafast terahertz (THz) techniques. In the first part of this chapter we describe the studies of carrier capture into the QDs, and thermionic carrier release from the QDs with (sub-)picosecond time resolution, using optical pump–THz probe measurements. In the second part of this chapter we investigate the direct manipulation of the quantum confinement potential of the QDs by an electric field of a strong THz pulse. The resulting THz-driven quantum-confined Stark effect leads to a strong modulation of a ground-state optical absorption in the QDs. Dynamically, such a THz-induced electro-absorption modulation in QDs (near-)instantaneously follows the absolute value of the electric field of the THz pulse, providing the capability for Tbit/s—rate all-optical switching in QDs using THz signals. The principles of experimental techniques used in our studies: optical pump–THz probe, and THz pump–optical probe spectroscopies, and strong-field THz generation, are also described in this chapter.

D. Turchinovich (✉)
DTU Fotonik, Department of Photonics Engineering, Technical University of Denmark, DK-2800 Kongens Lyngby, Denmark
e-mail: dmtu@fotonik.dtu.dk

M. C. Hoffmann
Max Planck Research Department for Structural Dynamics, University of Hamburg, CFEL, 22607 Hamburg, Germany
e-mail: matthias.c.hoffmann@desy.de

Z. M. Wang (ed.), *Quantum Dot Devices*, Lecture Notes in Nanoscale Science and Technology 13, DOI: 10.1007/978-1-4614-3570-9_11,
© Springer Science+Business Media New York 2012

Introduction

Understanding of ultrafast carrier dynamics in semiconductor quantum dots (QDs) is key to further improvement of operating performance of optoelectronic devices such as QD lasers [1, 2], QD infrared photodetectors (QDIPs) [3], and QD semiconductor saturable absorber mirrors (QD SESAMs) [4]. The growing demand for bandwidth in optical communications has already led to a demonstration of a fiber-optic communication systems operating at the data rates of several Tbit/s [5]. In order to support such an ultrahigh data rate, the subpicosecond switching times are required from individual optoelectronic components. Therefore, understanding of fundamental processes in semiconductors on ultrafast time scales, as well as demonstration of novel ultrafast modulation schemes leading to subpicosecond on/off switching in optoelectronic components become crucially important.

Here, we employ the combination of ultrafast optical and terahertz (THz) techniques to study the ultrafast carrier dynamics, and to achieve femtosecond-fast contact-free all-optical switching in QDs. A frequency of 1 THz corresponds to: 1 oscillation of electromagnetic field per 1 picosecond; a wavelength of 300 μm; or a photon energy of 4.1 meV. The use of ultrafast THz pulses in our experiment is dictated by their following advantages: First, the THz fields strongly couple to free, mobile charge carriers. This allows for observation of ultrafast dynamics in the systems where the carriers transit between the conducting states (CS) (e.g., barriers and wetting layers) which population is "visible" (i.e., absorbing) in the THz range; and the insulating states (e.g., QDs), which population will not contribute strongly to the absorption at THz frequencies. Second, ultrafast THz signals represent near-single cycle pulses of electric field, with the duration of less than a picosecond. Such pulses, incident onto a QD system, can therefore be used as ultrafast electrical switching signals applying the switching electric field to the QD system on a subpicosecond time scale, and, importantly, contact-free.

This chapter is structured as follows:

In "Ultrafast Dynamics of Capture and Release of Carriers in Quantum Dots" we will report on experiments elucidating carrier dynamics in QD systems using THz pulses as ultrafast conductivity probes. The principles of the underlying experiment, optical pump–THz probe spectroscopy will be also explained in this section.

In "Ultrafast All-Optical Switching in Quantum Dots with THz pulses: THz Electro-Absorption Effect" we will discuss ultrafast all-optical switching at THz frequencies, using the field of THz pulses to modulate the optical absorption in the QDs. A brief introduction to the underlying quantum-confined Stark effect in QD systems will be provided, the experimental demonstration of THz electro-absorption modulation in QDs will be presented, and potential applications will be discussed. The principles of the underlying experiment: THz pump–optical probe spectroscopy using strong-field THz pulses will be explained in this section.

Ultrafast Dynamics of Capture and Release of Carriers in Quantum Dots

Ultrafast dynamics in QDs has been studied intensively in the past two decades using ultrafast optical methods such as time-resolved photoluminescence (PL) [6, 7], and optical pump-probe spectroscopy [8, 9]. Here we observe the carrier release and capture dynamics in $In_{0.5}Ga_{0.5}As$/GaAs QDs, using an optical pump–THz probe technique. In such an experiment, an ultrafast optical excitation creates a population of electrons and holes, and the broadband THz probe pulse subsequently senses the change in the conductivity of the sample after the optical excitation. THz pulses are an ideal probe for conductivity since their frequency content is matched to the wavelength region of strong free carrier absorption in semiconductors, and subpicosecond pulse duration provides the corresponding time resolution in sampling of transient conductivity.

Principles of Transient Conductivity Measurements Using Optical Pump–THz Probe Spectroscopy

The dielectric function of a doped or photoexcited semiconductor in the THz frequency range is usually well described using Drude conductivity model [10], initially formulated to describe the conductivity of metals. In this formalism, the metal consists of light and mobile electrons that form plasma, and of heavy and immobile ions that form the crystal lattice. The lattice ions are assumed to act as scattering centers for the electrons, and between the individual acts of collision of an electron and an ion all other interactions (such as interactions of a given electron with other electrons and ions) are neglected. The collisions are assumed to be instantaneous, and upon the collision the electron velocity is changed abruptly. The time between the collisions—the scattering time, is assumed to be independent of the electron velocity. Although the original idea of free electrons colliding with the lattice ions was not correct (the electrons are actually freely moving within the bands that are provided by the overlapping Coulomb potentials of lattice ions, while the electron momentum-scattering collisions occur with phonons and other electrons), the Drude dielectric function still provides a fairly good agreement with experimental observations.

In particular, the Drude model is extensively used for accurate description of free-carrier conductivity in semiconductors in the THz range either in its original form (see e.g., [11, 12]), or with certain modifications (see e.g., [13–15]). An overview of the original Drude model and its various modifications applied to description of THz-range conductivity can be found in [16] and references therein. The free-carrier, Drude-like conductivity is usually the strongest factor contributing to the dielectric function describing the electronic response of semiconductor at THz frequencies. The contribution to the THz-frequency dielectric response

from the polarizability of localized carriers, or carriers bound into excitons, is usually much weaker [17, 18], and can often be neglected.

It is this high sensitivity of THz signals to the presence of free mobile carriers that makes the ultrafast THz probes an ideal tool to study the ultrafast carrier dynamics in the systems, where the carrier transitions between the conducting (i.e., strongly THz-absorbing) and localized (and thus not making significant contribution to the THz loss) states is of interest. The carrier dynamics in the systems where free carriers are captured onto (or released from) the localized crystal defects or 3D confinement potentials such as QDs or clusters have been studied successfully using optical pump–THz probe spectroscopy [9, 19–22].

The ultrafast THz pulses, the near-single-cycle transients of electromagnetic field with the duration on the order of (or even shorter than) a few hundreds of femtoseconds, can be generated by nonlinear optical downconversion of femtosecond laser pulses in a $\chi^{(2)}$—nonlinear crystal, phase-matched for co-propagation of both generating laser pulse and the generated THz signal. Since the resulting THz pulse is a product of coherent difference-frequency mixing of the laser modes within the bandwidth of the laser pulse, the THz pulse is per definition synchronized with the laser pulse in time, and is carrier-envelope stable.

One of the popular methods for coherent detection of THz pulses is free-space electro-optic sampling (FEOS) [23]—a method where the electric field of a THz pulse induces a Pockels effect in the electro-optic crystal, and a synchronized laser pulse senses the birefringence induced by the THz electric field with the time resolution corresponding to the laser pulse duration. Such a method allows to detect the electro-optic signal proportional to the *electric field* in the incident THz pulse including its sign, thus allowing for sampling of the complete THz waveform within the phase-matching bandwidth of the electro-optic crystal. This is in contrast to other methods of THz detection based on the intensity measurements, such as pyroelectric and bolometric detectors, Golay cells etc. The discussion on nonlinear optical THz generation and detection can be found in [16] and references therein.

An archetypal THz emitter and detector crystal used with the Ti:Sapphire femtosecond lasers operating around the wavelength of 800 nm is a $\langle 110 \rangle$ ZnTe crystal. The THz pulse generated and detected in a 1 mm thick $\langle 110 \rangle$ ZnTe crystal using 800 nm laser pulses of approximately 100 fs duration is shown in Fig. 11.1a. In Fig. 11.1b its Fourier amplitude and phase spectra are shown, covering the spectral range around 0–2.7 THz.

In Fig. 11.2 the layout of a typical optical pump–THz probe spectrometer is shown. Apart from the THs emitter and detector stages and guiding optics, it features two optical delay lines: DEL 1, used for scanning the FEOS delay, and thus to sample the waveform of the THz pulse; and DEL 2, used to control the delay of optical pump. By scanning the THz delay (DEL 1) at a fixed position of pump delay (DEL 2), a THz waveform transmitted through the sample at a fixed time-delay after excitation can be acquired. If a pump delay (DEL 2) is adjusted so that the probe THz pulse will interact with the sample before the pump pulse, then

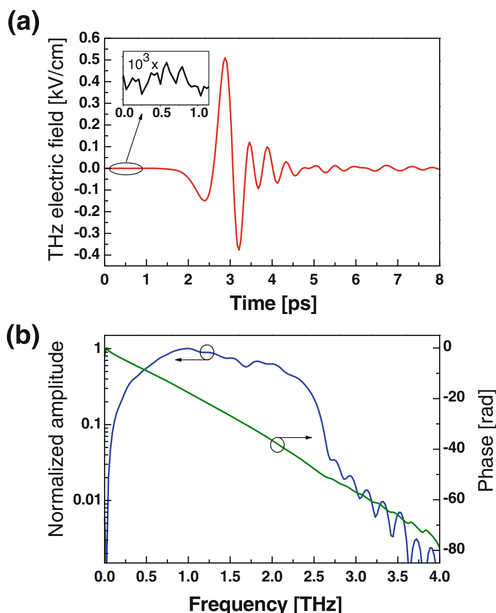

Fig. 11.1 **a** A THz pulse generated and detected in ⟨110⟩ ZnTe crystal with 100 fs laser pulses of 800 nm central wavelength, produced by an amplified Ti:Sapphire femtosecond laser. **b** Fourier amplitude and phase spectra of the THz pulse from **a**

the THz waveform transmitted through the unexcited sample will be acquired, which can serve as a reference measurement. Often, in order to increase the sensitivity of the transient THz spectroscopy measurements, only the transmitted THz signal associated with the pump interaction is recorded by modulating the pump beam at a certain modulation frequency and reading out the FEOS signals associated only with this modulation frequency. This signal is called a differential signal. The full shape of the THz waveform transmitted through the photoexcited sample is obtained by simple addition of the reference THz waveform (the one propagated through an unexcited sample), and the differential waveform associated with the modulated pump beam. The example of such measurements is shown in Fig. 11.3.

The differential THz signals recorded at various values of pump delays contain the spectral information of complex-valued photo-induced conductivity (or the equivalent properties such as absorption coefficient and refractive index), represented in temporal domain. In Fig. 11.4 the differential THz signals recorded at various time delays after 800 nm photoexcitation of a bulk intrinsic GaAs sample, and the sample containing one layer of InAs/GaAs QDs are shown. Note the rapid decay of photoconductivity in the sample containing QDs, as opposed to a simple bulk GaAs. This decay is due to the rapid capture of the mobile carriers from the GaAs barriers and wetting layers into the localized QD states featuring a full 3D confinement, thus making the carriers immobile, and hence greatly reducing their interaction with the THz field. This phenomenon will be described in detail in the next section.

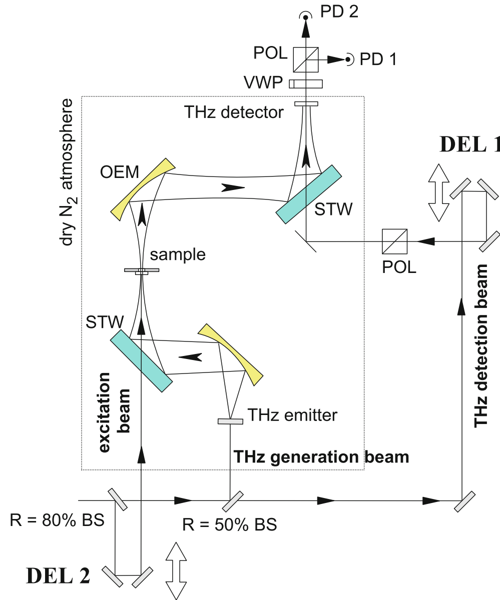

Fig. 11.2 The layout of a typical optical pump–THz probe spectrometer. *DEL 1* and *DEL 2* are the optical delay lines used for scanning the FEOS delay, and controlling the optical pump delay, respectively. *BS*-beam splitter, *OEM*-off-axis metallice mirror, *STW*-semitransparent window which is highly reflective for the THz beam and transparent for the optical beam. FEOS optics: *POL*-polarizer, *WP*-waveplate, *PD*-photodiode. From [24]

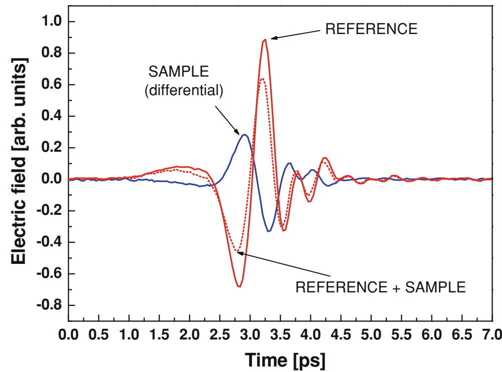

Fig. 11.3 Reference THz pulse propagated through the unexcited intrinsic GaAs sample (pump delay of-10 ps), and the differential THz signal propagated through the GaAs sample 10 ps after the excitation with 800 nm laser pulse. The full THz waveform of the THz pulse propagated through the photoexcited sample, constructed from the reference and the differential, is shown as a *dashed line*. From [24]

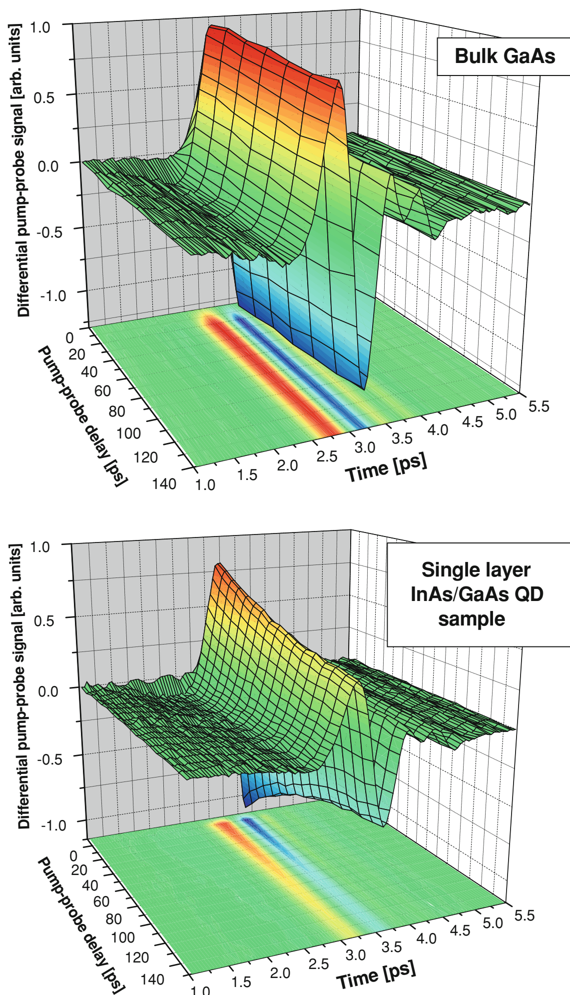

Fig. 11.4 Differential THz waveforms—the photo-induced THz conductivity represented in time domain, for the bulk intrinsic GaAs sample, and for the same GaAs sample overgrown with one layer of InAs/GaAs QDs. The excitation wavelength is 800 nm. Note the rapid decrease of conductivity for the QD sample. From [24]

The set of differential THz signals acquired in this fashion for various pump delays, together with a reference THz signal acquired with the pump pulse adjusted to negative time delay, allows for a calculation of the transient evolution of complex THz conductivity spectra of the photoexcited sample after the act of optical excitation. In Fig. 11.5 the evolution of complex-valued conductivity spectra after the photoexcitation of the sample containing QDs is shown. The methods for calculation of such frequency-domain spectra from the experimental time-domain data, and the influence of dynamic processes such as, e.g., carrier diffusion during the THz pulse propagation can be found in [16] and references therein.

In certain cases, when the nature of the photoexcited conductivity does not change, and the conductivity modulation associated with optical excitation does not have a sharp spectral dispersion, a simplified method of transient conductivity

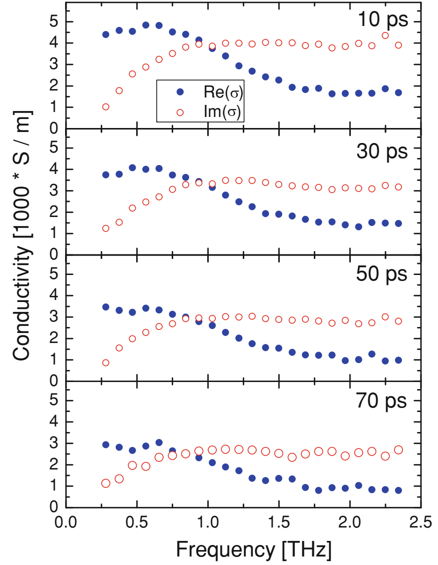

Fig. 11.5 Complex-valued THz conductivity of the GaAs sample containing one layer of InAs/GaAs QDs excited at 800 nm, calculated from the differential time-traces shown in Fig. 11.4. Time delay after excitation is indicated in the Figure

measurement can be used. In this case, instead of acquiring a full THz differential waveform by scanning the THz delay DEL 1, this delay is adjusted so that it coincides with the temporal position of the maximum of the differential THz pulse. Then, only the pump delay (DEL 2) is scanned, and the temporal evolution of the relative change in the maximum of the transmitted THz pulse $\Delta T(t)/T_0$ is recorded. Following the analysis presented in [25] and references therein, a THz frequency-integrated sheet conductivity can be calculated from such measurements using the equation:

$$\sigma_{2\mathrm{D,THz}} = en\mu(t)d = \frac{1+N}{Z_0}\left(\frac{1}{1+\Delta T(t)/T_0} - 1\right). \tag{11.1}$$

Here e is an electron charge, n is the carrier density, μ is the carrier mobility, d is the thickness of photoexcited layer usually estimated as an inverse pump absorption coefficient in the sample material $d \approx 1/\alpha_{\mathrm{pump}}$, N—the THz refractive index of the unexcited sample, and $Z_0 = 377\,\Omega$ is the impedance of the free space. In the section below we will use this method to analyze the transient conductivity dynamics associated with carrier capture and release in InGaAs/GaAs QDs.

We note here that the THz pulses are sensitive to the total conductivity of the sample, comprising both electronic and hole contributions $\sigma_{\mathrm{total}} = |e|[\mu_e n_e + \mu_h n_h]$. However, owing to the fact that in many material systems (such as the InGaAs/GaAs material system studied here) the hole effective mass is much larger than that of an electron, and thus the hole mobility is much smaller than that of an electron, in some cases it is safe to assume that the sample conductivity is dominated by the electrons, i.e., $\sigma_{\mathrm{total}} \approx \sigma_e$.

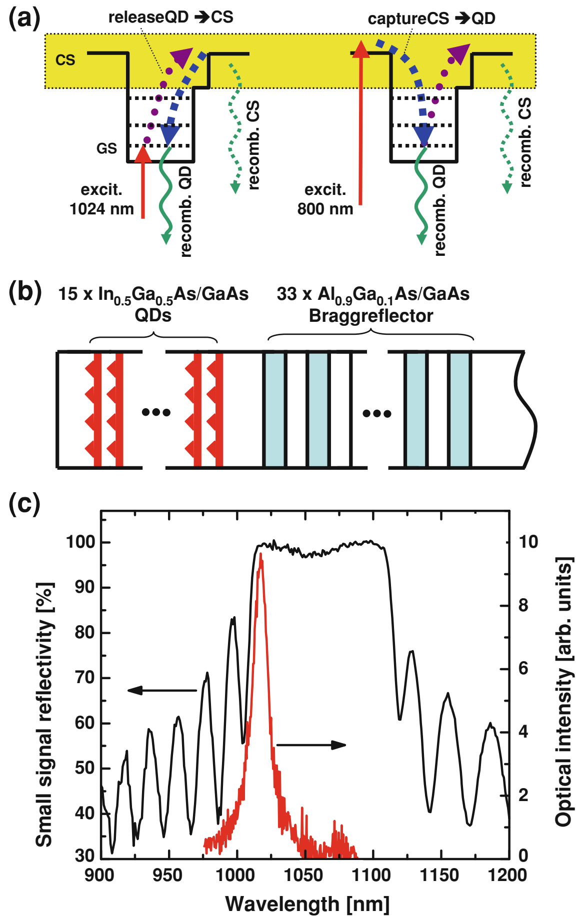

Fig. 11.6 **a** Schematic of InGaAs/GaAs QD SESAM sample. **b** Carrier dynamics processes in photoexcited QDs. *CS*-conducting state. *GS*-QD ground state. **c** Small signal reflectivity and room temperature optical emission spectra at 800 nm excitation of the QD SESAM. From [22]

Ultrafast Carrier Dynamics in Quantum Dots Observed by THz Spectroscopy: Experimental Results and Discussion

Now we will describe our experiments aimed at observation of carrier release and capture dynamics in InGaAs/GaAs QDs. This section is based on our results published in [22]. Our experiment was driven by a regenerative Ti:Sapphire femtosecond amplifier, operating at a repetition rate of 1 kHz, and generating 45 fs pulses at 800 nm central wavelength. A part of the amplifier output was used as a pump pulse: either directly, for excitation of the barrier states of the QDs at 800 nm; or after frequency conversion in an optical parametric amplifier (OPA) to 1024 nm, for resonant excitation of the QD ground state (GS), as shown in Fig. 11.6a. Another part of the amplifier output was used to power the nonlinear crystal-based THz time-domain spectrometer, such as described in the previous

subsection, with a sample positioned at its focal point. The THz probe pulses had a duration of approximately 300 fs, and were similar to the pulse shown in Fig. 11.1. All our measurements were performed at room temperature.

Our sample was a QD SESAM, grown by molecular beam epitaxy (MBE). It had 15 layers of $In_{0.5}Ga_{0.5}As$/GaAs QDs separated by GaAs spacers, grown on top of the $Al_{0.9}Ga_{0.1}As$/GaAs Bragg reflector. The total thickness of QD and spacer region was 611 nm. The sample was grown on a 0.5 mm thick semi-insulating GaAs substrate. The schematic of the sample is shown in Fig. 11.6b.

Ultrafast processes such as carrier capture, release, and recombination in a QD structure are schematically shown in Fig. 11.6a, exemplified by electrons in the conduction band. Also important for the ultrafast carrier dynamics are processes such as intradot carrier relaxation and carrier–carrier and carrier-phonon scattering, and interplay between the carriers in QD and the wetting layer (WL) states. These processes are temperature- and carrier density- dependent [8, 26]. In our experiments, the population of CS, consisting of the WL and barrier states, was monitored after optical excitation by measuring the relative transmission $-\Delta T/T_0$ of the THz probe pulse through the photoexcited sample. Here T_0 is the THz transmission through the sample before photoexcitation. The measured time dependencies of $-\Delta T/T_0$ are then converted into a photo-induced THz-frequency-integrated sheet conductivity $\Delta\sigma_{2D,THz} \propto [\mu_e n_e + \mu_h n_h]$, as described in a previous subsection, where $\mu_{e,h}$ and $n_{e,h}$ are the mobility and concentration of electrons and holes, respectively [25]. Both optical pump and THz probe pulses were incident on the sample at normal incidence. Therefore, the in-plane conductivity of the photoexcited sample was probed with the THz pulse. The energetic range of the probed CS (for the case of conduction band) is marked in yellow in Fig. 11.6a. We note here that in our experiments we were not able to distinguish between the carriers confined in the WLs, and the carriers present in the barriers, since both of these states are conducting in the plane of the sample. For the same reason we were not able to distinguish between electrons and holes in CS. However, as mentioned before, the electron contribution to the sample conductivity will be dominating, owing to their higher mobility.

The small-signal reflectivity spectrum of the studied QD SESAM, as well as the room-temperature optical emission spectrum at 800 nm excitation, indicating the energetic position of the QD GS, is shown in Fig. 11.6c. The Bragg reflector has a 100 nm wide stop band centered at 1060 nm. The emission spectrum is centered at a wavelength of 1017 nm. The 1024 nm optical pump pulse has a full width at half maximum (FWHM) bandwidth of 45 nm, ensuring good overlap with a QD GS in the case of its resonant excitation. The Bragg reflector blocked the propagation of the 1024 nm pump pulse further into the thick GaAs substrate of the sample, thus preventing free carrier generation in GaAs by two-photon absorption (TPA). This was very important, since the TPA-generated free carriers in a thick GaAs substrate would easily obscure the signal from the carriers released from the QDs at the resonant GS excitation.

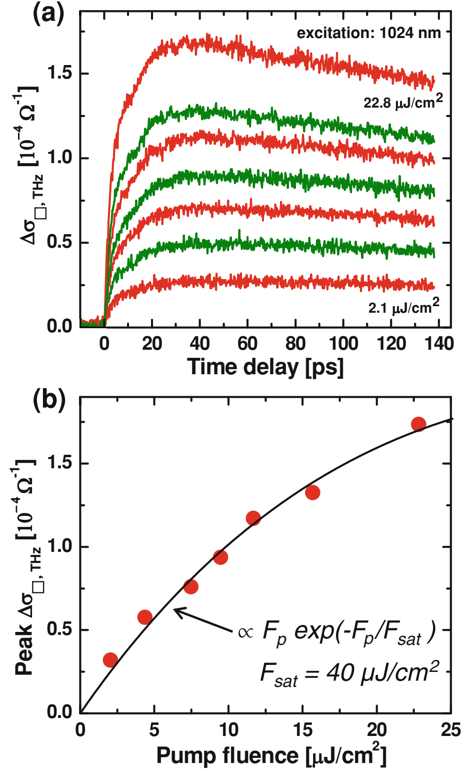

Fig. 11.7 Carrier release from the QD ground states: **a** Dynamics of photoinduced sheet conductivity $\Delta\sigma_{2D,THz}$ at resonant optical excitation of QD GS at 1024 nm, with the pump fluence 2.1–22.8 μJ/cm^2. **b** Maximum of $\Delta\sigma_{2D,THz}$ traces as a function of pump fluence for 1024 nm excitation. *Solid line* fit to the saturable absorption function with saturation fluence $F_s = 40\,\mu\text{J/cm}^2$. From [22]

In order to observe carrier release from the QD GS to the CS, we performed resonant optical excitation of QD GS at the wavelength of 1024 nm, with pump fluences in the range 2.1–22.8 μJ/cm^2. As can be seen in Fig. 11.7a, we observe a non-instantaneous rise in the sample conductivity, reaching its maximum at approximately 35 ps after photoexcitation, followed by a slow decay due to recombination in barriers, WLs, and QDs. The maximum of $\Delta\sigma_{2D,THz}$ as a function of pumping fluence exhibits a sub-linear behavior as plotted in Fig. 11.7b, which suggests that the photoexcitation mechanism leading to the supply of carriers to the CS has a one-photon saturable nature (with a reasonable assumption of constant carrier mobility), exactly as expected from resonant excitation of the QD GS in this pump fluence range. Fit of this dependency with the saturable absorption [27] function $\propto F_p \exp[-F_p/F_s]$, where F_p is the pump fluence, and F_s is the saturation fluence, revealed $F_s = 40\,\mu\text{J/cm}^2$. This is in reasonable agreement with the value of $F_s = 25\,\mu\text{J/cm}^2$, observed in [4] for a similar QD-based structure. Also, in the same Ref. [4] no TPA-driven carrier generation in the QDs was observed at resonant QD GS excitation with pumping fluences up to 1 mJ/cm^2, which agrees well with our observations. We note here that similar saturation fluence values were recently observed by us in saturable absorbers for THz frequency range, based on

completely different saturable absorption mechanism—the nonlinear carrier transport in doped bulk semiconductors in strong THz fields [28].

The $e1h1$-WL energy gap was measured to be 252 meV in a similar structure, shared approximately in 60/40 proportion between the electron and hole states [8]. This largely exceeds $k_{\mathrm{B}}T = 26\,\mathrm{meV}$ at room temperature for both electron and hole GS-CS transitions. However, the large difference in densities of states between the QD GS and CS should increase the probability of thermionic GS-CS carrier release.

In order to observe the carrier capture dynamics, the carriers were excited directly into the barrier states of conduction band with 800 nm excitation. In Fig. 11.8a the corresponding time dependencies of $\Delta\sigma_{2D,\mathrm{THz}}$ are shown for the pump fluences in the range 0.04–1.2 $\mu\mathrm{J/cm}^2$. In case of the barrier excitation, a near-instantaneous rise in photo-induced conductivity is observed, followed by a fast decay, and by a very long-lived contribution. We attribute this fast decay to capture of the carriers into the QDs [9, 19, 20], as supported by a slower initial conductivity decay dynamics observed in a bulk semi-insulating GaAs sample used here for control (dashed line in Fig. 11.8a). A very long-lived contribution, persistent even after an experimental cycle of 1 ms in case of the strongest excitation, is most likely due to spatially separated electrons and holes via Γ - X transfer [29] in the Type-II $\mathrm{Al_{0.9}Ga_{0.1}As}$/GaAs SESAM Bragg reflector, which was accessible to the pump light at this wavelength. This very long-lived contribution led to a small non-zero background in measured photoconductivities at time delays $t < 0$. In the QD SESAM data shown in Fig. 11.8a this background has been subtracted. A small kink in the 800 nm traces at around 22 ps is an experimental artifact, arising from a double reflection in a 2 mm thick pump beam attenuator during the measurements. The initial rise of $\Delta\sigma_{\mathrm{2D,THz}}$ shows linear dependency on excitation fluence (see Fig. 11.9), as expected from a non-saturable one-photon excitation process.

In order to estimate the carrier capture time, we have measured the time it takes for the photo-induced conductivity to decay by 10% in respect to its maximum. A 10% benchmark was chosen because the maximum value of fast decay in our data only reaches 20% due to the presence of a very long-lived component. This 10% time constant demonstrates near-linear growth from 1.2 to 5.7 ps with increase in pump fluence, as shown in Fig. 11.8b. We attribute this growth in carrier capture time constant to filling of the QD (trap) states at stronger excitation, which is in accordance with the observations made in Refs. [19, 20, 25, 30]. We note here that our observations are in contrast with the speeding up of carrier capture with increase in pump fluence, mentioned in Refs. [8, 9]. In Ref. [8] the population dynamics of only the GS of the QD was observed. However, one may speculate that suggested trapping mechanism—electron–electron scattering, may also provide for the scattering of the carriers from higher lying QD states back into the CS, thus slowing down the decay dynamics of the conductivity (which was not monitored in that experiment). The reason for the disagreement between our observations and those of Ref. [9] is not clear at this point.

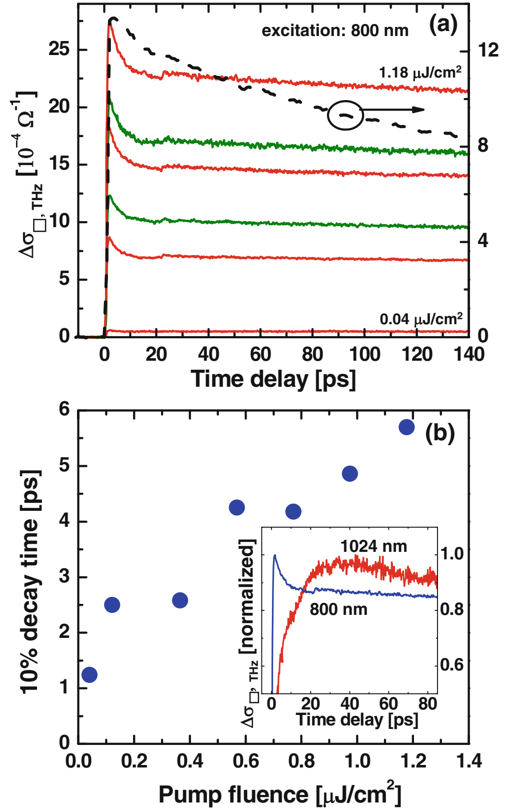

Fig. 11.8 Carrier capture from the conducting states into QDs: **a** *Solid lines* dynamics of photo-induced sheet conductivity $\Delta\sigma_{2D,THz}$ of a QD SESAM at optical excitation of barriers at 800 nm, with the pump fluence varied between 0.04 and 1.18 μJ/cm^2. *Dashed line* $\Delta\sigma_{2D,THz}$ for a bulk GaAs sample at 800 nm excitation with the pump fluence of 0.9μJ/cm^2. **b** 10% decay time constant of the QD SESAM $\Delta\sigma_{2D,THz}$ traces in Fig. 11.8a, as a function of 800 nm pump fluence. *Inset* Normalized $\Delta\sigma_{2D,THz}$ traces for QD GS and barrier excitation with the pump wavelength and fluence of 1024 nm and 22.8 μJ/cm^2, and 800 nm and 1.18 μJ/cm^2, respectively. From [22]

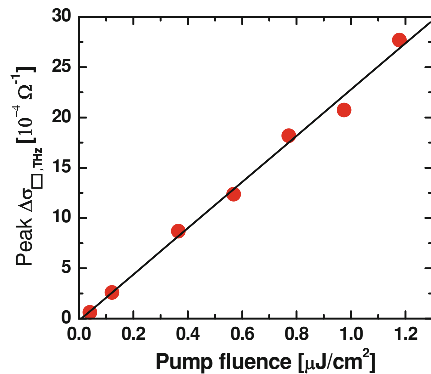

Fig. 11.9 Maximum of $\Delta\sigma_{2D,THz}$ traces as a function of pump fluence for 800 nm excitation. *Solid line*: linear fit, indicating that barrier excitation is a one-photon, non-saturable process

As a conclusion of this section, we have observed the conductivity dynamics in photoexcited InGaAs/GaAs QD structures associated with the carrier release from, and capture to QDs at room temperature (see inset of Fig. 11.8b). The time constant of carrier capture was found to be in the range of one to few picoseconds,

and was growing with pump fluence as indicative of saturating trapping capacity of the QDs. The time constant of carrier release from the QDs was found to be of approximately 35 ps, and it was independent of the pump fluence.

Ultrafast All-Optical Switching in Quantum Dots With THz Pulses: THz Electro-Absorption Effect

Recently demonstrated fiber-optic communication systems are reaching Tbit/s data rates in single serial communication channels [5]. Time and bandwidth considerations dictate that optical pulses of femtosecond duration and THz bandwidth should be used as data symbols in such systems. Following the same considerations, in order to implement a *wireless* (sub)Tbit/s system, such as, e.g., radio-over-fiber system, the signal frequency must be in the THz range [31, 32], and femtosecond, single-cycle THz pulses should be used as data symbols. On the receiver end of such a system, ultrafast THz signals should be encoded onto an optical carrier at (sub)THz repetition rate without the loss of bandwidth. In order to maintain the ultrafast speed of operation, the THz signal should bypass the inherently slow electrical domain, and should be encoded directly onto the optical signal. Therefore fast and direct THz-to-optical conversion devices have to be developed.

In this section we will describe ultrafast, contact-free electro-absorption modulation of optical absorption in InGaAs/GaAs QDs by the electric field of a strong-field single cycle THz pulse. Our THz-rate electro-absorption modulation scheme is based on the quantum-confined Stark effect induced by the electric field of an incident THz pulse. Optical absorption at the GS of the QD is modulated by the electric field of the THz pulse in a (near-)instantaneous manner, resulting in encoding of high-speed, high repetition rate THz pulses onto an optical signal resonant with the QD GS absorption [33, 34].

Principles of Strong-Field THz Pulse Generation, and THz Pump–Optical Probe Spectroscopy

As discussed in the Introduction, ultrashort near-single-cycle THz pulses are an excellent tool to study dynamical processes in various systems using time-resolved pump-probe spectroscopy. Changes in properties such as photoconductivity that are induced by an optical or near-infrared excitation pulse can be probed by a time-delayed THz pulse. A different class of experiments is based on taking advantage of strong THz fields that are used to *change* the optical properties of materials. Since these effects typically require high electric field strengths, and scale non-linearly with the applied THz field, it is crucial to use THz sources with high

enough fields in the experiments. The typical electric field strength, at which the THz-induced nonlinearities in most semiconductor systems become observable is of the order of 100 kV/cm.

The peak electric fields in the THz pulses used for the experiments described in "Principles of Transient Conductivity Measurements Using Optical Pump-THz Probe Spectroscopy" were relatively weak. These THz pulses were generated by optical rectification in a $\langle 110 \rangle$ cut ZnTe crystal and had an energy in the order of 1 nJ, corresponding to the peak electric field strengths not exceeding a few kV/cm (typically, less than 1 kV/cm). The ZnTe crystal is the most commonly used material for creating THz pulses from 800 nm amplified femtosecond laser systems. Its main advantage is that phase-matching conditions for the efficient co-propagation of generating 800 nm laser signal, and generated THz signal are approximately fulfilled in *collinear geometry* for the crystal thicknesses reaching a few millimeters (typically, 1–2 mm) and the THz frequencies below approxiamtely 3 THz. However, ZnTe has strong two-photon absorption at 800 nm, which leads to the generation of free carriers and, in turn, to increased THz reabsorption. Hence, the useful pump intensity is limited, which is a serious restriction in scaling up the process to higher generated THz pulse energies [35, 36].

Lithium niobate ($LiNbO_3$) is a material widely used in nonlinear optics and has favorable properties such as a high bandgap (which reduces two-photon absorption at 800 nm) and large second-order nonlinear coefficient. However, the phase-matching condition for THz generation by optical rectification of Ti:Sapphire laser pulses at 800 nm wavelength is not satisfied for a simple collinear geometry. This is caused by the large difference between group refractive index at optical frequencies ω_0 and phase refractive index at THz frequencies. Typical values are $n_g(\omega_0) = 2.2$ for a Ti:Saphire laser pump pulse at 800 nm wavelength and $n(\Omega) = 5$ at the frequency of 1 THz. In a purely collinear geometry, optical rectification in a non-phasematched crystal leads to an angle γ between the propagation direction of an optical pump pulse and that of a resulting THz wave, given by the relation

$$\cos\gamma = n_g(\omega_0)/n(\Omega) \tag{11.2}$$

This is reminiscent of the Cherenkov effect in the sense that speed of the source of radiation inside a material is exceeding the speed of light for the generated radiation. THz generation in $LiTaO_3$ and $LiNbO_3$ using this Cherenkov geometry has been demonstrated and used for experiments as early as in 1984 [37]. However, the THz generation efficiency is comparatively low because of geometric constrains and the lack of coherent superposition of waves. In order to improve THz generation efficiency, tilted-pulse-front pumping (TPFP) was proposed and demonstrated by Hebling et al. in 2002 for THz pulse generation in $LiNbO_3$ [38]. Here the intensity front of the pump laser is tilted at an angle corresponding to the Cherenkov angle γ. The THz radiation (Ω) generated by the tilted-pulse-front of the pump pulse propagates perpendicularly to this front with the THz phase velocity $v(\Omega)$ at an angle γ to the direction of propagation of the optical pump, traveling with a speed $v(\omega_0)$ (see Fig. 11.10).

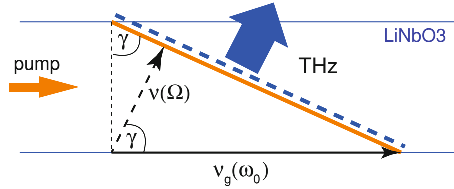

Fig. 11.10 THz generation by tilted-pulse-front pumping. The *thick solid line* indicates the pump pulse front, and the *thick dashed line* indicates the THz phase front. The *arrows* indicate the propagations direction and velocities of these two surfaces

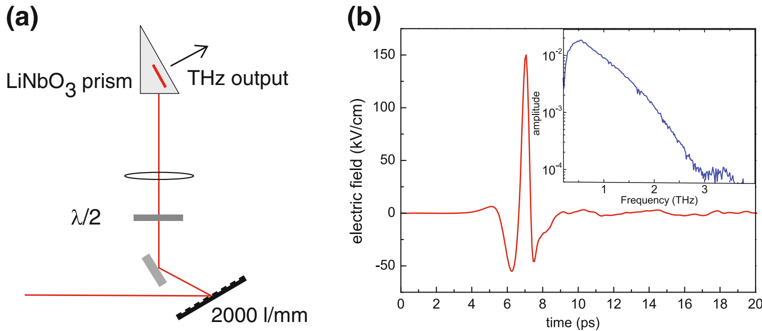

Fig. 11.11 **a** Experimental setup for THz generation by TPFP in $LiNbO_3$. **b** Typical pulse shape and spectrum obtained in our experiments

By adjusting the angle γ to match the known material properties, this technique provides *noncollinear phase matching*. Further, the tilted-pulse-front pumping technique allows for using an extended pump spot, thereby enabling high-energy THz pulse generation. Due to the large difference between $n_g(\omega_0)$ and $n(\Omega)$, TPFP in $LiNbO_3$ requires a pulse front tilt as large as 63°–65°. In order to provide such large tilt angle (and the corresponding large angular dispersion, see Eq. 11.2) a pulse-front-tilting setup consisting of a grating and a lens is used in experiments (Fig. 11.11). The angular dispersion introduced by the grating is further enlarged by the lens, which also recreates the original short pulse duration inside the medium by imaging the grating surface into the crystal. Additionally, a half wave plate is used to match the polarization of the pulse to the z-axis of the $LiNbO_3$ crystal. The generated THz wave is coupled out into free space through the surface of the crystal cut at the tilt angle γ.

By using this method, THz energies of 10 μJ [39] and 30 μJ [40] have been reported with pump-to-THz energy conversion efficiencies of 5×10^{-4} and 1.1×10^{-3}, respectively. These are the most energetic ultrashort THz pulses generated using a table-top source so far.

These strong THz pulses have been used in studies of semiconductors and semiconductor nanostructures to investigate strong field effects such as ballistic

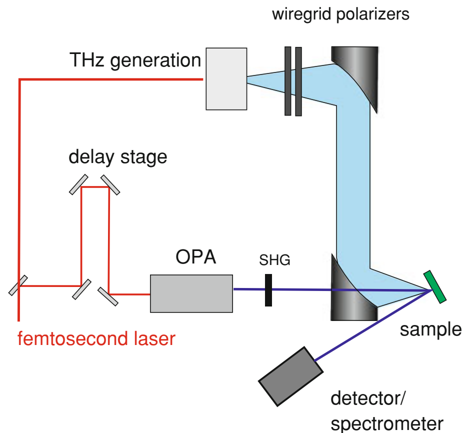

Fig. 11.12 Experimental setup for measuring the THz-induced quantum-confined Stark effect in QDs in a reflection geometry, using a TPFP in lithium niobate crystal for THz pump pulse generation, and an OPA for optical probe signal generation. A pair of linear polarizers is used to controllably attenuate the electric field in the pump THz pulses incident onto the QD sample

carrier acceleration, impact ionization as well as nonlinear propagation effects [28, 41].

For the THz pump–optical probe experiments on QDs described below we used intense THz pulses with an energy of 2 μJ generated from an 80 fs amplified Ti:Saphire laser system operating at 1 kHz repetition rate. The resulting THz pump pulses were focused tightly onto the QD sample yielding field strengths of 200 kV/cm as calibrated by electro-optical sampling. To controllably attenuate the THz pulses a pair of wire grid polarizers was used. A part of the laser output was split off and sent to an OPA and a SHG crystal to produce a tunable near-infrared probe signal at the wavelength around 1040 nm. This wavelength corresponded to the GS absorption in the QDs. These weak probe pulses were then delayed and detected. A sketch of the experimental setup is shown in Fig. 11.12. The change in the reflectivity of the optical probe pulse was recorded as a function of the time-delay between the optical probe pulse and a THz pump pulse.

Electro-Absorption Modulation in Quantum Dots: Quantum-Confined Stark Effect

The electro-absorption effect in a QD, a quantum-confined Stark effect (QCSE) [42] arises from the tilt in the confinement potential of a semiconductor nano-structure in the applied electric field E: U = Eex, where x is the coordinate along which the electric field E is applied. The QCSE manifests itself in two ways, as shown in Fig. 11.13: (1) in a decrease of the optical transition energy between electron and hole states (Stark shift); and (2) in a spatial separation of the envelope wavefunctions of electrons ψ_e and holes ψ_h in the presence of electric field, which leads to a reduced wavefunction overlap integral $M(E) = \langle\psi_e|\psi_h\rangle$. The value of $|M(E)|^2$ dictates the optical transition probability, and hence the optical absorption

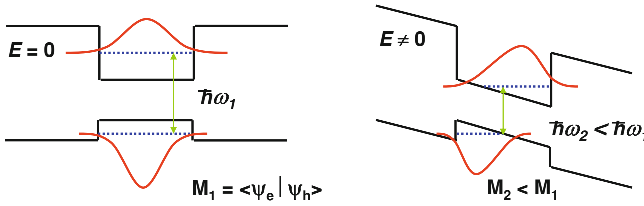

Fig. 11.13 An illustration of a quantum-confined Stark effect: application of electric field E to the quantum-confined system with initially rectangular confinement potential is leading to a decrease in optical transition energy $\Delta\hbar\omega$ and reduction in wavefunction overlap ΔM. The value of M^2 dictates the optical transition probability, and therefore the optical absorption coefficient

coefficient. Therefore, the optical absorption can be manipulated by the applied electric field.

Note, that in the case of a spatially-symmetric confinement potential at $E = 0$, the strength of the electro-absorption modulation effect only depends on the *absolute value* of the electric field, and not on its sign.

In Fig. 11.14 we show the lateral projections of wavefunctions for GS electrons and holes in disk-like $In_{0.5}Ga_{0.5}As$/GaAs QD without and with external electric field applied in the plane of the QD. Only the lateral components of the wavefunctions are modified in this case, as the confinement potential in the vertical, out-of-plane dimension is not affected by the in-plane electric field applied to a disk-like QD with "vertical" potential walls. The modified variational method (Turchinovich and Monozon, unpublished), initially developed for calculation of the QCSE in quantum wells [43] was applied here for calculations of the wavefunctions and eigenenergies of the GSs in the QD for arbitrary electric field strength. The material parameters of $In_xGa_{1-x}As$ compound were used [44], and the QD dimensions: radius of 5.3 nm, and height of 5 nm were chosen to approximately match the observed QD dimensions and GS optical transition wavelength around 1 μm [45].

In Fig. 11.15 the electric field dependency of Stark shift, and the values of wavefunction overlap integral M and the optical transition probability M^2 (i.e., the measure of optical absorption strength) is shown, as calculated for the disk-like QDs described above.

THz Switching in Quantum Dots: Experimental Results and Discussion

This subsection is based on our results published in [33] and [34]. Here we describe the femtosecond all-optical switching of optical absorption in InGaAs/GaAs QDs via QCSE induced by the electric field of an incident THz pulse. The

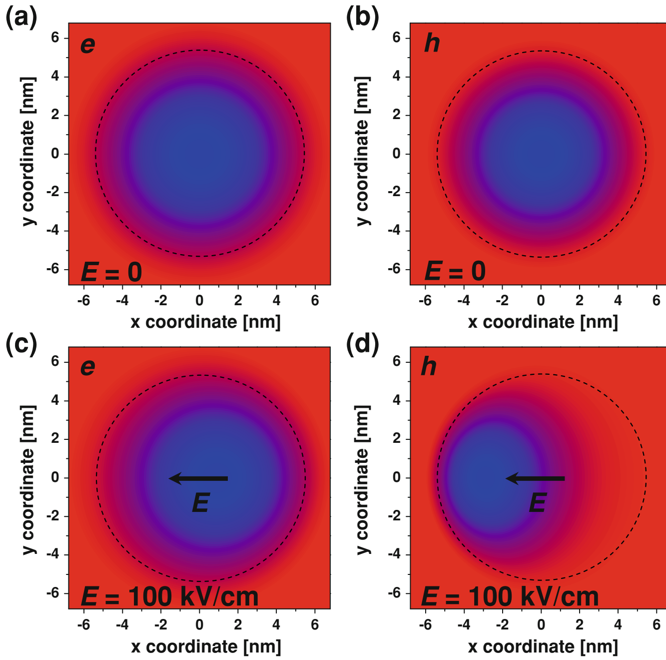

Fig. 11.14 Calculated lateral projections of wavefunctions for ground-state electrons and holes in disk-like $In_{0.5}Ga_{0.5}As$/GaAs QD without (**a**, **b**) and with (**c**, **d**) electric field applied in the plane of the QD. The electric field strength is 100 kV/cm. The QD dimensions are: radius of 5.3 nm, and height of 5 nm. The lateral projection of the physical dimensions of the QD is indicated with a dashed circle

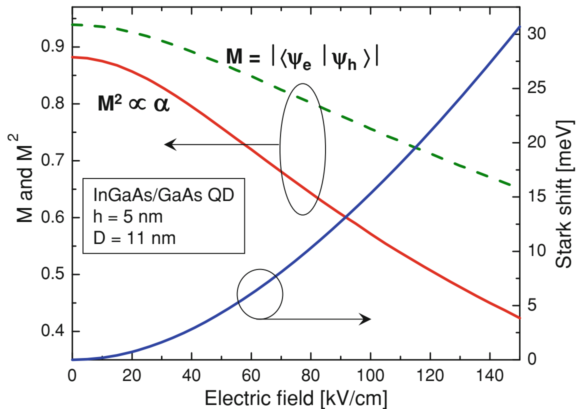

Fig. 11.15 Calculated Stark shift, and the values of wavefunction overlap integral M, and the measure of optical transition probability M^2 as a function of applied electric field for the disk-like $In_{0.5}Ga_{0.5}As$/GaAs QD from Fig. 11.14

QCSE, induced by the ac electric field oscillating at lower THz frequencies can be considered as an instantaneous effect, i.e., there is no delay between the instant when the electric field is applied to the quantum-confined nanostructures, and the

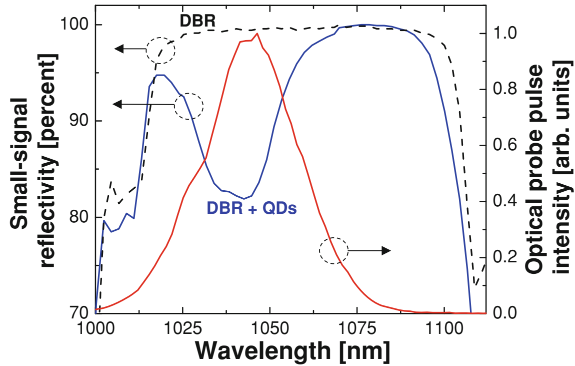

Fig. 11.16 Small-signal reflectivity spectrum of the whole QD sample (*solid line*), a bare DBR (*dashed line*), and the intensity spectrum of the probe laser pulse at QD ground-state resonance at 1040 nm. From [34]

instant when the optical properties in this nano-structure change. Once the field is removed, the optical properties of the nanostructure instantaneously return to the initial state, i.e., the relaxation time is essentially zero.

The mechanism of the interaction of an electric field with the QDs and the resulting electro-absorption modulation in QDs via QCSE was discussed in the previous subsection. We remind here that for the spatially-symmetric quantum confinement potential such as a disk-like quantum dot, the strength of QCSE will depend only on the absolute value of the applied electric field, and not on its sign. In traditional electro-absorption modulators, the electric field is applied to the QD structure via an external circuit. In our work instead of applying the modulating electric field to the whole QD structure via the hard-wired electrodes, which would slow down the modulation rate due to a large RC-constant involved, we have modulated the confinement potential of the QDs (which are the smallest possible semiconductor elements with a negligible RC constant) *directly* by the electric field of single-cycle THz pulses directed at the QD sample at normal incidence angle. As a result, we achieved a direct all-optical encoding of a free-space, ultrafast, high-bandwidth, and high repetition rate THz signal onto an optical signal probing the absorption in the QDs. We note that theoretical studies of THz-induced electro-absorption modulation in semiconductors has been performed in the past (see e.g., Ref. [46]).

The sample used in this experiments was somewhat similar to the one described in "Ultrafast Dynamics of Capture and Release of Carriers in Quantum Dots", based on our work [22]. It was an InGaAs/GaAs QD-based SESAM, comprising of a broadband GaAs/ $Al_{0.9}Ga_{0.1}As$ distributed Bragg reflector (DBR), and a QD absorber layer featuring 80 layers of submonolayer-grown $In_{0.5}Ga_{0.5}As$/GaAs QDs with the diameter of around 10 nm and the height of around 7 nm, alternated by the GaAs barriers of 10–14 nm thickness. Eight of these barriers were grown at low temperature (LT) in order to provide for the fast SESAM partial recovery with the exponential time constant of 4.3 ps for mode-locked laser applications, unrelated to this work. The QD absorber layer and the DBR were grown on a $(450 \pm 25) - \mu$m thick, $< 100 >$ -oriented semi-insulating GaAs substrate. The small-signal optical reflectivity spectra of the whole QD sample, and of a bare DBR measured prior to

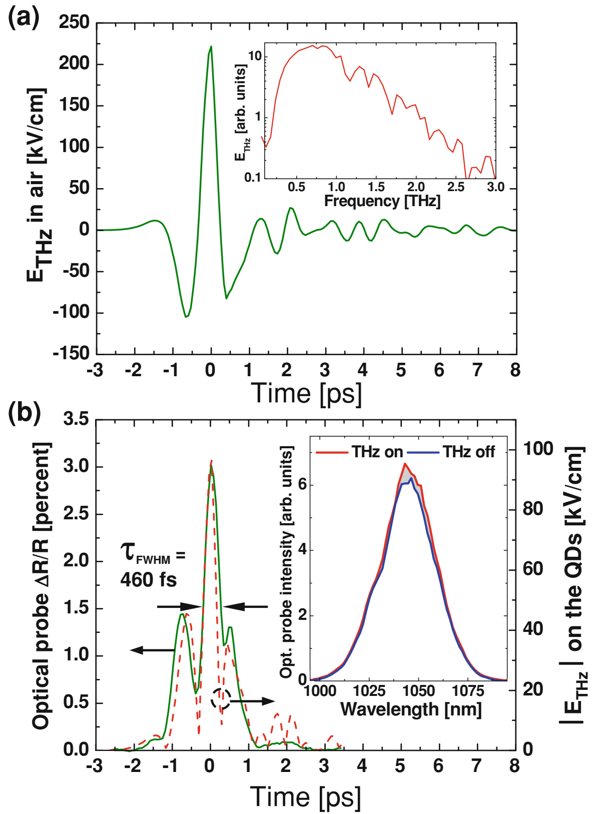

Fig. 11.17 **a** Electric field in free space as a function of time of the THz pulse with peak field strength of 220 kV/cm. Inset: its amplitude frequency spectrum. **b** *Solid line*—temporal reflectivity modulation $\Delta R/R$ of the probe signal at 1040 nm in the QD sample, under influence of the incident THz pulse from **a**. *Dashed line*—temporal dependency of absolute value of the electric field in the THz pulse from **a** experienced by the QDs. Inset: intensity spectrum of the optical probe signal with and without peak electric field of the THz signal from **a** on the QD sample. From [34]

the growth of the QD absorber layer, are shown in Fig. 11.16. The dip in the reflectivity of a QD sample positioned around 1040 nm is due to the GS absorption in the QDs. As described in "Ultrafast Dynamics of Capture and Release of Carriers in Quantum Dots" , the absence of the in-plane conductivity due to the carriers occupying the QD GS, and a 35 ps long carrier thermalization time was observed in a similarly grown structure, demonstrating the strong carrier confinement to the QDs at room temperature [22].

Single-cycle THz pump (i.e., switching) pulses were generated by TPFP in a lithium niobate crystal, yielding THz pulse energies of 2 μJ. We outlined the principles of strong-field THz pulse generation in the beginning of this section. The THz pulses were characterized in the time-domain using a standard free-space electro-optic sampling [23] in a combined ‘‘active-passive“ [47] 0.2 mm $<110>$–2 mm $<100>$ undoped GaP crystal, and showed a spectrum covering the range 0.2–3 THz. The peak electric field of the strongest THz transient was estimated [36] to be 220 kV/cm in air. The THz waveform and its amplitude spectrum are shown in Fig. 11.17a. A weak optical probe pulse around the wavelength of 1040 nm, coinciding with the GS absorption feature in the QDs

(see Fig. 11.16), was produced by conversion of part of the 800 nm laser output, using an OPA (see Fig. 11.12 for a sketch of the experiment).

We performed a THz pump–optical probe experiment on our sample, where the probe pulse reflectivity of the QD structure was modulated by the incident THz pulse. We measured the *absolute value* and the *sign* of the change in the optical probe reflectivity as a function of the time delay between the optical probe and THz pump pulses, using the photodiodes in a balanced detection arrangement (this layout is not shown in the Fig. 11.12). The angles of incidence with respect to normal of the pump THz and probe optical beams on the sample were 0° and 10°, respectively. The optical probe signal interacted with the QDs twice: on the way to and from the DBR. However, the total thickness of the QD absorber layer, including GaAs barriers, and spacer and cladding layers is only about 1.2μm, thus the interaction of both the THz pulse and the probe pulse with the QDs can be viewed as point interactions. All our measurements were performed at room temperature and in ambient atmospheric conditions. The dips in the amplitude spectrum of the THz signal in Fig. 11.17a are absorption lines of atmospheric water vapor.

In Fig. 11.17b our main result—a modulation of the reflectivity of the optical probe $\Delta R/R$ is shown, along with the absolute value of the electric field of the THz pulse $|E_{\mathrm{THz}}|$, experienced by the QDs. The latter was calculated taking into account the THz field transmission coefficient at the sample interface of 0.435, given the THz refractive index of GaAs of 3.6 [48]. The observed $\Delta R/R$ of the optical signal follows the shape of $|E_{\mathrm{THz}}|$ in a temporally coherent manner, reproduces most of the features of the THz signal, and does not exhibit an exponential-like decay features attributed to a relaxation process of any sort. This is precisely as expected from an “instantaneous” effect such as QCSE at lower THz frequencies. The THz pulse features as fast as 460 fs at FWHM are encoded all-optically onto the probe optical signal transmitted through the QDs. Obviously, these femtosecond-scale features cannot originate from a carrier depletion mechanism in QDs related to carrier trapping from the QDs into lattice defects in the LT-GaAs barriers. This process with a decay time constant of 4.3 ps is nearly ten times slower than the observed fast modulations. The maximum observed $\Delta R/R$ value was about 3%, at the peak THz electric field on the QDs of 96.5 kV/cm. Following Ref. [49] we calculated the small-signal loss S experienced by the optical probe with the spectrum $I(\lambda)$ in the QDs as $S = \int_\lambda I(\lambda)[R_{DBR}(\lambda) - R_{QD}(\lambda)]d\lambda / \int_\lambda I(\lambda)d\lambda = 10.3\%$, where $R_{DBR,QD}$ are the reflectivity spectra of the bare DBR and of the whole QD sample (see Fig. 11.16). We were thus able to reach a 3/10.3 = 30 % modulation of the total QD absorption experienced by the optical probe. This is comparable to the modulation depth observed in resonantly probed quantum wells (QWs) at similar *static* bias field strengths [49]. When the probe wavelength was detuned from the QD GS resonance, the magnitude of $\Delta R/R$ signal decreased by an order of magnitude, proving that the observed modulation is indeed due to the interaction of QDs with the THz field.

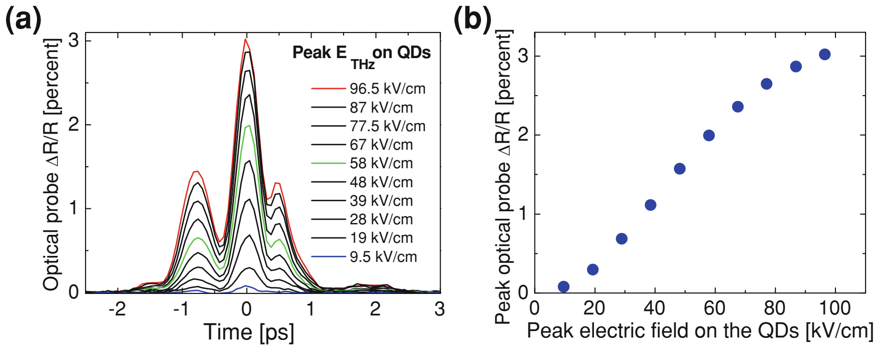

Fig. 11.18 **a** Temporal reflectivity modulation $\Delta R/R$ of the optical probe signal in the QD sample, under influence of the incident THz pulses with variable peak electric field strength. **b** Peak values of $\Delta R/R$ of the signals from **a**, as a function of peak THz electric field on the QDs. From [34]

The sign of the observed reflectivity change $\Delta R/R$ is positive, corresponding to a *decrease* in optical absorption at the probe wavelength in the presence of THz electric field. This positive sign of $\Delta R/R$ suggests that both manifestations of the QCSE may play a role: overall optical absorption quenching; and Stark shift of the QD absorption spectrum towards longer wavelengths, i.e., out of the probe pulse spectrum [49]. The inset of Fig. 11.17b shows the spectrum of the optical probe pulse in the case when the maximum of the THz pulse was in temporal overlap with the probe pulse, and when the THz pulse was blocked. The change in the probe pulse amplitude is more or less spectrally homogeneous, suggesting that the absorption quenching in the QDs is likely to be a dominating electro-absorption modulation effect here.

Figure 11.18a shows the optical probe modulation signals $\Delta R/R$ for different THz field strengths. The THz electric field was controlled using a pair of wire-grid polarizers [28]. In Fig. 11.18b the peak value of $\Delta R/R$ as a function of the peak THz electric field experienced by the QDs is shown, demonstrating a pronounced nonlinear scaling with the electric field, typical for the QCSE [42]—see the discussion in the previous subsection and Fig. 11.15.

We note, that THz-induced electro-absorption modulation was also recently observed at the exciton resonance in QWs [50] and carbon nanotubes [51]. The excitons were polarized by the THz field in the plane of QWs or along the nanotube long dimension. The stronger THz fields lead to ionization of excitons in QWs [50]. The THz modulation rate limit of around 1 THz was observed in Ref. [51], and was related to the exciton dephasing time (also see discussion in Ref. [50]).

The QD geometry should allow for polarization independence of the THz electro-absorption effect, since the application of the electric field in any direction will affect the overlap of *3D* wavefunctions of electrons and holes, and will always lead to the Stark shift. This possibility of inducing the QCSE by THz pulses normal-incident onto the sample is an advantage of QDs over, e.g., QWs or bulk

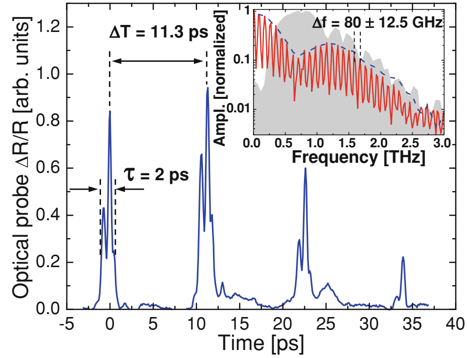

Fig. 11.19 Temporal reflectivity modulation $\Delta R/R$ of the optical probe signal in the QD sample, provided by the multiple reflections of a single THz pulse in the QD sample. Inset: Amplitude Fourier spectra of the isolated first $\Delta R/R$ modulation pulse around 0 ps (*dashed line*), and of the full multi-pulse sequence. Amplitude Fourier spectrum of a single THz pulse is shown in the background. From [34]

semiconductors without a strong excitonic effect. As expected, we found no dependency of the electro-absorption modulation efficiency on the orientation of the THz polarization with respect to the polarization of the optical signal or the orientation of the QD sample rotated about its normal axis. We found a weak dependency on the polarization of the optical probe signal with respect to the orientation of the sample rotated about its normal axis, which is likely due to the known effect of optical absorption anisotropy in QDs [52].

Finally, in Fig. 11.19 we show the modulation of optical absorption in the QDs induced by a *train of THz pulses* incident at high repetition rate. Such a demonstration is needed to confirm the potential of the THz electro-absorption modulation effect in QDs in Tbit/s—data rate signal processing applications, where the individual signals following at extremely high repetition rate should be recognized and processed without the cross-talk between the neighboring signals in the sequence. The THz pulse train in our experiment was produced by the multiple reflections of a single THz pulse within the sample, which was attached to a metal mirror with the back side of its substrate.

The individual pulses of $\Delta R/R$ have a temporal width of around 2 ps. Importantly, the contrast between the peak $\Delta R/R$ and the background is rather high. A certain reshaping of $\Delta R/R$ pulses in the sequence is due to the dispersion and scattering of the THz pulse experiencing multiple reflections within the sample. The interpulse interval of 11.3 ps (i.e., repetition rate of 88 GHz) corresponding to the round-trip time of the THz pulse within the sample shows the possibility of 88 Gbit/s data rate using this electro-absorption modulation scheme in RZ-OOK format. The ratio of interpulse interval to the individual pulse duration 11.3/2 ps = 5.65 suggests that the demonstrated data rate can be scaled accordingly, and crosstalk-free data rates of 88 Gbit/s $\times$ 5.65 = 0.5 Tbit/s can be supported.

In the inset of Fig. 11.19, the amplitude Fourier spectra of the isolated $\Delta R/R$ pulse, and of the whole multi-pulse sequence are shown, with the amplitude spectrum of the single THz pulse in the background. It can be clearly seen that the

full bandwidth of the THz pulse of 3 THz is encoded onto the optical probe signal. The spacing of $80 \pm 12.5\,\text{GHz}$ between the modes in the Fourier spectrum of the multipulse sequence reflects the pulse repetition rate of 88 GHz. These Fourier spectra of temporal $\Delta R/R$ signals are analogous to the THz sidebands observed in work [53] , and demonstrate the coherence in encoding of a THz signal onto an optical signal.

We note here, that this coherence of THz-to-optical encoding in our experiments is ensured by the fact that the THz electric field only contributes to the modulation of the quantum-confinement potential of the QDs. Indeed, the THz photons with the frequencies of less than 3 THz have energies less than 12.3 meV. These photon energies are too small to participate in any transitions in the QDs. Therefore, the THz electric field can be safely considered a quasi-static field in our experiments, and the THz electro-absorption modulation is thus fully coherent with the THz field. However, at THz frequencies of around 10 THz and higher, the intraband $1s - 2p$ absorption in the QDs can take place in the presence of the optical signal resonant with the QD GS. Therefore, these photon energies should be considered as a possible limit to the temporal coherence between the THz driving field and the electro-absorption modulation effect.

THz pulses with relatively high field strengths were used in our experiments, and the QD sample was not particularly optimized for the high THz-to-optical encoding efficiency. However, we note that the interaction between the QDs and THz field can be further enhanced considerably [33, 54]. This will lead to the emergence of QD-based optoelectronics components and devices capable of Tbit/s—rate all-optical signal processing and direct THz-to-optical encoding at low switching THz fields. Such devices should become the key in realizing wireless short-range data links with Tbit/s capacity, such as Tbit/s radio-over-fiber systems with the THz free-space channel. Such systems can be used e.g., as wireless interconnects in internet data centers. The coherent nature of the demonstrated THz electro-absorption modulation effect in QDs can also be utilized for the purpose of simple THz detectors based on the THz side-band generation in the spectrum of a well-defined reference optical signal. Therefore, analyzing the optical spectra will reveal the spectral information about the detected THz signal.

Conclusion

In conclusion, in this chapter we discussed the study of ultrafast phenomena in QDs related to carrier dynamics and ultrafast electro-absorption modulation, using ultrafast THz spectroscopy methods. We have described the foundations of the experimental techniques used in our studies: optical pump–THz probe spectroscopy for measurements of ultrafast conductivity dynamics, and high-field THz pulse generation and THz pump–optical probe spectroscopy for study of ultrafast THz switching in QDs. Also, the fundamentals of electro-absorption effect—the quantum-confined Stark effect in the QDs were presented.

Acknowledgements We are grateful to our colleagues H.P. Porte, P.U. Jepsen, K. Yvind and J. M. Hvam (DTU Fotonik), A.-P. Jauho (DTU Nanotech), B.S. Monozon (Marine Tech. Univ., St. Petersburg), E.U.Rafailov (Univ. Dundee), D. Livshits (Innolume GmbH), and A. Cavalleri (Univ. Hamburg) for contributing to the results described in this chapter, and for fruitful and stimulating discussions. We also thank Danish Proof of Concept Foundation (grant 7.7 Ultra-high-speed wireless data communications) and Max Planck Society for partial financial support.

References

1. Kirstaedter, N., Schmidt, O.G., Ledentsov, N.N., Bimberg, D., Ustinov, V.M., Egorov, A.Yu., Zhukov, A.E., Maximov, M.V., Kop'ev , P.S., Alferov, Zh.I.: Appl. Phys. Lett. **69**, 1226 (1996)
2. Rafailov, H.C., Cataluna, M.A., Sibbett, W.: Nat. Photonics **1**, 395 (2007)
3. Liu, H.C., Gao, M., McCaffrey, J., Wasilewski, Z.R., Fafarda, S.: Appl. Phys. Lett. **78**, 79 (2001)
4. Lagatsky, A.A., Bain, F.M., Brown, C.T.A., Sibbett, W., Livshits, D.A., Erbert, G., Rafailov, E.U.: Appl. Phys. Lett. **91**, 231111 (2007)
5. Mulvad, H.C.H., Galili, M., Oxenløwe, L.K., Hu, H., Clausen, A.T., Jensen, J.B., Peucheret, C., Jeppesen, P.: Opt. Express **18**, 1438 (2010)
6. Morris, D., Perret, N., Fafard, S.: Appl. Phys. Lett. **75**, 3593 (1999)
7. Gündogdu, K., Hall, K.C., Boggess, T.F., Deppe, D.G., Shchekin, O.B.: Appl. Phys. Lett. **85**, 4570 (2004)
8. Müller, T., Schrey, F.F., Strasser, G., Unterrainer, K.: Appl. Phys. Lett. **83**, 3572 (2003)
9. Yarotski, D.A., Averitt, R.D., Negre, N., Crooker, S.A., Taylor, A.J., Donati, G.P., Stintz, A., Lester, L.F., Malloy, K.J.: J. Opt. Soc. Am. B **19**, 1480 (2002).
10 Ashcroft, N.W., Mermin, N.D.: Solid State Physics. Saunders College Publishing, New York (1976)
11 Schall, M., Uhd Jepsen, P.: Opt. Lett. **25**, 13 (2000)
12 Huber, R., Tauser, F., Brodschelm, A., Bichler, M., Abstreiter, G., Leitenstorfer, A.: Nature **414**, 286 (2001)
13 Beard, M.C., Turner, G.M., Schmuttenmaer, C.A.: Phys. Rev. B **62**, 15764 (2000)
14 Smith, N.V.: Phys. Rev. B **64**, 155106 (2001)
15 Nemec, H., Kuel, P., Sundström, V.: Phys. Rev. B **79**, 115309 (2009)
16. Jepsen, P.U., Cooke, D.G., Koch, M.: Laser Photonics Rev. **5**, 124 (2011)
17. Wang, F., Shan, J., Islam, M.A., Herman, I.P., Bonn, M., Heinz, T.F.: Nat. Mater. **5**, 861 (2006)
18. Hendry, E., Koeberg, M., Bonn, M.: Phys. Rev. B **76**, 045214 (2007)
19. Turchinovich, D., Pierz, K., Uhd Jepsen, P.: Phys. Stat. Sol. (c) **0**, 1556 (2003)
20. Cooke, D.G., Hegmann, F.A., Mazur, Yu.I., Ma, W.Q., Wang, X., Wang, Z.M., Salamo, G.J., Xiao, M., Mishima, T.D., Johnson, M.B.: Appl. Phys. Lett. **85**, 3839 (2004)
21. Prasankumar, R.P., Scopatz, A., Hilton, D.J., Taylor, A.J., Averitt, R.D., Zide, J.M., Gossard, A.C.: Appl. Phys. Lett. **86**, 201107 (2005)
22. Porte, H.P., Jepsen, P.U., Daghestani, N., Rafailov, E.U., Turchinovich, D.: Appl. Phys. Lett. **94**, 262104 (2009)
23. Wu, Q., Zhang, X.-C.: Appl. Phys. Lett. **67**, 3523 (1995)
24. Turchinovich, D.: Study of ultrafast polarization and carrier dynamics in semiconductor nanostructures: a THz spectroscopy approach. Ph.D. Thesis, University of Freiburg (2004)
25. Lui, K.P.H., Hegmann, F.A.: Appl. Phys. Lett. **78**, 3478 (2001)
26. Nielsen, T.R., Gartner, P., Jahnke, F.: Phys. Rev. B **69**, 235314 (2004)
27. Haiml, M., Grange, R., Keller, U.: Appl. Phys. B: Lasers Opt. **79**, 331 (2004)
28. Hoffmann, M.C., Turchinovich, D.: Appl. Phys. Lett. **96**, 151110 (2010)

29. Feldmann, J., Nunnekamp, J., Peter, G., Göbel, E., Kuhl, J., Ploog, K., Dawson, P., Foxon, C.T: Phys. Rev. B. **42**, 5809 (1990)
30. Uhd Jepsen, P., Schairer, W., Libon, I.H., Lemmer, U., Hecker, N.E., Birkholz, M., Lips, K., Schall, M.: Appl. Phys. Lett. **79**, 1291 (2001)
31. Federici, J., Moeller, L.: J. Appl. Phys. **107**, 111101 (2010)
32. Kleine-Ostmann, T., Nagatsuma, T.: J. Infrared Millimeter, THz Waves **32**, 143 (2011)
33. Turchinovich, D.: Patent WO 2011/015200
34. Hoffmann, M.C., Monozon, B.S., Livshits, D., Rafailov, E.U., Turchinovich, D.: Appl. Phys. Lett. **97**, 231108 (2010)
35. Löffler, T., Hahn, T., Thomson, M., Jacob, F., Roskos, H.: Opt. Express **13**, 5353 (2005)
36. Blanchard, F., Razzari, L., Bandulet, H.C., Sharma, G., Morandotti, R., Kieffer, J.C., Ozaki, T., Reid, M., Tiedje, H.F., Haugen, H.K., Hegmann, F.A.: Opt. Express **15**, 13212 (2007)
37. Auston, D.H., Cheung, K.P., Valdmanis, J.A, et al.: Phys. Rev. Lett. **53**, 1555 (1984)
38. Hebling, J., Almasi, G., Kozma, I., Kuhl, J.: Opt. Express **10**, 1161 (2002)
39. Yeh, K.-L., Hoffmann, M.C., Hebling, J., Nelson, K.A.: Appl. Phys. Lett. **90**, 171121 (2007)
40. Stepanov, A.G., Bonacina, L., Chekalin, S.V., Wolf, J.-P.: Opt. Lett. **33**, 2497 (2008)
41. Hoffmann, M.C., Hebling, J., Hwang, H.Y., Yeh, K.-L., Nelson, K.A.: Phys. Rev. B **79**, 161201R (2009)
42. Miller, D.A.B., Chemla, D.S., Damen, T.C., Gossard, A.C., Wiegmann, W., Wood, T.H., Burrus, C.A.: Phys. Rev. Lett. **53**, 2173 (1984)
43. Bastard, G., Mendez, E.E., Chang, L.L., Esaki, L.: Phys. Rev. B **28**, 3241 (1983)
44. Vurgaftman, I., Meyer, J.R., Ram-Mohan, L.R.: J. Appl. Phys. **89**, 5815 (2001)
45. Mikhrin, S.S., Zhukov, A.E., Kovsh, A.R., Maleev, N.A., Ustinov, V.M., Shernyakov, Yu.M., Soshnikov, I.P., Livshits, D.A., Tarasov, I.S., Bedarev, D.A., Volovik, B.V., Maximov, M.V., Tsatsul'nikov, A.F., Ledentsov, N.N., Kop'ev, P.S., Bimberg, D., Alferov, Zh.A.: Semicond. Sci. Technol. **15**, 1061 (2000)
46. Johnsen, K., Jauho, A.-P.: Phys. Rev. B **57**, 8860 (1998)
47. Turchinovich, D., Dijkhuis, J.I.: Opt. Commun. **270**, 96 (2007)
48. Grischkowsky, D., Keiding, S., van Exter, M., Fattinger, Ch.: J. Opt. Soc. Am. B **7**, 2006 (1990)
49. Liu, X., Rafailov, E.U., Livshits, D., Turchinovich, D.: Appl. Phys. Lett. **97**, 051103 (2010)
50. Hirori, H., Nagai, M., Tanaka, K.: Phys. Rev. B. **81**, 081305(R) (2010)
51. Ogawa, T., Watanabe, S., Minami, N., Shimano, R.: Appl. Phys. Lett. **97**, 041111 (2010)
52. Cortez, S., Krebs, O., Voisin, P., Gérard, J.M.: Phys. Rev. B **63**, 233306 (2001)
53. Dhillon, S.S., Sirtori, C., Alton, J., Barbieri, S., De Rossi, A., Beere, H.E., Ritchie, D.A.: Nat. Photonics **1**, 411 (2007)
54. Seo, M.A., Park, H.R., Koo, S.M., Park, D.J., Kang, J.H., Suwal, O.K., Choi, S.S., Planken, P.C.M., Park, G.S., Park, N.K., Park, Q.H., Kim, D.S.: Nat. Photonics **3**, 152 (2009)
55. Hoffmann, M.C., Fülöp, J.A.: J. Phys. D **44**, 083001 (2011)

Chapter 12
Nonlinear Optics and Saturation Behavior of Quantum Dot Samples Under Continuous Wave Driving

T. Ackemann, A. Tierno, R. Kuszelewicz, S. Barbay, M. Brambilla, C. G. Leburn and C. T. A. Brown

Abstract The nonlinear optical response of self-assembled quantum dots (QD) is relevant to the application of QD-based devices in nonlinear optics, all-optical switching, slow light, and self-organization. Theoretical investigations are based on numerical simulations of a spatially and spectrally resolved rate equation

T. Ackemann (✉)
SUPA and Department of Physics, University of Strathclyde,
Glasgow G4 0NG, Scotland, UK
e-mail: thorsten.ackemann@strath.ac.uk

A. Tierno
Université de Nice Sophia Antipolis, Institut Non-Linéaire de Nice,
UMR 6618, 06560 Valbonne, France
e-mail: alessio.tierno@inln.cnrs.fr

R. Kuszelewicz · S. Barbay
Laboratoire de Photonique et de Nanostructures, CNRS, Route de Nozay,
91460 Marcoussis, France
e-mail: robert.kuszelewicz@lpn.cnrs.fr

S. Barbay
e-mail: sylvain.barbay@lpn.cnrs.fr

M. Brambilla
CNISM e Dipartimento Interateneo di Fisica, via Amendola 173, 70126 Bari, Italy
e-mail: brambilla@fisica.uniba.it

C. G. Leburn
SUPA and School of Engineering and Physical Sciences, Heriot-Watt University,
Edinburgh EH14 4AS, Scotland, UK
e-mail: C.G.Leburn@hw.ac.uk

C. T. A. Brown
SUPA and School of Physics and Astronomy, University of St. Andrews,
St. Andrews, KY16 9SS, Scotland, UK
e-mail: ctab@st-andrews.ac.uk

Z. M. Wang (ed.), *Quantum Dot Devices*, Lecture Notes in Nanoscale Science and Technology 13, DOI: 10.1007/978-1-4614-3570-9_12,
© Springer Science+Business Media New York 2012

model, which takes into account the strong coupling of the quantum dots to the carrier reservoir created by the wetting layer (WL) states. The complex dielectric susceptibility of the ground state is obtained. The saturation is shown to follow a behavior in between the one for a dominantly homogeneously and inhomogeneously broadened medium. Approaches to extract the nonlinear refractive index change by fringe shifts in a cavity or self-lensing are discussed. Experimental work on saturation characteristic of InGa/GaAs quantum dots close to the telecommunication O-band (1240–1280 nm) and of InAlAs/GaAlAs QD at 780 nm is described and the first demonstration of the cw saturation of absorption in room temperature QD samples is discussed in detail.

Introduction

As witnessed by the contributions in this book, semiconductor quantum dots (QD) are finding considerable interest for laser, amplifier, and quantum information devices. The 3D quantum confinement leads to a ‘quasi-atomic’ behavior with a delta function-like density of states resulting, from the applications point of view, in many realized or anticipated benefits such as low threshold currents, low temperature sensitivity, and low phase-amplitude coupling.

From the fundamental point of view, it seems interesting to revisit linear and nonlinear effects known for atoms—or their archetypical abstraction, the ‘two-level’ atom, in QD ‘artificial’ atoms. In contrast to real atoms, QD size, density, and material composition can be used to tailor emission wavelengths and other characteristics. The analogy between QD and atoms was most explored for single dots due to their relevance for quantum information devices, e.g. [1–3]. Saturation behavior typical for two-level atoms is reported in these Refs. However, in order to take advantage of long dephasing times cryogenic temperatures are required. Moving over to ensembles of QD, but still at cryogenic temperatures, self-induced transparency was demonstrated as a specific phenomenon in nonlinear beam propagation in two-level systems [4], and spectral hole burning in [5] mimicking the corresponding effect in Doppler broadened atomic systems.

At room temperature, work on nonlinear optical properties focused on the gain regime due to the relevance for semiconductor optical amplifiers (SOAs), most often under pulsed excitation [6–12], but also under cw conditions [6, 9, 13–16]. In contrast, studies under absorptive conditions seem to be limited either to pulsed excitation [7, 8, 17–19], motivated by applications as semiconductor saturable absorption mirrors (SESAMs), or to collodial ensembles [20, 21].

However, absorptive and refractive index nonlinearities of ensembles of QD without inversion might be useful for photonic devices displaying optical bistability, optical pattern formation, spatial solitons, or slow light [22–26]. In particular, many of the current authors have an interest in spatial cavity solitons (CS), i.e. self-confined solitary states in cw driven nonlinear cavities (see [27–29] for a

review). CS are bistable and have ‘mobility’, i.e. are easily being steered around within the device aperture. Hence, they are attractive for all-optical processing applications [30–32]. Though CS should exist for self-focusing, absorptive, and even self-defocusing situations, the self-focusing case appears to be the most robust by far [31, 33]. Hence the quasi-atomic character of the QD susceptibility is beneficial because a self-focusing or self-defocusing situation can be realized by simply changing the detuning whereas a bulk or quantum well semiconductor is always self-defocusing under absorptive and self-focusing under amplifying conditions. Obviously, this enhanced flexibility of QD might be not only beneficial for solitons but for nonlinear optics in general.

Moreover, characterizing the nonlinear index response to external optical driving provides also an alternative approach to the important problem of characterizing phase-amplitude coupling in QD. Due to their symmetric, atom-like gain spectrum, ‘ideal’ QD should have zero phase-amplitude coupling or linewidth enhancement factor (or α-factor [34]) at gain maximum and hence a reduced tendency to instabilities compared to quantum well and bulk devices. Indeed, a reduced α-factor and a reduced tendency to beam filamentation was observed in many QD samples under some operating conditions [35–38], but also fairly strong phase-amplitude coupling under different operating conditions [38–40]. Characterizing nonlinear phase shifts and/or the resulting self-lensing effects would give a direct indication of the tendency of the system to filamentation and help to identify the appropriate operation conditions for applications demanding low (lasers, amplifiers, absorptive nonlinearities) and high (dispersive optical nonlinearities) phase-amplitude coupling.

Hence, we are addressing in this chapter the room temperature, cw nonlinear optics of QDs. We review and give further details on a series of papers on modeling the complex nonlinear susceptibility of QD and more recently on the experimental observation of absorptive nonlinearities [22–25, 41, 42]. “Modeling and Simulation Results” provides the theoretical framework. Due to the significant coupling of QDs to the semiconductor matrix they are incorporated in, QDs are more complex than ‘simple’ atoms and we are adopting a model including QD and wetting layer (WL) dynamics with the basic coupling mechanisms using phenomenological rate constants. Another complication comes from the fact that QD spectra correspond to a ‘Voigt’-profile where neither the homogeneous nor the inhomogeneous broadening is strongly dominant. We derive the nonlinear dielectric susceptibility of the QD ground state (ES) and how it couples to nonlinear propagation and cavity equations. Predictions for the saturation behavior, nonlinear phase shifts, self-lensing, α-factor, and optical bistability are discussed. In “Experiments on InAs/GaAs QD Around 1,250 nm”, we investigate the saturation of InAs QD in a GaAs matrix emitting close to the telecommunication O-band. We demonstrate cw saturation of absorption and gain using a tunable Chromium forsterite laser as a pump laser. InAs/GaAs maybe the most established QD material system due to the fact that it provides good quality lasing devices in the 1,100–1,250 nm wavelength range, where quantum well-based devices are highly strained, and allows devices to reach the 1.3 μm telecommunication band

using the beneficial GaAs material system. This maturity and applicability at telecommunication wavelengths, where all-optical processing applications should happen, makes InAs QD attractive for these studies. They have, however, also a drawback, which is that their internal structures is not really simple but permits one or two excited QD states (ES) in addition to the GS. Hence, we are investigating in "Experiments on InAlAs/GaAlAs QD at 780 nm" InAlAs QD in an AlGaAs matrix operating around 780 nm. These QD are highly confined dots and a possible ES should be very close in energy to the WL, much closer than the energy difference between ES and GS. Hence, treating WL and ES as a common reservoir is expected to be a better approximation than in InAs QD. They can be also conveniently driven with a titanium-sapphire laser. We demonstrate saturation of absorption under cw driving also for these. "Summary and Conclusion" provides a brief summary of the issues discussed and an outlook on improving the nonlinear figure of merit of devices.

Modeling and Simulation Results

The Model

The modeling of semiconductor QD requires a number of assumptions, according to a variety of preconditions: in the first instance, the growth and sample characteristics, as well as the current and/or optical injection conditions. The most appealing feature of QD being their quasi-atomic susceptibility, one aims to have a clear set of discrete states from quantum confinement, the best separated as possible from the carriers states defined in the WL which is generally considered as a quantum well and the barrier substrate where the carriers are injected via electric contacts. The description of the QD states depends, in turn, on the sample inasmuch as, e.g. Stranski-Krastanow (SK) growth induces an inhomogeneous broadening of the energy dot states, while a submonolayer deposition yields a larger homogeneity of the dot size [36]. In this work, we will consider a system of small and/or shallow confined QD so that either there is only one electron and one hole bound states, or in case other discrete states exists, these are well separated from the inhomogeneously broadened fundamental transition. The InAlAs/AlGaAs QD discussed in "Experiments on InAlAs/GaAlAs QD at 780 nm" are an example for the latter, whereas in the InAs/GaAs QD discussed in "Experiments on InAs/GaAs QD Around 1,250 nm" several ES roughly equally spaced between WL and GS exist. In our treatment, the carriers in the ES [14, 16] are not explicitly taken into account but it is assumed that WL and excited states constitute a common reservoir for the QD ground state population [13]. Due to the large separation between the lifetimes of the carriers in the QD ground state (100 ps to 2 ns) and the fast coupling between the other states to the ground state (100 fs to some ps) [9, 16] the details of this coupling are not very important for the properties of the cw state, if probing and pumping are done at the same frequency. Hence, we will

use 'QD population' synonymous to 'QD ground state population' and 'WL layer population' synonymous to 'WL and excited QD state population'.

The WL continuum states are expected not to significantly contribute to the optical susceptibility in the vicinity of the fundamental transition. Hence, we are only taking into account the contribution of the GS transition to the susceptibility. However, the electromagnetic field couples to the GS transition of all the QDs, with varying strength, which reflects the inhomogeneous broadening. In addition, the optical response is affected indirectly by the WL states because they couple to the GS via the carrier dynamics and a change of carrier density in the GS changes the susceptibility. The optical response of our model is thus characterized by the nonlinear coupling of the QD fundamental transition to the WL. The presence of other discrete and continuous states is taken into account via the relaxation mechanism between the GS states and the outside world (WL).

In the model we describe the articulate and still partially unclear relaxation mechanisms of QD ensembles through phenomenological transition and escape/capture rates for intra-dot decays/recombinations and QD-WL carrier relaxations. The spin dynamics is neglected since the spin memory is lost very fast at room temperature [43, 44].

The coupling mechanisms between the WL and the QD considered are the carrier escape and capture by the dot via thermo-activation through emission or absorption of lattice phonons and Auger processes at first order in the WL populations, which include Pauli blocking effects, under the assumption that the sample is passive or weakly pumped [45].

Carrier Dynamics and Dielectric Susceptibility

Following [23], we derive the equations for the expectation values of the number of particles operator for the electrons and holes and for the corresponding polarization p:

$$\frac{\mathrm{d}n^{e,h}}{\mathrm{d}t} = -\gamma_{\mathrm{nr}} n^{e,h} - \Gamma_{\mathrm{sp}} n^e n^h + \frac{i}{\hbar}(\mu p^* - \mu^* p)\mathsf{E} + \left.\frac{\mathrm{d}n^{e,h}}{\mathrm{d}t}\right|_{\mathrm{QD-WL}} + \left.\frac{\mathrm{d}n^{e,h}}{\mathrm{d}t}\right|_{\mathrm{QD-WL}}^{\mathrm{Auger}}, \quad (12.1)$$

$$\frac{\mathrm{d}p}{\mathrm{d}t} = -\left(i\omega_a + \gamma_p\right)p - \frac{i}{\hbar}\left[n^e + n^h - 1\right]\mu\mathsf{E}, \quad (12.2)$$

where γ_{nr} is the non-radiative recombination rate, Γ_{sp} the bimolecular coefficient for spontaneous recombination, ω_a the electron-hole recombination pulsation, γ_p the polarization damping, $\mathsf{E} = E\exp(-i\omega_0 t) + c.c.$ is the electric field and μ the dipole transition matrix element.

If we consider the level degeneracy $\Pi = 2$ for the two opposite spins, we can introduce the QD population $n_{\mathrm{QD}}^{e,h} = \Pi n^{e,h}$, the total polarization $p_{\mathrm{QD}} = \Pi p$ and assume a real dipole moment μ. In the rotating wave approximation and introducing $p_{\mathrm{QD}} = P_{\mathrm{QD}}\exp(-i\omega_0 t) + c.c.$, Eqs. 12.1, 12.2 become

$$\frac{\mathrm{d}P_{\mathrm{QD}}}{\mathrm{d}t} = -\gamma_p(i\Delta+1)P_{\mathrm{QD}} - \frac{i\mu E}{\hbar}\left[n^e_{\mathrm{QD}} + n^h_{\mathrm{QD}} - \Pi\right], \tag{12.3}$$

$$\begin{aligned}\frac{\mathrm{d}n^{e,h}_{\mathrm{QD}}}{\mathrm{d}t} =& -\gamma_{\mathrm{nr}} n^{e,h}_{\mathrm{QD}} - \frac{\Gamma_{\mathrm{sp}}}{2} n^e_{\mathrm{QD}} n^h_{\mathrm{QD}} + \frac{i\mu}{\hbar}\left(EP^*_{\mathrm{QD}} - E^* P_{\mathrm{QD}}\right) \\ &+ \left.\frac{\partial n^{e,h}_{\mathrm{QD}}}{\partial t}\right|_{\mathrm{QD-WL}} + \left.\frac{\partial n^{e,h}_{\mathrm{QD}}}{\partial t}\right|^{\mathrm{Auger}}_{\mathrm{QD-WL}},\end{aligned} \tag{12.4}$$

where we have introduced the detuning from a single dot resonance $\Delta = (\omega_a - \omega_0)/\gamma_p$.

The first QD-WL relaxation term describes the thermo-activated processes. For the sake of simplicity we ignore the possible non-local interaction between the QD and the WL, drop the subscript QD in the variable names and write

$$\left.\frac{\partial n^{e,h}}{\partial t}\right|_{\mathrm{QD-WL}} = -\gamma^{e,h}_{\mathrm{esc}} n^{e,h} + \sigma^{e,h}_{\mathrm{cap}} N^{e,h}_{\mathrm{WL}}\left[\Pi - n^{e,h}\right], \tag{12.5}$$

where $N^{e,h}_{\mathrm{WL}}$ is the surface density carrier population in the WL. $\gamma^{e,h}_{\mathrm{esc}}$ and $\sigma^{e,h}_{\mathrm{cap}}$ are respectively the escape rate from the QD and the capture rate cross section into the QD. The second QD-WL relaxation terms describe the Auger processes [45]. For a low WL carrier density, we retain only those terms that are in first order in $N^{e,h}_{\mathrm{WL}}$:

$$\left.\frac{\partial n^e}{\partial t}\right|^{\mathrm{Auger}}_{\mathrm{QD-WL}} = -B_{\mathrm{he}} N^h_{\mathrm{WL}} n^e\left[\Pi - n^h\right] + B_{\mathrm{eh}} N^e_{\mathrm{WL}} n^h\left[\Pi - n^e\right]. \tag{12.6}$$

The first term describes the excitation of an electron to the WL via the interaction of a hole in the WL and in the QD, and the second term is a symmetric process that describes the capture of a WL electron in the QD via the interaction of a WL and a QD hole. For the sake of conciseness, we will refer to the symmetric process in the following by “sym.” in the equations. $B_{\mathrm{he,eh}}$ has the units of a cross-sectional rate (area/time). A similar term exists for the holes:

$$\left.\frac{\partial n^h}{\partial t}\right|^{\mathrm{Auger}}_{\mathrm{QD-WL}} = -\left.\frac{\partial n^e}{\partial t}\right|^{\mathrm{Auger}}_{\mathrm{QD-WL}}. \tag{12.7}$$

The QD polarization P_{QD} can be adiabatically eliminated due to the fast polarization decay time γ_p^{-1} with respect to the other ones so that its steady state values are:

$$P_{\mathrm{QD}} = -\frac{i\mu}{\hbar\gamma_p}\left(\frac{1-i\Delta}{1+\Delta^2}\right)\left[n^e + n^h - \Pi\right]E, \tag{12.8}$$

and can be substituted into Eq. 12.4 to obtain

$$\begin{aligned}\frac{\mathrm{d}n_{\mathrm{QD}}^{e,h}}{\mathrm{d}t} = &- \gamma_{\mathrm{nr}} n_{\mathrm{QD}}^{e,h} - \frac{\Gamma_{\mathrm{sp}}}{2} n_{\mathrm{QD}}^{e} n_{\mathrm{QD}}^{h} \\ &- \frac{2\mu^2}{\hbar^2 \gamma_p} \left(\frac{1}{1+\Delta^2} \right) \left[n^e + n^h - \Pi \right] |\mathbf{E}|^2 \\ &+ \left. \frac{\partial n_{\mathrm{QD}}^{e,h}}{\partial t} \right|_{\mathrm{QD-WL}} + \left. \frac{\partial n_{\mathrm{QD}}^{e,h}}{\partial t} \right|_{\mathrm{QD-WL}}^{\mathrm{Auger}} .\end{aligned} \tag{12.9}$$

The rate equation for the WL carrier population is given by

$$\begin{aligned}\frac{\partial N_{\mathrm{WL}}^{e,h}}{\partial t} = &\Lambda - \gamma_{\mathrm{nr}}^{\mathrm{WL}} N_{\mathrm{WL}}^{e,h} + \left. \frac{\partial N_{\mathrm{WL}}^{e,h}}{\partial t} \right|_{\mathrm{QD-WL}} \\ &+ \left. \frac{\partial N_{\mathrm{WL}}^{e,h}}{\partial t} \right|_{\mathrm{QD-WL}}^{\mathrm{Auger}} + D \nabla_{\perp}^2 N_{\mathrm{WL}}^{e,h},\end{aligned} \tag{12.10}$$

where $\gamma_{\mathrm{nr}}^{\mathrm{WL}}$ is the non-radiative decay term, $\Gamma_{\mathrm{sp}}^{\mathrm{WL}}$ is the spontaneous recombination term (that will be neglected consistently with the hypothesis of a low WL population), and Λ is a pumping term accounting for a possible current injection into the WL, moderate enough such that Coulomb effects remain negligible. Note the diffusion coefficient D which spreads out any initially localized excitation in the transverse plane and may contribute to diffusively couple QD at different locations. Again, spontaneous emission processes in the WL have been disregarded when considering first-order processes in N_{WL}. For a constant spatial density of QD N_{QD}, the Auger term and the capture term read:

$$\left. \frac{\partial N_{\mathrm{WL}}^{e,h}}{\partial t} \right|_{\mathrm{QD-WL}}^{\mathrm{Auger}} = -N_{\mathrm{QD}} \left. \frac{\partial n^{e,h}}{\partial t} \right|_{\mathrm{QD-WL}}^{\mathrm{Auger}}, \tag{12.11}$$

$$\left. \frac{\partial N_{\mathrm{WL}}^{e,h}}{\partial t} \right|_{\mathrm{QD-WL}} = -N_{\mathrm{QD}} \left. \frac{\partial n^{e,h}}{\partial t} \right|_{\mathrm{QD-WL}}. \tag{12.12}$$

It is now crucial to introduce the distribution of QD heights, intrinsic of the SK-growth, a phenomenon known to introduce an inhomogeneous broadening of the spectral linewidth of the dot ensemble. The contribution of each class of dots is weighed by a statistical factor,

$$G_{\Delta_i}(\Delta) = \frac{1}{\Gamma/\gamma\sqrt{\pi}} \exp - \left(\Delta_i - \frac{\gamma}{\Gamma} \Delta \right)^2, \tag{12.13}$$

as determined by the detuning from the center ω_i of the inhomogeneously broadened line as in [22]. $\Delta_i = (\omega_i - \omega_0)/\Gamma$ denotes the field detuning from the QD population line center and Γ is the inhomogeneous QD linewidth.

The WL Eq. 12.10 is only modified through the QD-WL interaction terms (12.11, 12.12). Since Auger or capture processes cannot involve two different dots, the carriers captured by all the dots (which equals the total population lost by the WL) is then just the capture rate for one spectral class of dots summed over the whole distribution :

$$\left.\frac{\partial N_{\mathrm{WL}}^{e,h}}{\partial t}\right|_{\mathrm{QD-WL}}^{\mathrm{Auger}} = -N_{\mathrm{QD}}\gamma_p \times \int \left(\mp B_{\mathrm{eh}} N_{\mathrm{WL}}^{e,h} n^{h,e}\left[\Pi - n^{e,h}\right] \pm sym.\right) \times G_{\Delta_i}(\Delta)\mathrm{d}\Delta, \tag{12.14}$$

$$\left.\frac{\partial N_{\mathrm{WL}}^{e,h}}{\partial t}\right|_{\mathrm{QD-WL}} = - N_{\mathrm{QD}}\gamma_p \times \int \left(-\gamma_{\mathrm{esc}}^{e,h} n^{e,h} + \sigma_{\mathrm{cap}}^{e,h} N_{\mathrm{WL}}^{e,h}\left[\Pi - n^{e,h}\right]\right) \times G_{\Delta_i}(\Delta)\mathrm{d}\Delta. \tag{12.15}$$

If we concentrate on the role of QD-WL interactions in determining the α-factor in a QD-based microcavity, a fundamental feature that must be taken into account is the distribution of the dot inhomogeneous sizes which changes the spectral distribution of carrier occupancy. A deeper QD will have a larger energy gap, so that when the difference in energy between the WL and the QD is larger, the carrier lasts longer in the GS, i.e. it is more difficult for it to escape into the WL [46, 47]. The rate γ_{esc} is just the inverse of the escape time and hence its dependence is proportional to $exp[(E_{\mathrm{QD}} - E_{\mathrm{WL}})/k_B T]$. For the carrier capture σ_{cap} the situation is the opposite in the sense that the transition from the WL into the excited state is favored when the difference $E_{\mathrm{WL}} - E_{\mathrm{QD}}$ is larger. If we account for this mechanism in the derivation of our model, it turns out that the escape and carrier rates depend on the spectral class of the carrier considered and, after some manipulations reported in [24], should be modified as:

$$\gamma_{\mathrm{esc}}(\Delta) = \gamma_{\mathrm{esc}}^{o} \exp\left(-\frac{\Gamma}{\gamma_p}\beta\Delta i\right)\exp(\beta\Delta), \tag{12.16}$$

$$\sigma_{\mathrm{cap}}(\Delta) = \sigma_{\mathrm{cap}}^{o} \exp\left(\frac{\Gamma}{\gamma}\beta\Delta i\right)\exp(\beta\Delta). \tag{12.17}$$

Here,

$$\beta = \hbar\gamma_p/k_B T \tag{12.18}$$

and its typical value at room temperature is around 0.01–0.02.

Finally, we introduce the same scalings reported in [23] to make the model compact, make all the interaction terms explicit and write the final form for the carrier equations as:

$$\frac{\mathrm{d}n_{\mathrm{QD}}^{e,h}}{\mathrm{d}t} = -\gamma_{\mathrm{nr}}\Bigg[n^{e,h} + \frac{\Gamma_{\mathrm{sp}}}{2}n^e n^h + \frac{|\mathbf{E}|^2}{1+\Delta^2}\left[n^e + n^h - \Pi\right] \\ \pm B_{\mathrm{he}}N_{\mathrm{WL}}^h n^e\left[\Pi - n^h\right] \mp B_{\mathrm{eh}}N_{\mathrm{WL}}^e n^h[\Pi - n^e] \\ + \gamma_{\mathrm{esc}}^{e,h}n^{e,h} - \sigma_{\mathrm{cap}}^{e,h}N_{\mathrm{WL}}^{e,h}\left[\Pi - n^{e,h}\right]\Bigg], \tag{12.19}$$

$$\frac{\partial N_{\mathrm{WL}}^{e,h}}{\partial t} = -\gamma_{\mathrm{nr}}^{\mathrm{WL}}\Big[-\Lambda + N_{\mathrm{WL}}^{e,h} - D\nabla_\perp^2 N_{\mathrm{WL}}^{e,h}. \\ \mp B_{\mathrm{he}}N_{\mathrm{WL}}^h\int n^e\left[\Pi - n^h\right]G_{\Delta_i}(\Delta)\mathrm{d}\Delta \pm B_{\mathrm{eh}}N_{\mathrm{WL}}^e\int n^h[\Pi - n^e]G_{\Delta_i}(\Delta)d\Delta \\ -\gamma_{\mathrm{esc}}^{e,h}\int n^{e,h}G_{\Delta_i}(\Delta)\mathrm{d}\Delta - \sigma_{\mathrm{cap}}^{e,h}N_{\mathrm{WL}}^{e,h}\int\left[\Pi - n^{e,h}\right]G_{\Delta_i}(\Delta)\mathrm{d}\Delta\Big]. \tag{12.20}$$

For our purposes, the most important scaling going from Eqs. 12.9–12.19 is the one of the field via the saturation field strength

$$E_{\mathrm{s}} = \sqrt{\frac{\hbar^2\gamma_p\gamma_{\mathrm{nr}}}{2\mu^2}}. \tag{12.21}$$

The saturation intensity is given by

$$I_{\mathrm{s}} = \frac{cn_b\varepsilon_0\hbar^2\gamma_p\gamma_{\mathrm{nr}}}{\mu^2}, \tag{12.22}$$

n_b denoting the background refractive index. The (normalized) susceptibility χ_I of the inhomogeneously broadened QD population then stems from the summation of the responses of individual QD weighed by their Gaussian statistical contribution,

$$\chi_I(\Delta_i, n_e, n_h) = \int\frac{1 - i\Delta}{1+\Delta^2}(n^e + n^h - \Pi)G_{\Delta_i}(\Delta)\mathrm{d}\Delta. \tag{12.23}$$

In order to make a connection to experiments, the scaled units need to be related to real ones. The unscaled susceptibility is:

$$\chi(\Delta_i, n_e, n_h) = \left(\frac{\mu^2 N_D}{\hbar\varepsilon_0\gamma_p}\right)\chi_I(\Delta_i, n_e, n_h). \tag{12.24}$$

Here, N_D defines an effective volume density. In vertical-cavity devices (VCSEL),

$$N_D = \frac{N_{\mathrm{QD}}N_l}{L_A}, \tag{12.25}$$

whereas in edge-emitting devices or lasers (EEL)

$$N_D = \frac{N_{\mathrm{QD}} N_l}{d}, \tag{12.26}$$

where N_l is the number of QD layers, d is the total thickness of the active zone (EEL) and L_A the total length of the active zone (VCSEL). From this, the absorption coefficient for the intensity can be obtained as

$$\alpha(\Delta_i, n_e, n_h) = \frac{\omega_0}{n_b c} \mathrm{Im}\chi(\Delta_i, n_e, n_h). \tag{12.27}$$

Analogously, the refractive index can be determined from the real part of the scaled susceptibility as:

$$n = \frac{1}{2n_b}\chi = \Delta n_0 Re\chi_I \tag{12.28}$$

where Δn_0 is equal to

$$\Delta n_0 = \frac{\mu^2}{2n_b \hbar \varepsilon_0 \gamma_p} N_D. \tag{12.29}$$

Note that these are the material coefficients, to obtain the modal coefficients for devices in which there is only a partial overlap between the active region and the field distribution (e.g. in EEL) one needs to multiply with a confinement factor Γ_{trans}, which is given by an overlap integral over the fast direction between the fundamental waveguide mode intensity distribution and the thin active layer.

Cavity Equation

The field equation is derived here in the case of a broad-area resonator, by following the same procedure as in [48, 49]. In the mean-field limit and introducing the appropriate scalings as in [23], we can write the equation for the intracavity field as:

$$\frac{\partial E}{\partial t} = -\left[(1+i\theta)E - E_I - i\nabla_\perp^2 E \; - \; 2C\,\chi(\Delta_i, n_e, n_h)\,E\right]. \tag{12.30}$$

The time here has been scaled to the field decay rate $\kappa = cT/2n_b L$ in the cavity. We also have introduced $\theta = (\omega_c - \omega_0)/\kappa$, the scaled cavity-field detuning and the cooperativity parameter

$$2C = \frac{\mu^2 \omega_0 N_{\mathrm{QD}}}{\varepsilon_0 \hbar \gamma_p n_b c T}. \tag{12.31}$$

E_I is an injected field while the transverse Laplacian $\nabla_\perp^2$ accounts for the diffraction inside the cavity. The spatial transverse coordinates are rescaled to the

diffraction coefficient $a = c/2n_b k_o \kappa$. L is the cavity length and T the mirror transmission.

Equation 12.19 for the electrons and holes and 12.20 for the WL with Eq. 12.30 for the field are the self-consistent set for a general description of a broad-area QD microresonator. (Due to the scaling of time with κ, γ_{nr} and $\gamma_{\mathrm{nr}}^{\mathrm{WL}}$ in Eqs. 12.19, 12.20 need to be scaled also to $\gamma_{\mathrm{nr}}/\kappa$ and $\gamma_{\mathrm{nr}}^{\mathrm{WL}}/\kappa$.)

Propagation Equations

The paraxial wave equation describing single-pass propagation of a light field $E(x, x, z)$ in a medium with a susceptibility χ is

$$\partial_z E = i\,\frac{c}{2n_b\omega_0}\,\nabla_\perp^2\, E + i\,\frac{\omega_0}{2n_b c}\,\Gamma_{\mathrm{trans}}\chi E. \tag{12.32}$$

The transmitted field after a thin layer of matter with thickness δz is (thin enough such that diffraction can be neglected)

$$E(x, y, z + \delta z) = \exp\left[i\frac{\omega_0}{2n_b c}\chi(x, y, z)\delta z\right] E(x, y, z). \tag{12.33}$$

In most investigations presented below, we will assume that this description is fine for the whole sample, i.e. we set $\delta z = L_A$ neglecting pump depletion (or amplification) and diffraction within the medium.

Numerical Results: Single-Pass Propagation

Parameters and Numerical Scheme

Calculations can be performed for the (two-dimensional) case of a surface-emitting geometry or for a (quasi-one-dimensional) edge-emitter. We concentrate on the latter because of the smallness of the optical density in a surface-emitter. Then, Eqs. 12.19, 12.20 are solved numerically for a cw Gaussian input beam $E(x) = E_0 \times \exp\left(-x^2/w_x^2\right)$ on a numerical grid with 64 space points and a beam waist w_x of 15 points or 15 μm. We resolve spectrally 61 size classes. About 8,000 iterations are needed until the solutions to the carrier equations relax to the stationary state. Due to the thinness of the active zone in the fast direction (y), $E(x)$ can be taken as the peak value of the field profile of the fundamental mode of the waveguide in the fast direction (with radius w_y) with the form $E(x, y) = E(x) \times \exp\left(-y^2/w_y^2\right)$. Note that we do not consider any built-in waveguide in the x-direction. The resulting spatial distributions $n^e(x)$ and $n^h(x)$ are then used to calculate the spatial distribution of the susceptibility by Eqs. 12.23 and 12.24.

In the experiment, one is not measuring the absorption coefficient (12.27) directly but transmission. Typically, the latter will be integrated over the beam in addition:

$$T = \int \exp\left[-\Gamma_{\text{trans}}\alpha(x)L_a\right]\left(\frac{2}{\pi}\right)^{1/2}\frac{1}{w_x}\exp\left(\frac{-2x^2}{w_x^2}\right)\mathrm{d}x, \tag{12.34}$$

where

$$\Gamma_{\text{trans}} = \frac{\int_{-d/2}^{d/2}|E(y)|\mathrm{d}y}{\int |E(y)|\mathrm{d}y} \tag{12.35}$$

is the confinement factor for an edge-emitting structure.

We are choosing parameters typical for InAs QD emitting in the 1.3 μm region at room temperature [9, 15, 16, 50, 51]. We assume the following set of parameters in normalized units: $B_{\text{eh,he}} = 200$, $\sigma_{\text{cap}} = 500$, $\gamma^e_{\text{esc}} = 0.01$, $\gamma^h_{\text{esc}} = 100$, $\gamma^{\text{WL}}_{\text{nr}} = 0.15$ and a time unit of 11.7 ps. This translates to a rate of (1/160 fs) for the capture and Auger processes coupling the WL to the QD in agreement with measurements for the refilling of the QD ground state from WL and excited states [9, 16].

Other parameters are [15, 51, 52]: $N_{\text{QD}} = 5 \times 10^{10}$ cm^{-2} QD dot sheet density, $N_l = 10$, $d = 10 \times 3.9 \times 10^{-8}$ m, $\omega_0 = 1.45 \times 10^{15}$ s^{-1}, $\lambda = 1.3$ μm, $\beta = 0.02$, $L_a = 1$ mm, $\gamma_p = 7.1 \times 10^{12}$ s^{-1}, $\Gamma/\gamma_p = 4$, corresponding to an inhomogeneous broadening of about 40 nm. A dipole matrix element of $\mu = 1.23 \times 10^{-28}$ Cm corresponding to a radiative lifetime of $1/\Gamma_1 = 0.5$ ns results then in a small-signal modal absorption coefficient in line center (Eq. 12.27 for $n_e = n_h = 0$, $\Gamma_{\text{trans}} = 0.094$) of $\alpha_0 = 26.7/\text{cm}$. Since reported small-signal modal gain values for these structure are between about 19 and 24/cm in the 1,250–1,290 nm range [9, 51] with small-signal absorption being about 30–100% larger than the small-signal gain [9], this is a conservative estimate. Note that in the remainder of "Modeling and Simulation Results" and in "Experiments on InAs/GaAs QD Around 1,250 nm" α, α_0, n, C denote modal absorption coefficients, refractive indices, and cooperativity parameters, whereas in "Experiments on InAlAs/GaAlAs QD at 780 nm" they denote the material parameters.

Results: Saturation of Absorption and Gain

Figure 12.1 displays the gain, respectively absorption, coefficient obtained from Eq. 12.34 in dependence of the input intensity for different detunings. For all curves, it starts at the small-signal value and then drops to the vacuum value of zero due to the generation of carriers and the resulting bleaching. Obviously, the small-signal absorption/gain is highest at $\Delta_i = 0$ and decreases for increasing modulus of detuning according to Eq. 12.27. The intensity where saturation becomes apparent seems to increase with increasing modulus of detuning.

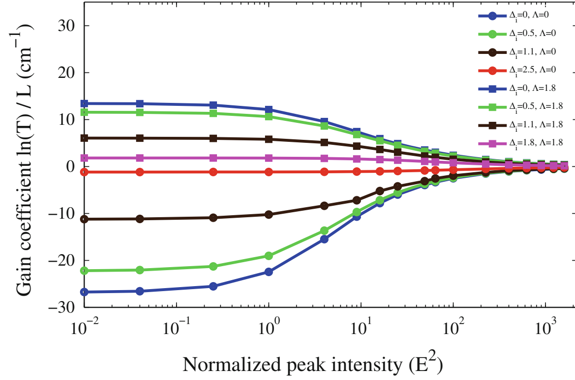

Fig. 12.1 (Color online) Modal gain coefficient as a function of the normalized intensity in the center of the Gaussian input beam for different values of the detuning in the absorption (*circles*) and gain regimes (*squares*). (Adapted from [25])

Since the ratio of $\Gamma/\gamma_p = 4$ refers to a Voigt-profile situation where neither homogeneous nor inhomogeneous broadening are clearly dominating, we fit the dependence of the gain coefficient on intensity with different models that describe saturable absorption in the case of two-level systems with inhomogeneous,

$$\alpha = \alpha_0 / \sqrt{(1 + E^2/E_s^2)}, \tag{12.36}$$

and homogeneous,

$$\alpha = \alpha_0 / (1 + E^2/E_s^2), \tag{12.37}$$

broadening [53]. The latter proves to fit best the simulation. We show in Fig. 12.2, the modulus squared of the saturation field strength vs Δ_i as extrapolated from the above formula. The saturation intensity is minimal at $\Delta_i = 0$ and is slightly different, about a factor of two, for the gain $(E^2 = 3.6)$ and the absorption case $(E^2 = 1.8)$. It strongly increases in both cases for increasing modulus of the detuning, whereas it should be constant in the strongly inhomogeneous limit [53]. As indicated above, a ratio of $\Gamma/\gamma_p = 4$ corresponds neither to strongly inhomogeneous broadening nor to pure homogenous one. Additional coupling is provided by the fact that different size classes of QD are coupled via the escape and recapture processes via the WL and lead to a stronger homogeneous broadening at room temperature than at lower temperatures [54]. Nevertheless, at least in quantum dash samples there is evidence for a strong coherent hole (the equivalent to the so-called Lamb-dip in Doppler-broadened atomic ensembles) at room temperature [55] indicating at least partial inhomogeneous broadening. This coherent hole is observed in our simulations also. Hence it seems to make sense that the saturation behavior shares features known from homogeneous and inhomogeneously broadened systems.

For an experimental situation with $w_x = 15$ μm and $w_y = 0.5$ μm, $E^2 = 1$ corresponds to a power of 7.1 mW. Hence the minimum value of the saturation power is 13 mW in the absorption case and 26 mW in the gain case. If instead of $\gamma = 0.15$

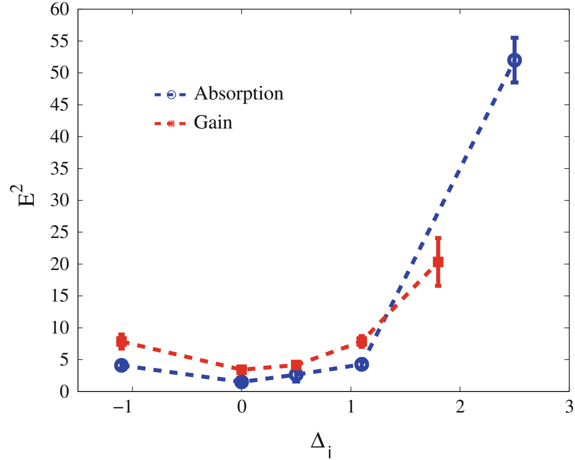

Fig. 12.2 (Color online) Modulus squared of saturation field strength (proportional to saturation intensity) obtained from a fit of the curves in Fig. 12.1 to Eq. 12.36 as a function of detuning. *Squares* represent the gain case (*red* online), *circles* the absorptive case (*blue* online). The lines are only a guide for the eye. (Adapted from [25])

(or 78 ps lifetime), the purely radiative lifetime is considered, the corresponding values are about a factor of 10 lower and easily accessible experimentally.

As indicated, the simulations presented neglect pump depletion within the medium. We have preliminary results using a split-step beam propagation method [56]. The term 'split-step' implies that the simultaneous action of diffraction and nonlinear refraction (determined by χ) in Eq. 12.32 is replaced by a step-wise scheme of alternating diffraction and refraction steps. This works by splitting the medium in m layers with a thickness $\delta z = L_A/m$. The diffraction part is solved in Fourier (transverse wave number) space, the refraction is solved in real space via Eq. 12.33. In each layer the carrier equations need to be solved providing a significant computational load. We find that for our case, $m = 16$ provides enough resolution (for $L_A = 1$ mm) so that the results do not depend on discretization. The principal shape of the saturation curves is not strongly affected by taking into account pump depletion but the saturation intensity for the absorption increases by a factor of about 1.6 and the saturation intensity for the gain decreases by a factor of about 0.7 (for $\Delta_i = 0$). As a result, the gain saturates now slightly easier than the absorption. This is easily understandable because the pump depletion due to absorption will hinder saturation in the subsequent layers. On the other hand, the amplification due to gain will help to saturate the gain in the subsequent layers. Similar considerations will be important in "Experiments on InAs/GaAs QD Around 1,250 nm" to interpret multi-pass effects.

Results: Self-Lensing

One effective method to assess the strength of a χ_3- or saturable refractive index nonlinearity is to look for self-lensing, e.g. in a so-called z-scan geometry [57]. Since the input beam is spatially varying, also the refractive index is. Around the

beam center, the variation is necessarily parabolic. According to [58] the radius of curvature acquired by a wave propagating a distance L_a in a medium is given by

$$\frac{1}{R(r)} = \frac{1}{r}\frac{\partial}{\partial r} n(r)\, L_a. \tag{12.38}$$

From that we can identify an effective focal power:

$$\frac{1}{f}(x) = -\frac{1}{x}\frac{\partial}{\partial x} n(x)\, L_a \tag{12.39}$$

$$= -\Delta n_0\, L_a \left(\frac{1}{x}\frac{\partial}{\partial x} \mathrm{Re}\chi_I(x)\right) \tag{12.40}$$

If the refractive index distribution would be a pure parabola, the focal power would be constant over the whole beam, thus implying an aberration-free equivalent lens. In reality, this is obviously not the case because the pumping Gaussian has an inflection point. Nevertheless the parabola is often a good approximation in beam center where most of the beam energy is. This was studied in detail in atomic vapors [59] and we will discuss it for the QD below. In any case, the curvature will give a quantitative indicator for the strength of beam shaping even if the lens is not perfect. The focusing can be experimentally detected by a change of the beam width in far field [60] or at some distance after the medium [59] (similar as in z-scan techniques [57]). In this first treatment, we will confine to a thin lens to demonstrate the principles. For a quantitative description of a real experiment it might be necessary to include absorption and nonlinear beam reshaping during propagation.

Figure 12.3 shows the spatial profile of the real part of the susceptibility imposed by the Gaussian pumping profile for low, intermediate, and high peak intensity. For low intensity it follows roughly the Gaussian intensity distribution of the input beam ('Kerr-limit') whereas at high intensities there is a broad plateau in beam center because the beam has sufficient intensity to saturate the sample even in the beam wings. At beam center, the variation is parabolic leading to lensing. Figure 12.4 shows how the lens power changes as function of input intensity for different detunings in the absorption case (a) as well as in the gain case (b). Apart from the $\Delta_i \approx 0$-case (discussed separately below), the focal power increases from zero with increasing intensity, reaches a peak at an intermediate intensity and decreases again if the intensity is increased further. The sign of the lensing depends on the sign of detuning and whether the sample is absorbing or providing gain, as expected. The maximum lens effect occurs at $\Delta_i = 1.1$ and $E^2 = 9$ ($P = 64$ mW). The focal power is maximum at an intermediate input power a few times higher than the saturation power. The intensity needed to obtain maximum lens power increases for increasing modulus of detuning. This is probably due to the fact that the saturation intensity increases with detuning and the maximum effect is found for the same saturation condition.

The fact that the maximum focal power is obtained at intermediate input intensity can be explained by looking at Fig. 12.3. For low intensity the curvature follows the curvature of the input profile ['Kerr-limit', $\Delta n(x) \sim |E|^2(x)$], but the

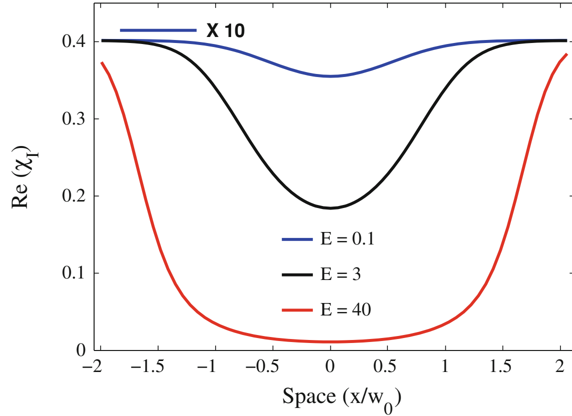

Fig. 12.3 (Color online) Spatial profile of the real part of the susceptibility for, from *top* to *bottom line*, low (*blue line*, amplitude enhanced by a factor of 10), intermediate (*black line*), and high excitation (*red line*). $\Lambda = 0,\ \Delta_i = 1.1$. The total excursion is $\Delta n = 1.6 \times 10^{-4}$. (From [25])

total effect is low because the excursion from the background refractive index is small (note that the curve is blown up by a factor of 10). For high intensity, the excursion is large (Re(χ_I) becomes nearly zero) but the total focal power is again low because the curvature is strongly reduced. This is due to the fact that saturation is effective over a large area at high intensities. The case of intermediate intensity is in between: On the one hand the excursion is of reasonable size, about half the maximal effect, on the other hand the curvature is still quite close to the one of the input beam. Both is characteristic for intensity levels around the saturation intensity, i.e. for the onset of saturation, and hence the total effect is maximal. Similar characteristics were found for atomic vapors [59]. Here, in the homogeneously broadened case, it can be demonstrated analytically that maximum focal power is found at the saturation power [59].

The lensing effect is minimal at $\Delta_i = 0$. Indeed, in a purely two-level system no effect at all is expected for $\Delta_i = 0$ because the contributions of blue and red detuned size classes cancel. It is the thermally induced coupling to the WL (described by the parameter β) which breaks that symmetry (see "Nonlinear Refractive Index and α-Factor").

In the peak, the predicted lensing effect is actually quite substantial, $|f_{\min}| \approx 1.7$ mm, in a sense, because the focal length reaches the length of the medium (assumed to be $L_a = 1$ mm), i.e. the point where the approximation by a thin lens becomes questionable. These values were calculated assuming an input beam radius of $w_x = 15$ µm chosen because it would be conveniently to work with experimentally and being somewhat larger than typical fundamental mode sizes in EEL, i.e. in a range where filamentation phenomena might occur. The size of cavity solitons is also in that range (about 10 µm [30, 61]).

Nevertheless, it turns out that an experimental confirmation is not straightforward. The modification of the input beam by the lensing of the sample can be detected by either measuring the on-axis amplitude (being proportional to the square of the new beam waist of the transmitted beam, w'^2_x) or the beam width in far field $(\sim 1/w'^2_x)$ [60] or, more sensitively, by measuring the beam size either

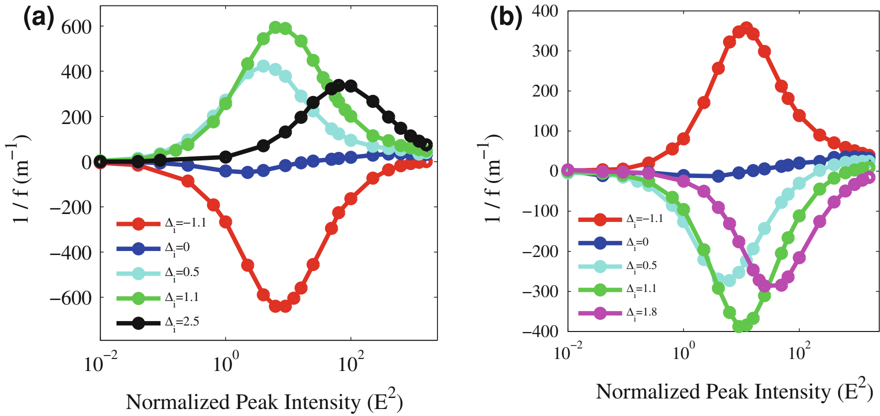

Fig. 12.4 (Color online) Focal power as function of normalized peak intensity for different detunings in the absorption case (**a**) and the gain case (**b**). ($\Lambda = 1.8$ was chosen because it reproduced the experimental finding that maximal gain is about half the absorption coefficient.) (From [25])

directly or via the transmission through a pinhole at some suitable chosen distance after the medium as it is done in usual z-scan techniques [57]. Replacing the medium by a thin lens of focal length f, the size of the new beam waist w'_x can be calculated by ABCD-matrix theory as

$$w'_x = w_x \frac{1}{1 + \frac{\pi w_x^4}{\lambda^2 f^2}}. \tag{12.41}$$

For an input beam waist of $w_x = 15$ μm and a thin lens with $f \approx 1.7$ mm, the new beam waist is $w_x = 14.3$ μm at a distance of 0.16 mm. This rather small change in beam is quite difficult to detect. Equation 12.41 says that the effect becomes more pronounced if the initial beam radius is increased (at constant f), being substantial if the Rayleigh length of the input beam $z_r = \pi w_x^2/\lambda$ is of the order of f. In reality, however, the focal length scales like $f \sim w_x^2$, since, as discussed for Fig. 12.3, the curvature of the susceptibility profile follows the curvature of the input beam in first approximation for not too strong saturation (see [59] for an analytical treatment). Hence, actually the strength of the detected signal cannot be influenced by choice of the input beam size.

However, due to the approximately quadratic dependence of the new beam waist on ratio of w_x^2/f, the situation rapidly improves with increasing focal power. For example, a change of size by 20%, which should be experimentally detectable, is reached already for a focal power of about 1,000/m, i.e. only about two times the maximum value reported in Fig. 12.4.

Since it appears that the numbers are somewhat at the edge, it is useful to discuss the influence of other uncertainties, e.g. the exact nature of the relaxation processes between the QD and WL states. Results reported in [25] indicate that the

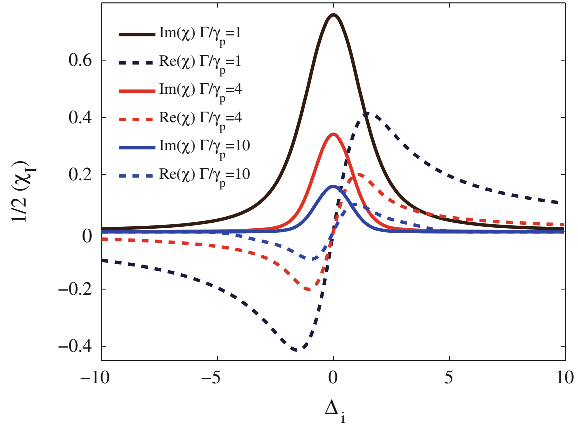

Fig. 12.5 (Color online) Real and Imaginary part of the linear susceptibility as function of detuning for different ratios between inhomogeneous and homogeneous broadening. (From [25])

changes are within the 20% range for the dominating part (real or imaginary) of the susceptibility for reasonable adjustments of parameters. The carrier lifetime in the QD was assumed to be 78 ps, much smaller than the radiative lifetime of 500 ps. This was done on the one hand to be on the conservative side with respect to the possible influence of defect induced recombination and on the other hand to reduce the computational load, which is rather high due to the separation of timescales between scattering processes between WL and QS and carrier lifetime in QD and due to the fact that the carrier density needs to be spectrally and spatially resolved in our case. We did some test runs using a lifetime of 0.5 ns which yield an increase of 10% in saturation and negligible effect in lensing. Note that the influence of the lifetime on the scaling of the saturation power can be treated exactly without additional calculations (as discussed above) due to the way the equations are scaled.

Finally, Fig. 12.5 shows how real and imaginary part of the linear susceptibility change as function of detuning for different ratios between homogeneous and inhomogeneous broadening. Since the linear susceptibility defines the maximum value of the nonlinear index change, this provides a good guidance on the maximum effect to be expected. Choosing a ratio of $\Gamma/\gamma_p = 10$ instead of 4 decreases the maximum of the real part of the susceptibility by a factor of 2.1. For a ratio of $\Gamma/\gamma_p = 1$, it is a factor of 2 higher. Hence, at constant γ_p, one can expect to benefit from improved growth with a reduced inhomogeneous broadening. Note that increasing γ_p at constant Γ is not beneficial because the increase of the scaled susceptibility is sublinear (cf. Fig. 12.5) and is overcompensated by the dependence of the proportionality factor between scaled and unscaled susceptibility on γ_p, see Eq. 12.24. We conclude that though uncertainties in the relaxation constants will influence the measurements quantitatively, our overall conclusion that the lensing is at the edge of being detectable is not changed. One reason for the somewhat low nonlinear phase shift is the inhomogeneous broadening. The peak phase shift from Fig. 12.5 for Γ/γ_p is only 40% of what a homogenously broadened transition with the same total QD density would give.

At this point it is worthwhile to note that a possible susceptibility contribution of the WL carrier population or ES population should be introduced here. Taking for example the curve with $\Gamma/\gamma_p = 4$ considered relevant here, the refractive index contribution of an ES 100–120 nm away from the GS (roughly the situation in InAs QD) will partially overlap and counteract the effect of the GS transition: With an inhomogenous broadening of $\Gamma \approx 40$ m the distance between the ES and the GS on the Δ_I-axis in Fig. 12.5 is 3. (The contribution is smaller for the imaginary part of the susceptibility (our main focus in the experiment later) because that tails off fast than the real part with detuning.) In particular, that implies that there might be a nonzero α-factor around the gain peak of the GS due to the off-resonant contributions from WL and ES. Though there are reports of fairly low α-factors [35–37] on the one hand, there is also significant evidence of contributions from the other states, discrete or continuous (WL or barrier based), whose contribution to the refractive index in particular could be significant for high injection values (and thus large carrier densities in the ES or WL) [38–40]. Modeling more complex contributions has been dealt with by means of properly balanced rate–equations models for the carriers and/or by inclusion of a contribution from the continuum and discrete states in WL and QD either in a semi-phenomenological or more first-principle way [39, 62–65].

Numerical Results: Cavity Dynamics

Nonlinear Refractive Index and α-Factor

As just discussed, the α-factor is an important, but still controversial factor in QD-based photonic devices. It depends very much on operating conditions and also on measurement method (see, e.g. the discussion in [39]). Commonly used techniques to measure the α-factor (e.g. [39]) are based on the FM/AM response of the laser output or the amplified spontaneous emission spectrum to a small modulation or variation of the injection current using the relation

$$\alpha_H = \frac{\frac{\mathrm{dRe}\chi}{\mathrm{d}N}}{\frac{\mathrm{dIm}\chi}{\mathrm{d}N}}, \tag{12.42}$$

where the change in carrier density (being it in the QD or the WL) is introduced via the variation of current around some working point. In another method one analyzes the output of a laser with injection (Huyet, 2005, "personal communication"). Since this latter method can be easily described by our formulation, Eq. 12.30, we use it here to point out one aspect of the carrier dynamics leading to an asymmetric gain spectrum and hence a nonzero α_H at gain peak in addition to the off-resonant effects of the WL and ES states. This is the different thermal occupation of the size dispersed QD GS states described by the factor β introduced in Eq. 12.18.

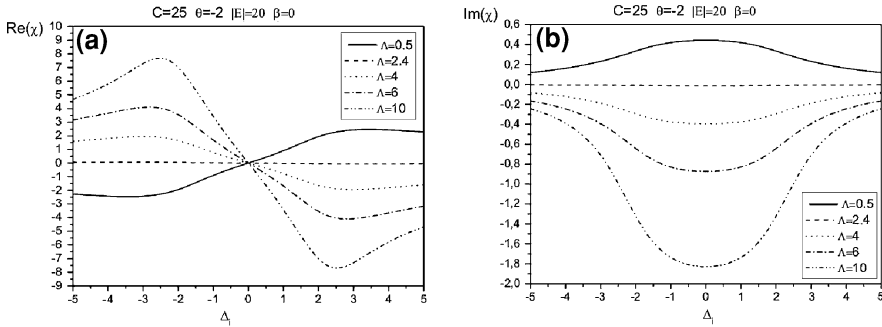

Fig. 12.6 Plot of the real and imaginary parts of the susceptibility spectrum versus the detuning from the QD population line center for $\beta = 0$ and for five values of the pump Λ from absorption to gain. Other parameters for these simulations are $\sigma_{\text{cap}}^{e,h} = 500,\ \gamma_{\text{esc}}^{h} = 100,\ \gamma_{\text{esc}}^{e} = 0.01,\ B_{\text{he,eh}} = 500,\ \gamma_p = 15,\ \Gamma = 60,\ \Gamma_{\text{sp}} = 2.5,\ \gamma_{\text{nr}} = \gamma_{\text{nr}}^{\text{WL}} = 0.15,\ C = 25,\ \Theta = -2,\ |E| = 20.$ (Reprinted with permission from [24]. Copyright 2007, American Institute of Physics)

We considered a pumped device with currents spanning from absorption to gain and evaluated the α-factor defined as in [24]. For vanishing β (meaning the neglect of the thermal distributions of the capture and escape rates) a symmetric, two-level like profile of the gain spectrum is maintained as shown in Fig. 12.6. The inhomogenous broadening does not influence the symmetry but decreases only the peak effect (as discussed above).

Figure 12.7 shows the situation for $\beta = 0.02$. When $\beta > 0$, the gain spectrum shows an asymmetry steadily growing with β and with carrier injection Λ (Fig. 12.7b) thus implying a non-vanishing α-factor. The real part of the susceptibility (Fig. 12.7a) is less affected, the point where all dispersion curves approximately intersect and hence where $\alpha_H \approx 0$ moves to slightly positive detuning (here $\Delta_i \approx 0.015$).

The α-factor can be evaluated by using the definition at the beginning of this section, i.e. varying Λ by a small amount around a working point and calculating the resulting differentials numerically. For a bias of $\Lambda = 2.36$ (pump slightly below transparency) and $\beta = 0.01$, we plot its value in Fig. 12.8.

By inspecting it, we see that for fixed current pump (below threshold) and input field values, the system exhibits a negative α-factor for higher energy (smaller wavelength) spectral values, consistently e.g. with [62], which increases to positive values, again, with a behavior qualitatively not dissimilar from the ones reported e.g. in Fig. 12.6 of [66], and experimentally in (Huyet, 2005, “personal communication“). The dispersion curve is strongly asymmetric, though the zero point is actually not much shifted for this relatively low values of β.

Nonlinear Phase Shift and Fabry-Perot Fringes

We discussed in “Results: Self-Lensing” self-lensing as a possible method to assess the nonlinear, intensity-dependent, phase shift and found that it is close to

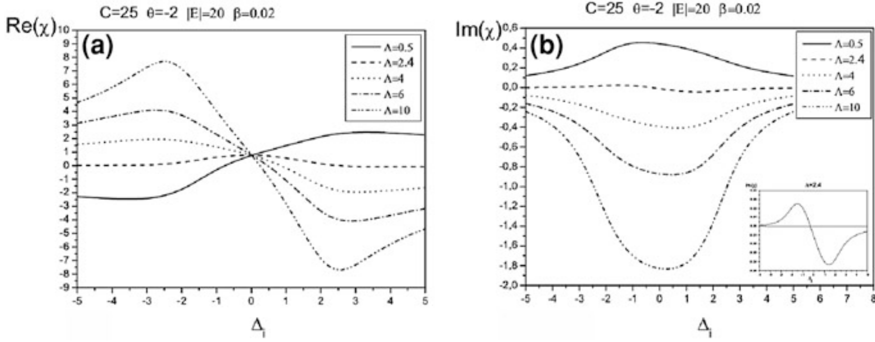

Fig. 12.7 Plot of the real and imaginary parts of the susceptibility spectrum versus the detuning from the QD population line center for $\beta = 0.02$ and five values of the pump Λ from absorption to gain. Other parameters as in Fig. 12.6. The inset is a blow-up of the curve for $\Lambda = 2.4$. (Reprinted with permission from [24]. Copyright 2007, American Institute of Physics)

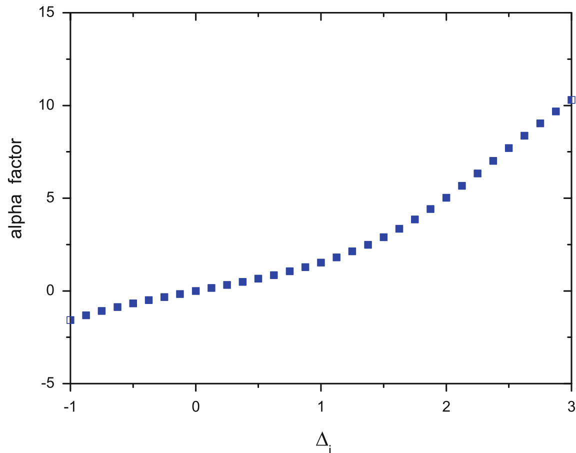

Fig. 12.8 α-factor versus the detuning from the QD population line center for $\beta = 0.01$ and $\Lambda = 2.36$. Other parameters as in Fig. 12.6 except $C = 20,\ \Theta = -3,\ |E| = 30$.

the detection limit. Interferometric methods are an attractive alternative in which a probing beam after having passed the QD sample might be interfered with a reference beam. Alternatively, one might measure the shift of cavity resonances with intensity. Note that contrary to the way the α-factor is normally measured, i.e. by changing the carrier density via changing the injection current (see previous section), we are interested here in the index shift generated by a coherent light beam via the carriers it generates (or takes out via stimulated emission).

In a Fabry-Perot cavity a refractive index change of δn causes a shift of the wavelength resonance by

$$\delta\lambda = \lambda_0 \frac{\delta n}{n_b}, \tag{12.43}$$

where λ_0 is the resonance wavelength belonging to the background index n_b. In order that a shift is detectable, it should be about half of a free spectral range

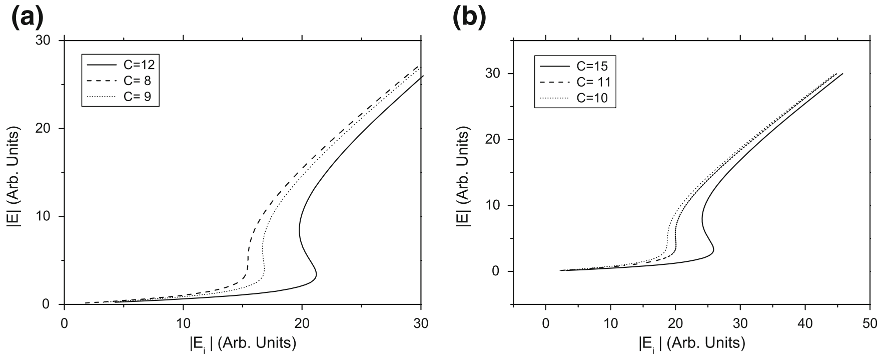

Fig. 12.9 Bistable and monostable steady state curves for the intracavity vs injected field amplitudes: (**a**) resonant case $\theta = \Delta_i = 0$ with $C = 12, 9, 8$ (respectively, *full*, *dotted*, and *dashed lines*) representatives of bistable, threshold, and monostable regimes; (**b**) dispersive case $\theta = -1,\ \Delta = 0$ with $C = 15, 11, 10$ (respectively, *full*, *dashed*, and *dotted lines*); representatives of bistable, threshold, and monostable regimes. Other parameters as specified in the text

(FSR) of the cavity given by $\Delta\lambda_{\mathrm{FSR}} = \lambda_0^2/(2n_bL)$. From this the detectable refractive index should be

$$\delta n = \frac{\lambda_0}{4L}. \tag{12.44}$$

For the simulation parameters used in "Parameters and Numerical Scheme", the maximum index shift is 1.6×10^{-4} at 1,280 nm. Hence, the nonlinear shift should be detectable in cavities of length of 2–4 mm. Note that this is only a rough estimation. On the one hand a shift of the fringes of less than half a FSR is detectable, on the other hand, the numbers given assume optimal tuning for the maximal index effect (Fig. 12.5) and complete saturation.

Optical Bistability

The set of equations proposed in "The Model" can be directly exploited to investigate the stationary emission states of a microresonator with coherent injection. In particular, an interest resides in the regimes where the stationary curve has a bistable character. This issue is interesting 'per se' for all-optical processing applications, but also because bistability is the fingerprint of highly nonlinear regimes and has also been investigated in relation to the search for modulational instabilities leading to pattern formation and cavity solitons (see, e.g. [27–29] for reviews).

In this research, the mainstream of the experimental investigations has been performed in absence of carrier pumping and with an injection resonant with the QD centerline and the cavity reference frequency (purely absorptive regime); in Fig. 12.9a we show the steady state field curves for the case $\theta = 0, \Delta_i = 0$ and we

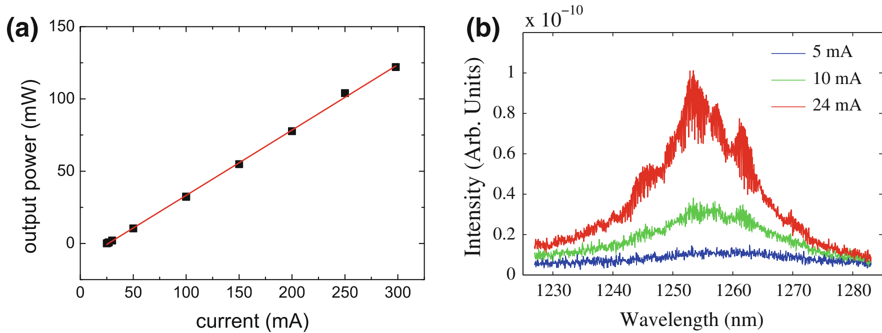

Fig. 12.10 (Color Online) **a** LI-curve (*squares*) of device with linear fit (*straight line*), $T = 15°\text{C}$. **b** Spontaneous emission spectra from the QDD for different injection currents below threshold. (Reprinted with permission from [41]. Copyright 2010, American Institute of Physics)

evidence the existence of a threshold in the C parameter, approximatively equal to 9, below which the curve is monostable. Other parameters in the simulations are the same as in "Nonlinear Refractive Index and α-Factor".

In the dispersive case, when the injected field is detuned from the cavity resonance, the bistability conditions are somewhat more demanding due to the diminished fraction of the spectral population distribution resonant with the external drive, as reported in Fig. 12.9b. The threshold for C is close to 11 for this case. Note that, there being no analytical expression for the steady states of the population variables, the threshold must be calculated by integrating the dynamical model to a stationary regime and identifying the curve where extrema disappear.

Globally, our model predicted bistability for C values of about 10–20 [23], within experimental reach, in principle. The cooperativity parameter of the edge-emitting InAs-based structure investigated in "Experiments on InAs/GaAs QD Around 1,250 nm" is estimated to be about 5 (with background waveguide losses of 1.5/cm determined for devices of this kind), i.e. roughly half the requirement for bistability. The analysis of Fig. 12.11 suggest an optical density of only $\alpha_0 \approx 14.5/\text{cm}$ giving $C \approx 3$. The InAlAs-based structure investigated in "Experiments on InAlAs/GaAlAs QD at 780 nm" is estimated to be about 7 (assuming the same background losses) or about 3, assuming losses of 10/cm suggested by the analysis in "Absorption Saturation". This means all present samples fall short of the requirement for bistability, but an optimization in terms of length and/or an improvement in growth density, number of layers, or a reduction in inhomogeneous broadening should open suitable parameter regimes (see also the discussion in "Summary and Conclusion").

The determination of the C parameter required for pattern formation has been discussed in [24] and suggested that QD densities needed (via Eq. 12.31) for such scopes are not outside reach. More precisely, pattern formation is predicted in the order of $N_{\text{QD}} \approx 10^{12}\,\text{cm}^{-2}$ (longitudinally integrated density for vertical-cavity devices) [22].

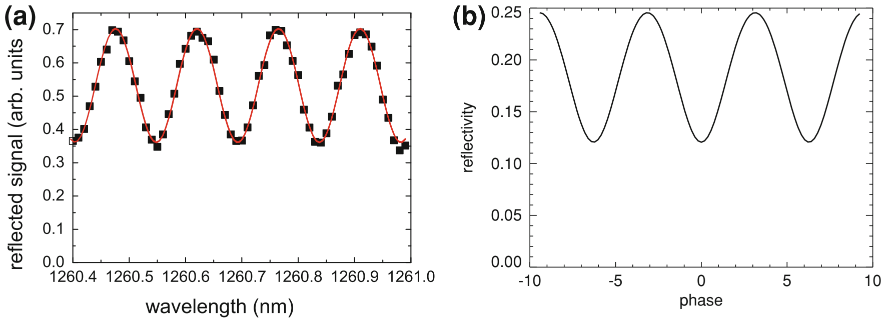

Fig. 12.11 (Color Online) **a** Linear reflection spectrum of QDD (*squares*) displaying Fabry-Perot fringes and fit to a sine-wave ($T = 15°\text{C}$, $I = 0$ mA). **b** Calculated Airy function in reflection for a Fabry-Perot interferometer for $R_1 = 0.18$, $R = 0.99$ and internal (intensity) losses of 16/cm

Experiments on InAs/GaAs QD Around 1,250 nm

Devices and Experimental Setup

The investigated sample is a quantum dot diode (QDD) from Innolume GmbH with a cavity length of $L = 1.5$ mm. It contains ten layers of InAs QD in a GaAs matrix. The epitaxial structure is similar to the one described in [9]. A single-mode ridge-waveguide ensures spatial fundamental mode operation. The device is designed as a laser with a front reflectivity of $R_1 = 0.18$ and a back reflectivity of $R_2 = 0.99$. The light-current (LI) characteristic is shown in Fig. 12.10, from which a threshold current of $I = 26.6$ mA at $T = 15°\text{C}$ is inferred. However, in our investigations, it is used only in absorptive mode (i.e. without current injection) or as an amplifier below threshold.

Figure 12.10b shows the spontaneous emission spectra taken with an optical spectrum analyzer (OSA, resolution 0.07 nm) for three injection current levels. The luminescence is centered around $\lambda = 1,255$ nm. No distinctive peaks or shoulders from excited state or WL emission are visible. The spectrum becomes somewhat jagged around the gain peak at high currents because the finesse of the cavity improves. We choose a current of 24 mA for the detailed investigations under gain conditions.

Figure 12.11a shows a linear reflection spectrum of the QDD obtained from a tunable laser (Santec TSL-210V). The free spectral range is fitted to be 0.15 nm in agreement with the length specification of the QDD by the manufacturer. The apparent Finesse is about 1. Finesse and modulation depth can be approximately fitted by a modal loss of 16/cm (see Fig. 12.10b), somewhat less than the 28.2/cm (1.5/cm waveguide loss and 26.7/cm absorption) expected from structures of this kind from "Parameters and Numerical Scheme", but indicating still a very reasonable interaction strength.

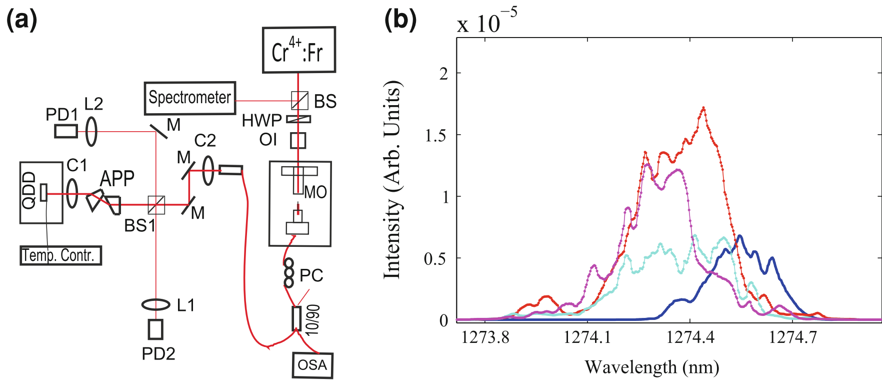

Fig. 12.12 **a** Experimental setup: Chromium forsterite laser (Cr^{4+} : Fr), beam splitter (*BS*, *BS*1), half-wave plate (*HWP*), optical isolator (*OI*), microscope objective (*MO*, 40×), optical spectrum analyzer (*OSA*), mirror (*M*), anamorphic prism pair (*APP*), aspherical collimator ($C1, f = 3$ mm; $C2, f = 13.9$ mm), lenses ($L1, f = 50$ mm; L2, $f = 35$ mm), amplified photodiode (*PD*1, *PD*2). **b** Examples for variation of spectra of Cr:Fr laser over time. (Reprinted with permission from [41]. Copyright 2010, American Institute of Physics)

The experimental setup is illustrated in Fig. 12.12a. The driving laser is a home-built Chromium forsterite (Cr:Fr) laser [67]. The 4-mirror asymmetric astigmatically compensated z-fold cavity was developed for mode-locked operation but had been re-configured to run in cw mode with a multi-mode output (see Fig. 12.12b); the free spectral range of about 100 MHz is obviously not resolved. A prism was included in the laser cavity to allow simple tunability of the system. The output spectra have a full width at half maximum of 0.3–0.2 nm, covering several longitudinal modes of the QDD. Hence, the coherence length of the Cr:Fr laser is less than the QDD cavity length and cavity resonance effects are expected to be weak. Since the laser is not optimized for cw operation, its modal envelope fluctuates slightly over time (some typical examples are shown in Fig. 12.12b). However, the fluctuations are small against the spectral broadening of the QD, which is on the several nm to tens of nm level.

After the laser a half-wave plate (HWP) and an optical isolator (OI) are present to avoid back reflection into the laser and for adjusting the power. The beam passing the OI is coupled through a microscope objective (MO) to a single-mode fiber. The single-mode fiber is then connected to a polarization controller (PC) and to a fiber coupler that splits the incoming beam into 10% and 90% components. The weak beam is sent to the OSA to monitor the spectra of the Cr:Fr laser. The main part (90 %) is collimated by an aspherical lens (C2) with a maximum power of about 100 mW at λ =1,240–1,280 nm. An anamorphic prism pair (APP) transforms the circular beam coming out of the fiber to an elliptical beam matching the waveguide mode of the QDD. The PC is used to select the polarization of the beam to be horizontal, matching the dominant polarization of the QDD (TE-polarized). With this scheme we have 100 mW

input power available at the QDD. In principle, further optimization is possible because the Cr:Fr laser is capable of producing up to 1 W in the gain maximum around 1,270 nm.

Then the beam is coupled into the QDD with an aspherical lens (C1). The procedure for the coupling is actually the opposite: The light coming out from the QDD diode is fiber coupled first, with an efficiency of 37%. Then we can conclude that the effective coupling efficiency of the Cr:Fr beam coupled out of the fiber to the QDD waveguide is $c_{\mathrm{eff}} = 0.37$. The data given below uses the raw data, i.e. the power incident on the device.

The light reflected by the sample and the light coming out of it is collected via a beam splitter (BS1, Fresnel reflection of 1% from front surface, back surface AR-coated) and focused onto the output photodiode (PD1). A similar photodiode monitors the input beam as well (PD2). In this experiment, the incident power is varied by turning the HWP and PD1 and PD2 are simultaneously monitored with a digitizer with 16 bit resolution. The reflection coefficient is derived from the ratio of the signal of the two detectors taking the known offsets and sensitivities into account. We plot in the following: R (in logarithmic scale) and $\ln R$ (in linear scale) because $\ln R$ should relate to the absorption (gain) coefficient as displayed in Fig. 12.1 without multi-pass effects, i.e. for a device with perfect anti-reflection coated input facet. Note that in [41] the data were presented as gain (absorption) coefficient per unit length with $L = 1.5$ mm in order to facilitate comparison with usual gain coefficients, but we prefer not to do the conversion here due to its strong limitations.

Experimental Results on Saturation of Gain and Absorption

Figure 12.13a shows how the gain coefficient changes as function of input power for $\lambda = 1,245$ nm under gain, $I = 24$ mA, and absorptive conditions, $I = 0$ mA. The reflection coefficient from the QDD shows a pronounced power dependence starting at power levels slightly less than 10 mW for the absorptive case indicating bleaching of absorption. The reduction of reflectivity due to gain depletion sets in somewhat earlier. Figure 12.13b shows the corresponding curves for $\lambda = 1,255$ nm showing similar trends.

The same holds for Fig. 12.14a displaying the situation for $\lambda = 1,265$ nm though the small-signal intercepts seem to be slightly reduced. This effect is much stronger in Fig. 12.14b displaying the data for $\lambda = 1,280$ nm. This is due to the increased detuning to line center. Under gain conditions, there is still a saturation effect, but the absorption is essentially constant (the small decrease at high power is probably an experimental artifact).

The curves in Figs. 12.13, 12.14 show the typical behavior of saturation curves, converging at high power to the linear background losses of the structure without active medium, e.g. Fig. 12.1 in "Results: Saturation of Absorption and Gain". Though the effective power within the structure will be affected by multi-pass

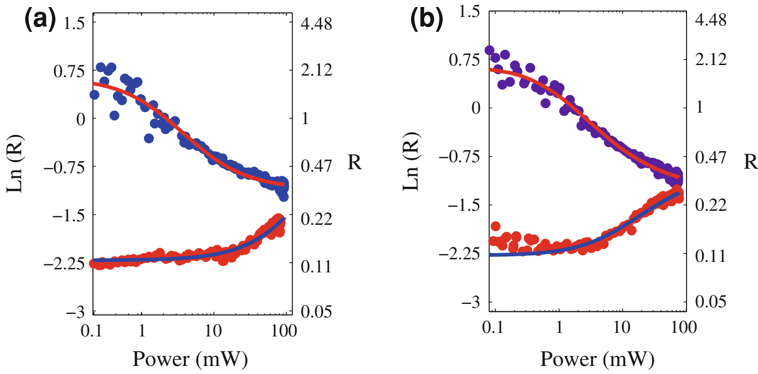

Fig. 12.13 (Color Online) Reflection coefficient as function of input power [*dark gray* (*blue*) data points for $I = 24$ mA, *light gray*(*red*) data points for $I = 0$ mA] and fit to an inhomogeneous broadening model [*dark gray* (*red*) *line* for $I = 24$ mA, *light gray* (*blue*) *line* for $I = 0$ mA). **a** $\lambda = 1,245$ nm. **b** $\lambda = 1,255$ nm. (Reprinted with permission from [41]. Copyright 2010, American Institute of Physics)

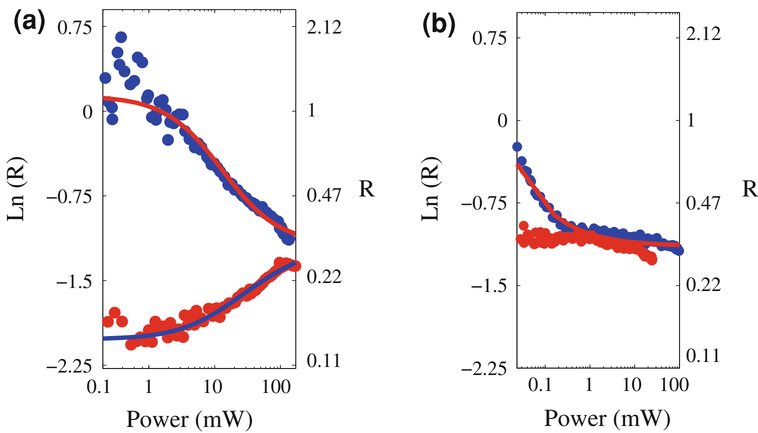

Fig. 12.14 (Color Online) Gain coefficient as function of input power at (**a**) $\lambda = 1,265$ nm, (**b**) $\lambda = 1,280$ nm. Legend as in Fig. 12.13. (Reprinted with permission from [41]. Copyright 2010, American Institute of Physics)

effects (see below), it seems to be instructive to use the incident powers only for a first analysis because the power within the sample is affected by the saturation level itself in a nontrivial manner. Hence, the dependence of the gain coefficient on power has been fitted with two models that describe saturable absorption in the case of two-level systems with inhomogeneous, Eq. 12.36, and homogeneous, Eq. 12.37, broadening. The results show that both models fit the data at $\lambda = 1,255$ nm and $\lambda = 1,265$ nm quite well but the inhomogeneous model proves to fit better and is the only model that fits the data well at $\lambda = 1,245$ nm and $\lambda = 1,280$ nm, Figs. 12.13a, 12.14b.

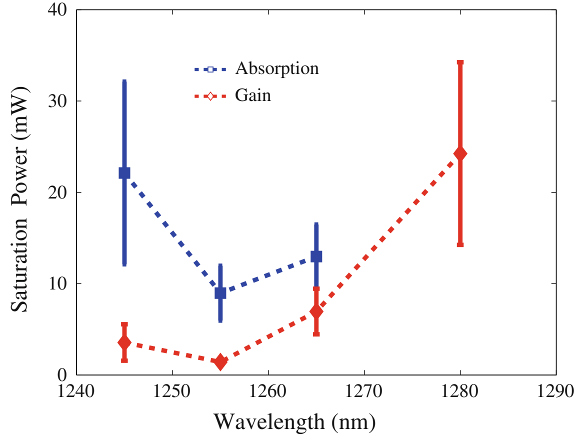

Fig. 12.15 (Color Online) Saturation power as function of wavelength in absorption and gain cases. (Reprinted with permission from [41]. Copyright 2010, American Institute of Physics)

Figure 12.15 shows the saturation power under absorptive and gain conditions as function of wavelength as obtained from the fits displayed in Figs. 12.13, 12.14. The minimum saturation power is reached at $\lambda = 1,255$ nm, i.e. line center, as expected, and is $P_{sat} = 9$ mW in the absorptive case and $P_{sat} = 1.4$ mW in the gain case. The saturation power increases for increasing detuning. These tendencies are in qualitative agreement with the simulations presented in "Numerical Results: Cavity Dynamics".

Analysis and Discussion

Via $I_{sat} = 2P_{sat}c_{eff}/(\pi w_x w_y)$, where P_{sat} are the saturation powers reported in Fig. 12.15 and $w_x = 3 \times 10^{-6}$ m and $w_y = 0.5 \times 10^{-6}$ m are the beam radii in the slow, respectively fast, axis, a saturation intensity in line center of $I_{sat} = 1.4 \times 10^9$ W/m^2 is obtained for the absorptive case. This value agrees with numerical predictions using the parameters from "Numerical Results: Cavity Dynamics" and Eq. 12.22 for a carrier lifetime in the ground state of 60 ps, i.e. a rather small value.

A qualitative difference between the experimental results and the simulations is that in the simulations the absorption saturates earlier than the gain, i.e. the theoretical expectation for the gain case based on "Numerical Results: Cavity Dynamics" is $I_{sat} = 2.8 \times 10^9$ W/m^2, whereas the fit from the experiments yields $I_{sat} = 0.2 \times 10^9$ W/m^2.

This feature, as well as the absolute scaling of the reflection coefficients, is strongly influenced by the fact that the sample does not have AR-coatings on both ends but the coatings are designed for laser operation. As indicated, we do not expect strong cavity resonance effects because of the low coherence length of the input laser, but nevertheless the device will behave as a two-pass amplifier due to

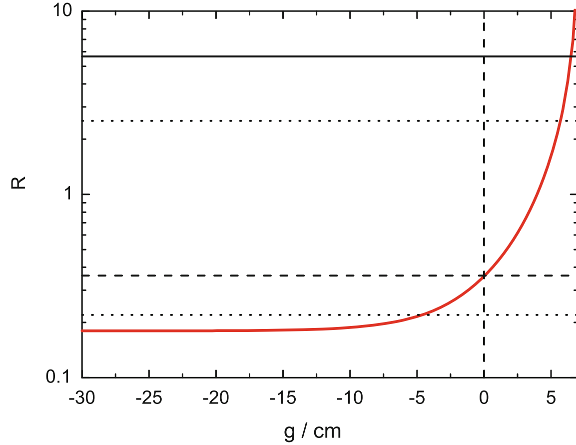

Fig. 12.16 (Color Online) Reflection coefficient calculated from Eq. 12.45 versus modal gain coefficient [*Light gray* (*red*) solid line]. *Dashed lines*: Value for high power asymptote ($g = 0$). Solid *black line*: Estimated maximal linear gain. *Dotted lines*: Reduction of linear absorption and gain by factor of $\sqrt{2}$.

the high reflectivity of the back mirror. Some portion of the light attenuated or amplified after one double pass $2L$ will be in turn retro-reflected into the sample due to the finite reflectivity of the front facet. The expected total reflectivity can be estimated from the incoherent sum of intensities of the multi-pass configuration,

$$R = R_1 + c_{\text{eff}}\,(1 - R_1)^2\,\frac{R_2 e^{(-\alpha_g + g)2L}}{1 - R_1 R_2 e^{(-\alpha_g + g)2L}}, \tag{12.45}$$

where $\alpha_g \approx 1.5/\text{cm}$ represents the waveguide loss and $g = -\alpha$ is the modal gain coefficient. (Qualitatively similar results are obtained if one averages the coherent Airy function over the resonator phase.) The corresponding function is displayed in Fig. 12.16 as the solid curve.

Obviously, the small-signal coefficient in the absorptive case ($g \approx -27/\text{cm}$) is totally determined by the reflectivity $R_1 \approx 0.18$ of the front facet. This is in rough agreement with the experiment assuming some additional linear losses. The reflection coefficient for the completely bleached QD, $g = 0/\text{cm}$, is about 0.36 (dashed black lines in Fig. 12.16) in rough agreement with the high power asymptotes. Finally, the threshold gain for the laser structure can be estimated to be 7.25/cm. Assuming a gain of 6.5/cm for the just below threshold case analyzed experimentally, the reflection coefficient is about 5.7 (solid black line in Fig. 12.16), again in rough agreement with the experiment assuming some additional linear losses. These multi-pass effects explain also the difference in saturation power between gain and absorption: A change of modal gain from 6.5/cm to only 5.7/cm is required to change the externally observed reflection coefficient by a factor of $\sqrt{2}$, whereas the modal absorption needs to change from -27 to $-4.6/\text{cm}$ to achieve the same effect. This is easy to understand hence absorption will reduce the intensity propagation further down into the structure and thus hinder saturation. In contrast, with gain the intensity increases with propagation in the structure and hence saturation becomes easier. Hence, the multi-pass effects delay saturation in absorption and favor it in gain explaining the observed asymmetry.

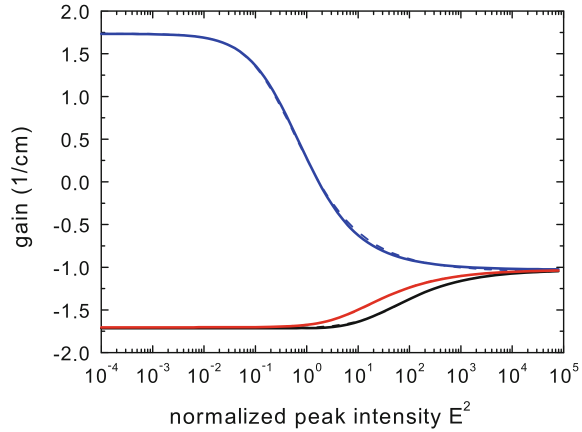

Fig. 12.17 (Color Online) Reflection coefficient calculated from Eqs. 12.36, 12.45 versus normalized intensity. *Black line*: $g(0) = -27/\mathrm{cm}$, *red* (*light gray*) *line*: $g(0) = -14.5/\mathrm{cm}$, *blue* (*dark gray*) *line*: $g(0) = +6.5/\mathrm{cm}$. *Dashed lines* denote fits of these plots to the saturation law (12.36) and are essentially not distinguishable from the data

One can now use the saturation law (12.36) to supply the intensity dependence of g in (12.45). The resulting reflection coefficient is displayed in Fig. 12.17 for different small-signal absorption and gain values. It is apparent that the curves have a qualitative similarity to the experimental curves in Fig. 12.13. Furthermore, they can be essentially perfectly fitted by the saturation law (12.36). From the fit one obtains $E_s^2 = 0.29$ for the gain case, $g(0) = +6.5/\mathrm{cm}$, and $E_s^2 = 33.3$ for the absorptive case, $g(0) = -27/\mathrm{cm}$. This confirms the asymmetry between saturation of absorption and gain discussed above, but the ratio between these values is very high, about 110, whereas the experimentally observed ratio is significantly smaller, around 7. It turns out that these values are very sensitive to the total absorption, e.g. for $g(0) = -14.5/\mathrm{cm}$ (inferred earlier from Fig. 12.11) $E_s^2 = 9.6$. This is reasonable since the depletion of the pump—and hence the delay of saturation—will be stronger, if the linear absorption coefficient is stronger. For this value of $g(0)$ the ratio between the saturation intensity of gain and absorption is about 30, still larger than in the experiment. In view of the uncertainties, one cannot make strong statements but it appears that the 'material' (i.e. not influenced by multiple-pass effects) saturation intensity is about $5 \times 10^8 \mathrm{W/m}^2$, in between the values observed for the gain and the absorption case. This would correspond to a lifetime of the GS of 170 ps, which is a low though still reasonable value.

For SESAM applications, saturation fluences for 1,280–1,340 nm QD under short-pulse excitation are reported to be $0.02-0.25\ \mathrm{J/m}^2$ [7, 8, 18]. If the carrier decay within the width of the probing pulse can be neglected, the saturation fluence can be converted to an equivalent cw saturation intensity by multiplying it with the carrier decay rate. Hence for a lifetime of 100 ps one concludes on saturation intensities of $(0.2 - 2.5) \times 10^9\ \mathrm{W/m}^2$ in line with our observation.

Experiments Addressing Nonlinear Index Shifts

As indicated from the discussion above, the data for the saturation of the imaginary part of the refractive index (i.e. gain or absorption) would be much cleaner and more straightforward to analyze if the sample would have been AR-coated at both input facets (or the waveguide would have been tilted with respect to the facets). The choice for a laser samples instead of an AR-coated amplifier stemmed from the desire to probe nonlinear index shifts via the shift of Fabry-Perot fringes as explained in "Nonlinear Refractive Index and α-Factor"

We briefly describe the experiment. A low-amplitude beam of a tunable laser was injected into the other input of the 90:10 fiber splitter. It is scanned over 0.5 nm, i.e. several FSR of the QDD, and its reflection is measured in presence of the strong pump laser. The tunable probe beam is chopped at a frequency of 800 Hz and its weak signal is filtered out of the total reflection signal with the help of a lock-in amplifier. We observe a change in shape and Finesse of the Airy function, i.e. a nonlinear version of Fig. 12.11a, dependent on the pump power, which is qualitatively as expected. This indicates that the idea of the measurement works in principle. However, the shift is about 0.001 nm/mW (external power) independent of wavelength and current. As one expect a different sign of the shift under absorptive and gain conditions, we conclude that we do not probe a carrier effect but some background absorption. For comparison, the fringe shift with temperature was determined to be 0.1 nm/K, i.e. the effect can be caused by very small temperature variations. The origin of this shift is unclear at the moment.

Experiments on InAlAs/GaAlAs QD at 780 nm

While QD have been developed first in the InAs/GaAs [68] system which operates typically at wavelengths larger than 1 μm, the question of connecting with wavelength domains compatible with the GaAlAs material system and with Ti:Sa lasers is actually being raised. InAs/GaAs QD can obviously not provide the solution since they lead to very shallow dots improper to the proposed target of realizing quasi 2-level electronic systems in this spectral range. Increasing the barrier height may be obtained by evenly incorporating aluminum in both the barrier and the dot materials leading to a higher confinement of quantum states and to the forsaken spectral overlap with the GaAlAs system. In this framework, InAlAs/GaAlAs QD [69, 70] open very promising perspectives both for cw and pulsed nonlinear or even self-organizing optical systems. Structural and optical properties of MBE-grown InAlAs/GaAlAs QD were investigated as a function of the growth kinetic and thermodynamical conditions [42]. Appropriate choice of growth conditions allows to control the density as well as the average size of QD and the carrier lifetimes during the growth stage [42], and introduces means of realizing either a slow focusing Kerr effect (FKE) material (ns-scale) or a fast (ps-scale) saturable absorber, as started in [12].

In this section, we report on linear and nonlinear measurements of the susceptibility of InAlAs/GaAlAs QD, after describing their growth conditions, which correlate to their structural properties in terms of dot and dislocation densities. Optical quality is established through spectral and temporal photoluminescence (PL) measurements. The core of the section is dedicated to the measurement of group index and nonlinear absorption using a long (high-order) Fabry-Perot cavity embedding InAlAs/GaAlAs QD. This approach leads to unprecedented measurements for this material and establishes, though not yet fully exploited, quite an efficient saturation behavior.

Description of the Experiments

Material Properties and Device Structure

The sample was MBE-grown on a GaAs substrate, using the Stransky-Krastanov growth regime. According to the criteria developed in the model, "The Model", there is a necessity to obtain a large volume of interaction between QDs and light by increasing the overall density of dots, and thereby the sensitivity of our experimental setup to the QD contribution to the susceptibility. Hence we were growing five superimposed planes of $In_{0.67}$ $Al_{0.33}As$ QDs with $Ga_{0.67}$ $Al_{0.33}As$ barriers as the nonlinear material (Fig. 12.18a). The symmetric step-graded barrier and cladding layers with corresponding material concentration follow and a GaAs cap terminates the structure. A cross-sectional visualization of QD was performed that gave information on the relaxation degree of the QDs which revealed appropriate for optical experiments. Due to the depth at which QD layers are located with respect to the surface, the density of dots ρ_D could only be inferred from a cross-sectional TEM image and lead to an integrated density for the 5 layers such as $2 \times 10^{11} < \rho_D < 5 \times 10^{11}\,\text{cm}^{-2}$. One-layer samples grown under nominally the same growth conditions had a density of about $2 \times 10^{11}\,\text{cm}^{-2}$.

The PL spectrum of this sample is sketched in Fig. 12.19. It exhibits a 40-nm wide inhomogeneous peak around 780 nm well separated from the other transitions with the $In_{0.67}$ $Al_{0.33}As$ WL and the $GaAl_{0.33}As$ barrier.

The complete structure was designed so as to form a planar waveguide inducing a vertical optical confinement (Fig. 12.18a and b). It comprises two 1.5 μm-thick $Ga_{0.14}$ $Al_{0.86}As$ cladding layers sandwiching the core layer consisting of the five layers of $In_{0.67}$ $Al_{0.33}As$ QDs spaced by 41.7 nm-thick $Ga_{0.67}$ $Al_{0.33}As$ barrier spacers. Finally, lateral optical confinement is introduced by etching the surface with a 0.4 μm deep, 3 μm wide ridge. The values were retained on the basis of finite element optical modeling with the finite element program © ALCOR warranting the monomode character of this waveguide around 800 nm. The optical mode area at half-intensity is 3×0.250 μm (Fig. 12.18b).

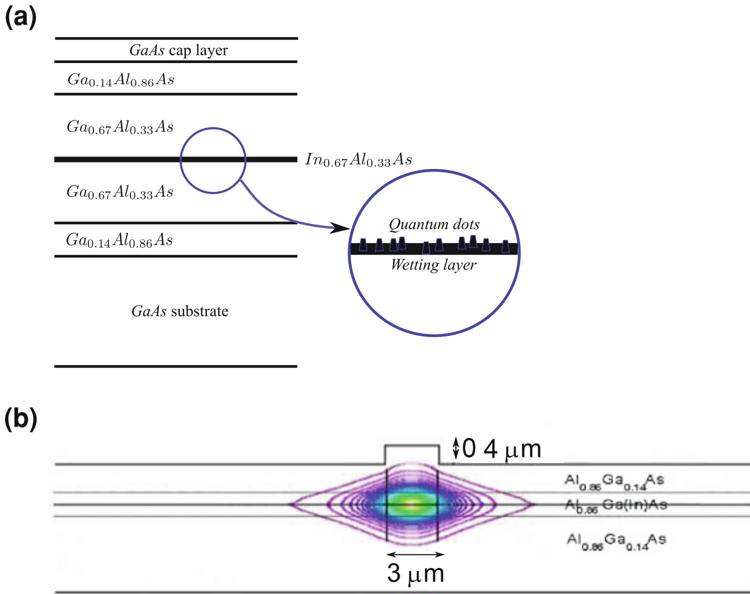

Fig. 12.18 **a** 5-layer AlGaAs/AlInAs QD structure. **b** Ridge waveguide formed by the initial stack modified for waveguiding properties (see text). The single-mode size calculated with a finite element program (ALCOR) is $3.0 \times 0.250\,\mu\text{m}^2$. (Reprinted with permission from [42]. Copyright 2012, American Institute of Physics)

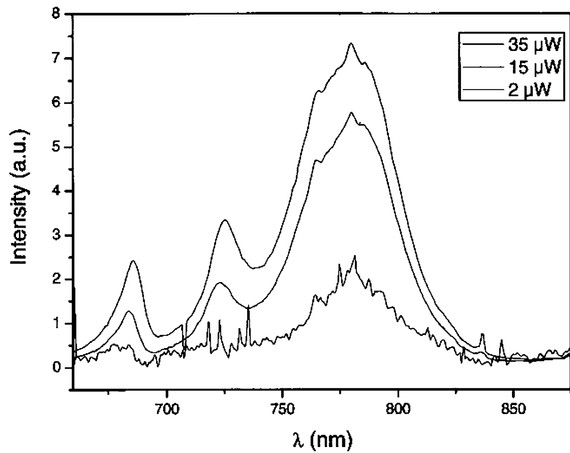

Fig. 12.19 PL spectrum of the InAlAs/GaAlAs QD used in the experiment at different excitation levels

Principle of the Experiment

In contrast to "Experiments on InAs/GaAs QD Around 1,250 nm", the driving TiSa-laser is a highly coherent single-frequency laser and hence interference effects in the Fabry-Perot sample investigated need to be taken into account. The measurements

rely on the use of the technique described in "Results: Saturation of Absorption and Gain and Nonlinear Phase Shift and Fabry-Perot Fringes" with $R = 0.30$ reflectivity mirrors provided by the uncoated cleaved facets of the sample.

In the presence of absorption with coefficient α, one uses the transmittance T defined as the ratio of the transmitted (I_t) to incident (I_i) intensities [71, 72]

$$T = \frac{(1-R)^2 e^{-\alpha L}}{(1-Re^{-\alpha L})^2 + 4Re^{-\alpha L}\sin^2(\phi)}, \tag{12.46}$$

where Φ is the phase accumulated during the propagation of light inside the cavity of length L. If it is filled with a material of intensity-dependent refractive index $n(I)$ the single-pass phase accumulated is

$$\phi \equiv \phi(I, L) = \int_0^L \frac{2\pi n(I(z))}{\lambda} \mathrm{d}z. \tag{12.47}$$

We neglect the eventual dependence of the intracavity intensity on the position and use instead the longitudinal average intensity $\bar{I} = \frac{1}{L}\int_0^L I(z)\mathrm{d}z$. T is thus a function of the intracavity intensity via ϕ and α. Similarly the incident intensity I_i can be connected to $\bar{I}$ via [72]

$$I_i = \frac{\alpha L}{(1-R)(1+Re^{-\alpha L})(1-e^{-\alpha L})}\left[(1-Re^{-\alpha L})^2 + 4Re^{-\alpha L}\sin^2(\phi)\right]\bar{I}. \tag{12.48}$$

From this point we shall drop the bar and write the average intensity as I. The general resolution for arbitrary and eventually nonlinear ϕ's may be found in solving Eq. 12.46 for $A = e^{-\alpha(I)L}$. Defining $S(I, \lambda) \equiv \sin^2(\phi)$ this leads to the equation

$$R^2TA^2 + \left[2RT(2S-1) - (1-R)^2\right]A + T = 0 \tag{12.49}$$

with the minus signed retained solution

$$A = \frac{-\beta - \sqrt{\beta^2 - 4R^2T^2}}{2R^2T}, \tag{12.50}$$

where $\beta(I, \lambda)$ is the coefficient of A in the second order Eq. 12.49. This gives in turn an experimental access to the nonlinear coefficients as the absorption coefficient comes straightforwardly as $\alpha = -lnA/L$ and can be deduced from the knowledge of the transmission T. In turn, the nonlinear index determination is not straightforward and can only be accessed through the determination of the phase as an adjustable parameter. However, in the present case, the QD are supposed to have a saturating absorption,

$$\alpha(I) = \alpha_0 \frac{I_s}{I + I_s}, \tag{12.51}$$

and a saturating index

$$n(I) = n_b - \delta n_s \frac{I_s}{I + I_s}. \tag{12.52}$$

This corresponds to the theory developed in "The Model", however, assuming strong homogeneous broadening for simplicity. Equation 12.50 reads as an implicit equation in A where the RHS of Eq. 12.50 depends on the transmission T and on A via β. This derivation of optical coefficients from experimental transmission measurements can be obtained via numerical or converging fit techniques.

The transmitted intensity I_t is known to be directly related to the intracavity field intensity I

$$I_t = \frac{\alpha L e^{-\alpha L}(1 - R)}{(1 + Re^{-\alpha L})(1 - e^{-\alpha L})} I. \tag{12.53}$$

Under the effect of the real and imaginary parts of the nonlinear susceptibility, both the transmission spectrum—via ϕ—and the transmission amplitude maximum—via saturation—are modulated. The combined measurement of I_t and I_i as a function of the wavenumber (wavelength) gives thus access to the transmittance and to the intracavity intensity. In the case of a waveguide, we use also the transverse confinement factor Γ_{trans} which weighs the QD layer contribution to the nonlinear index with respect to the mode area. As a general formulation, $n(I) \equiv n_0 + \Gamma_{\text{trans}} \delta n(I)$, should the dependence on I be linear or saturating.

The five InAlAs QD layers have a total thickness of approximately $5 \times 64 = 30$ nm. As they only partially overlap with the mode transverse dimension 250 nm we deduce a transverse confinement factor $\Gamma_{\text{trans}} \simeq 0.12$. Bulk and MQW semiconductors are known to exhibit nonlinear index saturation of the order of 10^{-2} [73]. Under these assumptions (other parameters in caption of Fig. 12.20) one can calculate now the expected transmission characteristics of the nonlinear Fabry-Perot interferometer in dependence on wavelength and intensity. Figure 12.20 shows the characteristic ripple structure of the transmission of a Fabry-Perot cavity. The modulation depths increases with intensity due to the increase of Finesse with saturation of absorption. The fringes shift due to the nonlinear index change. The figure confirms the back-of-the envelope calculation in "Nonlinear Phase Shift and Fabry-Perot Fringes" that phase shifts of some 10^{-4} should be detectable in mm-sized cavities due to the high interference order.

Experimental Setup

The experimental setup (see Fig. 12.21), similar to that used in "Experiments on InAs/GaAs QD Around 1,250 nm" uses a Ti-Sa laser source operating in the short wavelength range between 760 nm and 810 nm and emitting 100–500 mW cw power. A small fraction is collected via a beamsplitter (BS) into a Burleigh WA1100 wavemeter. In order to prevent thermal drifts of the sample properties, the beam intensity is modulated by an acousto-optic modulator (AOM) in the

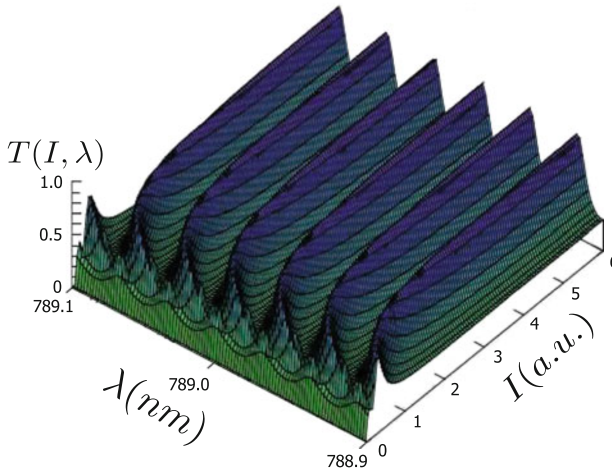

Fig. 12.20 Calculation of the transmission of nonlinear saturating Fabry-Perot resonator. The data used are: $R = 0.3$, $\Gamma_{\text{trans}}\alpha_0 = 14\ \text{cm}^{-1}$, $\alpha_g = 10\ \text{cm}^{-1}$, $L = 0.23\ \text{cm}, I_s = 2.8\ kW/cm^2$, $\Gamma_{\text{trans}}\delta n_s = 1.75 \times 10^{-3}$. I is scaled to the saturation intensity (Reprinted with permission from [42]. Copyright 2012, American Institute of Physics)

deflection mode into rectangular or triangular envelopes with a 10 kHz frequency and a duty cycle ranging from 10 to 20 converted from an electrical signal produced by an ANALOGIC 2000 arbitrary function generator. The modulated beam is then injected into a monomode fiber and directed to the monomode waveguide containing the QDs. In the path, light intensity is adjusted by a PC injecting a 10/90 directional coupler whose 10% branch allows the measurement of a signal proportional to the incident power onto the signal on Photodiode PD1. The 90% branch is coupled via the lensed end of a tapered fiber into the waveguide and its output, collected by a MO (L6), is detected by a second photodiode PD2 (Fig. 12.21).

The sample is mounted on a Peltier element holder giving a temperature control better than 0.1 K. The alignment procedure is performed with the help of two cameras. Camera 1 allows the precise pre-positioning of the fiber with respect to the front facet of the waveguide and Camera 2 allows the visualization of the rear facet and the optimization of the optical injection. Finally, three parameters could be measured: I_i, I_t and λ. In practice, the measurement sequence consisted in ramping I_i for a given λ and measuring I_t, then deducing the intracavity intensity I through Eq. 12.53 and finally recording and plotting the $3D$ curve

$$T \equiv T(I, \lambda).$$

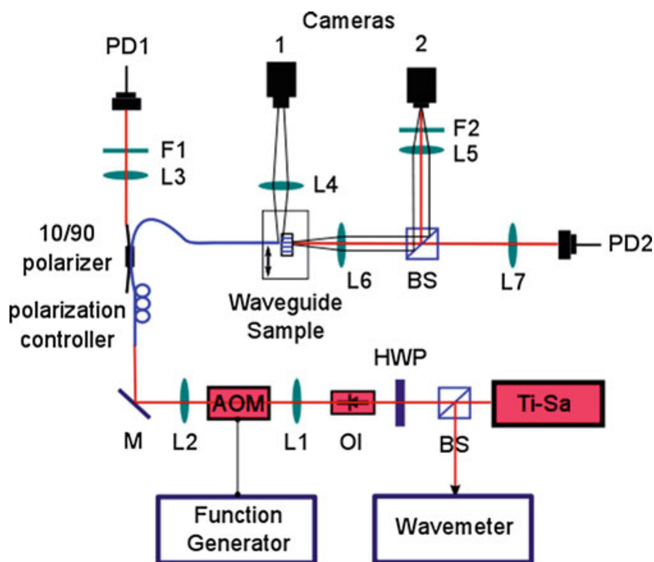

Fig. 12.21 Experimental setup: Ti:Sapphire laser (*Ti-Sa*), beam splitter (*BS*), half-wave plate (*HWP*), optical isolator (*OI*), acousto-optic modulator (*AOM*), lenses L1 ($f = 10$ mm), L2 ($f = 10$ mm), L3 ($f = 35$ mm), L4 ($f = 50$ mm), L5 ($f = 35$ mm), L6 ($f = 35$ mm), L7 ($f = 35$ mm); mirror (*M*), filters (*F*1, *F*2), photodiodes (*PD*1,*PD*2). (Reprinted with permission from [42]. Copyright 2012, American Institute of Physics)

Experimental Results on Saturation of Absorption

Measurements on Fabry-Perot Fringes

A first series of measurements was performed in order to detect the nonlinear index variation under increasing illumination. The waveguide length is $L = 0.23$ cm. Incident and transmitted intensities were recorded by ramping the incident intensity through the AOM at a fixed wavelength and iterating with 1 pm wavelength steps over a 14 pm range around the central wavelength. Such recordings were performed around 765, 780, 787, 790, 795, and 800 nm in order to scan different detunings from the inhomogeneously broadened line. Regular modulation is displayed at wavelengths around $\lambda = 787$ nm (Fig. 12.22a).

At low intensities, it was not possible to observe any drift of the Fabry-Perot resonances under increasing illumination while at higher intensities, absorption saturation restores the phase modulation, qualitatively as in Fig. 12.20 discussed above, but with a contrast poorer than expected. Both were attributed to the existence of a nonsaturable part of the absorption (α_g) that probably enforces the damping of the intracavity interferences at low intensities and maintain the cavity at a finesse lower than that of the cold cavity. This is confirmed by calculations (Fig. 12.22b) where absorption was modified as

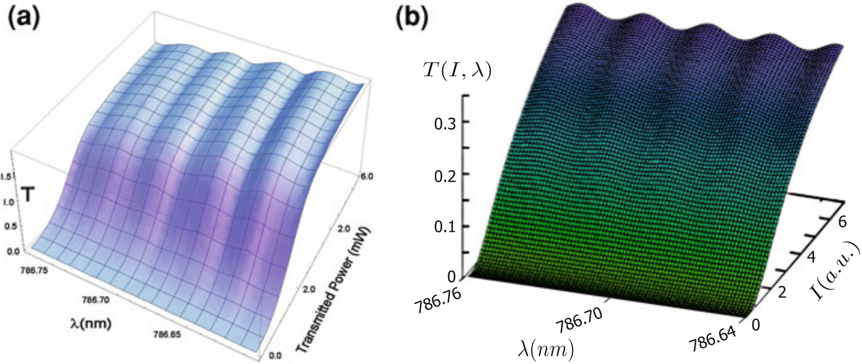

Fig. 12.22 **a** Plot of the transmission as function of wavelength for different transmitted intensities. **b** Theoretical plot assuming the fitting parameters obtained including nonsaturable losses as input parameters. (Reprinted with permission from [42]. Copyright 2012, American Institute of Physics)

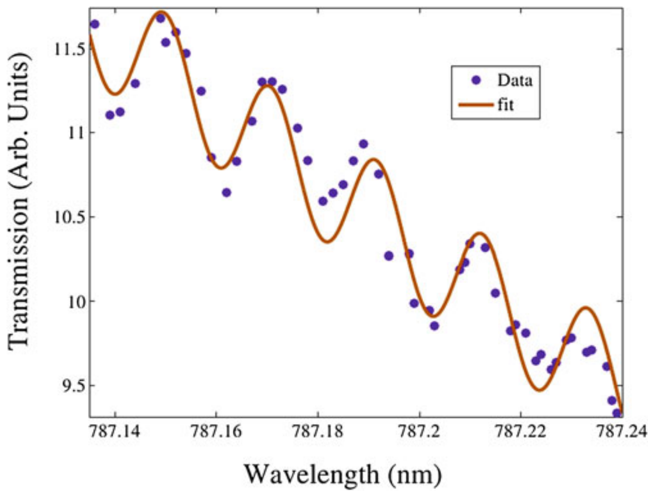

Fig. 12.23 Transmission spectrum at high intensities with saturated absorption at constant intracavity intensity around 787 nm. (Reprinted with permission from [42]. Copyright 2012, American Institute of Physics)

$$\alpha(I) = \alpha_g + \alpha_0 \frac{I_s}{I + I_s}. \tag{12.54}$$

From data at high transmission (see Fig. 12.23), a rather precise measurement of the free spectral range as 15.6 GHz or $0.52\,\mathrm{cm}^{-1}$ wavenumbers allowed to calculate the group index, incorporating the modal and spectral contributions to dispersion. This leads to the group index value $n_g = 4.16$. This is in good

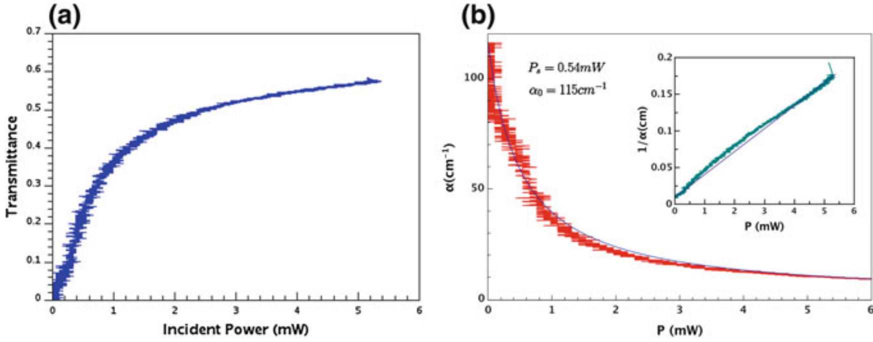

Fig. 12.24 **a** Plot of the transmission as a function of the incident intensity. **b** Material absorption vs incident intensity as deduced from Eq. 12.50, *red* (experimental), *black* (theoretical). The inset displays the same data in the form $1/\alpha = f(P_{inc})$ the linear dependence assesses a saturation law of the absorption. (Reprinted with permission from [42]. Copyright 2012, American Institute of Physics)

agreement with the literature value of 4.12 for the group index of $Al_{0.28}Ga_{0.72}As$ at 787 nm [74] allowing for waveguide dispersion.

In view of the fact that the measurement was done close to the absorption maximum, where the phase shifts are small (e.g. Figs. 12.5, 12.7) it is consistent that no shift of the Fabry-Perot fringes was detectable. Further investigations need to be focused on higher detunings to probe for phase shifts.

Absorption Saturation

As Fig. 12.22 indicated already, the experimental setup can be used to measure the absorption of the QD embedded in the waveguide section. The wavelength $\lambda =$ 789.00 nm is chosen so as to lie rather close to the maximum of QD absorption line. Transmission measurements as expressed by Eq. 12.50 give indeed access to absorption. This was done as previously by ramping the incident intensity and measuring the transmittance. Figure 12.24a shows the transmission as a function of the incident intensity. Figure 12.24b plots the absorption as deduced from Eq. 12.50 applied to the experimental data and fitted with the ansatz of Eq. 12.51. The difficulty lies in the dependance of T upon the nonlinear index via ϕ. Therefore, instead of using the intracavity intensity, which depends on this phase term, we used the measured incident intensity with the assumption that they are in a quasi constant ratio. We first adjusted the saturation parameters of the absorption in Eq. 12.24 so as to obtain the best possible fit. However, we noted that in a second step additional adjustments can be made by fine tuning the wavelength i.e the position with respect to the resonance and the saturation index. Further experiments will attempt to elucidate this point. However, from these adjusted values, we could extract the significant parameters of the QD material.

The calibration of the intracavity power was performed by using its relationship (Eq. 12.48) with incident power ($P^{\text{in}}_{\text{max}} = 5.2$ mW). In addition, we introduced the

coupling coefficient of light into the waveguide $\gamma = 0.083$ defined as the overlap ratio of the focused beam area $3 \times 3\ \mu m^2$ to that of the mode $S = 0.250 \times 3\ \mu m^2$. The maximum intracavity power is therefore $P_{\max} \simeq 0.54$ mW.

The absorption curve appears indeed to have a saturation behavior leading to a vanishing absorption coefficient at high intensities. In Fig. 12.24b two curves are presented for α and for $1/\alpha$ in the inset calculated with Eq. 12.50 and fitted according to a saturation ansatz also corrected with the transverse confinement factor Γ_{trans}

$$\alpha_{\text{measured}}(I) = \alpha_g + \Gamma_{\text{trans}}\alpha_0 \frac{P_s}{P + P_s},$$

where we used $\alpha_g = 10\ \text{cm}^{-1}$, as suggested by the analysis of Fig. 12.22. They yield an unsaturated absorption value of $\Gamma_{\text{trans}}\alpha_0 = 13.8\ \text{cm}^{-1}$, $\alpha_0 = 115\ \text{cm}^{-1}$ and a saturation power $P_s \simeq 0.021$ mW with excellent fidelity. The deduced saturation intensity is

$$I_s = \frac{P_s}{S} = 2.8\,\text{kW/cm}^2. \tag{12.55}$$

It could be interesting to compare this value with those obtained in other experiments. However the comparison must be performed accounting with the experimental conditions at which they were performed, cw or pulsed. In the cw regime, QD are expected in general to have a lower saturation intensity than material of lower confinement dimensionality. In [73] for example, a series of measurements were performed on bulk and MQW Urbach's tail, yielding a saturation intensity of $1\text{–}3 \times 10^5\ \text{W/cm}^2$ depending on detuning. In [73] it is argued also that—due to the detuning dependence—the relevant parameter for comparison is the factor $\alpha_0 I_s$ proportional to the transparency carrier density. We obtain here $\alpha_0 I_s \simeq 3 \times 10^5\ \text{Wcm}^{-3}$ which confirms the reduction of the saturation parameters in InAlAs/GaAlAs QDs whose values were respectively in the range $0.1\text{–}1 \times 10^8\ \text{Wcm}^{-3}$ for bulk GaAs and AlGaAs/GaAs multi quantum wells. In parallel, the saturation index was of the order of $\delta n_s \simeq 2\text{–}3 \times 10^{-2}$. These comparisons are only qualitative and would require a specific study including the dot density as one of the parameters where the techniques reported here may certainly be pursued.

Summary and Conclusion

In this chapter, we have discussed in detail the cw nonlinear optics of QD ensembles at room temperature. The model developed considers the important coupling between the QD states and the WL and the inhomogeneous broadening in determining the carrier populations in the dot in dependence on the incident light field. However, only the dielectric susceptibility of the GS is taken into account to

calculate the back action (absorption and refractive index) of the QD medium back onto the light. We find saturation behavior of the absorption and gain in between the ones expected for purely homogeneously or purely inhomogeneously broadened media reflecting the complex intermediate situation in typical QD. Experiments on InAs and InAlAs QD yield the first demonstration of the saturation of absorption and thus open up the prospect of cw room temperature nonlinear optics of QD. The saturation intensities inferred are about 5×10^8 W/m^2 for the InAs QD and 0.3×10^8 W/m^2 for the InAlAs QD. A detailed comparison between the values and with the theory is not only difficult because of the different nature of multi-pass effects involved in the measurements, but also because many of the other parameters involved are quite uncertain (e.g. defect density determining non-radiative lifetimes, the homogeneous broadening parameter γ_p) but the lower value observed for the InAlAs QD might indicate a better sample quality and less interaction with the semiconductor matrix due to the fact that there is only one well confined state. These uncertainties also make it difficult to compare the values obtained for the QD quantitatively to saturation intensities in bulk and quantum well samples. Values reported for good quality samples (i.e. lifetimes in the ns range) center around 2–8 $\times 10^7$ W/m^2 [75–77], but can reach 4×10^8 W/m^2 [78] whereas the excitonic contribution (lifetime of 20 ns) saturates already at 5.8×10^6 W/m^2 in the same sample [78]. We mentioned already that [73] reported a saturation intensity of 1–3$\times 10^5$ W/cm^2 for detuned excitation in the band tail of Ga/AlGaAs QW.

The modal absorption was determined to be about 14/cm for the InAlAs QD (material absorption about 120/cm) and about 14.5/cm (material absorption about 150/cm) for the InAs QD. The latter value is somewhat smaller than the estimated one of 27/cm. The maximum (modal) refractive index shift in edge-emitting samples is estimated to be on the order of 10^{-4}, up to a few times 10^{-4}, depending on the number of layers used. This should create a detectable phase shift in a nonlinear Fabry-Perot of a mm length or so, but preliminary corresponding experiments were unsuccessful in detecting these phase shifts, possibly the nonlinear interaction is reduced as indicated by the lower than expected values for the absorption.

For a clarification on the saturation behavior, future work should access the saturation properties of AR-coated or tilted samples such that the saturation is not influenced by multi-pass effects. Lifetime measurements need to be done on the very same samples in order to enable a more detailed comparison with the theoretical expectation. This can be expected to shed also some light on the influence of the coupling between WL (and ES) and GS states.

In order to promote devices for bistability, all-optical processing and solitons a high QD density, i.e. a high cooperativity parameter, and a low inhomogeneous broadening are important, as well as a low defect density. For the point of growth, these are partially conflicting aims and one needs to aim for a good compromise. State-of-the-art InAs QD devices as investigated in this chapter have a density of $N_{\mathrm{QD}} \approx 5 \times 10^{10}$ cm^{-2} and an inhomogeneous broadening of about 40 nm or

30 meV. Estimations indicate that in an edge-emitting device with 10 QD layers a cooperativity parameter of about $C \approx 20$, i.e. in the regime where bistability might be accessible, can be reached in a cavity with $L = 1.5$ mm provided the Finesse is high enough $(R_1 = R_2 = 0.99)$. A VCSEL with 20 QD layers could reach $C \approx 10$. Recent papers [79, 80] report $N_{QD} \approx 5.9 \times 10^{10}\mathrm{cm}^{-2}$, 8 layers and an inhomogeneous broadening of about 24 meV giving $C \approx 30$ for an edge-emitting cavity with the parameters given above. Similarly, Ref. [81] reports $N_{QD} \approx 8 \times 10^{10}\mathrm{cm}^{-2}$, 3 layers and an inhomogeneous broadening of about 24 meV. Hence it appears that optimized SK-growth can reach interesting nonlinear regimes, but it should be cautioned that for SK-growth inhomogenous broadening is intrinsic. The broadening can be reduced by seeding techniques (e.g. 21 meV [82], 17.5 meV [83]), but currently only at a density of $N_{QD} \approx 10^{10}\mathrm{cm}^{-2}$. Alternative growth techniques like site-controlled growth [84, 85] yield inhomogeneous broadening as low as 4 meV [84], but no QD density is given. Sub-monolayer QD are another promising material system with high gain and low broadening [84]. It should be noted that the single sheet density of $N_{QD} \approx 2 \times 10^{11}\mathrm{cm}^{-2}$ reported for InAlAs QD in "Experiments on InAlAs/GaAlAs QD at 780 nm" is probably close to the highest one achievable in a single layer before QD coalesce and optical properties degrade. This is in line with the fact that very high density samples with $N_{QD} \approx 7.8 \times 10^{11}\mathrm{cm}^{-2}$ were reported in [86], but apparently no devices were realized, yet.

In summary, it is hence our belief that devices based on staggered growth of optimized SK-layers or other advanced growth technologies can reach interesting nonlinear regimes and that the numerical and experimental investigations discussed in this chapter open up the prospect of cw nonlinear optics of QD, especially in the absorptive regime. Obviously, many details on the influence of inhomogeneous broadening and the influence of higher discrete and continuous states need to be worked out and explored, especially in view of devices relying on nonlinear phase shifts.

Acknowledgements T.A. and A.T. were supported by EPSRC project EP/E025021, A.T. gratefully acknowledges current funding of Région Provence Alpes Cote d'Azur (DEB 10-924) and a travel grant from COST action MP0702. M.B. acknowledges partial support from project FIRB PhoCOS project n. RBFR08QIP5. We are grateful to Innolume GmbH for supplying the InAs devices, J.-M. Benoit, A. Lemaître, G. Patriarche, and K. Meunier for supplying the 780 nm devices, T. Maggipinto for supplying part of the numerical code, and R. Martin for computational support. S. Moore and T. Krauss were supplying broad-area samples for preliminary studies, and E. Esposito and G. McConnel gave us the opportunity to perform preliminary measurements in their lab.

References

1. Alèn, B., Karrai, K., Warburton, R.J., Bickel, F., Petro, P.M., Martínez-Pastord, J.: Physica E **21**, 395 (2004)
2. Baier, M.H., Pelucchi, E., Kapon, E., Varoutsis, S., Gallart, M., Robert-Philip, I., Abram, I.: Appl. Phys. Lett. **84**, 648 (2004)
3. Mowbray, D.J., Skolnick, M.S.: J. Phys. D: Appl. Phys. **38**, 2059 (2005)

4. Schneider, S., Borri, P., Langbein, W., Woggon, U., Förstner, J., Knorr, A., Sellin, R.L., Ouyang, D., Bimberg, D.: Appl. Phys. Lett. **83**, 3668 (2003)
5. Sugiyama, Y., Nakata, Y., Muto, S., Futatsugi, T., Yokoyama, N.: IEEE Sel. Top. Quantum Electron. **4**, 880 (1998)
6. Akiyama, T., Kuwatsuka, H., Simoyama, T., Nakata, Y., Mukai, K., Sugawara, M., Wada, O., Ishikawa, H.: Opt. Quantum Electron. **33**, 927 (2001)
7. Nakamura, H., Kanamoto, K., Nakamura, Y., Ohkouchi, S., Ishikawa, H., Asakawa, K.: J. Appl. Phys. **96**, 1425 (2004)
8. Su, K.W., Lai, H.C., Li, A., Chen, Y.F., Huang, K.F.: Opt. Lett. **30**, 1482 (2005)
9. Cesari, V., Langbein, W., Borri, P., Rossetti, M., Fiore, A., Mikhrin, S., Krestnikov, I., Kovsh, A.: Appl. Phys. Lett. **90**, 201103 (2007)
10. Dommers, S., Temnov, V.V., Woggon, U., Gomis, J., Martinez-Pastor, J., Laemmlin, M., Bimberg, D.: Appl. Phys. Lett. **90**, 033508 (2007)
11. OâDriscoll, I., Piwonski, T., Houlihan, J., Huyet, G., Manning, R.J., Corbett, B.: Appl. Phys. Lett. **91**, 263606 (2007)
12. Pulka, J., Piwonski, T., Huyet, G., Houlihan, J., Barbay, S., Martinez, A., Merghem, K., Lemaître, A., Ramdane, A., Kuszelewicz, R.: IEEE J. Quantum Electron. **47**(8), 1094–1100 (2011)
13. Berg, T.W., Mørk, J., Hvam, J.M.: New J. Phys. **6**, 178 (2004)
14. Sugawara, M., Ebe, H., Hatori, N., Ishida, M., Arakawa, Y., Akiyama, T., Otsubo, K., Nakata, Y.: Phys. Rev. B **69**, 235332 (2004)
15. Uskov, A.V., O'Reilly, E., Laemmlin, M., Ledentsov, N.N., Bimberg, D.: Opt. Commun. **248**, 211 (2005)
16. Meuer, C., Kim, K., Laemmlin, M., Liebich, S., Capua, A., Eisenstein, G., Kovsh, A.R., Mikhrin, S.S., Krestnikov, I.L., Bimberg, D.: Opt. Express **16**, 8269 (2008)
17. Maas, D.J.H.C., Bellancourt, A.R., Hoffmann, M., Rudin, B., Barbarin, Y., Golling, M., Südmeyer, T., Keller, U.: Opt. Express **16**, 18646 (2008)
18. Lumb, M.P., Stavrinou, P.N., Clarke, E.M., Murray, R., Leburn, C.G., Jappy, C., Metzger, N.K., Brown, C.T.A., Sibbett, W.: Appl. Phys. B **97**, 53 (2009)
19. Piwonski, T., Pulka, J., Madden, G., Huyet, G., Houlihan, J., Viktorov, E.A., Erneux, T., Mandel, P.: Appl. Phys. Lett. **94**, 123504 (2009)
20. Wu, F., Tian, W., Chen, W., Zhang, G., Zhao, G., Cao, S., Xie, W.: J. Mod. Opt. **56**, 1868–1873 (2009)
21. Dancus, I., Vlad, V.I., Petris, A., Gaponik, N., Lesnyak, V., Eychmüller, A.: Opt. Lett. **35**, 1079 (2010)
22. Barbay, S., Koehler, J., Kuszelewicz, R., Maggipinto, T., Perrini, I.M., Brambilla, M.: IEEE J. Quantum Electron. **39**, 245 (2003)
23. Perrini, I.M., Barbay, S., Maggipinto, T., Brambilla, M., Kuszelewicz, R.: Appl. Phys. B **81**, 905 (2005)
24. Brambilla, M., Maggipinto, T., Perrini, I.M., Barbay, S., Kuszelewicz, R.: Chaos **17**, 037119 (2007)
25. Tierno, A., Ackemann, T., Maggipinto, T., Brambilla, M.: Phys. Rev. B **80**, 035314 (2009)
26. Su, H., Chuang, S.: Opt. Lett. **31**, 271 (2006)
27. Akhmediev, N., Ankiewicz, A. (eds.): *Dissipative Solitons*. In: Lecture Notes in Physics, vol. 661. Springer, Berlin (2005)
28. Ackemann, T., Oppo, G.L., Firth, W.J.: Adv. At. Mol. Opt. Phy. **57**, 323 (2009)
29. Kuszelewicz, R., Barbay, S., Tissoni, G., Almuneau, G.: Eur. Phys. J. D **59**, 1 (2010)
30. Barland, S., Tredicce, J.R., Brambilla, M., Lugiato, L.A., Balle, S., Giudici, M., Maggipinto, T., Spinelli, L., Tissoni, G., Knödel, T., Miller, M., Jäger, R.: Nature **419**, 699 (2002)
31. Ackemann, T., Firth, W.J.: Dissipative solitons. In: Akhmediev N., Ankiewicz A. (eds.) Lecture Notes in Physics, vol. 661, pp. 55–100. Springer, Berlin (2005)
32. Pedaci, F., Barland, S., Caboche, E., Genevet, P., Giudici, M., Tredicce, J.R., Ackemann, T., Scroggie, A.J., Firth, W.J., Oppo, G.L., Tissoni, G., Jäger, R.: Appl. Phys. Lett. **92**, 011101 (2008)

33. Taranenko, V.B., Slekys, G., Weiss, C.: Dissipative solitons. In: Akhmediev N., Ankiewicz A. (eds.) Lecture Notes in Physics, pp. 131–160. Springer, New York (2005)
34. Henry, C.H.: IEEE J. Quantum Electron. **18**, 259 (1982)
35. Smowton, P.M., Pearce, E.J., Schneider, H.C., Chow, W.W., Hopkinson, M.: Appl. Phys. Lett. **81**, 3251 (2002)
36. Xu, Z., Birkedal, D., Juhl, M., Hvam, J.M.: Appl. Phys. Lett. **85**, 3259 (2004)
37. Ribbat, C., Selin, R.L., Kaiander, I., Hopfer, F., Ledentsov, N.N., Bimberg, D., Kovsh, A.R., Ustinov, V.M., Zhukov, A.E., Maximov, M.V.: Appl. Phys. Lett. **82**, 952 (2003)
38. Schneider, S., Borri, P., Langbein, W., Woggon, U., Sellin, R.L., Ouyang, D., Bimberg, D.: IEEE J. Quantum Electron. **40**, 1423 (2004)
39. Melnik, S., Huyet, G., Uskov, A.V.: Opt. Exp. **14**, 2950 (2006)
40. Hegarty, S.P., Corbett, B., McInerney, J.G., Huyet, G.: Electron. Lett. **41**, 416 (2005)
41. Tierno, A., Ackemann, T., Leburn, C.G., Brown, C.T.A.: Appl. Phys. Lett. **97**, 231104 (2010)
42. Kuszelewicz, R., Benoit, J.M., Barbay, S., Lemaître, A., Patriarche, G., Meunier, K., Tierno, A., Ackemann, T.: J. Appl. Phys. **111**, 043107 (2012)
43. Paillard, M., Marie, X., Renucci, P., Amand, T., Jbeli, A., Gérard, J.M.: Phys. Rev. Lett. **86**, 1634 (2001)
44. Tsitsishvili, E., Baltz, R.V., Kalt, H.: Phys. Rev. B **66**, 161405(R) (2002)
45. Uskov, A.V., Boucher, Y., Le Bihan, J., McInerney, J.: Appl. Phys. Lett. **73**, 1499 (1998)
46. Markus, A., Chen, J.X., Gauthier-Lafaye, O., Provost, J.G., Paranthoen, C., Fiore, A.: IEEE Sel. Top. Quantum Electron. **9**, 1308 (2003)
47. Viktorov, E.A., Mandel, P., Tanguy, Y., Houlihan, J., Huyet, G.: Appl. Phys. Lett. **87**, 053113 (2005)
48. Brambilla, M., Lugiato, L.A., Prati, F., Spinelli, L., Firth, W.J.: Phys. Rev. Lett. **79**, 2042 (1997)
49. Spinelli, L., Tissoni, G., Brambilla, M., Prati, F., Lugiato, L.A.: Phys. Rev. A **58**, 2542 (1998)
50. Kovsh, A.R., Maleev, N.A., Zhukov, A.E., Mikhrin, S.S., Vasilâev, A.P., Shernyakov, Y.M., Maximov, M.V., Livshits, D.A., Ustinov, V.M., Alferov, Z.I., Ledentsov, N.N., Bimberg, D.: Electron. Lett. **38**, 1104 (2002)
51. Zhukov, A.E., Kovsh, A.R., Mikhrin, S.S., Vasil'ev, A.P., Semenova, E.S., Maleev, N.A., Ustinov, V.M., Kulagina, M.M., Nikitina, E.V., Soshnikov, I.P., Shernyakov, Y.M., Livshits, D.A., Kryjapovskykaya, N.V., Sizov, D.S., Maximov, M.V., Tsatsul'nikov, A.F., Ledentsov, N.N., , B.D., Alferov, Z.I.: Physica E **17**, 589 (2003)
52. Borri, P., Langbein, W., Mørk, J., Hvam, J.M., Heinrichsdorff, F., Mao, M.H., Bimberg, D.: Phys. Rev. B **60**, 7784 (2004)
53. Yariv, A.: Quantum Electronics. 3rd edn. John Wiley & Sons, New York (1988)
54. Sugawara, M., Mukai, K., Nakata, Y.: Appl. Phys. Lett. **74**, 1561 (1999)
55. Capua, A., Mikhelashvili, V., Eisenstein, G., Reithmaier, J.P., Somers, A., Forchel, A., Calligaro, M., Parillaud, O., Krakowski, M.: Opt. Express **16**, 2141–2146 (2008)
56. Thylén, L.: Opt. Quantum Electron. **15**, 433 (1983)
57. Sheik-Bahae, M., Said, A.A., Wei, T.H., Hagan, D.J., Stryland, E.W.V.: IEEE J. Quantum Electron. **26**, 760 (1990)
58. Siegman, A.E.: Lasers. University Science Books, Mill Valley, California (1986)
59. Ackemann, T., Scholz, T., Vorgerd, C., Nalik, J., Hoffer, L.M., Lippi, G.L.: Opt. Commun. **147**, 411 (1998)
60. Labeyrie, G., Ackemann, T., Klappauf, B., Pesch, M., Lippi, G.L., Kaiser, R.: Eur. Phys. J. D **22**, 473 (2003)
61. Tanguy, Y., Ackemann, T., Firth, W.J., Jäger, R.: Phys. Rev. Lett. **100**, 013907 (2008)
62. Gioannini, M., Sevega, A., Montrosset, V.: Opt. Quantum Electron. **38**, 381 (2006)
63. Tissoni, G., Spinelli, L., Lugiato, L.A., Brambilla, M.: In: Proceedings of SPIE, vol. 4283, p. 577 (2001)
64. Schneider, H.C., Chow, W.W., Koch, S.W.: Phys. Rev. B **64**, 115315 (2001)
65. Schneider, H.C., Chow, W.W., Koch, S.W.: Phys. Rev. B **66**, 041310(R) (2002)
66. Wong, H.C., Ren, G.B., Rorison, J.M.: Opt. Quantum Electron. **38**, 395 (2006)

67. Lagatsky, A.A., Leburn, C.G., Brown, C.T.A., Sibbett, W., Zolotovskaya, S., Rafailov, E.U.: Prog. Quantum Electron. **34**, 1 (2010)
68. Marzin, J.Y., Gérard, J.M., Izraël, A., Barrier, D.: Phys. Rev. Lett. **94**, 716 (1994)
69. Leon, R., Fafard, S., Leonard, D., Merz, J.L., Petroff, P.M.: Appl. Phys. Lett. **67**, 521 (1995)
70. Hinzer, K., Hawrylak, P., Korkusinski, M., Fafard, S., Bayer, M., Stern, O., Gorbunov, A., Forchel, A.: Phys. Rev. B **63**, 075314 (2001)
71. Miller, D.A.B.: IEEE J. Quantum Electron. **17**, 306 (1981)
72. Wherrett, B.S.: IEEE J. Quantum Electron. **20**, 646 (1984)
73. Sfez, B.G., Oudar, J.L., Kuszelewicz, R., Pellat, D.: Appl. Phys. Lett. **80**, 1163 (1992)
74. Adachi, S.: J. Appl. Phys. **58**(3), R1 (1985)
75. Weiner, J.S., Pearson, D.B., Miller, D.A.B., Chemla, D.S., Sivco, D., Cho, A.Y.: Appl. Phys. Lett. **49**, 531 (1986)
76. Lee, Y.H., Chavez-Pirson, A., Koch, S.W., Gibbs, H.M., Park, S.H., Morhange, J., Jeffery, A., Peyghambarian, N., Banyai, L., Gossard, A.C., Wiegmann, W.: Phys. Rev. Lett. **57**, 2446 (1986)
77. Tombling, C., Saitoh, T., Suzuki, Y., Tanaka, H.: Electron. Lett. **27**, 1374 (1991)
78. Miller, D.A.B., Chemla, D.S., Eilenberger, D.J., Smith, P.W., Gossard, A.C., Tsang, W.T.: Appl. Phys. Lett. **41**, 679 (1983)
79. Takada, K., Tanaka, Y., Matsumoto, T., Ekawa, M., Song, H.Z., Nakata, Y., Yamaguchi, M., Nishi, K., Yamamoto, T., Sugawara, M., Arakawa, Y.: Electron. Lett. **47**, 206 (2011)
80. Kageyama, T., Nishi, K., Yamaguchi, M., Mochida, R., Maeda, Y., Takemasa, K., Yamamoto, T., Sugawara, M., Arakawa, Y.: Extremely high temperature (220°C) continuous-wave operation of 1,300 nm-range quantum-dot lasers. In: Paper PDA.1, CLEO-Europe, Munich, (2011)
81. Amano, T., Sugaya, T., Komori, K.: IEEE Photonics Tech. Lett. **18**, 619 (2006)
82. Nishi, K., Saito, H., Sugou, S., Lee, J.S.: Appl. Phys. Lett. **74**, 1111 (1999)
83. Mi, Z., Bhattacharyaa, P.: J. Appl. Phys. **98**, 023510 (2005)
84. Leifer, K., Pelucchi, E., Watanabe, S., Michelini, F., Dwir, B., Kapon, E.: Appl. Phys. Lett. **91**, 081106 (2007)
85. Gogneau, N., Le Gratiet, L., Cambril, E., Beaudoin, G., Patriarche, G., Beveratos, A., Hostein, R., Robert-Philip, I., Marzin, J.Y., Sagnes, I.: J. Cryst. Growth **310**, 3413 (2008)
86. Chia, C.K., Zhang, Y.W., Wong, S.S., Yong, A.M., Chow, S.Y., Chua, S.J., Guo, J.: Appl. Phys. Lett. **90**, 161906 (2007)

Chapter 13
Quantum Dots with Built-in Charge for Enhancing Quantum Dot Solar Cells and Infrared Photodetectors

Kimberly A. Sablon, V. Mitin, J. W. Little, A. Sergeev and N. Vagidov

Abstract We present theoretical and experimental results of electron kinetics and transport in quantum dot structures with potential barriers created around dots via intentional or unintentional doping. Monte Carlo simulations demonstrate that photoelectron capture is substantially enhanced in strong fields and electron kinetics can be controlled by potential barriers. Therefore, by creating potential barriers around dots, we found that our novel quantum dots with built-in charge (Q-BIC) solar cells and infrared (IR) photodectors enhance electron intersubband transitions and suppress fast electron capture processes. These factors lead to a 60% increase in the photocurrent of the Q-BIC solar cells (without degradation of the open circuit voltage) and ~25 times increase in the photoresponse of the Q-BIC photodetectors.

Introduction

This chapter focuses on a novel approach for engineering nanostructures with advanced properties due to quantum dots with built-in charge (Q-BIC). By implementing this approach, a 50% increase in the photovoltaic efficiency in n-doped InAs/GaAs quantum dot solar cell (QDoSC) with a built-in-dot charge of ~6 electrons per dot have been achieved. In addition, we have also demonstrated

K. A. Sablon (✉) · J. W. Little
U.S. Army Research Laboratory, 2800 Powder Mill Road,
BLDG 207 (RDRL-SEE-I), Adelphi, MD 20783, USA
e-mail: kimberly.a.sablonramsey.civ@mail.mil

V. Mitin · A. Sergeev · N. Vagidov
University at Buffalo, Buffalo, NY 14260, USA

Z. M. Wang (ed.), *Quantum Dot Devices*, Lecture Notes in Nanoscale Science and Technology 13, DOI: 10.1007/978-1-4614-3570-9_13,
© Springer Science+Business Media New York (outside the USA) 2012

$\sim$25 times increase in the photoresponse of a quantum dot infrared photodetector (QDIP), with increasing the built-in-dot charge from one to six electrons per dot.

Self-assembled quantum dots have emerged as one of the most promising systems for a plethora of applications, including quantum computing, infrared (IR) sensing, solid-state lighting and lasing, and energy harvesting due to their fully quantized electron and hole states [1–7]. While knowledge of the tunable energy levels in QDs, which ultimately govern the electrical and optical properties, has been fully exploited, little efforts have been directed to controlling carrier kinetics within QD structures. For example, the phonon bottleneck concept assumes that the phonon-assisted bound-to-bound transitions in QDs are prohibited, unless the energy between two discrete levels matches the phonon energy [8], but completely ignores the interaction between electrons and corresponding modification of electron states. As a result, experimentally measured phonon-mediated electron relaxation turns out to be much faster than expected in the phonon bottleneck concept [9]. In response to this fundamental issue which impedes the performance of QD devices, an unique approach has been proposed for suppressing photoelectron relaxation and increase the photoelectron lifetime. This approach involves manipulating the interdot kinetics by using specially engineered potential barriers [10, 11]. As it will be shown in the next sections, there are two fundamental effects supporting the radical improvements observed in the QDoSCs and QDIPs as a result of these potential barriers. First, the built-in-dot charge strongly increases electron coupling to IR radiation, because a large electron population in QDs enhances the photoinduced intraband transitions in dots and transitions from QD localized states to conducting states in the matrix. Second, the built-in-dot charge creates potential barriers around dots and these barriers suppress capture processes for photocarriers of the same sign as the built-in-dot charge. As a result, the barriers decrease recombination via QDs and increase the photocarrier lifetime. High scalability of QD nano-blocks (single QDs, QD clusters, chains, etc.) allows for numerous possibilities for nano-engineering specifically three-dimensional (3D) potential barriers which provide unique optoelectronic characteristics.

This chapter begins with a brief description of the Stranski–Krastanow growth mode used for the self-assembled growth of InAs QDs. The photoelectron capture from a fundamental point of view with emphasis on controlling electron—hole kinetics via selective doping of the interdot space is then described followed by a detailed discussion on the effect of the potential barriers on the performance of QDoSCs and QDIPs.

Self-Assembled Growth of InAs/GaAs Quantum Dots Using MBE

Several methods including lithography have been reported for the fabrication of QDs, but most lithographic techniques suffer from size limitations, material defect formation, and poor interface quality [12, 13]. However, there are three

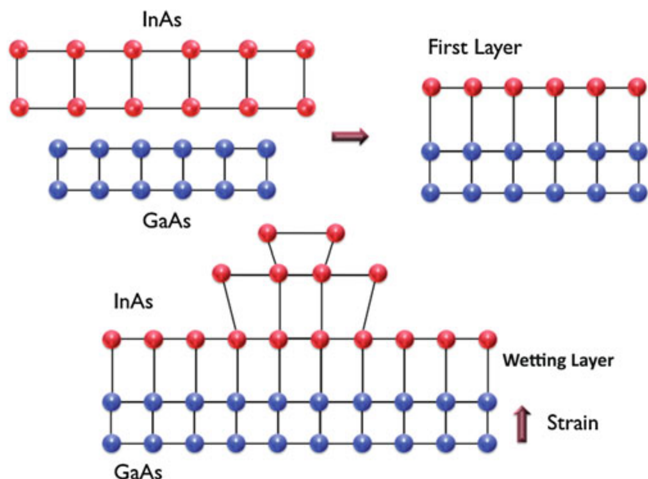

Fig. 13.1 The Stranski–Krastanow heteroepitaxial growth mode for the case of InAs/GaAs systems

well-established methods that are utilized in the heteroepitaxial growth of nanostructures [14]. The first is the Volmer-Weber growth mode which results in a direct 3D formation of islands. This occurs when deposited atoms strongly interact with each other rather than the surface. The second is the Frank van der Merwe mode which results in two-dimensional (2D) films via a 2D extension of clusters which in this case are interacting more strongly with the surface. The third is the Stranski–Krastanow growth mode which is the method of choice for fabricating the QD devices discussed in this chapter.

The Stranski–Krastanow mode has been extensively used in III–V material systems. This growth mechanism proceeds via a 2D–3D transition after depositing one or two monolayers (ML) of materials. Stranski–Krastanow growth is complex and extremely sensitive to surface stress, thickness, composition of the film, and lattice mismatch and typically results in high density defect-free QDs. This method is commonly used for lattice-mismatch systems of InAs/GaAs, where there is about a 7% lattice mismatch. Therefore, in this mode, the mismatched deposited material is accompanied by a compressive strain during the layer-by-layer 2D growth, which is generally referred to as the wetting layer. As more materials are deposited, the strain energy increases in the growth direction. Finally, after reaching a critical thickness, which has been found to be $\sim$2ML, the lattice relaxes, giving rise to 3D islands, termed QDs [15]. Figure 13.1 illustrates the Stranski–Krastanow growth mode for the InAs/GaAs heteroepitaxial system.

The advantage of the Stranski–Krastanow growth mode is that no ex-situ surface processing such as etching is required for the fabrication of QDs. Vertical ordering of QDs takes advantage of strain fields and have been predicted and observed experimentally [16–21] with the Stranski–Krastanow method. Nonetheless, this technique results in a random spatial ordering of QDs for single layers

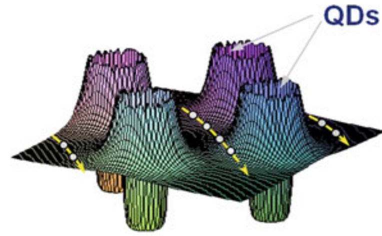

Fig. 13.2 Potential barriers around single dots in evenly distributed QD structures

[22]. Recent measurements [23] demonstrate that electron coupling between dots is in fact not essential for the operation of QDoSCs because the transitions via localized QD levels provide absorption of IR radiation. Therefore, employing more sophisticated growth approaches such as droplet epitaxy (DE) [24] for achieving spatial ordering of QDs is not a prerequisite for the devices explored in this chapter.

Potential Barriers in QD Structures

Photoelectron Capture

Progress in the field of QD technologies shows great potential for utilizing QD structures in solar cells and IR detectors. Nonetheless, a number of issues associated with the complex band structure, various electron transitions, and non-equilibrium processes in QD structures should be addressed to enhance the performance of QD devices. For example, electrons and phonons in QDs, and especially photocarrier capture processes in QDs play a crucial role in the optimization of photovoltaic power conversion in the case of solar cells [10] and detectivity and responsivity as in the case of photodetectors [11]. Therefore, complex optimization of QD structures and operating regimes can significantly improve the device performance.

An effective way to control the kinetics of electrons and phonons is to create potential barriers around the dots by selectively doping the interdot space [25, 26]. Potential barriers are created when electrons from dopants outside QDs are captured by the dots. For example, Fig. 13.2 shows the local potential barriers around single dots evenly distributed in QD planes (ordinary QD structures). The barriers are created by localized electrons within the dot and dopants within the interdot space. These barriers separate the dots from the conducting channel preventing photoelectron capture. As illustrated in Fig. 13.3, the carrier capture can be realized via electron tunneling (a) or via thermo-excitation above the potential barriers (b).

Relative probability of tunneling and thermo-excitation capture processes can be evaluated taking into account the position of the turning point for electron tunneling. Assuming that the barrier potential near the dot is close to the Coulomb

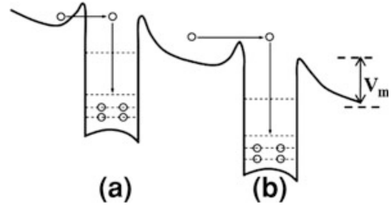

Fig. 13.3 Photoelectron capture due to electron tunneling (**a**), and thermo-excitation (**b**)

potential, the position of the turning point, R_t, averaged over the thermal electron distribution is given by [27]

$$R_t = a_B \left(\frac{Ry}{kT}\right)^{2/3} (Zm^*)^{1/3} \tag{13.1}$$

where a_B is the Bohr radius, Ry is the Rydberg constant, Z is the charge of the dot, and m^* is the electron effective mass. In particular, for GaAs at room temperatures, R_t, is about 4 nm. If dot radius is larger than R_t the thermo-excitation will dominate over tunneling. In the rest of the chapter, we will consider exactly this case. The photoelectron capture rate for the case of themo-excitation is given by

$$\tau_{capt}^{-1} = N_d \sigma \tilde{v} \tag{13.2}$$

with the trapping cross-section [27]

$$\sigma = \pi\alpha a^2 \exp\left(-\frac{eV_m}{kT}\right) \left(1 + \frac{3}{4}\frac{\alpha a}{\ell} F(V)\right)^{-1} \tag{13.3}$$

$$F = a \exp\left(-\frac{eV_m}{kT}\right) \int_a^b \frac{dr}{r^2} \exp\left(\frac{eV(r)}{kT}\right) \tag{13.4}$$

where $\tilde{v}$ is the electron thermal velocity, N_d is the concentration of quantum dots, a is the radius of the dot, ℓ is the electron mean free path with respect to elastic electron scattering, α is the probability for an electron at $r \le a$ to be captured by the quantum dot, and V_m is the maximum value of the potential barrier, i.e., $V_m = V(a)$. Describing the thermo-excitation processes, we accept that the inelastic interdot relaxation processes [28] are described by the relaxation time τ'_ε. In this case, the coefficient α can be evaluated as $\alpha \approx a/\ell'_\varepsilon$, where $\ell'_\varepsilon = \tilde{v}\tau'_\varepsilon$ and $\tilde{v}$ is the electron thermal velocity. Then, at $a^2 > \ell\ell'_\varepsilon$, the capture rate is independent of the coefficient α and is given by [24]

$$\frac{1}{\tau_{capt}} = \pi N_d D a^3 \frac{\tilde{v}}{\tilde{v}\prime}\frac{1}{\tau'_\varepsilon} \exp\left(-\frac{eV_m}{k_B T}\right) \tag{13.5}$$

where $D = \tilde{v}\ell/3$ is the diffusion coefficient. In the opposite case, $a^2 < \ell\ell'_\varepsilon$, the capture rate is

$$\frac{1}{\tau_{\text{capt}}} = \pi N_{\text{d}} a^3 \frac{\tilde{v}}{\tilde{v}'} \frac{1}{\tau'_{\varepsilon}} \exp\left(-\frac{eV_{\text{m}}}{k_{\text{B}}T}\right) \tag{13.6}$$

In both cases the exponential factor describes the effect of the potential barriers on capture processes. We would like to emphasize that Eqs. 13.3 and 13.4 are valid for any relation between ℓ, a and αa as well as for a wide variety of potentials.

In structures where the interdot space is homogeneously doped, the average number of electrons, N, trapped by a quantum dot is determined by the concentration of donors, and the potential barriers are given by [27]

$$V(r) = V_0\left(\frac{b}{r} + \frac{r^2}{2b^2} - \frac{3}{2}\right),\ V_0 = \frac{eN}{\varepsilon b(1-(a/b)^3)} \tag{13.7}$$

where a is the dot radius, b is the distance between dots, and ε is the dielectric permittivity of the interdot matrix. Thus, even in the case of homogenous doping, the potential barriers can be modified by changing the geometrical parameters of the structure and/or the doping level.

In summary, we should note that, while the formalism is general enough, it is applicable only for quasi-equilibrium electron distributions, i.e., in small electric fields. At the same time, optimal regimes for operating semiconductor devices are always achieved in strong fields, which generate non-equilibrium carrier distributions.

Carrier Capture in an Electric Field

By using a Monte Carlo simulation tool, the transport of 3D electrons in a GaAs matrix with dots was explored to investigate the dependence of the carrier capture on the electric field at various values of the potential barrier. The model assumes a regular lattice arrangement of dots with an interdot distance of b and a dot concentration, N_{d} which is given by $1/b^3$. If the interdot relaxation processes are described by the relaxation time τ'_{ε}, which is associated with inelastic electron–phonon scattering in the dot area (Fig. 13.4), the carrier capture process can be considered as a specific scattering process. This scattering process is limited in space by the dot volume and will occur when carriers transition from a conducting state with energy E_{c} above the potential barrier to a bound state E_{b} below the potential barrier.

By assuming that any carrier from the bound state will relax to the deep dot states much faster than it will return back to the conducting state, the capture time was found to be independent of the electric field up to the critical field, F_{c} which is in the order of 10^3 V/cm, and decreases substantially as the field increases as seen in Fig. 13.5. On the other hand, significant changes in the dependence of capture

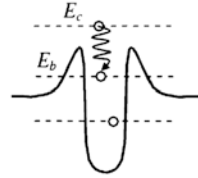

Fig. 13.4 The carrier capture as a result of electron–phonon scattering

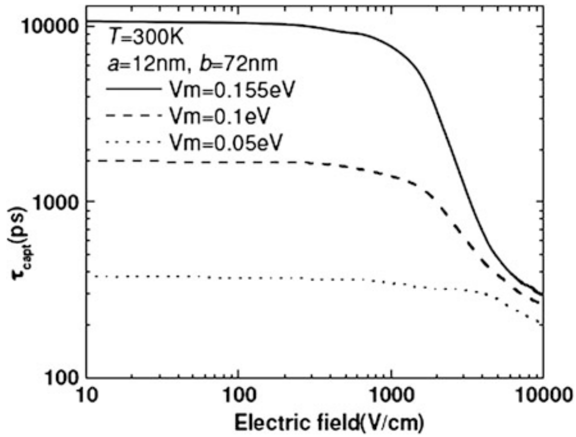

Fig. 13.5 Carrier capture as a function of the electric field at various potential barriers

time on the electric field are observed only for the case where the field is larger than 1 kV/cm as illustrated in Fig. 13.6.

A more important evaluation is the dependence of the capture time on the radius of the QD. To determine this, we compared data of the Monte Carlo simulations with analytical results taking into account that at room temperature, the electron mean free path, ℓ, is significantly larger than the dot radius. In this case, where the product of τ_{capt} and a^3 is a universal function of the electric field F, we can expect the capture rate to be proportional to a^3 as described by Eq. 13.5 and confirmed by the Monte Carlo modeling (see Fig. 13.7).

Analyzing the modeling data in terms of electron thermal energy, $\bar{\varepsilon}$, we see that the potential barriers do not change the average energy attained in the electric field. In fact, if we evaluate the logarithmic dependence of the capture time on the inverse value of $\bar{\varepsilon}$ (see Fig. 13.8), for various potential barriers the log τ_{capt} is proportional to $1/\bar{\varepsilon}$. In other words, the capture rate τ_{capt} is proportional to exp $(1/\bar{\varepsilon})$. This means that the carrier capture in the electric field can be described by Eq. 13.5, where the thermal energy kT is replaced by a factor of $\sim 2\bar{\varepsilon}/3$.

In summary, a wide range of novel properties can be realized through the manipulation of dots and potential barriers created by selectively doping QD structures. By employing potential barriers around the dots, we can separate the localized interdot electron states from the conducting states in the matrix and control all electron processes. In structures with barriers, electron kinetics and

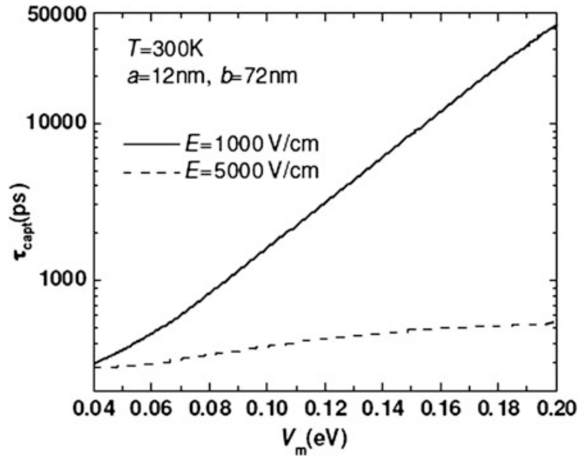

Fig. 13.6 Capture time as a function of the barrier at various electric fields

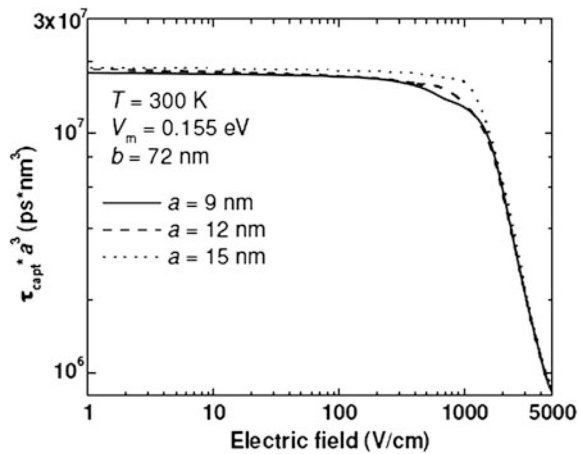

Fig. 13.7 Product of τ_{capt} and a^3 as a function of electric field

transport in the electric field based on the model of electron heating is well understood. Because the potential barriers strongly suppress the capture processes to the point where the average electron energy is comparable to the barrier height enabling better control and management of electron kinetics, a significant increase in the photocurrent and photovoltage in QDoSCs and device detectivity, photoconductive gain, and responsivity in QD IR detectors can be expected.

In the following sections, we will discuss the fundamental issues in QDoSCs and QDIPs and the effect of potential barriers in QD structures on the performance of these devices.

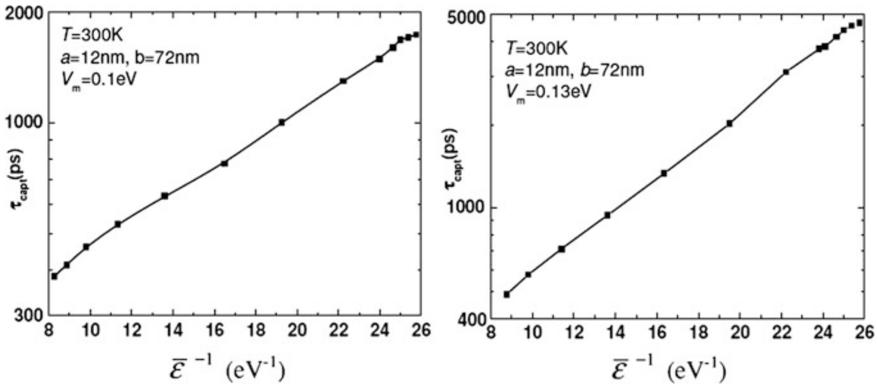

Fig. 13.8 The capture time as a function of inverse average electron energy attained in the electric field

Strong Enhancement of QD Solar Cell Efficiency due to Potential Barriers

Fundamental Issues in Solar Cells

According to Shockley and Queisser [29], the maximum efficiency for the conversion of unconcentrated solar radiation is 31%. One of the major factors that have limited the conversion efficiency in single junction cells is that subbandgap photons are not absorbed. In response, several approaches including heterostructure cells, multijunction cells, hot carrier cells, intermediate band cells, and cells based on multiple exciton generation through impact ionization were proposed to reduce losses in efficiency. Heterostructure solar cells, first proposed by Alferov [30] in 1966 are presently dominating the market of concentrator solar cells with a record conversion efficiency (up to 40%) and high degradation robustness. Despite the impressive achievements in the field of heterostructure solar cells, their efficiency remains at or below 40% primarily due to: thermalization loss, low junction voltage, contact-voltage drop, recombination loss, contact non-radiative recombination, resistivity-related heating (see Fig. 13.9). Thermalization loss is an important and fundamental problem. The bandgap of the solar cell should be small enough to absorb the major part of the solar spectrum. However, the shorter wavelength part of the solar spectrum generates hot electron–hole pairs, and most of the photon energy is lost via a thermalization process.

Multijunction cells are currently the state of the art and are based on stacking junctions with different badgaps [31]. Each p-n junction cascade is designed to effectively absorb photons, within a certain window of energies, close to the bandgap for better use of the solar spectrum. This approach has a predicted efficiency of 52% in the case of three cascades and 70% for four or more cascades.

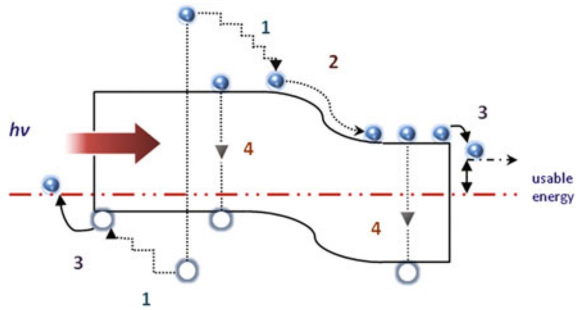

Fig. 13.9 Losses in a solar cell: *1* thermalization losses, *2* and *3* losses related to junction and contact voltages, and *4* recombination losses

However, the need for lattice matching, current matching, and use of tunnel junctions to cascade the junctions presently enables only triple-junction cells (Ge-substrate junction—InGaAs—AlInGaP) with a maximum conversion efficiency of 41%.

Recently, low-dimensional quantum structures were proposed to be used in solar cells, providing an approach complementary to the multijunction solar cells. A significant enhancement in the short circuit current and conversion efficiency were observed in solar cells based on planar quantum wells (QW) [30, 32, 33]. However, due to the continuum nature of states in QWs, losses due to thermalization of carriers cannot be avoided. For that reason, QDs have attracted much interest for photovoltaic applications [23, 34–42]. QDs have the potential to create energy levels that can better match the solar spectrum, i.e., for minimization of thermalization losses, and provide greater freedom in absorption band and strain engineering as compared with bulk materials and QWs, with predicted efficiencies of ~64% for a single junction cell [38]. However, experimental results remain substantially lower than this limit. In fact, introducing dots into the intrinsic region of solar cells gives rise to additional channels of recombination, which increases the recombination losses. Thus, while QD structures minimize thermalization losses, they simultaneously increase recombination losses.

Q-BIC Solar Cell

To increase IR harvesting and minimize the recombination losses in QDoSCs, we have identified the physical mechanisms that control recombination processes in QDs heterostructures and propose a novel approach for improving the basic parameters of QDoSCs. Our approach is based on the effective control of photoelectron capture into QDs by selectively doping the interdot space to create potential barriers around the dots. As discussed in "Photoelectron Capture", potential barriers are created when electrons from dopants outside QDs are captured by the dots. By charging the QDs, we can drastically affect photoelectron capture processes.

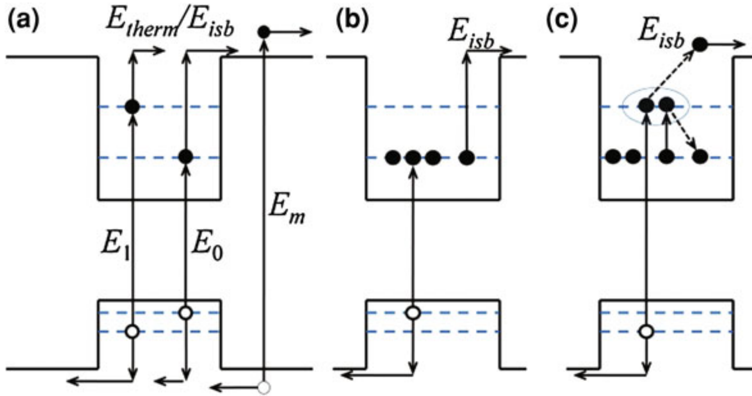

Fig. 13.10 **a** Photogeneration of electron–hole pairs into the ground QD state (E_0) and into the excited QD state (E_1) followed by either thermionic emission (E_{therm}) or intersuband photoexcitation (E_{isb}) into the conducting channel; E_{m} is the direct photogeneration in the GaAs matrix. **b** Process induced by n-doping with IR transition of an electron from the localized to the conducting state. **c** Another doping-induced process, where the radiation excites two electrons to the QD excited states, then due to strong interelectron interaction in a QD one of these electrons transfers to the conducting state and the other transfers to a low-energy state

If we consider the positive effects of doping on the open circuit voltage (V_{OC}) and IR harvesting of solar energy, we can expect that doping will stabilize the V_{OC} as well as generate additional carriers in QDs, enhance the IR absorption and photocurrent as shown in Fig. 13.10.

Figure 13.10a presents the processes in a QD structure without doping. Figure 13.10b and c shows the doping-induced process associated with free electrons in the ground state due to intentional doping of dots. Figure 13.10c demonstrates a two-step process, where two electrons are excited by IR radiation to the excited localized QD states. Consequently, strong electron–electron interaction in QDs [43, 44] causes one of these electrons to transfer to some low-energy state (for example, to the ground state) while another electron transfers to the conducting state and leaves the dot. N-doping enhances electron interdot transitions shown in Fig. 13.10b and c without substantially changing the hole kinetics.

In undoped QDs, differences in the capture rates of electrons and holes can lead to an accumulation of the built-in dot charge. As we have demonstrated in "Potential Barriers in QD Structures", capture rates depend strongly on the electric field even in relatively small fields. Therefore, the built-in dot charge can substantially affect the electric field around the dot and alter capture processes. For that reason, both the potential barriers around dots and the built-in dot charge will play a significant role in the IR harvesting and carrier capture processes in QDoSCs. To evaluate the proposed approach on the solar cell parameters (short circuit current, J_{SC}; open circuit voltage, V_{OC}; efficiency, η) and understand the IR-induced transitions and capture processes, we investigated p- and n-doped InAs/GaAs QDoSCs with various doping levels compared with GaAs reference and undoped QD cells.

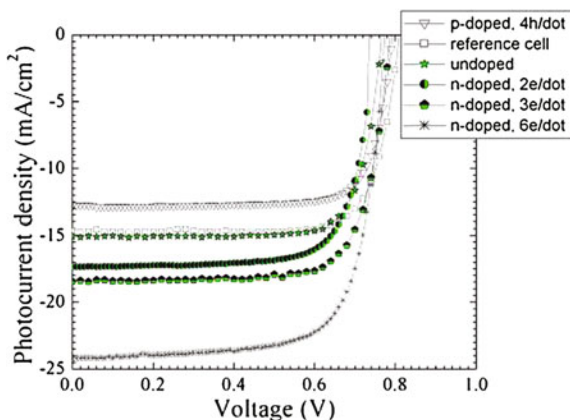

Fig. 13.11 I–V characteristics under 1 Sun at 100 mW/cm^2 of QDoSCs as a function of doping: p-doped QD cell with four holes per dot, GaAs reference cell, undoped QD cell, n-doped QD cells with two, three, and six electrons per dot

Figure 13.11 shows the current–voltage (I–V) curves obtained under 1 Sun (AM1.5G) illumination. This result demonstrates that while p-doping degrades the J_{SC}, the n-doped structures show a monotonic increase in J_{SC} with increasing doping level. Similarly, the power conversion efficiency increases by 4.5, 30, and 50% for doping levels of two, three, and six electrons per dot, respectively. To determine the exact contribution of the IR portion of the solar spectrum to the overall photoresponse of our QDoSCs, a GaAs filter was used to block all wavelengths below 880 nm. The I–V characteristics obtained with the filter is shown in Fig. 13.12.

The photoresponse due to radiation at wavelengths greater than 880 nm increases substantially with doping. Photocurrents of ~7.0 and ~9 mA/cm^2 were observed in the devices doped to provide two and six electrons per dot, respectively, compared with the undoped sample. As expected, the GaAs reference cell does not show any photoresponse to the long-wavelength part of solar spectrum.

To further determine the harvesting role of IR photons, we measured the spectral dependence of the photocurrent under low illumination conditions using a Nicolet Fourier Transform Infrared (FTIR) spectrometer. Figure 13.13 shows partial contributions of the band-to-band, wetting layer, QD ground state, and subband transitions to the photocurrent. The photocurrent due to band-to-band transitions (below ~880 nm) and transitions in the wetting layer (~880–920 nm) are not significantly affected by n-doping. However, the IR harvesting via electron transitions shown in Fig. 13.10b and c increases with n-doping. In fact, it was observed that doping further reduces the photoresponse due to short-wavelength (above bandgap of GaAs) photons while enhancing the long-wavelength photons contribution via QDs. Interestingly, the spectral density monotonically decreases when the radiation wavelength increases up to 4.8 μm. From the onset of Fig. 13.13b, the spectral density for the sample with six electrons per dot shows a sharp rise at 4.8 μm (250 meV), which we believe corresponds to the transition from the dot ground state to the low-energy resonance conducting state (E_{isb} in Fig. 13.10b). A broad peak is observed between 4.8 and ~8 μm which is close to

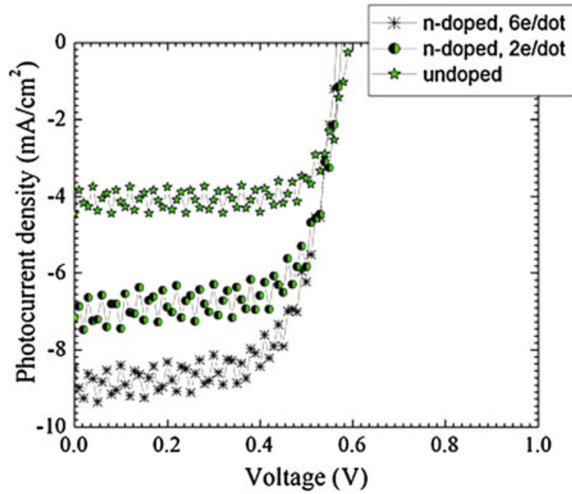

Fig. 13.12 The long-wavelength photoresponse for undoped QD solar cell and n-doped cells with two and six electrons per dot under 1 Sun (AM1.5G) light passed through short-wavelength GaAs absorber

the cutoff of the experiment. As the doping level decreases, the peak decreases and completely disappears in the reference cell.

So far, we have discussed the effect of doping on the generation of free electrons and subsequent harvesting of IR radiation. How does doping affect the carrier capture and relaxation processes via the built-in-dot charge? To understand relaxation processes via the built-in dot charge, we studied potential barriers around QDs as a function of dot population using a simulation tool based on the nextnano^3 software [45]. The potential profile in QD structures where the positions of dots are correlated in QD planes is shown in Fig. 13.14a. As seen, the potential barriers in the QD planes are smaller than those between QD planes. Therefore, photoelectron capture via thermo-excitation is mainly expected to come from the QD planes. Figure 13.14b shows the potential barriers around single dots in QD planes as a function of the quantum dot population.

According to these results, the barrier height is proportional to the number of electrons trapped in a dot, i.e., $V_b = k_e \times n$, where n is the dot population and $k_e = 2.5$ meV. The coefficient k_e depends on the dot form and increases for smaller dots. The built-in negative charge suppresses the fast electron capture processes and accelerates the capture of holes. Taking into account an exponential dependence of the capture rates on the built-in charge [11, 46], the corresponding dot population may be evaluated as

$$n_d \approx (k_B T / k_e) \ln\left(\tau_c^p(0) / \tau_c^n(0)\right) \tag{13.8}$$

where $1/\tau_c^p$ and $1/\tau_c^n$ are capture rates for holes and electrons, respectively. Therefore, even a relatively small difference in initial capture rates may provide a very significant built-in-dot charge. The study on quantum well structures by Ridley [47] has shown that a difference in electron and hole capture rates can lead to charge accumulation in the wells. In fact, experimental works, where both

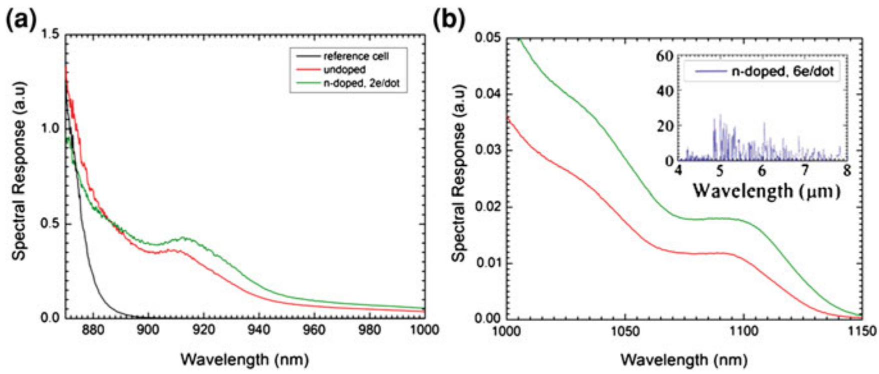

Fig. 13.13 **a** Spectral response of GaAs reference, doped and undoped solar cell structures. **b** Magnified view of the spectral response in the range from 1,000 to 1,150 nm. The inset shows the spectral response of QD structures with six electrons per dot in the range of 4–8 μm

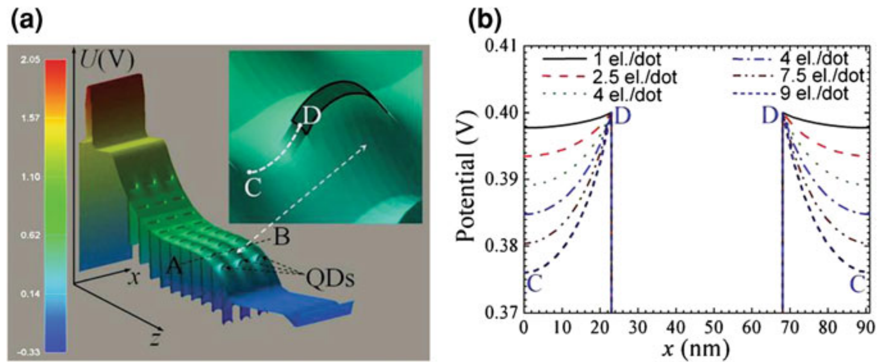

Fig. 13.14 **a** 3D potential profile of the conduction band in the QD solar cell with correlated positions of QDs. *Inset*: Potential barriers around QD suppress the capture of photoelectrons. In the QD plane A–B the potential between QDs varies from the maximum (D) to minimum (C). **b** Corresponding potential barriers for electrons in QD plane A–B as a function of built-in electron charge

capture processes have been studied, show electron relaxation via emission of an optical phonon is much faster than the corresponding hole relaxation in QDs which is different from bulk materials. Although there has been some controversy in the reported values of capture rates for electrons and holes, if as an example, we use the ratio obtained from Ref. [48] which was determined to be $\tau_c^p(0)/\tau_c^p(0) = 2\,\mathrm{ps}/0.5\,\mathrm{ps} = 4$, we get seven electrons localized in the dot at room temperature. This suggest that if the built-in-dot charge is not provided by doping, then the corresponding charge comes from p^+ and n^+ contacts and changes the potential profile in the active area. Therefore, to avoid this negative effect, the doping level that provides the dot population given by Eq. 13.7 should be considered.

Table 13.1 QD solar cell parameters

Dot population	J_{SC} (mA/cm^2)	V_{OC} (V)	Fill factor (%)	Efficiency (%)
0	15.1	0.77	77	9.31
2	17.3	0.74	76	9.73
3	18.5	0.79	75	12.1
6	24.3	0.78	72	14.0

N-doping of the interdot space of QDoSCs has shown to enhance the harvesting of IR energy. As it is summarized in Table 13.1, the efficiency of the photovoltaic conversion increases from 9.3% in QDoSCs without doping to 14% in cells doped to provide $\sim$6 electrons per dot, which was the maximum doping level in our investigations.

Further improvements are expected with higher doping levels. The improvement of IR harvesting is anticipated to be even stronger at higher radiation intensities due to an optical pumping effect which will be discussed in the following section.

Application of Potential Barriers for QD IR Ohotodetectors

Currently, IR technologies based on quantum well IR photodetectors (QWIPs) are widely utilized in various sensors and imaging devices operating at 77 K and below [49–52]. However, QWIPs have drawbacks such as insensitivity to the normal incidence radiation and fast carrier capture at room temperature [51, 52]. Consequently, the detectivity and responsivity decreases drastically at room temperature. The factors limiting the high temperature operation of QWIPs are well understood. In fact, various reports in the literature have unambiguously demonstrated that this limitation is caused by the reduced photocarrier lifetime at temperatures above 77 K. Fast electron relaxation increases the generation-recombination noise, hence compromising the sensitivity of the detector. To solve the sensitivity and responsivity issue, QDs are widely considered for use in IR photodetectors due to the many possible routes for manipulating electron processes in QD structures. In fact, QDIPS have already demonstrated detectivities of $D^* \sim 10^8$ cm Hz$^{1/2}$/W. To further enhance the sensitivity and responsivity of QDIPs, local potential barriers around QDs were explored for suppressing fast electron capture processes.

To determine the effects of potential barriers on the photoresponse of QDIPs, we studied variations of potential barriers and their effects on the device performance. Since barriers can be controlled by varying the dot size, doping levels, and host materials, we modified dopant positions and levels and computed the corresponding barrier height. The doping levels were varied to provide 2.4, 2.8, 4.7, and 6.1 electrons per dot as shown in Table 13.2.

Table 13.2 Device variations explored

Device	Dopant position	Dopant concentration (cm^{-2})	Electrons per dot	Barrier height (meV)
B44	QD layer	2.7×10^{11}	2.4	25
B45	Middle of AlGaAs layers	2.7×10^{11}	2.8	70
B52	QD layer	5.4×10^{11}	4.7	79
B53	Middle of AlGaAs layers	5.4×10^{11}	6.1	130

The height of the potential barriers for electrons located in the interdot area is defined as the difference between the maximum of the conduction band in QDs and minimum in the depletion regions that occur as a result of interdot doping, as shown in Fig. 13.15. Comparing the photoresponse of structures doped in the QD layer (B44), middle of the AlGaAs layer (B45), and modulately doped (B46), we observed that the photoresponse of structures doped at the interdot space, i.e., in the middle of the AlGaAs layers is several times larger than that of the other samples. Figure 13.16 shows the photoresponse as a function of the built-in-dot charge at 80 K for the various device geometries. The photoresponse increases with increasing dot population.

To verify the effect of the potential barriers on the performance of the QDIPs, the potential height was computed as a function of dot population. As it is shown in Fig. 13.14, the 3D potential barriers around dots are strongly anisotropic. The barriers in the QD planes, i.e., in the direction perpendicular to the current, are substantially smaller than the barriers in the direction of the current. Therefore, the thermo-activated capture processes occur mainly in QD planes. Calculating the height of the potential barriers in the direction perpendicular to the current, we found that the barrier height is proportional to the QD charge: $V = k_e q$, where q is the dot charge, i.e., $q = n$ is the dot population in the case of the interdot doping, and $q = n - p$ is the dot population n reduced by the number of dopants p in the dot in the case of the interdot doping. The coefficient k_e depends on the dot size and concentration and was found to be $\sim$2.5 meV.

In Fig. 13.16, we present the fitting of the experimental data for the photoresponse of samples B44, B45, B52, and B53 (blue squares) by the theoretical dependence

$$I = A \times n \exp(k_e q / k_B T) \tag{13.9}$$

where the pre-exponential factor $A \times n$ describes the probability of the photo excitation, which is proportional to the number electrons in dot, n, and the exponential factor describes the suppression of the photocarrier capture processes due to potential barriers around dots and the built-in-dot charge, q. As seen, the theoretical modeling (red circles) is in a very good agreement with experimental data (blue squares). The red dashed line shows the modeling results for the interdot doping ($q = n$), which was used for doping of the samples B45 and B53.

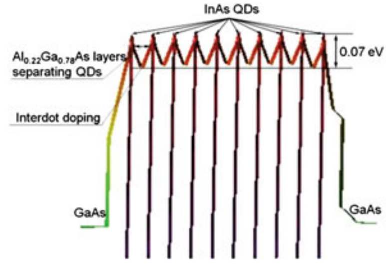

Fig. 13.15 A 2D slice of the calculated conduction band structure of sample *B45,* where the dopant was inserted in the middle of the AlGaAs layers with a concentration of 2.7×10^{11} cm^{-2}

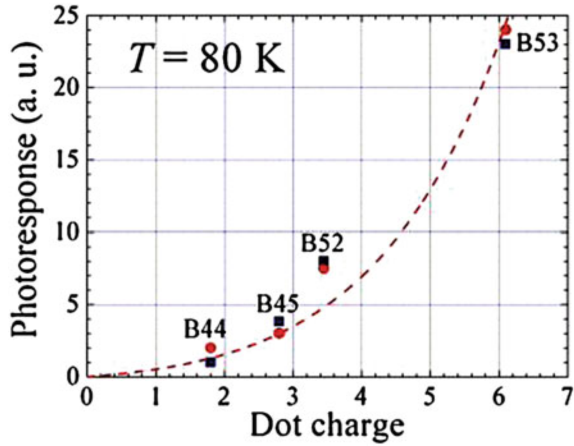

Fig. 13.16 QDIP photoresponse (T = 80 K) vs the dot population; *blue squares* are for experimental data, *red circles* show modeling results, and the *red line* is for the theoretical prediction for the interdot doping

For samples B44 and B52 with the doping of QD layers, the dot charge was formed by the electrons captured in the dot and dopants placed in the dot. From the fitting of experimental data, the parameter k_e was found to be equal to 2.7 meV, i.e., $k_e/k_BT = 0.4$, which is in a good agreement with $k_e = 2.5$ meV that we obtained from the independent modeling of the potential barriers. Thus, our model provides an adequate description of the photoresponse enhancement due to potential barriers.

To further understand IR harvesting in Q-BIC structures, we investigated the IR photocurrent under high optical pumping. A red light-emitting diode (LED) with a 620 nm wavelength was used to optically pump the samples. Figure 13.17 shows the photocurrent densities for sample B45 at different intensities. The measurements demonstrate an increase by three orders of magnitude in the photocurrent density due to the short-wavelength pumping. This result is in agreement with Ref. [53] which demonstrated that the IR response is significantly enhanced by optical pumping. In this case, optical pumping is equivalent to the effects of doping QDs. As seen in Fig. 13.17, the high-energy radiation increases the number of carriers captured into QDs, which in turn significantly enhances the IR electron transitions from localized states in QDs to the conducting states in the matrix as it is shown in Fig. 13.10b and c.

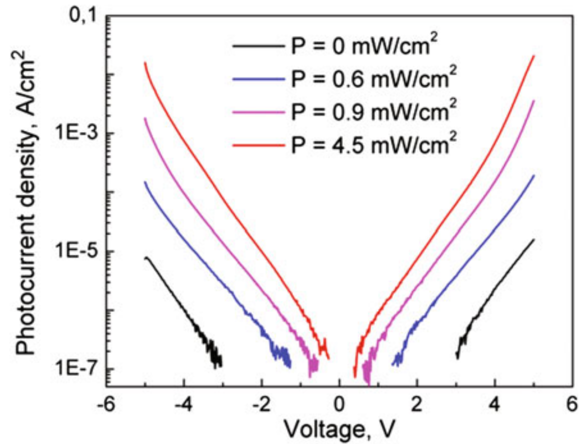

Fig. 13.17 Photocurrent density of sample B45 at T = 80 K as a function of optical pumping from a *red* LED

Let us note that the same effect known for QDIPs, where the IR response is significantly enhanced by the optical pumping could potentially provide a significant increase in the photocurrent of our Q-BIC solar cells. The difference between the photoresponse under high illumination (Fig. 13.11) and the low intensity spectral response (Fig. 13.13) could be the result of optical pumping under high intensity conditions. Therefore, due to the optical pumping effect we can expect strong enhancement of IR harvesting and conversion in concentrator Q-BIC solar cells.

Conclusion

To conclude, this chapter reviewed both theoretical and experimental studies of Q-BIC devices. We presented the effects of the built-in-dot charge on the solar energy harvesting, IR transitions, and recombination processes. By using an analytical approach and Monte Carlo simulations, the capture rates of photocarriers in Q-BIC structures were investigated as a function of the built-in-dot charge, dot concentration, dot radius, and electric field. Based on this analysis, we optimized our devices and demonstrated the effects of potential barriers due to interdot n-doping on the overall performance of our QD devices. As the theoretical models predicted, the effective separation of conducting and localized states by potential barriers provides a 60% increase in the photocurrent of the QDoSCs (without degradation of the open circuit voltage) and $\sim$25 times increase in the photoresponse of the QDIPs. Further improvements due to the built-in-dot charge are expected for higher doping levels. The IR harvesting in Q-BIC solar cells is anticipated to be even stronger at higher radiation intensities due to the optical pumping effect.

Acknowledgments The authors would like to thank Kimberley Olver, Fred Towner, and Gregory Salamo's group for their contributions.

References

1. Shoji, H., Nakata, Y., Mukai, K., Sugiyama, Y., Sugawara, M., Yokoyama, N., Ishikawa, H.: Appl. Phys. Lett. **71**, 193 (1997)
2. Bimberg, D., Grundmann, M., Lendenstov, N.N.: Quantum Dots Heterostructures, 1st edn. Wiley, New York (1999)
3. Bhattacharya, P., Stiff-Roberts, A.D., Krishna, S., Kennerly, S.: Int. J. High Speed Electron. Syst. **12**, 969 (2002)
4. Krishna, S.: J. Phys. D **38**, 2142 (2005)
5. Towe, E., Pan, D.: IEEE J. Sel. Top. Quantum Electron. **6**, 408 (2000)
6. Oga, R., Lee, W.S., Fujiwara, Y., Takeda, Y.: Appl. Phys. Lett. **82**, 4546 (2003)
7. Jone-Bey, H.A.: Laser Focus World **42**, 10 (2006)
8. Bockelmann, U., Bastard, G.: Phys. Rev. B **42**, 8947 (1990)
9. Ferreira, R., Bastard, G.: Appl. Phys. Lett. **74**, 2818 (1999)
10. Sablon, K.A., Little, J.W., Mitin, V., Sergeev, A., Vagidov, N., Reinhardt, K.: Nano Lett. **11**, 2311–2317 (2011)
11. Mitin, V., Antipov, A., Sergeev, A., Vagidov, N., Eason, D., Strasser, G.: Nanoscale Res. Lett. **6**, 21 (2011)
12. Ohshima, T., Song, H.Z., Okada, Y., Akahane, K., Miyazawa, T., Kawabe, M., Yokoyama, N.: Phys. Status Solidi C **4**, 1364 (2003)
13. Schneider, C., Strau, M., Sünner, T., Huggenberger, A., Wiener, D., Reitzenstein, S., Kamp, M., Höfling, S., Forchel, A.: Appl. Phys. Lett. **92**, 183101 (2008)
14. Stranski, I.N., Krastanow, L.: AMA Arch. Opthalmol **146**, 797 (1937)
15. Schchukin, V.A., Ledentsov, N.N., Bimberg, D.: Epitaxy of Nanostructures. Springer, Berlin (2004)
16. Srolovitz, D.J.: Acta Metall. **37**, 621 (1989)
17. Snyder, C.W., Orr, B.G., Kessler, D., Sander, L.M.: Phys. Rev. Lett. **66**, 3032 (1991)
18. Eaglesham, D.J., Cerullo, M.: Phys. Rev. Lett. **64**, 1943 (1990)
19. Gao, H.: J. Mech. Solids **39**, 443 (1991)
20. Ratsch, C., Zangwill, A.: Surf. Sci. **293**, 123 (1993)
21. Tersoff, J., LeGoues, F.K.: Phys. Rev. Lett. **72**, 3570 (1994)
22. Wang, Z.M., Churchill, H., George, C.E., Salamo, G.J.: Temperature dependent lasing characteristics of multi-stacked quantum dot lasers. J. Appl. Phys. **96**
23. Guimard, D., Morihara, R., Bordel, D., Tanabe, K., Wakayama, Y., Nishioka, M., Arakawa, Y.: Appl. Phys. Lett. **96**, 203507 (2010)
24. Koguchi, N., Ishige, K.: Jpn. J. Appl. Phys. **32**, 2052 (1993)
25. Mitin, V., Pipa, V.I., Sergeev, A., Dutta, M., Stroscio, M.: Infrared phys. Technol. **42**, 467 (2001)
26. Vagidov, N., Sergeev, A., Mitin, V.: Int. J. High Speed Electron. Syst. **17**, 585 (2007)
27. Chien, L.H., Sergeev, A., Vagidov, N., Mitin, V.: Int. J. High Speed Electron. Syst. **18**, 255 (2008)
28. Lim, H., Movaghar, B., Tsao, S., et al.: Phys. Rev. B **74**, 205321 (2006)
29. Shockley, W., Queisser, H.J.: J. Appl. Phys. **32**, 510 (1961)
30. Alferov, Z.I.: Rev. Mod. Phys. **73**, 767 (2001)
31. Cotal, H., Fetzer, C., Boisvert, J., Kinsey, G., King, R., Hebert, P., Yoon, H., Karam, N.: Energy Environ. Sci. **2**, 174 (2009)
32. Sachenko, A.V., Sololovskyi, I.O.: Semicond. Phys. Quantum Electron. Optoelectron. **11**, 1 (2008)

33. Alemu, A., Williams, L., Bhusal, L., Freundlich, A.: In: Proceedings of 19th European Photovoltaic Solar Energy Conference, 359 (Paris, France 2004)
34. Nozik, A.J.: Nano Lett. **10**, 2735 (2010)
35. Laghumavarapu, R.B., El-Emawy, M., Nuntawong, N., Moscho, A., Lester, L.F., Huffaker, D.L.: Appl. Phys. Lett. **91**, 243115 (2007)
36. Hubbard, S.M., Raffaelle, R., Robinson, R., Bailey, C., Wilt, D., Wolford, D., Maurer, W., Bailey, S.: Mater. Res. Soc. Symp. Proc. **1017**, 13 (2007)
37. Sablon, K.A., Little, J.W., Olver, K.A., Wang, Zh.M., Dorogan, V.G., Mazur, Yu.I., Salamo, G.J., Towner, F.J.: J. Appl. Phys. **108**, 074305 (2010)
38. Luque, A., Martı, A.: Phys. Rev. Lett. **78**, 5014 (1997)
39. Wei, G., Shiu, K.T., Giebink, N.C., Forrest, S.R.: Appl. Phys. Lett. **92**, 066102 (2008)
40. Zhou, D., Vullum, P.E., Sharma, G., Thomassen, S.F., Holmestad, R., Reenaas, T.W., Fimland, B.O.: Appl. Phys. Lett. **96**, 083108 (2010)
41. Hubbard, S.M., Cress, C.D., Bailey, C.G., Raffaelle, R.P., Bailey, S.G., Wilt, D.M.: Appl. Phys. Lett. **92**, 123512 (2008)
42. Oshima, R., Takata, A., Okada, Y.: Appl. Phys. Lett. **93**, 083111 (2008)
43. Schaller, R.D., Klimov, V.I.: Phys. Rev. Lett. **92**, 186601 (2004)
44. Ellingson, R.J., Beard, M.C., Johnson, J.C., Yu, P., Micic, O.I., Nozik, A.J., Shabaev, A., Efros, A.L.: Nano Lett. **5**, 865 (2005)
45. http://www.nextnano.de/nextnano3
46. Sergeev, A., Mitin, V., Stroscio, M.: Phys. B **316–317**, 369 (2002)
47. Ridley, B.K.: Phys. Rev. B **50**, 1717 (1994)
48. Yarotski, D.A., Averitt, R.D., Negre, N., Crooker, S.A., Taylor, A.J., Donati, G.P., Stintz, A., Lester, L.F., Malloy, K.J.: J. Opt. Soc. Am. B **19**, 1480 (2002)
49. Tidrrow, M.Z.: Quantum sensing and nanophotonic devices II. In: Razeghi, M., Brown, G.J. (Eds.) Proceedings of SPIE, vol. 5732, p. 217 (2005)
50. Rogalski, A.: Prog. Quantum Electron. **27**, 59 (2003)
51. Gunapala, S.D., Bandara, S.V., Liu, J.K., et al.: Semicond. Sci. Technol. **20**, 473 (2005)
52. Levine, B.F.: J. Appl. Phys. Lett. **74**, R1 (1993)
53. Höglund, L., Holtz, P.O., Pettersson, H., Asplund, C., Wang, Q., Malm, H., Almqvist, S., Petrini, E., Andersson, J.Y.: Appl. Phys. Lett. **94**, 053503 (2009)

Chapter 14
Semiconductor Quantum Dot-Sensitized Solar Cells Employing TiO_2 Nanostructured Photoanodes with Different Morphologies

Qing Shen and Taro Toyoda

Abstract CdSe quantum dot (QD)-sensitized solar cells (QDSCs) were synthesized by adsorbing CdSe QDs onto TiO_2 nanostructured electrodes with different morphologies, i.e., nanoparticles, nanotubes, and inverse opals. The optical absorption, photoelectrochemical, and photovoltaic properties of the QDSCs were characterized and the dependences of these properties on the QD deposition time and the TiO_2 nanostructure are discussed. To improve the photovoltaic performance of the CdSe QDSCs, surface passivation with a ZnS coating was introduced and Cu_2S counter electrodes were applied. All aspects of the photovoltaic performance, including the short-circuit photocurrent density, open-circuit voltage, fill factor, and efficiency, were found to be significantly improved by the surface modification with ZnS. For the counter electrode, the Cu_2S electrode was demonstrated to be more efficient than platinum against the polysulfide electrolytes usually used as redox couples in CdSe QDSCs. Moreover, CdS QD adsorption on the TiO_2 electrodes prior to CdSe QD adsorption also resulted in better solar cell performance. In addition, we found that the morphology of the TiO_2 electrodes had a great influence on the photovoltaic properties of the QDSCs. Finally, a power conversion efficiency as high as 4.9% was achieved for a combined CdS/CdSe QDSC under solar illumination of 100 mW/cm^2.

Q. Shen (✉) · T. Toyoda
Department of Engineering Science, Faculty of Informatics and Engineering,
The University of Electro-Communications, 1-5-1 Chofugaoka,
Chofu, Tokyo 182-8585, Japan
e-mail: shen@pc.uec.ac.jp; qingshen3@yahoo.co.jp

Q. Shen
PRESTO, Japan Science and Technology Agency, 4-1-8 Honcho,
Kawaguchi, Saitama 332-0012, Japan

Z. M. Wang (ed.), *Quantum Dot Devices*, Lecture Notes in Nanoscale Science and Technology 13, DOI: 10.1007/978-1-4614-3570-9_14,
© Springer Science+Business Media New York 2012

Introduction

The increasing demand for renewable and low-cost energy has engendered some outstanding research in the field of photovoltaics, especially, next generation solar cells. Potential candidates for next generation solar cells are dye-sensitized solar cells (DSCs). Much attention has been directed toward DSCs employing nano-structured TiO_2 photoanodes and organic-ruthenium dye molecules as light-harvesting media. The high porosity of nanostructured TiO_2 photoanodes enables a large concentration of the sensitizing dye molecules to be adsorbed. The attached dye molecules absorb light and inject electrons into the TiO_2 conduction band upon excitation. The electrons are then collected at a back conducting electrode, generating a photocurrent. DSCs exhibit high photovoltaic conversion efficiencies of about 11% and good long-term stability. In addition, they are relatively simple to assemble and are low cost [1–3]. However, in order to replace conventional Si-based solar cells in practical applications, further effort is needed to improve the efficiency of DSCs and also the production cost should be lowered.

One key factor in improving the performance of DSCs is the design of the photosensitizer. The ideal dye photosensitizer for DSCs should be highly absorbing across the entire solar light spectrum, bind strongly to the TiO_2 surface, and inject photoexcited electrons into the TiO_2 conduction band efficiently. Many different dye compounds have been designed and synthesized to fulfill the above requirements. It is likely that the ideal photosensitizer for DSCs will only be realized by co-adsorption of a few different dyes, for absorption of visible light, near infrared (NIR) light, and/or infrared (IR) light [4, 5]. However, attempts to sensitize electrodes with multiple dyes have achieved only limited success to date. Narrow-bandgap semiconductor quantum dots (QDs), such as CdS, CdSe, PbS, PbSe, and InAs, have also been the subject of considerable interest as promising candidates for replacing the sensitizer dyes in DSCs [6–26]. These devices are called QD-sensitized solar cells (QDSCs) [22, 27, 28]. Figure 14.1 shows the working principle of QDSCs, which is very similar to that of DSCs (only the sensitizer is changed from dyes to semiconductor QDs). A comparison of the working principles between QDSCs and DSCs was given by Hodes in his seminal review [29]. The use of semiconductor QDs as sensitizers has some advantages over the use of traditional dyes (such as Ru-polypyridine complexes and organic dyes) in solar cell applications [27, 28] due to the unique properties of QDs. First, the energy gaps of the QDs can be tuned by controlling their size, and therefore the absorption spectra of the QDs can be tuned to match the spectral distribution of sunlight. Second, the semiconductor QDs have large extinction coefficients due to the quantum confinement effect. Third, these QDs have large intrinsic dipole moments, which may lead to rapid charge separation. Finally, semiconductor QDs have the potential to generate multiple electron–hole pairs with one single-photon absorption [27, 28, 30], which would lead to incident photon-to-current (IPCE) efficiencies of over 100%. Therefore, it has been predicted theoretically that the maximum thermodynamic efficiency for photovoltaic devices with a single

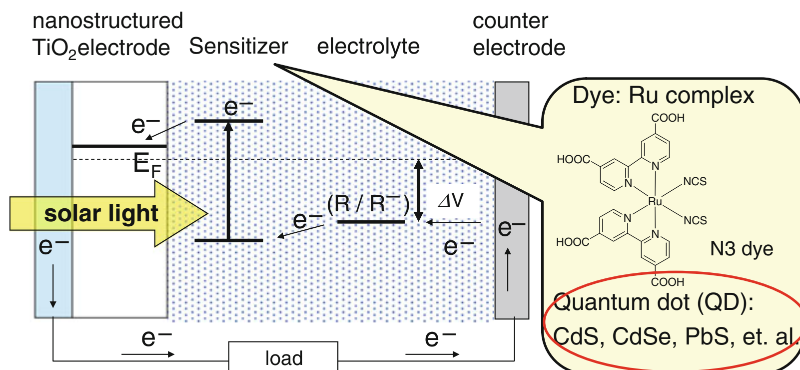

Fig. 14.1 Schematic illustration of the working principle of quantum dot-sensitized solar cells

sensitizer could be improved to as much as ~44% by employing semiconductor QDs [31]. Since QDSCs could be made very cheaply using simple chemical methods, the expectation was that QDSCs would become one of the promising next generation cost-effective high efficiency solar cells and would attract much attention.

However, at present, the maximum reported energy conversion efficiency of QDSCs is in the range of 4–5% [32, 33], which is significantly lower than the maximum efficiency of DSCs, which is more than 11%. Therefore, fundamental studies on the mechanism and preparation of QDSCs, including the development of materials, such as light-harvesting QDs, nanostructured photoanodes, electron and hole conductors and counter electrodes, and appropriate surface modification, are necessary and very important for boosting the photovoltaic performance of QDSCs.

One of the main factors limiting the photovoltaic performance of QDSCs is the assembly of the QDs onto the TiO_2 photoanode, which is related to the QD deposition method. Usually there are two different deposition methods for adsorbing QDs onto TiO_2 photoanodes. One is a pre-synthesis method, in which the semiconductor QDs are pre-synthesized and attached to the photoanodes directly or with the aid of bifunctional linker molecules [14, 15]. The other is the direct growth of the QDs on the TiO_2 photoanode surface by chemical bath deposition (CBD) [13, 34] or by successive ionic layer adsorption and reaction (SILAR) [33, 35]. So far, better photovoltaic performance has been achieved by the latter method because of the effective coverage of the QDs on the surface of the TiO_2 nanostructured photoanode.

The morphology of the TiO_2 nanostructured photoanodes is very important for satisfactory assembly of the QDs and for improving the energy conversion efficiency. On the other hand, another limiting factor for the overall photovoltaic performance of the QDSCs is the transport of photogenerated electrons through the TiO_2 nanostructure network. Thus, TiO_2 photoanodes with a higher degree of order than those made from a disordered assembly of nanoparticles, such as 1D

nanorods, nanowires, nanotubes, are desirable for achieving high efficiency QDSCs through improvements in the electron transfer rate and the effective QD assembly, as well as good hole electrolyte penetration [17–19, 21, 36, 37].

This chapter will focus on some of our recent studies on CdSe and combined CdS/CdSe QDSCs, of which the various morphologies of TiO_2 photoanodes, such as nanoparticulate, nanotube, and inverse opal, were employed [12, 13, 17–21, 38–40]. The optical absorption, photoelectrochemical properties, and photovoltaic characteristics of the QDSCs are discussed. It is very interesting that the photovoltaic properties of the QDSCs were found to depend greatly on the TiO_2 morphology. The effects of surface modification and the type of counter electrodes on the photovoltaic properties are also described. For further details on recent general studies of QDSCs, readers are referred to a number of excellent review articles listed at the end of the chapter [22, 26, 29].

Sample Preparation and Characterization

TiO_2 Nanoparticulate Photoanodes

TiO_2 nanoparticulate photoanodes were made from nanocrystalline particles with a diameter of 10–30 nm [41]. First, a TiO_2 paste was prepared by mixing the TiO_2 nanocrystals (with diameters of 15 nm) and polyethylene glycol (PEG) [molecular weight (MW) of PEG was 500,000] in pure water. The resultant paste was then deposited onto transparent conducting substrates [F-doped SnO_2 (FTO)]. The TiO_2 films were sintered in air at 450°C for 30 min to obtain good necking. Thus, highly porous nanostructured TiO_2 films with a continuous network (pore sizes were of the order of a few tens of nanometers) were formed, which was confirmed through scanning electron microscopy (SEM) images (Fig. 14.2). To improve the light absorption in the long wavelength region by enhancing the optical light path, a scattering TiO_2 layer made from larger nanoparticles (300–400 nm in diameter) was added to the TiO_2 photoanodes in some experiments [32].

TiO_2 Nanotube Photoanodes

Ti foils (0.25 mm, 99.7% purity, Aldrich) were degreased by sonicating in acetone, isopropanol, and methanol, rinsed with deionized water and dried in a nitrogen stream. The Ti foils were anodized in ethylene glycol containing 0.25 wt% NH_4F using a conventional two-electrode configuration with a platinum gauze as a counter electrode [42]. The applied voltage was changed from 20 to 50 V, and anodization was performed at different temperatures (from 10 to 40°C). After anodization, the samples were annealed at 480°C for 3 h in air. XRD patterns

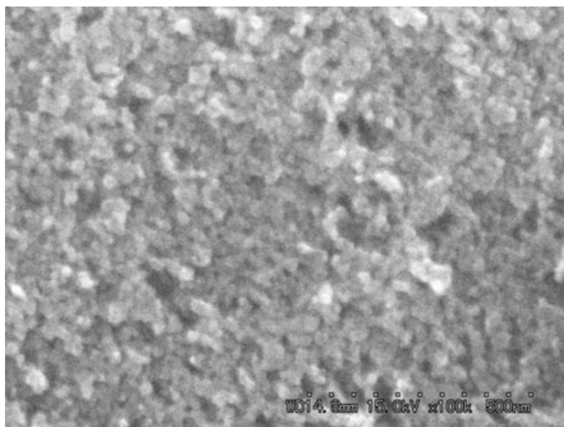

Fig. 14.2 SEM image of a nanostructured TiO_2 film made from nanoparticles

show that the crystal structure of the TiO_2 nanotubes was anatase. Figure 14.3 shows top (a), bottom (b), cross sectional (c), and lateral views of FESEM images of TiO_2 nanotubes prepared at a potential of 50 V for 1 h at 30°C. The average inner and outer diameters of the TiO_2 nanotubes are around 100 and 120 nm, respectively. The length of the TiO_2 nanotubes is about 10 μm. It was found that the diameters and lengths depend greatly on the applied potential and anodization temperature. Figure 14.4 shows top (a) and cross sectional (b) views of FESEM images of TiO_2 nanotubes prepared at a potential of 20 V for 1 h at 30°C. Figure 14.5 shows top views of FESEM images of TiO_2 nanotubes prepared at a potential of 20 V for 1 h at different temperatures. It was confirmed that both the diameters and lengths increased as the applied potential and anodization temperature increased.

TiO_2 Inverse Opal Photoanodes

Inverse opal TiO_2 films were prepared on fluorine-doped tin oxide (FTO)-coated glass by the replication of a self-organizing material used as a template [38, 39, 43]. Substrates were cleaned ultrasonically with soap, KOH, water, and methanol. Monodispersed polystyrene latex suspensions were sonicated for 30 min to break down the aggregated particles. The synthetic opal templates were assembled by immersing the FTO substrates vertically in a 0.1 wt% monodispersed polystyrene suspension and evaporating the solvent in an oven at 40°C for 1–2 days until the solvent had completely disappeared, leaving behind a colloidal crystal film on the substrate. Then TiO_2 was brought into the void of the template by the following method. A 10 μl drop of 2% $TiCl_4$ in methanol was added via a micropipette onto the 1.3×2.3 cm^2 colloidal crystal surface. After hydrolysis for 30 min, the sample was subsequently heated to 80°C in air for 10 min. This process was

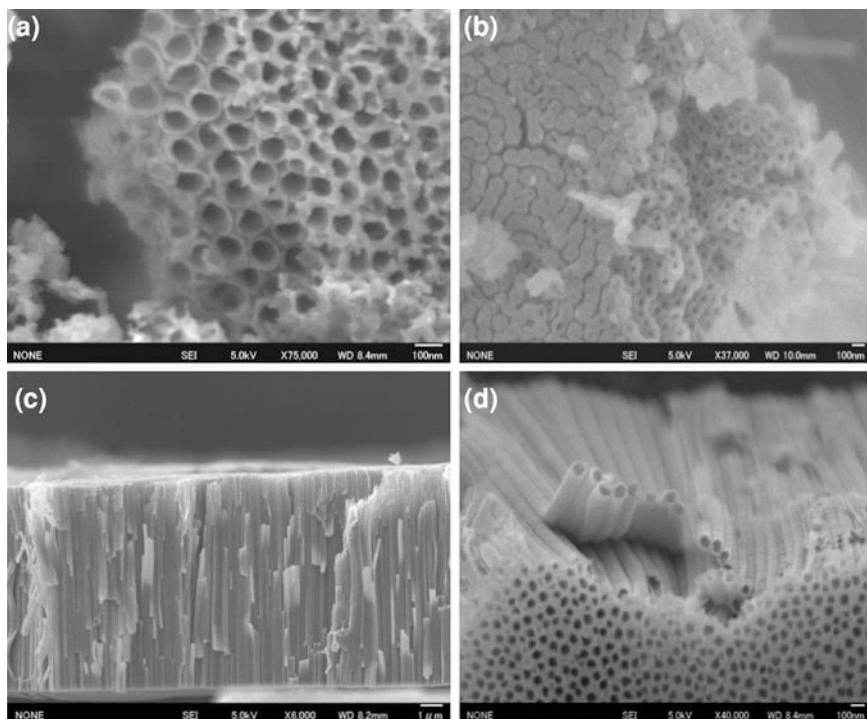

Fig. 14.3 *Top* (**a**), *bottom* (**b**), *cross sectional* (**c**), and lateral views of SEM images of TiO_2 nanotubes prepared at a potential of 50 V for 1 h at 30°C

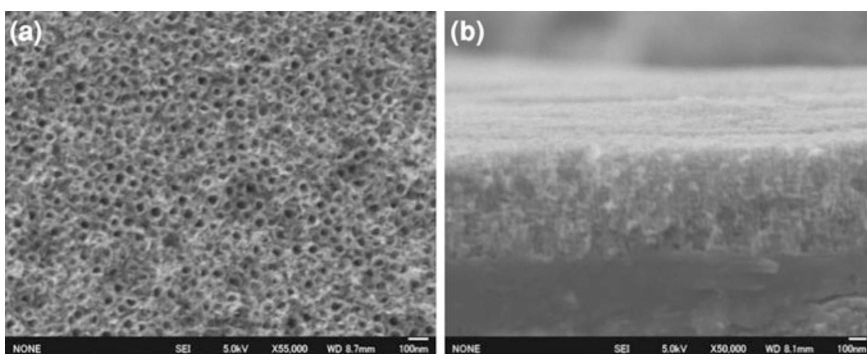

Fig. 14.4 *Top* (**a**), and *cross sectional* (**b**) views of SEM images of TiO_2 nanotubes prepared at a potential of 20 V for 1 h at 30°C

repeated several times to ensure the filling of all the voids. Finally, the sample was heated at 450°C for 1 h in air with a heating rate of 0.5°C/min to calcinate the template and anneal the TiO_2.

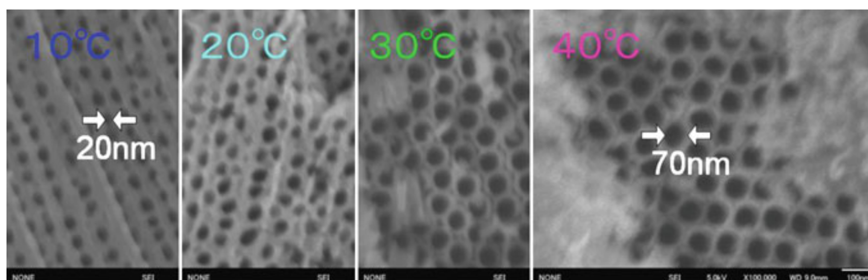

Fig. 14.5 *Top* views of SEM images of TiO_2 nanotubes prepared at a potential of 50 V for 1 h at different temperatures

The XRD pattern shows that the inverse opal TiO_2 has the crystalline structure of anatase. Typical SEM images of the latex sphere template, with sphere diameters of 309 nm, and the obtained TiO_2 inverse opal are shown in Fig. 14.6. The latex spheres are arranged in the fcc lattice (Fig. 14.6a) with a thickness (Fig. 14.6b), depending on the concentration of the original colloidal latex suspension, before the vertical immersion of the FTO substrate and evaporation of the aqueous solvent. After the calcination process, replication of this template with the titanium dioxide resulted in a honeycomb structure with an ordered hexagonal pattern of spherical pores that connected each sphere to its nearest neighbors, as shown in Fig. 14.6c. The diameter or center to center distance of the pores, referred to as the periodic lattice constant of the inverse opal TiO_2, was determined to be $\sim$270 nm (Fig. 14.6c) which shows the latex spheres had shrunk from their initial diameter of 309 nm. This structure also consists of several layers, connected to each other, as shown in Fig. 14.6d with a possible maximum thickness similar to the initial latex film. The thickness of the obtained TiO_2 inverse opal film was measured to be the same as that of the latex film, while thinner inverse opal films could be made using smaller amounts of $TiCl_4$.

Adsorption of CdSe QDs and Combined CdS/CdSe QDs

For combined CdS/CdSe QD-sensitized TiO_2 photoanodes, CdS QDs were first adsorbed using a CBD method before CdSe QD adsorption [16, 40]. CdS QDs were adsorbed from the common NH_3 bath with a solution composition of 20 mM $CdCl_2$, 66 mM NH_4Cl, 140 mM thiourea, and 0.23 M ammonia with a final pH $\sim$ 9.5 [16, 40, 44]. The TiO_2 electrodes were immersed in a container filled with the final solution. The adsorption was carried out at a constant temperature in the dark for various times.

CdSe QDs were adsorbed onto the TiO_2 nanostructured electrodes using CBD [13, 34]. First, for the Se source, an 80 mM sodium selenosulfate (Na_2SeSO_3) solution was prepared by dissolving elemental Se powder in a 200 mM Na_2SO_3

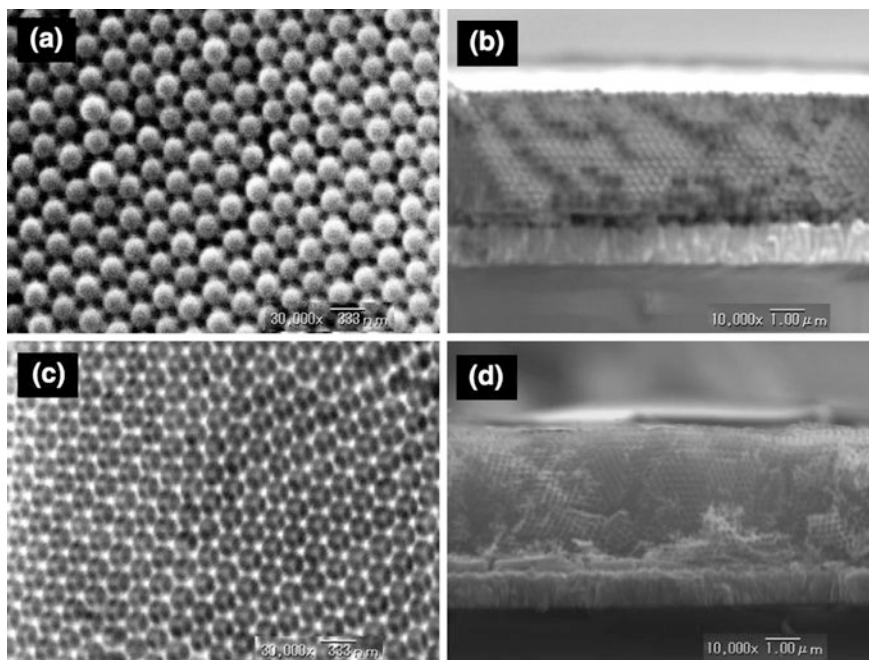

Fig. 14.6 SEM images of a latex sphere template (diameter of 309 nm) **a** surface, **b** cross section, together with the replicated inverse opal TiO_2, **c** surface, **d** cross section

solution. Second, 80 mM $CdSO_4$ and 120 mM of the trisodium salt of nitrilotriacetic acid ($N(CH_2COONa)_3$) were mixed with the 80 mM Na_2SeSO_3 solution in a volume ratio of 1:1:1. The TiO_2 films were placed in a glass container filled with the final solution at a constant temperature (from 2 to 40°C) in the dark for various times to promote CdSe adsorption. Afterwards the samples were rinsed with water and dried in an N_2 flow.

After the adsorption of CdSe QDs, the samples were coated with ZnS to surface passivate the QDs by SILAR for several times in 0.1 M $Zn(CH_3COO)_2$ and 0.1 M Na_2S aqueous solutions for 1 min for each dip [20, 45].

Optical Absorption Measurements

The optical absorption properties of nanostructured TiO_2 electrodes adsorbed with and without QDs were investigated using photoacoustic (PA) spectroscopy [46]. The scattering effects in the optical absorption by nanostructured TiO_2 electrodes and the adsorbed QDs can be minimized by employing the PA method [12, 13, 20]. A typical gas-microphone method was applied in the PA spectroscopic investigation [8, 46]. Figure 14.7 shows a schematic diagram of the PA spectrometer.

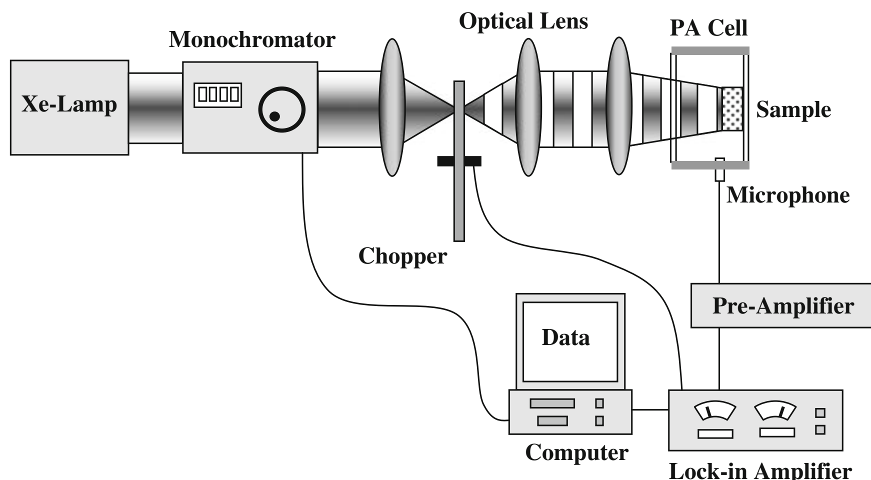

Fig. 14.7 Schematic diagram of a photoacoustic (PA) spectrometer, comprising a light source, monochrometer, mechanical chopper, photoacoustic cell, preamplifier, lock-in-amplifier, etc

The PA cell is composed of an aluminum cylinder with a small channel at the periphery in which a microphone is inserted. The inner volume of the cell is approximately 0.5 cm^3 and the cell is suspended by four rubber bands to prevent interference from external vibration. The cell window, made of quartz, is highly transparent throughout the observed wavelength range, and the sample holder can be easily removed from the cell to maintain the optical configuration. A 300 W Xe arc lamp is used as the light source. Monochromatic light is modulated at 33 Hz by the mechanical chopper. The modulated light is focused on the sample inside the PA cell and the PA signal is monitored with a microphone and amplified using a preamplifier and a lock-in amplifier. Spectra were measured at room temperature in the wavelength range of 250–800 nm and normalized using a PA spectrum obtained with a carbon black sheet.

Incident Photon-Current Conversion Efficiency (IPCE) and Photovoltaic Property Measurements

The IPCE and photovoltaic measurements were performed in a sandwich structured cell (i.e., in the two-electrode configuration) with a counter electrode. An FTO electrode with sputtered platinum (200 nm thick) (termed the Pt counter electrode) or a Cu_2S film on brass (termed the Cu_2S counter electrode) was used as the counter electrode. The electrolyte used was polysulfide solution (1 M Na_2S + 1 M S) for both CdSe and combined CdS/CdSe QDSCs. It is well known that the electrocatalytic activity of Pt in a polysulfide electrolyte is not

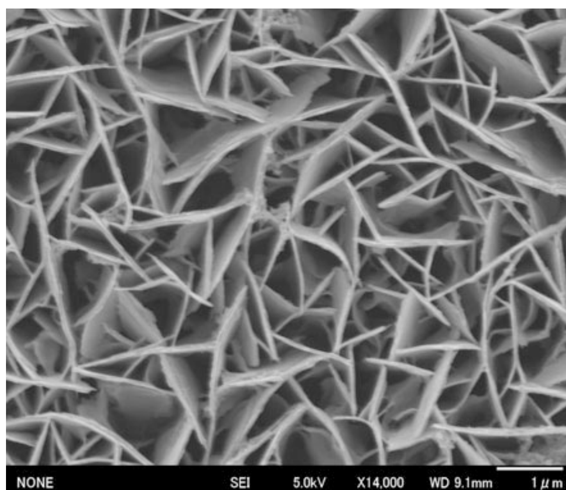

Fig. 14.8 SEM image of the surface of a Cu_2S counter electrode

satisfactory for photovoltaic cell applications and alternative counter electrode materials with higher activity such as Cu_2S and CoS have been reported by Hodes and co-workers [47, 48]. The higher electrocatalytic activities of these materials are due to a reduction in the charge transfer resistance between the redox couple and the counter electrode [23]. The Cu_2S counter electrodes were prepared by immersing brass in HCl solution at 70°C for 5 min and subsequently dipping them into polysulfide solution for 10 min [40, 47, 48], resulting in porous Cu_2S electrodes, as shown in Fig. 14.8. The solar cells were prepared by sealing the Cu_2S counter electrode and nanostructured TiO_2 electrode adsorbed with QDs using a silicone spacer ($\sim$50 μm) after the introduction of the polysulfide electrolyte.

The IPCE value, determined by the sensitizer's light-harvesting efficiency, the quantum yield for electron injection from the excited sensitizer to the conduction band of the semiconductor (TiO_2), and the collection efficiency of the injected electrons at the back contact, was measured from the short-circuit photocurrent with a zero shunt meter using the same apparatus and conditions used for the PA measurements shown in Fig. 14.7. For the IPCE measurement, the incident light was directly irradiated onto the sample, without modulation through the chopper. The incident light intensity was measured by an optical powermeter. The conditions for all the measurements (optical configuration, path-length, irradiation area, excitation light intensity, etc.) were fixed as much as possible to compare the IPCE values and spectra directly. The photovoltaic properties were characterized under illumination of one sun (AM 1.5: 100 mW/cm^2) using a solar simulator by measurements of the photocurrent versus photovoltage to investigate the short-circuit current (J_{sc}), open-circuit voltage (V_{oc}), fill factor (FF), and photovoltaic conversion efficiency (η), together with the series and parallel resistance values.

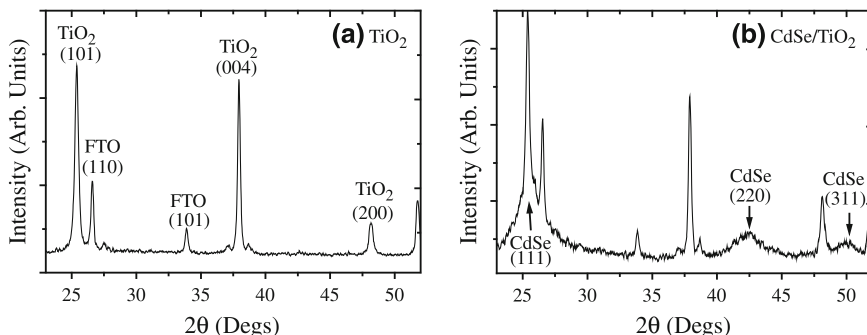

Fig. 14.9 XRD patterns of TiO_2 electrodes A (15 nm) **a** without, and **b** with CdSe deposition (at 20°C for 120 h) [12]

Results and Discussion

CdSe and Combined CdS/CdSe QDSCs Employing TiO_2 Nanoparticulate Photoanodes

TiO_2 nanoparticulate photoanodes are most easily prepared and most commonly used for QDSCs. We used these photoanodes for CdSe and combined CdS/CdSe QDSCs. In this section, we will describe the dependences of the optical absorption, photoelectrochemical, and photovoltaic properties of the QDSCs on the QD deposition time. We will discuss how ZnS surface modification and the type of counter electrode influence the photovoltaic performance of QDSCs.

Figure 14.9 shows the X-ray diffraction (XRD) patterns of TiO_2 nanoparticulate electrodes without (a) and with (b) CdSe deposition (120 h) at 20°C, respectively [12]. The pattern without CdSe deposition (Fig. 14.9a) can be matched with the anatase form of TiO_2 and the FTO substrates. The formation of CdSe QDs on the TiO_2 electrodes can be confirmed clearly in Fig. 14.9b, although the peak at $2\theta = 25.5°$ is substantially broadened at the base. In Fig. 14.9b, two new diffraction peaks appear at $2\theta = 42.4°$, and 50.0°. These three peaks correspond to the (111), (220), and (311) reflections of the cubic CdSe crystal [34]. The broadening of the peaks implies that the size of the CdSe particles is very small. The average size of the CdSe crystals was estimated to be approximately 6 nm from the full-width at half maximum of the diffraction peaks, using the Scherrer equation [49].

Figure 14.10 displays SEM micrographs of TiO_2 photoanode surfaces with different CdSe deposition times ((a) without, (b) 5 h, (c) 13 h, and (d) 60 h [12]). It is clearly seen that small particles (white dots) were formed after CdSe deposition and that the number of particles increases with increased deposition time. From SEM images on a high magnification scale, spherical particles with an average size of a few tens of nm can be seen. This size deviates greatly from the

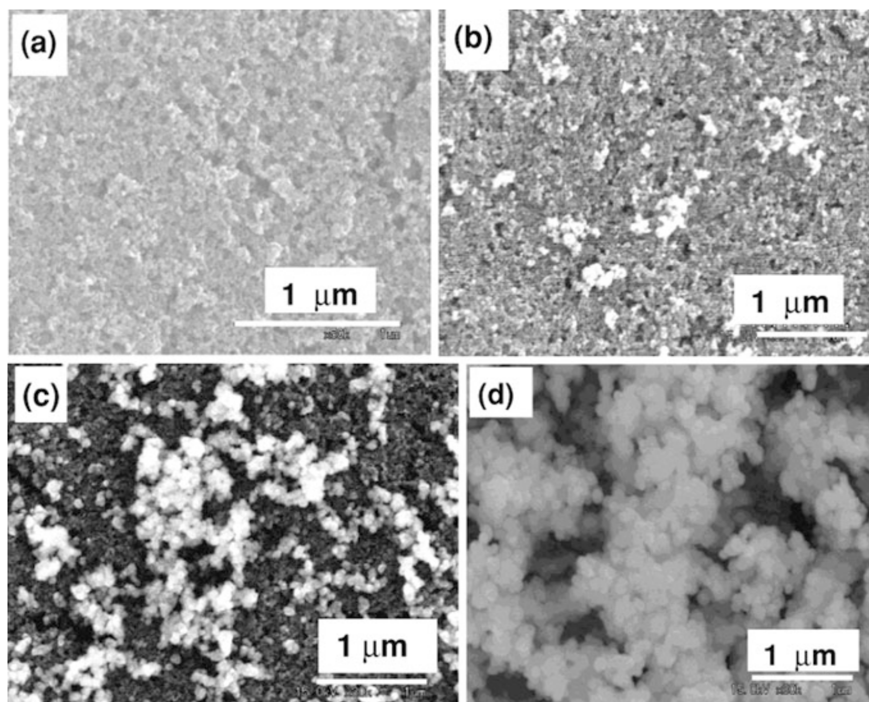

Fig. 14.10 SEM images of TiO_2 nanoparticulate electrode surfaces with different CdSe deposition times (**a** without, **b** 5 h, **c** 13 h, and **d** 60 h) [12]

average size calculated from the XRD results. The CdSe particles observed in the SEM micrographs can be considered to be secondary particles of aggregations of small CdSe QDs. This result can also be confirmed from the results of the optical absorption spectra measured by PA spectroscopy, which is shown below. TEM observations also confirmed that the average size of cdSe QDs is a few nm.

Figure 14.11a shows the PA spectra of TiO_2 electrodes with CdSe adsorption for different deposition times before the ZnS coating. The spectra are normalized at the photon energy of 3.75 eV. Compared with the PA spectrum of a bare TiO_2 electrode, optical absorption in the visible light region due to the adsorbed CdSe QDs can be observed. With increasing adsorption time, a redshift of the optical absorption shoulder point (indicated by arrows) can be clearly observed, implying growth of the CdSe QDs. An increase in the PA intensity at the shoulder with increasing adsorption time can also be observed, indicating an increase in the amount of CdSe adsorbed. Relative to the bandgap energy of 1.73 eV (E_g) for bulk CdSe, as shown in Fig. 14.11a the optical absorption shoulder points in the PA spectra of the CdSe-adsorbed samples show blueshifts, which is indicative of the quantum confinement effect. This implies that the radii of the CdSe QDs are smaller than the Bohr radius of the exciton in bulk CdSe, i.e., 5.6 nm. We assumed

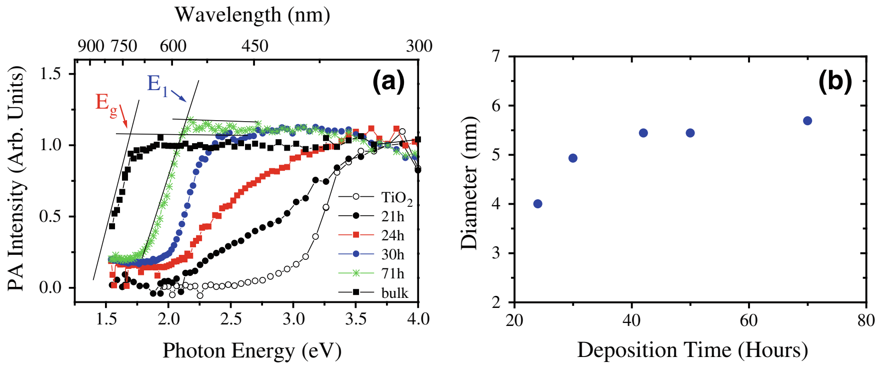

Fig. 14.11 **a** Photoacoustic (PA) spectra of the nanostructured TiO_2 electrodes with and without CdSe adsorption, as well as the PA spectrum of bulk CdSe. E_1 is the photon energy of the optical absorption shoulder of each PA spectrum and Eg is the bandgap energy of bulk CdSe. **b** Variation of the average diameter of the CdSe QDs with adsorption time

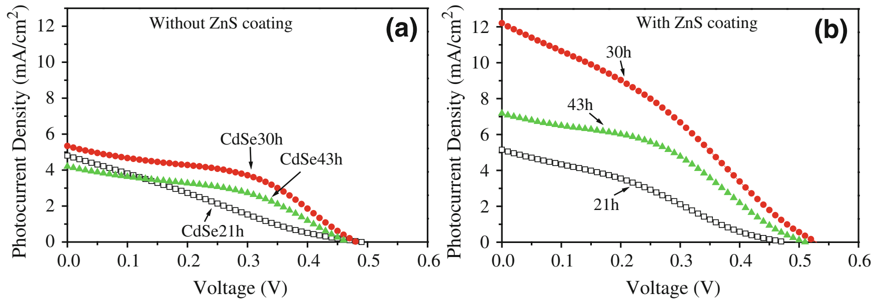

Fig. 14.12 Photocurrent density-photovoltage characteristics of CdSe quantum dot-sensitized solar cells with different adsorption times (21, 30, and 43 h) without a ZnS coating (**a**), and with a ZnS coating (**b**) [20]

that the photon energy of the optical absorption shoulder point corresponds to the lowest excitation energy E_1 of the CdSe QDs [12, 13, 20]. The average diameter of the CdSe QDs for each deposition time can be estimated using Eq. 14.1 with an effective mass approximation [12, 13, 20, 49, 50]:

$$\Delta E = E_1 - E_g = \frac{h^2}{8r^2}\left(\frac{1}{m_e} + \frac{1}{m_h}\right) \tag{14.1}$$

where ΔE is the bandgap shift, r is the QD radius, and m_e, m_h, and m_0 are the effective electron mass, the hole mass, and the electron rest mass, respectively ($m_e = 0.13\ m_0$, $m_h = 0.44\ m_0$, and $m_0 = 9.11 \times 10^{-31}$ kg) [49]. The dependence of the average diameter on the adsorption time is shown in Fig. 14.11b. It can be seen that the QDs grow rapidly during the initial adsorption process, and, after a certain time, the crystal growth rate slows down [51]. When the adsorption time is sufficiently long, the QD diameter becomes constant at about 5.5 nm.

This result is in good agreement with that estimated from the XRD measurements [12] and also with that obtained from TEM observations. The PA spectra of the CdSe QDs with the ZnS coating were also measured and no changes in the PA spectra in the wavelength range of 320–800 nm were observed after the ZnS coating.

The photocurrent density–voltage (*J–V*) curves of the sandwich-type CdSe QDSCs with different CdSe adsorption times were measured under illumination of one sun (AM1.5, 100 mW/cm^2), in which Pt counter electrodes were used. Figure 14.12a and b show the *J–V* characteristics of the CdSe QDSCs with adsorption times of 21, 30, and 43 h, without and with the ZnS coating, respectively [20]. The dependences of the values of the short-circuit current density (J_{sc}), the open-circuit voltage (V_{oc}), the FF, and the photovoltaic conversion efficiency (η) on the CdSe deposition time are shown in Fig. 14.13. For the electrodes without the ZnS coating, J_{sc} increases as the adsorption time increases and has a maximum value of 5.53 mA/cm^2 at 24 h. It then decreases as the adsorption time increases and has a value of around 4.3 mA/cm^2 at longer adsorption times. On the other hand, V_{oc} decreases a little from 0.49 to 0.46 V and the FF remains almost constant (0.42–0.43) with increasing adsorption time up to 48 h. As a result, with increasing CdSe adsorption time, the photovoltaic conversion efficiency η first increases, and then decreases after reaching a maximum value of 1.16% for 24 h CdSe adsorption. For the CdSe QDSCs with the ZnS coating, as shown in Fig. 14.13, J_{sc} increases with adsorption time and has a maximum value of 12.2 mA/cm^2 at an adsorption time of 30 h. Then, J_{sc} decreases with further increases in adsorption time and at 48 h reaches a value of about 6.5 mA/cm^2. V_{oc} increases with adsorption time and reaches a maximum value of 0.56 V for 24 h adsorption, after which it decreases. The FF is around 0.3–0.4. As a result, the photovoltaic conversion efficiency η first increases with increasing CdSe adsorption time, and has a maximum value of 2.02% at 30 h, and then decreases to 1.29% at 48 h. For both without and with the ZnS coating, the photovoltaic conversion efficiency η depends predominantly on the short-circuit current density J_{sc} as shown in Fig. 14.13 and there is an optimum CdSe adsorption time for achieving the maximum energy conversion efficiency. We can understand the results as follows. The amount of CdSe adsorbed onto the electrodes increases as the adsorption time increases; thus, initially, J_{sc} increases with increasing adsorption time. However, there is also an increase in the CdSe–CdSe boundaries present in the nanostructured TiO_2 electrodes with longer CdSe adsorption times. The increased CdSe–CdSe boundaries cause an increase in the loss of electrons and holes during their transport from the CdSe QDs to the TiO_2 nanoparticles and the electrolyte, due to increased exciton recombination in the QDs before the electrons and holes can completely separate, and also due to increased trapping at the interfaces. Thus, J_{sc} decreases for longer CdSe adsorption times and there is an optimum adsorption time at which the maximum values of J_{sc} and η occur. The FFs of the CdSe QDSCs in this study are poor compared to those of the DSCs, which are normally around 0.7. The poor FFs are attributable to resistance losses in the system, such as those at the CdSe/TiO_2 interface, the CdSe/CdSe interface, the CdSe/polysulfide electrolyte interface, the Pt counter electrode/polysulfide

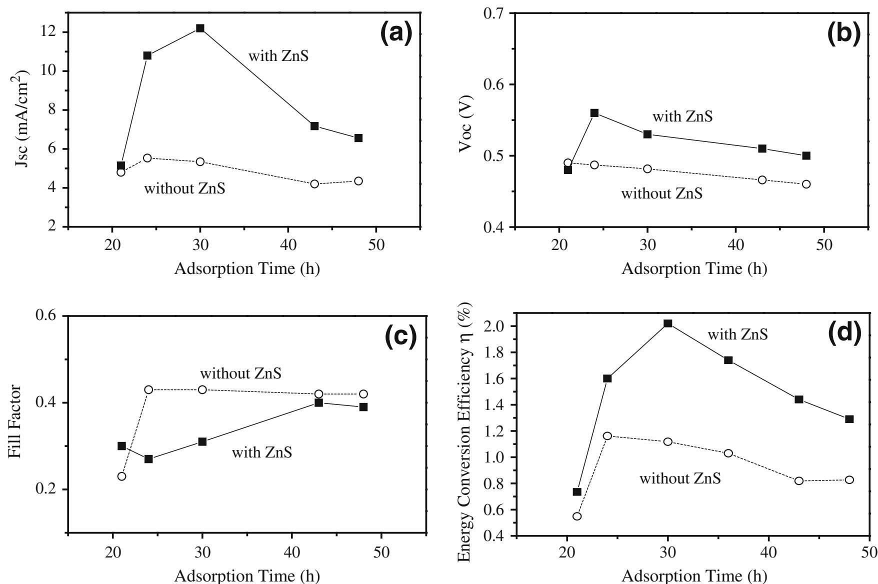

Fig. 14.13 Dependences of the short-circuit current density Jsc (**a**), open-circuit voltage Voc (**b**), fill factor FF (**c**), and (**d**) the photovoltaic conversion efficiency of CdSe quantum dot-sensitized solar cells on the CdSe adsorption time with (*square*) and without (*circle*) a ZnS coating

electrolyte interface, and those in the electrolyte. It is worth noting that the Pt counter electrode used here is not a good electrocatalyst for the polysulfide redox reaction, as reported by Hodes and co-workers [47, 48]. We confirmed that much higher FF and much higher photovoltaic conversion efficiency can be achieved by using an optimum counter electrode for the polysulfide solution, such as Cu_2S, as shown below [23, 40].

Compared to the CdSe QDSCs without the ZnS coating, the values of J_{sc} for the electrodes with the ZnS coating increase dramatically and almost double (e.g., from 5.34 to 12.2 mA/cm^2 for the electrodes with 30 h CdSe adsorption) for those electrodes with optimum CdSe adsorption times, as shown in Fig. 14.13. V_{oc} also increases greatly as a result of the ZnS coating (e.g., from 0.49 to 0.56 V for the electrodes with 24 h CdSe adsorption). On the other hand, the FFs of the coated samples decrease a little compared to the samples without coating. Figure 14.13d shows the dependences of the photovoltaic conversion efficiencies of the CdSe QDSCs on the CdSe adsorption time without and with the ZnS coating. The maximum value of η increases from 1.16 to 2.02% after the ZnS coating. The above results can be explained as follows. One of the main effects of the ZnS coating is to passivate the surface states of CdSe, which results in suppression of the surface trapping of photoexcited electrons and holes in the CdSe QDs. Thus, the photoexcited electrons can transfer efficiently into the TiO_2 conduction band, and a higher photocurrent density J_{sc} is obtained. This is also demonstrated by the large increase in the IPCE values of the CdSe QDSCs with the ZnS coating

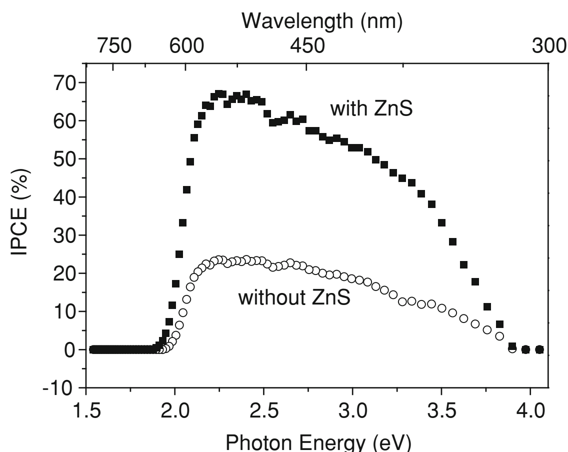

Fig. 14.14 The incident photon to current conversion efficiency (IPCE) spectra of CdSe quantum dot-sensitized solar cells for 30 h CdSe adsorption with (*square*) and without (*circle*) a ZnS coating [20]

compared to those without it. As an example, Fig. 14.14 shows the IPCE spectra of the CdSe QDSCs with and without the ZnS coating for 30 h CdSe adsorption. The IPCE peak value increases from 23 to 67% after the ZnS coating. Accordingly, V_{oc} is also enhanced because the quasi-Fermi level in the TiO_2 increases with the increase in density of the electrons injected from the CdSe QDs into the TiO_2 conduction band [52]. The ZnS coating can also be considered to be a potential barrier at the CdSe/electrolyte interface, since the ZnS band gap of 3.8 eV is much larger than that of CdSe. Consequently, the leakage of electrons from the CdSe into the electrolyte can be suppressed. This might also help to enhance both J_{sc} and V_{oc}. Based on the above interpretation, an increase in the FF of the CdSe QDSCs with the ZnS coating is predictable. However, the ZnS coating resulted in a small decrease in the FF. One possible reason for this phenomenon is blocking of the mesopores in the nanostructured TiO_2 electrodes by the ZnS coating. Thus, the electrolyte in the pores would decrease, resulting in a small decrease in the FF. Recently, through electrochemical (including impedance spectroscopy) and ultra-fast photoexcited carrier dynamic measurements, Guijarro et al. have demonstrated that the ZnS layer plays a 3-fold role: (1) passivation of the QDs, (2) blockage of the TiO_2 surface, and (3) increase of the electron injection rate [53].

To improve the photovoltaic performance of QDSCs based on a CdSe QD sensitizer on a nanostructured TiO_2 electrode, Hodes and co-workers proposed the idea of adsorbing a pre-adsorbed layer of CdS QDs between the TiO_2 and the CdSe QDs (termed the combined CdS/CdSe QDs) [16]. This was then developed by other groups [54]. We investigated the detailed function of the combined CdS/CdSe QD sensitizer on the performance of the QDSCs, together with basic studies of the optical absorption and photocurrent characteristics [40]. Optical absorption spectra were measured using PA spectroscopy and the average diameter of the CdSe QDs was determined from the optical spectra using the effective mass approximation equation as described above. The dependence of the average diameter on the CdSe adsorption time is shown in Fig. 14.15, both for combined

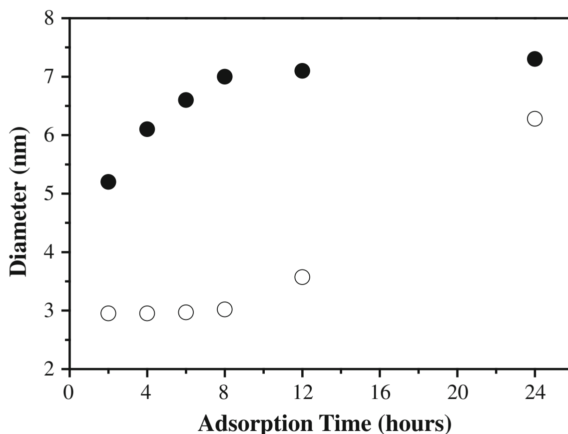

Fig. 14.15 Dependence of the average diameter on the adsorption time, both of combined CdS/CdSe (black dot) and CdSe without a pre-adsorbed CdS layer (*circle*) [40]

CdS/CdSe (black dot) and CdSe without a pre-adsorbed CdS layer (circle) (the CdS deposition was carried out at 10°C for 40 min.) [40]. It can be observed that the CdSe QDs on the nanostructured TiO_2 electrodes with a pre-adsorbed CdS layer grow rapidly during the initial adsorption process (less than 2 h adsorption). After a certain time, the crystal growth rate slows down, which is similar to the previous results [51]. When the adsorption time is sufficiently long (in this case ~24 h), the average diameter of the CdSe QDs becomes constant at about 7.1 nm. On the other hand, it can be observed that the CdSe QDs adsorbed on the nanostructured TiO_2 electrodes without a pre-adsorbed CdS layer show very slow growth or no growth during the initial adsorption process (less than 8 h). Therefore, the crystal growth rate of CdSe QDs adsorbed on a TiO_2 electrode with a pre-adsorbed CdS layer is faster than that of CdSe QDs adsorbed on the TiO_2 electrodes without a pre-adsorbed CdS layer. There are several possibilities for the faster crystal growth rate of CdSe QDs adsorbed on the nanostructured TiO_2 electrode with a pre-adsorbed CdS layer. First, it is possible that the active CdSe QDs form from the excess Cd remaining after CdS adsorption directly on the nanostructured TiO_2 electrode [16]. This suggests that CdS QDs act as a seed layer for subsequent CdSe growth [54]. The second possibility is that the passivation effect of CdS QDs on the nanostructured TiO_2 surface reduces defects or dislocations. Thirdly, CdSe QDs are grown on an assembly of CdS QDs, indicating that the growth on a similar crystal structure (or close lattice constant) is different from the growth on TiO_2 [40].

Figure 14.16a shows the IPCE spectra of the nanostructured TiO_2 electrodes adsorbed with combined CdS/CdSe QDs for different adsorption times, together with that adsorbed with CdS QDs only. The pre-adsorption time for CdS QDs was fixed at 40 min. Photoelectrochemical current in the visible light region due to the adsorbed CdSe QDs can be observed, indicating photosensitization by the combined CdS/CdSe QDs. With increasing adsorption time, a redshift in the photoelectrochemical current can be clearly observed, implying the growth of

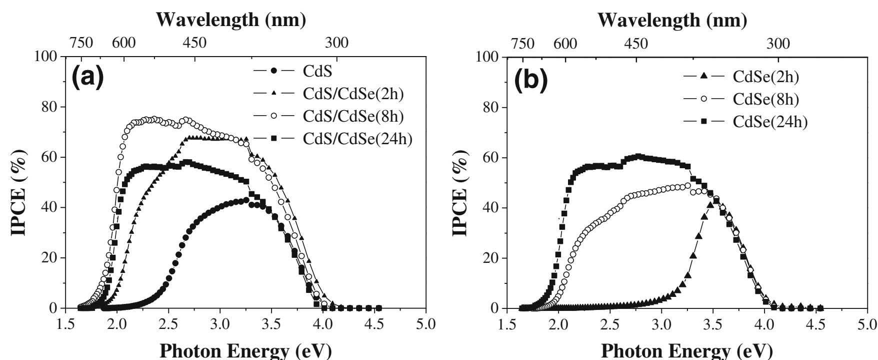

Fig. 14.16 **a** IPCE spectra of nanostructured TiO_2 electrodes adsorbed with combined CdS/CdSe QDs for different adsorption times together with that adsorbed with CdS QDs only. **b** IPCE spectra of the nanostructured TiO_2 electrodes adsorbed with CdSe QDs without a pre-adsorbed CdS layer for different adsorption times [40]

CdSe QDs. The IPCE peak value increases with increasing adsorption time up to 8 h (~75%), then decreases until 24 h adsorption owing to the increase in recombination centers or interface states, together with a decrease in the energy difference between the LUMO in CdSe QDs and the bottom of the conduction band of TiO_2. Also, a comparison between the adsorption of CdSe QDs on the TiO_2 electrodes with and without the pre-adsorbed CdS layer was carried out to evaluate the difference in IPCE spectra. For that, Fig. 14.16b shows the IPCE spectra of the nanostructured TiO_2 electrodes adsorbed with CdSe QDs without a pre-adsorbed CdS layer for different adsorption times. Photoelectrochemical current in the visible light region due to the adsorbed CdSe QDs can be observed in Fig. 14.16b, also indicating photosensitization by the CdSe QDs. With increasing adsorption time, a redshift in the photoelectrochemical current can be clearly observed, implying the growth of CdSe QDs. However, the appearance of the spectrum in Fig. 14.16b is different from that of the combined CdS/CdSe QDs, namely in the reduction of the maximum IPCE value (~60%) and the adsorption time dependence of the spectrum shape. These results demonstrate that the spectral response of the IPCE is enhanced with combined CdS/CdSe sensitization rather than single CdSe QD sensitization, indicating the possibility of a reduction in recombination centers and interface states owing to possible active CdSe QDs being formed by the excess Cd remaining after CdS adsorption and the passivation effect of CdS QDs on the nanostructured TiO_2 surface.

Figure 14.17 illustrates the photovoltaic parameters [(a) J_{sc}; (b) V_{oc}; (c) FF; (d) η] of combined CdS/CdSe QD-sensitized (black dot) and CdSe QD-sensitized (circle) solar cells as a function of CdSe QD adsorption time [40]. A Cu_2S counter electrode was used in each case. It can be seen that the parameter J_{sc} in combined CdS/CdSe QDSCs increases with increasing CdSe QD adsorption time up to 8 h. On the other hand, V_{oc} and FF are independent of adsorption time. The performance of solar cells improves with increasing adsorption time up to 8 h mainly

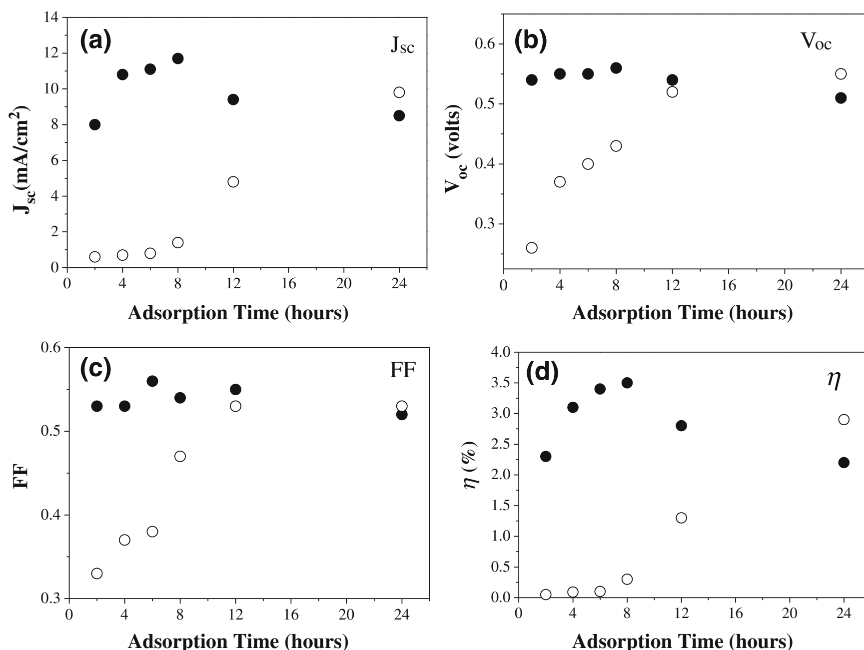

Fig. 14.17 Dependence of the photovoltaic parameters on the adsorption time, both of combined CdS/CdSe (black dot) and CdSe without a pre-adsorbed CdS layer (*circle*) (**a** J_{sc}; **b** V_{oc}; **c** FF; **d**) [40]

due to the increase in the amount of CdSe QDs, but also to the improvement in crystal quality and decrease in interface states. However, the increase in adsorption time after more than 8 h leads to deteriorations in J_{sc} and V_{oc}. High adsorption times for the CdSe QDs might cause an increase in recombination centers, poor penetration of the CdSe QDs, and a decrease in the energy difference between the LUMO in the CdSe QDs, and the bottom of the conduction band in TiO_2. Therefore, η of the combined CdS/CdSe QD-sensitized solar cell shows a maximum of 3.5% at 8 h adsorption time. On the other hand, J_{sc} and η below the CdSe QD adsorption time of 8 h without a pre-adsorbed CdS layer show very small values close to zero, indicating a very small amount of CdSe QD adsorption similar to the results of the PA and IPCE characterizations. We can observe that J_{sc}, V_{oc}, FF, and η in CdSe QDSCs without a pre-adsorbed CdS layer increase with increasing adsorption time up to 24 h, indicating differences in the crystal growth and the formation of recombination centers in the combined CdS/CdSe and CdSe QDs. It is worth noting that, by using the Cu_2S counter electrode, FF is as high as 0.55, which is much better than those obtained with a Pt counter electrode shown earlier (Fig. 14.13c). Recently, by employing a scattering layer in the TiO_2 nanostructured electrode, the photovoltaic properties of combined CdS/CdSe QDSCs have been improved and a maximum efficiency as high as 4.9% was achieved [32]. As far as we know, this value of the power conversion efficiency is the best result for CdSe and combined CdS/CdSe QDSCs reported up to now.

CdSe QDSCs Employing TiO_2 Nanotube Photoanodes

To date, only a few studies concerned with the photosensitization of TiO_2 nanotubes prepared on Ti foils by CdS, CdSe and CdTe QDs have been reported [36, 55–57]. Almost all were carried out in a three-electrode configuration and the maximum observed photocurrent values, J_{max}, under 100 mW/cm^2 white light illumination and 0 V bias versus a reference electrode were reported. Grimes and co-workers attained a J_{max} of 2.5 mA/cm^2 when using CdS QDs as sensitizers [55] and 0.44 mA/cm^2 when using CdTe QDs as sensitizers [56]. Kamat and co-workers achieved a J_{max} of 6.1 mA/cm^2 using CdS QDs as sensitizers [36]. Very recently, Lee and co-workers reported that they attained an IPCE peak value of 36% for a sandwich-structured solar cell consisting of CdSe QD-sensitized TiO_2 nanotubes [57]. However, the photovoltaic properties of QD-sensitized TiO_2 nanotube electrodes on Ti substrates in a sandwich structure have not yet been reported. Recently, we proposed a novel CdSe QDSC employing TiO_2 nanotubes, without the use of FTO and Pt [21]. A highly ordered TiO_2 nanotube film was prepared on a Ti foil using an electrochemical anodizing method as mentioned in [21]. The 1D tubular structure of TiO_2 nanotubes is useful for separating and transporting electrons to the Ti substrate. In addition, Ti has higher electronic conductivity and is much cheaper than FTO substrates, which will be advantageous for the production of low-cost large-area solar cells. One key factor in our novel QDSC is that a Cu_2S film with a ring shape, prepared on a brass sheet, was used as the counter electrode. The preparation method for the Cu_2S counter electrode was very easy and the production cost was very low. The ring-shaped Cu_2S counter electrode was prepared as follows: A brass plate with a hole (diameter: 5.5 mm) was etched in an HCl solution for 5 min. Then, Scotch tape with a hole (diameter: 7 mm) was used as a frame on the above brass plate, and only the ring region (with inner and outer diameters of 5.5 and 7 mm, respectively) on the brass plate was reacted with a polysulfide solution (1 M Na_2S and 1 M S) for 5 min to produce the Cu_2S film. Finally, a glass sheet was glued on the brass plate to function as a window in the counter electrode, through which the light was incident. For the photovoltaic properties and IPCE measurements, sandwich-structured solar cells as shown in Fig. 14.18 were used.

Figure 14.19 shows SEM images of the surface and a cross section of the TiO_2 nanotube electrode after CdSe QD adsorption for 24 h. The TiO_2 nanotubes are fully covered with CdSe QDs both on the surface and in the depth direction. Figure 14.20 shows the PA spectra of the TiO_2 nanotube electrode before and after CdSe adsorption for 12 and 48 h, respectively [21]. Compared with the PA spectrum of a bare TiO_2 nanotube electrode, optical absorption in the visible light region due to the adsorbed CdSe QDs can be clearly observed. Optical shoulders (indicated by the arrows) can be observed in the PA spectra of the CdSe-adsorbed samples, which are considered to correspond to the first excitation energy, E_1, of the CdSe QDs. Relative to the bandgap energy of 1.73 eV for bulk CdSe, E_1 exhibits a blueshift, which is indicative of the quantum confinement effect.

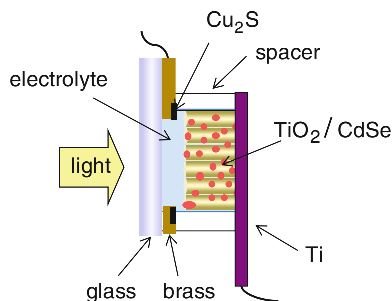

Fig. 14.18 Schematic illustration of the sandwichstructured QD-sensitized TiO_2 nanotube solar cells with a ring shaped Cu_2S counter electrode

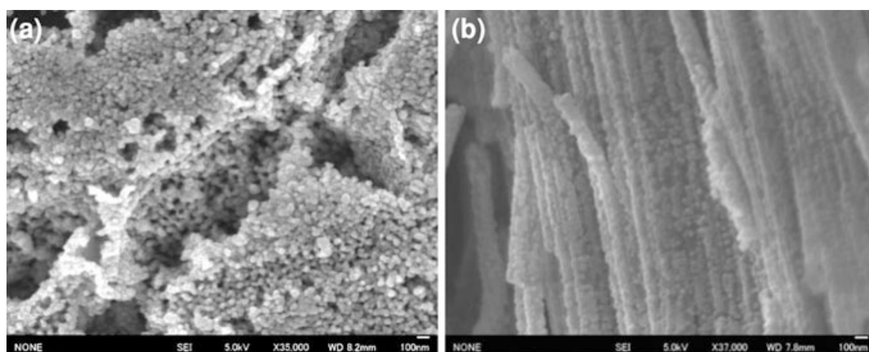

Fig. 14.19 SEM images of the surface **a** and a cross section, **b** of the TiO_2 nanotube electrode after CdSe QD adsorption for 24 h [21]

The average sizes of the CdSe QDs were calculated using an effective mass approximation [20, 49, 50], and were found to increase from 4.8 to 6 nm as the CdSe deposition time increased from 12 to 48 h.

Figure 14.21a shows the IPCE spectra of the samples for different CdSe adsorption times. There is a redshift in the IPCE spectra with increasing adsorption time, which is consistent with the redshift in the optical absorption spectra with increasing adsorption time shown in Fig. 14.20. The IPCE peak value increases with increasing adsorption time and a maximum of 65% is achieved for 24 h adsorption, and then decreases for longer adsorption times. As the adsorption time increases, the amount of CdSe adsorbed onto the electrodes increases; thus, initially, IPCE increases with increasing adsorption time. However, there is also an increase in the CdSe–CdSe boundaries present in the TiO_2 electrodes with longer CdSe adsorption times. The increased CdSe–CdSe boundaries cause an increasing loss of electrons and holes during their transport from the CdSe QDs to the TiO_2 nanotubes and the electrolyte, due to increased exciton recombination in the QDs before the electrons and holes can completely separate, and also due to increased trapping at the

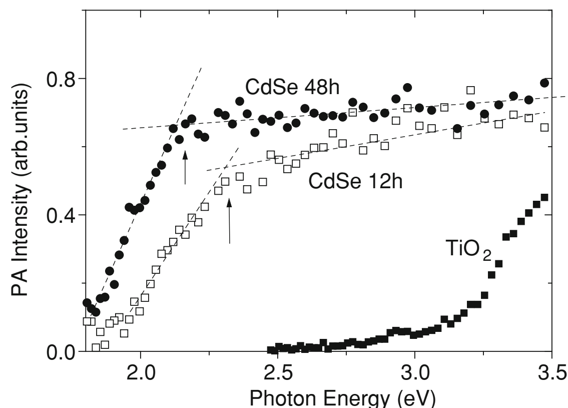

Fig. 14.20 Photoacoustic (PA) spectra of TiO_2 nanotube electrodes before and after CdSe QD adsorption for 12 and 48 h, respectively [21]

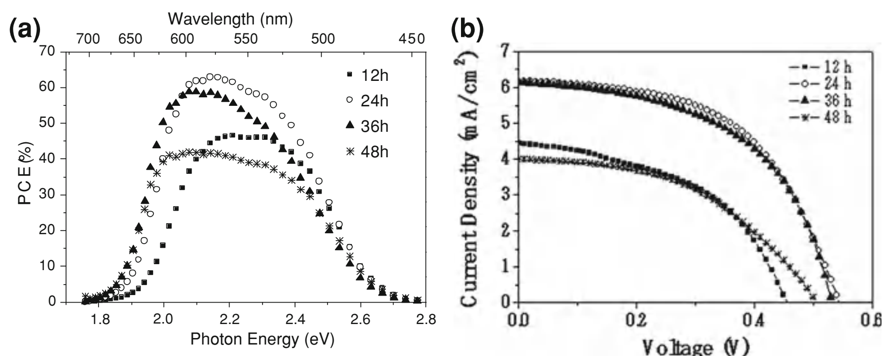

Fig. 14.21 **a** The incident photon to current conversion efficiency (IPCE) spectra of CdSe quantum dot-sensitized TiO_2 nanotube solar cells. **b** Photocurrent density-photovoltage characteristics of CdSe quantum dot-sensitized TiO_2 nanotube solar cells [21]

interfaces. Thus, IPCE decreases for longer CdSe adsorption times and there is an optimum adsorption time at which the maximum value of IPCE occurs.

Figure 14.21b shows the photovoltaic characteristics of sandwich-type solar cells with different adsorption times. The values of J_{sc}, V_{oc}, FF, and η, are given in Table 14.1. As the adsorption time increases, J_{sc}, V_{oc}, and FF increase and show maximum values of 6.2 mA/cm^2, 0.54 V, and 0.53 at 24 h, respectively. Then J_{sc}, V_{oc}, and FF decrease for longer adsorption times. As a result, with increasing CdSe adsorption time, the photovoltaic conversion efficiency η first increases, and then decreases after reaching a maximum value of 1.8% for 24 h CdSe adsorption. It should be noted that the FFs of the QDSCs have been improved greatly to be as high as 0.53 by using the Cu_2S counter electrode compared to those (about 0.4) using the Pt counter electrodes, although the area of the Cu_2S counter electrode is

Table 14.1 Photovoltaic properties of CdSe QD-sensitized TiO_2 nanotube solar cells with different adsorption times. J_{sc}, V_{oc}, FF and are the short-circuit current density, open-circuit voltage, fill factor, and photovoltaic conversion efficiency, respectively

Adsorption time (h)	J_{sc} (mA/cm^2)	V_{oc} (V)	FF	(%)
12	4.5	0.46	0.48	0.98
24	6.2	0.54	0.53	1.8
36	6.2	0.53	0.53	1.7
48	4.0	0.51	0.47	0.94

quite small (about 0.15 cm^2). We also confirmed that the electrocatalytic activity of the Cu_2S electrodes was much better than that of the Pt electrodes used in our experiments by means of current–potential measurements. Thus, the great improvement in the FFs achieved by using Cu_2S as a counter electrode is due to its good electrocatalytic activity for the reduction reaction occurring in the polysulfide electrolyte. However, the FF is still poor compared with that obtained in the DSCs (about 0.7). This result implies that the FF of the CdSe QDSCs prepared by our method also depends greatly on the resistance at each interface in the CdSe-adsorbed TiO_2 photoanode and the resistance in the electrolyte, and that the FF can be improved further by reducing these. Further optimization of the structure of the TiO_2 nanotubes, the conditions of CdSe adsorption, the electrolyte concentration, together with the structure of the Cu_2S counter electrodes is in progress and it is expected that better solar cell performance will be achieved in the near future.

In summary, we have demonstrated a unique sandwich style CdSe QD-sensitized TiO_2 nanotube solar cell. A photovoltaic conversion efficiency as high as 1.8% under solar illumination of 100 mW/cm^2 has been achieved by using a small area Cu_2S counter electrode and irradiating the light from the counter electrode side. To our knowledge, this is the first time that the photovoltaic properties of QD-sensitized TiO_2 nanotube electrodes on Ti substrates have been studied with a two-electrode configuration measurement method. In addition, the production costs of the Cu_2S counter electrode and the Ti substrate used in our QDSCs are much lower than those of the Pt counter electrode and FTO substrate used in normal QDSCs. This is very important for the practical application of QDSCs in the future.

CdSe QDSCs Employing TiO_2 Inverse Opal Photoanodes

The relatively low efficiency compared to the theoretical value obtained in DSCs is ascribed to the poor penetration of materials into thick TiO_2 films, and the detachment of hole transport layers from TiO_2 electrodes [58]. To address the penetration of both sensitizers and redox couples, a novel approach has been proposed using mesoporous inverse opal titania originating from self-organizing systems, such as polystyrene, as templates [43]. A method of enhancing the light-harvesting efficiency has been proposed by Nishimura et al. [59], by confining photons to the high refractive index layer of dye-sensitized TiO_2. The absorbance

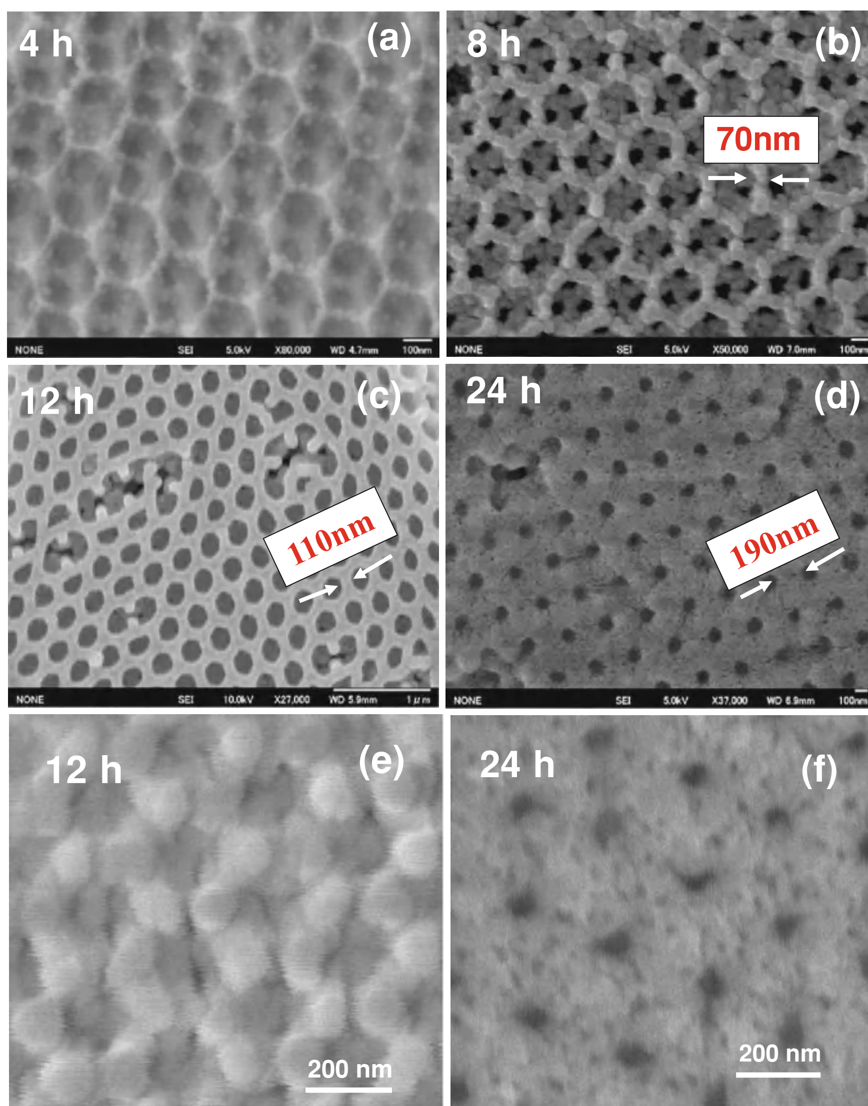

Fig. 14.22 SEM images of the surfaces of TiO_2 inverse opal electrodes (latex sphere diameter: 431 nm) adsorbed with CdSe QDs for different times of 4 h (**a**), 8 h (**b**), 12 h (**c**), and 24 h (**d**), (**e**) and (**f**) are high resolution SEM images of the surfaces of TiO_2 inverse opal electrodes (latex sphere diameter: 308 nm) adsorbed with CdSe QDs for 12 and 24 h, respectively

was enhanced significantly, at energies toward the red edge of the photonic bandgap, for dye adsorbed on TiO_2 inverse opal, and coupling of an inverse opal layer to a conventional film of TiO_2 nanoparticles produced an increase in photocurrent due to multiple scattering, but, unfortunately, the photovoltaic

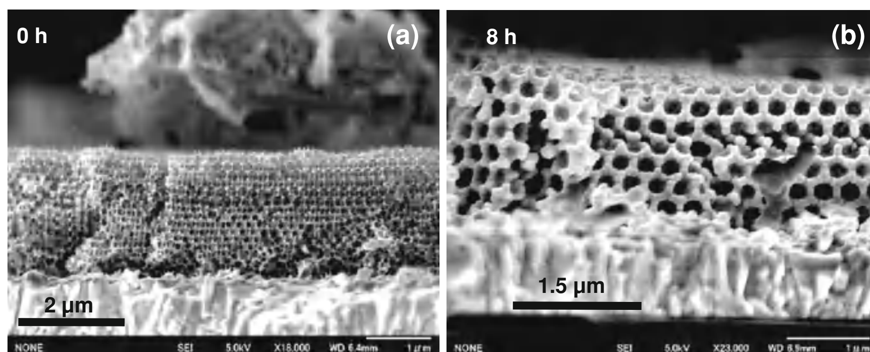

Fig. 14.23 SEM cross sectional images of TiO_2 inverse opal electrodes before (**a**), and after CdSe adsorption for 8 h (**b**)

properties were not characterized. Huiman et al. [60] reported a 0.6% photovoltaic conversion efficiency of dye-sensitized TiO_2 inverse opal, which is much lower than that found for common DSCs, possibly because of a difference in film thickness. However, in the case of solid state DSCs, Somani et al. [61] demonstrated that a higher efficiency could be obtained by using TiO_2 inverse opal, due to the fact that its ordered interconnected pores led to better infiltration of both the sensitizers and the hole transporting material, throughout the whole depth of the TiO_2 film.

Recently, we proposed the use of TiO_2 inverse opal solar cells in QDSCs sensitized with CdSe QDs prepared by CBD, and gave a suggestion for improving solar cells, in addition to surface passivation with ZnS, namely, the insertion of fluoride (F^-) ions into the TiO_2/CdSe and CdSe/ZnS interfaces [19].

Figure 14.22 shows SEM images of TiO_2 inverse opal electrodes originated from latex spheres with diameters of 431 nm, with and without CdSe QD adsorption. For 4 h adsorption time, CdSe QDs were formed on the TiO_2 surface. During adsorption, CdSe QDs grow increasingly on the TiO_2 inverse opal surface, indicated by the thicker wall in the inverse opal structure. The adsorbed CdSe surrounding the TiO_2 inverse opal wall might become thicker than the TiO_2 inverse opal wall itself. Furthermore, increasing the CdSe adsorption time consequently gives smaller porous size, especially for 24 h adsorption. From the cross sections shown in Fig. 14.23, CdSe adsorption was confirmed not only on the portion near the surface of the inverse opal structure but also within the entire inverse opal structure.

The optical absorption properties of TiO_2 inverse opal with CdSe adsorption were characterized using the PA technique. The normalized PA spectra of TiO_2 inverse opal with various CdSe QD adsorption times at 10°C are shown in Fig. 14.24. The shift of the spectra to the lower energy region and increasing intensity can be clearly observed with increasing CdSe deposition time. This may demonstrate a change in CdSe optical absorption with deposition time, because the optical absorption in the visible region is caused by CdSe QDs. The first excitation energy of the CdSe QDs for each deposition time is estimated from the position of

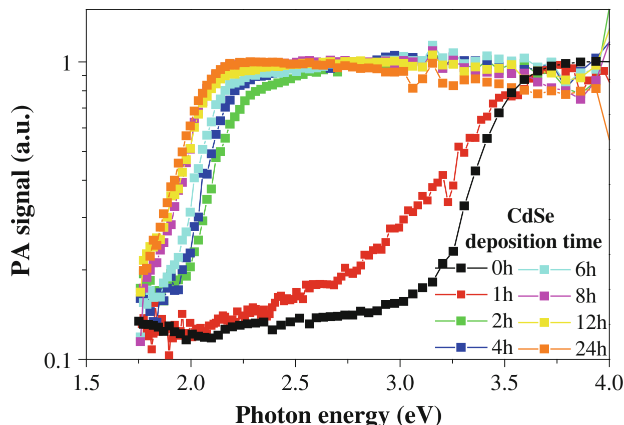

Fig. 14.24 Normalized PA spectra of TiO_2 inverse opal with various CdSe QD adsorption times at 10°C

the edge in the lower energy region of the shoulder. Figure 14.25 shows the dependence of CdSe QD size on adsorption time.

Figure 14.26 shows the IPCE spectra of inverse opal TiO_2 (latex sphere diameter: 431 nm) with CdSe deposition for different deposition times at 10°C with a TiO_2 thickness of 3 μm. The photosensitization of CdSe QDs on inverse opal TiO_2 in the visible region can be clearly seen. IPCE increases with increasing deposition time, and decreases for deposition times longer than 8 h due to the over-adsorption of CdSe inside the electrode. As shown in the SEM images (Fig. 14.22), CdSe adsorption for more than 8 h makes the pores in the inverse opal structure much smaller, thus disturbing the penetration of the redox couple used to scavenge the photoexcited holes in CdSe QDs. On the other hand, the large CdSe clustering indicated by the thick wall in the inverse opal structure may cause the photoexcited electrons (mostly generated in CdSe located on the wall surface, far away from the TiO_2) to experience longer pathways to transport across before being transferred to the TiO_2 conduction band. Therefore, it increases the possibility of hole and electron recombination, which results in a decrease in IPCE.

The photocurrent density (J) versus photovoltage (V) curves of TiO_2 inverse opal (latex sphere diameter: 431 nm) with various CdSe QDs adsorption times were taken with polysulfide electrolyte as the redox couple and Cu_2S-coated FTO as the counter electrode (shown in Fig. 14.27). The detailed photovoltaic properties are described in Table 14.2. The short circuit current density (J_{sc}) increases with adsorption time and has a maximum value of 8.3 mA/cm^2 at an adsorption time of 8 h. Then, J_{sc} decreases for longer adsorption times, and reaches a value of 3.1 mA/cm^2 at 24 h. The photovoltage (V_{oc}) has a maximum value of 0.69 V at 8 h and decreases as the deposition time gets longer. The FF is around 0.54–0.57. Consequently, the energy conversion efficiency first increases with increasing CdSe adsorption time and reaches a maximum value of 3.1% at 8 h, and then

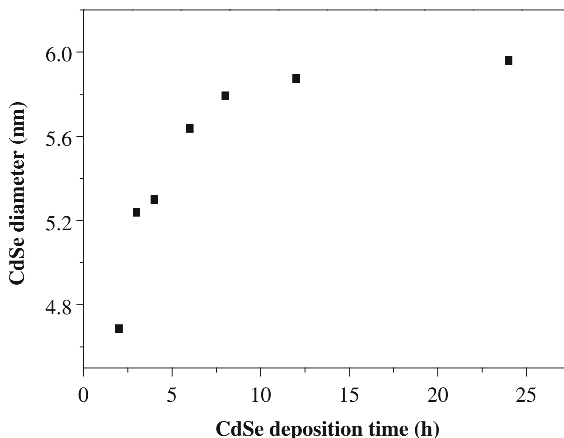

Fig. 14.25 Dependence of CdSe QD diameter on adsorption time

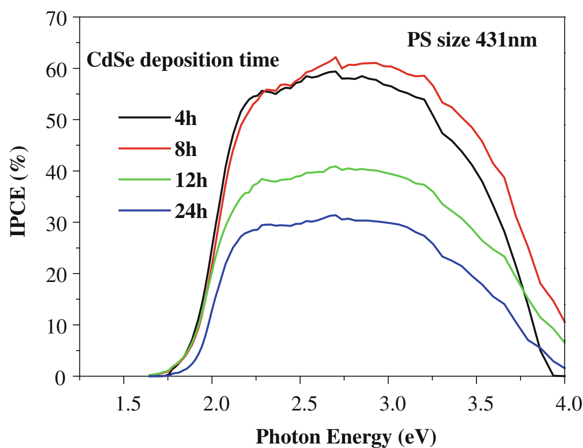

Fig. 14.26 The IPCE spectra of CdSe quantum dot-sensitized TiO_2 inverse opal solar cells for different CdSe deposition times of 4, 8, 12, and 24 h

decreases to 1.0% for 24 h adsorption time. With increasing adsorption time, the amount of CdSe adsorbed onto the TiO_2 inverse opal electrode increases, thus larger amounts of light will be adsorbed resulting in higher J_{sc}. However, as shown in the SEM image (Fig. 14.22) greater growth of CdSe on the TiO_2 inverse opal results in a thicker wall on the inverse opal structure. Finally for deposition times longer than 12 h the pore size in the inverse opal structure becomes so small that the redox couple cannot easily penetrate through the structure, resulting in poor charge transfer at the CdSe QDs/electrolyte interfaces. From the electron point of view, the thicker layer of CdSe adsorbed on the TiO_2 surface also causes longer electron transport through the CdSe clusters before finally reaching the TiO_2 surface and being transferred. So there is an optimum adsorption time at which the maximum efficiency occurs. Furthermore, the lower FF compared to those of DSSCs may be attributed to resistance losses in the cell, such as those in the

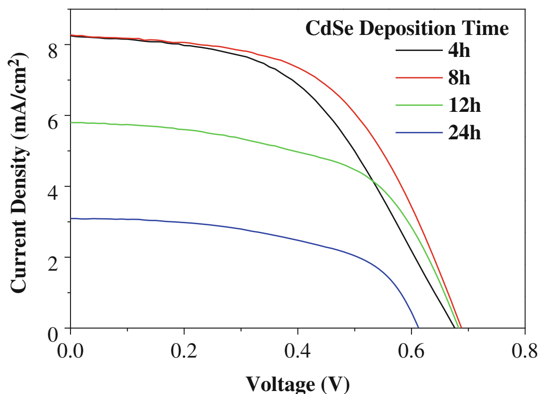

Fig. 14.27 Photocurrent density-photovoltage characteristics of CdSe quantum dot-sensitized TiO_2 inverse opal solar cells for different CdSe deposition times of 4, 8, 12, and 24 h

TiO_2/CdSe, CdSe/CdSe, CdSe/polysulfide electrolyte interfaces. Higher energy conversion efficiency should be achieved by overcoming those problems.

In order to appreciate the unique properties of inverse opal structures in sensitized solar cell applications, the typical photovoltaic performances of CdSe QD-sensitized TiO_2 inverse opal and nanoparticulate TiO_2 solar cells were compared as shown in Fig. 14.28. The thicknesses of both the nanoparticulate and inverse opal TiO_2 electrodes are 9 μm. The measurements were taken under the same conditions with the polysulfide as the redox couple and Cu_2S as the counter electrode, while both CdSe QD-sensitized TiO_2 electrodes were coated twice with ZnS. The short-circuit photocurrent density (J_{sc}), open-circuit photovoltage (V_{oc}), FF, and efficiency () were found to be 9.3 mA/cm^2, 0.51 V, 0.52 and 2.4% for the QD-sensitized nanoparticulate solar cell, while for the QD-sensitized inverse opal solar cell they were 9.0 mA/cm^2, 0.71 V, 0.51 and 3.5%, respectively (Table 14.3). Although having lower J_{sc}, the QD-adsorbed inverse opal solar cell seems to give higher efficiency due to the higher V_{oc} compared with that of the nanoparticulate TiO_2. The higher V_{oc} in the inverse opal structure is due to the orderly adsorption of the QDs along the ordered inverse opal structure, which results in a higher quasi Fermi level. This is because that the orderly adsorption of the QDs along the ordered TiO_2 inverse opal walls allows a sufficient physical blockage of the inverse opal TiO_2 surface preventing its contact with the electrolyte. The higher V_{oc} observed in the TiO_2 inverse opal structure is a superior characteristic compared to the nanoparticulate TiO_2 in sensitized solar cell applications, while its photocurrent property may be increased by fabricating thicker inverse opal films, using a QD sensitizer with a narrower energy level and/or combining two or more QD sensitizers.

Thus, we have demonstrated a new approach to sensitized solar cells, based on TiO_2 inverse opal and the use of QDs as sensitizers. Relative to a QD-sensitized nanoparticulate TiO_2 solar cell, the QD-sensitized TiO_2 inverse opal solar cell typically has higher open-circuit voltage due to orderly adsorption of the QDs along the ordered TiO_2 inverse opal walls allowing a sufficient physical blockage

Table 14.2 Photovoltaic properties of CdSe QD-sensitized TiO_2 inverse opal solar cells with different adsorption times. J_{sc}, V_{oc}, FF and are the short-circuit current density, open-circuit voltage, fill factor, and photovoltaic conversion efficiency, respectively

Adsorption time (h)	J_{sc} (mA/cm^2)	V_{oc} (V)	FF	(%)
4	8.2	0.68	0.54	2.8
8	8.3	0.69	0.57	3.1
12	5.8	0.68	0.57	2.2
24	3.1	0.61	0.55	1.0

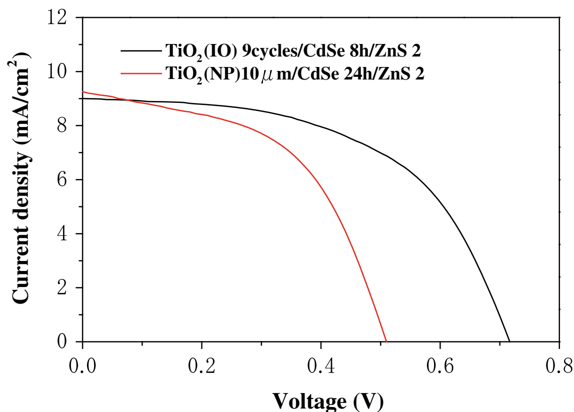

Fig. 14.28 Photocurrent density-photovoltage characteristics of typical CdSe QD-sensitized TiO_2 inverse opal and nanocrystalline TiO_2 solar cells with the same TiO_2 thickness (9 μm)

Table 14.3 Photovoltaic properties of typical CdSe QD-sensitized TiO_2 nanoparticulate and inverse opal solar cells with different adsorption times. J_{sc}, V_{oc}, FF and are the short-circuit current density, open-circuit voltage, fill factor, and photovoltaic conversion efficiency, respectively. The thicknesses of both the TiO_2 nanoparticulate and TiO2 inverse opal electrodes are 9 μm

Electrode	J_{sc} (mA/cm^2)	V_{oc} (V)	FF	(%)
TiO_2(NP)/CdSe/ZnS	9.3	0.51	0.52	2.4
TiO_2(IO)/CdSe/ZnS	9.0	0.71	0.51	3.5

of the TiO_2 surface, which is superior in solar cell applications. A power conversion efficiency of about 3.5% has been attained for TiO_2 inverse opal based QDSCs, under solar illumination of 100 mW/cm^2.

Summary

In summary, we have prepared CdSe and combined CdS/CdSe QDSCs on TiO_2 electrodes with different morphologies, i.e., nanoparticles, nanotubes, and inverse opals. We characterized the optical absorption, photoelectrochemical, and photovoltaic properties of the QDSCs. To improve the photovoltaic performance,

we introduced surface passivation with ZnS and employed a Cu_2S counter electrode to replace the platinum electrode. In addition, we discussed the dependences of the photovoltaic properties of the QDSCs on the QD preparation conditions such as the deposition time and the TiO_2 nanostructure. Each aspect of the photovoltaic performance, including the short-circuit photocurrent density, open-circuit voltage, FF, and efficiency, was significantly improved by surface modification with ZnS. For the counter electrode, the Cu_2S electrode was demonstrated to be more efficient than platinum against the polysulfide electrolytes usually used for the redox couples in CdSe and combined CdS/CdSe QDSCs. Thus applying the Cu_2S as the counter electrode has significantly increased the photovoltaic performance. Moreover, CdS adsorption on TiO_2 electrodes prior to CdSe adsorption also resulted in better solar cell performance. In addition, we found that the morphology of the TiO_2 electrodes had a great influence on the photovoltaic properties of the QDSCs. Finally, a power conversion efficiency as high as 4.9% was achieved for a combined CdS/CdSe QDSC by employing a scattering layer on the TiO_2 nanoparticulate electrode, under solar illumination of 100 mW/cm^2.

Acknowledgments Part of this research was supported by the JST PRESTO program, Grant in Aid for Scientific Research (No. 21310073) from the Ministry of Education, Sports, Science and Technology of the Japanese Government. The authors would like to thank Dr. Lina J. Diguna, Mr. Junya Kobayashi, Mr. Yasumasa Ayuzawa, Mr. Satoru Tamura, Mr. Keita Oshikane, Mrs. Akari Yamada for their helps in the experiments. The authors thank Prof. Q.B. Meng, Prof. D.M. Li and Prof. Y.H. Luo for their cooperations.

References

1. O'Regan, B., Grätzel, M.: A low-cost, high-efficiency solar cell based on dye-sensitized colloidal TiO_2 films. Nature **353**, 737–740 (1991)
2. Grätzel, M.: Dye-sensitized solar cells. J. Photochem. Photobiol. C: Photochem. Rev. **4**, 145–153 (2003)
3. Chiba, Y., Islam, A., Watanabe, Y., Koyama, R., Koide, N., Han, L.: Dye-sensitized solar cells with conversion efficiency of 11.1%. Jpn. J. Appl. Phys. **43**, L638–L640 (2006)
4. Polo, A.S., Itokatu, M.K., Iha, N.Y.M.: Metal complex sensitizers in dye-sensitized solar cells. Coord. Chem. Rev. **248**, 1343–1361 (2004)
5. Park, B.-W., Inoue, T., Ogomi, Y., Miyamoto, A., Fujita, S., Pandey, S.S., Hayase, S.: Electron injection from linearly linked two dye molecules to metal oxide nanoparticles for dye-sensitized solar cells covering wavelength range from 400 to 950 nm. Appl. Phys. Express **4**, 012301 (2011)
6. Vogel, R., Pohl, K., Weller, H.: Sensitization of highly porous, polycrystalline TiO2 electrodes by quantum sized CdS. Chem. Phys. Lett. **174**, 241–246 (1990)
7. Vogel, R., Hoyer, P., Weller, H.: Quantum-sized PbS, CdS, Ag_2S, Sb_2S_3 and Bi_2S_3 particles as sensitizers for various nanoporous wide-bandgap semiconductors. J. Phys. Chem. **98**, 3183–3188 (1994)
8. Toyoda, T., Saikusa, K., Shen, Q.: Photoacoustic and photocurrent studies of highly porous TiO_2 electrodes sensitized by quantum-sized CdS. Jpn. J. Appl. Phys. **38**, 3185–3186 (1999)
9. Toyoda, T., Sato, J., Shen, Q.: Effect of sensitization by quantum-sized CdS on photoacoustic and photoelectrochemical current spectra of porous TiO_2 electrodes. Rev. Sci. Instrum. **74**, 297–299 (2003)

10. Peter, L.M., Riley, D.J., Tull, E.J., Wijayanta, K.G.U.: Photosensitization of nanocrystalline TiO_2 by self-assembled layers of CdS quantum dots. Chem. Commun. **2002**, 1030–1031 (2002)
11. Plass, R., Pelet, S., Krueger, J., Gratzel, M., Bach, U.: Quantum dot sensitization of organic—inorganic hybrid solar cells. J. Phys. Chem. B **106**, 7578–7580 (2002)
12. Shen, Q., Toyoda, T.: Characterization of nanostructured TiO_2 electrodes sensitized with CdSe quantum dots using photoacoustic and photoelectrochemical current methods. Jpn. J. Appl. Phys. **43**, 2946–2951 (2004)
13. Shen, Q., Arae, D., Toyoda, T.: Photosensitization of nanostructured TiO_2 with CdSe quantum dots: effects of microstructure and electron transport in TiO_2 substrates. J. Photochem. Photobiol. A: Chem. **164**, 75–80 (2004)
14. Yu, P.R., Zhu, K., Norman, A.G., Ferrere, S., Frank, A.J., Nozik, A.J.: Nanocrystalline TiO_2 solar cells sensitized with InAs quantum dots. J. Phys. Chem. B **110**, 25451–25454 (2006)
15. Robel, I., Subramanian, V., Kuno, M., Kamat, P.V.: Quantum dot solar cells. Harvesting light energy with CdSe nanocrystals molecularly linked to mesoscopic TiO_2 films. J. Am. Chem. Soc. **128**, 2385–2393 (2006)
16. Niitsoo, O., Sarkar, S.K., Pejoux, P., Rühle, S., Cahen, D., Hodes, G.: Chemical bath deposited CdS/CdSe-sensitized porous TiO_2 solar cells. J. Photochem. Photobiol. A **182**, 306–313 (2006)
17. Shen, Q., Katayama, K., Sawada, T., Yamaguchi, M., Toyoda, T.: Optical absorption, photoelectrochemical, and ultrafast carrier dynamic investigations of TiO_2 electrodes composed of nanotubes and nanowires sensitized with CdSe quantum dots. Jpn. J. Appl. Phys. **45**, 5569–5574 (2006)
18. Shen, Q., Sato, T., Hashimoto, M., Chen, C.C., Toyoda, T.: Photoacoustic and photoelectrochemical characterization of CdSe-sensitized TiO_2 electrodes composed of nanotubes and nanowires. Thin Solid Films **499**, 299–305 (2006)
19. Diguna, L.J., Shen, Q., Kobayashi, J., Toyoda, T.: High efficiency of CdSe quantum-dot-sensitized TiO_2 inverse opal solar cells. Appl. Phys. Lett. **91**, 023116 (2007)
20. Shen, Q., Kobayashi, J., Diguna, L.J., Toyoda, T.: Effect of ZnS coating on the photovoltaic properties of CdSe quantum dot-sensitized solar cells. J. Appl. Phys. **103**, 084304 (2008)
21. Shen, Q., Yamada, A., Tamura, S., Toyoda, T.: CdSe quantum dot-sensitized solar cell employing TiO_2 nanotube working-electrode and Cu_2S counter- electrode. Appl. Phys. Lett. **97**, 123107 (2010)
22. Kamat, P.V.: Quantum dot solar cells. Semiconductor nanocrystals as light harvester. J. Phys. Chem. C **112**, 18737–18753 (2008)
23. Gimenez, S., Mora-Sero, I., Macor, L., Guijarro, N., Lana-Villarreal, L., Gomez, R., Diguna, L.J., Shen, Q., Toyoda, T.: Bisquert, J: Improving the performance of colloidal quantum-dot-sensitized solar cells. Nanotechnology **20**, 295204 (2009)
24. Mora-Sero, I., Gimenez, S., Fabregat-Santiago, F., Gomez, R., Shen, Q., Toyoda, T., Bisquert, J.: Recombination in quantum dot sensitized solar cells. Acc. Chem. Res. **42**, 1848–1857 (2009)
25. Mora-Seró, I., Bisquert, J.: Breakthrough in the development of semiconductor-sensitized solar cells. J. Phys. Chem. Lett. **1**, 3046–3052 (2010)
26. Ruhle, S., Shalom, M., Zaban, A.: Quantum-dot-sensitized solar cells. Chem. Phys. Chem. **11**, 2290–2304 (2010)
27. Nozik, A.J.: Quantum dot solar cells. Physica E **14**, 115–120 (2002)
28. Nozik, A.J.: Multiple exciton generation in semiconductor quantum dots. Chem. Phys. Lett. **457**, 3–11 (2008)
29. Hodes, G.: Comparison of dye- and semiconductor-sensitized porous nanocrystalline liquid junction solar cells. J. Phys. Chem. C **112**, 17778–17787 (2008)
30. Schaller, R.D., Klimov, V.I.: High efficiency carrier multiplication in PbSe nanocrystals: implications for solar energy conversion. Phys. Rev. Lett. **92**, 186601 (2004)
31. Hanna, M.C., Nozik, A.J.: Solar conversion efficiency of photovoltaic and photoelectrolysis cells with carrier multiplication absorbers. J. Appl. Phys. **100**, 074510 (2006)

32. Zhang, Q.X., Guo, X.Z., Huang, X.M., Huang, S.Q., Li, D.M., Luo, Y.H., Shen, Q., Toyoda, T., Meng, Q.B.: Highly efficient CdS/CdSe-sensitized solar cells controlled by the structural properties of mesoporous TiO_2 photoelectrodes. Phys. Chem. Chem. Phys. **13**, 4659–4667 (2011)
33. Gonzalez-Pedro, V., Xu, X., Mora-Sero, I., Bisquert, J.: Modeling high-efficiency quantum dot sensitized solar cells. ACS Nano **4**, 5783–5790 (2010)
34. Gorer, S., Hode, G.: Quantum size effects in the study of chemical solution deposition mechanisms of semiconductor films. J. Phys. Chem. **98**, 5338–5346 (1994)
35. Guijarro, N., Lana-Villarreal, T., Shen, Q., Toyoda, T., Gómez, R.: Sensitization of titanium dioxide photoanodes with cadmium selenide quantum dots prepared by SILAR: photoelectrochemical and carrier dynamics studies. J. Phys. Chem. C **114**, 21928–21937 (2010)
36. Baker, D.R., Kamat, P.V.: Photosensitization of TiO_2 nanostructures with CdS quantum dots: particulate versus tubular support architectures. Adv. Funct. Mater. **19**, 805–811 (2009)
37. Bang, J.H., Kamat, P.V.: Soalr cells by design: photoelectrochemistry of TiO_2 nanorods arrays decorated with CdSe. Adv. Funct. Mater. **20**, 1970–1976 (2010)
38. Diguna, L.J., Murakami, M., Sato, A., Kumagai, Y., Ishihara, T., Kobayashi, N., Shen, Q., Toyoda, T.: Photoacoustic and photoelectrochemical characterization of inverse opal TiO_2 sensitized with CdSe quantum dots. Jpn. J. Appl. Phys. **45**, 5563–5568 (2006)
39. Diguna, L.J., Shen, Q., Sato, A., Katayama, K., Sawada, T., Toyoda, T.: Optical absorption and ultrafast carrier dynamics characterization of CdSe quantum dots deposited on different morphologies of nanostructured TiO_2 films. Mater. Sci. Eng. C **27**, 1514–1520 (2007)
40. Toyoda, T., Oshikane, K., Li, D.M., Luo, Y.H., Meng, Q.B., Shen, Q.: Photoacoustic and photoelectrochemical current spectra of combined CdS/CdSe quantum dots adsorbed on nanostructured TiO_2 electrodes, together with photovoltaic characteristics. J. Appl. Phys. **108**, 114304 (2010)
41. Shen, Q., Toyoda, T.: Studies of optical absorption and electron transport in nanocrystalline TiO_2 electrodes. Thin Solid Films **438–439**, 167–170 (2003)
42. Macak, J.M., Schmuki, P.: Anodic growth of self-organized anodic TiO2 nanotubes in viscous electrolytes. Electro. Acta **52**, 1258–1264 (2006)
43. Wijnhoven, J., Vos, W.: Preparation of photonic crystals made of air spheres in titania. Science **281**, 802–804 (1998)
44. Jayakrishnan, R., Nair, J.P., Kuruvilla, B.A., Kulkarni, S.K., Pandy, R.K.: Composition, structure and morphology of dip-coated rapid thermal annealed CdS and non-aqueous electrodeposited CdTe. Semicond. Sci. Tech. **11**, 116 (1996)
45. Yang, S.M., Huang, C.H., Zhai, J., Wang, Z.S., Jiang, L.: High photostability and quantum yield of nanoporous TiO_2 thin film electrodes co-sensitized with capped sulfides. J. Mater. Chem. **12**, 1459–1464 (2002)
46. Rosencwaig, A., Gersho, A.: Theory of the photoacoustic effect with solids. J. Appl. Phys. **47**, 64–69 (1977)
47. Hodes, G., Manassen, J., Cahen, D.: Photo-electrochemical energy conversion: electrocatalytic sulphur electrodes. J. Appl. Electrochem. **7**, 181–182 (1977)
48. Hodes, G., Manassen, J., Cahen, D.: Electrocatalytic electrodes for the polysulfide redox system. J. Electrochem. Soc. **127**, 544–549 (1980)
49. Bawendi, M.G., Kortan, A.R., Steigerwald, M.L., Brus, L.E.: X-ray structural characterization of larger CdSe semiconductor clusters. J. Chem. Phys. **91**, 7282–7290 (1989)
50. Brus, L.E.: Electron–electron and electron-hole interactions in small semiconductor crystallites: The size dependence of the lowest excited electronic state. J. Chem. Phys. **80**, 4403–4409 (1984)
51. Toyoda, T., Uehata, T., Suganuma, R., Tamura, T., Sato, A., Yamamoto, K., Shen, Q., Kobayashi, N.: Crystal growth of CdSe quantum dots adsorbed on nanoparticle, inverse opal, and nanotube TiO_2 photoelectrodes characterized by photoacoustic spectroscopy. Jpn. J. Appl. Phys. **46**, 4616–4621 (2007)

52. Bisquert, J., Zaban, A., Salvador, P.: Analysis of the mechanisms of electron recombination in nanoporous TiO_2 dye-sensitized solar cells nonequilibrium steady-state statistics and interfacial electron transfer via surface states. J. Phys. Chem. B **106**, 8774–8782 (2002)
53. Guijarro, N., Campiña, J.M., Shen, Q., Toyoda, T., Lana-Villarreal, T., Gómez, R.: Uncovering the role of the ZnS treatment in the performance of quantum dot sensitized solar cells. Phys. Chem. Chem. Phys. **13**, 12024–12032 (2011)
54. Sudhagar, P., Jung, J.H., Park, S., Lee, Y.-G., Sathyamoorthy, R., Kang, Y.S., Ahn, H.: The performance of coupled (CdS:CdSe) quantum dot-sensitized TiO_2 nanofibrous solar cells. Electrochem. Commun. **11**, 2220–2224 (2009)
55. Chen, S., Paulose, M., Ruan, C., Mor, G.K., Varghese, O.K., Kouzoudis, D., Grimes, C.A.: Electrochemically synthesized CdS nanoparticle-modified TiO2 nanotube-array photoelectrodes: preparation, characterization, and application to photoelectrochemical cells. J. Photochem. Photobiol. A **177**, 177–184 (2006)
56. Seabold, J.A., Shanker, K., Wilke, R.H.T., Paulose, M., Varghese, O.K., Grimes, C.A., Choi, K.: Photoelectrochemical properties of heterojunction CdTe/TiO2 electrodes constructed using highly ordered TiO_2 nanotube arrays. Chem. Mater. **20**, 5266–5273 (2008)
57. Lee, W., Kang, S.H., Kim, J.Y., Kolekar, G.B., Sung, Y.E., Han, S.H.: TiO_2 nanotubes with a ZnO thin energy barrier for improved current efficiency of CdSe quantum-dot-sensitized solar cells. Nanotechnology **20**, 335706 (2009)
58. Tanaka, S.: Performance simulation for dye-sensitized solar cells: Toward high efficiency and solid state. Jpn. J. Appl. Phys. **40**, 97–107 (2001)
59. Nishimura, S., Abrams, N., Lewis, B.A., Halaoui, L.I., Mallouk, T.E., Benkstein, K.D., Lagemaat, J., Frank, A.J.: Standing wave enhancement of red absorbance and photocurrent in dye—sensitized Titanium dioxide photoelectrodes coupled to photonic crystals. J. Am. Chem. Soc. **125**, 6306–6310 (2003)
60. Huisman, C.L., Schoonman, J., Goossens, A.: The application of inverse titania opals in nanostructured solar cells. Sol. Energy Mater. Sol. Cells **85**, 115–124 (2005)
61. Somani, P.R., Dionigi, C., Murgia, M., Palles, D., Nozar, P., Ruani, G.: Solid-state dye PV cells using inverse opal TiO_2 films. Sol. Energy Mater. Sol. Cells **87**, 513–519 (2005)

Chapter 15
Optoelectronic Applications of Colloidal Quantum Dots

Zhiping Wang, Nanzhu Zhang, Kimber Brenneman, Tsai Chin Wu, Hyeson Jung, Sushmita Biswas, Banani Sen, Kitt Reinhardt, Sicheng Liao, Michael A. Stroscio and Mitra Dutta

Abstract This chapter highlights recent optoelectronic applications of colloidal quantum dots (QDs). In recent years, many colloidal QD-based optoelectronic devices, and device concepts have been proposed and studied. Many of these device concepts build on traditional optoelectronic device concepts. Increasingly, many new optoelectronic device concepts have been based on the use of biomolecule QD complexes. In this chapter, both types of structures are discussed. Special emphasis is placed on new optoelectronic device concepts that incorporate DNA-based aptamers in biomolecule QD complexes. Not only are the extensions of traditional devices and concepts realizable, such as QD-based photo detectors, displays, photoluminescent and photovoltaic devices, light-emitting diodes (LEDs), photovoltaic devices, and solar cells, but new devices concepts such a biomolecule-based molecular sensors possible. This chapter highlights a number of such novel QD-based devices and device concepts.

Z. Wang · N. Zhang · H. Jung · S. Biswas · B. Sen · M. A. Stroscio (✉) · M. Dutta
Electrical and Computer Engineering Department, University of Illinois at Chicago (UIC), 851 S. Morgan Street, Chicago, IL 60607, USA
e-mail: stroscio@uic.edu

S. Liao · M. A. Stroscio · M. Dutta
Physics Department, University of Illinois at Chicago, 851 S. Morgan Street, Chicago, IL 60607, USA

K. Brenneman · T. C. Wu · M. A. Stroscio
Bioengineering Department, University of Illinois at Chicago, 851 S. Morgan Street, Chicago, IL 60607, USA

K. Reinhardt
Physics and Electronics Directorate, Air Force Office of Scientific Research, Suite 325, 875 N. Randolph Street, Arlington, VA 22203, USA

Z. Wang
Department of Physics, Inner Mongolia University, 235 West University Road, Hohhot 010021, China

Z. M. Wang (ed.), *Quantum Dot Devices*, Lecture Notes in Nanoscale Science and Technology 13, DOI: 10.1007/978-1-4614-3570-9_15,
© Springer Science+Business Media New York 2012

Introduction

In this chapter optoelectronic applications of colloidal quantum dots (QDs) are highlighted. The study of colloidal QDs has a long history going back at least to the early studies of Michael Faraday. However, the traditional optoelectronic device community did not study the use of QDs until a little over 20 years ago and those devices were based not on colloidal QDs but on self-assembled QDs. Representative studies of this type include those of Linder et al. [1], Stiff-Roberts et al. [2], Su et al. [3], Chakrabarti et al. [4], Bockelmann and Bastard [5], Inoshita and Sakaki [6], and Leburton et al. [7]. These early contributions to optoelectronics based on self-assembled QDs have been the subject of excellent reviews including those of Bhattacharya et al. [8], and Skolnick and Mowbray [9]. The work of Bhattacharya and Ghosh [10] illustrates the application of such self-assembled QD structures in novel tunnel injection $In_{0.4}Ga_{0.6}As$/GaAs QD lasers with 15 GHz modulation bandwidth at room temperature. Moreover, Blakesley et al. [11] have demonstrated efficient single photon detection by QD resonant tunneling diodes. In related work, Shields et al. [12] have used a field-effect transistor gated by a layer of QDs for the detection of single photons. The technological advances based on self-assembled QD structures have indeed been impressive and future developments in this promising discipline are expected.

Optoelectronic applications of colloidal QDs, as opposed to self-assembled QDs, have flourished during the last decade. This chapter highlights a variety of applications of colloidal QDs in optoelectronic devices and optical sensors. Colloidal QD-based structures have found a large number of applications in optoelectronic devices and in related device concepts as well as in novel nanoscale detectors as highlighted in this chapter. Among such applications and concepts, the following are discussed in this chapter: photodetectors; multicolor photodetectors, novel nanoscale devices for converting optical radiation into electrical currents; and optical signal-based detectors of nanoscale structures including biomolecules and even ions. In addition, this chapter will discuss selected observations of the electrical properties of these optoelectronic and optics-based devices and structures. While some of these applications are extensions of conventional optoelectronic devices, some have unique properties that are directly related to the use of colloidal QDs. Indeed, the use of colloidal QDs facilitates designing devices with multicolor capability as a result of the availability of colloidal QDs having different bandgaps as well as designing flexible optoelectronic structures by embedding colloidal QDs in a matrix of flexibility polymer matrix materials. The variety of available bandgaps stems directly from the ability to synthesis colloidal QDs from a wide variety of semiconductors having different conduction band edges, E_c, and different valence band edges, E_v. Among such colloidal QD materials are CdSe, CdTe, CdSe-CdTe, CdSe-ZnS, CdS, Fe_2O_3, GaN, PbS, PbSe, Si, SnO_2, and WO_3. Moreover, there are many available conductive polymers with different highest occupied molecular orbitals (HOMO) and lowest unoccupied molecular orbital (LUMO) levels. Poly-[2-methoxy-5-(2′-ethylhexoxy)-1,4-

phenylenevinylene] (MEH-PPV), poly-(3,4-dicyanothiophene) (PDCTh), poly-(phenylenevinylene) (PPV), peroxydisulfate (PDS), poly-3-hexylthiophene (P3HT), and polyvinylpyrrolidone (PVP) have been selected for inclusion in this summary as a result of the suitability of their LUMOs and the HOMOs having energies suitable for device applications.

Synthesis and Properties of QD-Based Structures Incorporating Colloidal QDs

Colloidal QDs (QDs) are generally synthesized as suspensions in liquids. These suspensions of QDs are due to the like charges on the QDs that cause them to remain in suspensions. In many cases, the QD surfaces are functionalized with a surfactant molecule to facilitate subsequent binding of the QD to the desired entity. The presence of a solution as well as the QD surfactants raises the possibility that the optical and electrical properties of the QDs may be altered as a result of the solutions or surfactants. Alexson et al. [13], Ramadurai et al. [14], and Stroscio and Dutta [15] are among the authors discussing such effects. In many cases, the energies of the luminescent peaks associated with the QDs are not affected greatly by the surfactants; however, there are exceptions and the photoluminescent intensity may be altered by such surfactants. In applications, it is essential to study the photoluminescence (PL) for each case of interest in device applications. As an early example of the use of CdSe-ZnS QDs, Zhao et al. [16] have investigated the electro- and PL spectra of CdSe/ZnS core–shell QDs functionalized with organic ligands. Moreover, they have incorporated these QDs into multilayered light-emitting diodes (LEDs). These authors found that the peak energies of the electro- and PL are shifted only several nanometers for diluted QDs. Finally, these authors found no appreciable energy shifts due to the surface ligands, QD orientation, surface ligands, or the presence of conductive polymers in the vicinity of these QDs. In other studies, new latent chemically cross-linked gel electrolyte precursors for quasi-solid dye-sensitized solar cells (QDSC) where identified by Kato et al. [17]; in particular, the gel electrolyte precursors consisted of nanoparticles and dicarboxylic acids as the latent gelators. These authors report that the viscosity of the precursor is low initi87uq ally, but that when baked at 80°C, it was observed to solidify. Importantly, these authors found that the photovoltaic characteristics of these QDSC structures were maintained after solidification. In addition, Bakkers et al. [18] have described a class of assemblies in which photoexcitable QDs—as an example—are linked covalently to a metal by spacer molecules of variable length; in these studies, a series of bisulfide spacer molecules—with lengths of 0.34, 0.77, and 1.18 nm—are used to assemble QD ensembles. In other studies, the robust mechanical properties of the metal/spacer/QD (CdSe) structures have been interpreted as evidence for a covalent linking of the nanocrystals to the spacer molecule by S-Cd bonds [18]. Size-dependent effects for QDs of disparate size

have been investigated by Crooker et al. [19]. These authors considered the dynamics of resonant energy transfer in mixed-size, monodisperse, and energy gradient (layered) assemblies of CdSe nanocrystal QDs. In addition, these authors used time-resolved and spectrally resolved PL techniques to investigate the energy-dependent transfer rate of excitons for a range of dot' sizes and show that energy transfer occurs on timescales of 0.7–1.9 ns. Moreover, these authors present evidence that interdot energy transfer rates can be of the magnitude of picoseconds in structurally optimized systems. In research on fluorescent resonant energy transfer between QDs and photosystem I (PSI), Jung et al. [20] showed that the time associated with fluorescence resonance energy transfer (FRET) is to occur in 0.12 ps.

Many of the promising techniques for embedding QDs in conductive polymers involve assembling multiple layers of QDs with intervening layers of conductive polymers. Of particular interest in this connection, Constantine et al. [21] examined layer-by-layer (LBL) assembly techniques and they have shown that these techniques may be used to fabricate an ultrathin film of polyelectrolytes. The particular LBL structures considered by Constantine et al. [21] were composed of chitosan and organophosphorus hydrolase polycations as well as thioglycolic acid-capped CdSe QDs as the polyanion. These authors examined the topography of the films using epifluorescence microscopy imaging. Of particular interest, the PL property of the functionalized QDs was found to be enhanced when sandwiched between the polycation layers. The presence of organophosphorus compounds was confirmed through UV-vis and emission spectroscopies. Jaffer et al. [22] also demonstrated LBL deposition in structures incorporating ZnS-capped CdSe QD surfaces modified with polyelectrolyte coatings. In complementary techniques, Tang et al. [23] and Pacifico et al. [24] have demonstrated the use of self-assembled monolayer (SAM) methods for the synthesis of QD films. Of particular interest, Tang et al. [23] demonstrated the production of a high coverage photo-active surface for use in a surface sensitized Schottky barrier photovoltaic structure was possible by controlling the pH during deposition. In the related work of Pacifico et al. [24], two-dimensional ordered arrays of QDs were fabricated using bifunctional alkanes to form SAMs. In related studies, Ouyang and Awschalon [25] used bifunctional chemical linkers as a means of providing control over the spacings between adjacent QDs. In yet another approach to self-assembly, Stroscio et al. [26] have used biomolecular peptides to chemically assemble alternating layers of CdSe-ZnS and CdS on an Au substrate.

For applications of QD structures as photodetectors, the absorption coefficient and the related extinction coefficient are of special importance. The extinction coefficients of CdTe, CdSe, and CdS nanocrystal have been determined by Yu et al. [27]. As expected, these results confirmed that (for high-quality CdTe, CdSe, and CdS nanocrystals) that the extinction coefficient per mole of nanocrystals at the first exitonic absorption peak was strongly dependent on the size of the nanocrystals. There is a growing body of literature indicating relatively large extinction coefficients for colloidal QDs at the first exciton peak [27–29]. The extinction coefficient, ε, is related to the absorbance, A, through, $A = \varepsilon CL$, where

C is molar concentration, the QD concentration in mol/liter and *L* is the optical path length in cm. Experimentally determined extinction coefficients of CdTe, CdSe, and CdSe nanocrystals for colloidal QDs indicate significant absorption levels near the first exciton peaks; indeed, these experimental measurements yield values of extinction coefficients corresponding to *A*/*L* (absorbance per length) values of: $29.6 \times 3 \times 10^5\ cm^{-1}$ CdSe, $24.4 \times 6 \times 10^5\ cm^{-1}$ for CdTe and $33.7 \times 5 \times 10^5\ cm^{-1}$ for CdS [27]. In part, these relatively large values are due to quantum confinement effects. Moreover, Albanesi et al. [28] predict absorption coefficients in PbS, PbTe, and PdSe with peak values in excess of $10^6\ cm^{-1}$, and Tsuchiya et al. [29] predict absorption coefficients in excess of $10^6\ cm^{-1}$.

In designing devices and structures incorporating colloidal QDs it is essential that the energy level structure of each component material will be understood. In this regard, Al Kuhaimi [30] has investigated the conduction and valence band offsets of CdS/CdTe solar cell structures; in this study, the conduction band offsets was determined to be between 0.23 and 0.3 eV, and that of the valence band offsets was determined to be between 0.67 and 0.74 eV. Of special importance for designs with period structures of QDs, Lazarenkova and Balandin [31] have analyzed the carrier energy band structure in three-dimensional arrays of uniformly spaced semiconductor QDs; in this work, the anticipated splitting of carrier energy levels that results in three-dimensional miniband formation was investigated. As expected, changing the sizes of QDs as well as the spacings between QDs and the associated barrier heights made it possible to control the electronic band structure of these artificial QD crystals. These authors also demonstrated that the effective-mass tensor and density of states for these QD crystals are different from those of bulk semiconductors. Moreover, they found that the electronic properties of these artificial crystals are more sensitive to interdot spacings than dot geometries. In subsequent studies, Balandin and Lazarenkova [32] found a thermoelectric figure-of-merit enhancement in regimented QD superlattices that can be an order of magnitude or more greater than that in bulk semiconductors. Accordingly, these authors have demonstrated that the thermal and electrical of three-dimensional QD arrays may be engineered to alter device properties as suggested by Lyanda-Geller and Leburton [33] and Dmitriev and Suris [34]. Furthermore, Yamanaka et al. [35] and Vasudev et al. [36] analyzed the transmission coefficients of carriers of GaN, TiO_2, and CdSe QDs arranged three-dimensional arrays for a variety of conductive polymer matrices. These three-dimensional structures had both regular and irregular interdot spacings. These analyses indicated that carrier transmission coefficients may be large (>50%) at selected band energies for suitably designed arrays.

Biswas et al. [37] reported that in nanocomposite heterostructures made of semiconducting QDs and conductive polymers, the peak to valley ratio of the current is 91 at room temperature while 2,965 at 77 k. The current voltage characteristics were simulated for a double-barrier resonant tunneling device and the location of the NDR peaks agreed with the experimental results. The negative differential resistance phenomenon is of potential interest in memory cells, electronic switches, and oscillators.

Phenomena Dealing with PL and LED Applications Using QD-Based Structures

This section deals with PL and LED applications using QD-based structures. In early work underlying LED applications, Coe-Sullivan et al. [38] studied techniques underlying the fabrication of large-area ordered QD monolayers via phase separation during spin-casting. Moreover, Coe-Sullivan et al. [39] have demonstrated that a phase segregation process can be applied to the fabrication of Quantum-dot LED (QD-LEDs) containing a wide range of CdSe QD sizes. QD core diameters from 3.2 to 5.8 nm, the peak electroluminescence was tuned from 540 to 635 nm. Coe-Sullivan et al. [39] have demonstrated that for both all-organic LEDs and QD-LEDs with thin emissive layers, there is an increase in the exciton recombination region width as the drive current density is increased. Coe-Sullivan et al. [40] have fabricated a QD-LED that has a monolayer of QDs, sandwiched between two organic thin films; these authors used a fabrication method that employed material phase segregation between the QD aliphatic capping groups and the aromatic organic materials. In these studies, a 25-fold improvement in luminescence efficiency (1.6 cd A^{-1} at 2,000 cd m^{-2}) was found relative to best previous QD-LED results at that time.

As a preliminary to developing displays, Lee et al. [41] have demonstrated nearly full color emission using semiconductor nanocrystals, QDs, and polymer composites. Lee et al. [41] fabricated composites by stabilizing chemically synthesized II–VI semiconductor QDs into polylaurylmethacrylate (PLMA) matrices in the presence of tri-*n*-octylphosphine (TOP). With the resulting structures, Lee et al. [41] observed that the fluorescence of the resulting composites covered the entire visible range with narrow emission profiles and high PL quantum yields when the excitation was accomplished with ultraviolet or blue light; these authors also observed that controlling the mixing ratio of different-sized QDs resulted in mixed colors. In related studies, Anikeeva et al. [42] performed a study of the enhancement of PL of CdSe/ZnS core/shell QDs by energy transfer from a phosphorescent donor. For the system considered by Anikeeva et al. [42] the photoluminescent dynamics was dominated by exciton diffusion within a *fac* tris(2-phenylpyridine) iridium (Ir(ppy)3) film to the QD layer. Photonic bandgap effects have been considered by Lin et al. [43] who self-organized CdS-coated PMMA (poly(methyl methacrylate)) microspheres to form a photonic crystal that provides spectrally and angularly dependent electromagnetic structural resonances; these studies identified photonic stop band with PL from the nanocrystals. Yang et al. [44] studied the optical characterization of the ZnO. They measured the PL as a function of temperature and Raman scattering data at room temperature. ZnO has a large exciton binding energy of 60 meV which is very important for light emitting applications. They also studied the electron and hole transmission mini bands of colloidal ZnO QDs and conductive polymers which is a potential material in the field of optoelectronic device.

Photodetector Concepts Based on QD Arrays

Photodetectors based on treated CdSe QD films have been investigated by Oertel et al. [45]. PEDOT-PSS (poly-3,4-ethylenedioxythiophene doped with polystyrene sulfonate) was used as the conductive polymer in these studies. (PEDOT:PSS). An effective bandgap energy shift to lower energy via strong Förster energy transfer was observed by Kang et al. [46] in studies of the PL characteristics of the self-assembled silica nanospheres containing coupled CdSe/ZnS core–shell QDs on the surface of the sphere. In the infrared region, Konstantatos et al. [47] analyzed infrared photodetectors fabricated using solution-based process; these infrared photodetectors were superior in their normalized detectivity, D^*, to the best epitaxially grown devices operating at room temperature. In related work, McDonald et al. [48] used a nanocomposite approach in which PbS nanocrystals tuned by the quantum size effect sensitize the conjugated polymer poly2-methoxy-5-(2′-ethylhexyloxy-pphenylenevinylene) (MEH-PPV) into the infrared. These were able to realize photocurrent spectra with peaks tailored to 980 nm, 1.200 μm, and 1.355 μm by varying the size of the nanocrystals during processing.

Boberl et al. [49] formed columns by filling colloidal QDs into nanoporous alumina membranes with aspect ratios of 300:1. They fabricated the QD column photodetectors with two different QDs HgTe and PbS and different QD sizes. Electrical transport and photocurrent up to long wavelengths of 3 μm are demonstrated. The potential application of colloidal QDs is that they provide a good way to low-cost large-area devices and high flexibility.

Liao et al. [50] proposed a novel design for a photodetector that is based on QD coupled resonant-tunneling diodes (QDRTDs) with the QDs embedded in with conductive polymers adjacent to the RTD. In the studies of Liao et al. [50], an AlGaN-based double-barrier quantum well (DBQW) and PbS colloidal QDs form the QDRTD. By using PPV, PVK, and SiHMFPV with embedded PbS QDs as the photon absorption regions, the device is capable of detecting photons with three different wavelengths simultaneously. In the specific design discussed herein, the resonant-tunneling diode (RTD) is made of an $Al_{0.46}Ga_{0.54}N/Al_{0.6}Ga_{0.4}N/Al_{0.46}Ga_{0.54}N$ quantum heterostructure, and a layer of lead sulfide (PbS) QDs is embedded in the conductive polymer on top of the RTD structure. The polymers Poly(phenylene vinylene) (PPV), Poly(N-vinylcarbazole) (PVK), and Poly(hexylmethyl-silylene-*p*- phenylene vinylene-9,9-dihexylfluorene vinylene-*p*-phenylene) (SiHMFPV) were selected for the three absorption regions because with an Al composition fraction, x, in the $Al_xGa_{1-x}N$ compound of 0.46 the conduction band E_c of the DBQW emitter is aligned with the LUMO of the PPV and PVK polymers, and the LUMO of the SiHMFPV polymer is slightly lower than the E_c of the emitter.

Figure 15.1 depicts the energy diagram of AlGaN-based DBQW coupled with conductive polymer as the collector–photon absorption region-with PbS QDs embedded in the conductive polymer. The widths of both the well and barrier of the double-barrier are 3 ML. Figure 15.2 presents the calculated current–voltage (IV) characteristics of the device with different polymers at 300 K.

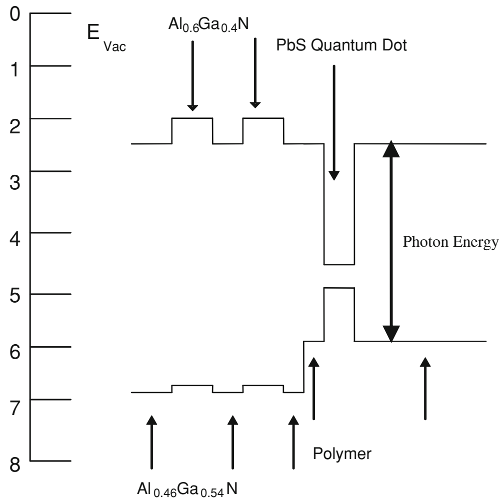

Fig. 15.1 Energy diagram of AlGaN-based DBQW coupled with conductive polymer as the collector with PbS QDs embedded in the polymer

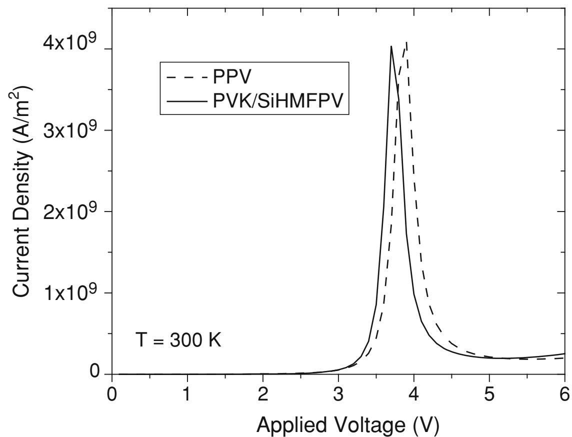

Fig. 15.2 Current–voltage characteristics of the device with different polymers at 300 K

Liao et al. [50] applied a modified Hooge's empirical model to analyze the low frequency noise of the QDRTD and polymer-based photodetector. Based on this analysis was estimated the minimum light sensitivity of the order of 0.01 nW/cm^2. The photodetector designs considered by Liao et al. [50] may be used to extend to different three-color detectors as a result of the great variety of available conductive polymers, QDs, and DBQWs.

Solar Cell Structures Incorporating QDs

There has been considerable effort aimed at using QD arrays as the basis for solar cells. Nozik et al. [51] have assessed QD-based solar cells and have specifically considered using hot photogenerated carriers to produce higher photovoltages

or higher photocurrents. This analysis lead to the result that QD-based structures have the potential to increase the maximum attainable thermodynamic conversion efficiency of solar photon conversion up to 66%. The works of Boudreaux et al. [52] and Benistry [53] underlie the conclusion that relaxation dynamics of photogenerated carriers may be markedly affected by quantization effects in dimensionally confined semiconductors. Indeed, Boudreaux et al. [52] performed an analysis of the energy of injected electronic minority carriers from an illuminated semiconductor into an electrolyte. In another potentially critical observation, phonon-bottleneck effects in QDs were introduced by Benistry [53]. More recently Stroscio and Dutta [54] have considered phonon-related effects in semiconductor nanostructures.

Hagen et al. [55] have presented an innovative three-layer concept for efficient solid-state solar cells based on nanoparticle-based solar cells. The devices considered by Hagen et al. [55] consisted of a TiO_2 nanocrystalline layer for electron conduction, an organic triphenyldiamine layer for the transport of holes, and a surface-absorbed ruthenium dye complex for light absorption. Importantly, high charge storage capability of porous titanium dioxide layers was demonstrated.

Arango et al. [56] have investigated charge transfer in photovoltaics; the structures consisted of interpenetrating networks of TiO_2 nanoparticles and conjugated polymer—poly2-methoxy-5(2′-ethylhexoxy-phenylene-vinylene) (MEH-PPV). These layered structures exhibited a two order of magnitude increase in photoconductivity and sharp saturation relative to blended structures.

Photoelectrochemical cells based, in part, on novel photovoltaic cells fabricated from nanocrystalline materials and conducting polymers films have been assessed and reviewed by Gratzel [57]; high conversion efficiencies, flexibility, and inexpensive fabrication were highlighted for selected device designs. Dye-sensitized solid heterojunctions, extremely thin absorber (ETA) solar cells and organic solar cells incorporating interpenetrating polymer networks were among the structures considered by Gratzel [57]. Of special significance, Gratzel [57] reviewed photovoltaic devices based on interpenetrating mesoscopic networks characterized by ultrafast initial charge separation and much slower back-reaction that facilitates the collection of charge carriers as an electric current before recombination can occur. Low-cost high-efficiency solar cells based on dye-sensitized colloidal TiO_2 films have been considered by O’Regan and Gratzel [58]; these material structures have large internal surface area and are attractive as a result of the need for dye-sensitized solar cells to absorb more incident light. In addition, O’Regan and Gratzel [58] considered interconnected mesoporous materials to facilitate electronic conduction.

Solid-state dye-sensitized solar cells employing a solid organic hole-transport material (HTM) have been considered by Kroeze et al. [59] who have pointed out that they offer a number of practical advantages over liquid electrolyte junction devices. These authors have emphasized the practical importance of the control of interfacial charge transfer in the design of these devices.

InAs self-assembled QDs incorporated in an AlGaAs/GaAs heterostructure for solar cell applications have been studied by Suraprapapich et al. [60] who have reported potentially high device efficiencies based on these structures.

Concepts for nanostructured solar cells enhance the potential for applications of such devices. However, potential difficulties associated with realizing efficient nanostructured solar cells have been pointed out. In the case of quantum well-based solar cells, these considerations include: (a) the polarization-sensitive nature of the absorption reduces absorption efficiency and necessitates the use of elaborate incident optics; (b) the localization of carriers increases the difficulty of carrier collection and has motivated carrier collection through complex means such as hot-carrier transport or miniband transport; and (c) the voltage drop across complex structures leads to reduced power output. In the case of QD-based solar cells, the same difficulties arise except for point (a) made previously. Notwithstanding these difficulties, there are numerous efforts aimed at realizing QD-based solar cells. Ruangdet et al. [61] have studied the performance of structures based on multi-stacked high-density InAs QDs. This study provides an example of the difficulty of achieving high efficiencies; however, it should be pointed out that it was based on self-assembled QDs instead of colloidal QD-based devices. In this work, Ruangdet et al. [61] use a thin-capping-and-regrowth molecular beam epitaxy (MBE) process to fabricate multiple layers of InAs-based QDs with areal densities of 10^{10}–10^{12} cm^{-2}. Importantly, by electrical characterization of homojunction p-n solar cells with one layer of QDs and five layers of QDs these authors show that a short-circuit of 9.6 mA/cm^2 for the one-layer case as opposed to 14.4 mA/cm^2 results for the five-layer case. Significantly, the efficiency for the five-layer case is only 5.1%. In other investigation underlying QD-based solar cells, Marti et al. [62], Luque and Marti [63, 64], have investigated the considered role of intermediate bands in QD-based solar cells. Indeed, an analysis of a solar cell with an impurity level in the semiconductor bandgap under ideal conditions has been presented by Luque and Marti [63]. It was argued that under these ideal conditions that an efficiency of 63.1% was possible instead of the 40.7% predicted in the Shockley and Queisser model limit; this is discussed further by Werner et al. [65]. Thus, this analysis predicts high efficiencies for an idealized system with an impurity having energy in the semiconductor bandgap. However, the implementation of this approach through the use of QDs to provide the intermediate level (or band) has resulted [64] in the observation and conclusion that the absorption of light in a ten-layer system is low and that increasing the number of layers might lead to material defects.

Jung et al. [20] have demonstrated energy transfer between colloidal CdSe QDs and PSI. The work of Jung et al. [20] was motivated by the fact that in the natural photosynthesis process, light harvesting complexes (LHCs) absorb light and pass excitation energy to PSI and photosystem II (PSII). They used nanocrystalline QDs as an artificial LHC by integrating them with PSI to extend their spectral range. Based on PL and ultrafast time-resolved absorption measurements, these investigators have demonstrated that when the nanocrystalline QDs and PSI are within the Forster radius that the emission from the nanocrystalline QDs is quenched and the fluorescence from PSI is enhanced. Moreover, using absorption and bleaching results, Jung et al. [20] demonstrate FRET from the nanocrystalline QDs to the PSI; the non-radiative energy transfer was determined to occur in 0.12 ps.

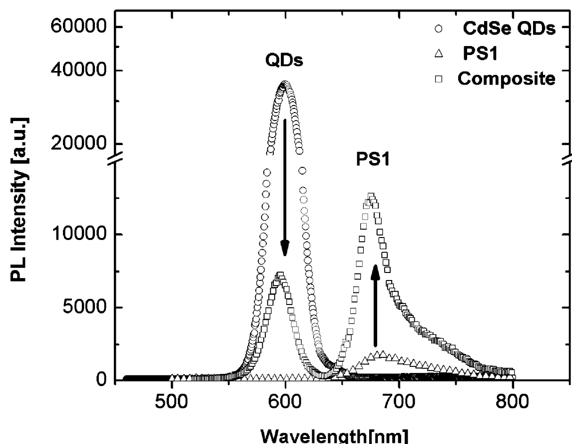

Fig. 15.3 PL of CdSe QDs (595 nm, *circle*), PSI (682 nm, *triangle*), and QD-PSI composite (*square*) using excitation at 442 nm. The intensity of the peaks of QDs are decreased while that of PSI are increased in the composite, showing the energy transfer

Figure 15.3 demonstrates the FRET effect for the composite QD-PSI system. Since green plants including PSI have very few green pigments, as a result of refection green light by plants, it may be possible to increase/engineer/expending light absorption by adding nanocrystalline QDs in green range.

Rao et al. [66] studied organic photovoltaic devices using transient optical absorption spectroscopy. They focused on pentacene/C_{60} bilayers which exhibited high quantum efficiencies which is a drawback of organic phtotovoltaic devices. They demonstrated that the reason for the high quantum efficiencies of their structure is that spin-singlet excitons in pentancene thin film undergo fission to two spin-triplet excitions on a sub-200 fs timescale who diffuse to a heterojunction then and dissociated there leading to charge formation on a 2–10 ns timescale and get high quantum efficiencies. Inspired by this structure and mechanism, the photocurrent of OPVs can be enhanced and in the future anticipate the developmental organic photovoltaic devices having suitability for flexible and large-area applications while at the same time with high efficiencies.

Biomolecule-Based Molecular Sensors Based on Colloidal QDs

There have been studies using colloidal QDs to construct detectors of ions. Wu et al. [67] designed the QD-based aptamer beacon for potassium ion detection in the potassium concentration range from 0 to 300 mM. Wu et al. [67] used the thrombin-binding aptamer (TBA) as the probe, CdSe/ZnS QDs as the donor and gold nanoparticles as the acceptor in this design. The TBA has the following sequence 5′ GGG TGG TGT GGT TGG 3′. In the presence of potassium ions that stabilize the tetraplex structure (structure with four GG pairs) formed by the TBA, the donor and acceptor are brought together within several nanometers, and therefore FRET occurs. As a result, the intensity of the fluorescence from the

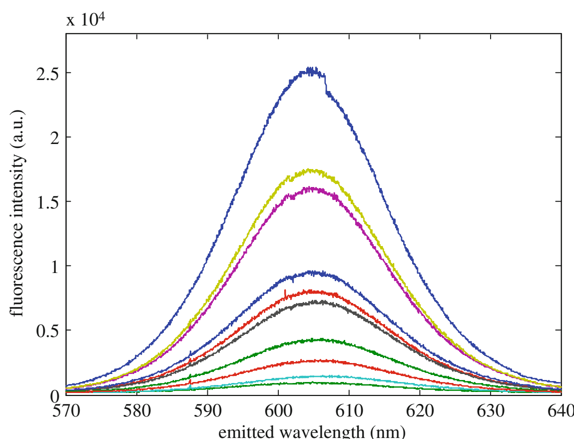

Fig. 15.4 The fluorescence response of the QD-based potassium detector solution to the potassium level range from 0 to 304 mM; the concentrations going from the upper curves to the lowest curve are 0, 20, 39, 58, 77, 96, 115, 134, 153, 190, 208, 235, 262, and 289 mM, respectively. The CdSe/ZnS QDs have a narrow, symmetric emission spectrum with peak centered at 605 nm

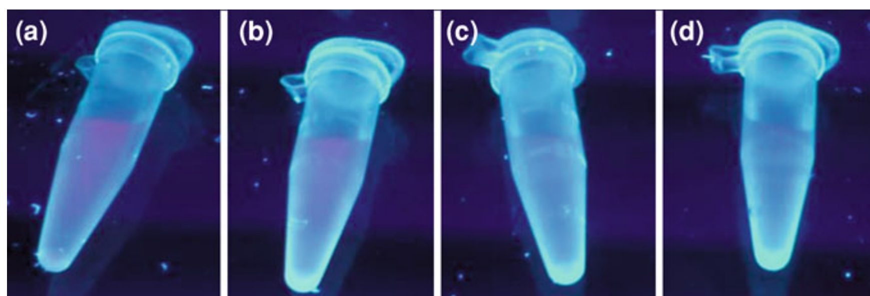

Fig. 15.5 This picture shows that the fluorescence intensity change is large enough to be seen by the naked eye, which makes this design promising in applications as a simple diagnostic device. In this picture, each of the four vials, (**a**)–(**d**), contain 1 L of 907 6-base-spacer beacons. 0, 1 L, 10 L, 100 L of 5.69 M saturated potassium chloride are added into the vials from left to right while all of the volumes are designed to be equal to 1,112 L. This photograph was taken in a dark room with a Panasonic LX3 one minute after potassium ions were added into the beacon solution. The overall potassium ion concentrations are 0 mM (**a**), 5.11 mM (**b**), 51.1 mM (**c**), and 511 mM (**d**). The overall beacon concentrations of these four vials are the same, 907 μM

solution depends on the percentage of probes that stay in the quenching stage, and, therefore, gives information of the potassium ion concentration. It was found that the fluorescence intensity of the potassium probe decreases with increasing potassium level when they are excited by a laser with a wavelength of 305 nm; see Fig. 15.4. These results indicate that it may be possible to design a potassium sensor based on the observation of the fluorescence of a sample solution added by

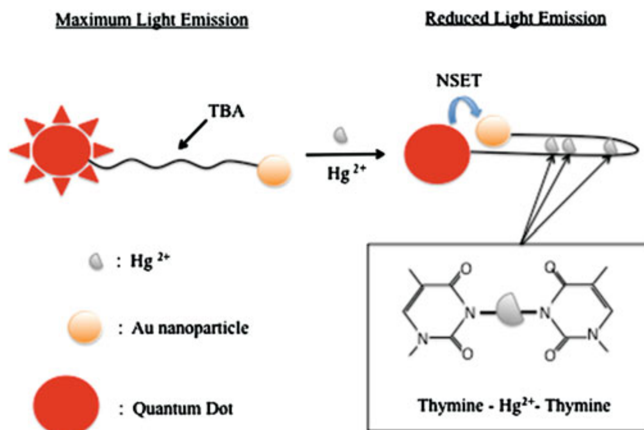

Fig. 15.6 Schematic of Hg^{2+} ion probe. The interaction between Hg^{2+} and thymine bases leads to the folding of the aptamer which allows NSET between QD and Au nanoparticle

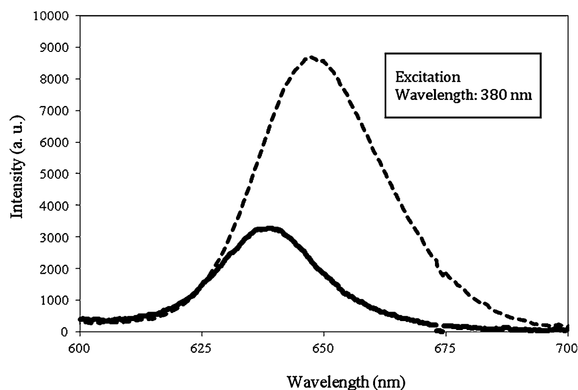

Fig. 15.7 PL of aptamer probe assay at 10 nM probe concentration. *Dashed line* is a control containing the probe only with maximum emission at 650 nm and the solid line is the probe plus 500 nM Hg^{2+} present. Light emission is reduced

the probe. Furthermore, the fluorescence response is so significant that it can be sensed with the naked eye as shown in Fig. 15.5; this design shows promising potential in the development of take-home diagnostic devices.

Brenneman et al. [68] used semiconductor QDs and the same DNA aptamer as Wu et al. [67] for the detection of Hg^{2+} ions. Oligonucleotides can be used for Hg^{2+} ion detection because they interact with thymine (T) bases to create T- Hg^{2+}-T structures [69]. Since the TBA (5′-GGT TGG TGT GGT TGG-3′) used for K^{+} detection contains 6 thymine bases, it can also be employed in Hg ion detection. The symmetry of the thymine bases in the TBA will cause the DNA to fold into a hairpin structure when Hg^{2+} binds to it (Fig. 15.6). When this occurs the Au nanoparticle, which acts as a quencher through the phenomenon of nanometal surface energy transfer (NSET), is brought closer to the QD. Therefore, this conformational change causes a reduction in the emission of the excited QD.

The process of NSET is similar to that of FRET, except the energy transfer is between dipole-surface rather than dipole–dipole [70].

This reduction in fluorescence is related to the presence of mercury(II) ions. The emission spectra in Fig. 15.7 was measured using a spectrometer. Both assays contained 10 nM of the probe, but the solid line shows a quenching efficiency of 62% with the addition of 500 nM Hg^{2+}.

Summary

In this chapter we highlight recent optoelectronic applications of colloidal QDs. We have showed the great potential of application of such structure in the fields of photoluminescent devices, LEDs, displays, photodetectors solar cells, and other novel devices. It is expected that the research on this structure will continue so that more possibility of application will be opened.

References

1. Linder, K.K., Phillips, J., Osasaimeh, O., Liu, X.F., Krishina, S., Bhattacharya, P., Jiang, J.C.: Self-organised In0.4Ga0.6As quantum-dot lasers grown on Si substrates. Appl. Phys. Lett. **74**, 1355–1357 (1999)
2. Stiff-Roberts, A.D., Chakrabarti, S., Su, X., Bhattacharya, P.: Research propels quantum dots forward. Laser Focus World **41**, 103–108 (2005)
3. Su, X.H., Chakrabarti, S., Stiff-Roberts, A.D., Singh, J., Bhattacharya, P.: Quantum dot infrared photodetector design based on double-barrier resonant tunneling. Electron. Lett. **40**, 1082–1083 (2004)
4. Chakrabarti, S., Stiff-Roberts, A.D., Bhattacharya, P., Kennerly, S.W.: Heterostructures for achieving large responsivity InAs/GaAs quantum dot infrared photodetectors. J. Vac. Sci. Technol. B **22**, 1499–1502 (2004)
5. Bockelmann, I., Bastard, G.: Phonon scattering and energy relaxation in two-, one-, and zero-dimensional electron gases. Phys. Rev. B **42**, 8947–8951 (1990)
6. Inoshita, T., Sakaki, H.: Electron relaxation in a quantum dot: significance of multiphonon processes. Phys. Rev. B **46**, 7260–7263 (1992)
7. Leburton, J.P., Fonseca, R.C., Nagaraja, S., Shumway, J., Ceperley, D., Martin, R.M.: Electronic structure and many-body effects in self-assembled quantum dots. J. Phys.: Condens. Matter **11**, 5953–5967 (1999)
8. Bhattacharya, P., Ghosh, S., Stiff-Roberts, A.D.: Quantum dot optoelectronic devices. Annu. Rev. Mater. Res. **34**, 1–40 (2004)
9. Skolnick, M.S., Mowbray, D.J.: Self-assembled semiconductor quantum dots: fundamental physics and device applications. Annu. Rev. Mater. Res. **34**, 181–218 (2004)
10. Bhattacharya, P.K., Ghosh, S.: Tunnel injection In0.4Ga0.6As/GaAs quantum dot lasers with a 15 GHz modulation bandwidth at room temperature. Appl. Phys. Lett. **80**, 3482–3484 (2002)
11. Blakesley, C., See, P., Shields, A.J., Kardynal, B.E., Atkinson, P., Farrer, I., Ritchie, D.A.: Efficient single photon detection by quantum dot resonant tunneling diodes. Phys. Rev. Lett. **94**, 067401-1-4 (2005)

12. Shields, A.J., O'Sullivan, M.P., Farrer, I., Ritchie, D.A., Hogg, R.A., Leadbeater, M.L., Norman, C.E., Pepper, M.: Detection of single photons using a field-effect transistor gated by a layer of quantum dots. Appl. Phys. Lett. **76**, 3673–3675 (2000)
13. Alexson, D., Li, Y., Ramadurai, D., Shi, P., George, L., George, L., Uddin, M., Thomas, P., Rufo, S., Dutta, M., Stroscio, M.A.: Binding of semiconductor quantum dots to cellular integrins. IEEE Trans. Nanotechnol. **3**, 86–92 (2004)
14. Ramadurai, D., Geerpuram, D., Alexson, D., Dutta, M., Kotov, N.A., Tang, Z., Stroscio, M.A.: Electrical and optical properties of colloidal semiconductor nanocrystals in aqueous environments. Superlattices Microstruct. **40**, 38–44 (2006)
15. Stroscio, M.A., Dutta, M.: Integrated biological-semiconductor devices. Proc. IEEE **93**, 1772–1783 (2005)
16. Zhao, J., Zhang, J., Jiang, C., Bohnenberger, J., Basche, T., Mews, A.: Electroluminescence from isolated CdSe/ZnS quantum dots in multilayered light-emitting diodes. J. Appl. Phys. **96**, 3206–3210 (2004)
17. Kato, T., Okazaki, A., Hayase, S.: Latent gel electrolyte precursors for quasi-solid dye sensitized solar cells. Chem. Commun. **3**, 363–365 (2005)
18. Bakkers, E.P.A.M., Marsman, A.W., Jenneskens, L., Vanmaekelbergh, D.: Distance-dependent electron transfer in Au/spacer/Q-CdSe Assemblies. Angew. Chem. **39**, 2297–2299 (2000)
19. Crooker, S.A., Hollingsworth, J.A., Tretiak, S., Klimov, V.I.: Spectrally resolved dynamics of energy transfer in quantum-dot assemblies: toward engineered energy flows in artificial materials. Phys. Rev. Lett. **89**, 186802–186809 (2002)
20. Jung, H., Gulis, G., Gupta, S., Redding, K., Gosztola, D.J., Wiederrecht, G.P., Stroscio, M.A., Dutta, M.: Optical and electrical measurement of energy transfer between nanocrystalline quantum dots and photosystem I. J. Phys. Chem. B **114**, 14544–14549 (2010)
21. Constantine, C.A., Gattas-Asfura, K.M., Mello, S.V., Crespo, G., Rastogi, V., Cheng, T.C., DeFrank, J.J., Leblanc, R.M.: Layer-by-layer biosensor assembly incorporating functionalized quantum dots. Langmuir **19**, 9863–9867 (2003)
22. Jaffar, S., Nam, K.T., Khademhosseini, A., Xing, J., Langer, R.S., Belcher, A.M.: Layer-by-layer surface modification and patterned electrostatic deposition of quantum dots. Nano Lett. **4**, 1421–1425 (2004)
23. Tang, J., Birkeldal, H., McFarland, E.W., Stucky, G.D.: Self-assembly of CdSe/CdS quantum dots by hydrogen bonding on Au surfaces for photoreception. Chem. Commun. **18**, 2278–2279 (2003)
24. Pacifico, J., Gomez, D., Mulvaney, P.: A simple route to tunable two-dimensional arrays of quantum dots. Adv. Mater. **17**, 415–419 (2005)
25. Ouyang, M., Awschalom, D.D.: Coherent spin transfer between molecularly bridged quantum dots. Science **301**, 1074–1078 (2003)
26. Stroscio, M.A., Dutta, M., Ramadurai, D., Shi, P., Li, Y., Vasudev, M., Alexson, D., Kohanpour, B., Sethuraman, A., Saini, V., Raichura, A., Yang, J.: Optical and electrical properties of colloidal quantum dots in electrolytic environments: using biomolecular links in chemically-directed assembly of quantum dot networks. J. Comput. Electron. **4**, 21–25 (2005)
27. Yu, W.W., Qu, L., Guo, W., Peng, X.: Experimental determination of the extinction coefficient of CdTe, CdSe, and CdS nanocrystals. Chem. Mater. **15**, 2854–2860 (2003)
28. Albanesi, E.A., Peltzer y Blanca, E.L., Petukhov, A.G.: Calculated optical spectra of IV–VI semiconductors PbS, PbSe and PbTe. Comput. Mater. Sci. **32**, 85–95 (2005)
29. Tsuchiya, T., Ozaki, S., Adachi, S.: Modelling the optical constants of cubic ZnS in the 0–20 eV spectral region. J. Phys.: Condens. Matter **15**, 3717–3730 (2003)
30. Al Kuhaimi, S.A.: Conduction and valence band offsets of CdS/CdTe solar cells. Energy **25**, 731–739 (2000)
31. Lazarenkova, O.L., Balandin, A.A.: Miniband formation in a quantum dot crystal. J. Appl. Phys. **89**, 5509–5515 (2001)
32. Balandin, A.A., Lazarenkova, O.L.: Mechanism for thermoelectric figure-of-merit enhancement in regimented quantum dot superlattices. Appl. Phys. Lett. **82**, 415–417 (2003)

33. Lyang-Geller, Y.B., Leburton, J.P.: Resonant tunnelling through arrays of nanostructures. Semicond. Sci. Technol. **13**, 35–42 (1998)
34. Dmitriev, I.A., Suris, R.A.: Electron localization and bloch oscillations in quantum-dot superlattices under a constant electric field. Low-Dimensional Systems **35**, 219–226 (2001)
35. Yamanaka, T., Sun, K., Li, Y., Dutta, M., Stroscio, M.A.: Spontaneous polarizations, electrical properties, and phononic properties of GaN nanostructures and systems. In: Morkoc, H., Litton, C.W. (eds.) GaN Materials and Devices II, SPIE 6473, 64730F-1-14 (2007)
36. Vasudev, M., Yamanaka, T., Sun, K., Li, Y., Yang, J., Ramadurai, D., Stroscio, M.A., Dutta, M.: Colloidal quantum dots as optoelectronic elements. In Razeghi, M., Brown, G.J. (eds.) Quantum Sensing and Nanophotonic Devices IV, SPIE 6479, 64790I-1-12 (2007)
37. Biswas, S., Dutta, M., Stroscio, M.A.: Negative differential resistance in conductive polymer and semiconducting quantum dot nanocomposite systems. Appl. Phys. Lett. **95**, 1821011–3 (2009)
38. Coe-Sullivan, S., Steckel, J.S., Woo, W.R., Bawendi, M.G., Bulović, V.: Large-area ordered quantum-dot monolayers via phase separation during spin-casting. Adv. Funct. Mater. **15**, 1117–1124 (2005)
39. Coe-Sullivan, S., Woo, W.K., Steckel, J.S., Bawendi, M.G., Bulović, V.: Tuning the performance of hybrid organic/inorganic quantum dot light-emitting devices. Org. Electron. **4**, 123–130 (2003)
40. Coe, S., Woo, W.K., Bawendi, M., Bulović, V.: Electroluminescence from single monolayers of nanocrystals in molecular organic devices. Nature **420**, 800–803 (2002). (Letter to Nature)
41. Lee, J., Sundar, V.C., Heine, J.R., Bawendi, M.G., Jensen, K.F.: Full color emission from II-VI semiconductor quantum dot-polymer composites. Adv. Mater. **12**, 1102–1105 (2000)
42. Anikeeva, P.O., Madigan, C.F., Coe-Sullivan, S.A., Steckel, J.S., Bawendi, M.G., Bulović, V.: Photoluminescence of CdSe/ZnS Core/Shell quantum dots enhanced by energy transfer from a phosphorescent donor. Chem. Phys. Lett. **424**, 120–125 (2006)
43. Lin, Y., Zhang, J., Sargent, E.H., Kumacheva, E.: Photonic pseudo-gap-based modification of photoluminescence from CdS nanocrystal satellites around polymer microspheres in a photonic crystal. Appl. Phys. Lett. **81**, 3134–3136 (2002)
44. Yang, J., Yamanaka, T., Sun, K., Stroscio, M.A., Dutta, M., Zhong, J., Chen, H., Saraf, G., Lu, Y.: Optoelectronic properties for ZnO and related semiconductors in various nanoscale geometries. ECS Trans. **6**, 149–160 (2007)
45. Oertel, D.C., Bawendi, M.G., Arango, A.C., Bulović, V.: Photodetectors based on treated CdSe quantum-dot films. Appl. Phys. Lett. **87**, 213505-1-3 (2005)
46. Kang, K.S., Ju, H.L., Han, W.H., Lee, J.H., Choi, J.G., Boo, D.W.: Photoluminescence characteristics of coupled CdSe/ZnS quantum dots on self-assembled silica nanospheres. Appl. Phys. Lett. **87**, 141909–141911 (2005)
47. Konstantatos, G., Howard, I., Fischer, A., Hoogland, S., Clifford, J., Klem, E., Levina, L., Sargent, E.H.: Utrasensitive solution-cast quantum dot photodetectors. Nature **442**, 180–183 (2006). (Letter to Editor)
48. McDonald, S., Konstantatos, G., Zhang, S., Cyr, P.W., Klem, E.J.D., Levina, L., Sargent, E.H.: Solution-processed PbS quantum dot infrared photodetectors and photovoltaics. Nature Mat. **4**, 138–142 (2005). (Letter to Editor)
49. Boberl, M., Kovalenko, M.V., Pillwein, G., Brunthaler, G., Heiss, W.: Quantum dot nanocolumn photodetectors for light detection in the infrared. Appl. Phys. Lett. **92**, 261113-1-3 (2008)
50. Liao, S., Sun, K., Dutta, M., Stroscio, M.A.: Three-color photodetector based on quantum dots and resonant-tunneling diodes coupled with conductive polymers. Solid-State Electron. **54**, 1066–1070 (2010)
51. Nozik, A.J.: Quantum dot solar cells. Physica E **14**, 115–120 (2002)
52. Boudreaux, D.S., Williams, F., Nozik, A.J.: Hot carrier injection at semiconductor-electrolyte junctions. J. Appl. Phys. **51**, 2158–2163 (1980)

53. Benistry, H.: Reduced electron-phonon relaxation rates in quantum box systems: theoretical analysis. Phys. Rev. B **51**, 13281–13293 (1995)
54. Stroscio, M.A., Dutta, M.: Phonons in nanostructures. Cambridge University Press, Cambridge (2001)
55. Hagen, J., Schaffrath, W., Otschik, P., Fink, R., Bacher, A., Schmidt, H., Haarer, D.: Novel hybrid solar cells consisting of inorganic nanoparticles and an organic hole transport material. Synth. Met. **89**, 215–220 (1997)
56. Arango, A.C., Carter, S.A., Brock, P.J.: Charge transfer in photovoltaics consisting of interpenetrating networks of conjugated polymer and TiO_2 nanoparticles. Appl. Phys. Lett. **74**, 1698–1700 (1999)
57. Grätzel, M.: Photoelectrochemical cells. Nature **414**, 338–344 (2001)
58. O'Regan, B., Gratzel, M.: A low-cost, high-efficiency solar cell based on dye-sensitized colloidal TiO_2 films. Nature **353**, 737–740 (1991)
59. Kroeze, E., Hirata, N., Schmidt-Mende, L., Orizu, C., Ogier, S.D., Carr, K., Gratzel, M., Durrant, J.R.: Parameters influencing charge separation in solid-state dye-sensitized solar cells using novel hole conductors. Adv. Funct. Mater. **16**, 1832–1838 (2006)
60. Suraprapapich, S., Thainoi, S., Kanjanachuchai, S., Panyakeow, S.: Quantum dot integration in heterostructure solar cells. Sol. Energy Mater. Sol. Cells **90**, 2968–2974 (2006)
61. Ruangdet, S., Thainoi, S., Kanajnachuchai, S., Panyakeow, S.: Improvement of PV performance by using multi-stacked high density InAs quantum dot molecules. In: IEEE Proceedings of the 4th World Conference on Photovoltaic Energy Conversion, pp. 225–228. Waikoloa 1-4244-0016-3 (2006)
62. Marti, A., Cuadra, L., Luque, A.: Partial filling of a quantum dot intermediate band for solar cells. IEE Trans. Electron Devices **48**, 2394–2399 (2001)
63. Luque, A., Marti, A.: Increasing the efficiency of ideal solar cells by photon induced transitions at intermediate levels. Phys. Rev. Lett. **78**, 5014–5017 (1997)
64. Luque, A., Marti, A.: Recent progress in intermediate band solar cells. In: IEEE Proceedings of the 4th World Conference on Photovoltaic Energy Conversion, pp. 49–52. Waikoloa 1-4244-0016-3 (2006)
65. Werner, J.H., Kodolinski, S., Queisser, H.J.: Novel optimization principles and efficiency limits for semiconductor solar cells. Phys. Rev. Lett. **72**, 3851–3854 (1994)
66. Rao, A., Wilson, M.W.B., Hodgkiss, J.M., Albert-Seifried, S., Bassler, H., Friend, R.H.: Exciton fission and charge generation via triplet excitons in pentacene/C60 bilayers. J. Am. Chem. Soc. **132**, 12698–12703 (2010)
67. Wu, T.C., Biswas, S., Dutta, M., Stroscio, M.A.: Quantum dot based aptamer beacon for detection of potassium ions. IEEE Trans. Nanotechnol. **10**(5), 991–995 (2011)
68. Brenneman, K.L., Sen, B., Stroscio, M.A., Dutta, M.: Aptamer-based optical bionano sensor for mercury(II) ions. In: IEEE Nanotechnology Materials and Devices Conference Proceedings, Monterey CA, 12–15 Oct 2010
69. Ono, A., Togashi, H.: Highly selective oligonucleotide-based Sensor for mercury(II) in aqueous solutions. Angew. Chem. Int. Ed. **43**, 4300–4302 (2004)
70. Yun, C.S., Javier, A., Jennings, T., Fisher, M., Hira, S., Peterson, S., Hopkins, B., Reich, N.O., Strouse, G.F.: Nanometal surface energy transfer in optical rulers, breaking the FRET barrier. J. Am. Chem. Soc. **127**, 3115–3119 (2005)

Index

C
Catastrophic optical damage, 93, 110
CdSe, 317, 323–325, 327, 356
Chaos, 5, 20, 74
Class A versus Class B, 2, 10
Colloidal nanocrystals, 353–357

D
Delta doping, 252
Detectivity, 300, 304, 311, 357

E
Electrical injection, 134
Electron kinetics, 297, 303, 304
Excitability, 1, 4, 21

F
Fiber-optic communications, 167

G
Group III interstitials, 116

H
Holey, 160

I
InGaAs, 24, 37, 44, 51, 58, 94, 112, 139, 146, 159, 160
Intermixing, 100, 102, 105, 109–121, 126

L
Laser, 1, 3, 9–11, 14, 24, 26, 35, 41, 52, 69, 101, 143, 148, 253
Laser annealing, 93, 101, 126
Laser diodes, 95, 112, 198
Light extraction, 160, 168
Light-emitting diode, 144, 159, 351

M
Mach-Zehnder interferometer, 216
Mass sensor, 134
Modulation doping, 117
Multistability, 1
Multi-wavelength emission, 49, 50

N
Nanomechanical resonator, 173, 175, 184, 188
Non-absorbing mirror, 93, 99, 101, 102, 104

Z. M. Wang (ed.), *Quantum Dot Devices*, Lecture Notes in Nanoscale Science and Technology 13, DOI: 10.1007/978-1-4614-3570-9,
© Springer Science+Business Media New York 2012

O
Optical nonlinearity, 197, 200, 201, 213
Optical resonator, 131
Optical switch, 200, 203, 206, 209
Optically injected QD lasers, 2, 8
Optoelectronic devices, 224, 352

P
Passive mode locking, 28, 49, 50, 52, 54, 58
Phase shift, 31, 215, 217, 268, 270, 291
Photonic crystal, 134, 159, 160, 173, 175, 181, 192
Photonic crystal cavity, 131
Photonic integrated circuits, 110
Photonic-crystal, 159, 160
Photoresponse, 297, 298, 308, 311, 312
Post-growth intermixing, 109, 119, 122, 127
Potential barriers, 297, 298, 300, 306, 312, 314
Power efficiency, 199–201
Pulse width narrowing, 49, 50, 56, 62

Q
Quantum dot, 1, 4, 10, 23, 65, 159, 175, 242
Quantum dots with built-in charge, 297
Quantum memory, 173, 182, 189, 191
Quantum well;, 2, 24, 94, 109, 144, 198, 240, 306
Quantum-dot, 159, 160, 356
Quantum-dot photodetectors, 366
Quantum-dot solar cells, 193
Quantum optical transistor, 173–176, 180, 191

R
Ridge waveguide laser, 104

S
Self assembly, 354
Semiconductor quantum dots, 197, 223, 252, 318
Sensitized solar cells, 317, 318, 344, 353, 359
Submonolayer, 159, 242, 259
Surface Plasmon, 175

T
Thermal runaway, 94, 96–98, 105
TiO_2 inverse opal, 321, 323, 340, 344
TiO_2 nanoparticles, 330, 340, 359
TiO_2 nanotubes, 321, 336, 337, 339
Tunable dual state mode locking, 49, 50

U
Ultrafast photonics, 198

V
Vertical cavity, 2, 134, 160, 197, 201, 205, 206, 209, 214, 215, 218, 273